CEOS CALIBRATION/VALIDATION WORKING GROUP
SAR CALIBRATION SUB-GROUP

SAR Calibration Workshop Proceedings

20 - 24 September 1993
ESTEC, NOORDWIJK, THE NETHERLANDS

Workshop Organiser
Yves-Louis Desnos
ESA/ESTEC/XRI
P.O.Box 299
2200 AG Noordwijk
The Netherlands

Editor
Evert Attema
ESA/ESTEC/JWS
P.O.Box 299
2200 AG Noordwijk
The Netherlands

Chairman
CEOS Sub-group on SAR Calibration
A. Freeman
M/S 300-235
Jet Propulsion Laboratory
Pasadena, CA 91109
United States

Cover

Signature of ESTEC High Precision Calibration Transponder from an ERS-1 Single Look Complex SAR Image (by J-L. Valero, ESA/ESTEC/XRI)

Disclaimer

This document is published in the ESA WPP (Workshop Preliminary Proceedings) series. This is an informal series and the documents do not necessarily carry the full authority of the formal ESA publications series. Such documents are intended for issue to workshop participants and as working documents. Some papers in the ESA WPP series may be selected for editing and inclusion in a formal ESA publication at a later date.

There is no formal distribution of ESA WPP publications; distribution is arranged by the workshop organisers.

Table of Contents

INTRODUCTION

The sixth general meeting of the Committee on Earth Observation Satellites (CEOS) Subgroup on SAR Calibration was held at the ESA/ESTEC Conference Centre in Noordwijk, The Netherlands during the week of September 20 to 24 1993. The meeting was co-hosted by the ESA Technical Directorate and the ESA Directorate of Observation of the Earth and its Environment.

The workshop, attended by approximately 120 participants from ESA member states, Canada, USA, Japan, Russia, consisted of 9 serial plenary sessions in which three selected formal presentations where made to all participants followed by two times 4 parallel working group meetings starting with shorter formal presentations. This structure facilitated everyone to get an overview and identify the issues which needed further discussion.

The smaller more specialized working groups for which "Seed questions" were prepared in advance, could carry the discussion further and draw conclusions, an action plan and recommendations. Each working group was asked to present to the plenary a summary of its findings on the last day of the workshop.

This volume brings together the results presented at the workshop through the full length papers, the seed questions prepared for the working groups, the summary reports of the 8 working groups and finally the recommendations brought up to the CEOS Calibration/Validation Working Group.

As a result of this fruitful and productive meeting significant progress has been made in our understanding of Synthetic Aperture Radar Calibration/Validation issues for the benefit of the worldwide community.

CEOS CAL/VAL WORKING GROUP

SAR CALIBRATION SUB GROUP

A Word from the Chairman:

The latest in the series of workshops held by the SAR Calibration Subgroup was, for me, enormously successful. This was mainly due to the efforts of the organizers at ESTEC, particularly Yves-Louis Desnos, to whom we should offer our special thanks.

The SAR Calibration Workshops have evolved into a forum for technical interchange at the highest level in the SAR System Engineering field: for setting up joint projects and experiments; for resolving key technical arguments/questions; for setting requirements for radar system calibration; and for helping define future radar instruments and their performance. There are still questions to be resolved in this area and the sub-group will continue to meet on an annual basis to address them.

I would also like to take this opportunity to thank the attendees for all their efforts in making this workshop a great success. I look forward to seeing all of you again at the next workshop.

Anthony Freeman

CALIBRATION REQUIREMENTS

Session 1

Chair: E.ATTEMA, ESA-ESTEC

APPLICATION ORIENTED REQUIREMENTS TO SAR-DATA CALIBRATION
THE SOIL MOISTURE CASE

M. Rombach, J. Kellndorfer, W. Mauser

Institute of Geography, University of Munich
Luisenstraße 37, D-80333 München
phone: +49-89-5203-335
fax: +49-89-5203-321

ABSTRACT

From August to December 1991 28 SLC-images of the Freiburg test-site (upper Rhine valley, Germany) have been collected during the Commissioning Phase of ERS-1. At the same time an extensive ground truth campaign on this test site took place (continuously recorded soil-moisture, LAI (weekly), plant height (weekly), wet and dry biomass (weekly), vegetation cover (weekly) a. o.).

This made it possible, to carry out investigations on the determination of soil-moisture with SAR-DATA. Correlations were calculated between soil-moisture and the average backscatter from the five test fields (three corn and two harvested barley fields) under investigation (correlation-coefficient >0,8). Furthermore the results of these analyses provide a good feed back for the necessary accuracy of different calibration parameters.

1. Introduction

The 1991 campaign (sponsored by DARA) took place to validate and calibrate ERS-1 data and to apply this data for different geoscientific issues. In this context soil-moisture estimates are of great importance for the hydrological cycle within soil-plant-atmosphere models. To understand more frequent changes in this continuum, soil-moisture detection is one of the keys for explanations. Models are working on micro-scale level with ground truth but our aim is the meso-scale where no ground truth is available. Therefore remotely sensed soil-moisture values are necessary.

2. Ground Truth Measurements

The Freiburg test site has an extension of $6 \cdot 8$ km^2 and is almost flat. The climate in the Upper Rhine Valley is characterized by high temperatures and low precipitation. The soil consist of loamy to gravelly sand with a low clay content. This indicates that at least corn as the main agricultural crop must be irrigated, which in fact is done. Corn covered almost 30% of the whole test area in 1991.

Field measurements were carried out on 7 test fields (3 corn fields, 3 cereals and one fallow land) spread over the whole test site (soil moisture was only monitored on 3 corn and 2 harvested barley fields). Field sizes varied between one and three hectares. A digital soil type and actual land use map of the area supports the ground truth data of the selected single fields.

Measurements of plant parameters were carried out from May to October. Leaf area index (Fig. 1), wet and dry weight of the plant leaves, stem and fruit, wet and dry biomass, plant height and (Fig. 2) vegetation cover were sampled every week during the growing season on all test fields.

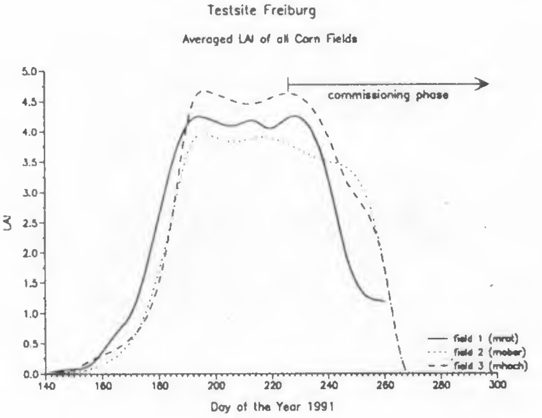

Fig. 1: Course of the green leaf area index for three corn fields (May 20 - Oct. 27, 1991)

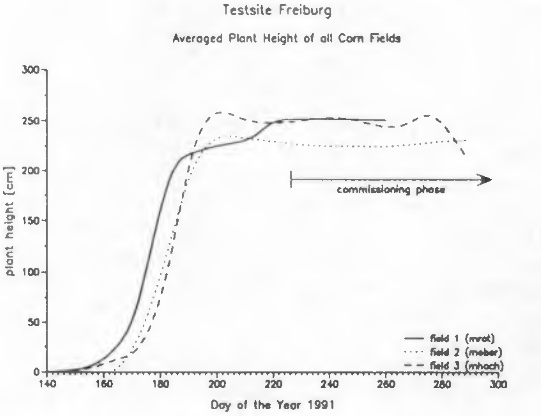

Fig. 2: Course of the plant height for corn fields (May 20 - Oct. 27, 1991)

Surface soil moisture (0-5 cm) was recorded continuously on an hourly basis at 4 different depth on 5 test fields from the beginning of August to the end of October (Fig. 3). These measurements are difficult by nature. The accuracy of these measurements is limited by the knowledge of the relation between soil suction and soil moisture for the given soil and the variable soil moisture gradients within the top soil layer. It is estimated to be within a 5% range. The methods used were tensiometric (soil suction), gypsum blocks (electrical conductivity) and gravimetric (only once a week).

In addition several meteorological and pedological parameters were acquired during this campaign.

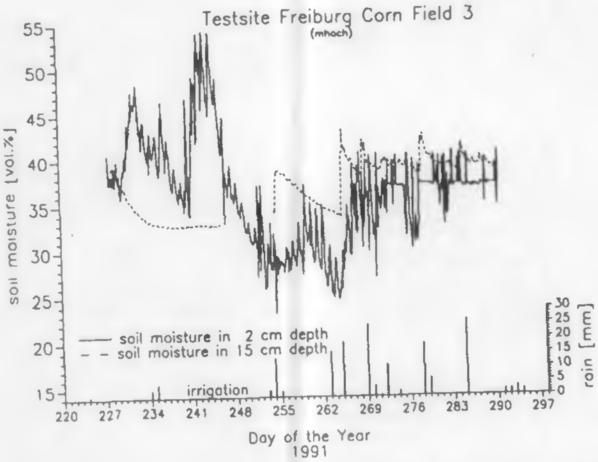

Fig. 3: Course of soil moisture for corn field 3 in 2 and 15 cm depth (Aug. 8 - Oct. 25, 1991)

3. ERS-1 SAR-DATA Calibration

Although a first attempt to derive soil moisture information from SLC-derived power values showed promising results (Demircan, 1992) it is expected, that the correlation between AMI-backscatter and soil moisture can be somewhat improved by calibrating the SLC-Data.

The SAR-data research started with several attempts to convert ERS-1 SLC-data into backscattering coefficient $\beta°$ [dB] ($\beta° \cdot \sin\theta = \sigma°$; $\sin\theta$: local incidence angle; $\sigma°$[dB]: final calibrated backscattering coefficient including terrain corrections).

Programms for calibrating the complex pixel values into backscattering coefficient $\beta°$ in dB were developed, including correction of the antenna pattern, determination of the incidence and look angle at each pixel, compensation of range spreading loss and correction of the PAF dependent calibration constant, using header information and the GEM6 ELLIPSOID. (Kellndorfer, 1993)

The calibration of the SLC-data was carried out on the original 16 bit values after conversion of the inphase/quatrature component data into power values. The calibration program was developed at the Institute of Geography of the University of Munich. All calibrations were done in slant range, which ensures the highest possible information in each pixel. For the calibration the following algorithm (Laur, H. 1992) was applied to the power values:

$$\beta° = \frac{\langle I \rangle}{K} * \frac{\sin\alpha}{\sin\alpha_{ref}} * \frac{R^3}{R_{ref}} * \frac{1}{g^2(\theta)} \qquad (Eq.1)$$

and

$$\beta°_{(dB)} = 10 * \log_{10} \beta° \qquad (Eq.2)$$

$\langle I \rangle$	:	intensity at any pixel (power)
K	:	PAF related calibration constat
$\sin\alpha$	:	incidence angle at any pixel
$\sin\alpha_{ref}$	:	reference incidence angle
R^3	:	slant range distance at each pixel
R^3_{ref}	:	reference slant range distance
$g^2(\theta)$	:	in-flight ERS-1 antenna pattern

The actual altitude and local look angle for each pixel were introduced in the calibration procedure. The in-flight antenna pattern is provided by ESA. (Laur, 1992; Zink, 1992)

Since the K-value of equation 1 was subject to some discussion and has now obviously stabilized to K = 65026 (except D-PAF, which used K = 186618 before 15.11.92), these values were used for the final calibration.

Values like zero-Doppler range time at the first pixel, the incidence angle at the first pixel, geodetic latitude and others, were taken from header information. The precision of these header values is somewhat unstable, because of the changes in the number of digits of some values from orbit to orbit. The zero-Doppler range time in fact, varies only because the number of digits has been raised to seven in the header annotations at the beginning of 1993.

Calibrated intensity images of 28 overflights were then produced. The locations of the test fields were determined and the average test field intensity calculated. As the test fields were almost flat, a calculation of the local incidence angle was not necessary. Figure 4 shows the influence of the calibration on test field 3. The slope direction of the two curves is only changed twice (between day 241, 247 and 253, 259). The slope of the curves itself differs in almost any case.

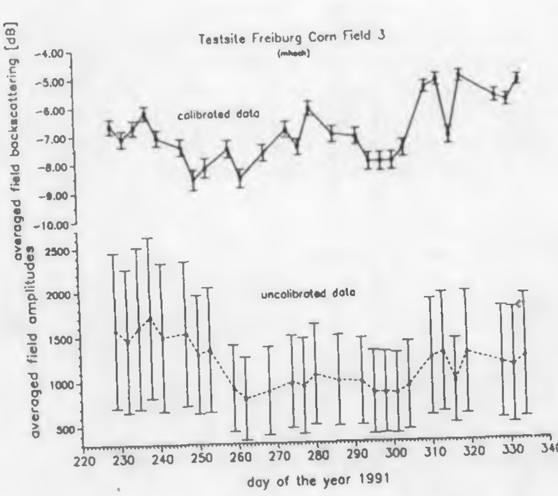

Fig. 4: Influence of calibration at one test field (Aug. 8 - Dez. 6, 1991)

4. Results

After calibration and removal of obvious artefacts in the soil moisture data the backscatter and soil moisture curves were compared. Figure 5 shows the course of soil moisture and backscattering coefficient averaged over one corn field. The strong and direct influence of the water content of the soil on the surface-scattering behaviour of high frequency microwaves is easily visible.

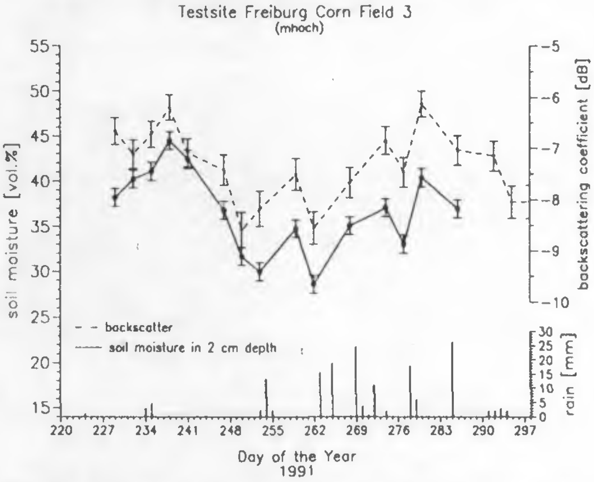

Fig. 5: Course of backscattering and soil moisture over one corn field (Aug. 8 - Oct. 25, 1991)

The change of soil surface random roughness (RMS) during this champagne on the monitored fields, was negligibly small since the corn plants were harvested after the measurements were taken. The surface roughness was considered as continuously medium during soil moisture measurements with a tendency to smooth, which implies that backscatter is independent from surface roughness (Ulaby, 1982, Vol.II, Chap. 11). Therefore no corrections on the soil moisture backscatter regression line was applied. Plant row direction (eq. soil row direction) of the corn fields with continuous soil moisture measurements is constant.

Looking at Fig. 1 and 2, one can see that the leaf area index of the corn fields were on its maximum already at the start of the commissioning phase. The green leaf area index decreased to 0 during the first phase, which is due to the maturity of the plants. Nevertheless the plant height did not change at all after launch of ERS-1 until the end of moisture measurements.

The barley fields were all harvested already at the beginning of the measurements and were ploughed after the end of the measurements. The harvested barley fields were covered with some irregularly spread weeds together with dried up and half-cut barley stems. Surface roughness was as stable as at the corn fields. The backscatter behaviour was therefore similar, only depending on different soil moisture content due to different precipitation and transpiration. All this guarantied a stable surface geometry over the whole measurement period.

Combining the measurements of soil moisture and backscattering coefficient θ°, the regression line in Fig. 6 was retrieved. As it is necessary to estimate soil moisture values with an accuracy of at least ±5,0 Vol. % to be meaningful for input and calibration of hydrological models, the accuracy of the total calibration of the backscattering coefficient θ° have to be better than 0,72 dB (if the testsite is flat !). Including additional errorsthat add to the precision of SAR-DATA calibration, (field boundaries, errors in soil moisture measurements a.o.) the requirement for the total SAR-data calibration increases to a recommended accuracy of better than 0.5 dB.

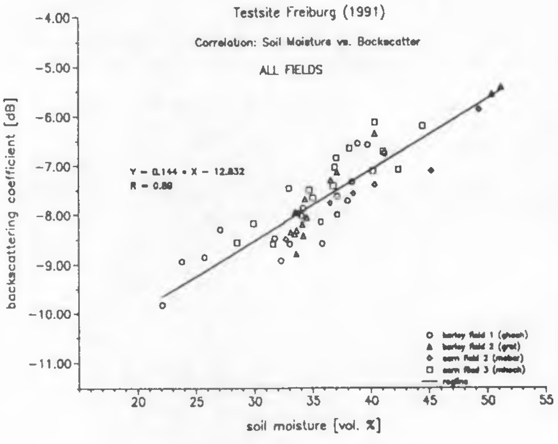

Fig. 6: Correlation of all field (soil moisture vs. backscattering).

As a result it can be stated that the ERS-1 microwave configuration is well suited for soil moisture measurements in the top soil layer. Taking into account the inaccuracies in the determination of the surface soil moisture it can be stated that the accuracy of the ERS-1 data for the determination of soil moisture is at least 5% in our case. This cam be considered to be sufficient for numerous practical applications in hydrology and agriculture. The spatial resolution of nominally <10 x <10m and pixel spacing of about 3.9 x 7.9m respectively in azimuth and slant range (ERS-1 SLC-data) is sufficient for the fields, which were considered.

5. Outlook

As consequence of these results, the accuracy of the determination of surface soil moisture has to be improved to be able to reach the limits of microwave sensing systems. This will be one of the aims of ongoing ground truth campaigns in testsites now situated near Munich using ERS-1, ERS-2, JERS-1 and the airborne DLR E-SAR system.

For future studies it is necessary to conduct interferometric analyses. This is necessary to derive DEMs from SAR-data which allow the calibration of SLC-images also on sloping testsites. This, together with multitemporal and multifrequency SAR-data may enable the production of reliable soil moisture maps over larger areas. To reach this goal a commissioning phase of ERS-2 with a similar temporal resolution to the one of ERS-1 is necessary.

6. Acknowledgement

This study has been sponsored by the Deutsche Agentur für Raumfahrtangelegenheiten (DARA) within the framework of its Calibration and Land Application (CALA) activities.

The ERS-1 data have been supplied by ESA through its ERS-1-PI program.

Thanks to Mr. A. Demircan for supplying the plant parameter data.

7. References

Beaudoin, A.; Le Toan; Gwyn, Q. (1990): SAR Observations and Modelling of the C-Band Backscatter Variability Due to Multiscale Geometry and Soil Moisture, *IEEE Trans. Geosci. Remote Sens.* Vol. 28 No.5 886-894.

Borgeaud, M.; Noll, J. (1992): Comparisons of Theoretical Surface Scattering Models for Polarimetric Microwave Remote Sensing, *IGRASS'92*, Vol. I, 180-182, Houston.

Brisco, B.; et al. (1990): The Diurnal Pattern of Microwave Backscattering by Wheat, *Remote Sens. Environ.* 34:37-47.

Buckler, L.; et al. (1988): Near Surface Soil Moisture Estimation From Microwave Measurements, *Remote Sens. Environ.* 26:101-121, New York.

Cihlar, J.; et al. (1992): Change Detection with Synthetic Aperature Radar, *Int. J. Remote Sensing*, Vol. 13 No.3 401-414.

Demircan, A.; Rombach, M.; Mauser, W. (1992): Extraction of Plant and Soil Parameters from Multitemporal ERS-1 SLC Data of the Freiburg Testsite, *Proceedings first ERS-1 Symp.*, esa sp-359, Vol II, Noordwijk.

Kellndorfer, J. (1993): Landnutzungsklassifikation mit multitemporalen ERS-1 SAR Daten unter Anwendung von Segment-Informationen im Verfahren "Majoritätsfilter", MS-thesis, Institute for Geography, Ludwig Maximilians Universität, München.

Laur, H. (1992): Derivation of Backscattering Coefficient %° in ERS-1 SAR PRI Products, Issue 1, Rev. 0, ESA, PAFs.

Ulaby, F.T.; et al. (1981-1986): Microwave Remote Sensing, Vol I-III, London.

Ulaby, F.T. (1992): Short Course Notes, DLR, Oberpfaffenhofen.

Zink, M.; Seifert, P. (1992): Inflight Antenna Diagram Determination of Spaceborne and Airborne Sar-Systems, *IGRASS92*, Vol. I, 117-119, Houston.

SAR CALIBRATION REQUIREMENTS FOR CROP AND SOIL STUDIES

M.G.Wooding, A.D.Zmuda & G.H. Griffiths
Remote Sensing Applications Consultants,
Merlin Court, 82 Alexandra Rd., Farnborough, Hampshire. GU14 6DD, UK.

ABSTRACT

Multi-temporal ERS-1 backscatter measurements for a variety of crop types are being analysed as part of the UK Calibration and Crop Backscatter Experiment, to investigate the effects of crop growth and soil moisture on backscatter.

This paper describes the type and magnitude of different sources of error that affect the accuracy of backscatter measurements for a variety of crops and soil moisture conditions. These potential errors arise from the difficulties involved in achieving precise absolute calibration, estimating mean field backscatter and accounting for the disturbing effect of meteorological events.

Examples of each of these types of error, determined from measurements of corner reflector radar cross section and from multi-temporal ERS-1 backscatter measurements for a large number of agricultural fields, are presented. The importance of absolute calibration accuracy and the effect of speckle statistics and meterological conditions is discussed in the context of crop discrimination and soil moisture monitoring.

1. INTRODUCTION

This paper addresses aspects of backscatter measurement accuracy from the perspective of a user with interest in crop and soil studies. The results presented have been derived from research beginning in 1991, on the backscatter properties of soil and crops as part of the UK Calibration and Crop Backscatter Experiment (Bird et al., 1992, Wooding et al, 1993 (a), 1993 (b)).

2. CALIBRATION REQUIREMENTS

Accurate absolute measurements of backscatter are necessary to understand the backscatter properties of crops and soil and to develop techniques for mapping crop type and monitoring soil moisture. Without accurate measurements it is difficult to gain a precise understanding of the nature of crop and soil backscatter for a range of environmental conditions and to compare data-sets from different instruments with varying sensor characteristics.

The sources of error which affect the reliable calibration of ERS-1 SAR imagery are many and include errors associated with propogation, orbit and sensor parameters, processing and calibration device. This paper is not intended to be a detailed examination of such error, but a summary of the experience gained during the UK Calibration and Crop Backscatter Experiment in determining acceptable levels of accuracy for crop discrimination and soil moisture monitoring. Three calibration aspects covered include, the problems of absolute calibration, the statistical problems associated with estimating mean backscatter per field and the effect of meteorological variables, especially rainfall.

2.1 ABSOLUTE CALIBRATION

Results from a number of studies have demonstrated (Laur, 1992) the highly stable nature of the ERS-1 SAR. For example, the published calibration constant (K) delivered for ESA products remained the same for the period September 1991 to end August 1992. This contrasts with the problems encountered in calibrating multi-frequency multi-polarisation airborne SAR data (ESA/ESTEC, 1992).

Although the ERS-1 SAR provides radiometrically stable measurements of backscatter, errors introduced during processing may reduce the reliability of the calibration. Two examples of processing problems encountered during the experiment and which resulted in significant calibration errors, are presented.

Figure 1 shows two temporal backscatter profiles for shingle, an unvegetated surface of water worn pebbles distributed along a stretch of the south coast of England at Dungeness. The unvegetated nature of this mostly dry surface means that its backscatter properties are extremly stable in comparison to agricultural fields. The first profile in Figure 1 (a) is based on a calibration factor (K) calculated from the measurement of mainlobe power for a corner reflector deployed close to the shingle area on 19th August 1991. The profile displays an unexpected increase in backscatter of approximately 2dB between August 25 (day 237) and October 15 (day 288). This was attributed to the replica power varying independently of the transmitted power, thus spurious replica power values were used for image normalisation resulting in the observed variation in corner reflector response (Bird et al., 1992).

The second profile (b) is derived from individual measurements of corner reflector radar cross section (RCS) obtained from each of the 18 ERS-1 scenes acquired between 13 August and 29 November A different calibration factor was subsequently applied to each ERS-1 scene to compensate for the observed differences in mainlobe power caused by variations in the replica power signal. The result is a much flatter profile with a dB deviation about the mean value of ± 0.5dB, an acceptable error given the stable nature of the shingle surface.

In this example the RCS measurements of corner reflectors at each overpass date enabled the processing error to be detected and corrected. The consequences of not correcting for errors of this type are illustrated in Figure 2.The relationship betwen volumetric soil moisture (M_υ) and the backscattering coefficient (σ^0) for a single field of bare soil for which soil moisture measurements were obtained on nine dates, is shown for backscatter data calibrated using a single date calibration factor (August 13) and for data calibrated separately for each date. The slope and intercept of the linear regression line for the single date calibrated data are different to the more reliable multi-date calibrated data, indicating the magnitude of the systematic processing errors.

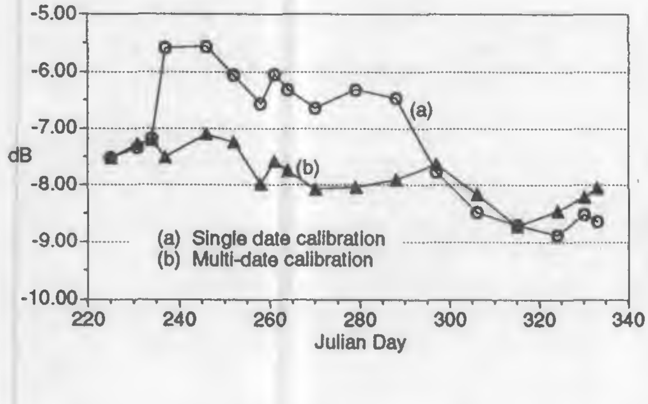

Figure 1. Comparison of backscatter for shingle surfaces based on single and multi-date calibration factors. (Romney Marsh Test Site, UK Calibration and Crop Backscatter Experiment 1992).

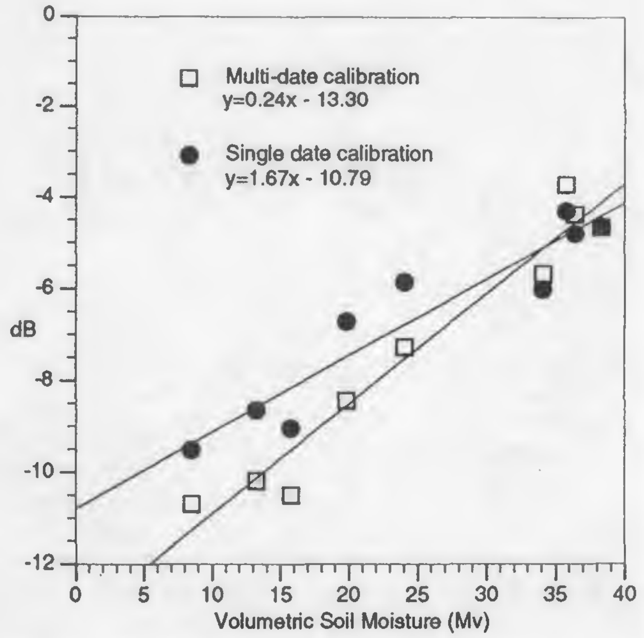

Figure 2. The relationship between volumetric soil moisture ($M\upsilon$) and σ^0 for backscatter data calibrated using a single date calibration factor and multi-date factors. (Romney Marsh Test Site, UK Calibration and Crop Backscatter Experiment, 1992).

In the second example, ERS-1 SAR PRI products processed by the UK-PAF in the period September 1992 to April 1993, were found to contain systematic errors caused by incorrect application of the elevation antenna gain pattern. The magnitude of the error varies as a function of image mode (3/ 35 day repeat), latitude of acquisition and swath position (Figure 3). The error, which resulted in a maximum miscalibration of -1.55dB for sites monitored during the 1993 UK Calibration and Crop Backscatter Experiment was detected from RCS measurements of corner reflectors deployed at the test site in E. Anglia.

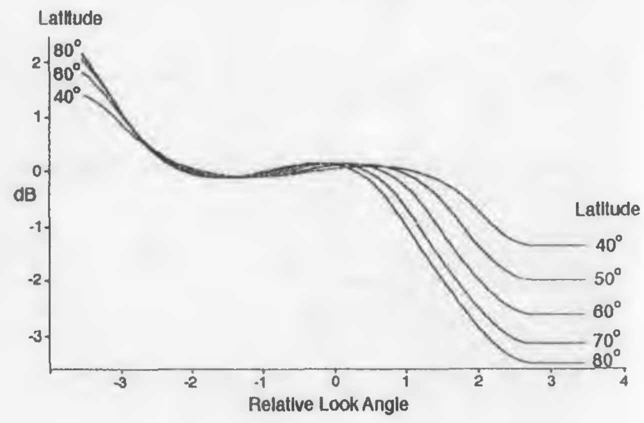

Figure 3. Intensity correction for a selection of latitudes during the 35 day repeat cycle (Source: UK PAF ERS-1 SAR Health Report, 1993).

2.2 ACCURACY OF FIELD BACKSCATTER MEASUREMENTS

Speckle within a SAR image affects the reliability with which the mean intensity value for an extended target, such as a field of crops, can be estimated.

An empirical approach was used in this study, based on measurements of backscatter for random pixels to determine the minimum number of samples that are required to give a reliable estimate of mean backscatter per field. A large sample (n >200) of pixels within a field was taken and randomised. The mean, standard deviation (S.D.) and standard error (S.E.) was calculated for sample sizes from 1-n and plotted for fields containing different crop types. The results for three potato fields are shown in Figure 4 and demonstrate that a minimum of 60 pixels are required to give an estimate of the mean which is within ±0.4dB of the true mean. Although the mean backscatter profiles for these three fields is very different, their speckle properties are similar and the same number of samples is required in each case to obtain an accurate mean value.

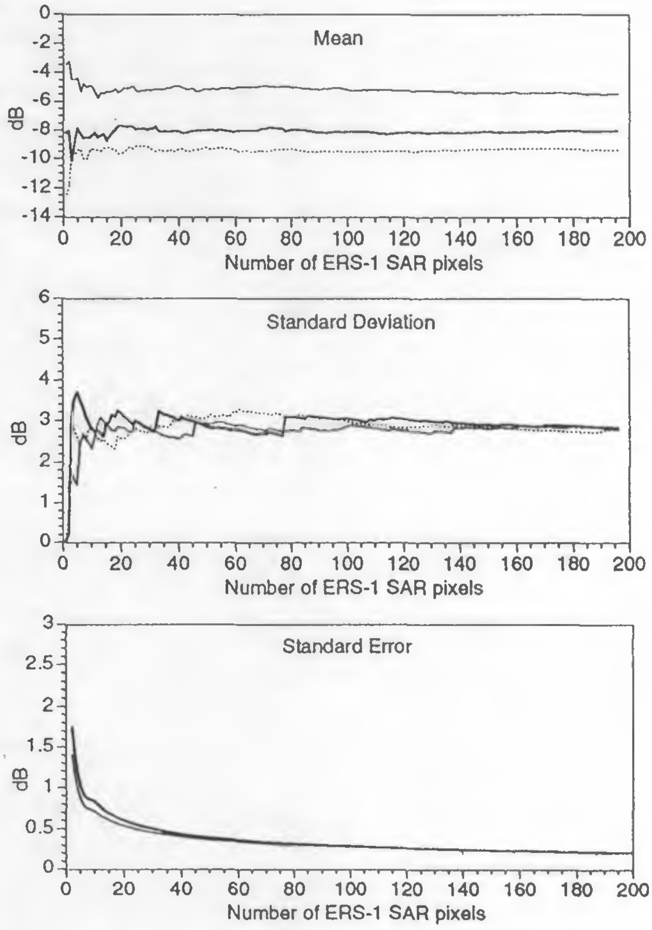

Figure 4. Effects of Increasing Sample Size on Measurement Accuracy for Potato Fields. (Terrington, Norfolk, UK Calibration and Crop Backscatter Experiment, 1993).

For practical purposes most fields are sufficiently large (> 1ha) such that simple averaging of backscatter within a field for the 3-look PRI SAR data, provides a useable estimate of the backscatter.

2.3 METEOROLOGICAL EFFECTS

A form of non-systematic or random noise in the data is caused by the unpredictability of meteorological events, especially rainfall. The random nature of this variable makes it difficult to establish temporal profiles for a crop which can definitively be attributed to crop phenology.

In Figure 5 the temporal backscatter profile for winter wheat at a site in the Fenland Region of Eastern England, is superimposed onto the daily rainfall records for the same region. The strong dip in the wheat profile at day 170 coincides with a prolonged dry period which began on day 158. It might be concluded that the dry conditions were inducing the decrease in backscatter but other evidence, notably from the establishment of similar winter wheat backscatter profiles for the following season (1993), indicates that this decrease in backscatter is phenological and relates to the period of maximum crop productivity (anthesis).

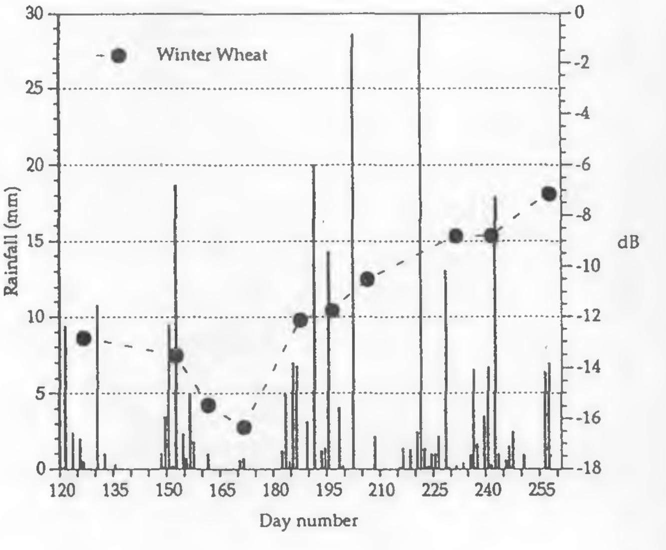

Figure 5. Variation in Rainfall and Winter Wheat Backscatter. (Terrington, Norfolk, UK Calibration and Crop Backscatter Experiment, 1993).

The effect of rainfall may make it difficult to compare measurements both on short term time-scales, e.g. within and between seasons. This may adversely affect the statistical separation between the mean backscatter for different crops and reduce the potential for accurate discrimination. However, with sufficient number of measurements over long time periods it may be possible to isolate statistically meteorological effects on backscatter trends displayed by the crop profiles.

3. DISCUSSION

Further work is required to quantify the magnitude of the errors introduced by calibration problems, speckle statistics and meteorological effects and to consider their impact on crop discrimination and the measurement of soil moisture.

Methodological problems involved in separting the predictable effects of crop growth on backscatter from short-term and unpredictable meteorological effects, can be addressed by establishing temporal profiles for a variety of crops across seasons for a range of meteorological conditions. Figure 6 compares the winter wheat temporal profile for 1992 (see Figure 5) with the 1993 temporal profile of this crop. The similarity in the shape of the two profiles at the beginning of the growing season reinforces the conclusion that the observed decrease in backscatter is attributable to crop phenology and not to the prolonged period of dry weather in 1992 which coincided with maximum productivity in the crop cycle. However, the deviation of the 1992 winter wheat profile from the 1993 profile can probably be attributed to a higher rainfall on day 150, clearly seen in Figure 5.

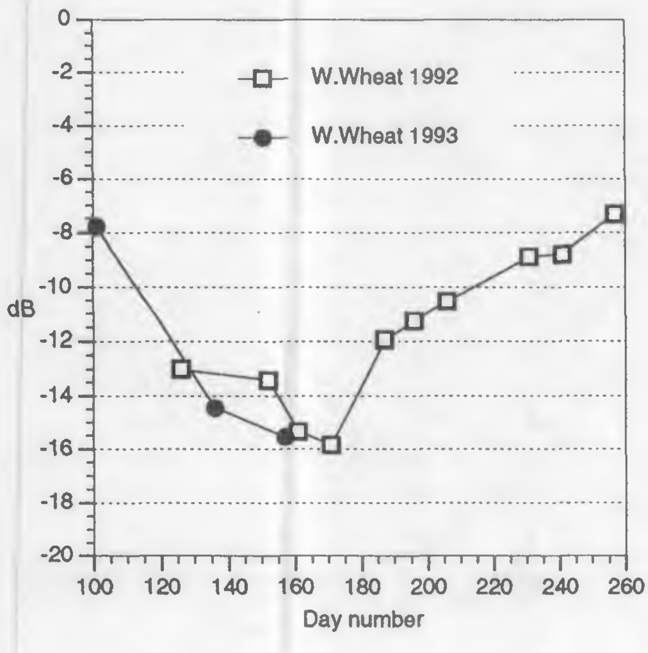

Figure 6. Comparison of winter wheat profiles for the 1992/1993 growing seasons. (Terrington, Norfolk, UK Calibration and Crop Backscatter Experiment, 1993).

Further work is also required to determine the effect of speckle, especially at field edges, on the true estimate of the mean backscatter for fields of different crop and soil conditions. A related problem is the effect of resampling the ERS-1 SAR imagery to a specific map projection, on the radiometric properties of the data.

Finally a monitoring programme based on backscatter measurements of corner reflectors, should be continued for a range of crop types and conditions to ensure that processing errors are detected and can be corrected. Further work is required to determine the effect of absolute calibration errors on crop discrimination and the accuracy of soil moisture retrieval, and to define acceptable minimum levels of accuracy

REFERENCES

P.J. Bird, G.E.Keyte & D.R.D.Kenward, 1992.An experiment for the radiometric calibration of the ERS-1 SAR.*Proceedings of the First ERS-1 Symposium, Space at the Service of our Environment*, 4-6 November 1992, Cannes, France.

ESA/ESTEC, 1992. MAESTRO-1/AGRISCATT, *Radar Techniques for Forestry and Agricultural Applications.* Final Workshop, March 1992, ESTEC, Noordwijk, The Netherlands. ESA wpp-31, May 1992.

Laur, H., ESRIN 1992. *Derivation of Backscattering Coefficient σ^0 in ERS1.SAR.PRI Products.*

M.G.Wooding, G.H.Griffiths, R. Evans, P.J. Bird, & G.E. Keyte, 1993 (a). Temporal Monitoring of Soil Moisture using ERS-1 SAR Data. *Proceedings First ERS-1 Symposium - Space at the Service of our Environment,* Cannes, France, 4-6 November 1992. ESA SP-359.

M.G. Wooding, A.D. Zmuda, G.H. Griffiths, P.J. Bird & G.E. Keyte, 1993 (b). Crop Discrimination using Multi-temporal ERS-1 SAR Data. *Proceedings Second ERS-1 Symposium - Space at the Service of our Environment,* Hamburg, Germany, 11-14 October 1993 (in press).

UK-PAF, 1993. UK-PAF ERS-1.SAR.PRI Health Report, (unpublished).

Implication of the User Requirements for the Calibration of SAR Images over Land

Maurice Borgeaud, Josef Noll, and Andrea Bellini
European Space Agency, ESTEC–XEP
P.O. Box 299, 2200 AG Noordwijk, The Netherlands

Andre Beaudoin
Ecole Nationale du Genie Rural, des Eaux et des Forêts
34033 Montpellier, France

Thuy LeToan
Centre d'Etude Spatiale des Rayonnements
31029 Toulouse, France

Abstract

In order to meet the user requirements for retrieving geo- and bio-physical parameters using SAR images, it is necessary to carefully estimate the errors arising from the quality of the SAR data, their calibration, and the accuracy of the applied retrieval algorithms. For land targets such as forests and bare soils, a retrieval accuracy of 20 to 40 tons/ha is desirable by the user community for forest biomass while, for surface soil moisture, an accuracy of 5% between a range of 10 to 40% might be accepted. This paper investigates how these users requirements can be met with the current existing retrieval algorithms and what are the implications on the calibration requirements for the SAR images. Examples of these requirements are illustrated using SAR data from ERS-1, JERS-1, and the NASA-JPL AIRSAR airborne polarimetric radar. A sensitivity analysis of the models to predict the forest biomass and the surface soil moisture is performed in order to determine the variation range of the backscattering coefficient and, consequently, the requirements of the calibration of the SAR images.

1 Introduction

This paper is divided in two parts. The first one will concentrate on the forest biomass and the implication of the accuracy of σ_0 on the retrieval of that parameter. The second part looks at the surface moisture for bare soils and used validated theoretical models to derive requirements for the backscattering coefficient.

2 Forest biomass

In recent years, there has been an increasing interest in the use of radar data for the retrieval of forest biomass. From regression analysis using airborne SAR data, it was demonstrated that the intensity in a SAR image at L-band was highly related to the above-ground biomass or related characteristics (tree age, height, diameter) of pine forests [1, 2]. Beaudoin *et al.*[3] confirmed the correlation and sensitivity of L-band HH (both transmitted and received polarizations are horizontal) to biomass. Even better correlation and sensitivity to forest biomass was obtained at the lower frequency of P-band [4, 5]. The cross-polarization factor (HV) was found to have the highest correlation to forest biomass, compared to HH or VV. Similar results were obtained

by Dobson [6] on two different pine forests: maritime pine at Les Landes forest in France and loblolly pine at Duke forest in the USA.
Therefore, it is possible to estimate forest biomass with a simple statistical law, using either spaceborne JERS-1 data at L-HH 35° or airborne P-HV 45° , which should be validated by theoretical modeling. This validation assesses the use of the statistical law valid at least for pine forests and other excurrent types of coniferous trees on flat terrain [3, 6]. However, for practical applications, the impact of these empirical relations along with backscattering coefficient σ_0 accuracy from SAR sensors must be matched to user's requirements concerning biomass retrieval. Timber volume estimates, often related to trunk biomass and total biomass, requires accuracy of the order of or better than 20 tons/ha, whereas for regional and global studies such as atmosphere/vegetation exchange, 40 tons/ha are sufficient. The goal of this section is to specify which accuracy of σ_0 is necessary to enable biomass retrieval within such limits.
In previous paper, biomass estimate was expressed as a linear function of σ_0 expressed in natural units [3]. However as accuracy is usually expressed in dB, a biomass estimate as a function of σ_0 in dB is preferred and the empirical law derived from regression analysis takes the following form:

$$\hat{B} = ae^{b\sigma_0} \tag{1}$$

where $\hat{B}$ is the total biomass estimate, a and b are empirical coefficients, and σ_0 is the backscattering coefficient expressed in [dB]. Table 1 lists the values of the coefficients a,b along with model RMS error, saturation level and dynamic range for P-HV (optimal configuration) and L-HH configurations.

	P-HV 45° (Airsar)	L-HH 35° (JERS-1)
a	8852.8	503852
b	0.27	0.85
R^2	0.94	0.79
RMS error on $\Delta\hat{B}$ (tons/ha)	14.9	21.0
Saturation level (tons/ha)	120	100
Dynamic range (dB)	15	2.5

Table 1: *Parameters extracted from AIRSAR and JERS-1 data*

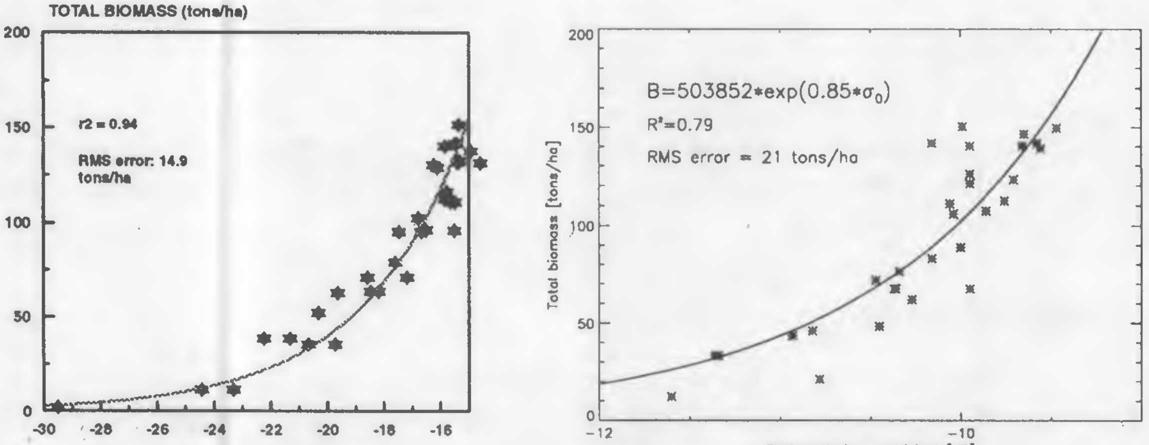

Figure 1: *Biomass retrieval using AIRSAR data at P-band (left) and JERS-1 at L-band (right)*

Fig. 1 features these empirical laws along with observations, respectively for L-HH and P-HV configuration. Correlation coefficient of 0.94 is achieved with P-HV, with an RMS error of

15 tons/ha while a lower correlation coefficient of 0.79 with an RMS error or 21 tons/ha is obtained for L-HH. At this step, it is already clear that P-HV is significantly better than L-HH for biomass retrieval. Nevertheless, L-HH should be investigated to find if it can meet partially user's requirements.
To estimate the impact of σ_0 accuracy on biomass retrieval, the following equation is used:

$$B = \hat{B} \pm \Delta B_1 \pm \Delta B_2 \tag{2}$$

where B is the total biomass, $\hat{B}$ is the biomass estimate from empirical relation, ΔB_1 is the RMS error due to the empirical relation, and ΔB_2 is the RMS error due to the variation of the backscattering coefficient $\Delta\sigma_0$ (assumed to be known or given by system specification). It must be stressed that ΔB_2 depends on the level of σ_0 as it can be derived from Eq. 1:

$$\Delta B_2 = abe^{b\sigma_0}\Delta\sigma_0 \tag{3}$$

Fig. 2 illustrates the biomass RMS error (tons/ha) as a function of σ_0 for three levels of $\Delta\sigma_0$ accuracy: 0.5, 1.0, and 1.5 dB, respectively for L-HH and P-HV configuration.

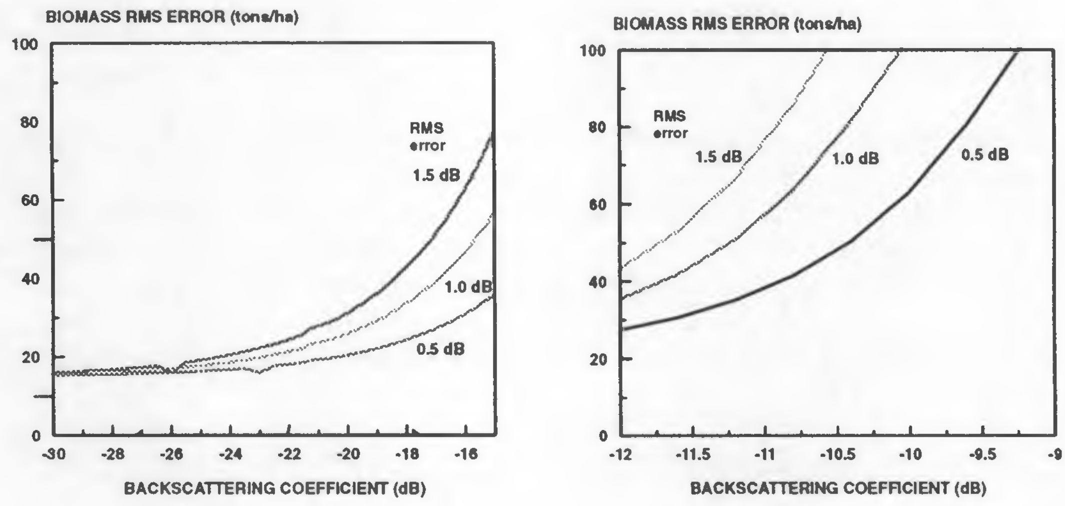

Figure 2: *Error on the retrieval of the biomass with AIRSAR data (left) and JERS-1 data (right)*

For P-HV, it is found that an accuracy of 1 dB on σ_0 is sufficient to meet biomass estimate accuracy necessary for timber inventories (<20 dB), except for high biomass values (σ_0 > -19 dB). At L-HH, due to lower saturation level and sensitivity to biomass, the biomass RMS error is higher and increases rapidly with σ_0 level. The best σ_0 accuracy of 0.5 dB that can be achieved in practice gives RMS error up to 60 tons/ha. Therefore, L-HH should be used only for regional/global studies with lower requirements on biomass accuracy, if the accuracy of 0.5 dB can be achieved.

3 Surface soil moisture

An important parameter to be retrieved from SAR data is the volumetric soil surface moisture. In this paper, only bare soils are considered and the effect of surface roughness compared to soil moisture can be identified using models to predict the backscattering coefficients σ_0 . The requirements for soil surface moisture have been identified [7, 8] and show that an accuracy of 5% between a range of 10 to 40% might be accepted by the user community. In order to see the impact of this requirement on the soil moisture, theoretical models based on Maxell's equations are applied [9, 10, 11].

Using a statistical description of a rough surface, an RMS height σ (roughness factor) and an correlation length l (lateral direction) are introduced. Furthermore, the volumetric soil moisture is converted in a corresponding permittivity value [12] required as input for the models. Depending on the values of σ and l with respect to the wavelength, different approximations are used to solve Maxwell's equation. For very rough surface, the geometric optics (GO) is used or physical optics (PO) for less rough terrains. The backscattering coefficient of smooth surfaces is derived by applying the small perturbation method (SMP). These three input parameters are used in the models to predict σ_0 and an example of model output is illustrated in Fig. 3.

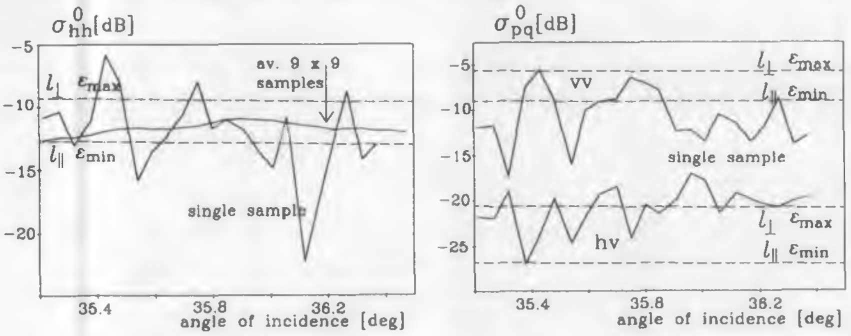

Figure 3: *Data from Maestro'89 for bare soil at L-band, field 114 with SPM model*

σ_{hh}, σ_{vv}, and σ_{hv} are shown in function of the incidence angle. The model used is SMP and two limiting curves are displayed depending on the maximum and minimum values of the permittivity ϵ and lateral correlation length measured parallel or perpendicular to the flight direction. The data comes from the NASA-JPL AIRSAR and were collected during the Maestro'89 campaign [13]. Either a single sample or an average of 9x9 pixels is shown. A good comparison can be seen between theoretical prediction and the data measured. Based upon this model and input parameters, a variation of the soil surface can be performed in function of the value of σ_0 as illustrated on the left of Fig. 4.

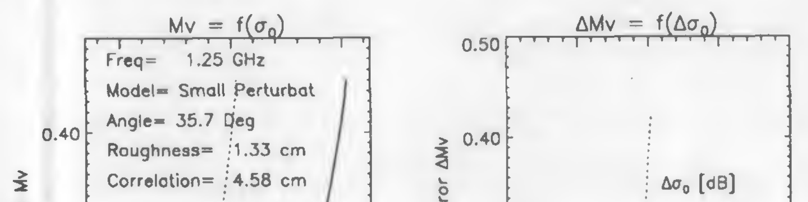

Figure 4: *Surface moisture error as a function of σ_0 for field 114, SMP model at L-band and 35° of incidence angle*

Taking the derivative of the soil moisture in function of the backscattering coefficient, a sensitivity analysis can be performed as a function of the value of σ_0 . This is shown on the right side of Fig. 4. Depending on the accuracy on σ_0 (0.5, 1 , or 2 dB), the corresponding accuracy on the surface moisture is shown. As example, an error of 0.5 dB on σ_0 will produce an error most of the time smaller than 5% for the soil moisture retrieval (except for higher values of σ_0). A similar result can be obtained using data from ERS-1 as illustrated in Fig. 5.

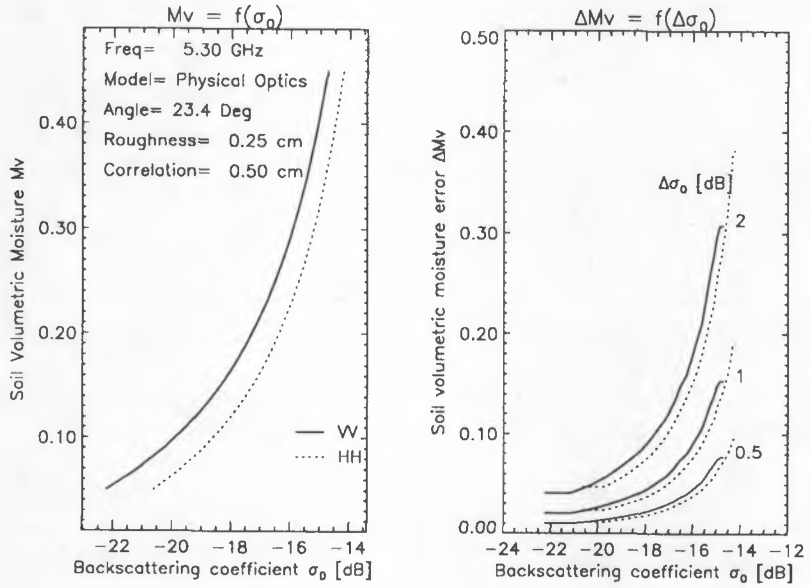

Figure 5: *Surface moisture error as a function of σ_0 for ERS-1 data taken on 1 June 1993 at C-band and 23° of incidence angle compared to PO model*

Due to the different values of ground parameters (roughness and moisture), the GO (geometric optics) model is used in Fig. 5 to describe the variation of the surface moisture in function of σ_0 . Interesting enough, though the frequency, incidence angle, and model are different, a similar value of 5% of error on the retrieval of the surface moisture for an accuracy of 0.5 dB on σ_0 can be observed.

4 Conclusions

P-HV can be used for biomass retrieval for forest with biomass level <150 tons/ha (temperate, boreal or regeneration areas) if accuracy of 1 dB is achieved, giving a minimal biomass error off the order of 20 tons/ha. On the other hand, better accuracy of the order of 0.5 dB should be realized to use L-HH data for regional/global studies, for low biomass forest, with minimal RMS error of 30 tons/ha. In this case, L-band data should be used for classification in larger biomass classes (when biomass <100 tons/ha) instead of data inversion using empirical law.
For the soil surface moisture, a requirement of 5% of the retrieval of the soil surface moisture implies an accuracy of 0.5 dB on the value of the backscattering coefficient.

References

[1] S.T. Wu, "Potential application of multipolarization SAR for pine-plantation biomass estimation", *IEEE Transactions on Geoscience and Remote Sensing*, Vol. 25, No 3, pp. 403-409, 1987

[2] Y.A. Hussin, R.M. Reich and R.M. Hoffer, "Estimating slash pine biomass using radar backscatter", *IEEE Transactions on Geoscience and Remote Sensing*, Vol. 29, No 3, pp. 427-431, 1991

[3] A. Beaudoin, T. Le Toan, S. Goze, E. Nezry, A. Lopes, E. Mougin, C.C. Hsu, H.C. Han, J.A. Kong and R.T. Shin, "Retrieval of forest biomass from SAR data", accepted for publication in *International Journal of Remote Sensing*

[4] T. Le Toan, A. Beaudoin, J. Riom and D. Guyon (1992), "Relating forest biomass to SAR data", *IEEE Transactions on Geoscience and Remote Sensing*, Vol. 30, No 2, pp. 403-411, March 1992

[5] E.S. Kasischke, L. Chavez, N.L. Christensen and M.C. Dobson (1991), "The relationship between aboveground biomass and radar backscatter as observed on airborne SAR imagery", *Proceedings of the 3rd AIRSAR Workshop*, May 23-24, Jet Propulsion Laboratory, Pasadena CA, JPL Publication 91-30, pp. 11-21

[6] M.C. Dobson, F.T. Ulaby, T. Le Toan, A. Beaudoin, E. Kasischke and N. Christensen, "Dependence of radar backscatter on coniferous forest biomass", *IEEE Transactions on Geoscience and Remote Sensing*, Vol. 30, No 2, pp. 412-415, March 1992

[7] A. Freeman, "SAR calibration: an overview", *IEEE Transactions on Geoscience and Remote Sensing*, Vol. 30, No 6, pp. 1107-1121, November 1992

[8] R.J. Brown, B. Brisco, F. Alhern, C. Bjerkelund, M. Manore, V. Singhroy, P. Vachon, "SAR calibration requirements for science applications", *CEOS Workshop on SAR calibration*, Ottawa, 21-25 September 1992

[9] F.T. Ulaby and C. Elachi, *Radar Polarimetry for Geoscience Applications,* Artech House, Norwood (MA), 1990

[10] S. Oh, K. Sarabandi, F.T. Ulaby, "An empirical model and an inversion technique for radar scattering from bare soil surfaces", *IEEE Transactions on Geoscience and Remote Sensing*, Vol. 30, No 2, pp. 370-381, March 1992

[11] M. Borgeaud and J. Noll, 1993, "Analysis of Theoretical Surface Scattering Models for Polarimetric Microwave Remote Sensing of Bare Soils", *International Journal of Remote Sensing*, May 1993

[12] M. Hallikainen, F.T. Ulaby, M.C. Dobson, M.A. El-Rayes, and L.K. Wu, "Microwave Dielectric Behavior of Wet Soil — Part I: Empirical Models and Experimental Observations", *IEEE Transactions on Geoscience and Remote Sensing*, GE–23, pp. 25–34, 1985

[13] W.J. Droesen, D.H. Hoekman, H.J.C Leeuwen, J.J. van der Sanden, S.A.M.Bouman, D. Uenk, M.A.M Vissers, and G.G. Lemoine, "MAESTRO'89 Ground Data Collection Horsterwold/Speulderbos/Flevoland (NL)", Wageningen Agricultural University, 1989

TOPOGRAPHIC EFFECTS ON RADAR CROSS SECTION

Francesco Holecz, Erich Meier, Jens Piesbergen, and Daniel Nüesch

Remote Sensing Laboratories, University of Zürich
Winterthurerstrasse 190, CH-8057 Zürich - Switzerland
Fax: +41 1 362 52 27
email: franci@rsl.geogr.unizh.ch

ABSTRACT

Synthetic Aperture Radar (SAR) data can presently be calibrated with an accuracy approaching ± 1 dB. However, relief induced geometric distortions strongly affect the backscattered signals through variations in the local resolution as well as the local incidence angle. In order to derive the radar cross section per unit area σ^0 (or normalized radar cross section) and therefore to retrieve geophysical parameters, the effect of the changing size of the resolution element on the ground must be removed by using a high resolution Digital Elevation Model (10 x 10 m). This paper demonstrates the importance of deriving an accurate estimate of σ^0, and that geometric calibration is a fundamental requirement for a correct radiometric calibration. As an example, ERS-1 magnitude data in a mountainous region have been selected for use in snowcover determination. Results show, that despite the extreme geometric and radiometric distortions some thematic information remains and can be extracted if an appropriate calibration procedure is carried out. The poor local spatial resolution in sloped areas limits the accuracy of the geophysical parameters. In rugged terrain, layover effects make it mandatory that images from at least two crossing orbits be used.

Keywords: Normalized radar cross section, geometric and radiometric calibration, value added products, optimal resolution approach, snowcover determination.

1. INTRODUCTION

A SAR system is an active microwave sensor capable of measuring the radar reflectivity of a surface. The SAR image formation process can be described as follows [1]:

$$E\{P(x,y)\} = K_s \sigma_{pq}(x,y) \otimes h(x,y) + K_n \sigma_n(x,y)$$

where $E\{P(x,y)\}$ is the expected value of square-law detected data, x and y are the spatial coordinates, h is the system impulse response function, σ_{pq} is the radar cross section for the receive (q) and transmit (p) polarizations, σ_n is the additive noise present in the backscatter measurements, K_n is the radar gain term for the noise, and K_s contains contributions from all possible sources. For the internal calibration of the instrument the two gain terms K_n and K_s should be equal unity.

The largest obstacle in developing a consistent set of SAR calibration specifications is that the calibration measures are referenced to individual elements of the system and not to the end product. When reference is made to radiometric calibration of a sensor, it typically refers to the various types of internal calibration signals to measure transmitter power or receiver gain. In other cases, it refers to external calibration (estimate of the calibration relations from measurements of external targets) or absolute calibration (a calibration wherein the physical property has been measured in units relatable to accepted physical units of mass) or relative calibration (a calibration which is not related to physical units) [2,3].

However, the concept of the radiometric calibration has a wider meaning. It implies requirements concerning the accuracy and the precision of each calibration parameter, which are hightly application-dependent. In addition to these standard requirements, further prerequisites, often neglected or only approximated, are the geometric calibration and the Digital Elevation Model (DEM) accuracy. When the exact area of the pixel projected onto the ground A and the local incidence angle θ_i at the scattering surface are known, the normalized radar cross section σ°_{pq} and γ_{pq} can be derived from σ_{pq}, namely [3]:

$$\sigma^\circ_{pq} = \frac{\sigma_{pq}}{A}$$

and: $$\gamma_{pq} = \frac{\sigma^\circ_{pq}}{\cos\theta_i}$$

Normally, a flat or curved earth is assumed when calculating the normalized radar cross section σ°_{pq}. But this is not adequate when imaging a surface even with moderate terrain height variations. In terrain with relief variations active radar signals are strongly distorted, exhibiting extreme changes in local mean intensity, while layover and radar shadow produce signals lacking interpretable geophysical information. The goal of this paper is to point out the importance of deriving an accurate estimate of σ^0, for the retrieval of geophysical parameters (e.g. snowcover), and to show that geometric calibration is a fundamental requirement for a correct radiometric calibration. As an example, ERS-1 magnitude data in a mountainous region have been selected.

After the speckle reduction, radiometric distortions caused by the relief are removed using value added products such as local incidence angle and local resolution maps. These products are calculated directly from the DEM by reconstructing the original illumination geometry for each individual backscatter element. This information is transformed into the initial SAR geometry (Ground Range Geometry) and used to calculate the normalized radar cross section σ^o (Figure 1).

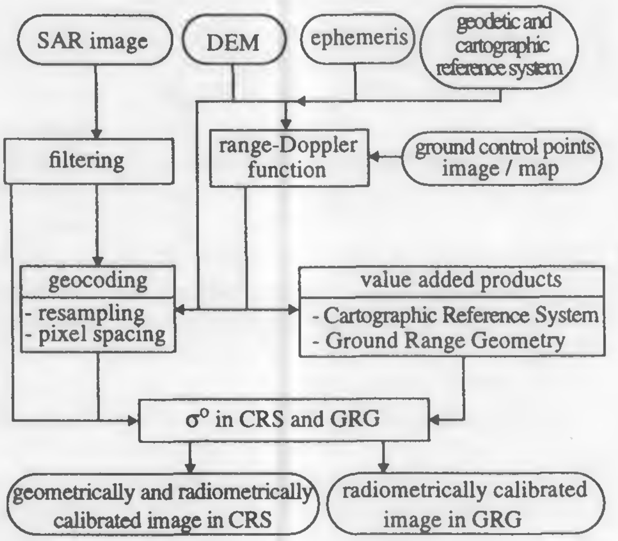

Figure 1: Derivation of the normalized radar cross section (σ^o or γ).

Due to severe foreshortening and layover effects images from two crossing orbits are used. The normalized radar cross section values of both orbits are transformed into the cartographic reference system and combined using an optimal resolution approach. In the resulting synthetic image the normalized radar cross section is taken from the orbit with the higher spatial local resolution.

2. RIGOROUS DERIVATION OF σ^o

A. Speckle Reduction

It is assumed that speckle has the characteristics of a random multiplicative noise (i.e. noise level increases with the average gray level of the local area). A requirement for its filtering is adaptivity: homogeneous areas must be smoothed, while edges and structures must be preserved, all with a minimal information loss. In previous works [4,5], it was shown, that the Frost filter [6] allows a good preservation of the information. One should note that no texture model is applied in this filter.

B. Range-Doppler Approach and Generation of Value Added Products

The removal of relief induced radiometric distortions requires a high precision geocoding of the image information. This geometric correction has to consider the sensor and the processor characteristics and therefore must be based on a range-Doppler approach [7]. For each picture element the following two relations must be fulfilled:

$$R_S = \sqrt{(S-P)\ (S-P)}$$

$$f_D = \frac{2f_0}{c} \cdot \frac{(v_p - v_s)}{|R_S|}$$

where:
R_s = slant range
S, P = spacecraft and backscatter element position
v_s, v_p = spacecraft and backscatter element velocity
f_0 = carrier frequency
c = speed of light
f_D = Doppler frequency

Using these equations the spatial relationship between the sensor, each single backscatter element, and their related velocities are calculated and therefore not only the illuminating geometry but also the processor characteristics are considered. Through this complete reconstruction of the imaging and processing geometry the

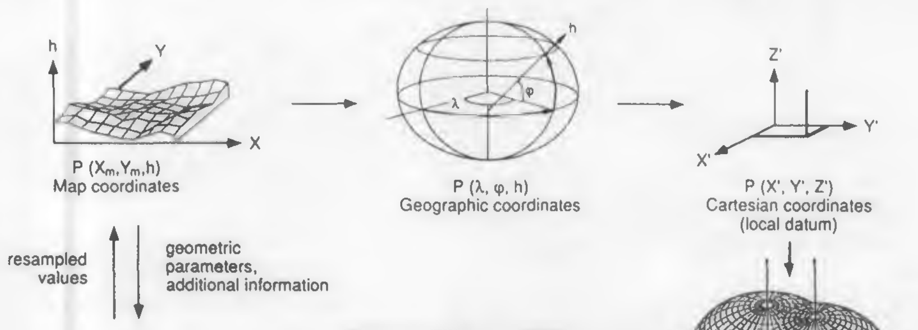

Figure 2: Rectification procedure and its inverse functionality.

primary topographic effects (foreshortening, layover) as well as the influence of earth rotation and terrain height on the azimuth geometry are calculated. Figure 2 summarizes the rectification procedure and its inverse functionality.

Resampling algorithms, as they are applied during geometric rectification, are only approximations of the sinc-function and cause radiometric and geometric distortions of the radar signal. As shown in [5,8] the geometric and radiometric distortions of the backscatter element can be minimized by selecting an appropriate resampling method and pixel spacing. Figure 3 shows the mean-to-standard deviation ratio as a function of the resampling and pixel spacing for a forest sample. Note that the bold lines at the rear of the diagram indicate the level of the corresponding value of the same area in the original SAR geometry.

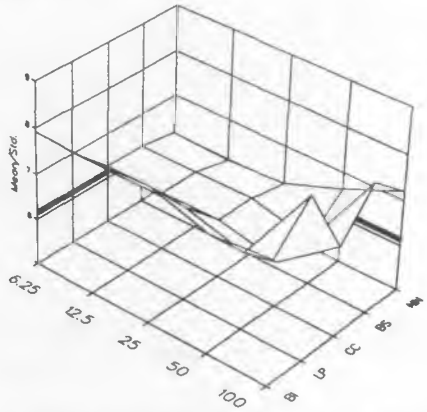

Figure 3: Mean-to-standard deviation of a forest sample. NN = Nearest Neighbour, CC = Cubic Convolution, BS = Bicubic Spline Interpolation, LP = Lagrange Polynomial, BI = Bilinear Interpolation.

Instead of the resampling procedure and in order to avoid radiometric and geometric distortions, any geometric parameters such as the local resolution, the local incidence angle and layover areas can be calculated directly from the DEM. These results can be stored in the same reference geometry as the DEM and at the calculated azimuth and range coordinate in a frame buffer of the same size, location and orientation as the original SAR image. To avoid gaps in this new data matrix four slant range coordinates, corresponding to four neighbouring DEM points, define the orientation of a backscatter element. They are combined and, if necessary, the area between is filled with the selected parameters. For that purpose a polygon-fill algorithm is used. The contents of the frame buffer then is stored in a data set and directly combined with the original SAR image, which is the basis for all subsequent radiometric calculations. We have to consider, that while the backscattered signals are preserved, the accuracy of the value added products is reduced, and therefore affecting the quality of the subsequent radiometric corrections.

For the retrieval of geophysical information in areas with severe terrain variations it is very important to have detailed knowledge of the backscatter behaviour. For example, layover disqualifies some areas from image interpretation, particularly if the depression angle of the sensor is large. A further limitation in mountainous areas is the local spatial resolution. It is defined as the area on the earth that is equivalent to a processed pixel in the SAR slant range image. Due to the properties of the SAR system one should distinguish between the local range resolution and the local azimuth resolution. The local resolution in cross-track direction corresponds to the projection of the nominal range resolution onto a cross-track profile. It is the dominant factor, causing the greatest radiometric variations in hilly and mountainous areas (Figure 4A). The local resolution in flight direction is defined by the nominal processed azimuth resolution onto an along-track profile at the targets position (Figure 4B). Although the nominal resolution of the ERS-1 SAR system is about 20 m^2, the local spatial resolution near layover areas can amount to several thousand square meters. As a result the geophysical interpretation will be dramatically reduced. A further required value for the calculation of the normalized radar cross section γ is the local incidence angle θ_i. It is defined as the angle between the surface normal of the backscattering element and the incoming radiation (Figure 4C).

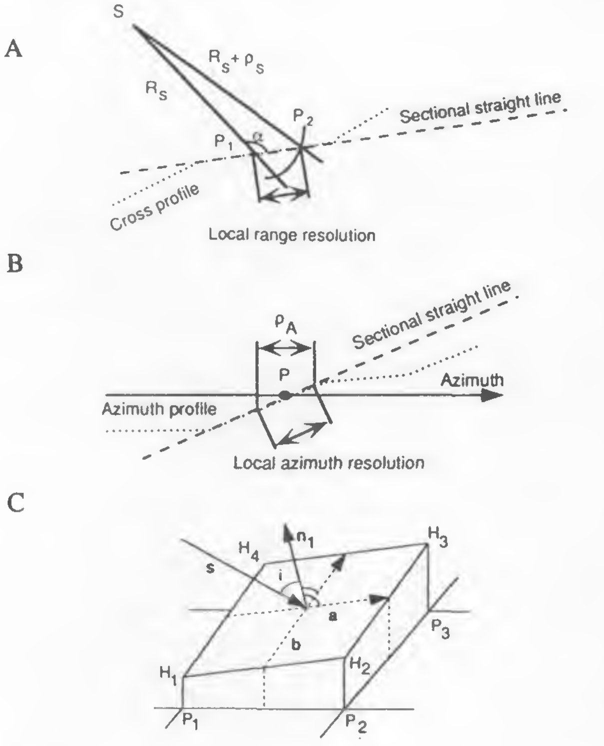

Figure 4: Local spatial resolution in range (A) and azimuth (B) , and local incidence angle (C).

Figure 5 shows layover and local resolution maps of the testsite (for ascending A-D) and for descending orbits (E-F) in the cartographic reference system. Layover areas are black, while local resolution is gray and split into four classes. Due to the large depression angle of ERS-1 SAR, about 28% of the ascending and 45% of the descending image are layover areas for the scene. The local resolution decreases strongly in regions near layover:

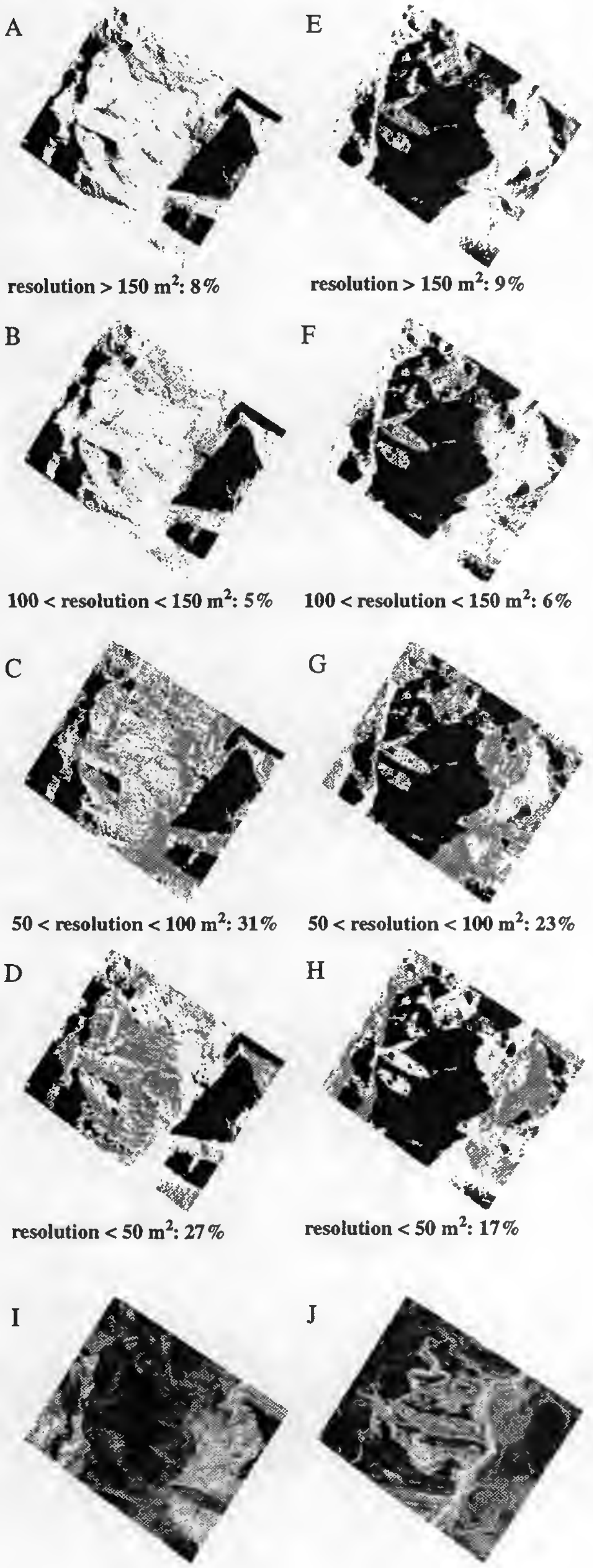

Figure 5: Layover and local resolution maps of the testsite (Grison, Switzerland) for the ascending (A-D) and for the descending orbit (E-H) in the cartographic reference system, while I and J show the geocoded images from ascending and descending orbit (acquistion dates April 27th and April 30th, 1992). Note, that the images I and J have not yet been radiometrically calibrated.

theoretical values up to 70'000 m^2 are computed. The mean local resolution (layover areas excluded), was computed to be 209 m^2 for the ascending image and 337 m^2 for the descending image.

Figure 6 shows the local incidence angle in the cartographic reference system (A and B) as well as in the original SAR geometry (C and D). The gray tones correspond to the cosine of the local incidence angle, and reach their brightest values in areas close to layover.

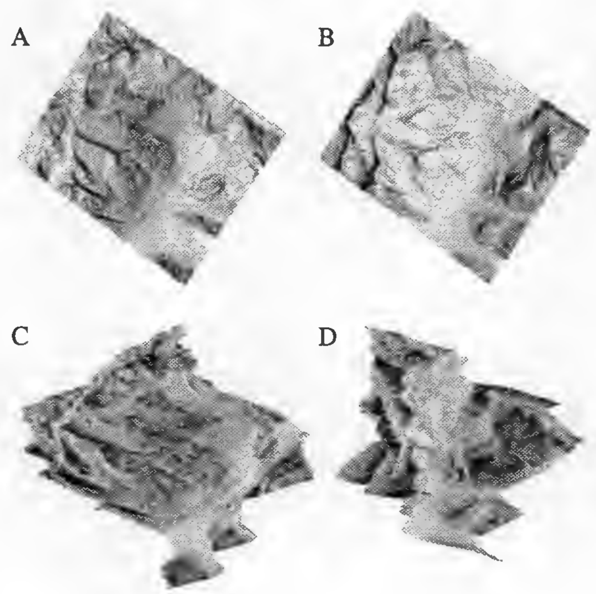

Figure 6: Local incidence angle maps of the testsite for the ERS-1 ascending (A and C) and descending orbit (B and D).

C. Derivation of the Normal Radar Cross Section and Optimal Resolution Approach

Due to the low signal-to-noise-ratio and the strong modulation in radar signals, the intrinsic spatial variability, called intrinsic texture, is difficult to detect in spaceborne SAR images. After [9,11] it was demonstrated, that the tonal information (e.g. the local mean backscattering) for spaceborne SAR systems, contains without question almost all of the useful information. For this reason textural analysis is not pursued further here.

Since the local spatial resolution as well as the local incidence angle for each backscattered element is known, σ^0 and γ can be derived. To avoid geometric and radiometric distortions of the radar signal, the normalized radar cross section γ is calculated in the original SAR geometry. Figure 7 shows the resulting γ values. Note, that the white areas in the images correspond to layover, which are omitted from the analysis.

The crossing images can now be combined to produce a synthetic product containing better geophysical information. To avoid radiometric changes and to minimize geometric distortions, a nearest neighbour resampling method with a pixel spacing of 25 m was used.

A

B

Figure 7: γ values of the testsite for ascending orbit (A) and descending orbit (B).

The new synthetic image was obtained from the two geocoded images by applying an optimal resolution approach: the normalized radar cross section γ was taken from the orbit with the better local resolution. The result is shown in Figure 8. While Figure 8A represents the new synthetic γ-map in the cartographic reference system, Figure 8B indicates the data source used for each area of the scene. The unusable layover area could be reduced to only 5% and the resulting mean local resolution improved from 273 m^2 to 127 m^2. 56% of the geophysical information is derived from the ascending orbit, and 39% from the descending orbit.

A

B

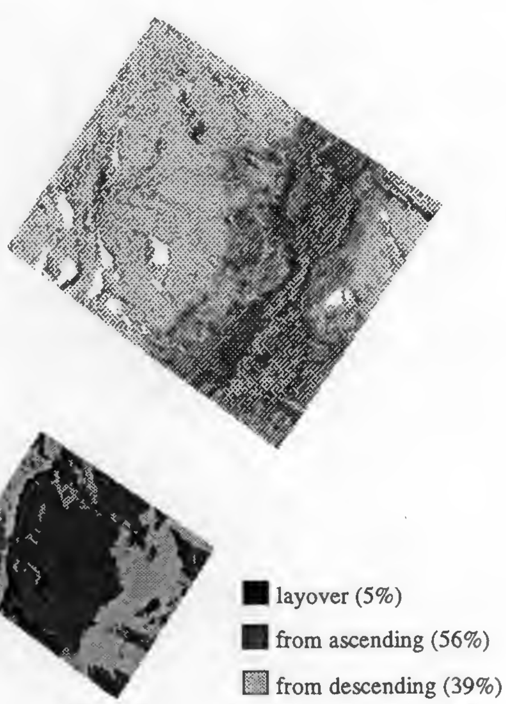

Figure 8: γ values [dB] in the cartographic reference system after optimal resolution approach (A) and data source of the synthetic product (B).

3. SNOWCOVER MAPPING AND DISCUSSION

A snowcover segmentation using a simple thresholding of the normalized radar cross section was carried out and compared to the previously segmented TM imagery [9]. The results are compared in Figure 9.

A

B

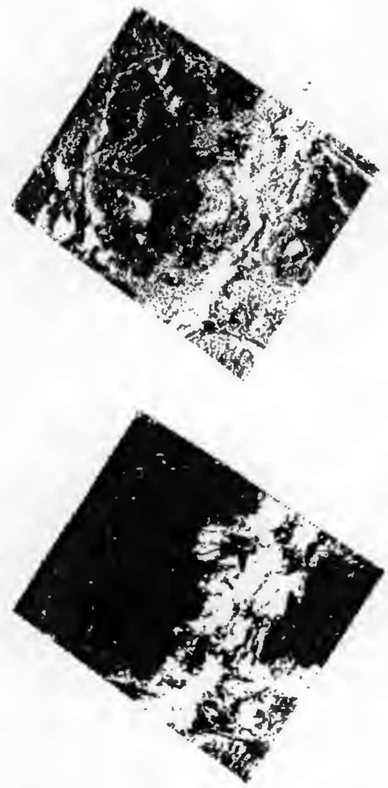

Figure 9: Snowcover discrimination based on γ values (A) and on TM image (B).

Snowcover determination using TM image (Figure 9B) clearly provides the better result. The snow discrimination of the TM image is applied using only band 4 (0.76 - 0.90 μm). For the ERS-1 SAR data (Figure 9A) a coarse snowcover discrimination could be achieved. But several limitations must be taken into account. Omitting the layover areas from the evaluation three considerations can be made: a) Regions near layover areas are generally not correctly classified. The reason lies in the poor local spatial resolution despite of the optimal resolution approach. b) Between snow-covered and snow-free zones a few areas are erroneously classified as snow-covered. This confusion may be caused by wet soil conditions and has already been observed and reported in [10]. c) Due to the vegetation, which dominates the backscattered energy, only snow determination in wide open areas can be made. This result confirms the work reported in [11].

What has to be clarified now is the potential of a synergism between the two sensors. Since the TM image reveals a very good snowcover discrimination, the resulting snow mask can be superimposed to the derived γ values to determine the statistical distribution of the normalized radar cross section. Figure 10 shows the snow-

cover distribution of the γ values linearly scaled. The values are normally distributed. This confirms together with the spatial distribution of the γ values in Figure 8A, that no additional information concerning the snow conditions could be extracted from the ERS-1 SAR data.

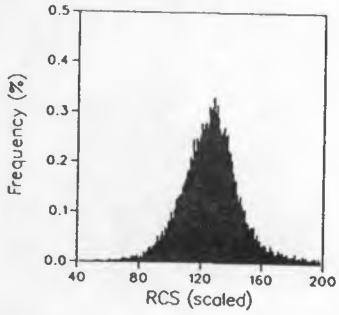

Figure 9: Statistical distribution of snowcover, γ values in [dB], linearly scaled.

4. CONCLUSIONS

In a case study it could be demonstrated, that geometric calibration is a fundamental requirement for a correct radiometric calibration. Furthermore the accuracy of the radiomentric calibration depends upon the DEM accuracy. This was previously reported in [12].

A comparison of SAR derived normalized radar cross section with optical imagery and with ground truth information leads to the following conclusions. A coarse snowcover discrimination using ERS-1 SAR magnitude data can be made but several limitations have to be taken into account: a) no discrimination between wet soil and wet snow is possible, b) the detection of snow can be carried out only in wide open areas. In addition, in rugged terrain, layover effects lead to a requirement for images from at least two crossing orbits. The optimal resolution approach, combining ascending and descending orbits, reduce layover areas and enables a better mean local spatial resolution as well as an improved geophysical information extraction. The result is a snowcover map taking into account two different acquisition times and therefore two different snow type conditions. For this reason additional information, i.e. meteorological data (such as temperature, wind, humidity, radiation, cloud cover) is required.

The poor local spatial resolution in sloped areas also limits the accuracy of the snowcover discrimination. In this paper it also could be shown, that in mountainous regions with wet snow conditions the ERS-1 SAR sensor is not the most suitable remote sensing system. The advantage of ERS-1 SAR data compared to optical imagery is to acquire time independent data. Because spaceborne SAR images are often the only input for snowmelt runoff models, due to the cloud coverage in optical images, ERS-1 can be used as a complementary information source.

5. REFERENCES

1. A. Freeman, "SAR Calibration: An Overview", CEOS Working Group on SAR Calibration, DLR, Oberpfaffenhofen, 1991.
2. A. Freeman and J.C. Curlander, "Radiometric Correction and Calibration of SAR Images", Photogrammetric Engineering and Remote Sensing, Vol. 55, No. 9, pp 1295-1301, 1989.
3. A. Freeman, "White Paper on Calibration Definitions", CEOS Working Group on SAR Calibration, DLR, Oberpfaffenhofen, 1991.
4. F. Holecz, "A Study on Texture Measurements Applied to SAR Images", Final Report to CEC Joint Research Centre, Ispra, 1989.
5. F. Holecz, E. Meier and D. Nüesch, "Postprocessing of relief induced radiometric distorted spaceborne SAR imagery", Chapter 14 in SAR-Geocoding - Data and Systems, Wichmann-Verlag, edited by Schreier, pp 299- 352, 1993.
6. Frost V.S., J.A. Stiles, K.S. Shanmugan and J.C. Holtzman, "A Model for Radar Images and its Application to Adaptive Digital Filtering of Multiplicative Noise", IEEE Transactions on Pattern Analysis and Machine Intelligence, Vol. PAMI-4, pp 157-165, 1982.
7. E. Meier, "Geometrische Korrektur von Bildern orbitgestützer SAR-Systeme", Remote Sensing Series, Vol. 15, University of Zurich, 1989.
8. F. Holecz, "Postprocessing von SAR-Satellitenbilddaten", Remote Sensing Series, Vol. 23, University of Zurich, 1993.
9. F. Holecz, M. Datcu and D. Small, "Model Based Radiometric Correction of Optical Imagery in Mountainous Regions for Snowcover Segmentation", Proceedings IGARSS Symposium Tokyo, pp 401-403, 1993.
10. R. Hüppi, "RASAM: A Radiometer-Scatterometer to Measure Microwave Signatures of Soil, Vegetation and Snow", Ph.D. Thesis University of Bern, 1987.
11. J.R. Donald, F.R. Seglenieks, E.D. Soulis, N. Kouwen and D.W. Mullins, "Mapping Partial Snowcover During the Melt Season Using C-Band SAR Imagery", Canadian Journal of Remote Sensing, pp 68-76, 1993.
12. F. Holecz, E. Meier and D. Nüesch, "Classification of SAR Images in Areas with Severe Terrain Variations", Proceedings IGARSS Symposium Houston, pp 1123-1125, 1992.

DIELECTRIC BEHAVIOUR OF SOILS: COMPARISON BETWEEN TDR MEASUREMENTS AND SAR DATA WITHIN MAC-EUROPE '91 IN MONTESPERTOLI (ITALY).

G.D'Urso [*], M.Mancini [**], P.Troch [***]

[*] University of Molise, V.Cavour 50, 86100 Campobasso Italy

[**] DIIAR Politecnico, L. da Vinci 32, 20133 Milano Italy

[***] Lab. Hydrology and Water Manag., University of Ghent, Ghent B9000, Belgium

ABSTRACT

The knowledge of soil dielectric behaviour is of great importance when interpreting SAR backscattering data for surface soil water content detection. Preliminary investigations carried out during Mac-Europe '91 experiment in Montespertoli are presented. In-situ non destructive measurements of soil dielectric characteristics have been performed on bare soil plots by using Time Domain Reflectometry (TDR) in coincidence of a JPL-AirSAR flight over the test site. Measured values of dielectric constant are used to calibrate an empirical inversion model of SAR backscattering at radar resolution on a basin spot. Results from calibrated model are discussed and compared with TDR measurements.

Keywords: soil water content, JPL-AirSAR, backscattering, dieletric constant, TDR.

1. INTRODUCTION.

The possibility of detecting surface soil water content by means of active remote sensing is very attractive in many hydrological studies. Due to the role played in the energy balance, soil water content is recognised as one of the most important variables in the hydrological cycle for its implication on climate.

The availability of spaceborne active sensors may provide a powerful and cost-effective tool for the estimate of spatial distribution of soil water content over large areas. Several studies have shown how water content influences soil dielectric behaviour and as a consequence its response to microwave backscattering phenomena (Ref.11). Nevertheless, retrieval of soil water contents from backscattering coefficients is not a straightforward procedure and in most cases it does not take into account of soil physical properties. This approach may lead to large uncertainity of results, especially when soil variability conditions occur. On the other hand, the areal distribution of soil water content can be derived from the knowledge of corresponding value of dielectric constant and different soil physical characteristics may be considered (Ref.7). Moving from this consideration, soil dielectric behaviour has been investigated by means of Time Domain Reflectometry in coincidence of JPL-AirSAR flight during MAC-Europe '91 experiment carried out in Montespertoli (Italy). The dielectric measurements have been used to calibrate the inversion model of SAR backscattering signals proposed by Oh et al. (Ref.6). The resulting relationship has been successively tested in a second site comparing measured soil dielectric constant with estimated value from SAR images.

2. THEORY AND DEFINITIONS

2.1 TDR operating principles.

The development of Time Domain Reflectometry -shortly TDR- for detection of impendance mismatching in long cables has made available reliable and portable instrumentations for the measurement of dielectric properties of materials. Since 1980, this technique has been intensively used for in-situ non destructive soil water content determinations in hydrological studies and agricultural applications. Multiple regressions of experimental data (Refs. 9-10) has led to the definition of a commonly accepted relationship between the soil dielectric constant ϵ, as determined by TDR, and the volumetric soil water content θ for all mineral soils:

$$\theta=(-530+292\epsilon-5.5\epsilon^2+0.043\epsilon^3)10^{-4} \quad (1)$$

When an accuracy better of 5% is asked, a soil specific calibration is required. A more physical interpretation of ϵ-θ relationship has been tried out by applying Maxwell equation to homogeneous mixtures of four-component system having differentiated dielectric properties (Ref.1). A comparison of this approach with Eq.1 and other empirical models has been investigated by Dirksen and Dasberg (Ref.2).

The TDR technique is based on the measure of time propagation T of a pulse travelling along a transmission line of lenght L, formed by two metallic conductors, embedded into the soil which is the dielectric medium. A step pulse of 300 mV with a rising time of 0.2 ns and width of 25 ns is sent through the transmission line by the TDR apparatus, consisting of a commercially available coaxial cable tester. At the end of transmission line, the pulse is reflected back to the tester, where it is sampled and recorded. Although it is inappropriate to give frequency specifications in the time domain, it is possible to relate the pulse rise time and width to the frequency band limits of TDR, thus corresponding approximately to 25 KHz and 1.75 GHz (Ref.4).

The dielectric constant of bulk soil ϵ can be expressed by a complex function of d.c. electrical conducibility γ, frequency f and permittivity μ_0 (8.854×10^{-12} F/m):

$$\epsilon=\epsilon'-i(\epsilon''+\frac{\gamma}{2\pi f\mu_0}) \quad (2)$$

When operating above 100 MHz frequency range, as in this application of TDR, the complex term of dielectric constant can be neglected and $\epsilon=\epsilon'$ is assumed (Ref.4). The TDR pulse speed along the transmission line, given by:

$$v=\frac{2L}{T} \qquad (3)$$

is related to the dielectric characteristics of the medium by means of the function (Refs.1,3):

$$v=c/(\epsilon'\frac{1+(1+\tan\delta^2)^{1/2}}{2})^{1/2} \qquad (4)$$

where the tangent loss $\tan\delta$ is given by the ratio of complex and real part of dielectric constant:

$$\tan\delta=(\epsilon''+\frac{v}{\omega\mu_0})/\epsilon' \qquad (5)$$

Under the assumtions made and with reference to soil measurements, Eq.4 may be rewritten in the following form:

$$v=\frac{c}{\epsilon} \qquad (6)$$

thus giving:

$$\epsilon=(\frac{cT}{2L})^2 \qquad (7)$$

which is the fundamental relationship for the measurement of dielectric constant by means of Time Domain Reflectometry.

The travel time T can be read on the display of TDR tester, which shows a waveform similar to that illustred in fig.1.

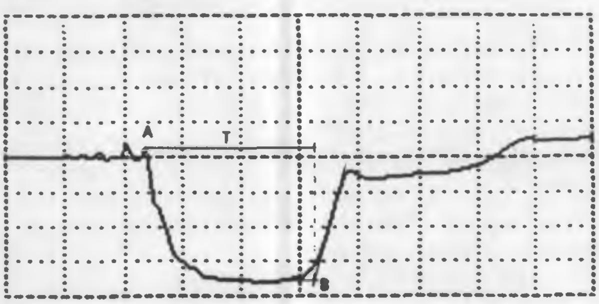

Fig.1: TDR waveform display.

The time T is given on graph abscissas and pulse amplitude (V) on vertical axis; point A represents the entrance of the pulse into the soil, while point B corresponds to its reflection at the end of transmission line. Thus, the interpretation of TDR display allows for travel time determination which can be entered into Eq.7. for the calculation of dielectric constant. The measure can be considered as the average value along the transmission line of length L. The value of travel time T may be directly used for the calculation of Fresnel reflectivity index $\Gamma(\alpha)$, which at nadir is given by the known expression:

$$\Gamma_0=|\frac{1-\sqrt{\epsilon}}{1+\sqrt{\epsilon}}|^2=|\frac{1-\frac{cT}{2L}}{1+\frac{cT}{2L}}|^2 \qquad (8)$$

2.2 Estimation of soil dielectric constant from backscattering data.

Radar backscattering phenomenon over soil surface can be formulated in different ways (Small Perturbation, Physical-Optical and Geometrical-Optical models; Ref.11). In most cases, backscattering coefficients are mainly related to the incidence angle α, the reflective index of surface Γ, which is a function of dielectric constant ϵ, and the soil surface roughness k_s. The theoretical models available still show many severe constraints for their inverse solution, as required when retrieving soil dielectric constant from backscattering data. At present moment, it seems that this task may be achieved more easily by means of empirical models, as recently proposed by Oh et al. (Ref.6), based on L-, C- and X-band backscattering measurements. In brief, according to this model, the co-polarized and cross-polarized ratios (p,q) of backscattering coefficients can be expressed as follows:

$$\sqrt{p}=\sqrt{\frac{\sigma^0_{hh}}{\sigma^0_{vv}}}=1-(\frac{2\alpha}{\pi})^{\frac{1}{A\Gamma_0}}\exp(-k_s) \qquad (9)$$

$$q=\frac{\sigma^0_{hv}}{\sigma^0_{vv}}=B\sqrt{\Gamma_0}[1-\exp(-k_s)] \qquad (10)$$

where A and B are empirical coefficients depending on soil characteristics. By eliminating k_s from Eq.9 and 10 the following equation can be obtained:

$$(\frac{2\alpha}{\pi})^{\frac{1}{A\Gamma_0}}[1-\frac{q}{B\sqrt{\Gamma_0}}]+\sqrt{p}+1=0 \qquad (11)$$

If dielectric measurements are available, parameters A and B may be derived for the specific site conditions; successively, Eq.11 may be used for retrieval of dielectric values from backscattering ratios.

This approach has been attempted here, by applying the model at pixel scale for the given sites on the basin surface utilizing the radar backscattering coefficients for the three polarizations (hh,vv,hv).

3. EXPERIMENT DESCRIPTION.

The MAC-EUROPE 1991 italian experiment was carried out in Tuscany over the Virginiolo basin. This is a first order basin of the Arno river with a drainage area of 4.5 km^2 and it shows the typical hilly landscape of the central Italian Apennines. The basin appears as one elongated valley through which a small stream flows northwards. A digital elevation model at a resolution of 30m was available. The climate of this area is classified as Mediterranean with dry summers and an average annual precipitation of 1000 mm. The flight route of NASA JPL-Airsar carrier (Jet Propulsion Laboratory) was fixed in 275 W-degrees so that the direction of radar illumination was practically aligned in the valley direction. This avoided the local incidence angle being affected differently by the local topography on both sides of the valley.

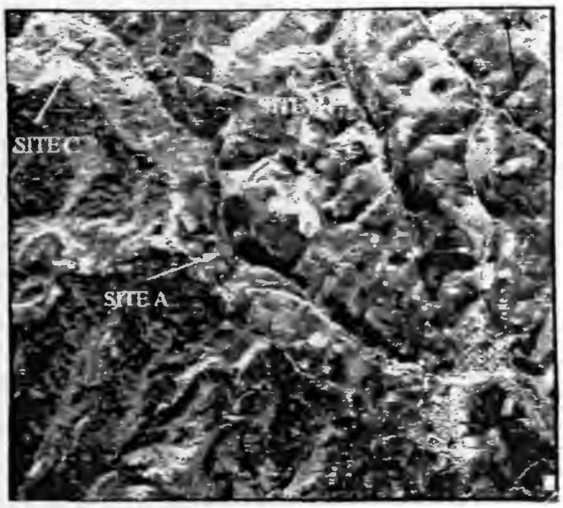

Fig.2: SAR image L-band (hh pol.) of test site area.

Airborne SAR data were acquired over the sites on dates June 22nd and 29th for thee bands C, L, P corresponding to the frequencies f=5.33 Gz, f=1.25 GHz, and f=0.44 GHz respectively at an incidence angle of 25 degrees with hh, vv, hv polarization (fig.2). The slant range and azimuth resolution were 3.3 m and 6.1 m. The radar data were processed using the JPL AirSAR processor 3.55 (Ref.12) and were calibrated using trihedral corner reflectors located on sites B and C. To ensure that each pixel of the analyzed images refers to the same ground measurements locations, SAR image was georeferenced by using the basin DEM. For more comment on signal analysis we refer to Lin et al. (Ref.5).

In coincidence of SAR acquisition, dielectric measurements with TDR were performed in two different test sites, A and C, with a mean slope of about 25% characterized by tilled bare soil. Soil texture, classified as sandy clay, was determined by the granulometric curves made for each site to a depth of 40 cm. Some gravels were also visible on the ground surface. Measurements were taken along prefixed transects at a distance of 20 meters approximately

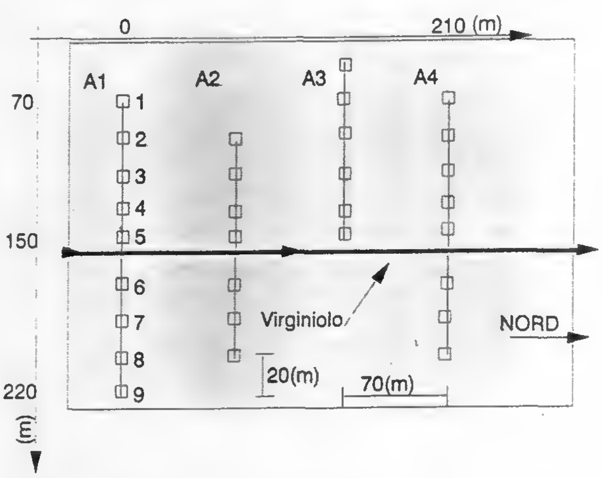

Fig.3: Measurement grid on site A.

(fig.3). The transects were set for each test-site orthogonally to the stream direction and at an interdistance of about 70 meters. TDR Tektronix cable tester 1502 B with built-in printer has been used. The transmission line was consisting of a three rods coaxial hand probe (Ref.13); the electrical probe lenght, which also determines the investigated soil volume, was 14 cm with rods interaxis of 4 cm. The probe was gently pushed vertically into the soil, after having flattened its surface by taking away the first 2-3 cm of soil.

4. DISCUSSION OF RESULTS.

The application of inversion technique of Oh model has been performed according to a two steps procedure: in first instance, A and B parameters of Eq.9 and 10 had to be estimated for the site C conditions by using the measured values of ϵ from TDR; secondly, retrieval of dielectric constant from Eq.11 has been tried out refering to site A and resulting values have been compared with measured TDR dielectric constant. In order to consider meaningful value of backscatter in correspondance of each TDR measurements along the transects, a set of contiguos pixel of georeferenced SAR image has been selected around each TDR location and their average backscattering coefficient has been determined for further elaborations. This sampling procedure allowed for minimizing possible errors of transect position in the SAR georeferenced image. Signal variance with respect of different pixel aggregation windows has been examined.

Backscattering coefficients in L-band along the

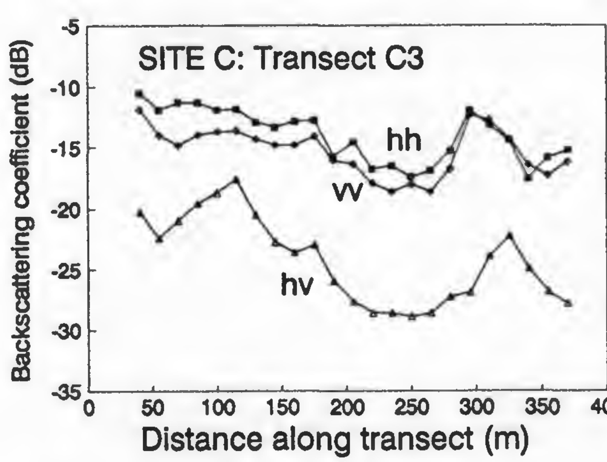

Fig.4: Backscattering coefficients σ_o along a transect on site C.

transect C3 are shown in fig.4: values of backscatter refer to full co-polarizations hh and vv and cross-polarization hv. Considering the frequency bandwidth of TDR measurements and the length of hand probe used, backscattering signal in L-band has been considered as the most suitable for the present analysis. In this case, the dielectric constant value retrieved from L-band backscatter is expected to be the closest to that given by TDR either for the frequency range and for the volume of the soil investigated.

Correlation between parameters A and B (Eq.9-10) and backscattering ratios p and q (as derived from SAR L-band values for site C) has been investigated. In

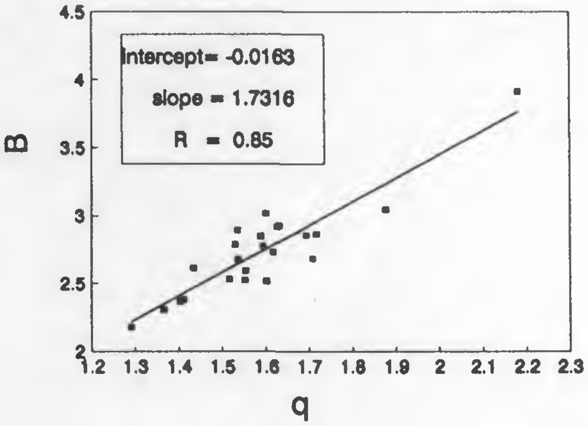

Fig.5: Linear interpolation of B parameter values with ratio q on site C.

the first case, parameter A resulted to be indipendent from the value of backscatter and its constant value has been set to 3, as given by Oh (Ref.6). Diversely, evident correlation has been found between the value assumed by the parameter B and corresponding measured values of cross-polarized backscatter ratio q (fig.5); parameter B has been found ranging from 1.2 and 2.3, one order of magnitude larger than Oh empirical value (0.23). Introducing this relationship in Eq.11, the latter has been solved with respect to Γ_0 with an iterative algorithm (tollerancy less than 10^{-3}), from which soil dielectric constant values have been derived.

The backscattering coefficients used to calculate the ratio q and p for the transect A1 of site A are shown in fig.6.

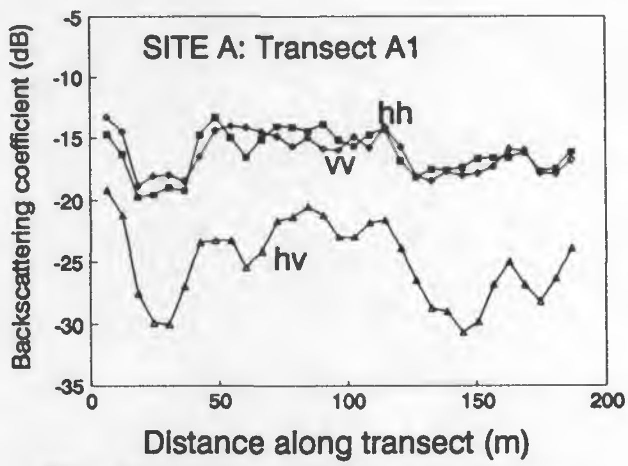

Fig.6: Backscattering coefficients σ_o along transect A1.

The comparison between TDR values and those resulting from the solution of Eq.11 is depicted in fig.7. Dielectric constant values retrieved from backscatter data are characterized by abrupt variations, which are not confirmed by field measurements. Indeed, the regression of ϵ_{TDR} versus ϵ_{SAR} given in fig.8 is not very encouraging. If data are averaged at grid level, the agreement between mean value of SAR dielectric constant over the site ($\epsilon_{SAR}=14.22$) and TDR transect average ($\epsilon_{TDR}=12.20$) is quite satisfactory.

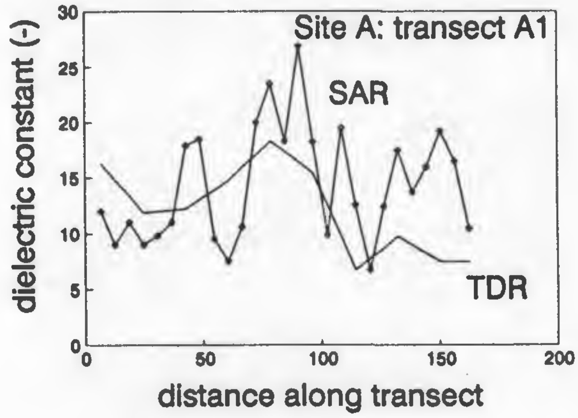

Fig.7: Dielectric constant values determined with TDR and SAR along transect A1.

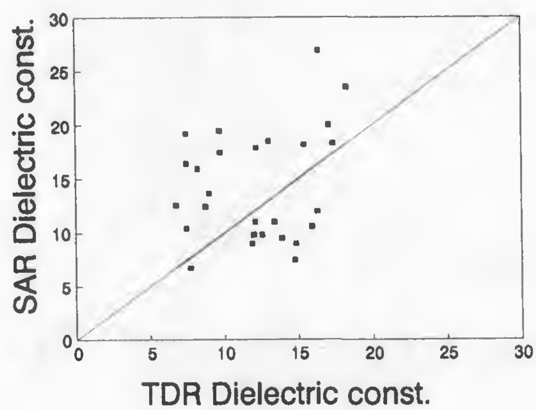

Fig.8: Measured dielectric constant (TDR) versus SAR derived value.

5. CONCLUSIONS.

The methodology proposed in this study indicates a possible way for the retieval of soil dielectric constant from SAR backscattering measurements. TDR technique offers the attractiveness of *in situ* non destructive measurements of soil dielectric properties, from which water content can be easily derived. The analogy of physical principles between TDR and SAR can bring new perspectives in the geophysical calibration of active microwave remote sensing. The use of inversion modeling algorithms, such as that one adopted in this study, allow for a more physically sound approach for SAR data analysis. The results presented here have shown the possibility of retrieving the average value of dielectric constant over

a plot, by applying the inversion model of SAR data to a grid of pixels. Further investigations are needed for searching other formulations which do not rely on empirical basis.

The outcome of this research issue may turn into useful indications for the use of SAR digital products in many application of hydrology and water resources management.

ACKNOWLEDGEMENTS.

The financial support to this study has been granted within the framework of Italian Research and University Ministry Project "Processi idrologici fondamentali" (M.U.R.S.T. 40%).

List of symbols.

A,B	: calibration parameter (-)
c	: e.m. celerity ($3x10^8$ m/s)
f	: frequency (Hz)
k_s	: roughness coefficient (-)
L	: transmission line lenght (m)
p	: co-polarized backsc. ratio (-)
q	: cross-polarized backsc ratio (-)
T	: pulse travelling time (s)
v	: e.m.propagation speed (m/s)
α	: SAR incidence angle (rad)
γ	: d.c. conductivity (S/m)
Γ	: Fresnel reflectivity index (-)
δ	: dielectric loss angle (-)
ϵ	: dielectric constant (-)
μ_0	: air permittivity (F/m)
σ_0	: backscattering coefficient (dB)
θ	: volum.soil water content (-)

References.

1. De Loor G.P., 1990. *The dielectric properties of wet soils.* BCRS Rep. n.90-13, TNO Phys. Electr. Lab., Den Haag, 39 pg.

2. Dirksen C., Dasberg S., 1993. Improved calibration of Time Domain Reflectometry soil water content measurements. *Soil Sci. Am. J.*, 57, 660-667.

3. Fellner-Feldegg H., 1969. The measurements of dielectrics in time domain. *J. Phys. Chem.*, 73, 616-623

4. Heimovaara T.J., 1993. *Time Domain Reflectometry in soil science: theoretical backgrounds, measurements and models.* Doctoral Thesis, University of Amsterdam, 55-80

5. Lin, D. S., E. F. Wood, M.Mancini, P.Troch, and T. Jackson, 1992. Comparison Between Remotely Sensed and Model Simulated Soil Moisture on a Heterogeneous Watershead, subm. to *Remote Sensing Environ.*

6. Oh Y., Sarabandi K., Ulaby F.T., 1992. An empirical Model and an inversion technique for radar scattering from bare soil surface, *IEEE Trans. Geosci. and Remote Sensing*, 30(2), 370-381

7. Schmugge T., 1985. Remote Sensing of soil Moisture, *Hydrological Forecasting*, ed. M.G. Andersonand T. P. Burt, John Wiley & Soons

8. Shy J. J.,V. Soares, L. Hess, E.T. Engman, J. van Zyl, SAR-derived soil moisture Measurements for bare Fields, *IEEE Trans. Geosci. and Remote Sensing*, 30(2), 1992

9. Topp G.C., Davis J.L., Annan A.P., 1980. Electromagnetic determination of soil water content: measurements in coaxial transmission lines. *Water Resour. Res.*, 16, 574-582

10. Topp G.C., Davis J.L. 1985. Measurements of soil water content using Time Domain Reflectometry: a field evaluation. *Soil Sci. Am. J.*, 49, 19-24

11. Ulaby, F.T., Moore R.K., Fung A.K., 1985. *Microwave remote sensing.* Vol.II, Artech House, Washington

12. Van Zyl, J.J., C.F Burnette, H.A Zebker, A. Freeman and J. Holt, 1990. *POLCAL User Manual*, JPL, Cal. Tec., Pasadena

13. Zegelin S., White I., Jenkins D.R., 1989. Improved field probe for soil water content and electrical conductivity measurements using Time Domain Reflectometry. *Water Resour. Res.*, 25, 2367-2376

CALIBRATION DEVICES

Session 2

Chair: H.LENTZ, INS, GERMANY

ESTEC RF SYSTEMS DIVISION SAR CALIBRATION ACTIVITIES

H.Jackson, J.Kleijweg, A.Woode

Introduction

ESA-ESTEC has built up considerable experience in SAR calibration with the design, construction and deployment of ground transponders for the calibration and validation of the ERS-1 SAR. The three ERS-1 C-band transponders are deployed in Flevoland in the Netherlands. Test and analysis suggest that the long term stability of these units is < 0.1 dB and calibration accuracy of < 0.2 dB. Both figures fulfilling the original specification.
In early 1993 an L-band transponder, for calibration of the Japanese JERS-1 satellite, was also deployed at the Flevopolder test site. This unit having similar stability but slightly worse absolute calibration accuracy <0.5 dB.

Future activities planned are calibration of the ERS-2 satellite, being launched in 1995 and for the ENVISAT ASAR to be launched in 1998. In the shorter term it is planned to support the SIR-C shuttle SAR campaign and hopefully to achieve cross calibration between this mission and the two satellite borne SAR instruments.

It is important for ESTEC that the calibration standards achieved with the current range of transponders are continued with new applications such as dual polarisation or interferometry. Both creating their own problem of achieving good stability and accuracy.

ERS-1 C-Band Transponders

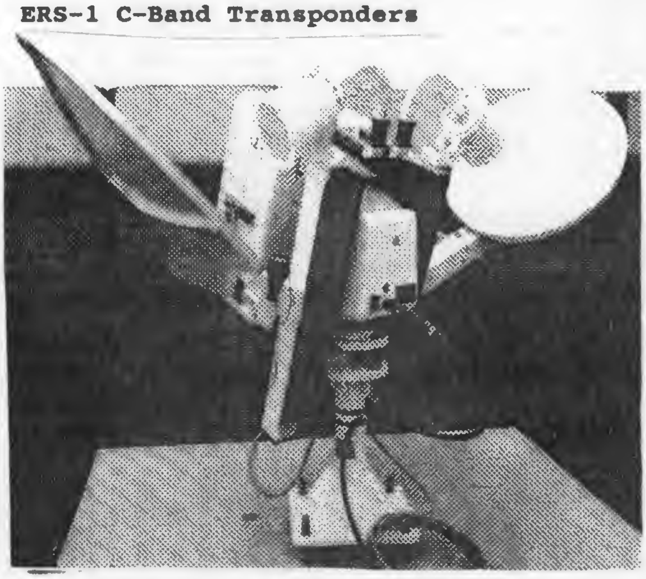

Fig. 2 ERS-1 TRANSPONDER BASED IN FLEVOLAND

The design and operation of these precision transponders has been well documented [1], [2] so will not be fully described here. The simplified block diagram Fig 1 shows the principle of operation. An injected calibration pulse is sampled at the diode detector D1 and also sampled after amplification and delay in the electronics unit. Any unbalance between these two signals causes the control unit to increment the digital attenuator.
A key component for good stability is the optical delay line, this reducing

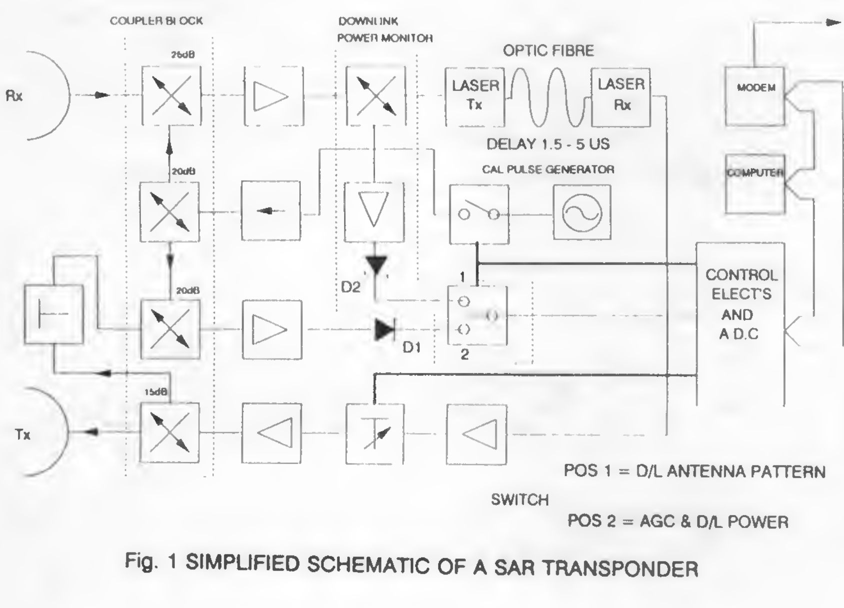

Fig. 1 SIMPLIFIED SCHEMATIC OF A SAR TRANSPONDER

errors caused through antenna leakage and coherent feedback within the electronics. It also allows single point sampling to be used. An additional and sometimes important advantage is that it displaces the image within the swath, so by the choice of delay used the transponder image can be placed in an area of low background return. The delay of the C-band transponders was chosen as 1.5 μsec.

Operation of the transponders has been continuous since the launch of ERS-1, in August 1991, Fig 2 shows one at Lelystad in Flevoland. During the first month of operation it was necessary to reduce the radar return of the transponders from 65 dBm^2 to 58 dBm^2 to avoid saturation of the processed data.

As shown in Fig 3, the combined instrument processing and transponder stabilities for ERS-1 were believed to be about 0.4 dB. Recent work in ESRIN to correct for small a.d.c. non linearities has now reduced this uncertainty to 0.2 dB [3].

An operational summary of the three transponders is given in Table 1, this

Table 1 OPERATION SUMMARY OF THE

THREE ERS-1 TRANSPONDERS

413		TOTAL OVERPASSES
24		SAR not detected (*)
40		Missed due to deployment and calibration
349		CALIBRATION OPPORTUNITIES
30		Lost due to ARC failures: (*2 coincide)
	18	Software crashes or timing errors
	5	Positioner failures
	3	RF electronics failure
	2	Prime power failures
	2	Operator error
321		SUCCESSFUL

(Launch to 31/8/93)

shows that taking all failures into account the success rate is >90%. Being fully automatic, operation of the transponders is routine and requires a minimum of manpower.

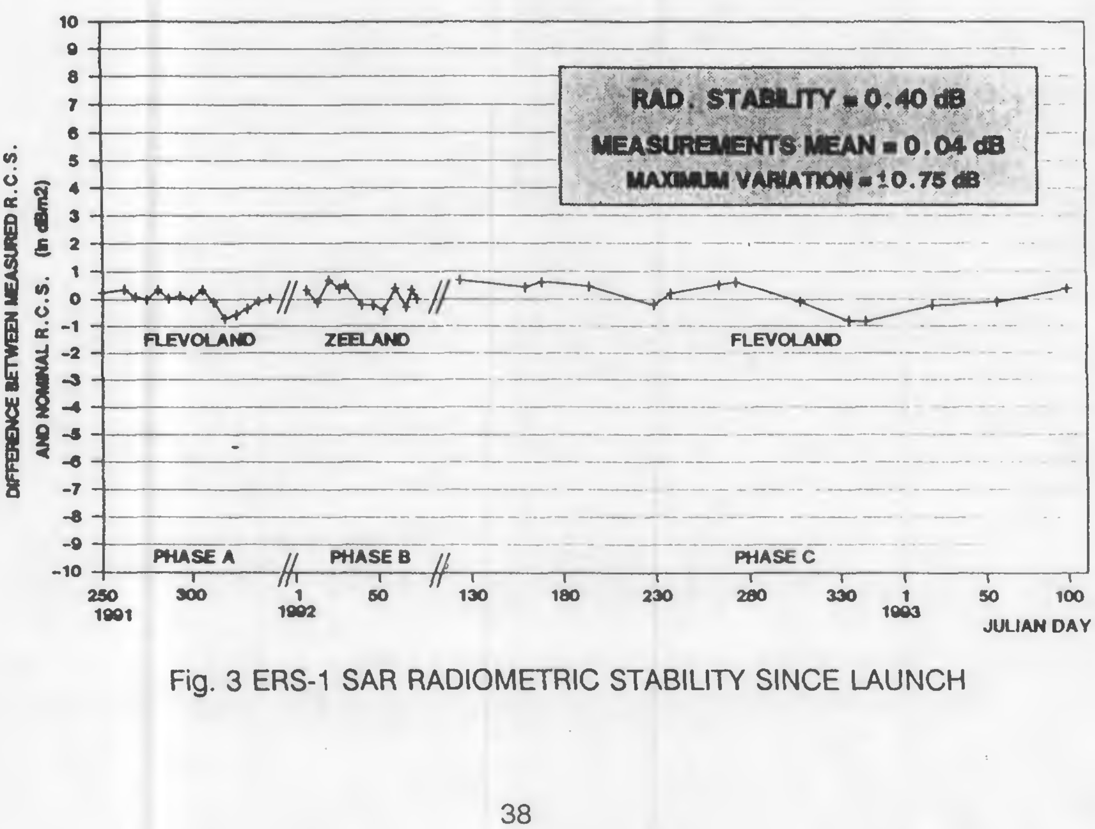

Fig. 3 ERS-1 SAR RADIOMETRIC STABILITY SINCE LAUNCH

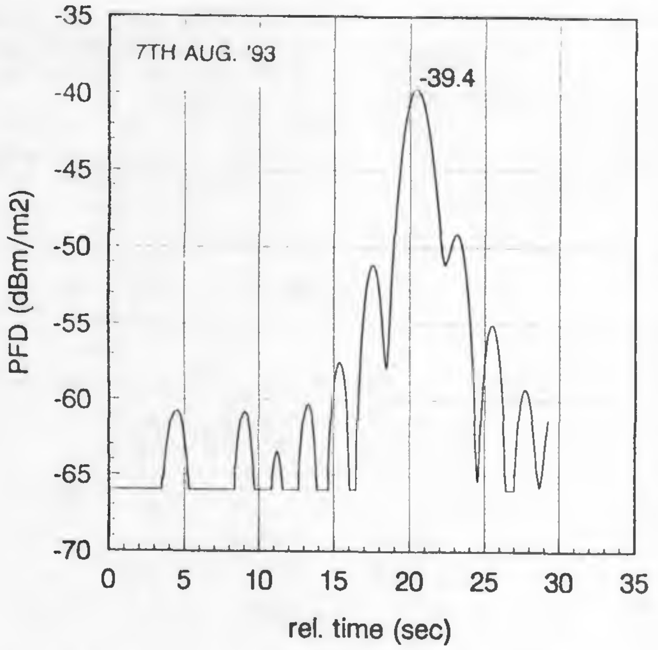

Fig. 4 JERS-1 DOWNLINK FLUX DENSITY MEASUREMENT

L-Band Calibration Activities

As Principal Investigator in the JERS-1 System Verification Program, ESTEC has built an active L-band transponder and deployed it in Flevoland in February 1993 [4]. The design of this transponder was more versatile than those built for calibrating ERS-1, including the capability for dual polarisation and downlink power monitoring, the basic schematic as (Fig 1). In operation the fundamental microwave frequency was 1.26 GHz and the delay used was 5μsec. Horn antennas were used in place of parabolic reflectors and designed to use either V or H polarisation, if required.

With reference to Fig 1, downlink power monitoring is a combination of measurements made both before and after the delay line. The measurements made after the delay with detector D1 are the most accurate, being within the gain loop, they are however limited in dynamic range due to the high intrinsic noise level of the delay line. The highest sensitivity is achieved by measurements made before the delay line

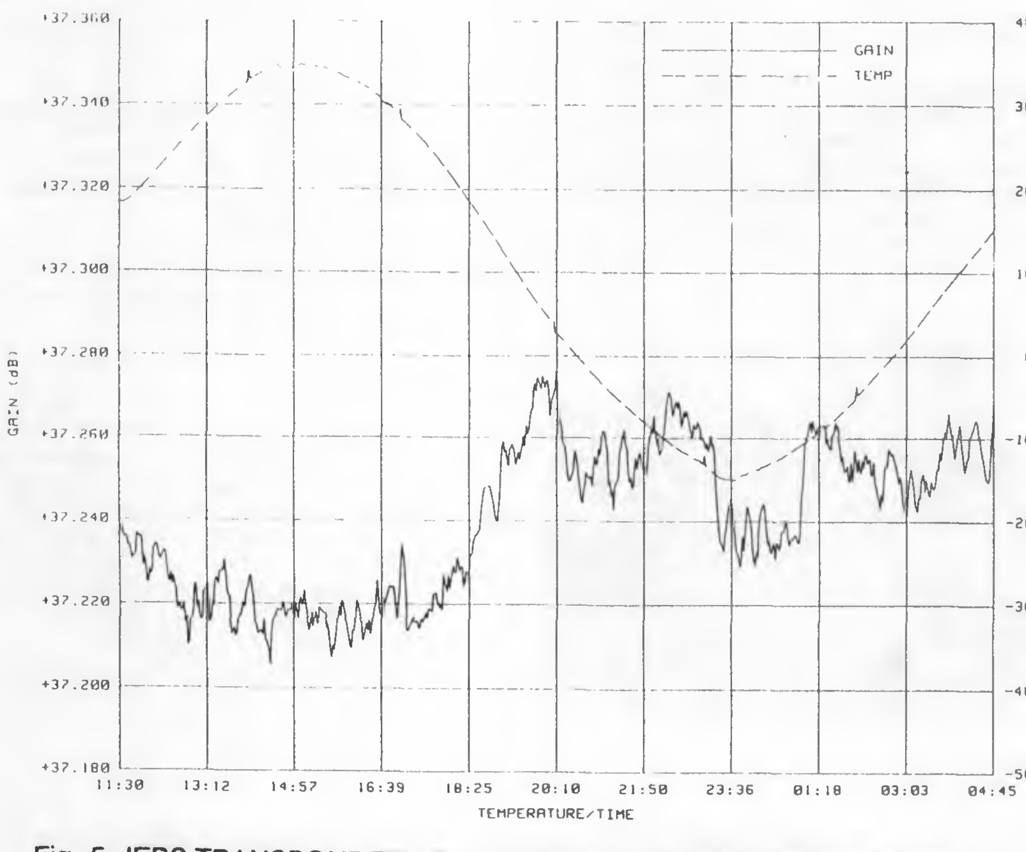

Fig. 5 JERS TRANSPONDER RF UNIT GAIN STABILITY WITH TEMPERATURE

with detector D2. The downlink power flux is extracted from these two data sets and approximately 18 seconds of data can be stored. Figure 4 gives an example of the JERS-1 transmit flux density.

Testing and Calibrating the JERS-1 Transponder

The test program for the JERS-1 transponder follows the same principle as that established for the ERS-1 transponders [1], [2]. The RF and Electronics unit was temperature cycled between -15° and +35°C while measuring the gain stability, Fig 5 shows the overall stability obtained.
The calibration method used is a novel one, being fully described in [1] & [2]. The transponder is set up in an outside range at a distance from a large metal plate. The transponder transmits a series of calibration pulses, which are reflected from the plate and received back by the transponder. The 5μsec delay in the electronics unit allows the transmitted, the received and re-transmitted pulses etc, to be displayed as a decaying series. From the range parameters, the plate RCS and the difference between pulses the RCS of the transponder can be derived.

The flat plate is an accepted standard of RCS provided correct dimensional and alignment accuracies are achieved. The reference plate was of bonded honeycomb construction with the dimensions of 2.5 x 2.5 m^2 and a specified flatness of $\pm$2mm, Fig 6. To minimize edge

Fig. 6 CALIBRATION PLATE USED FOR JERS TRANSP.

diffraction the plate was $\lambda/4$ thick and the edges coated with a microwave absorbing compound. Correct alignment was obtained by a telescope mounted through the centre of the plate which was removed once aligned.
The calibration routine included the estimation of multipath effects, but no significant contributions were found. The main contribution to calibration error were background reflections

Table 2 JERS TRANSPONDER STABILITY AND OVERALL CALIBRATION ERROR

SOURCE	STABILITY (dB)*	ABSOLUTE CALIBRATION ERROR (dB)*	NOTES
1) ANTENNA POINTING			Budget Table 1
with JERS track error +-1 km	<0.001**	<0.002**	
+-5 km	<0.002**	<0.002**	
2) THERMAL STABILITY			
Antenna	0.005	0.005	ERA report 90-0221
Electronics	0.040	0.040	XRI test
3) IMPULSE DISTORSION		0.010	
4) CALIBRATION			
Target plate		0.029	
Range measurement		0.008	+- 5 cm
Multipath + background		0.455	
measurement resolution		0.005	XRI test/ stand. dev
Mutual alignment		0.015	+-1.1 deg.
TOTAL ABSOLUTE CAL. ERROR	0.045	0.567	
RSS	0.040	0.463	

* values given in +- dB
** neglected

STABILITY Variation in RCS of the deployed ARC with multiple observation
ABSOLUTE CALIBRATION ERROR Error in the quoted RCS.

caused by the relatively broad polar diagram of the horn antennas (3dB B.W.= 32°) and the buildings in the vicinity of the test range. Nevertheless the overall calibration error of 0.5 dB meets the specified requirements, Table 2.

Operation
The L-band transponder was built in industry with the Radar Cross Section set to the JERS-1 system requirement of 42 dBm^2. After the extended test and calibration campaign at ESTEC, the transponder was deployed at the Flevoland test site, 1 km south-west of Lelystad airport. This location offers a good opportunity for joint calibration between both ERS-1 and JERS-1 satellites. The deployed unit is shown in Fig 7.

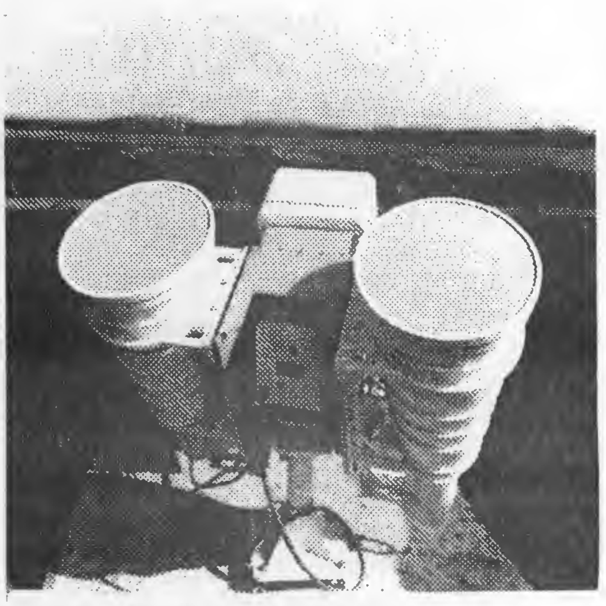

Fig. 7 JERS-1 TRANSPONDER BASED IN FLEVOLAND

Phase stable SAR Calibration

In response to the current interest in differential interferometry, some thought has been given to the long term (>1 day) phase stability of various point targets. Passive reflectors are clearly adequate for many applications but suffer from the same limitations applicable to radiometric stability. Namely, signal to clutter, signal to bi-static multipath, physical aspects such as mounting rigidity, distortion due to wind or temperature differentials and susceptibility to debris accumulation.

Active targets have additional sources of phase instability such as antenna leakage and contributions from both passive and active internal components. Table 3 attempts to quantify some of these errors when used with a 5.3 GHz SAR such as ERS-1. No information on the mechanical aspects of corner reflectors could be found but the figures shown are thought typical. Likewise, no information on active targets using standard gain horns was available but the error due to multipath is likely to be significant. The errors due to bi-static multipath were analysed in [5] and for corner reflectors refer to the square based variety. Rigid mounting requirements are common to all targets and are excluded. Parameters associated with active targets refer, of course, to the ESA transponders the subject of this paper.

The table shows that for movement detection of >1mm, corner reflectors are the obvious candidate, with some reservations associated to long term unattended operation. The table also suggests that the 1mm criteria is a practical fundamental limitation for corner reflectors due to signal/clutter ratio and/or mechanical distortions.

Should < 1mm movement detection become a real requirement, then, for the ESA Transponders, some method of reducing the excessive variation is needed and discussed below.

A Phase Stable Transponder

Figure 8 shows a simplified block diagram of an ESA type transponder modified for phase and group delay stability. The internally generated calibration pulse length is made longer than the delay of the delay line used, creating a portion where the two signals overlap. When seen at the detector these two signals interfere with a resultant amplitude defined by the relative phase of the two signals. The resulting waveform is then digitally sampled and a programmable phase shifter used to correct the input/output phase relationship.

The control loop provides relative phase stability with a 180° control range, this is not sufficient to compensate for the full 5π phase variation of the delay line over the

Table 3 COMPARISON OF POINT TARGET PHASE STABILITY (5.3 GHz)

		1m CORNER REFLECTOR		2.5m CORNER REFLECTOR		ESA ARC	
		+-mm		+-mm		+-mm	
a) SIGNAL/CLUTTER		1.01	19dB	0.40	27dB	0.09	40dB
b) SIGNAL/BISTATIC		0.03	51dB	0.03	51dB	0.07	43dB
c) EFF. ANTENNA ISOLATION		-		-		0.01	96dB
d) MOUNTING RIGIDITY	(40 Km/Hr)	0.5	Est	1	Est	0.2	Est
e) REFLECTOR RIGIDITY	"	0.5	Est	1	Est	0.03	ERA meas
f) REFLECTOR THERMAL	(+- 25deg)	0.5	Est	1	Est	0.46	ERA anal.
g) ANTENNA FEED THERMAL	"	-		-		0.64	Analysis
h) ELECTRONICS	"	-		-		75	XRL meas
	RSS	1.3		1.8		75	

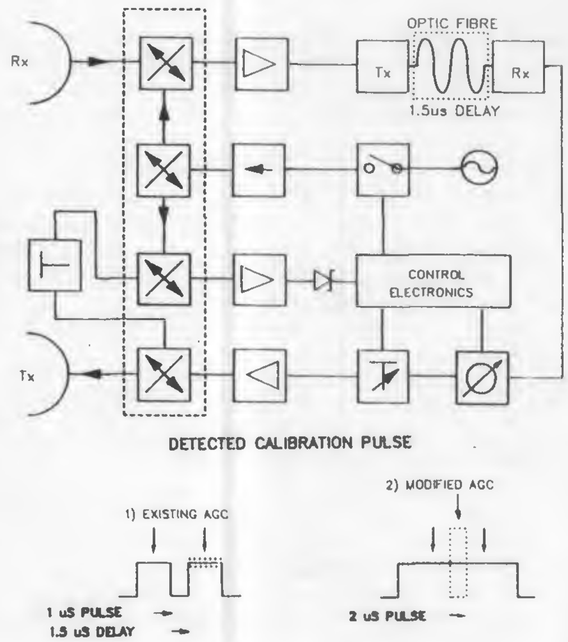

Fig. 8 TRANSPONDER SCHEMATIC WITH PHASE STABILITY MODIFICATION

temperature range of -15 to +35°C. It is thus not possible to obtain stable phase calibration without some other form of compensation. The preferred approach is to temperature stabilise the fibre-optic to about ± 5°C, this limiting the phase variations in the delay line to < 180° and the absolute phase, or group delay of the transponder will be held stable.

Phase instabilities due to thermal effects on the antennas and antenna feeds are predominantly linear with temperature and can be reduced by monitoring the equipment external temperature and introducing compensation into the phase control loop via a look up table.

Conclusions

The ESTEC C-band ground transponders have been used for calibration of ERS-1 since its launch in August 1991. In early 1993, an L-band transponder has also been deployed as part of the System Verification Program for the Japanese JERS-1 satellite. The performance of all the units has met the requirements placed on them and they continue to play a major part in the verification of the data obtained from both satellites.

The R.F. Systems Division of ESTEC is now preparing for future activities in calibration of the new generation of remote sensing satellites such as ERS-2 and ENVISAT ASAR. Other applications such as dual polarisation and interferometry are also being actively considered.

References

1) Development of the ERS-1 Active Radar Calibration Unit. H.Jackson A.Woode. IEEE Trans MTT, Vol 40 No 6, June 1992.

2) The Development and Provisional Results from the ESTEC ERS-1 Active Radar Calibration Unit. A.Woode, Y-L Desnos and H.Jackson. IEEE Trans on Geoscience and Remote sensing Vol 30 No 6 11/1992.

3) ESRIN presentation at this workshop

4) J-ERS-1 and ERS-1 SAR calibration experiments over Flevoland. Y-l. Desnos, J-L Valero, M. Loiselet. Proceedings IGARSS'93, pp.:955-957

5) Internal ESTEC Communication. E.Attema

CORNER REFLECTOR IMAGING BY HIGH RESOLUTION SAR

Jos Groot, Matern Otten
TNO-FEL
P.O.Box 96864
2509 JG The Hague
The Netherlands

September 16, 1993

Abstract

Corner reflectors are commonly used to calibrate and characterise the quality of SAR images. For this purpose it is important that these reflectors behave as point targets. Taking the example of trihedral triangular corner reflectors, it can be shown that these do indeed behave as point targets, even when their physical size is larger than the spatial resolution of the SAR. This has also been verified experimentally by imaging small and large reflectors with high resolution. For SAR calibration using the so-called peak method, large reflectors offer an advantage in that they shield a significant part of the background from the radar, so that the peak of the impulse response function contains practically no background contribution.

Keywords: SAR, corner reflector, impulse response function, calibration

1 Introduction

Radiometric calibration factors and image quality parameters for SAR data are most commonly derived from the impulse response function (IRF) [1]. The IRF of a SAR image is the response to a point target, which is a target with negligible dimensions compared to the spatial resolution, and a large radar backscattering cross section (RCS) which does not depend on the aspect angle. Triangular trihedral corner reflectors (TTCR) are often used as an approximation to point targets, because these are relatively small and have a large RCS over a large beamwidth ($\approx 40°$) [2,3]. Most current SAR systems operate in the wavelength range from X- ($\approx$3 cm) to P-band ($\approx$68 cm), while corner reflector dimensions range from well below 1 m to 2.5 m [4]. The highest resolution obtained by civil modern airborne SAR systems is better than 1 m (azimuth) or 2 m (range) [5,6,7]. Military radars are known to attain resolutions down to a few decimeters. The TCR's are thus often as large as or even larger than the resolution. It is not clear beforehand what kind of effect this has on the measured IRF, for example with respect to the 3 dB resolution, and on radiometric calibration. This paper discusses these matters.

Section 2 gives results of the geometrical optics theory applied to the corner reflector backscattering problem. This is used in Section 3 to derive the IRF for a corner reflector which is large compared to the resolution, followed by a discussion of the implications. Section 4 contains results of processing C-band SAR data up to 1.1/4.5 m azimuth/range resolution, confirming the findings of Section 3.

2 Geometrical optics theory for corner reflectors

The most frequently used corner reflector type is the triangular trihedral corner reflector (TTCR). It consists of three identical metal triangular plates, connected at right angles to each other (Fig.1).

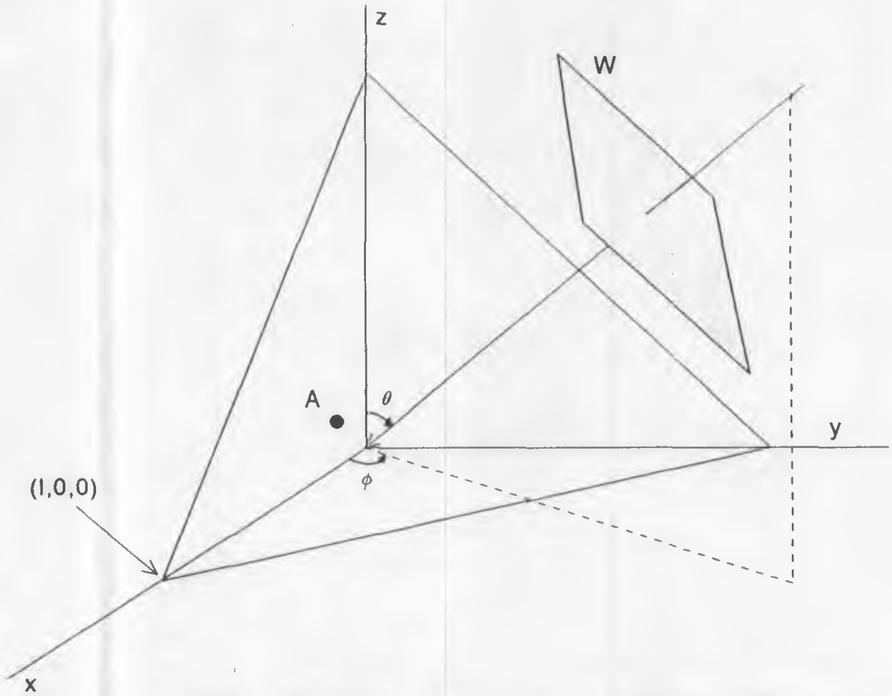

Figure 1: Triangular trihedral corner reflector (TTCR).

The length of the short sides of any of the triangles is l. Its RCS depends on the radar wavelength, the leg length l, and the aspect angle (azimuth ϕ, incidence angle θ in Fig.1). When the TTCR is large compared to the wavelength, the geometrical optics approximation may be used to compute the backscattered field induced by a plane wave incidence on the TTCR [8]. In this approximation electromagnetic fields are represented by rays oriented in the propagation direction. Assume that a plane wave is incident on the TTCR from the direction (ϕ,θ), with wavefront W. The wavefront is represented by rays which are directed towards the corner reflector. The following statements hold [9,10,11]:

1. A ray is 0, 1, 2 or 3 times reflected, depending on its incidence angle and incidence position A on the TTCR. Rays reflected three times return in the exact opposite direction.
2. The distance travelled by the rays between leaving plane W and crossing it again after three reflections is the same for all rays and independent of the aspect angle, and equals twice the shortest distance between the plane and the apex (the origin in Fig.1).
3. Because of 1. and 2. the RCS is large, and relatively independent of the direction of incidence (beamwidth $\approx 40°$). The RCS is the same as that of a flat plate, *oriented orthogonal to the incident direction.* The shape (and size) of this 'equivalent flat plate' is found by projecting all points A for which three reflections occur onto a plane through the apex, perpendicular to the incident direction. Because not all points result in three reflections, the flat plate is always included in the projection of the boundary of the TTCR onto the same plane. The flat plate includes the apex because of 2. Fig.2 shows the plate shape for a TTCR as a function of incidence angle θ, for a fixed azimuth of $\phi = 45°$.

For decreasing TTCR size to wavelength ratios diffractional effects become increasingly important, and geometrical optics results will differ from experimental results. Differences also occur for incidence far from boresight, because single- and double bounce backscattering give rise to interference. However, research conducted in the past [3,10] proved that geometrical optics results are valid, as long as the TTCR aperture size exceeds 2-3 wavelengths.

It is implicitly assumed that the incident field on the TTCR does not exhibit significant wavefront curvature. This assumption is valid as long as the following inequality holds:

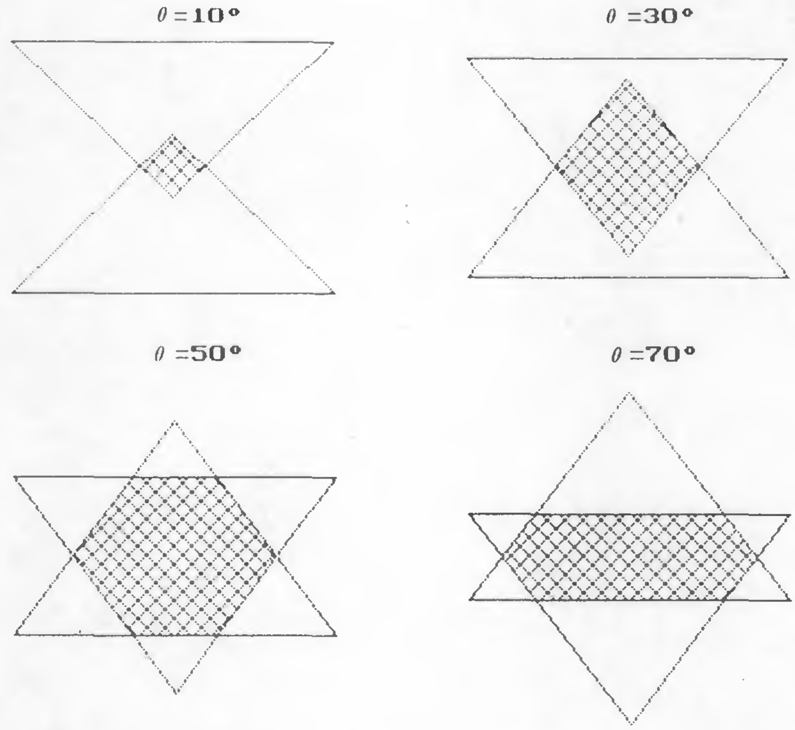

Figure 2: Equivalent flat plate shape (cross-hatched) for a TTCR as a function of incidence angle θ, for a fixed azimuth of $\phi = 45°$ (from [11]).

$$a < \frac{\sqrt{\lambda R}}{2}, \tag{1}$$

with λ the wavelength, a the maximum flat plate dimension, and R the antenna-plate distance. This, in fact, means that the change in range from a fixed point to a point on the plate does not vary more than one 8^{th} of a wavelength. For a minimum wavelength of 5 cm and minimum range of 5 km, the TTCR size should be no more than 8 m, according to this criterion.

3 SAR imaging of corner reflectors

3.1 Range imaging

SAR achieves its high slant range resolution by conventional pulse compression techniques. If the TTCR can be modelled as a flat plate, the range curvature criterion is satisfied, and so the two way path length travelled by the transmitted pulse will vary only a fraction of the wavelength over the extent of the TTCR. It will therefore appear as an object much smaller than the range resolution, i.e., as a point target.

3.2 Azimuth imaging

SAR achieves high azimuth resolution by correlating the received complex signal with a reference function containing the point target phase history. This corresponds to the formation of synthetic apertures along the flight direction. Consider the received signal over the synthetic aperture length. When the TTCR is fully illuminated during the synthetic aperture time, and the SAR antenna stays within the beamwidth of the TTCR, the received signal has constant amplitude and the phase varies according to the range variation. In other words, the signal is identical to that of an actual point target, and thus the response after processing will be the IRF. The first condition *must* be satisfied in order for the SAR principle to work. It can be shown that the second condition is then also satisfied. The first condition implies that the synthetic aperture length L cannot be longer than the illuminated area (in azimuth) which is determined by the *real* beamwidth of the SAR antenna, so that:

$$L < \frac{\lambda}{D} R, \tag{2}$$

where D is the real aperture size, and R the antenna-TTCR distance. For the second condition to be satisfied, the SAR antenna must stay within the corner reflector beamwidth θ_{CR} over an interval equal to L, so the following inequality should hold:

$$L < \theta_{CR} R, \tag{3}$$

This inequality is certainly satisfied when:

$$\frac{\lambda}{D} < \theta_{CR}, \tag{4}$$

since inequality (3) can be derived from (2) and (4). If for θ_{CR} the 1-dB beamwidth of a TTCR is substituted, which is about 0.4 radians, the second condition becomes:

$$D > 2.5\lambda, \tag{5}$$

This is true for all practical SAR antennas.

3.3 Implications

The preceding sections showed that, with realistic assumptions, the response function of a TTCR is the IRF itself, despite the fact that its dimensions may exceed the spatial resolution. Image quality parameters (resolution, peak side lobe ratio etc.) can be savely derived from a TTCR response. Fig.3 shows the simulated response of a high resolution SAR to a TTCR.

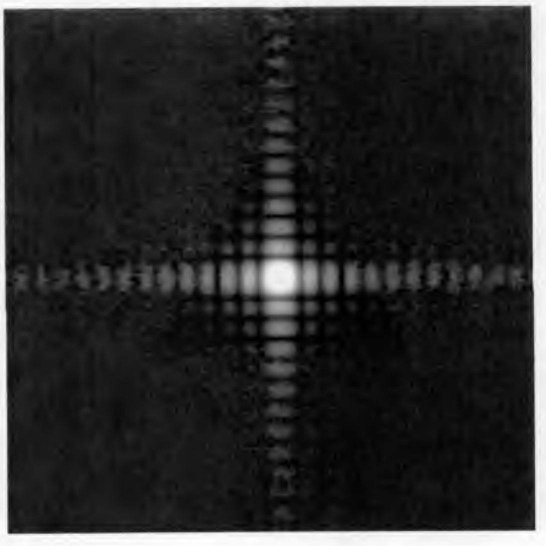

Figure 3: Simulated response (pixel size 5 cm) of a 25 cm azimuth/range resolution C-band SAR to an $l = 2.5$ m TTCR imaged at boresight (RCS= 47 dBm^2), with background scattering coefficient σ^0 =20 dB.

The corner reflector covers part of the background and causes a triangular low response region in the background, with the IRF main lobe at the centre. To enhance the visibility of the triangle, the background σ^0 was set to the (unrealistically high) value of 20 dB. The image was produced by generating speckle, eliminating the speckle in the triangular projection of the TTCR's aperture, convolving the result with the IRF (causing the low response in the triangle), and finally superposing the IRF.

Radiometric calibration of SAR data with TTCR's is usually done with one of two methods, the integral or the peak method [12,13]. The integral method calibration factor involves the integral of the image pixel power over a small area containing the IRF, minus an estimate of the background contribution due to clutter and noise. The peak method calibration factor involves the IRF peak value, which cannot be corrected for the background contribution. It has been proven that the RMS error resulting from the peak method is always smaller than or equal to that from the integral method for a well-focused SAR. However, the integral method is to be preferred because it is insensitive to focus errors and does not require detailed knowledge of the IRF.

From Fig.3 it is clear that if the triangular region is larger than the resolution cell, the peak method has the additional advantage of being (almost) independent of the background backscatter. In case of the integral method the background subtraction should ideally be corrected for the low response part. This correction is usually negligible.

SAR images of urban areas are often dominated by high responses resulting from scattering by dihedral or trihedral corner reflector structures, formed by the vertical walls of buildings and the horizontal ground ([2], section 11-3.4). From the preceding sections it follows that the spatial extent of the SAR response to these structures may often be smaller than the structures themselves.

4 Experimental verification

Current civil SAR systems have resolutions which do not permit direct detection of the low response triangle. In 1991 data was obtained with the C-band PHARS system [6] of two series of corner reflectors with sizes of 0.65, 0.93, 1.43 and 2.44 m. The three smaller size corner reflectors had a square base plate instead of the triangular plate of the 2.44 m TTCR. The data was processed for an azimuth/slant range resolution of 1.0/4.4 m (Fig.4), without weighting, utilizing the maximum Doppler- and system bandwidths of the PHARS. Obviously, the azimuth resolution is much smaller than the two largest reflector sizes.

Figure 4: PHARS image of row with 7 corner reflectors.

Before interpreting the experimental results, the relation between the size of an object and its SAR response width was investigated for the case of two separated identical point targets and a flat plate. The 1-dimensional SAR response to two point targets separated by a distance l is the sum of two $\operatorname{sinc} x \equiv \sin x/x$ functions, i.e.,

$$p(x) \propto \left| \mathrm{sinc}(a(x - \frac{l}{2})) + \mathrm{sinc}(a(x + \frac{l}{2})) \right|^2, \tag{6}$$

with $p(x)$ the pixel power at azimuth or slant range image coordinate x, and $r \approx 2.783/a$ the resolution of the IRF of a single point target. A physical optics approximation of the response to a flat plate of length l was taken from [14]. Fig.5 gives the fractional increase of the response width relative to the system resolution r with increasing l/r ratio.

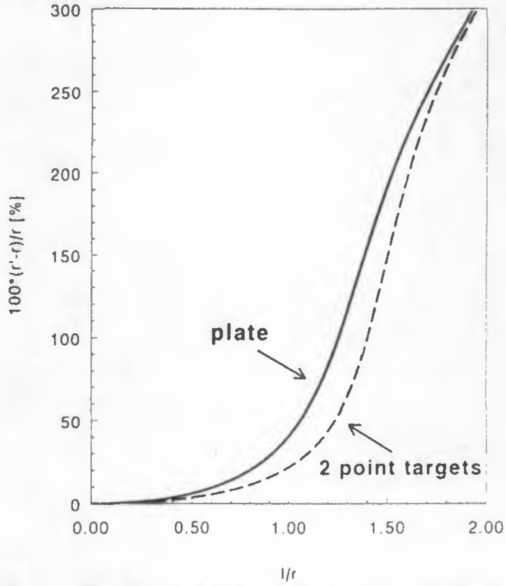

Figure 5: Fractional response width increase as a function of increasing plate length and point target separation l.

It shows that the effect of size on the apparent resolution becomes important (exceeds 10%) as soon as the plate size (point target separation) exceeds 0.60 (0.75) times the actual system resolution. This strongly suggests that if corner reflectors do *not* behave as single point targets, some of the imaged corner reflectors are large enough to reveal any broadening effect.

Table 1 shows the PHARS data analysis results. Two groups of corner reflectors were placed at different incidence angle ranges in bare soil fields in the Flevopolder, the Netherlands. The apparent resolutions are close to the expected resolution.

	$\theta = 35° - 42°$		$\theta = 50° - 55°$	
l	ρ_r	ρ_a	ρ_r	ρ_a
2.44	4.93	1.09	4.76	1.11
2.44	4.71	1.09	4.52	1.13
1.43	4.56	1.10	4.47	1.15
1.43	4.47	1.09	4.45	1.13
0.93	4.47	1.08	4.43	1.16
0.93	4.55	1.14	4.43	1.13
0.65	4.71	1.12	4.53	1.11
average	4.63	1.10	4.51	1.13
st.dev.	0.17	0.02	0.12	0.02

Table 1: Apparent resolutions determined from TTCRs, in meters.

Figure 6 shows a range- and azimuth response of one of the corner reflectors.

In range, there is some deformation of the response, causing a resolution slightly exceeding 4.4 m, due to phase distortion in the receive channel. There is also some spread in the measured values. Whether this

6

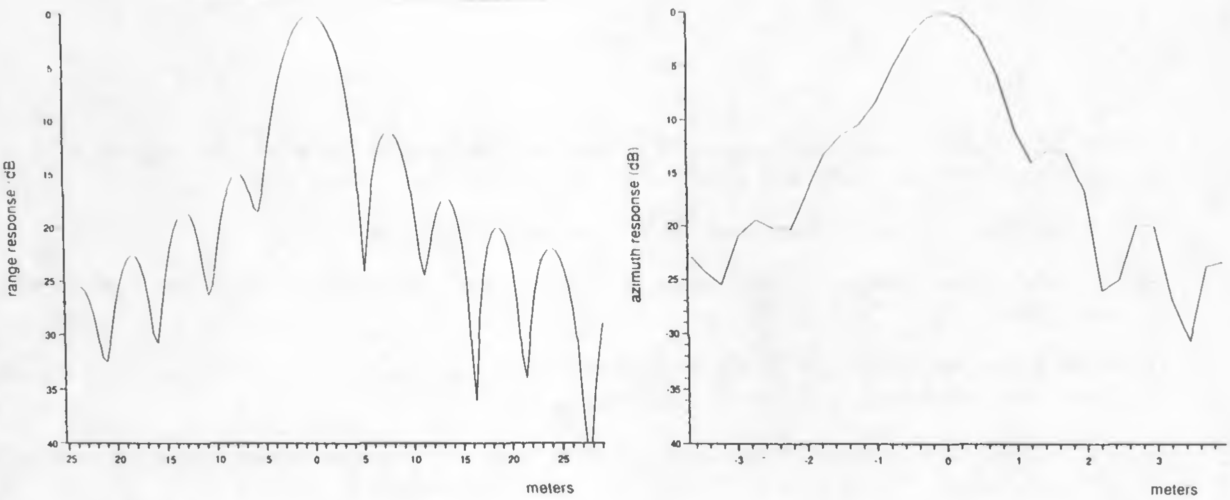

Figure 6: Range and azimuth responses of a 2.44 m corner reflector.

is caused by some system instability, or other factors is not quite clear. In any case, there is hardly any correlation with reflector size. In azimuth this is even more evident. The small deviation from the ideal 1.0 m resolution is most likely caused by a residual velocity error (no autofocus was used).

5 Conclusions

It can be argued, using geometrical optics, that Triangular Trihedral Corner Reflectors appears to a SAR imaging system as a single point target, even when the physical size of the TTCR is larger than the spatial resolution of the SAR. This has been verified experimentally, by imaging TTCRs of different sizes with high resolution. In fact, no significant correlation was found between physical size and SAR response width, while this width was less than the actual size of the larger TTCRs. For SAR calibration, a large TTCR even offers an advantage when the peak method is used: the IRF peak value contains practically no background contribution, since the background is shielded from the radar by the TTCR itself.

6 Acknowledgements

We thank R.J. Dekker for carefully (and repeatedly!) processing and analyzing the PHARS data, and JPL for the use of their 2.44 m corner reflectors.

References

[1] A. Freeman. SAR calibration: an overview. *IEEE Tr. on GeoS. and RS.*, 30(6):1107–1121, November 1992.

[2] F.T. Ulaby et al. *Microwave Remote Sensing.* Volume II, Addison-Wesley, 1982.

[3] G.T. Ruck *et al. Radar Cross Section Handbook.* Volume 2, Plenum Press, New York, 1970.

[4] A. Freeman, J.C. Curlander, F. Heel, M. Zink, P. Hoogeboom, J. Groot, A. Dawkins, J. Baker, M. Reich, and H. Lentz. Preliminary results of the multi-sensor, multi-polarization SAR calibration experiments in Europe 1989. In *Proc. IGARSS'90, Washington D.C., USA*, pages 783–787, May 1990. Ref. ESA SP-284.

[5] S.N. Madsen, E.L. Christensen, N. Skou, and J. Dall. The Danish SAR system: design and initial tests. *IEEE Tr. on Geos. and RS.*, 29(3):417–426, May 1991.

[6] P.J. Koomen P. Hoogeboom, P. Snoeij and H. Pouwels. The PHARUS project, results of the definition study including the SAR testbed PHARS. *IEEE Tr. on GeoS. and RS.*, 30(4):723–735, July 1992.

[7] M. Zink, F. Heel, and H. Kietzmann. The Oberpfaffenhofen SAR calibration experiment of 1989. *J. of Electromagnetic Waves and Applications*, 5(9):935–951, September 1991.

[8] M. Born and E. Wolf. *Principles of Optics*. Pergamon Press, 1964.

[9] S.D. Robertson. Targets for microwave radar navigation. *Bell Systems Technical Journal*, 26:852–869, 1947.

[10] K.M. Keen. New technique for the evaluation of the scattering cross-sections of radar corner reflectors. *IEE proceedings Pt.H*, 130:322–326, August 1983.

[11] J.S. Groot. Cross section computation of trihedrals with the geometrical optics approximation. *European Tr. on Telecom. and RT.*, 3(6):637–642, November 1992.

[12] A.L. Gray et al. Synthetic aperture radar calibration using reference reflectors. *IEEE Transactions on Geoscience and Remote Sensing*, 28(3):374–383, May 1990.

[13] L.M.H. Ulander. Accuracy of using point targets for SAR calibration. *IEEE Tr. on Aerosp. and Elect.*, 27(1):139–148, January 1991.

[14] E.L. Johansen. The synthetic-array radar image of a flat plate. *IEEE Tr. Aerosp. and Elect.*, 395–398, May 1970.

CALIBRATION OF ERS-1 SAR

P.J. Bird, G.E. Keyte, D.R.D. Kenward

Defence Research Agency
Farnborough, UK.

ABSTRACT

A calibration site containing a number of large (47 dBm^2) corner reflectors was established at Romney Marsh, UK for the ERS-1 SAR Commissioning Phase. The reflectors were constructed with a radar cross-section accuracy of ± 0.3 dB and were found to have a stability of approximately the same order. Subsequently, the site has been in continuous use, which has allowed assessment of ERS-1 SAR and the targets over a period of two years. Results indicate that the SAR has been stable to within ± 1 dB and that there appears to be no long-term drift in performance. In addition, the cross-track calibration has been measured during the Multi-disciplinary Phase using a further set of reflectors deployed in East Anglia, UK. Analysis of images corrected for antenna gain has revealed a residual effect of approximately 1 dB across the swath-width. Measurements carried out at both sites have also allowed investigation of a reflector radome and a comparison to be made between day and night-time passes.

Keywords: ERS-1 SAR calibration, corner reflector, radome.

1. INTRODUCTION

Future SAR systems are expected to utilise active phased array antennas with electronic beam steering and beam shaping. For these the antenna gain pattern will generally vary depending on how the beam is steered. There may also be temporal variations in the overall transmitted power and in the antenna gain pattern caused by fluctuations in temperature of active elements in the antenna and also by ageing effects. With active antennas the implementation of effective on-board calibration systems is difficult and it will generally be necessary to use external calibration targets as a means of measuring the antenna pattern as well as to verify the overall system performance.

A number of calibration targets having an accurately known radar cross-section may be used in principle to provide a means of measuring the antenna gain pattern, whilst repeated observations of a fixed set of calibration targets over a period of time will enable temporal variations to be monitored. This paper describes the development and test of calibration targets for space SAR using the opportunity offered by ERS-1 SAR to investigate the ability of such devices to measure the antenna gain pattern and long-term stability.

2. SAR CALIBRATION STRATEGY

2.1. Calibration target selection

The main calibration targets used for ERS-1 SAR were trihedral corner reflectors. These were chosen because they were relatively inexpensive to construct and because their radar cross-section can be accurately determined from a precise measurement of their dimensions, i.e. they are primary calibration targets. The precision corner reflector used for the ERS-1 trials is described in section 3. Additionally, a prototype transponder was developed at DRA and the results of initial tests are noted in section 4.

2.2. Deployment plan

The corner reflector deployment plan was based on the different phases of ERS-1 operation. These were:-

(i) Commissioning Phase (July - December 1991) - 3 day repeat orbit.

(ii) First Ice Phase (December 1991 - March 1992) - 3 day repeat orbit.

(iii) Multi-disciplinary Phase (April 1992 - December 1993) - 35 day repeat orbit.

The Commissioning Phase provided an opportunity to obtain frequent revisits of a calibration site and thus allowed the stability of the reflectors to be monitored and established confidence in their use for long-term calibration. The Commissioning Phase experiment was carried out at Romney Marsh, UK and is summarised in section 4.

No calibration activities were performed during the Ice Phase due to the shift in the position of the 3-day repeat orbit. For the Multi-disciplinary phase the following activities were carried out:-

(i) Cross-track calibration measurements using five precision corner reflectors deployed in East Anglia, UK.

(ii) Long-term assessment of the ERS-1 SAR calibration using the Romney Marsh calibration site for both descending (day-time) and ascending (night-time) passes. During this period the corner reflector configuration was changed to investigate differences between descending and ascending passes and the effect of radome attenuation.

2.3. Analysis procedure

The analysis of the calibration target signatures was carried out using standard ESA ERS-1 PRI products, produced mainly by the UK processing centre but with some additional products supplied by the German and ESRIN processing centres. The PRI product is a single frame measuring approximately 100 km by 100 km and is presented as a 3 - look amplitude image sampled on a 12.5 m grid in azimuth and ground range.

The following corrections were applied to the images where necessary:-

(i) Antenna gain pattern : applied to correct for images processed without cross-track antenna gain (Ref.1).

(ii) Range spreading loss : applied to correct for variation in range (R^3) (Ref.1).

(iii) Processor bias : applied to correct for differences in gain between the different processing centres (Ref.1).

(iv) Mis-alignment of corner reflectors.

(v) Replica pulse power : errors in the replica pulse power were found during the Commissioning Phase which required corrections to be made. The replica power has been relatively stable since this time.

The procedure used to measure the target image response is described below. The software used was developed by DRA and implemented on an IBM PC.

A sub-image of 50 by 50 pixels centred on the point target was extracted from the image. Next, the background intensity was determined; the size and position of the pixel regions used were selected from the area surrounding the point target. This ensured that nearby bright points were avoided, thus allowing accurate determination of the mean background. The mean background was subtracted from the sub-image, to leave an image containing only the point target. The integrated point target power was then calculated from a 9 by 9 pixel region centred on the peak pixel intensity and chosen to ensure that the mainlobe and first sidelobes were included. The absolute calibration of the SAR image requires that the system noise be taken into account and that an additional correction be applied for sidelobe energy (approximately 0.1 dB).

3. CORNER REFLECTOR DESIGN

The principle targets used for ERS-1 SAR calibration were trihedral corner reflectors (Ref.2). The reflectors were made from sheets of aluminium faced honeycomb sandwich on jig built frames, using shims to ensure that the faces are exactly orthogonal and flat. The frames were erected on a purpose built base frame which was accurately aligned with the satellite track and permitted an incidence angle adjustment of ± 5 deg. The side length of the reflectors was 2.570 m providing a theoretical radar cross-section of 47.56 dBm^2. The calculated radar cross-section error budget (taking into account deviation from flatness and orthogonality) was found to be less than ± 0.3 dB. This was also confirmed by antenna range measurements.

In an attempt to maintain a constant radar cross-section in all weather conditions a radome was developed consisting of a Gore-Tex fabric stretched over the trihedral aperture. Figure 1 shows a 2.57 m corner reflector at the Romney Marsh calibration site.

4. PRELIMINARY TRIALS (ERS-1 COMMISSIONING PHASE)

Four 2.57 m corner reflectors were assessed during the Commissioning Phase at a site on Romney Marsh, Kent (Ref.3). The location of the site and the 3-day repeat swath are shown in Figure 2. The reflectors were deployed on large, level bare soil and grass fields. These were found to provide a target signal-to-clutter ratio of approximately 30 dB for the standard ERS-1 PRI (3-look) SAR image. A radome cover was tested on one of the reflectors.

The corner reflector signatures were measured for 18 images all produced at the UK processing centre using the procedure described in section 2. The results, which are plotted in Figure 3, show variations in the signatures of nearly 2 dB in August and again in October. These variations were found to be due to errors in the replica pulse power. The reflector powers were corrected relative to the replica power level for the pass on 24 October, which was believed to be uncorrupted. The resulting graph is shown in Figure 4. The large decrease in the response of reflector 3 on 11 November is believed to be due to the effect of rain water droplets on the radome cover.

An assessment of the variations in the reflector image signatures was carried out. Table 1 summarises the results, together with results for the DRA transponder which was operated at the Romney Marsh site for 6 passes with a radar cross-section of 58.0 dBm^2 (Ref.4). It has been shown experimentally (Ref.5) and theoretically (Ref.6) that a peak signal-to-clutter ratio of 30 dB will give a standard deviation for the integral estimate of the point target signature of approximately 0.2 dB. The variations shown in Table 1 are consistent with this result, indicating that the targets were stable and that the overall ERS-1 SAR radiometric stability was good during the Commissioning Phase.

Table 1. Variations of reflector and transponder image signatures during the Commissioning Phase.

Target	Number of images analysed	Mean power in mainlobe (dB)	Standard deviation (dB)
Reflector 1	18	85.64	0.24
Reflector 2	18	85.41	0.22
Reflector 3*	16	85.22	0.21
Reflector 4	18	85.42	0.25
Transponder	6	96.14	0.21

* Radome cover.

Conclusions resulting from the preliminary trials can be summarised as follows:-

(i) The corner reflectors were constructed with a radar cross-section accuracy of ± 0.3 dB.

(ii) The deployment methodology and rigidity of the corner reflector panels provided a very stable calibration target. Although the accuracy of the reflectors was maintained by regular cleaning and inspection, the use of radomes should allow them to be used unattended for long periods of time.

(iii) The radome cover produced a signal attenuation of 0.2 - 0.4 dB although this increased in the presence of rain water droplets. Further investigation is required to develop an all-weather radome.

(iv) The stability of the corner reflector image response was high comparable to that of the DRA transponder.

5. CROSS-TRACK CALIBRATION (ERS-1 MULTI-DISCIPLINARY PHASE)

5.1. Background

The aim of this work was:-

(i) To verify the stated ERS-1 SAR antenna pattern(Ref.2).

(ii) Investigate the problems of using arrays of targets for steered beam SAR calibration.

The corner reflectors used were made to the same design as those described in section 3. Five locations were selected in East Anglia, UK, chosen because this area is generally level and is relatively free of features which could cause interference with the target signatures. Figure 5 shows the location of the sites and the position of the ERS-1 descending swaths during the Multi-disciplinary Phase. Swath 51 covers all five reflectors, with the adjacent swaths (280 and 323) providing partial coverage.

The reflectors were deployed from mid-1992 onwards and were occasionally moved or adjusted as a result of image analysis. None of the targets were covered by radomes and each of them were inspected and if necessary cleaned before a satellite pass.

5.2. Results

Figure 6 shows the cross-track variation in the reflector signatures for three consecutive passes for swath 51. The images were supplied by the UK processing centre and included corrections for the antenna gain pattern and range spreading loss. Other corrections outlined in section 2 were applied.

A slope from the near edge to the far edge of the swath is seen with an apparent 'kink' for the reflector at Feltwell. The latter was explained when an inspection of the Feltwell target revealed a minor distortion in one of the reflector faces which has since been corrected. The antenna power distortion appears to be uniform with a gradient of approximately 1 dB over the full swath-width indicating that the antenna pattern has been correctly applied to within 1 dB.

An attempt was made to include reflector signatures measured from the adjacent swaths (280 and 323) in the cross-track analysis. However, correlation between the target powers from these swaths was not good. As yet, the cause of the discrepancies is not known.

6. LONG-TERM TRIALS (ERS-1 MULTI-DISCIPLINARY PHASE)

6.1. Background

After the preliminary trials at Romney Marsh a long-term evaluation of ERS-1 SAR calibration was conducted using the same site. The prime objective was to investigate whether any long-term drift had occurred in either the transmitter or receiver of ERS-1 SAR. In addition, the relationship between descending (day-time) and ascending (night-time) passes was investigated (this is important because the SAR antenna may change shape in going from eclipse into sunlight and hence the gain may alter). Also, further tests were made on the radome in an attempt to assess it's performance when rain was falling. The corner reflector deployment sequence is shown in Table 2.

Table 2. Corner reflector deployment at Romney Marsh during the Multi-disciplinary Phase.

Period	Descending	Ascending	Comment
12/5/92 - 28/7/92	2R	1R	Comparison of descending (day) and ascending (night) passes.
29/7/92 - 23/10/92	2R + 2U	—	Comparison of radome with open reflectors.
24/10/92	4U	—	Stability check on all reflectors.
4/11/92 - 26/5/93	2R	2R	Comparison of descending and ascending passes.

R : Radome. U : Uncovered.

During the Multi-disciplinary phase the Romney Marsh site was imaged by two descending and two ascending swaths. The corrections outlined in section 2 were applied in order to allow comparison of the target signatures for these different swaths.

6.2. Results

6.2.1. Overall radiometric stability

Figure 7 shows the variation in corner reflector signatures for descending passes over the period August 1991 to May 1993, i.e. ~ 9000 orbits. The first set of data (orbits 0-2000) show the signatures measured during the Commissioning Phase. This set of data is identical to that shown in Figure 4 and is shown here for comparison.

The data plotted for orbits 4500-9500 are those obtained during the Multi-disciplinary phase. The results for this period show significant variations in the reflector signatures in the order of 1 dB. Since the graph shown in Figure 7 includes data from two adjacent swaths, the variability may partly be explained by the antenna gain variation found for the East Anglia experiment, i.e. the targets are located at different across-track positions for the different swaths. A further contribution to the variability may be explained by the inclusion of data from several images produced at the German and Esrin processing centres. For these images no correction was made for the replica pulse power.

Figure 8 shows data plotted for just one of the descending swaths, with all images being produced at the UK processing centre. A significant reduction in variability is observed. Table 3 summarises the data plotted in

Figure 7 for reflectors 4B and 4D. A correction was made to allow comparison of radome covered and open reflectors. The mean target power has decreased from the Commissioning Phase by approximately 0.6 dB and the variability is significantly greater (compare with Table 1). Table 4 summarises the data plotted in Figure 8 for reflectors 4B and 4D. By considering one swath and UK processed images only, the variability is reduced but still larger than that found during the Commissioning Phase.

Table 3. Variation of reflector signatures for all descending passes at Romney Marsh during the Multi-disciplinary Phase.

Reflector	Number of images analysed	Mean power in mainlobe (dB)	Standard deviation (dB)
4B*	17	84.57	0.52
4D*	19	84.67	0.45

* Radome cover.

Table 4. Variation of reflector signatures for one swath and UK processed images only.

Reflector	Number of images analysed	Mean power in mainlobe (dB)	Standard deviation
4B*	7	84.57	0.44
4D*	9	84.60	0.33

* Radome cover

These results seem to indicate that over the 24 month period ERS-1 SAR is stable to within ± 1 dB but the variation does not appear to indicate a long-term drift due, for example, to ageing of the high power amplifier. The variations appear to be due to other systematic causes which if corrected could provide an overall system stability of < 1 dB.

6.2.2. Radome assessment

The results obtained for the four passes between orbits 5400-6500 (Figure 7) allowed a comparison of reflectors fitted with radomes to those left uncovered. The radome caused a mean attenuation of approximately 0.3 dB which confirmed the results obtained during the Commissioning Phase. For orbit 6666, where all four reflectors were uncovered, the signatures are almost identical indicating that the reflector radar cross-sections are in very good agreement.

The remaining data in Figure 7 (orbits 7000 - 9500) show the results for two covered reflectors. There is increased variation between the reflectors themselves for this period, which is attributed to a combination of increased background clutter and changes in radome transmittance caused by rainfall or condensation. Table 5 shows a comparison of covered and open reflector stability. Variations in the differences between target signatures were calculated for the covered reflectors 4B and 4E (at Romney Marsh) and for the open reflectors at the Boxworth and Feltwell sites, East Anglia. The images used were spread over the same time period and the background clutter was similar for all reflectors. The smaller variations seen between the open reflectors indicate that the radome does account for some of the signature variability, probably as a result of increased rainfall during this period. This is currently being verified by use of a weather station which records any rainfall at the time of the satellite pass.

Table 5. Comparison of covered and open reflector stability.

Reflector	Number of images analysed	Mean difference in signatures (dB)	Standard deviation (dB)
4D* - 4B*	12	0.14	0.27
Boxworth+ - Feltwell+	6	0.21	0.17

* Radome cover.
\+ Open.

6.2.3. Descending (day-time) and ascending (night-time) comparison

Figure 9 shows the variation in reflector signatures for ascending passes during the Multi-disciplinary Phase. No data was obtained for orbits 5000 - 7000 when all reflectors were aligned for descending passes. The results show variations in the signatures of a similar magnitude as found for descending passes. Note, data is included from two adjacent swaths and was measured from a combination of UK and ESRIN processed images.

Table 6 summarises the data plotted in Figure 9. Both reflectors were fitted with radomes for all ascending passes. The mean target powers and signature variability are similar to that found for descending passes (compare with Table 3).

Table 6. Variation of reflector signatures for all ascending passes at Romney Marsh during the Multi-disciplinary Phase.

Reflector	Number of images analysed	Mean power in mainlobe (dB)	Standard deviation (dB)
4A*	12	84.68	0.53
4C*	9	84.41	0.47

* Radome cover.

Figure 10 compares the variation in reflector signatures for a number of descending and ascending passes. Two swaths were considered (one descending and one ascending) with all images produced at the UK processing centre. No significant differences between day and night images are evident.

Finally, the stability of the reflectors themselves was checked for ascending passes by assessing the variation between the signatures. The results, shown in Table 7, indicate that the reflectors are less stable for the night-time passes (compare with Table 5) possibly as a result of condensation on the radome.

Table 7. Assessment of reflector stability for ascending passes.

Reflector	Number of images analysed	Mean difference in signatures (dB)	Standard deviation (dB)
4A* - 4C*	9	0.19	0.42

* Radome cover.

7. FUTURE WORK

The corner reflectors were originally designed for use at a specified azimuth and elevation setting. An improved base has now evolved which allows the target to be rotated to align with descending and ascending passes. This base is planned for use in measuring the antenna pattern for descending and ascending passes where thermal stresses on the SAR antenna may cause significant changes. A second design of base is now in use at Romney and this incorporates both azimuthal and elevation adjustments. This design is being evaluated as a means of calibrating the different beams used by RADARSAT and ASAR and will be tested using the shuttle imaging radar, SIR-C.

A further improvement to the corner reflector design involves the development of a new radome. Although the radome concept has been demonstrated as being feasible, the trials conducted using ERS-1 SAR have shown that improvements in design are required to ensure better stability. Consequently, a more stable rigid radome is currently under development which should allow the reflectors to be used unattended for long periods of time in all weather conditions.

Considering the future development of active phased array radars it is clear that the requirement for ground-based calibration targets will increase. At the present time it is considered that for C-band SAR, transponders and corner reflectors can be made to similar levels of accuracy in radar cross-section. The advantage of transponders is their ability to produce radar cross-sections of different values to suit the imaging mode of the SAR. However, transponders are considerably more expensive (2-6 times) than corner reflectors and this will inhibit their use is significant numbers. Hence, a requirement exists for both kinds of targets and development of both is planned for the future. A low cost, accurate transponder has recently been developed at DRA and is currently being tested using ERS-1 SAR.

Further calibration work includes more tests of ERS-1 SAR to investigate the reason for apparent changes of up to 1 dB in overall gain and also further tests to establish the number of targets needed for accurate antenna pattern measurement.

8. CONCLUSIONS

It has been shown that the DRA corner reflectors can be constructed with a radar cross-section accuracy of within ± 0.3 dB and have a stability of approximately the same order. This compares favourably with transponders. However, work is required to improve the radome design to allow reliable use in all weathers.The work conducted to date using ERS-1 SAR shows external targets are essential if full use is to be made of space SAR systems. Several anomalies were discovered in ERS-1 SAR PRI products as a result of measurements made using corner reflectors. These include, errors in the replica pulse power, error in application of the antenna gain correction and apparent long-term variation in overall gain. It has been shown that corner reflector targets can be used to verify the cross-track antenna pattern correction. However, more work is required to determine the accuracy with which the antenna pattern can be measured (as distinct from being corrected) using a relatively small number of targets.

9. ACKNOWLEDGEMENTS

This work has been carried out as part of the Earth Observation programme of the British National Space Centre.

10. REFERENCES

1. Laur, H., Derivation of Backscatter Coefficient $\sigma°$ in ERS-1 SAR PRI Products, *ESA note*, 17 October 1992 (Issue 1).

2. Kenward, D.R.D., A Precision Corner Reflector for ERS-1 SAR Calibration, *DRA working paper SP (92) WP90*, December 1992.

3. Bird, P.J. et al., An Experiment for the Radiometric Calibration of the ERS-1 SAR, *Proceedings of the First ERS-1 Symposium*, November 1992.

4. Dawkins, A.W.J. et al., Calibration of the ERS-1 Synthetic Aperture Radar (SAR) using a Transponder at the UK Romney Marsh site, *DRA working paper SP (92) WP47*, July 1993.

5. Gray, A.L. *et al.*, Synthetic Aperture Radar Calibration Using Reference Reflectors, *IEEE Trans. Geosci. Remote Sensing, vol.GE-28, pp. 374-383*, May 1990.

6. Ulander, L.M.H., Accuracy of Using Point Targets for SAR Calibration, *IEEE Trans. Aerosp. Electron. Syst., Vol. GE-27, pp.139-148*, Jan. 1991.

Figure 1. 2.57m corner reflector at the Romney Marsh calibration site.

Figure 2. Location of the Romney Marsh calibration site.

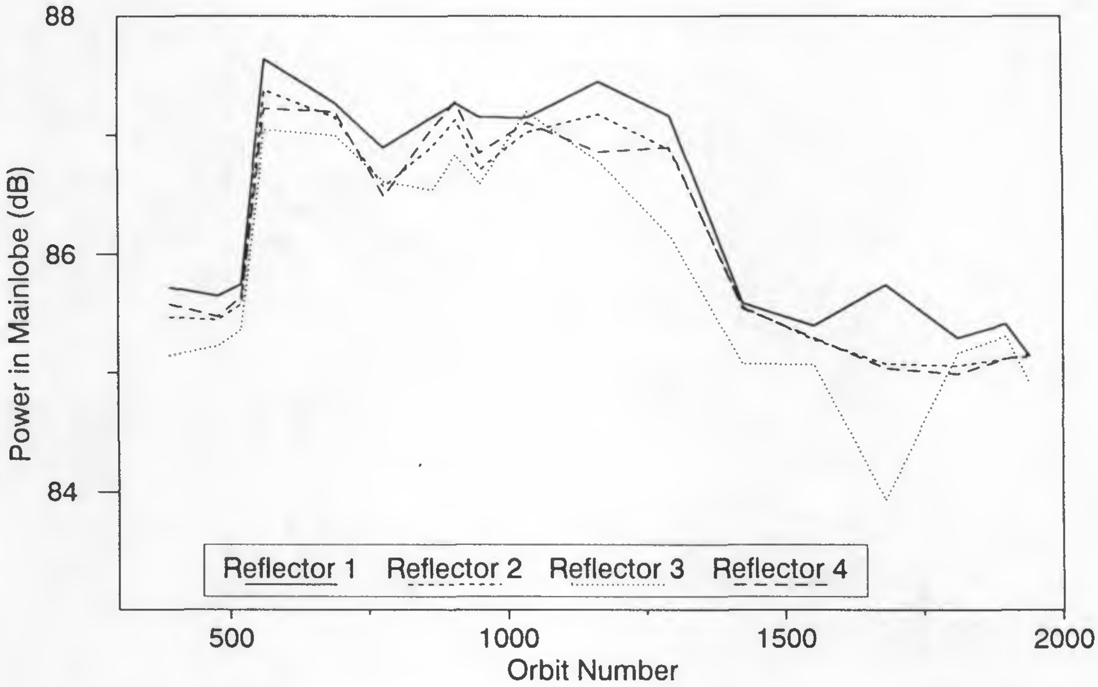

Figure 3. Variation of reflector signatures at Romney Marsh during the ERS-1 Commissioning Phase.

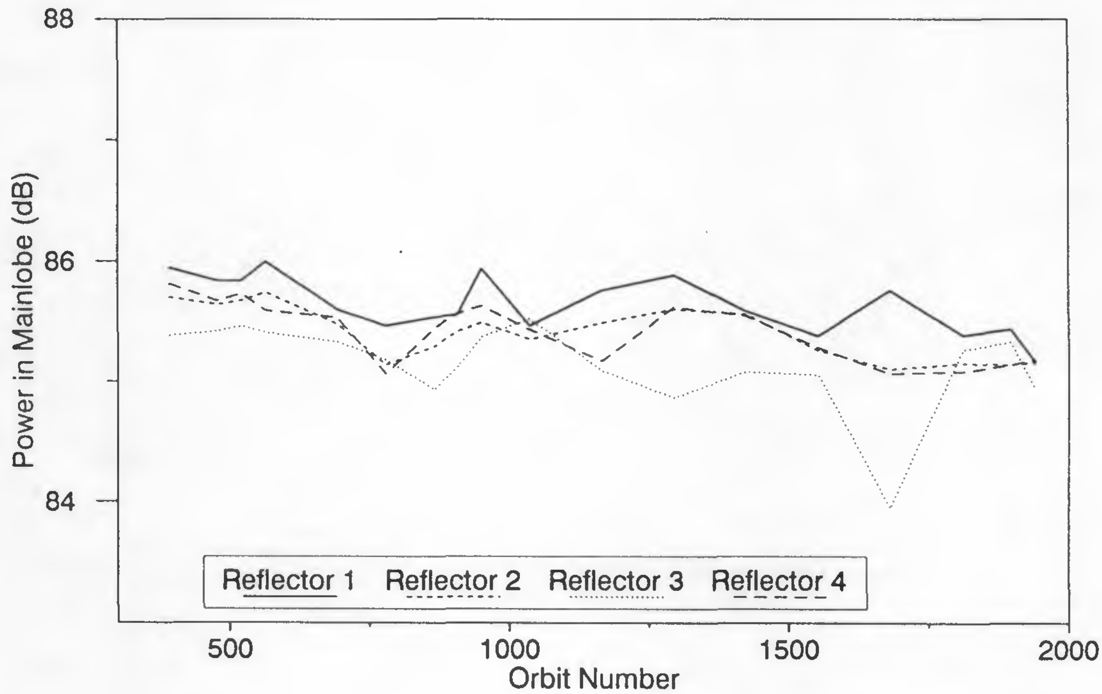

Figure 4. Reflector signatures corrected for errors in the replica pulse power.

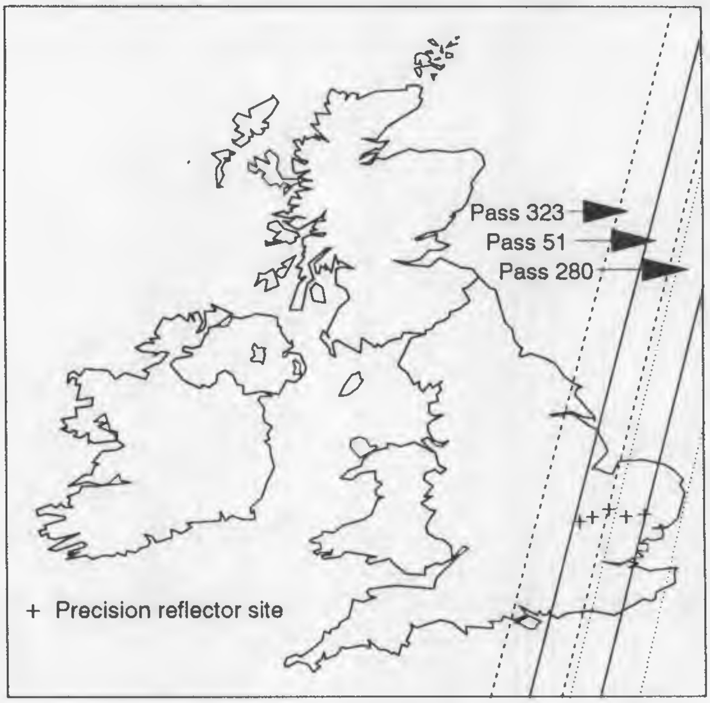

Figure 5. Location of reflector sites in East Anglia.

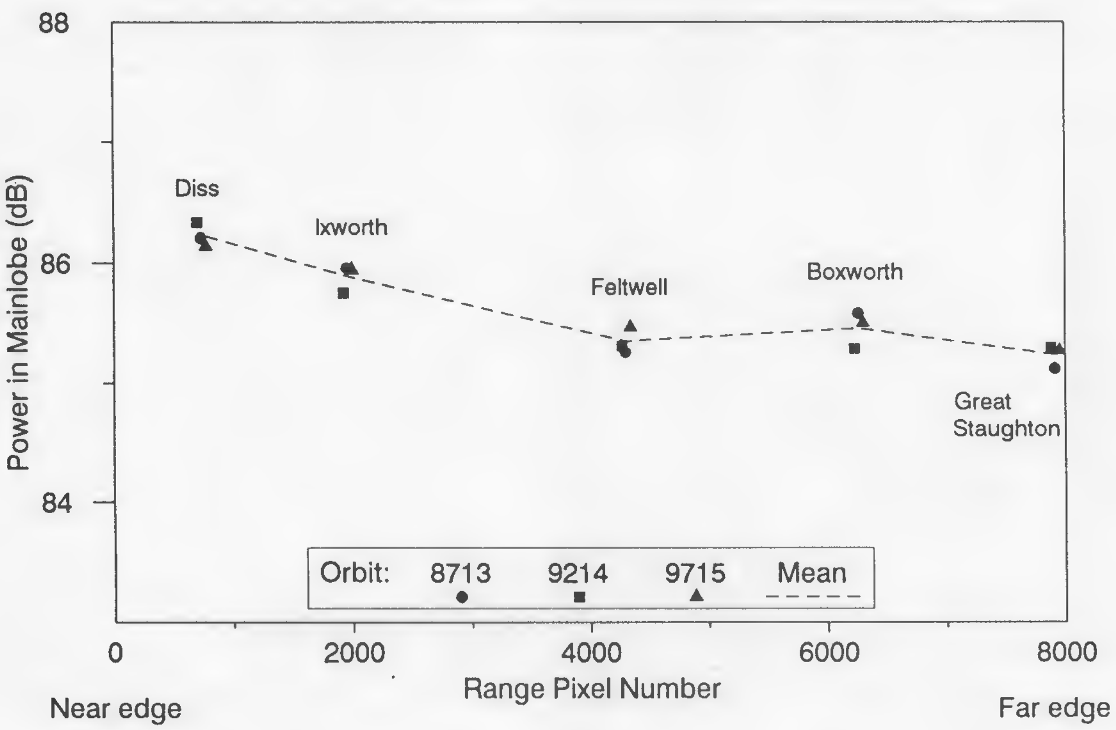

Figure 6. Variation of reflector signatures across swath 51.

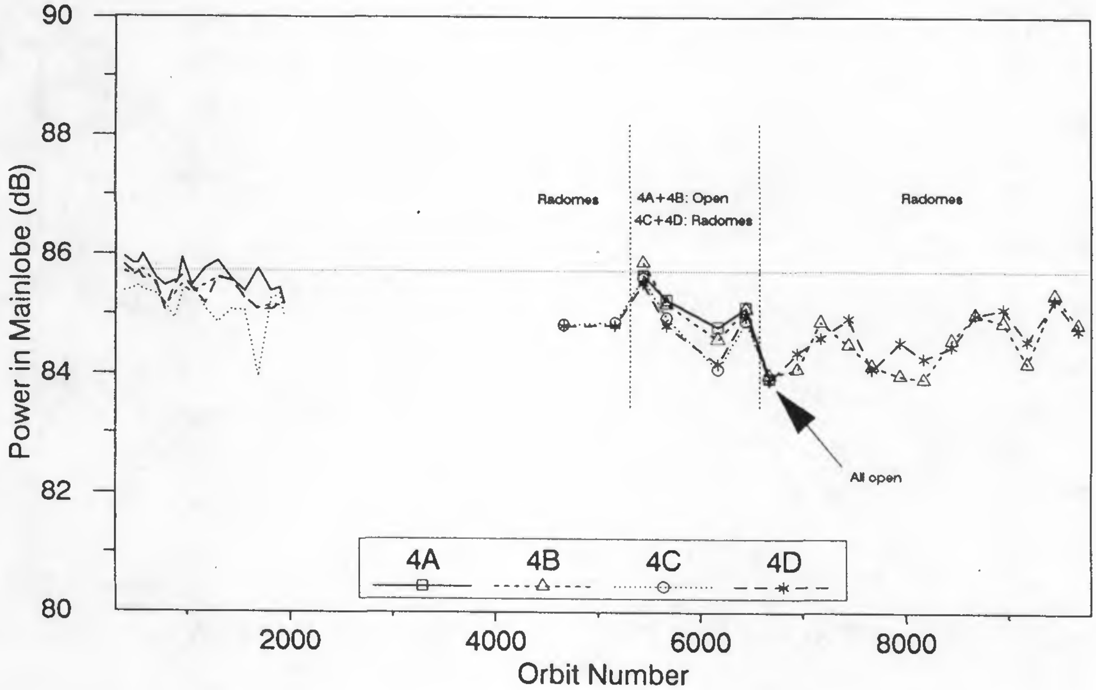

Figure 7. Reflector signature history for ERS-1 descending passes at Romney Marsh.

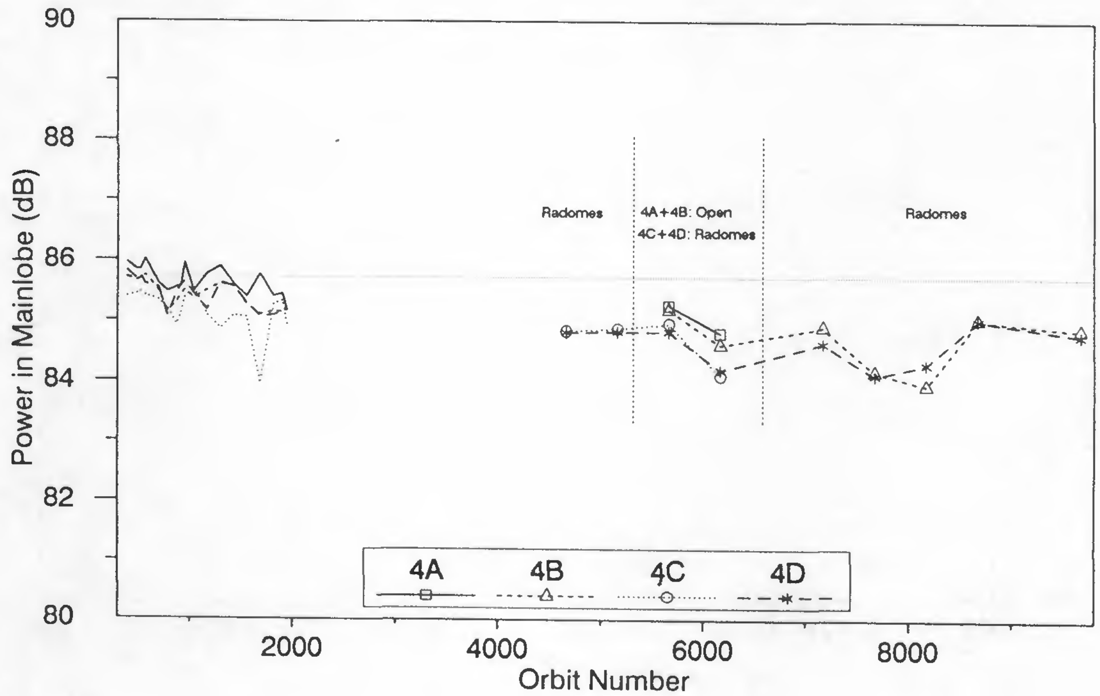

Figure 8. Reflector signature history for one swath and UK processed images only.

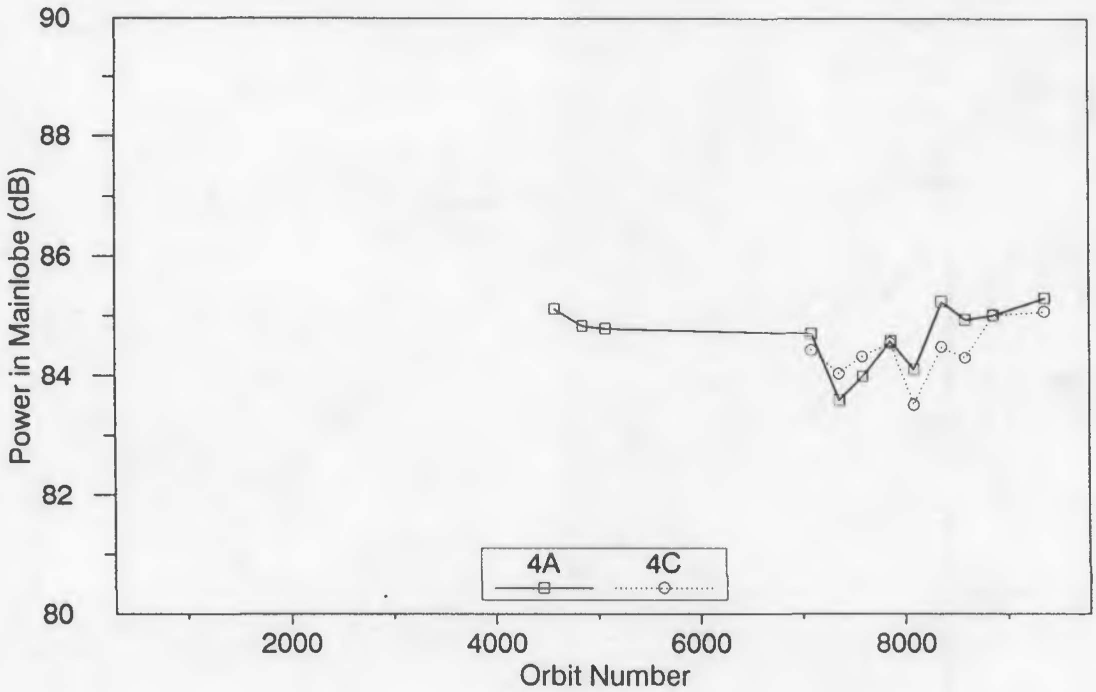

Figure 9. Reflector signature history for ERS-1 ascending passes at Romney Marsh.

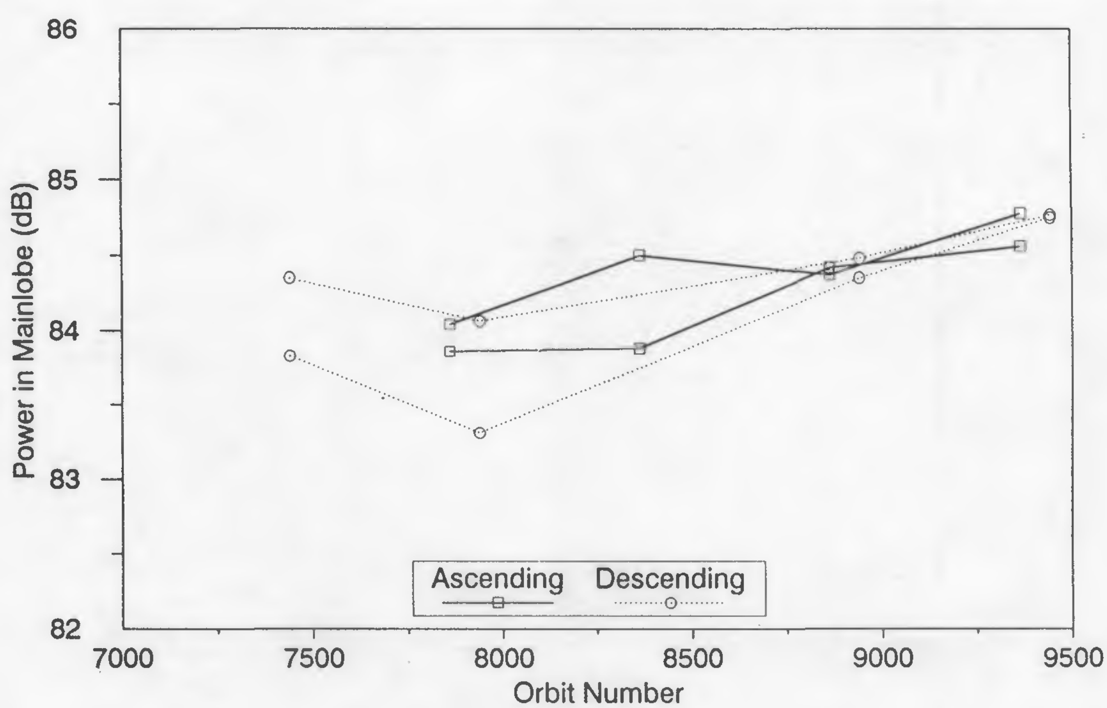

Figure 10. Comparison of descending (day-time) and ascending (night-time) passes.

GENERATION OF INVISIBLE SAR TARGETS USING CODED TRANSPONDERS

Stefan Dill
David Hounam
Karl Hans Wägel

Deutsche Forschungsanstalt für Luft- und Raumfahrt e.V. (DLR)
Oberpfaffenhofen
Germany

ABSTRACT

Conventional SAR transponders act as strong point targets and appear as bright reference points of known intensity in SAR images. The paper describes a transponder which is coded in such a way that it can only be imaged by suitably processing the SAR data. With conventional processing, the background is focused, but the coded transponder is invisible. Processing with the transponder code defocuses the background but reveals the transponder.

Use of such transponders could be to identify and localize objects too small to be resolved by the SAR sensor and the location of calibration transponders in areas of high reflectivity.

The paper describes the transponder design and demonstrates the technique with the ERS-1 AMI operating in image mode.

Keywords: Transponder, Pseudo-Noise Code, Radiometric Calibration, Microwave Tagging

1. INTRODUCTION

For many applications the spatial resolution of imaging radars is insufficient. This is particularly true for satellite radars, such as the ERS-1 Active Microwave Instrument, and where objects need to be positively identified. The classic solution to identify objects with radars is to use transponders which transmit an identification signal. An example of this is an air traffic control radar, where each airliner carries a transponder to identify the echoes on the radar screen.

With this problem in mind, an experimental transponder was desgined to enable positive identification of the transponders in SAR images. Identification is provided by modulating the transponder with an individual code. The code modulation means that the transponder will only be focused, if the SAR data is appropriately processed. After such processing the background will be defocused. Providing the power of the transponder is chosen carefully, the transponder will not be seen in the normally processed SAR image. As will be seen later, this can be a useful feature for some applications.

Although the motivation behind the work was to provide identification of targets, some advantages can be foreseen for radiometric calibration.

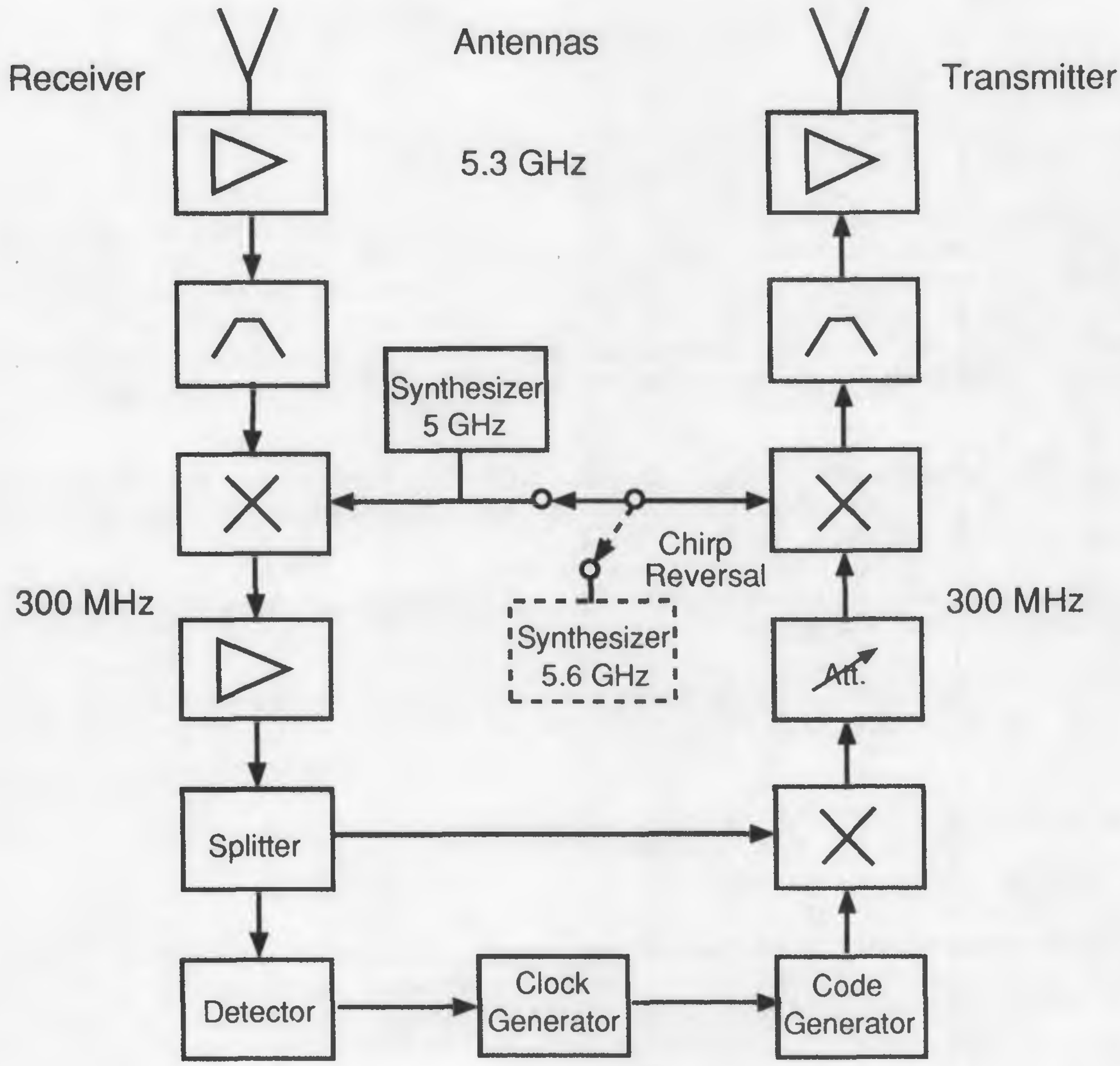

Fig 1: Block Diagram of the Coded Transponder

2. TRANSPONDER CONCEPT

The principle of the coded transponder can best be explained with the aid of the block diagram in Fig. 1.

The transponder uses separate transmit and receive horn antennas to ensure good decoupling. The receive signal is amplified and band pass filtered before being mixed down to 300 MHz with a local oscillator at 5.0 GHz. After further amplification, the signal is split into two paths, one leading to the transmit chain and the other to a detector. The latter provides trigger pulses for the clock generator, which clocks the code generator. The latter produces a pseudo-random-noise (PRN) sequence. The code chosen is a Gold code, as used for the GPS satellites, with a length of 1023 bits.

The code is applied to a double-balanced mixer, which phase shift keys the received intermediate frequency signal from the power splitter. A variable attenuator enables the radar cross section of the transponder to be adjusted. The code modulated signal is now mixed back up to 5.3 GHz. For the initial experiments, the same local oscillator (5 GHz synthesizer) was used for both the receive and transmit channels. After filtering and amplification the signal is transmitted via the transmit antenna.

Hence, the transponder is transparent to the received signal, except that the phase of the signal is keyed between $+\pi$ and $-\pi$ in synchronism with the chosen code.

The transponder was built in a 19" rack unit with the antennas attached to the case.

A first experiment was performed using a pass of the ERS-1 satellite over Oberpfaffenhofen on 12. April 1993 and with the transponder set to a high output power. The result is shown in the multilook image in Fig. 2. The range direction is horizontal and azimuth vertical. The transponder, far from being invisible, can be clearly seen as a bright line passing through the DLR centre.

To compress the transponder, a single-look complex image data set with 30 m azimuth resolution was used (see Fig. 3). The uncompressed elongated return from the transponder is shorter than in Fig. 2, because of the reduced overall Doppler bandwidth.

The complex image data were now correlated with the code from the transponder. The result can be seen in the lower image which has been reduced in intensity. The background is defocused and only the transponder appears as a bright point in the lower part of the image.

The position of the transponder in the image does not coincide with its true position as it depends on the time delay between the transponder code and the along track position of the satellite. If the datation of the SAR data, the timing of the code and the orbit of the satellite are known, the along track position of the transponder can be determined with an accuracy commensurate with the resolution cell size.

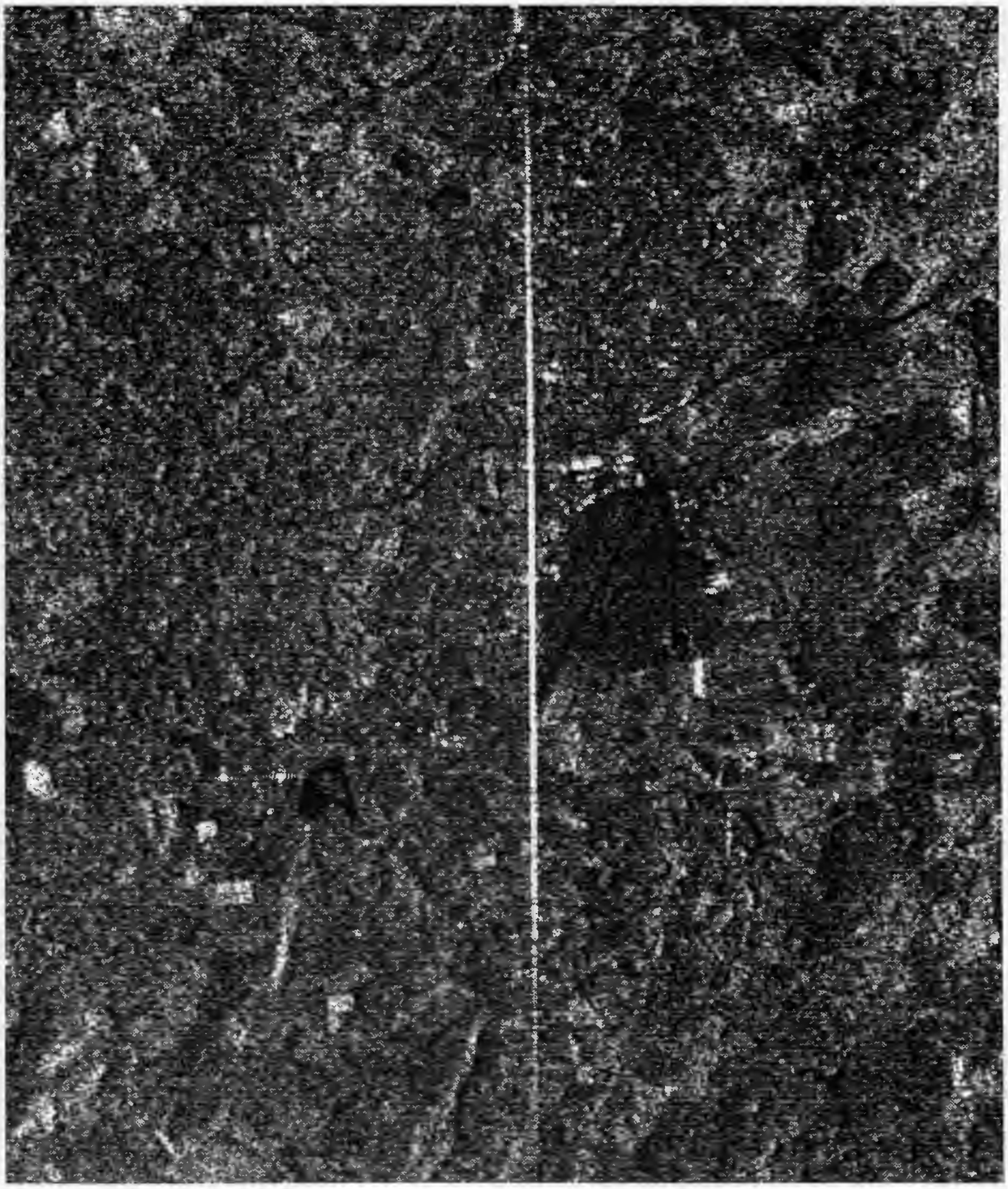

ERS-1 12-April-1993

Fig 2: Multilook Image of the Oberpfaffenhofen Area showing the Coded Transponder

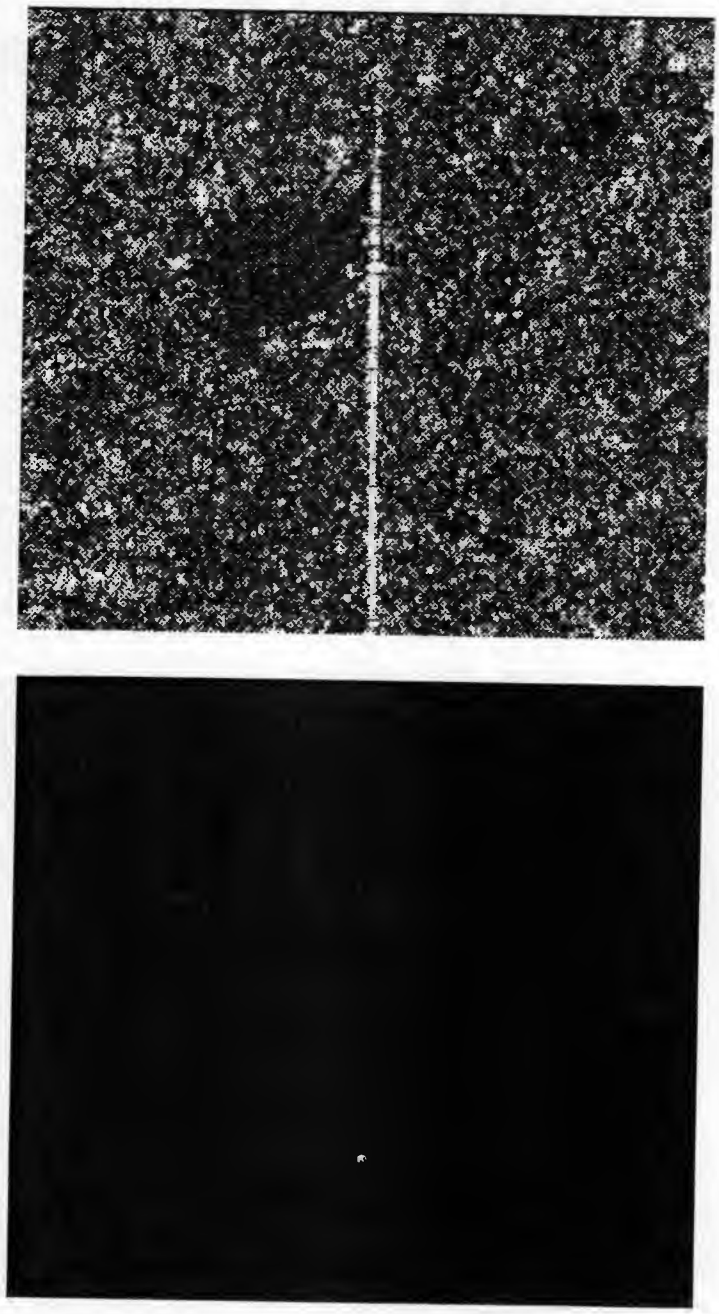

Fig 3: Upper Image: Single-look Image used for the Analysis
Lower Image: Correlated Image showing Compressed Transponder

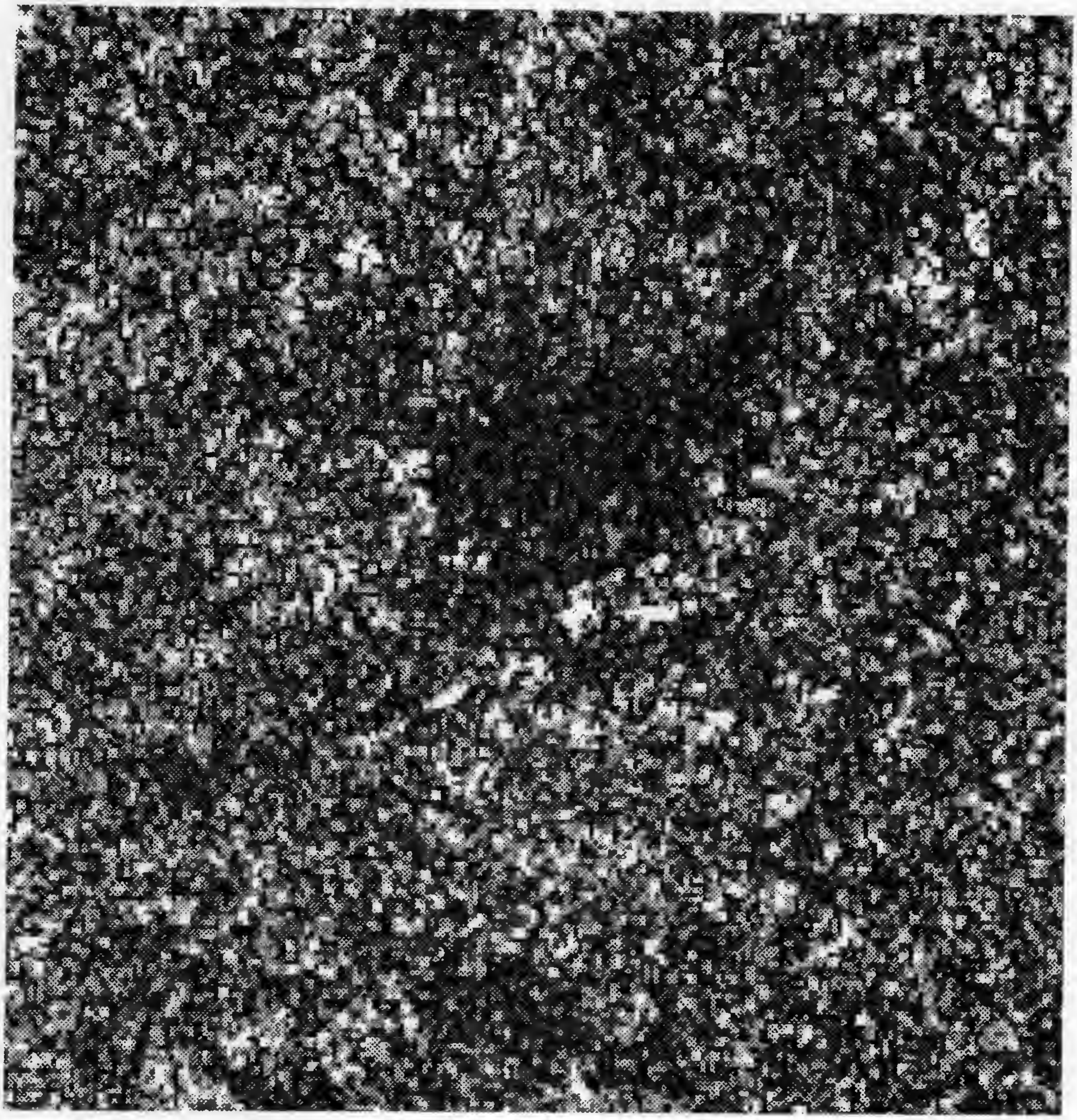

Fig. 4: Single-look ERS-1 Image with the Transponder Invisible

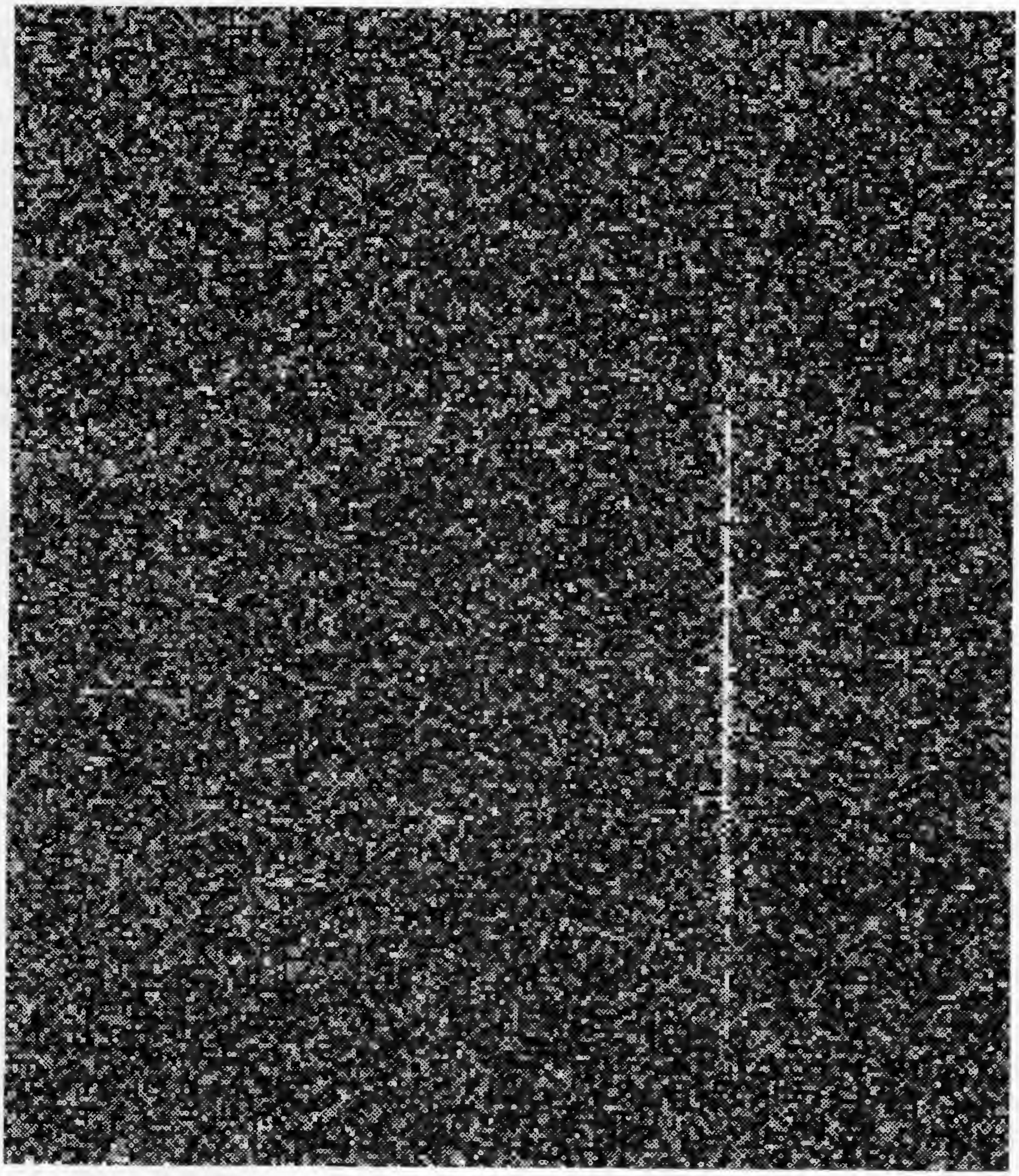

Fig. 5: Range Compressed Data with the Transponder Focused in Range

3. INVISIBLE TRANSPONDER

In this first experiment, the transponder was far from invisible, due to the high power and the transponder being focused in the range direction. To provide total invisibility in a normally processed SAR image the SAR transponder was provided with a facility to reverse the pulse expansion chirp. Referring to Fig. 1, this was achieved by switching the transmit mixer to a second synthesizer operating higher than the receive frequency at 5.6 GHz. Mixing with a low local oscillator on receive and a high local oscillator on transmit reverses the chirp received from ERS-1 and completely decorrelates the transponder and the background. But this mixing scheme has a second effect. Because any phase shift on the down path to the transponder is reversed in the transponder, it is cancelled by the phase shift on the upward return path. Hence, the Doppler modulation is cancelled out.

A second experiment was performed with this mixing scheme and with reduced transponder power. The single look image with 30 m resolution is shown in Fig. 4. The transponder cannot be identified in this scene. The first processing step was to range compress the raw data with the range chirp reversed (see Fig. 5). The transponder can now be seen as a bright line, it now being focused in range. The background is totally defocused, because the range chirp is mismatched and no azimuth compression is performed.

The next step is to correlate the image with the transponder code. The equivalent block diagram of a time domain correlator is shown in Fig. 6.

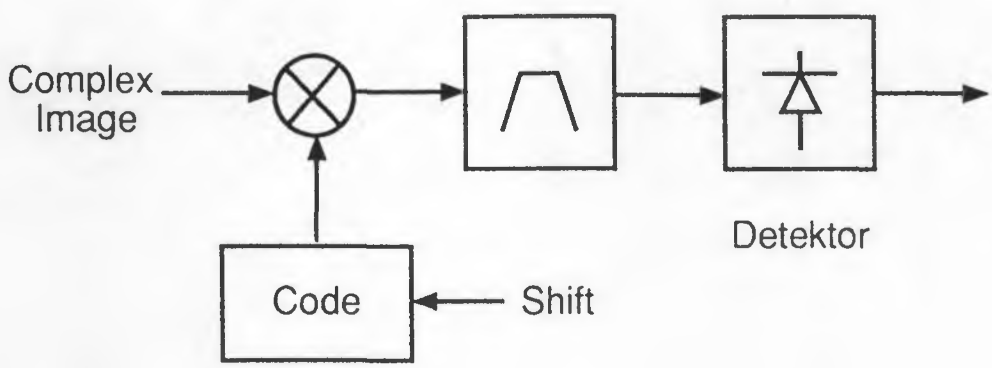

Fig. 6: Equivalent Diagram of a Time Domain Correlator

The complex image data is multiplied with the code signal, the latter being shifted through all 1023 code positions. The resulting signal is band-pass filtered and then detected. The band-pass filter is required, as opposed to a low-pass filter, because, after the mixer, the signal has a frequency offset. This offset is partially due to delay in the transponder and partially to the imperfect cancelling of the Doppler modulation on the down and up paths, resulting from the slight difference in the down and up signal delay.

If realised in this way, correlation would be searched for by shifting the code and observing the detected output. In reality, the correlation was performed with the frequency domain algorithm illustrated in Fig. 7.

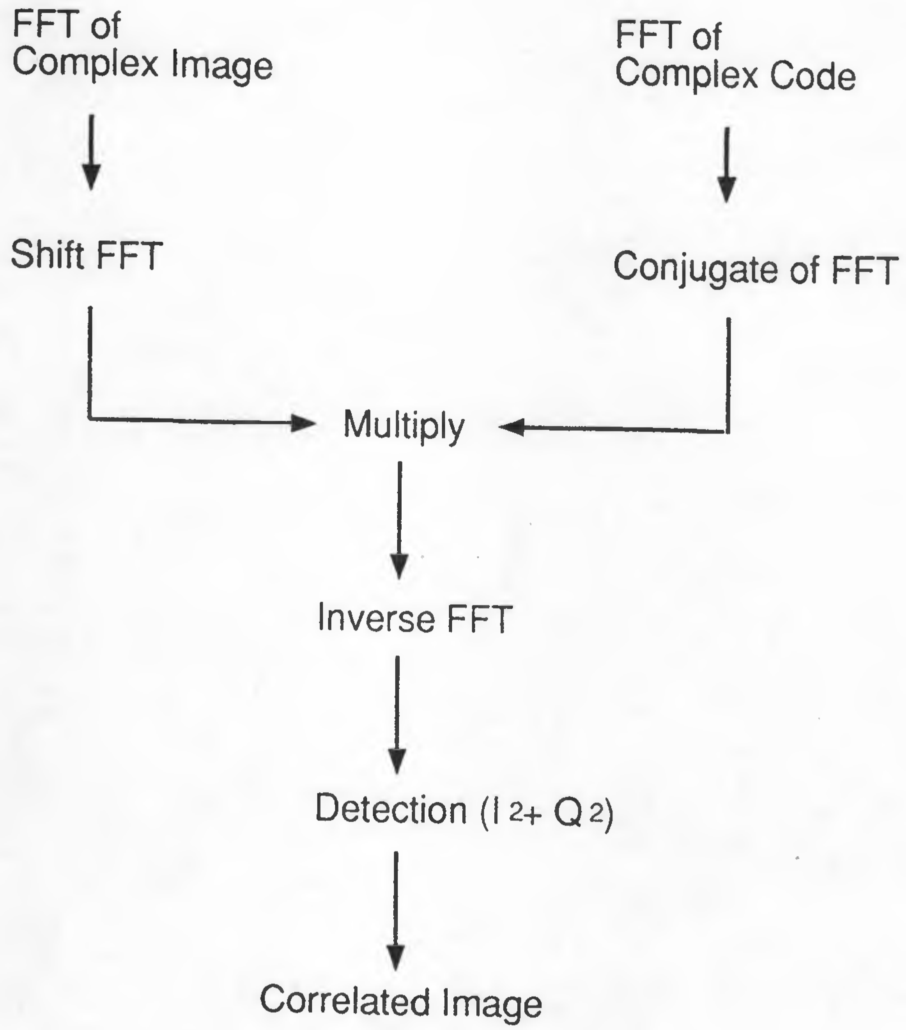

Fig. 7: Frequency Domain Correlation

The complex conjugate of the FFT of the code signal is multiplied with the FFT of the complex image data. The latter has first to be shifted according to the frequency offset discussed above. After multiplication, the inverse FFT is formed and the result detected to obtain the image intensity. The outcome is an image only fully compressed and correlated for the transponder.

The result is shown in Fig. 8. The background is decorrelated and the transponder is visible as two bright points of differing intensity. The azimuth line containing the transponder is somewhat brighter than the other lines due to some instability in the transponder code.

Fig. 10 is a plot of the intensity of the range bin containing the transponder. It can be seen that the peaks in the curve, i.e. bright points in the image, are spaced 1023 azimuth bins apart. The appearance of this second correlation maximum is due to the code length (1023 bits) being shorter than the real aperture length. For ERS-1, a longer code would be needed to produce an unambiguous result. The transponder response is more than 20 dB above the background and has a width of one azimuth sample spacing, i.e. approx 4.2 m. Providing the relative timing of the code and

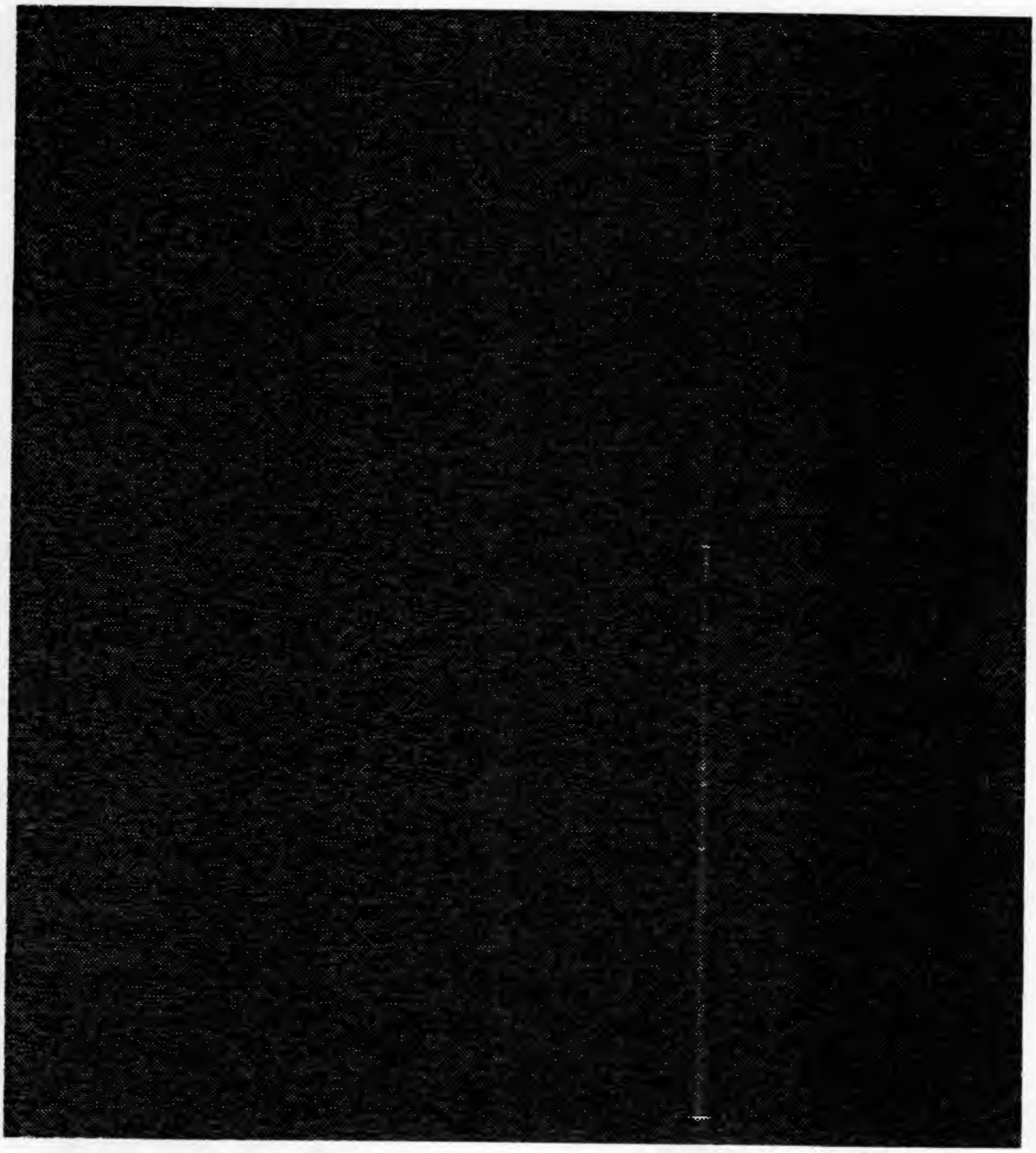

Fig. 8: Image with the Transponder Correlated

the satellite position is known, the transponder can be localised with an accuracy of approx 4 m.

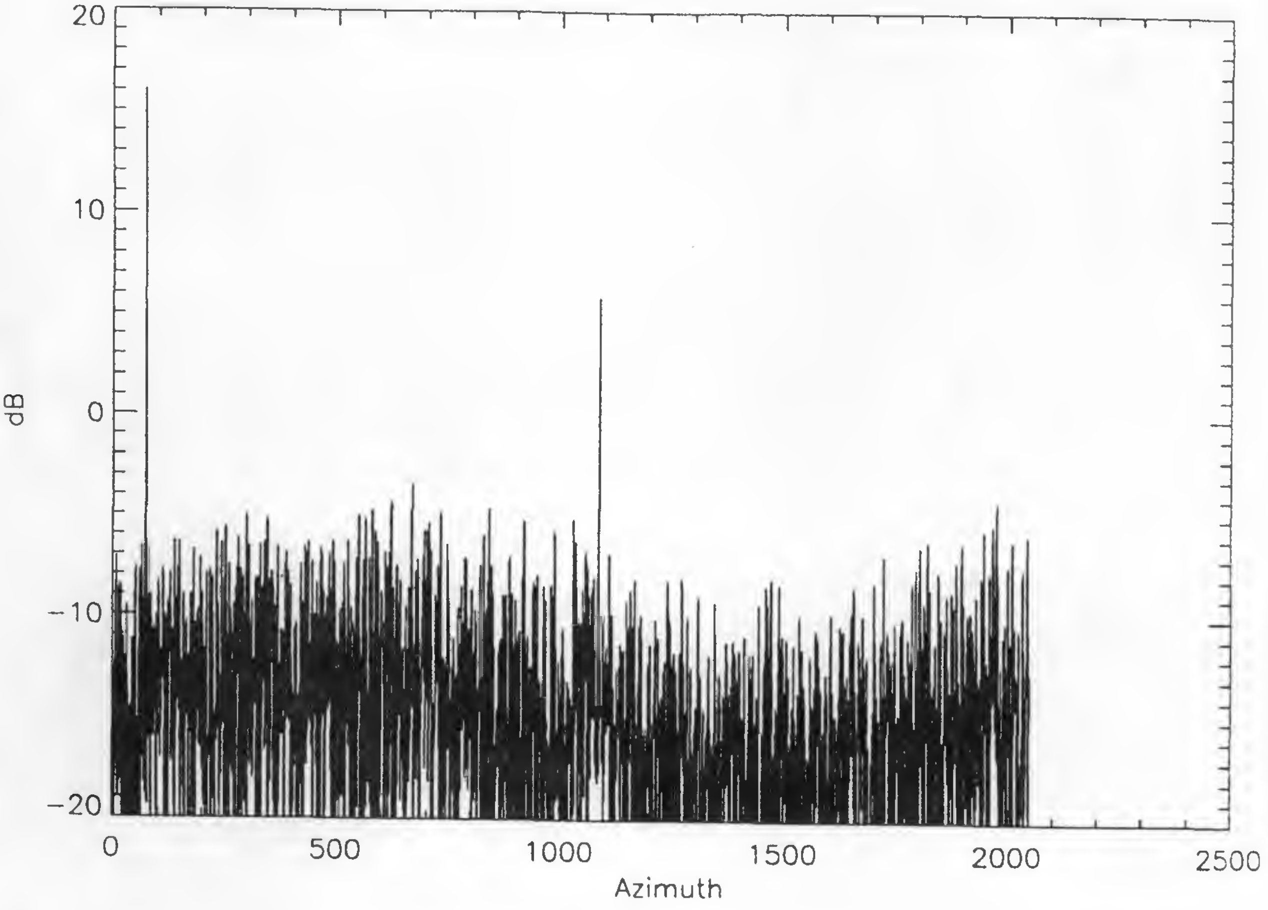

Fig. 9: Plot of the Range Bin containing the Transponder.

In the range direction, the transponder response is resolved with the usual slant range resolution, i.e. approx. 11 m. Localisation accuracy in range is the same as for normally processed image pixels.

4. CONCLUSIONS

The above experiments demonstrate the feasibility of using coded transponders to identify and localise objects. A similar experiment with the airborne SAR of the DLR E-SAR is being evaluated and should show similar results.

The first ERS-1 experiments, referred to above, were performed with some instability in the generated code, resulting in poorer correlation than would be expected. This is under investigation.

The identification of objects using such transponders has a number of possible applications. The one stimulating the work was the monitoring of treaty limited equipment (TLE) for arms control verification. With a few passes of a satellite or airborne SAR sensor, not only could the region of interest be imaged but it could check the correct location of all TLEs. The transponders would represent microwave tags readable at great distances. A number of similar identification/localisation tasks could be envisaged in other fields, like the monitoring of vehicles, ships and maybe for tracking migrant earth features, like ice flows. For many of these applications, it would be both desirable and feasible to greatly reduce the size of the transponder.

Advantages can also be foreseen for the radiometric and geometric calibration of SAR sensors. The defocusing of the background means the transponder does not have to be located in areas of low reflectivity, providing an alternative to conventional response shifting methods. Also, the coded transponder enables calibration points to be quickly, positively and even automatically identified.

Looking to the future, one could foresee such a transponder correlator being implemented in the SAR data chain, maybe even on board the satellite. The correlator could automatically locate and evaluate calibration transponders, merging the resulting data with the SAR data. This would give the user immediate access to external calibration data without the delay, experienced at present, due to the long calibration data chain.

MAC EUROPE 1991 CAMPAIGN: DESIGN AND PERFORMANCE EVALUATION OF AN ACTIVE RADAR CALIBRATOR

S. Ponte
Faculty of Engineering, University of Naples "Federico II"
Napoli, Italy

F. Posa
c/o Physics Dept., Polytechnic of Bari
Bari, Italy

V. Schena, S. Vetrella
Consortium for Research on Advanced Remote Sensing Systems (Co.Ri.S.T.A.)
Napoli, Italy

ABSTRACT

This paper describes the characteristics and performance of an Active Radar Calibrator (ARC) used during the MAC Europe 1991 Campaign conducted in Southern Italy (Matera) to calibrate the Airborne Synthetic Aperture Radar (AIRSAR) and Topographic Synthetic Aperture Radar (TOPSAR) instruments which were flown onboard the NASA/JPL-DC8 aircraft. The main design considerations and the ARC hardware performance are presented. The laboratory measured values of radar cross section and propagation delay time are compared to those obtained from the images acquired during the flight. The TOPSAR raw data have been compressed with a Range-Doppler processor which includes range migration correction. The radiometric calibration, performed with the intensity integration method, gave a backscattering coefficient accuracy of ±0.8 dB. The ARCs' radar cross-sections extracted from the calibrated images have been compared with the laboratory experimental data, giving results in good agreement with the anechoic chamber tests. The laboratory tests gave an absolute calibration error of ±0.6 dB.

Keywords: Active Radar Calibrator, Performance Evaluation, Radiometric Calibration, SAR Processing

1. INTRODUCTION

The Active Radar Calibrator (ARC) is a versatile and useful tool for external calibration of SAR images, due to its design flexibility, reduced dimensions, relatively small sensitivity to positioning errors, large and adjustable Radar Cross Section (RCS) and fully polarimetric capabilities. An ARC is essentially a high gain amplifier coupled with a receiving and a transmitting antenna, which reradiates the received radar signal, with different polarization when requested, towards the (airborne or spaceborne) SAR sensor. The "absolute" backscatter reference given by an ARC has been widely used in past airborne SAR campaigns with the objective of achieving absolute calibration (Refs. 1, 2). The variable polarization signature, easily accomplished by relative rotation of the two antennas, has been effectively used to derive the amplitude and phase characteristics of multichannel polarimetric SARs by means of Polarimetric ARC (PARC) devices (Ref. 3). Furthermore, the high calibration accuracy (typical values are 0.1÷0.5 dB) make the ARC suitable for evaluating in-flight antenna patterns, by using either ARCs (Ref. 4) or PARCs (Ref. 5). The ground calibration plans of future missions such as SIR-C/X-SAR (Ref. 6) require an extensive use of ground-based active calibrators, whereas operating sensors are being very accurately characterized in terms of system performance by using sophisticated and reliable ARCs, such as those used for ERS-1 mission (Ref. 7).

This paper is addressed to the description and the performance analysis of the ARCs developed under a collaboration between the Italian Consortium for Research on Advanced Remote Sensors (Co.Ri.S.T.A.) and the Polytechnic of Bari (Italy), and deployed on the Matera test-site in June 1991, during the MAC Europe Campaign. After a short description of the campaign, the main design considerations of the transponder are presented. Next, a comparison between the laboratory measurements and on-site performance is carried out by analyzing the C-band calibrated data. The concluding remarks point out some considerations about the use of active devices for SAR external calibration campaigns.

2. 1991 CAMPAIGN

In the framework of the MAC Europe 1991 campaign, SAR raw data were gathered by the NASA DC-8 AIRSAR instrument, augmented with a pair of C-band antennas displaced across track, in order to obtain interferometric fringes and topographic information from the imaged surface (TOPSAR, Ref. 8). The test-site was covered five times, with three descending and two ascending runs. Table 1 shows the TOPSAR system parameters of interest for radiometric calibration.

Frequency	5.2875 GHz (C-band)
Wavelength	5.65 cm
Aircraft speed	214.4 m/s
Side-looking angle (ϑ)	45° (nominal); 30°-60°
Altitude	$\cong$9 km
Swath width	4630 m (slant range)
Slant range	11200 m (ϑ=45°)
Ground range resolution	5.30 m
Slant range resolution	3.75 m
Azimuth resolution	0.8 m (1 look, nominal)
Chirp bandwidth	40 MHz
Pulse length	5.0 μs
Sampling frequency	90 MHz
SNR (distributed targets)	13 dB
SNR (point targets)	18 dB
PRF	567 Hz

Table 1: *TOPSAR radar system parameters*

The Matera test-site, in Southern Italy, extends over about 128 km^2, and consists of prevailingly bare soil, except for two small hilly areas with argillaceous formations. In conjunction with the flight (June 25th, 1991), an extensive ground truth campaign has been carried out, addressed to the classification of 50 sample areas and to the evaluation of texture, soil moisture content and surface roughness on 26 sample points, in correspondence of the location of 26 calibration devices (Ref.9). The point targets are three ARCs and 23 triangular trihedral Corner Reflectors (CR), subdivided in 15, five and three with leg lengths of 95, 150 and 70 cm, respectively. Fig. 1 shows the deployment scheme of the CRs and ARCs on the test-site: the two parallel lines in the horizontal (range) direction were at a distance of 800 m, with a spacing of 200 m between two successive CRs, to avoid coupling effects. All the point targets were deployed on a homogeneous background. The mean temperature during the TOPSAR overpass was 30° C.

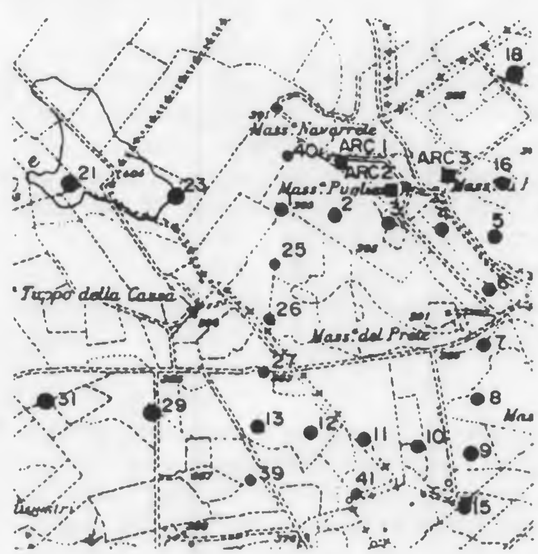

Figure 1: *Istituto Geografico Militare Italiano (IGMI) map of the test site, with the deployment scheme of all Corner Reflectors and ARCs*

3. ARC CONFIGURATION AND HARDWARE PERFORMANCE

Fig. 2 shows a block diagram of the C-band ARC used in the Matera experiment. It basically consists of a receiving antenna and a transmitting antenna coupled with a RF amplifier, together with signal detection circuitry, in order to feed a small part of the received power to a digital section capable of acquiring the in-flight azimuth antenna pattern (Acquisition Section).

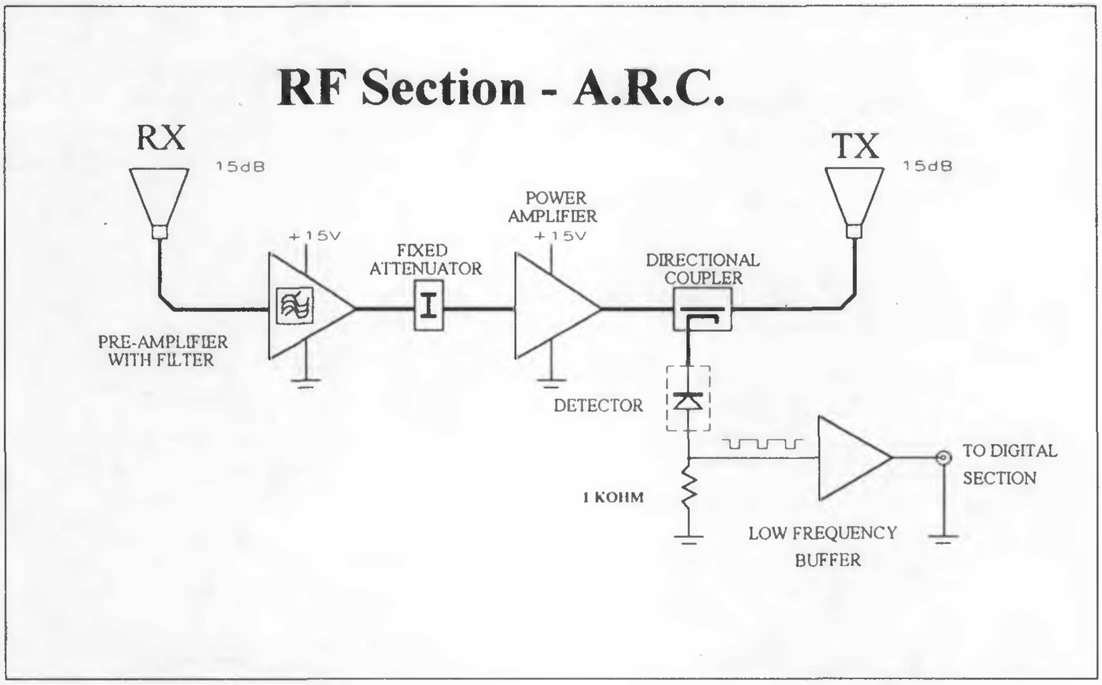

Figure 2: *ARC block diagram*

The receiving antenna is connected to a pre-amplifier, built in hybrid technology and cascaded with a bandpass filter, centred on 5.3 GHz and with a bandwidth of 300 MHz, chosen as a compromise between the need of filtering out spurious signals and noise, and the possibility of using the same ARC for future or different SAR systems. A fixed attenuator arranges the dynamic range of the received signal between the two amplification stages. A variable attenuator has been used, in order to provide a range of RCS values and to avoid saturation of the SAR impulse response function and positive feedback in the RF section. A directional coupler collects a fraction of the received power (10 dB below the input signal level) which is fed to a detector diode. The envelope of the radar signal is demodulated and a negative pulse train at the Pulse Repetition Frequency (PRF) is achieved, with a duty cycle dependent on the SAR system (0.3% for the TOPSAR system). Finally, the signal is transmitted to the synthetic aperture radar via a standard C-band horn, with the same characteristics of the receiving horn. The ARC has been developed with a modular concept, particularly for the signal detection unit, allowing a complete interchangeability between electronical and mechanical components.

ARCs Nos. 1 and 2 have the same hardware characteristics, while ARC No. 3 has been realized without the preamplifier and with the two antennas closer each other. The reduced RCS value (about 15 dBm^2 less than ARCs 1 and 3) could not satisfy the >20-dB requirement on signal-to-clutter ratio necessary to avoid that the ARC's response is hidden in the baeground return (Ref. 10). However, by properly deploying such an active calibrator, both precision and accuracy in evaluating radiometric bounds for the linear region of the SAR system transfer function could be improved, in order to reduce the error budget (Ref. 11).

In the following we give a short synthesis of the main aspects and characteristics of the ARC:

• **Packaging.** The ARC is a compact device which weighs about 20 kg. Electronics and antennas are weatherproof and the structure is able to withstand normal winds without readjustment. The deployment and orientation are easily accomplished, and the adjusting/locking mechanisms are manual, independent for each antenna which can be oriented at 45°, 90°, 180° with respect to the other.

• **Power requirements.** Lead-gel airtight rechargeable batteries supply 24V, 10 Ah, and an electronic power regulator supplies 15 V DC to the RF section. The power supply is sufficient to operate at full capacity for 10 hours continuously, with a current absorption of 700 mA. The external power source is easy to connect and to replace, with circuitry to protect against wrong insertions.

• **Amplifier section.** A LED turns on when the ARC is receiving a power greater than or equal to the peak expected power. Both the preamplifier and the power amplifier have gain flatness of ±0.05 dB over the 300 MHz bandwidth, with a noise figure of 3.6 dB at the central frequency of 5.3 GHz. Table 2 and Fig. 3 show the laboratory tests on both the preamplifier (Model JCA56-353) and the power amplifier (Model JCA56-519), and the gain curves over the available bandwidth. In agreement with the manufacturer's data, the return and mismatch losses at 5.3 GHz have been found to be 16.5 dB and less than 0.1 dB, respectively. The one-dB compression point of the cascaded amplifiers is when the input power is -40 dBm, and the linearity range is 30 dBm, from -70 to -40 dBm input power.

MODEL N.	JCA56-353 (Pre-Amp)
DC SUPPLY	+15 Vdc

Frequency [GHz]	**Gain [dB]**	**Noise figure [dB]**	**Input VSWR**	**Output VSWR**	**Compression @+10 dBm**
5.15	see	3.5	1.84	1.24	.2
5.25	plot	3.6	1.41	1.23	.2
5.45	(Fig. 4a)	3.5	1.27	1.24	.2

MODEL N.	JCA56-519 (Power Amp)
DC SUPPLY	+15 Vdc

Frequency [GHz]	**Gain [dB]**	**Noise figure [dB]**	**Input VSWR**	**Output VSWR**	**Compression @+25 dBm**
5.00	see	3.4	1.16	1.50	.8
5.30	plot	3.6	1.35	1.50	.7
5.60	(Fig. 4b)	3.8	1.60	1.60	.7

Table 2: *Results of the laboratory tests on the RF section (pre-amplifier and power amplifier)*

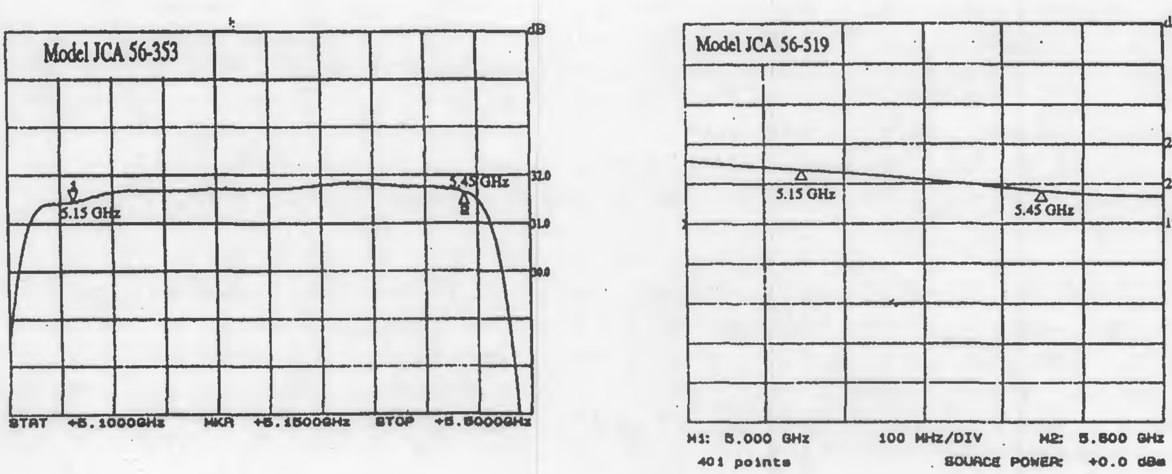

(a) (b)

Figure 3: *Measured frequency response of the preamplifier (a) and of the power amplifier (b)*

The temperature test chamber measurements detected a relative variation of the gain over temperature of 5.7%, i. e., 0.08 dB/°C. Fig. 4 shows the RCS of the ARC as a function of temperature, from -10° C to +40° C, at 5° C increments, with an input power of -60 dBm, which is located in the central region of the allowable input dynamic range. This characteristic affects the RCS during the operation of the ARC which requires the thermal compensation of both the RCS and the received power values through a look-up table.

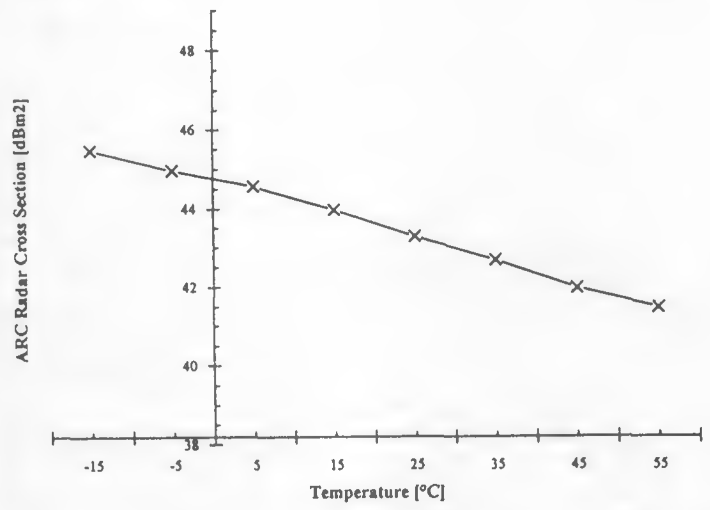

Figure 4: *Climatic room tests: diagram of radar cross-section over temperature. The input power level is -60 dBm*

• **Antennas.** Both RX and TX antennas, labeled for easy identification, are C-band pyramidal horns with rectangular aperture (13.2x9.4 cm). The -3 dB beamwidths in the E and H-planes are respectively 25° and 34°, values which overcome orientation problems. To achieve a good cross-coupling performance, the distance between the center of simmetry of the two horns has been set to 62 cm. At the central frequency of 5.3 GHz, the antennas have a bandwidth of 300 MHz. The peak gain declared by the manufacturer is 15 dB, with typical sidelobes level of -20 dB which allows to minimize multipath effects and background noise. In addition to the orientation of the antennas with respect to the flight line, a different polarization state is achieved by rotating each antenna about its boresight at 45° steps, with a system of hexagonal-head bolts on a frame structure. The minimal cross-polarization isolation is 32 dB. Echo-absorbing material surrounds the horns, in order to avoid resonance effects and to minimize the re-radiation effects of the structure (see Fig. 5). The decoupling between the antennas, defined as $10\log_{10}(P_p^t / P_q^r)$, where P_p^t is the transmitted power with polarization state p, and P_q^r is the power received with polarization q, is >80 dB in the HV and VH configurations, >60 dB in the VV orientation, and >54 dB in the HH mode. The mismatch loss is less than 0.05 dB and the return loss is 20 dB, with a corresponding voltage standing wave ratio (VSWR) of 1.22.

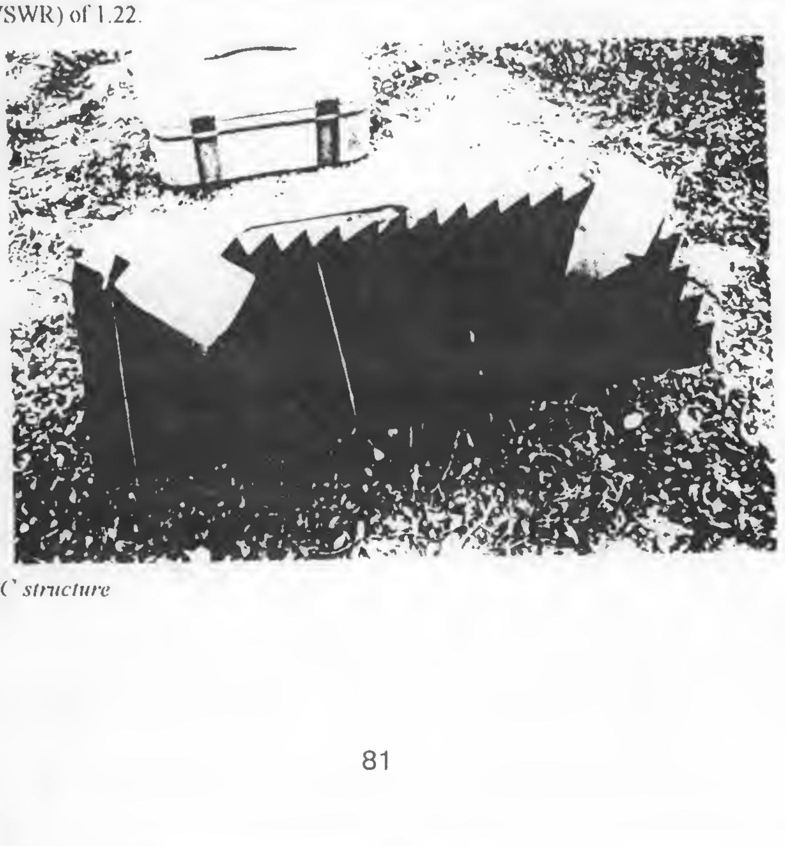

Figure 5: *ARC structure*

4. ARC PERFORMANCE EVALUATION

In order to validate the laboratory measurements of the main ARC parameters, we performed a full compression and radiometric calibration of the SAR raw data acquired by the two antennas of the TOPSAR instrument. The raw data were focused in the frequency domain, with a Range-Doppler processor, developed by Co.Ri.S.T.A.. The range reference function emulated the on-board Digital Chirp Generator (DCG), and the compressed data were frequency-shifted at baseband, to remove the video offset frequency. The Hamming-weighted azimuth reference function was of variable length, depending on the incidence angle. The range migration was not negligible (about 2 range bins at a mean incidence angle of 47.5°), and it was corrected by a frequency-domain trajectory restoration algorithm, based on clutterlock/autofocus algorithms and on resampling techniques by means of *sinc* weighting functions. Multiple pixel averaging of the intensity images (1024x1024 pixels) was performed to achieve a square pixel (Fig.6). Slant range and azimuth spacings are 3.33 m and 3.03 m respectively.

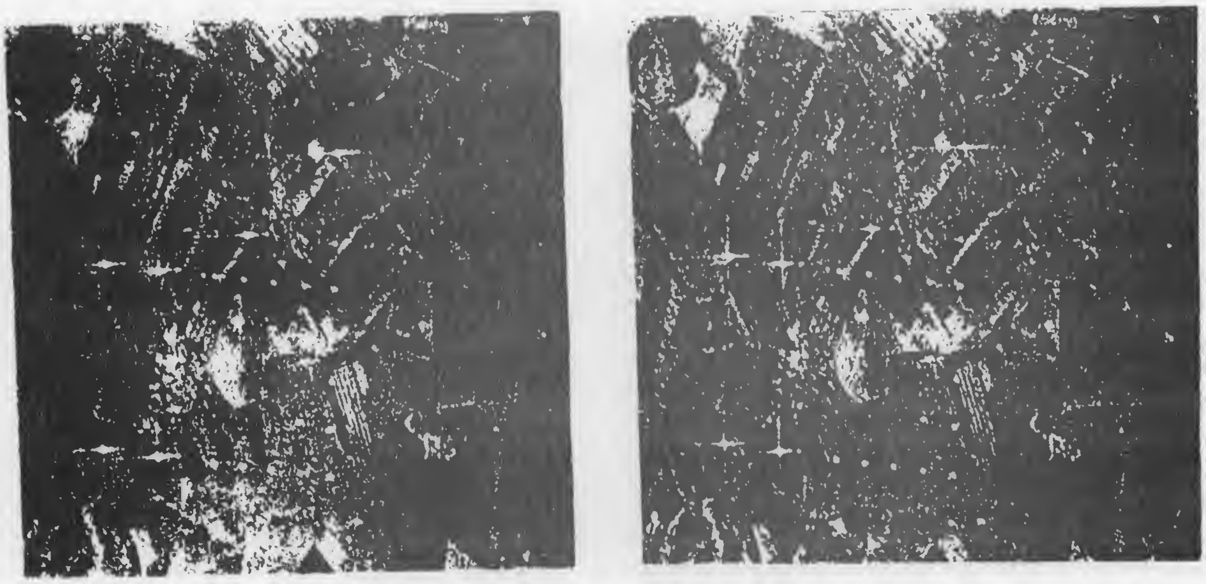

(a) (b)

Figure 6: *Image of the test site obtained from raw data gathered by antenna 1 (transmitting/receiving) (a) and antenna 2 (receiving) (b)*

Unfortunately, ARC No. 2 did not work during the TOPSAR overpass, due to a hardware malfunctioning, and it is not visible, while ARCs Nos. 1 and 3 are clearly recognizable above the upper horizontal line of corner reflectors. Fig. 7 shows a three-dimensional plot of the ARC response, with z-axis representing amplitudes in dB.

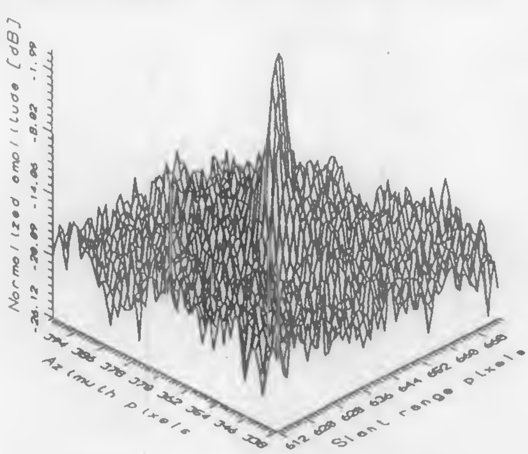

Figure 7: *Three-dimensional representation of the response of ARC No. 1*

A set of standard quality tests were conducted to test the processor performance, in terms of one-dimensional resolution, Integrated Sidelobe Ratio (ISLR) and Peak Sidelobe Ratio (PSLR) in both range and azimuth directions (Tab. 3).

ARC No.	ϑ_i [deg]	ρ_{gr} [m]	ρ_{sr} [m]	Range ISLR [dB]	Range PSLR [dB]	ρ_{az} [m]	Azimuth ISLR [dB]	Azimuth PSLR [dB]
1	46.3	5.61	4.06	-8.95	-11.16	8.82	-18.69	-27.22
3	47.6	5.67	4.19	-6.44	-9.68	8.68	-12.61	-17.75
1	46.3	5.87	4.24	-9.38	-25.42	8.82	-16.75	-16.07
3	47.6	5.29	3.90	-7.59	-11.79	7.71	-11.07	-13.52

Table 3: *Ground range (ρ_{gr}), slant range (ρ_{sr}) and azimuth (ρ_{az}) resolutions, ISLR and PSLR in range and azimuth directions for ARCs Nos. 1 and 3. The mean broadening factors are 15% in range and 25% in azimuth. Second column reports the calculated incidence angle (ϑ_i)*

The radiometric calibration of the images was performed by using the intensity integration method (Ref. 12), which is insensitive to misfocussing and to scene and/or processor coherence. After having estimated $\mathcal{E}_{gp}$, the integrated energy associated to the reference target (a CR), $\mathcal{E}_{gu}$, the background clutter energy, and the image noise power, the average backscattering coefficient $<\sigma^0>$ in correspondence of each point target was evaluated by applying the equation:

$$<\sigma^0> = \sigma_{ref} \frac{\mathcal{E}_{gu}}{A_u \mathcal{E}_{gp}} \sin\vartheta_u \qquad (1)$$

where $A_u = \delta_{sr}\delta_{az}$ is the uniform target area, given by the product of the slant range and azimuth spacings δ_{sr} and δ_{az}, ϑ_u is the incidence angle of the uniform target area, σ_{ref} is the reference RCS value of the CR. The error on each σ^0 determination is associated to the integral estimate of the point target energy ($\mathcal{E}_{gp}$), and it depends on the speckle autocovariance function (Ref. 13), integrated over the area A_p, containing the point target response function. We found for the standard deviation of $\mathcal{E}_{gp}$, and therefore for the calibration accuracy of the method, a mean value of 0.7 dB. The reference RCS value and the estimate of the energy term $\mathcal{E}_{gp}$ were derived from the eleven C-band CRs (95-cm leg length) deployed on the test-site: we chose the CR deployed on the area with the smallest standard deviation of the background clutter (0.02 dB, CR no. 5). On the amplitude image (proportional to $\sqrt{\sigma^0}$) obtained from the pixel-by-pixel calibration algorithm, we derived the values of σ for ARC No. 1 by evaluating the product $\mathcal{E}_{gp}A_p$ on the area containing the ARC response. The theoretical RCS (30.3 dBm^2) of the eleven CRs was derived within ±0.8 dB, which consequently represents the minimal accuracy in the estimation of σ.

A further step was the estimation of the ARC delay time, which was obtained by measuring the ground range R_G of CR No. 40, that is the nearest to ARC No. 1 (Fig. 8 depicts the geometry), and comparing this value with the Universal Transverse Mercator (UTM) co-ordinates known after the ground truth information, in order to compensate local bias effects due to geometric errors such as scale and skew. We evaluated R_G of the ARC and, after removal of geometric distortion effects estimated on the CR, we got the ground range difference between the location on the image and the actual position of the ARC. This offset was converted to a slant range displacement of two range bins, which corresponds (see Table 1) to a delay time of 44 ns.

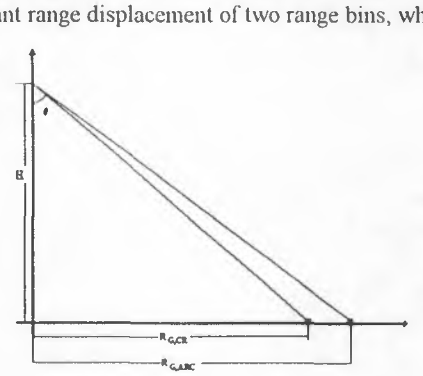

Figure 8: *Geometry for the evaluation of the ARC's delay*

5. RESULTS

An extensive set of anechoic chamber measurements have been carried out on the ARCs, and RCS and delay time of the active devices were evaluated on the compressed data with the techniques described in the previous section. A synoptic view of nominal, laboratory and calibration results is shown on Table 4 for ARC No. 1.

	Nominal Value	Laboratory Measurement	Measurement on calibrated SAR Images
Antenna Gain [dB]	15	16.0±0.6	-
RF Gain [dB]	51.2	49.2±0.6	-
RX-TX decoupling [dB]	>60 (VV) >54 (HH) >80(VH,HV)	~70 (VV)	-
RCS [dBm^2]	45.2	43.28±0.6	43.6±0.8
Delay time [ns]	-	30±0.5	44±11

Table 4: *Results: nominal values, laboratory measurements and estimated values from SAR images*

The first row reports the antenna gains. At boresight, the combined gain $G_{r,ARC} \cdot G_{t,ARC}$ of the ARCs' receiving and transmitting antennas, has been found to be 32.0 dB, measured with a standard-gain test antenna. The second row shows the laboratory measurements of G_a, the RF gain, performed at room temperature (22.5 °C). The differences from the nominal values are ascribable to the sum of L_{ATT}, the attenuator insertion loss, and L_{MIS}, the overall mismatch loss, which was 1.0 + 0.97 dB. The cross-polarization isolation measurements (HH and HV modes) gave a value below 32 dB, troughout the dynamic range. The third row reports the decoupling measurements, in different polarization configurations. The measured gain values have been used to evaluate σ_{ARC}, the peak RCS, with the basic equation (Ref. 14):

$$\sigma_{ARC} = \frac{\lambda^2}{4\pi} \frac{G_{r,ARC} G_{t,ARC} G_a}{L_{ATT} L_{MIS}} \tag{2}$$

where λ is the wavelength. The laboratory results, on the fourth row of Table 4, gave an RCS which satisfies the ±1dB precision requirement on a bare soil background (Ref. 15). The absolute radiometric bias factor K, defined after (1) as:

$$K = \frac{\sigma_{ref}}{A_u \mathcal{E}_{gp}} \tag{3}$$

was 52.4 dB. The RCS values have also been calculated by using the two radiometrically corrected images, and Table 4 reports the mean value.

The error budget on the laboratory calibration of the ARCs gave on the estimated accuracy on the RCS a value of ±0.6 dB. Error sources are summarized as follows:

- measurement accuracy due to the gain-measuring system: 0.2÷0.3 dB;
- antenna gain instability over temperature, evaluated by using the manufacturer's data: 0.1 dB;
- thermal noise, antenna pointing errors, multipath errors: ±0.2÷0.3 dB.

Finally, in far-field conditions, by positioning the active devices about 20 m away from the measurement equipment, we measured the propagation delay of each ARC, obtaining a value of 30±5 ns. The corresponding delay time (ARC No. 1) measured on the images is shown in the last row of Table 4. The accuracy of the delay measurement on the SAR images is δ_{sr}/c, where c is the velocity of light, and is ±11 ns.

6. CONCLUDING REMARKS

We have presented the design considerations and the validation strategy of an ARC, a high-and-tunable-RCS point target which can guarantee an accurate radiometric and geometric calibration of a SAR system, overcoming the stability and size problems of passive calibrators with the same RCS values. ARCs have some drawbacks, such as the relatively high cost, the inability of measuring the SAR transfer funtcion far from the high end of the allowable dynamic range, and therefore the risk of saturation on the digitized image, due to their high RCS. Nevertheless, ARCs have special characteristics which make them unique as external calibration devices, such as:

- the possibility of collecting a small portion of the received signal and feeding it to a Ground Receiver, or Acquisition, Section, capable of monitoring the in-flight azimuth antenna pattern by detecting the field strength during the synthetic aperture formation time;

- high signal-to-clutter ratios (SCR) in critical situations where a dark background (i.e. low σ^0) is not available;

- the availability of measurements of the SAR cross- and co-polarized transfer characteristics without different deployments;

- the variability of the propagation delay due to the waveguides and electronics of the RF section. This delay could be controlled in order to force the point target response in a more convenient location in the final image. For example, the ARC could be placed on the edge of a quasi-absorbing surface (a small lake or a large uniform field), and by inserting a suitable value of the delay time, the active device would be imaged on areas with very low backscattering;

- the possibility of inserting controlled phase errors on the interferometric data, by tuning the delay time. This could be a useful feature for interferometric phase calibration and for the estimation of processor-induced phase errors.

Currently, successful laboratory tests on a prototype ground acquisition section, interfaced to a PC, allow us to use the ARC with azimuth pattern recording features, and an X-band ARC with its Acquisition Section is being developed and tested. Future developments on our ARCs concern a better characterization of the error sources and a reduction of the absolute calibration error, together with the thermal stabilization of the RF section, mandatory when using the active calibrator as a ground receiver.

ACKNOWLEDGEMENTS

This work has been partly supported by the Italian Space Agency (ASI) under the contract ASI-90-RS70. Special thanks are due to Dr. E. Serena and Mr. G. Spaccarelli of Alenia Spazio for their contribution to the ARC's testing.

REFERENCES

1. Hartl P, Reich M, Bhagavathula S. 1987, An Attempt to Calibrate Air-borne SAR Images Using Active Radar Calibrators and Ground Based Scatterometers, *Proc. IGARSS '87 Symposium*, Ann Arbor, MI, pp. 501-508

2. Holt J, Freeman A 1990, Calibration of Bonanza Creek, Alaska, SAR Imagery Using Along-Track Calibration Targets, *Proc. IGARSS '90*, College Park, Maryland, Vol. III, pp. 2309-2312

3. Freeman A, Shen Y & Werner C L 1990, Polarimetric SAR Calibration Experiment Using Active Radar Calibrators, *IEEE Trans. Geosc. & Remote Sensing*, Vol.28, No. 2, pp. 224-240

4. Dobson M C, Ulaby F. T., Brunfeldt D. R. & Held D. N. 1986, External Calibration of SIR-B Imagery with Area-Extended and Point Targets, *IEEE Trans. Geosc. & Remote Sensing*, Vol. GE-24, No. 4, pp. 453-461

5. Seifert P., Lentz H., Zink M. & Heel F. 1992, Ground-Based Measurements of Inflight Antenna Patterns for Imaging Radar Systems, *IEEE Trans. Geosc. & Remote Sensing*, Vol. 30, No. 6, pp. 1131-1136

6. Freeman A. 1990, *SIR-C Ground Calibration Plan*, JPL D-6999

7. Woode A. D., Desnos Y.-L. & Jackson H. 1992, The Development and First Results from the ESTEC ERS-1 Active Radar Calibration Unit, *IEEE Trans. Geos. & Remote Sensing*, Vol. 30, No. 6, pp. 1122-1130

8. Zebker H. A., Madsen S. N., Martin J., Wheeler K. B., Miller T., Lou Y, Alberti G., Vetrella S., Cucci A. 1992, The TOPSAR Interferometric Radar Topographic Mapping Instrument, *IEEE Trans. Geosc. & Remote Sensing*, Vol 30, No. 3, pp. 933-940

9. Co.Ri.S.T.A.-AQUATER 1992, *Progetto SAR 1991: Rapporto Finale Campagna AGRISAR '91*, Co.Ri.S.T.A. internal document

10. Blacksmith P. Jr., Hiatt R. E., Mack R. B. 1965, Introduction to Radar Cross Section Measurement, *Proceedings of the IEEE*, Vol. 53, pp- 901-920

11. De Carolis G., Posa F., Veneziani N. 1991, Estimation of Linearity and Confidence Level for the SAR Radiometric Transfer Function, *Proc. 11th EARSeL Symposium*, Graz (Austria), pp. 130-139.

12. Gray A. L., Vachon P. W., Livingstone C. E. & Lukowski T. I. 1990, Synthetic Aperture Radar Calibration Using Reference Reflectors, *IEEE Trans. Geosc. & Remote Sensing*, Vol. GE-28, pp. 374-383

13. Ulander L. M. H. 1991, Accuracy of Using Point Targets for SAR Calibration, *IEEE Trans. Aerosp. & Elec. Syst.*, Vol. 27, No. 1, pp. 139-148

14. Brunfeldt D. R. & Ulaby F. T. 1984, Active Reflector for Radar Calibration, *IEEE Trans. Geos. & Remote Sensing*, Vol GE-22, No. 2, pp. 165-169

15. Ulaby F. T., Moore R. K. & Fung A. K. 1982, *Microwave Remote Sensing: Active and Passive*, Vol II, Addison-Wesley, Reading, MA

GERMAN SAR CALIBRATION ACTIVITIES: DEVICES AND RESULTS

Harald Lentz
University of Stuttgart
Institute of Navigation (INS)
Keplerstr. 11
70174 Stuttgart, Germany
Phone: +49 711 121 3400, Fax: +49 711 121 3500

ABSTRACT

The INS developed receivers and transponders for external SAR calibration in L-, C- and X-band. Approximately 100 devices have been manufactured or will be completed in the next weeks. This paper gives an overview on performance test results and on how the devices are calibrated. Furthermore first results from forest canopy penetration measurements and from campaigns to measure the antenna elevation pattern of ERS-1 and JERS-1 are given.

Keywords: Antenna elevation pattern, ground receivers, receiver calibration, receiver tests

CALIBRATION

A lot of receivers and transponders have been manufactured at INS. Their principle and their universal properties have been described previously [1], [2], [3]. Further reports are currently under preparation.
The special features of the calibration devices are:

- broad bandwidth,
- very high dynamic range,
- microcomputer controlled sampling and storage of radar pulses
- flexibility in PRF and pulselength
- resistance against distortion by ability to lock onto the desired signal
- synchronizable internal clocks (for beam alignement measurements)
- suitability for field deployment

Since a considerable quantity of these devices had to be manufactured, the question of how to achieve a high performance with regards to required manpower and costs got in the focus of the design philosophy. The calibration procedure necessarily had to be automated in some way.
The solution was to limit the efforts to build a 'perfect' hardware. A good hardware performance is the prerequisite and the final specifications of the devices are the result of an additional data correction by means of software.
For this reason the process of calibrating the receivers and transponders consists of the measurement of their behaviour under all circumstances occuring during field deployment. That means to determine temperature- and frequency-dependencies and nonlinearities. The knowledge of the remaining hardware imperfections then is used to correct the measured SAR-data and to determine the actual RCS-value in the case of a transponder. The internal temperature of the calibration devices therefore is measured by a built-in sensor and written into the memory to be read out together with the sampled SAR pulses. The correction is automatically performed by the special data evaluation software, developed at INS. The center frequency of the SAR sensor has to be specified manually and the software automatically reads the temperature from the measured data set to apply the correction data.
To perform the calibration process for a lot of devices, an automated facility has been installed at INS (Fig. 1). A computer controls a climate chamber, a microwave generator, a pulse generator and, in the case of a transponder, a power-meter. The computer adjusts 21000 combinations of power levels, frequencies and temperatures to get the total characterization of each individual calibration device. The chirp generator is only used to ensure that the calibration device affects no phase distortion. All measurements are referenced to the very accurate power-meter. By means of the individual ID of each device installed in their memory, the data

evaluation software applies the corresponding correction data set.

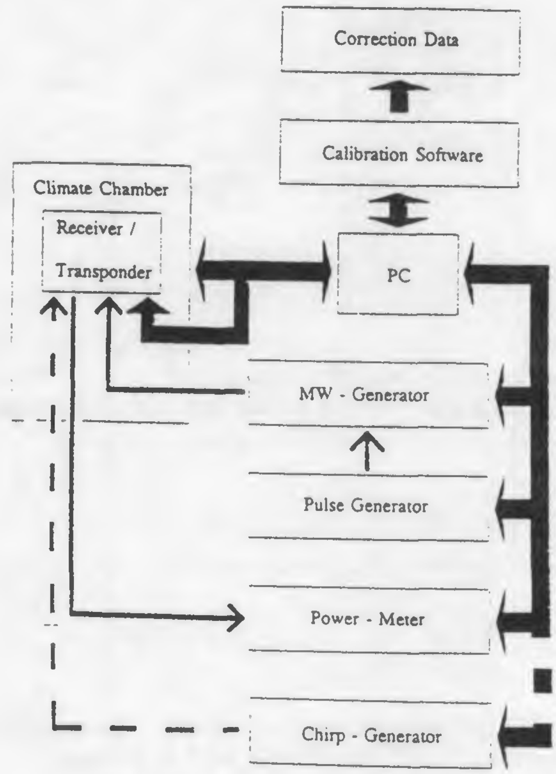

Fig. 1: Automatic facility for calibration of receivers and transponders

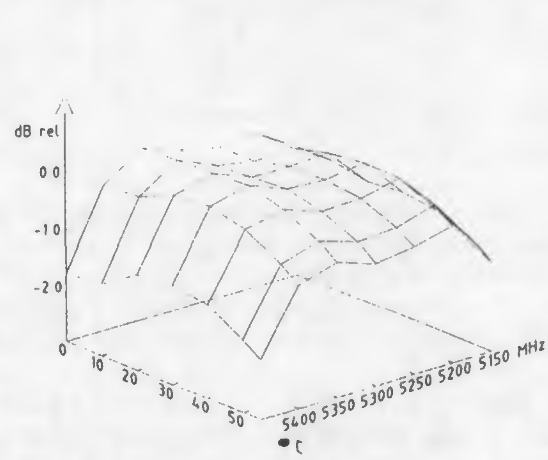

Fig. 2: Typical sensitivity behaviour of a receiver versus temperature and frequency. This variation is taken into account by the data evaluation software to perform the correction.

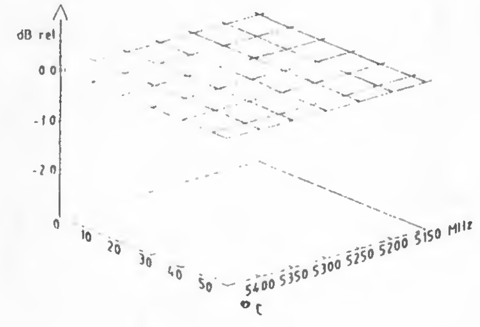

Fig. 3: Goal of the correction - a thermal- and frequency independent sensitivity.

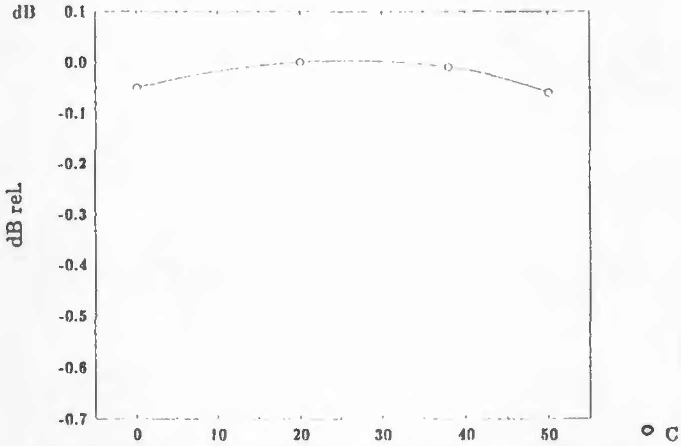

Fig. 4: Residual gain variation of the receiver after correction by software

Fig. 2 depicts the typical hardware behaviour of a C-band receiver for a particular input-power level. Since these properties are stored in the correction data set, the hardware imperfections can be removed from the measured SAR-signal. The goal is to achieve an ideal behaviour as shown in Fig. 3. Fig. 4 depicts the remaining error of a receiver for one particular input-power level and frequency. For higher power levels corresponding to a higher A/D-converter resolution, the results are even better.
Applying this strategy, remaining errors only occur due to a limited repeatability and ageing effects.
The antennas are measured seperately on test range at DLR, angle and frequency dependence are specified and stored in additional correction files.

ACTIVITIES

The activities in 1993 focused on the inflight antenna pattern measurement of ERS-1 and JERS-1. The campaigns have been carried out together with our colleagues from DLR. The test site is located near DLR/Oberpfaffenhofen in the northern surroundings of Munich. For both satellites, about 30 calibration receivers have been lined up - as straight as possible - perpendicular to the ground tracks of the satellites (Fig. 5). For ERS-1 the distance between the first and the last receiver was 170 km, approximately 100 km in the case of JERS-1 (Fig. 6). Each receiver led to one azimuth cut. The maximum-values of these cuts delivered the elevation pattern. The individual locations had been exactly measured by means of differential GPS and the built-in clocks of the calibration receivers had been synchronized by means of the time output of a GPS-receiver in order to perform a beam alignement measurement. The total procedure was quite similar to the campaign in 1992 [2], which only delivered results with limited accuracy due to extreme weather conditions with heavy rain. Fig. 7 depicts the measured antenna elevation pattern of ERS-1.
Since the satellite attitude and orbit parameters have not yet been evaluated, the results only can be considered preliminary. Especially the squint angles still have to be evaluated. Details will be discussed in a further paper.

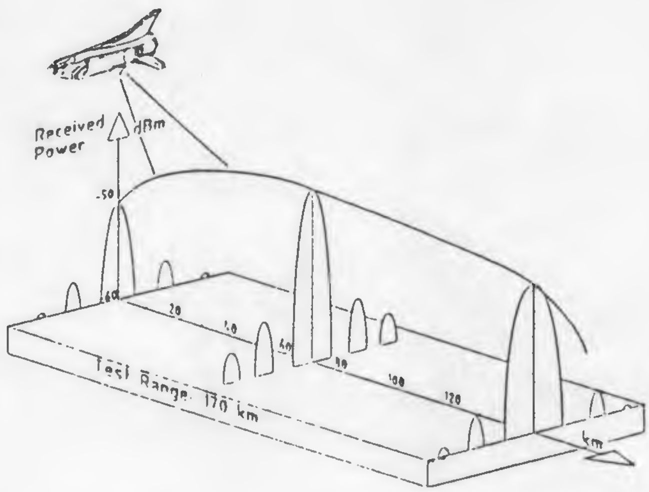

Fig. 5: Measurement of the SAR-antenna pattern, using the azimuth cuts

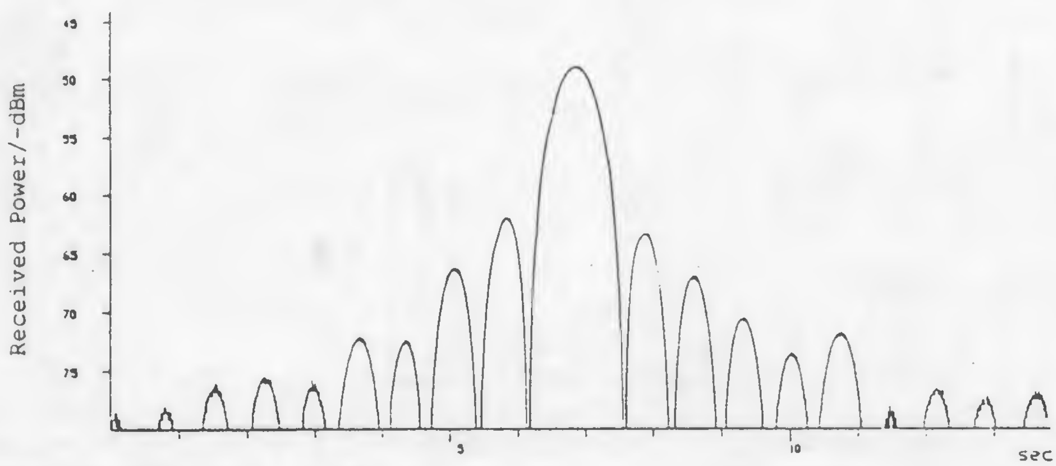

Fig. 6: One antenna azimuth cut of ERS-1

Fig. 7: Measured antenna elevation pattern for ERS-1

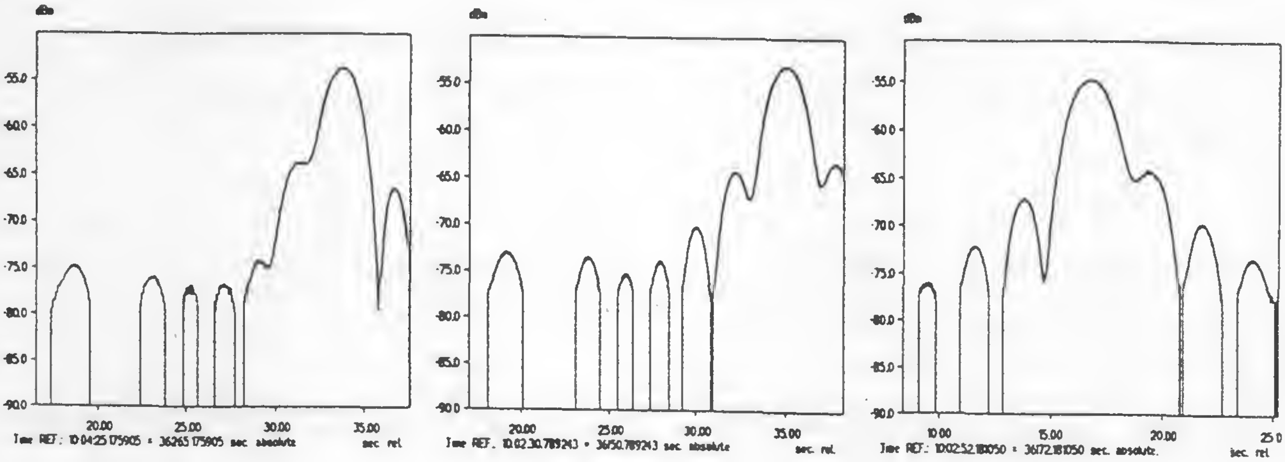

near mid far

Fig. 8, 9 and 10: Antenna azimuth cuts for JERS-1 measured at different range positions

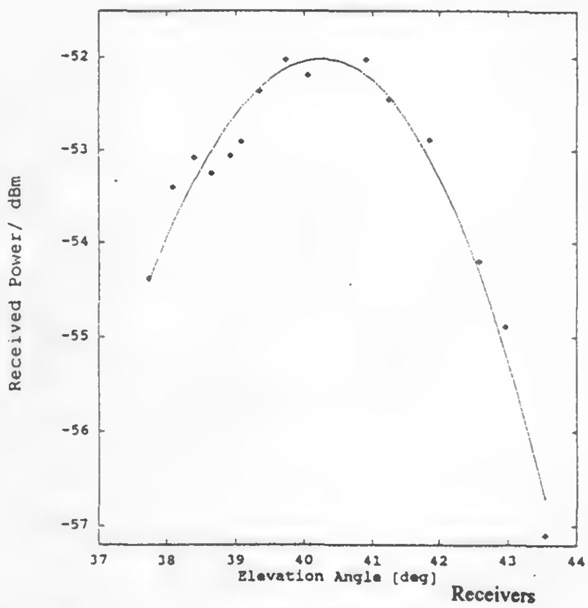

Fig. 11: Measured antenna elevation pattern of JERS-1

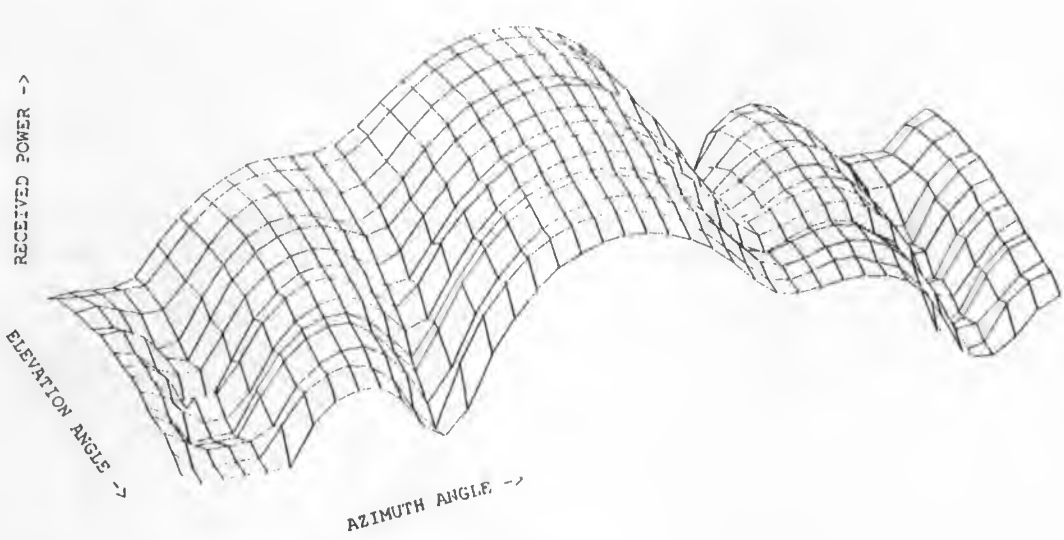

Fig. 12: Measured 3 dimensional antenna pattern of JERS-1

Considering Fig. 8, 9, 10 and 12 for JERS-1, a strange behaviour of the first sidelobes can be realized indicating a malfunction of the SAR antenna. This effect might be due to problems related to antenna unfolding. Furthermore the received power is 8 dB lower than expected which additionally indicates an output power reduction.

Recently the INS started vegetation canopy penetration measurements using ERS-1. For this purpose several receivers have been deployed beneath different species of trees, each with different foilage thickness. The final goal is to be able to distintinguish between the contribution of the trees and the soil in the radar image. Since the efforts started recently, there is only a small database for comparison and averageing. Therefore Fig. 13 is only very preliminary. It depicts the one way effect on the incident waves. The locations of the ground based receivers try to avoid direct influences by the logs of the trees. The measurements are referenced to two receivers which have direct sight to the SAR-transmitter. The studies will be continued.

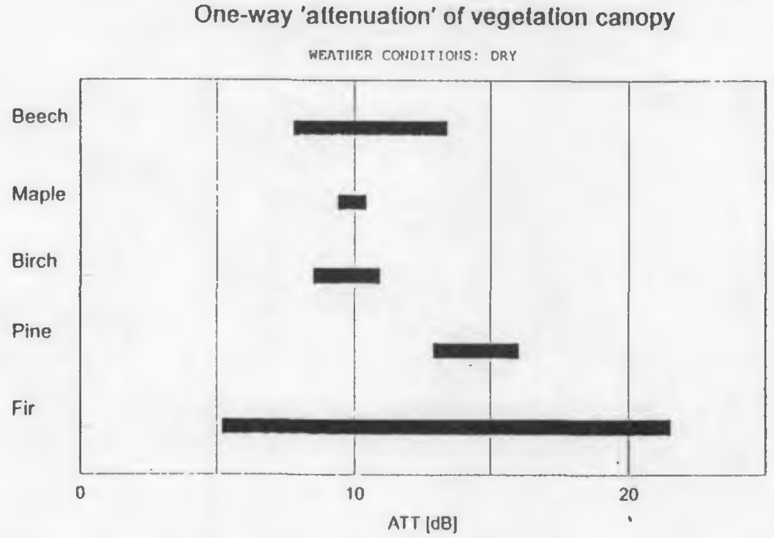

Fig. 13: 'Attenuation' of the incident waves by different kinds of vegetation canopy

ACKNOWLEDGEMENTS

The author wishes to thank all colleagues from INS and DLR involved in the campaigns and especially the team from INS which is responsible for manufacturing and calibrating the devices.

REFERENCES

[1] P. Seifert, H. Lentz, M. Zink, F. Heel; "Ground-Based Measurements of Inflight Antenna Patterns for Imaging Radar Systems", *IEEE Transactions on Geoscience and Remote Sensing*, Vol. 30, No.6, pp 1131-1136, Nov 1992

[2] P. Seifert, H. Lentz, M. Zink;"ERS-1 Preliminary Antenna Elevation Pattern Measured by Ground Receivers", *Proceedings of the First ERS-1 Symposium*, ESA SP-359, pp 157-159, March 1993

[3] H. Lentz;"Receivers and Transponders for SAR-Calibration",Status Report XSAR/SIR-C Project, DARA-contract No. 01QS89024, Dec. 1992

POLARIMETRIC CALIBRATION

Session 3

Chair: R.CORDEY, GEC-Marconi, UK

THE EFFECTS OF NOISE ON POLARIMETRIC SAR DATA

A. Freeman

Jet Propulsion Laboratory
California Institute of Technology
4800 Oak Grove Drive
Pasadena, CA 91109, USA.
Tel: (818) 354 1887
Fax: (818) 393 6943
e-mail: Freeman@jplpol.jpl.nasa.gov

ABSTRACT

Polarimetric SAR data can provide a great deal of information about the scattering behavior of the surface under observation. Polarimetric SAR systems often measure the scattering matrices of the areas under observation in linear polarizations (H and V). From the scattering matrix commonly used forms such as the covariance matrix and the Stokes matrix can be easily derived. Other measures derived from polarimetric SAR data include correlation coefficients between scattering matrix terms and the mode and variance of phase differences between scattering matrix terms. The effects of additive system noise on these measurements is not often considered in the literature on this subject.

In this paper, the effects of additive system noise on measurements derived from polarimetric SAR data will be examined. It will be shown how first-order noise effects can be removed and how second-order noise effects can be reduced for some measurements. Some commonly occurring characteristics of polarimetric SAR data which may be attributed to noise, such as the pedestal on a polarization signature, or a broadening in the distribution of the HH-VV phase difference over an area, or a reduction in the magnitude of a correlation coefficient, will be identified. The appearance of azimuth ambiguities in polarimetric SAR data is also addressed.

Keywords: Polarimetric SAR, Data Analysis, Azimuth ambiguities

BASIC POLARIMETRIC SAR MEASUREMENTS

For nominally calibrated polarimetric SAR measurements, the measured matrix, **M**, should be related to the scattering matrix of interest, S, via:

$$\mathbf{M} = \begin{pmatrix} S_{HH} & S_{VH} \\ S_{HV} & S_{VV} \end{pmatrix} + \begin{pmatrix} n_{HH} & n_{VH} \\ n_{HV} & n_{VV} \end{pmatrix} \equiv \mathbf{S} + \mathbf{N}$$

where N is a matrix representing the noise in each polarization channel. This noise cannot be removed from the measurements. It remains to characterize this additive noise, examine the sources which give rise to it and its effects on measures commonly derived from polarimetric SAR data.

NOISE SOURCES

Potential sources of additive noise in polarimetric SAR data are:

- Thermal noise - from the radar receiver, antenna and background radiation (e.g. earth noise)

- Analog-to-Digital (ADC) conversion noise - includes both quantization (rounding or truncation) and saturation noise
- Interference - due to transponders on the ground or to transmitters
- Ambiguities - 'ghost' images visible in both range and azimuth directions

In this paper, saturation noise and interference will not be included in the discussion.

SNR GOALS

Goals for Signal-to-Noise ratios in polarimetric SAR data are 20dB [1].

NOISE CHARACTERISTICS

Thermal noise and quantization noise are usually characterized as white noise inputs. That is, they have constant spectral density over all bandwidths. We characterize this type of noise term as having two-dimensional (real and imaginary), zero-mean, Gaussian distributions, with the following properties:

$$\langle n_{jk} \rangle = 0$$

$$\langle n_{jk} n_{jk}^{*} \rangle = \sigma_{jk}^{*}$$

$$\langle n_{jk} n_{lm}^{*} \rangle = 0 \text{ , for } j \neq l \text{ or } k \neq m.$$

$$\langle n_{jk} S_{lm}^{*} \rangle = 0 \text{ , for any } j, k, l, m.$$

where σ_{jk}^{n} is the noise power (or noise-equivalent sigma-zero) in the polarization channel jk. We assume that the noise terms are uncorrelated with each other and with the scattering matrix (signal) terms.

The assumption of constant spectral density for thermal noise and quantization noise may not apply after SAR processing, in which several filters (azimuth matched filter, range matched filter, multi-looking, etc.) are applied. The net effect of these filters is usually to leave the noise spectrum shaped instead of constant over some bandwidth. This is known as colored noise.

AMBIGUITIES

Ambiguities are caused by aliasing in the azimuth dimension and by receiving echoes from different pulses simultaneously in the range dimension. Ambiguities are unlike other forms of 'noise' in that they can appear to be focused and look like 'ghost' images. Azimuth ambiguities occur at fixed along-track repeat positions with respect to the position, x_o, of the actual feature, i.e. at positions:

$$x = x_o + \frac{n \lambda R_o PRF}{V} \equiv x_o + n\Delta A$$

where n is an integer denoting the number of the ambiguity, λ is the wavelength, R_0 the range at closest approach, V the relative speed between platform and target and PRF the pulse repetition frequency.

When collecting polarimetric SAR data, some systems, such as the NASA/JPL AIRSAR, collect HH, HV and VH, VV returns separately, i.e. on adjacent pulses. The returns are separated by intervals 1/2PRF in time or V/2PRF in the along-track dimension, where 2PRF is the frequency at which pulses are transmitted, but PRF is the frequency at which H or V polarized pulses are transmitted.. If the HH, HV response occurs at position x_o, the VH, VV response occurs at position

$$x = x_o + \frac{V}{2PRF} \equiv x_o + \Delta x$$

The VH, VV returns are then resampled so that they are registered with the HH, HV returns.

The azimuth phase history for a target positioned at x_o can be represented by:

$$s(x) = \exp\left\{j\frac{4\pi R_o}{\lambda}\right\} \exp\left\{ j\frac{2\pi}{\lambda R_o}(x - x_o)^2\right\}$$

Suppose the HH, HV returns are from a target positioned at x_o. After resampling the VH, VV returns will still have a phase shift $2\pi(\Delta x)^2/\lambda R_o$ with respect to the HH, HV returns. It is straightforward to remove this phase shift with an appropriate multiplication by a complex number.

Now consider what happens to azimuth ambiguous returns when the above procedure is applied. The HH, HV ambiguous responses occur at the position $x_o + n\Delta A$, while the VH, VV ambiguous responses occur at $x_o + n\Delta A + \Delta x$. Using the expression for the azimuth phase history given in (3), it can be shown that, after resampling and correction for the nominal phase shift, the phase difference between the ambiguous HH, HV and the VH, VV returns is $n\pi$. This can readily be seen in AIRSAR images of bright point targets: the first ambiguities lie at a distance ΔA either side of the main response and the phase difference between HH and VV is π radians. Thus the first (and strongest) ambiguities often look like 'ghosts' of the real thing but with the HH-VV phase difference changed by ~180 degrees. In Figure 1 is shown a point target HH response from a corner reflector at a calibration site, together with the 1st ambiguity on the right. The peak level of the ambiguity is 22dB down from the peak of the actual response. The HH-VV phase difference for the peak of the ambiguity is 168°, while the corresponding value for the actual response is -6°.

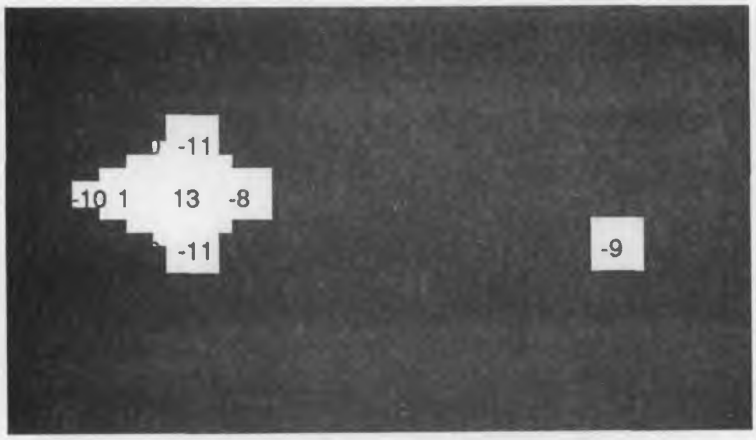

Figure 1: Point target response from C-band HH AIRSAR image, showing position of 1st azimuth ambiguity on the right-hand side

POLARIMETRIC SAR MEASUREMENTS

In this section, the effects of noise on several common measures used in analysis of polarimetric SAR data are examined. It is assumed that the scattering matrix measurements have been 'symmetrized', i.e. that the HV and VH measurements have been averaged together, as is the case for NASA/JPL AIRSAR data. Note that, after symmetrization, the noise power in the HV measurement should be:

$$\sigma^n_{HV} = \frac{(\sigma^n_{HV} + \sigma^n_{VH})}{4}$$

COVARIANCE MATRIX

Forming cross-products between the elements of the measured matrix, **M**, yields the elements of the covariance matrix associated with the measurements. Under the assumption that the backscatter is reciprocal, the expected value of these six cross-products can be shown to be:

$$\left\langle M_{HH} M^*_{HH} \right\rangle = |S_{HH}|^2 + \sigma^n_{HH}$$

$$\left\langle M_{HV} M^*_{HV} \right\rangle = |S_{HV}|^2 + \sigma^n_{HV}$$

$$\left\langle M_{VV} M^*_{VV} \right\rangle = |S_{VV}|^2 + \sigma^n_{VV}$$

$$\left\langle M_{HH} M^*_{VV} \right\rangle = \left\langle S_{HH} S^*_{VV} \right\rangle$$

$$\left\langle M_{HH} M^*_{HV} \right\rangle = \left\langle S_{HH} S^*_{HV} \right\rangle$$

$$\left\langle M_{HV} M^*_{VV} \right\rangle = \left\langle S_{HV} S^*_{VV} \right\rangle$$

where the σ^n_{XY} terms are the noise powers in the HH, HV and VV measurements. The average values of these noise powers, if known, ca subtracted off cross-product measurements which have been averaged areas. This corrects for the first-order noise effects. Spatial averaging reduces the variance of higher order noise fluctuations.

STOKES MATRIX

Another way of representing the cross-products derived from the scat matrix elements is in the Stokes matrix format [13]. For reciprocal scat the Stokes matrix F is a 4x4 symmetric matrix, with the following elements:

$$F_{11} = 0.25(M_{HH} M_{HH}^* + 2M_{HV} M_{HV}^* + M_{VV} M_{VV}^*)$$

$$F_{12} = 0.25(M_{HH} M_{HH}^* - M_{VV} M_{VV}^*)$$

$$F_{13} = 0.5\mathrm{Re}\,(M_{HH}^* M_{HV}) + 0.5\mathrm{Re}\,(M_{HV}^* M_{VV})$$

$$F_{14} = 0.5\mathrm{Im}\,(M_{HH}^* M_{HV}) + 0.5\mathrm{Im}\,(M_{HV}^* M_{VV})$$

$$F_{22} = 0.25(M_{HH} M_{HH}^* - 2M_{HV} M_{HV}^* + M_{VV} M_{VV}^*)$$

$$F_{23} = 0.5\mathrm{Re}\,(M_{HH}^* M_{HV}) - 0.5\mathrm{Re}\,(M_{HV}^* M_{VV})$$

$$F_{24} = 0.5\mathrm{Im}\,(M_{HH}^* M_{HV}) - 0.5\mathrm{Im}\,(M_{HV}^* M_{VV})$$

$$F_{33} = 0.5\,(M_{HV} M_{HV}^*) + 0.5\mathrm{Re}\,(M_{HH}^* M_{VV})$$

$$F_{34} = 0.5\mathrm{Im}\,(M_{HH}^* M_{VV})$$

$$F_{44} = 0.5(M_{HV} M_{HV}^*) - 0.5\mathrm{Re}\,(M_{HH}^* M_{VV})$$

When there is no signal present, i.e. the scattering matrix elements ar zero, the expected values of the Stokes matrix terms are:

$$\langle F_{11}\rangle = 0.25\left(\sigma_{HH}^n + 2\sigma_{HV}^n + \sigma_{VV}^n\right)$$

$$\langle F_{12}\rangle = 0.25\left(\sigma_{HH}^n - \sigma_{VV}^n\right)$$

$$\langle F_{13}\rangle = \langle F_{14}\rangle = \langle F_{23}\rangle = \langle F_{24}\rangle = \langle F_{34}\rangle = 0$$

$$\langle F_{22}\rangle = 0.25\left(\sigma_{HH}^n - 2\sigma_{HV}^n + \sigma_{VV}^n\right)$$

$$\langle F_{33}\rangle = \langle F_{44}\rangle = 0.5\,\sigma_{HV}^n$$

These are the first-order, additive noise powers to be corrected in the presence of a signal. Note that if the noise powers in each of the channels are equal (before symmetrization), only the F_{11}, F_{22}, F_{33} and F_{44} terms contain significant first-order noise terms. As for the covariance matrix, spatial averaging will reduce the variance of higher order noise fluctuations in the Stokes matrix measurements.

CORRELATION COEFFICIENTS

When forming a correlation coefficient between the HH and VV scattering matrix measurements, the following is calculated by averaging over an area:

$$\frac{\langle M_{HH} M_{VV}^{*}\rangle}{\sqrt{\langle M_{HH} M_{HH}^{*}\rangle \langle M_{VV} M_{VV}^{*}\rangle}}$$

This can be corrected for first-order noise effects by initially correcting the covariance matrix elements used to calculate the correlation coefficient. If this is not done, the estimated correlation coefficient will be lower than the actual one. The same applies to correlation coefficients formed from other combinations of scattering matrix elements. Again, spatial averaging will reduce the variance of higher order noise fluctuations in the correlation coefficient measurements.

POLARIZATION SIGNATURES

For any given radar receive and transmit polarization, the radar cross-section (RCS) can be calculated from the scattering matrix, $\mathbf{S}$, via:

$$\sigma_{pq} = 4\pi \left| \bar{\mathbf{q}}^{r}\, \mathbf{S}\, \bar{\mathbf{p}}^{t} \right|^{2}$$

where $\mathbf{q}^{r}$, $\mathbf{p}^{t}$ are polarization field vectors for the radar receive and transmit polarizations, respectively. This procedure is called polarization synthesis. Polarization signature plots are a useful tool for visualizing polarimetric scattering properties of a target. They represent the synthesized response of the target to all possible like-polarized or cross-polarized radar transmit/receive combinations. The polarization signature plots are given as functions of orientation and ellipticity angle, and are normalized with respect to the total power, F_{11}.

The scattering matrix model for Bragg scattering from an idealized rough surface, such as wind-blown water, is:

$$\mathbf{S} = \begin{pmatrix} a & 0 \\ 0 & b \end{pmatrix} \quad \begin{matrix} \text{with } a,b \text{ real}, b>a>0 \\ \text{and } \langle ab^{*}\rangle = ab \end{matrix}$$

i.e., a scattering matrix with zero cross-polarized return, HH and VV returns which are completely correlated and zero phase difference between the HH and VV returns. A polarization signature corresponding to a typical Bragg scatterer is shown in Figure 2.

Rosamond 170-4

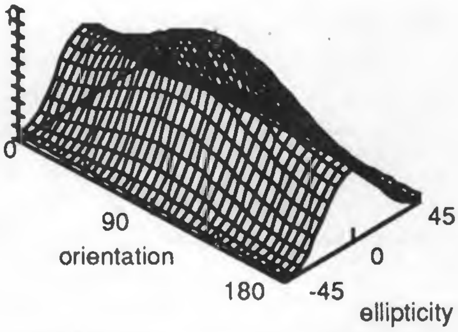

Figure 2: Like-polarized polarization signature of a typical Bragg scatterer with high SNR

The polarization signature in Figure 2 shows the case where there is a high SNR (>18dB). Figure 3 contains an example of a polarization signature of a Bragg scatterer when the SNR is low (<7dB). Note that the pedestal (minimum level of the polarization signature) is significantly increased.

Rosamond 170-4

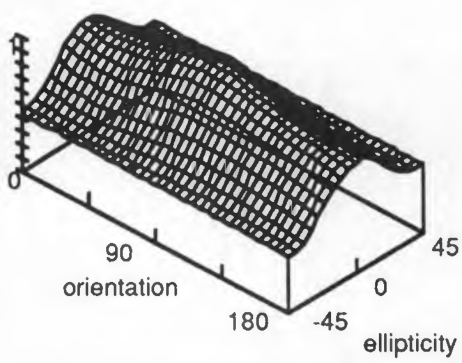

Figure 3: Like-polarized polarization signature of a typical Bragg scatterer with low SNR

PHASE DIFFERENCE PLOTS

In Figure 4, HH-VV phase difference plots for the same scatterers examined in Figure 3 are shown. The presence of noise in the low SNR case broadens the distribution of the phase histogram but does not significantly alter the mode of the distribution.

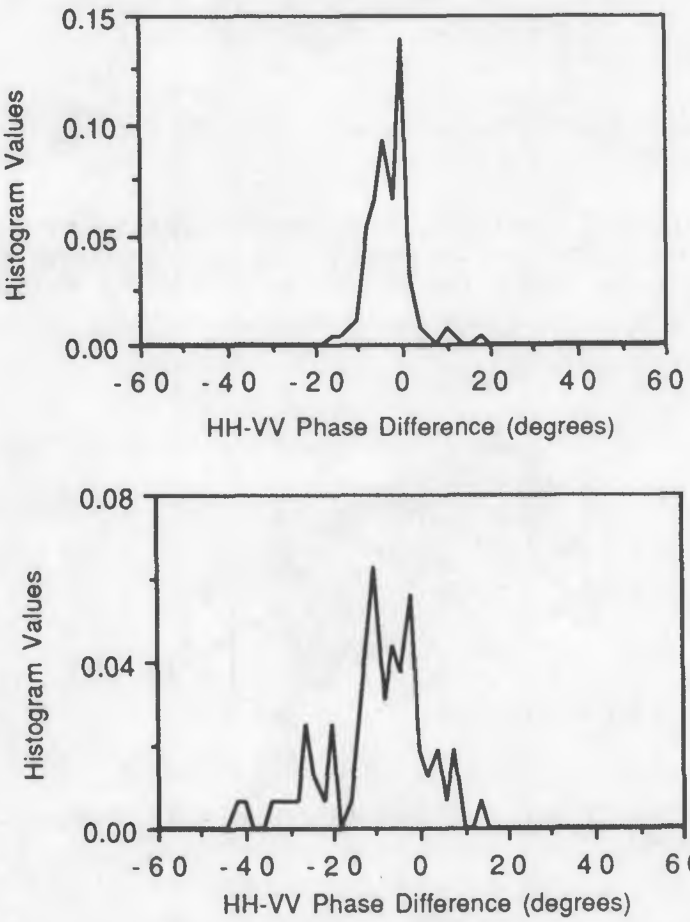

Figure 4: HH-VV phase difference histogram plots for typical Bragg scatterers with a) high SNR and b) low SNR

SUMMARY AND DISCUSSION

The importance of knowledge of the noise power present in the HH, HV, VH and VV measurements made by a polarimetric SAR system has been demonstrated above. If the noise powers are known, they can be used to apply a first order correction to averaged covariance matrix or Stokes matrix values. If such first order noise corrections are not applied, several measures commonly derived from polarimetric SAR data may give erroneous results. Spatial averaging reduces the higher order fluctuations in the noise.

The noise power values as a function of range position in the image should, ideally, be provided with the data. In the absence of information on the noise powers, the user can get a crude estimate of an upper bound to the noise floor by examining the HV backscatter corresponding to a target demonstrating known Bragg scattering behavior (e.g. a water surface or a dry lake bed). This should give an estimate for the noise power in the HV measurements. For "symmetrized" data, if the noise powers were all equal before symmetrization, the HH and VV noise powers would then be 3dB higher than the HV.

Also, it was shown that the first and brightest azimuth ambiguities (i.e. those closest to the main response) occur at predictable locations and with an HH-VV phase difference 180 degrees away from the phase difference associated with the main response. Thus, in polarimetric SAR data, very bright single-bounce or double-bounce scatterers will give rise to ambiguities in azimuth that look like fairly bright double-bounce or single-bounce scatterers, respectively.

ACKNOWLEDGMENT

The research described in this paper was carried out by the Jet Propulsion Laboratory, California Institute of Technology, under a contract with the National Aeronautics and Space Administration.

REFERENCES

[1] Dubois, P.C., Evans, D. and van Zyl, J.J., "Approach to Derivation of Science Requirements for Calibration, IEEE Trans. on Geoscience and Remote Sensing, vol. 30, No. 6, Nov. 1992, pp. 1145-1149.

STATISTICAL ASPECTS OF POLARIMETRIC CALIBRATION AND MEASUREMENT

S. Quegan
School of Mathematics and Statistics
University of Sheffield, UK

ABSTRACT

The K distribution model for polarimetric data appears consistent with AirSAR observations from vegetation. This implies that the properties of single frequency measurements from distributed targets are completely described by an order parameter, the powers in each channel and the cross-channel correlation coefficients. Estimators for these quantities are described. For the Gaussian case, the effects of both noise and spatial correlation on the covariance estimates are also derived.

Keywords: Product model, target characterisation, parameter estimation

1. INTRODUCTION

The purpose of calibration is to define a type of measurement and to guarantee that the data provided is a true representation of this measurement, with known limitations, such as those due to noise. At the lowest level, this is a guarantee that the pixel values in a scattering matrix or a Muller matrix image are not corrupted by cross-talk, antenna pattern, channel imbalance, etc.

A more general view of calibration may include the definition of the useful parameters which can be extracted from the data, i.e. the minimal set of measurements which completely characterises the scattering behaviour of particular types of targets, especially extended scatterers. This presupposes the existence of a reliable data model, hence may seem to greatly extend the concept of calibration (or, in fact, stretch it too far). However, in polarimetric calibration, this extended view of calibration is already part of the process, because of the importance of the behaviour of distributed scatterers in providing calibration information.

It is also sensible to take such an extended view of calibration if the purpose is to provide reliable data for applications purposes. The user should be aware of the range of independent measurements which may be available, especially from distributed targets. He/she should also be aware of:

- the optimal methods to estimate parameters from the data
- limitations due to sampling
- limitations due to noise
- the effects of (spatial) correlation.

Particularly in polarimetric data, the relevance of the parameters extracted to observables (such as phase difference) should also be made clear.

This paper begins by describing a data model for polarimetric data, including image texture, and evidence for its validity. This data model provides a concise definition of information content and useful measurements for distributed targets. It also provides descriptions of the distributions of observables, such as data moments and histograms. Analytic results are available for most of the important distributions and moments, for both single look and multi-look data. After describing these, the maximum likelihood estimators of the defining parameters are discussed. This is followed by a discussion of the effects of noise on the estimators, and the effects of spatial correlation.

2. DATA MODELS

A natural extension of models for single channel data from extended targets is derived in [Ref.1], where an N-dimensional K distributed model for polarimetric data is developed. This is more general than, and includes, the N-dimensional Gaussian model used by several authors in their analyses of polarimetric data [Refs. 2, 3]. The simplest description of this data model is as a product model; the observed values $\mathbf{z}$ of the scattering matrix can be regarded as a product

$$\mathbf{z} = \sqrt{\gamma}\omega \tag{1}$$

where γ is a unit mean (scalar) gamma distributed variable, and ω is a multi-variate zero-mean complex Gaussian variable. For calibrated data, the vector $\mathbf{z}$ can be taken as

$$\mathbf{z} \equiv (z_1, z_2, z_3)^t \equiv (S_{hh}, S_{hv}, S_{vv})^t \tag{2}$$

where the S_{ij} are the (symmetric) scattering matrix values and ^{t} denotes transpose.

The gamma-distributed part of the product is described by a single number, its order parameter, ν, and characterises surface fluctuations. The Gaussian part is completely described by the covariance matrix of the complex channels

$$C[i,j] = \langle z_i z_j^* \rangle \tag{3}$$

where $\langle\cdot\rangle$ denotes expected value. We can write, up to a constant of proportionality,

$$C = \begin{pmatrix} \sigma_1 & \sqrt{\sigma_1\sigma_2}\rho_{12} & \sqrt{\sigma_1\sigma_3}\rho_{13} \\ \sqrt{\sigma_1\sigma_2}\rho_{12}^* & \sigma_2 & \sqrt{\sigma_2\sigma_3}\rho_{23} \\ \sqrt{\sigma_1\sigma_3}\rho_{13}^* & \sqrt{\sigma_2\sigma_3}\rho_{23}^* & \sigma_3 \end{pmatrix} \tag{4}$$

where $\sigma_i = \langle | z_i |^2 \rangle$ is the RCS of channel i, and

$$\rho_{ij} = \frac{\langle z_i z_j^* \rangle}{\sqrt{\sigma_i \sigma_j}} \tag{5}$$

is the complex correlation coefficient of channels i and j. Since the σ_i are real, this means that there are 10 potential pieces of information in the data, viz. the three real values of σ_i, the three phases and amplitudes of the ρ_{ij}, and the order parameter ν. As is well-known, for azimuthally symmetric targets only ρ_{13} would be non-zero, which reduces the number of free parameters to six. Where surface fluctuations are not significant, there is a further reduction to only five variables.

3. CONSEQUENCES OF THE DATA MODEL

In principle, any observable property of a distributed target can be constructed from the 10 numbers of the model. It has proved possible to derive analytic formulae for many of the observables thought to be useful. In particular, analytic expressions are available for the following:

1. The phase and amplitude distributions of z_i/z_j, which are independent of ν. The phase of this ratio is the phase difference of the two channels. The cumulative density functions are also analytic, and can be used to derive formulae for the mean and variance of phase.

2. The real and imaginary parts and the phase and amplitude of the Hermitian product $z_i z_j^*$

$$z_i z_j^* \equiv A + jB \equiv Qe^{j\theta}. \tag{6}$$

The phase of this product is again the phase-difference of the two channels. The moments of A, B and Q are also known.

3. The distributions of the in-phase and quadrature components and amplitude of each channel.

Other aspects of the model which relate to observables are:

1. The order parameter ν is calculable from each channel separately, and should not depend on channel.
2. There is a predicted relationship between the correlation coefficients of the intensity and complex scattering matrix data. If the intensity of channel i is written $I_i = |z_i|^2$, then

$$\rho_{ij}^{(I)} = \frac{\langle I_i I_j\rangle - \langle I_i\rangle\langle I_j\rangle}{\sqrt{\langle (I_i - \langle I_i\rangle)^2\rangle\langle (I_j - \langle I_j\rangle)^2\rangle}} = |\rho_{ij}|^2 \tag{7}$$

Derivations of these results can be found in [Refs. 1, 4, 5], where analytic results are also derived for distributions of the amplitude, phase and real and imaginary parts of the averaged Hermitian product

$$\frac{1}{M}\sum_{k=1}^{M} z_i^{(k)} z_j^{(k)*} \tag{8}$$

This is the key quantity in dealing with multi-look data. As a reference, a few of the less well-known results for single look data are given in the Appendix.

4. COMPARISON OF DATA WITH THEORY

Though the theory is well developed, it has not been extensively tested. Results are reported in [Refs. 1, 3, 6, 7], in all cases restricted to vegetated areas. A thorough investigation dealing with other surface types and temporal changes has yet to be made. However, the most comprehensive set of measurements [Ref. 7] confirms the theoretical predictions. This study, based on data from the MacEurope campaign, shows that at shorter wavelengths (C-band) and the comparatively low resolution of the AirSAR data (15.5 × 11 m in azimuth and slant range), all the vegetation types considered exhibited Gaussian behaviour. At longer wavelengths, there are marked departures from the Gaussian model, which are well-reproduced by the K distribution model. Phase difference and amplitude ratio distributions also coincide with theory, and the order parameter shows similar behaviour between channels. (Different channels did not give exactly the same value of the order parameter, but this may be due to estimation error; see below.)

5. ESTIMATORS

The K distribution model focusses attention on a small number of quantities in order to fully describe the parameters of the data. These are:

- the mean power in each channel (the RCS of each channel, σ_i);
- the phase and amplitude of the inter-channel complex correlation coefficients, ρ_{ij} ;
- the order parameter, ν.

We need to know how to recover the best estimate of each of these parameters from the data, which may be in scattering matrix or Muller matrix form. In the first instance, the effects of noise and spatial correlation will be ignored.

For single-look data, the estimation of σ_i, $r = |\rho_{ij}|$ and $\theta_0 = \angle\rho_{ij}$ contains few surprises. Given M independent measurements, it is easy to show [Blacknell, private communication] that the maximum likelihood estimators (MLEs) for these quantities are given by:

$$\hat{\sigma}_i = \frac{1}{M}\sum_{p=1}^{M} \mid z_i^{(p)} \mid^2 \tag{9}$$

$$\hat{r}e^{i\hat{\theta_0}} = \frac{1}{M}\frac{\sum_1^M z_i^p z_j^{(p)*}}{\sqrt{\hat{\sigma}_i\hat{\sigma}_j}} \tag{10}$$

where the individual measurements in channel i are indexed by p, $1 \leq p \leq M$. These are obvious estimators and easy to apply. Their asymptotic variances are also known:

$$\begin{aligned} Var(\hat{\sigma}_i) &= \tfrac{1}{M}\sigma_i^2 \\ Var(\hat{r}) &= \tfrac{\sigma_i\sigma_j}{2M}(1+r^2) \\ Var(\hat{\theta_0}) &= \tfrac{1}{2M}\left(\tfrac{1}{r^2}-1\right). \end{aligned} \tag{11}$$

The first of these is the familiar result that variances of independent measurements add.
Notice that, since $0 \leq r^2 \leq 1$,

$$\frac{\sigma_i\sigma_j}{2M} \leq Var(\hat{r}) \leq \frac{\sigma_i\sigma_j}{M} \tag{12}$$

and that the estimation error increases as the channels become more correlated (again, no surprise). The estimation error in θ_0 is not so well-behaved. For highly correlated channels, the error is small and the phase difference is very well defined. When r is small, however, the accuracy of the estimate becomes very poor. This is to be expected, since θ_0 is in fact the mode of the phase difference distribution. As $r \longrightarrow 0$, this distribution becomes flat, and hence the mode is undefined (or can take any value in the range $-\pi < \theta_0 \leq \pi$).
As an aside, the expression for $Var(\theta_0)$ should not be regarded as complete, since it has not properly exploited the condition $\mid \hat{\theta_0} \mid\leq \pi$. If this is used, we find that $Var(\hat{\theta_0}) \leq \pi^2/3$.
The best estimate of the order parameter ν is more complicated. Since ν should be the same for all channels, it can be estimated from a single channel (though this is not optimal). The simplest estimate is based on the moment relation

$$\frac{\langle I^2\rangle}{\langle I\rangle^2} = 2\left(1+\frac{1}{\nu}\right) \tag{13}$$

as was used in [Ref. 1] and [Ref. 6]. A better estimate is in fact provided by solving the equation

$$\psi(\nu) + \psi(1) - \ln\nu = \langle \ln I\rangle - \ln\langle I\rangle \tag{14}$$

where $\psi(\cdot)$ is the digamma function. This is significantly less biased and has smaller variance than an estimate based on (13) [Refs. 8, 9], but is computationally more demanding.
The MLE of ν requires the simultaneous solution of the pair of equations

$$\frac{(\nu+1)}{\alpha} = \frac{1}{M}\sum_{j=1}^{M} A_j \frac{K_\nu(2\alpha A_j) + K_{\nu-2}(2\alpha A_j)}{K_{\nu-1}(2\alpha A_j)} \tag{15}$$

and

$$\ln\psi(\nu) - \ln\alpha = \frac{1}{M}\sum_{j=1}^{M}\left(\ln A_j + \frac{\frac{\partial}{\partial\nu}K_{\nu-1}(2\alpha A_j)}{K_{\nu-1}(2\alpha A_j)}\right) \tag{16}$$

for ν and the mean power σ_i, where $\alpha = \sqrt{\nu/\sigma_i}$, and $\{A_j\}$, $1 \leq j \leq M$, are the amplitude values of the data. This presents practical difficulties, so that use of (14) is preferable.

6. NOISE

Equation (1) does not provide a full description of the observations, since the noise in each channel should be taken into account. In this case, (1) becomes

$$z = \sqrt{\gamma}\omega + n \tag{17}$$

where n is a noise vector. Equation (17) is directly applicable to the observed data before calibration. However, if the calibration procedure is linear (as is the case, at least for cross-talk calibration, in the methods proposed in [Refs. 10-12]) then it can also be used to model the data after calibration, when z can be taken to represent true scattering matrix data (this ignores errors in the calibration procedure introduced by noise effects).

The effects of noise on the estimated covariance elements are relatively straightforward to describe, under the assumptions that noise is zero-mean, uncorrelated between channels and uncorrelated with the signal. Then

$$\hat{C}_{ij} = \frac{1}{M}\sum_{p=1}^{M} z_i^{(p)} z_j^{(p)*} \tag{18}$$

so that

$$\langle \hat{C}_{ij} \rangle = C_{ij} + N_i \delta_{ij} \tag{19}$$

where N_i is the mean noise power in channel i and δ_{ij} is the Kronecker delta. This means that all the channel powers are positively biased, but the covariances are unbiased. The variance of the estimator is given by

$$Var(\hat{C}_{ij}) = \frac{1}{M}\left(N_i N_j + \sigma_i N_j + \sigma_j N_i + \langle \mid z_i \mid^2 \mid z_j \mid^2 \rangle - \mid C_{ij} \mid^2\right) \tag{20}$$

which in the case of Gaussian data reduces to

$$Var(\hat{C}_{ij}) = \frac{1}{M}(\sigma_i + N_i)(\sigma_j + N_j). \tag{21}$$

Assuming Gaussian noise, these results apply to both $i = j$ and $i \neq j$.

We have seen in Section 4 that the important term in defining the variance of the amplitude and phase of the complex correlation coefficient is the actual correlation coefficient of the data. For noisy data,

$$\begin{aligned} \rho'_{ij} &= \frac{\langle z_i z_j^* \rangle}{\sqrt{\langle |z_i|^2 \rangle \langle z_j|^2 \rangle}} \\ &= \frac{\rho_{ij}}{\sqrt{\left(1+\frac{N_i}{\sigma_i}\right)\left(1+\frac{N_j}{\sigma_j}\right)}} \end{aligned} \tag{22}$$

so that the correlation coefficient is reduced. This reduction does not change the expected value of the phase, but will have particularly deleterious effects on the phase variance (see Eq. (11)).

Notice that the discussion here only relates to system noise. Other effects, such as those due to ambiguities, are included in a discussion in [Ref. 14].

7. SPATIAL CORRELATION

The properties of the estimators discussed in Section 5 and 6 assume independent data values. In practice, the data is spatially correlated, essentially because of oversampling. As is well known, mean values calculated using correlated data have a higher variance than when uncorrelated data is available. This problem has been discussed by many authors; a recent discussion in the context of single channel SAR is given by [Ref. 14], though with a different noise model than that used below.

For polarimetric data, we reconsider the estimated covariance given by equation (18). As expected, the mean value is unchanged by the effects of spatial correlation, but the variance of the estimator is more complicated. Writing

$$z_i = \omega_i + n_i \tag{23}$$

(i.e. just dealing with Gaussian data, without surface fluctuations) and assuming that C_{ij} is estimated over a rectangular window of dimensions $P \times Q$, then

$$Var(\hat{C}_{ij}) = \frac{1}{PQ} \sum_{|p|<P} \sum_{|q|<Q} \left(1 - \frac{|p|}{P}\right)\left(1 - \frac{|q|}{Q}\right) (\sigma_i \rho_i(p,q) + N_i \rho_{ni}(p,q))(\sigma_j \rho_j^*(p,q) + N_j \rho_{nj}^*(p,q)) \tag{24}$$

which is valid both for $i = j$ and $i \neq j$. In this equation, the following notation has been used:

$$\rho_i(p,q) = \frac{1}{\sigma_i} \langle \omega_i(a+p,\ b+q) \omega_i^*(a,b) \rangle, \tag{25}$$

with analogous definitions for ρ_j and the two noise spatial correlation functions ρ_{ni} and ρ_{nj}. To arrive at this expression, the assumptions about noise in Section 6 are used, together with statistical stationarity and one further assumption about the signal:

$$\langle \omega_i(a+p, b+q) \omega_j(a,b) \rangle = 0 \quad \text{for all } (p,q). \tag{26}$$

This is to be expected since both terms in the product are randomly phased. While phase differences may not be uniformly distributed, phase sums are likely to be. Nonetheless, this assumption needs confirmation.

Notice that for uncorrelated data, (24) reduces to (21) again, since the only non-zero terms in the summation occur for $p = q = 0$, when all the correlation functions take the value 1.

An important simplifying feature of (24) is that it does not involve cross-channel spatial correlations, only those of **individual channels**. Because all channels are processed in the same way, and it is the processing which imposes the spatial correlation on the data, we would expect

$$\rho_i = \rho_j \quad \text{and} \quad \rho_{ni} = \rho_{nj} \tag{27}$$

The correlation functions of signal and noise are also related, since both signal and noise have passed through the SAR processor. However, the signal has additional correlation imposed on it due to the effects of the prefilter (the azimuth antenna pattern weighting and doppler shift) so that in general we expect

$$\rho_i \neq \rho_{ni}. \tag{28}$$

Further discussion of this point relies on a processing model, and is the subject of current work.

APPENDIX

Below are given some of the less well-known analytic results useful in dealing with single look polarimetric data. A more complete treatment will be found in [Refs. 1, 4, 5]. The equations all refer to a pair of channels z_i and z_j, with powers σ_i and σ_j, and correlation coefficient $\rho_{ij} = |\rho| \exp(j\theta_0)$.

Amplitude ratio PDF: set $t = |z_i|/|z_j|$ and $\alpha = |\sigma_i|/|\sigma_j|$

$$p(t) = 2\alpha \frac{(1-|\rho|^2)(\alpha+t^2)t}{[(\alpha+t^2)^2 - 4\alpha|\rho|^2t^2]^{\frac{3}{2}}} \qquad t \geq 0 \tag{29}$$

with cumulative density function:

$$P(t) = \frac{1}{2}\left(1 + \frac{t^2 - \alpha}{[(\alpha+t^2)^2 - 4\alpha|\rho|^2t^2]^{\frac{1}{2}}}\right) \qquad t \geq 0 \tag{30}$$

Phase difference PDF: set $y = |\rho|\cos(\theta - \theta_0)$

$$p(\theta) = \frac{1}{2\pi}\left(\frac{1-|\rho|^2}{1-y^2}\right)\left(1 + \frac{y}{\sqrt{1-y^2}}\left[\frac{\pi}{2} + \sin^{-1}(y)\right]\right) \qquad -\pi < \theta \leq \pi \tag{31}$$

with cumulative density function:

$$P(\theta) = f(\theta - \theta_0) + f(\pi + \theta_0) \qquad -\pi < \theta \leq \pi \tag{32}$$

where

$$f(\theta) = \frac{1}{2\pi}\left(\theta + \frac{|\rho|(\pi/2 + \sin^{-1}(|\rho|\cos\theta))\sin\theta}{\sqrt{1-|\rho|^2\cos^2\theta}}\right)$$

First and second moments of θ:

$$\langle\theta\rangle = \frac{|\rho|\sin\theta_0\cos^{-1}(|\rho|\cos\theta_0)}{\sqrt{1-|\rho|^2\cos\theta_0^2}} \tag{33}$$

and

$$\langle\theta^2\rangle = \frac{\pi^2}{3} - \pi\sin^{-1}(|\rho|\cos\theta_0) + [\sin^{-1}(|\rho|\cos\theta_0)]^2 - \frac{1}{2}\sum_{n=1}^{\infty}\frac{|\rho|^{2n}}{n^2} \tag{34}$$

The Hermitian product $z_i z_j^* = A + jB = Q\cos\theta$ has several important PDFs associated with it.

Marginal PDF of A:

$$p(A) = \frac{4\nu^{(\nu+1)/2}}{\Gamma(\nu)(1-|\rho|^2)g} \times \begin{cases} ([g-f]A)^{(\nu-1)/2}K_{\nu-1}\left(2\sqrt{[g-f]\nu A}\right) & \text{if } A \geq 0 \\ ([g+f]|A|)^{(\nu-1)/2}K_{\nu-1}\left(2\sqrt{[g+f]\nu|A|}\right) & \text{if } A < 0 \end{cases} \tag{35}$$

where

$$f = \frac{2}{\sqrt{\sigma_i\sigma_j}(1-|\rho|^2)} \mid \rho \mid \cos\theta_0$$

$$g = \frac{2}{\sqrt{\sigma_i\sigma_j}(1-|\rho|^2)}\sqrt{1 - \mid \rho^2 \mid \sin^2\theta_0}.$$

The PDF of B is found by replacing $\cos\theta_0$ by $\sin\theta_0$ and vice versa in the expressions for f and g.

In the Gaussian case, (35) reduces to

$$p(A) = \frac{2}{(1-|\rho|^2g}\left\{e^{-(g-f)A}H(A) + e^{(g+f)A}H(-A)\right\} \tag{36}$$

where $H(A)$ is the unit step function. In the Gaussian case, it is also possible to find the PDF of Q:

$$p(Q) = \frac{4Q}{\sigma_i\sigma_j(1-|\rho|^2)} I_0\left(\frac{2|\rho|Q}{\psi}\right) K_0\left(\frac{2Q}{\psi}\right) \tag{37}$$

where $K_0(.)$ and $I_0(.)$ are modified Bessel functions.

References

[1] Yueh S.H. 1990, K-distribution and polarimetric radar clutter, in *Progress in Electromagnetics Research 3: Polarimetric Remote Sensing*, Elsevier.

[2] Sarabandi K. 1992, Derivation of phase statistics from the Mueller matrix, *Radio Science*, 27, 553-560.

[3] Quegan S., Dutra L.V. and Grover K. 1993, Phase measurements in MAESTRO polarimetric data from the UK test sites, *Int. J. Remote Sensing* (in press).

[4] Quegan S. 1993, Application of Principal Components Analysis to Quadpolarised Data, Tech, Rpt. RAE 1B/89, University of Sheffield.

[5] Tough R.J.A. 1991, Interferometric detection of sea surface features, RSRE Memo. 4446

[6] Sheen D.R. and Johnston L.P. 1992, Statistical and spatial properties of forest clutter measured with polarimetric synthetic aperture radar, *IEEE Trans. Geoscience and Remote Sensing* 30, 578-588.

[7] Quegan S. and Rhodes I. 1993, Statistical models for polarimetric data: consequences, testing and validity, *Int. Jnl. Remote Sensing* (submitted)

[8] Blacknell D. and White R.G. 1993, Optimum classification of non-Gaussian processes using neural networks.

[9] Caves R.G. 1993, Automatic Matching of Features in Synthetic Aperture Radar Data to Digital Map Data, PhD Thesis, University of Sheffield.

[10] van Zyl J.J. 1990, Calibration of polarimetric radar images using only image parameters and trihedral corner reflector responses, *IEEE Trans. Geoscience and Remote Sensing* 28, 337-348.

[11] A. Freeman et al. 1992, Calibration of Stokes and scattering matrix format polarimetric SAR data, *IEEE Trans. Geoscience and Remote Sensing* 30, 531-539.

[12] Quegan S. 1993, A unified algorithm for phase and crosstalk calibration - theory and observations, *IEEE Trans. Geoscience and Remote Sensing* (in press).

[13] Freeman A. 1993, The effects of noise on polarimetric SAR data, Proc. IGARSS 93, Tokyo.

[14] Rignot E. and Kwok R. 1993, Characterization of spatial statistics of distributed targets in SAR, *Int. J. Remote Sensing* 14, 345-363.

Phase calibration from smooth surfaces and corner reflectors

A. Guissard and J.L. Fernandez

Département d'Electricité, Université Catholique de Louvain (UCL)
Louvain-la-Neuve
Belgium

Abstract

The phase calibration problem for polarimetric radars is discussed. The use of smooth surfaces and point targets is considered. The assumption that the copolar vertical and horizontal returns from a smooth surface are in phase is critically reviewed. It is concluded that the phase difference is not negligible for sea water and moist soils at large incidences, but that the assumption of zero phase difference is a good approximation for dry soils and low frequencies. The use of corner reflectors is also considered and illustrated by an example showing the crucial necessity of phase calibration.

1 Introduction

The development of airborne radars and synthetic aperture radars (SAR), having the capability of measuring the four elements of a ground target scattering matrix, both in amplitude and phase, has given to radar polarimetry a new field of applications in remote sensing. Let us mention more particularly the airborne SAR developed by the Jet Propulsion Laboratory (NASA/JPL airborne SAR), which provides complete polarimetric measurements in three frequency bands (P, L and C) with the high resolution of the SAR technique. This instrument has been flown above a number of test areas in Europe in 1989, in the frame of the so-called MAESTRO-1 campaign. Other polarimetric SAR's will be flown in 1994-95 during the EMAC campaign, jointly organised by the European Spatial Agency (ESA) and the EEC Joint Research Center (JRC). Some of these instruments are operating in X, K and even W-band.

For the production of meaningfull polarization signatures of ground targets, from airborne or spaceborne polarimetric radar or SAR, the phase calibration of the instrument is of particular importance. Two methods are in common use for removing the transmitter and receiver phase errors. Both methods are based on the assumption that the scattering matrix is symmetric in the backscattering configuration, provided a proper choice is made for the fields reference base (*backscattering alignment*, or BSA, as defined in [16]).

In the first method it is further assumed that for a smooth surface the HH and VV returns are in phase [17] (V and H stand respectively for linear vertical and horizontal polarizations). Such an approach is incorporated into the calibration procedure, called POLCAL, developed at the Jet Propulsion Laboratory [14]. The second method is applicable only if corner reflectors are available in the scene. Use is made of the fact that the scattering matrix is, within a proportionnality factor, a unit matrix. From the assumption of symmetry, an estimate of the difference between the transmitter and receiver phase errors is obtained as the argument of the mean product of S_{VH} and S_{HV}^*, evaluated over all the image. On the other hand the sum of the transmitter and receiver phase errors is obtained by forcing the mean value of the product $S_{HH} S_{VV}^*$ to be real, either over the smooth surface, or on the available reflectors.

We have considered in some details the assumption of equal phases for the VV and HH returns from a smooth surface. From Rice approach for scattering by a slightly rough random surface [6], as extended by Valenzuela [11] and others using a Fourier transform technique, the expression of the backscattered electric field for emitted polarization Q and received polarization P $(P, Q = V, H)$, can be written as the product $E_{PQ} = g\alpha_{PQ}$ of a geometric factor g and a polarization dependent scattering function α_{PQ}. From this result, the phase difference between E_{HH} and E_{VV} has been computed for a number of surfaces (sea water, moist soil, dry soil) and frequencies in the range 0.4 to 15 GHz.

On the other hand, the corner reflector method has been applied to polarimetric data collected above the Freiburg test-site, during the MAESTRO-1 campaign in 1989. Phase errors for the transmitter and receiver have been evaluated by forcing the point target response of the reflectors to be proportional to the unit matrix. The phase errors appear to be so important that the corner reflectors polarization signatures are completely distorded, if no phase calibration is applied. After phase correction however, the signatures appear to correspond rather well to the theoretical signature to be expected.

2 Calibration

A proper interpretation of polarimetric radar measurements implies that a well defined calibration scheme is applied, more particularly for the phases of the scattering matrix elements. This last problem has been addressed by a number of groups, among them the group at JPL being the more active. Let us writte the scattering matrix as usual

$$\mathbf{S} = \begin{pmatrix} S_{HH} & S_{HV} \\ S_{VH} & S_{VV} \end{pmatrix} \tag{1}$$

where H and V denote the horizontal and vertical polarizations respectively. Two assumptions are generally made [12, 15] :

1) From reciprocity for the backscattering case, the scattering matrix $\mathbf{S}$ should be symmetric, if the *backward scattering alignment* convention is used [7, chapter 2].

2) There exists in the scene some target (point or distributed) which has a known scattering matrix $\mathbf{S}$, from which the phase difference between S_{HH} and S_{VV} can be determined.

For assumption (2), use is generally made of two kinds of targets :

1) Trihedral corner reflectors for which, in the vicinity of the boresight direction, the scattering matrix has the following form, to within a constant factor,

$$\mathbf{S} = \begin{pmatrix} 1 & 0 \\ 0 & 1 \end{pmatrix} \tag{2}$$

and the phase difference between S_{HH} and S_{VV} is exactly zero.

2) A uniform smooth surface of enough extension that a proper average can be obtained. It is generally claimed that the phase difference between S_{HH} and S_{VV} for that case is also zero. When this second kind of target is used, an average must

necessarily be considered over an extended area, in order to minimize the effect of noise.

The claim is made by a number of people (see for instance [2, p.780], [17, p.537], [13, p.694], [14, p.22]) that the copolar HH and VV returns from a smooth surface are in phase. Reference is made to the small perturbation theory applied to a slightly rough surface. It is clearly stated in [2] that "in the case of a slightly rough dielectric surface the HH and VV signals are in phase, because there is little multiple scatter". In [13] it is claimed that "the Bragg model for the ocean has the property that the phases of S_{HH} and S_{VV} are equal", and in [14] the authors write that "for smooth, homogeneous surfaces, the small perturbation model predicts an $HHVV$ phase difference close to zero degree". In [17], the claim is somewhat less affirmative. It is noted "that for normal incidence on a dielectric plane interface, the scattering matrix is

$$\mathbf{S} = \frac{1-\sqrt{\epsilon}}{1+\sqrt{\epsilon}} \begin{pmatrix} 1 & 0 \\ 0 & 1 \end{pmatrix} \tag{3}$$

A similar kind of signature is expected to occur in radar images in situations where specular reflections occur. These situations include reflection from smoother surfaces near normal incidence and specular reflection from very rough surfaces".

Although Van Zyl et al. [17] introduce an important restriction on the validity of the assumption, no such restrictions appear in [2, 13, 14], and the calibration procedure *POLCAL* developed in [14] is based on the use of a smooth surface, whatever the incidence angle might be. One must point out that the *POLCAL* calibration scheme is developed specifically for the NASA/JPL DC-8 Aircraft SAR, a three channels instrument (P-, L- and C-band) with an incidence angle from 20° to 70° [3]. Thus the condition specified in [17] of being near normal incidence, is generally not met.

We shall first recall the expressions of the electric field scattered by a slightly rough surface, as obtained by the small perturbation method. From these expressions, the phase difference between the HH and the VV components is then evaluated in the backscattering case, for a number of realistic sufaces (soil and ocean). In the last section, phase calibration by corner reflectors is discussed and some results from data of the MAESTRO campaign are presented.

3 Rice approach

Let us consider the scattering of electromagnetic waves by a slightly rough surface, which is horizontal in the mean and is represented by the equation

$$z = f(x,y)$$

It is assumed that the surface can be described by a two-dimensional random process. The small perturbation method requires that two assumptions be satisfied :

(1) the rms surface displacement σ should be small as compared to the electromagnetic wavelength λ,

(2) the average slopes should be small.

These conditions can be expressed as follows

$$\begin{aligned} k\sigma &< 0.3 \\ \sqrt{2}\,\frac{\sigma}{l} &< 0.3 \end{aligned} \tag{4}$$

where $k = 2\pi/\lambda$ is the electromagnetic wavenumber and l is the surface correlation length.

In the approach by Rice [6], it is assumed that the surface $z = f(x, y)$ can be represented in the form of a Fourier series

$$z = \sum_{m,n} P(m,n) \exp[-ia(mx + ny)] \tag{5}$$

where $L = 2\pi/a$ is the periodicity of the surface. The coefficients $P(m,n)$ obey the property

$$\langle P(m,n)\, P(-m,-n)\rangle = \frac{a^2}{4}\, W(am, an) \tag{6}$$

where $W(k_x, k_y)$ is the energy spectral density of the surface, and the $\langle . \rangle$ symbol denotes the ensemble average.

The results obtained by Rice are applied by Valenzuela [9, 10] to backscattering from a tilted slightly rough surface. The tilt angle is δ ; in our case we just let $\delta = 0$. The case considered is backscattering and a time dependence $\exp(j\omega t)$ is assumed. In the notations of Valenzuela, one finds the following expressions of the backscattered field

$$\begin{aligned}
E_{HH} &= E_{\perp\perp} = E_{HH}^{(1)} + E_{HH}^{(2)} \\
E_{VV} &= E_{\|\|} = E_{VV}^{(1)} + E_{VV}^{(2)} \\
E_{HV} &= E_{\perp\|} = E_{HV}^{(2)} \\
E_{VH} &= E_{\|\perp} = E_{VH}^{(2)}
\end{aligned} \tag{7}$$

where $E_{PQ}^{(1)}$ and $E_{PQ}^{(2)}$ are first order and higher order contributions respectively, in the small parameter $k\sigma$. To first order, one thus has

$$E_{HV} = E_{VH} \cong 0 \tag{8}$$

and, to that order, there is no depolarization in the field backscattered from a slightly rough surface.

For the copolar terms, one obtains to first order that

$$\begin{aligned}
E_{HH} &= E_{HH}^{(1)} = -2jk\,\gamma_i\, T_{\perp\perp}\, P \\
E_{VV} &= E_{VV}^{(1)} = -2jk\,\gamma_i\, T_{\|\|}\, [\epsilon(1 + \alpha_i^2) - \alpha_i^2]\, P
\end{aligned} \tag{9}$$

where ϵ is the relative permittivity of the medium below the surface (it is assumed that the above medium is air) and

$$\begin{aligned}
\alpha_i &= \sin\theta_i \quad \gamma_i = \cos\theta_i \\
P &= P(-2\nu, 0) \quad a\nu = k\alpha_i \\
T_{\perp\perp} &= \frac{\epsilon - 1}{(\gamma_i + \gamma'')^2} \\
T_{\|\|} &= \frac{\epsilon - 1}{(\epsilon\gamma_i + \gamma'')^2} \\
\gamma'' &= \sqrt{\epsilon - \alpha_i^2}
\end{aligned} \tag{10}$$

It is clear from the above expressions that for a complex permittivity ϵ, the copolar fields E_{HH} and E_{VV} are *not* in phase (except for $\theta_i = 0$, where the result (3) is obtained, to within a constant factor).

4 Generalization of Rice approach

The above approach can be generalized (see for instance [8] in section 12.5 and appendix 12.I) by taking the Fourier transform (FT) of the surface displacement

$$Z(k_x, k_y) = \mathrm{FT}\{ z(x,y) \} \tag{11}$$

and by representing the scattered field as a spectrum of plane waves

$$\vec{E}(x,y,z) = \frac{1}{2\pi} \int\int \vec{U}(k_x, k_y)\, f(k_x, k_y)\, dk_x dk_y \tag{12}$$

where

$$f(k_x, k_y) = \exp(jk_x x + jk_y y - jk_z z) \tag{13}$$

and

$$k_z = (k^2 - k_x^2 - k_y^2)^{1/2} \tag{14}$$

In [8] general expressions are obtained for the bistatic case ; the incident direction is (θ_i, π) and the scattering direction is (θ_s, ϕ_s). The expression of the scattered field, for any polarization combination (P,Q) is

$$E_{PQ} = \frac{1}{2\pi} \int\int (j2k\cos\theta)\, \alpha_{PQ}\, Z\, f\, dk_x dk_y \tag{15}$$

where

$$Z = Z(k_x + k\cos\theta_i,\ k_y) \tag{16}$$

It should be observed that the results for the various polarizations differ only by the scattering functions α_{PQ} (called "polarization amplitudes" in [8]). Complete expressions are given in [8] for the general case of a medium with permittivity ϵ and permeability μ. General expressions can also be found in [5]. For the case of interest here, we have $\mu = 1$ and the following expressions are obtained, as can also be found in [4, section 21.5]. Defining the following quantities for the facility

$$\begin{aligned} D_1 &= \cos\theta_i + (\epsilon - \sin^2\theta_i)^{1/2} \\ D_2 &= \cos\theta_s + (\epsilon - \sin^2\theta_s)^{1/2} \\ D_3 &= \epsilon\cos\theta_i + (\epsilon - \sin^2\theta_i)^{1/2} \\ D_4 &= \epsilon\cos\theta_s + (\epsilon - \sin^2\theta_s)^{1/2} \end{aligned} \tag{17}$$

one has (note that in [8] the expression of α_{VV} has the wrong sign)

$$\begin{aligned} \alpha_{HH} &= -\frac{(\epsilon - 1)}{D_1 D_2} \cos\phi_s \\ \alpha_{VV} &= \frac{(\epsilon - 1)}{D_3 D_4} \left[\epsilon \sin\theta_i \sin\theta_s - \cos\phi_s (\epsilon - \sin^2\theta_i)^{1/2} (\epsilon - \sin^2\theta_s)^{1/2} \right] \end{aligned}$$

$$\alpha_{HV} = \frac{(\epsilon - 1)(\epsilon - \sin^2\theta_i)^{1/2}}{D_2\,D_3}\sin\phi_s$$
$$\alpha_{VH} = \frac{(\epsilon - 1)(\epsilon - \sin^2\theta_s)^{1/2}}{D_1\,D_4}\sin\phi_s \tag{18}$$

One observes that for the backscattering case ($\phi_s = \pi$), there is no depolarized return since $\alpha_{HV} = \alpha_{VH} = 0$, as was concluded by Valenzuela [10].

Clearly, the scattering functions α_{PQ} do depend only on the directions of incidence and of scattering and on the properties of the medium ; they do not depend on the variables k_x and k_y in (15). On the other hand, the remaining factors in the integral do not depend on the polarization. Consequently, the scattered field can be written in the form

$$E_{PQ} = g(z)\,\alpha_{PQ} \tag{19}$$

where $g(z)$ is a common factor, depending only on the geometry of the surface. The ratio of the HH component to the VV component, we are interested in, is given by

$$\frac{E_{HH}}{E_{VV}} = \frac{\alpha_{HH}}{\alpha_{VV}} \tag{20}$$

In the backscattering case, the expressions (18) simplifies somewhat. One has for $\theta_s = \theta_i$ and $\phi_s = \pi$,

$$D_1 = D_2 = \cos\theta_i + b$$
$$D_3 = D_4 = \epsilon\cos\theta_i + b \tag{21}$$

where

$$b = (\epsilon - \sin^2\theta_i)^{1/2} \tag{22}$$

One obtains from (18) the following expressions

$$\alpha_{HH} = \frac{\epsilon - 1}{D_1^2}$$
$$\alpha_{VV} = \frac{(\epsilon - 1)}{D_3^2}N_{VV} \tag{23}$$

where

$$N_{VV} = \epsilon\sin^2\theta_i + (\epsilon - \sin^2\theta_i) = \epsilon\sin^2\theta_i + b^2 \tag{24}$$

Exactly the same result is obtained, starting from the expressions (9) and (10) of Rice.

5 Evaluation of the $HHVV$ phase difference

The above results will be used now to evaluate the phase difference between the HH and the VV fields by a smooth surface. Let us write the field ratio in (20) as

$$\frac{E_{HH}}{E_{VV}} = \left|\frac{E_{HH}}{E_{VV}}\right|\exp(j\phi) \tag{25}$$

where ϕ is the phase difference. We have calculated ϕ for the three NASA-JPL SAR frequencies : $f_1 = 0.44$, $f_2 = 1.25$ and $f_3 = 5.30$ GHz, for incidence angles between 20° and 70° and for typical surfaces. A fourth frequency has also been included : $f_4 = 15$ GHz.

The complex relative permittivity can be written as

$$\epsilon = \epsilon' - j\epsilon'' \tag{26}$$

where the imaginary part is related to the conductivity σ by

$$\epsilon'' = \frac{\sigma}{\omega\epsilon_0} = 60\,\lambda\,\sigma \tag{27}$$

with $\omega = 2\pi f$ and $\lambda = c/f$; ϵ_0 is the absolute permittivity of free space. Values of ϵ' and σ have been taken from Boithias [1, chap.3,fig.3.1], for the following four cases :

- A sea water
- B moist soil
- C dry soil
- D very dry soil.

The values of the parameters are given in table 1, where ϵ'' is obtained by (27) from σ. Two values of ϵ'' have, however, been taken from [8, chap.11, fig.11.11].

		f_1			f_2			f_3			f_4	
	ϵ'_r	σ	ϵ''_r	ϵ'_r	σ	ϵ''_r	ϵ'_r	σ	ϵ''_r	ϵ'_r	σ	ϵ''_r
Sea water (A)	80	5	204	80	5	72	80	10	34	40	25	30
Moist soil (B)	30	0.055	2.2	30		7*	18	1.5	5.1	7	6	7.2
Dry soil (C)	15	0.01	0.4	15		3*	14	0.8	2.7	7	3	3.6
Very dry soil (D)	3	10^{-4}	0.004	3	$2\ 10^{-4}$	0.003	3	0.015	0.05	3	0.1	0.12

Table 1: Permittivity and conductivity of various natural surfaces at four frequencies. All values are taken from [1], with the exception of those marked by $\star$ taken from [8].

The phase diffference ϕ is drawn for the four frequencies in figure 1 (a) to (d), for the four surfaces. For the frequencies f_1 to f_3 of the NASA-JPL instrument, it can be seen that the error introduced by assuming that $\phi = 0°$, will be less than 3° for incidence angles less than 50°, and less than 6° for all incidence angles, if only soil surfaces are considered. For the sea surface, the error is larger, up to 10°, contrary to the assertion in [13] that the phase difference is equal to zero for the Bragg model applied to the ocean surface. The error is seen to increase for higher frequencies (note the different scale for ϕ in figure 1(d)).

6 Corner reflectors

In this section we recall briefly the principle of the phase calibration procedure, based on the use of point reflectors, in the form of trihedral corner reflectors. The method is then applied to the data collected over the Freiburg test-site, during the MAESTRO campaign. As already discussed in section 2, the phase calibration is based on the assumptions that, in the backscattering situation, the scattering matrix should be symmetric for any pixel of the image, and that the scattering matrix of the corner reflector should be proportionnal to the unit matrix.

Following the procedure proposed by the group at JPL [14, 15], we define ϕ_t and ϕ_r as the differences between the phase errors in H and V polarizations, for the transmitter and receiver

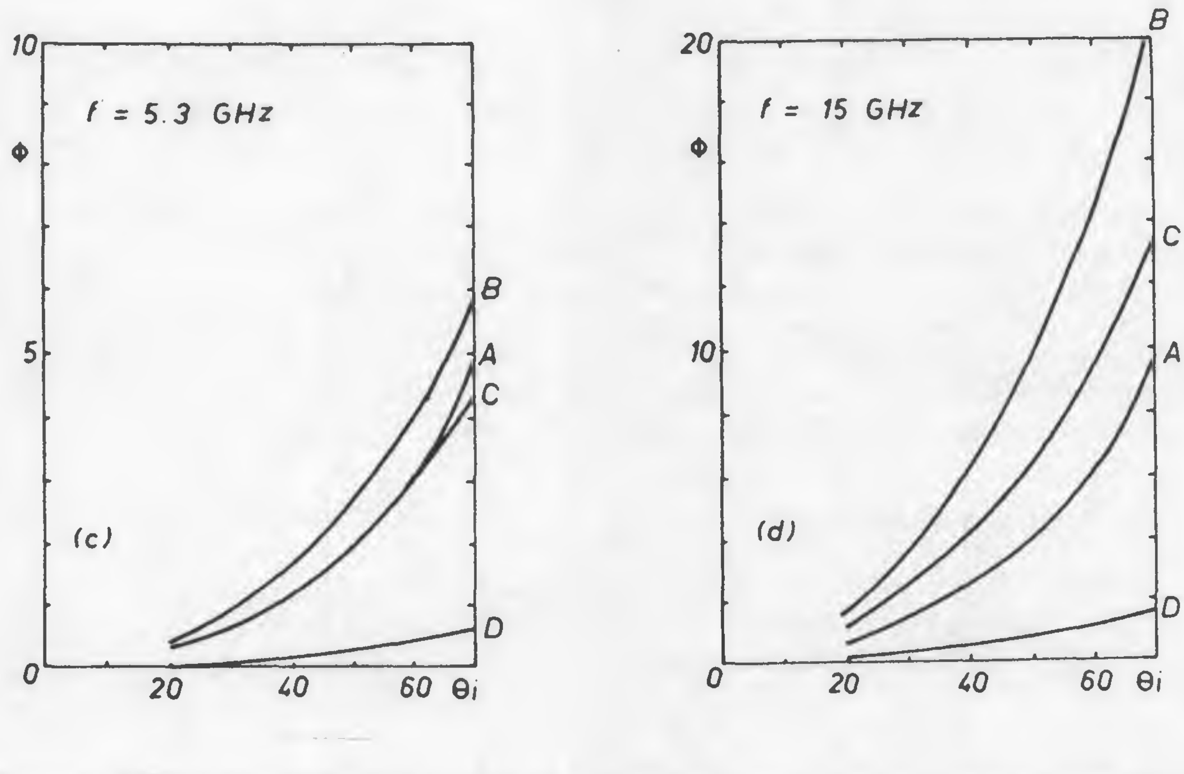

Figure 1: $HHVV$ phase difference as a function of incidence angle, for the four surfaces specified in table 1 : (a) 0.44 GHz ; (b) 1.25 GHz ; (c) 5.3 GHz ; (d) 15 GHz

respectively. Ignoring an absolute phase term, the measured scattering matrix can be written as follows

$$\mathbf{S}^{m} = \begin{pmatrix} S_{HH}\exp[j(\phi_t + \phi_r)] & S_{HV}\exp(j\phi_r) \\ S_{VH}\exp(j\phi_t) & S_{VV} \end{pmatrix} \tag{28}$$

From the assumption of reciprocity, an estimate of the difference $\phi_t - \phi_r$ is obtained from the average over the image of the product of one non-diagonal element with the complex conjugate of the other

$$\widehat{\phi_t - \phi_r} = \arg\langle S^m_{VH}\, S^{m*}_{HV}\rangle \tag{29}$$

Here the notation $\langle\rangle$ stands for the ensemble average. From the measured scattering matrix of the corner reflector, an estimate of the sum of the errors is obtained as follows

$$\widehat{\phi_t + \phi_r} = \arg(S^m_{HH}\, S^{m*}_{VV}) \tag{30}$$

from the diagonal elements. If several corner reflectors are available in the scene, an average can be performed over all reflectors.

The method has been applied to the Freiburg test-site, on the C-band SAR high resolution complex data. Five trihedral corner reflectors, and one polarimetric active radar calibrator (PARC), were installed on the site, with geographical coordinates as given in table 2. The site is roughly 12×8 km^2 and is displayed in figure 2, where the localisation of the reflectors is indicated. Reflectors 1,2 and 4 are clearly visible, reflector 3 is totally masked and reflector 6 is partially masked by the forest canopy. Number 5 is the active calibrator. The data were stored into four files, corresponding to four vertical strips of roughly 3 km width.

The localisation of the reflectors was performed by the following procedure. In a first step the positions of the reflectors are determined approximately and a partial scene is extracted. In a second step a clipping process is applied, by searching pixels with values of $|S_{HH}| + |S_{VV}|$ above an appropriate treshold. In the last step, those pixels with a ratio $|S_{HH}|/|S_{VV}|$ near to unity are selected. We give in table 3, the complex scattering matrices of the six reflectors, together with their pixel localisation.

From equation (30), we find the following values for reflectors 1, 2, 4 and 6 : 173.1°, 178.9°, 164.4° and 180.0°. We do not consider the active calibrator neither reflector 3, which is completely masked. We find for the four reflectors a mean value

$$\widehat{\phi_t + \phi_r} = 174.1^\circ$$

On the other hand the mean difference (29) has been evaluated separately for the four strips, composing the total image. The corresponding values are respectively : −7.5°, −7.3°, −7.5° and −7.6°, giving a mean value of 7.5°. The resulting phase errors are therefore

$$\hat{\phi}_t = 83.2^\circ \qquad \text{and} \qquad \hat{\phi}_r = 90.7^\circ$$

and are seen to be very important. To illustrate the effect of the phase calibration, we show in figure 3 and 4 the copolar polarimetric signature of reflector 4, before and after calibration respectively. Without calibration, the signature is similar to that of a dihedral corner reflector, while with the phase calibration the signature approaches rather well that of the trihedral corner reflector. Note that no amplitude calibration has been applied.

reflecteur	*right value*	*left value*
1	3453.7	5319.8
2	3454.95	5321.2
3	3451.95	5323.65
4	3452.4	5322.3
5	3452.15	5322.9
6	3451.16	5321.78

Table 2: Geographical coordinates of the reflectors

	type	*pixel*	*Shh*		*Shv*		*Svh*		*Svv*	
1	trièdre	[125, 1488]	63.19	[133.5°	3.68	[164.1°	3.19	[162.4°	82.76	[-39.6°
2	trièdre	[266, 2049]	86.56	[131.6°	6.9	[146.7°	6.31	[132°	99	[-47.3°
4	trièdre	[366, 2891]	265.3	[-36.2°	12.3	[-151°	13.7	[-165°	258.6	[159.4°
5	PARC	[423, 2960]	305.9	[32.8°	17	[-214°	17.8	[-125°	343.5	[147°
6	trièdre	[310, 3113]	12.06	[116.5°	2	[-79°	-2.5	[-100	10.55	[-63.5°

Table 3: Pixel coordinates and complex scattering matrices of the reflectors (with the exception of reflector 6 which is masked)

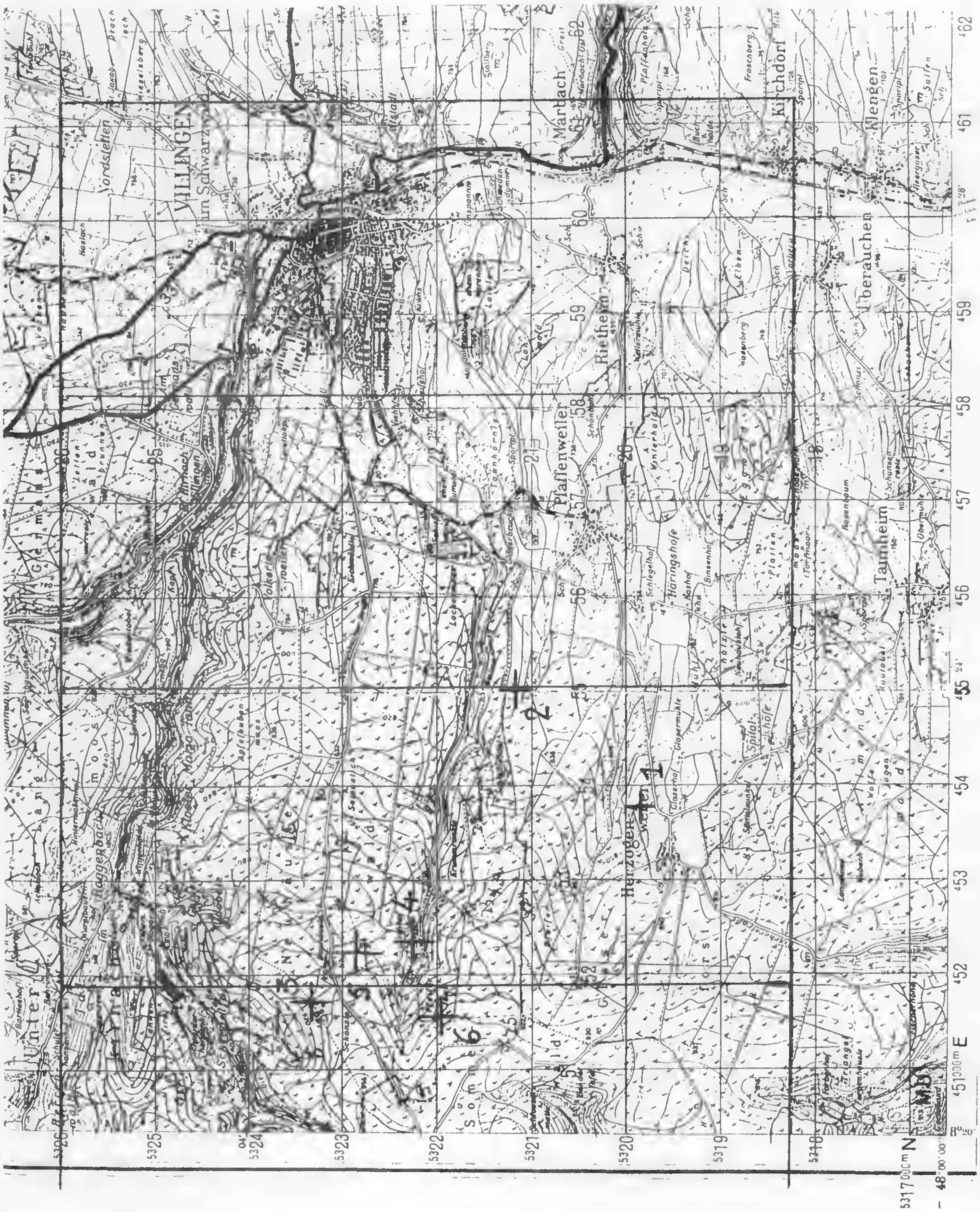

Figure 2: Map of the test-site, with the localisation of the six reflectors

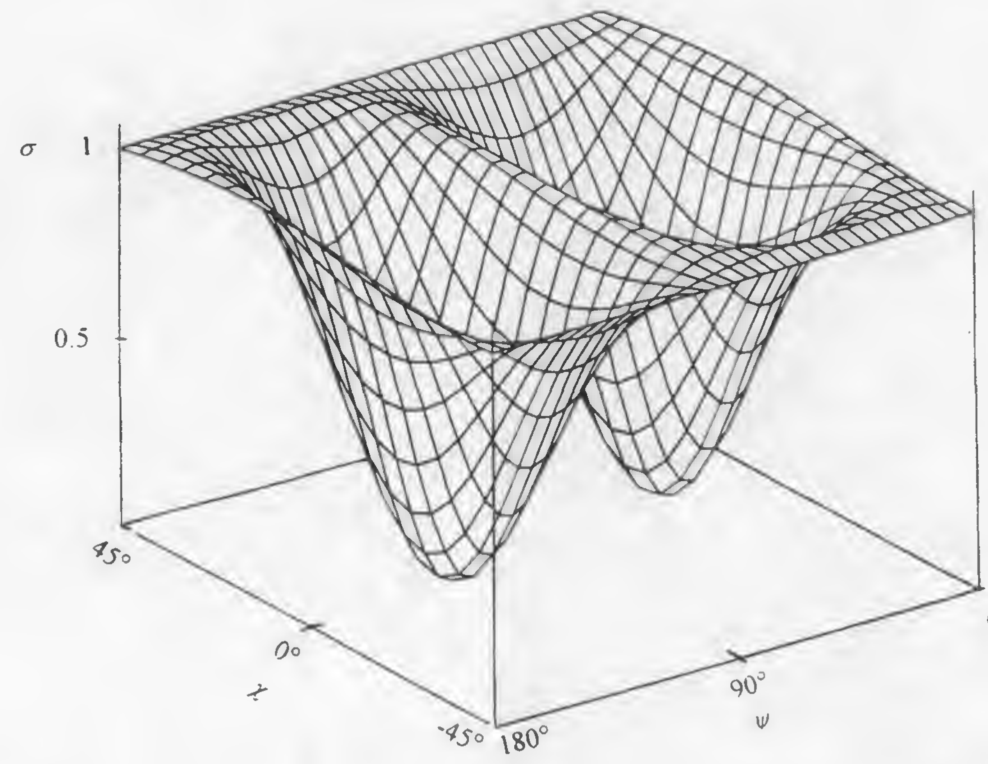

Figure 3: Copolar polarimetric signature of reflector 4, without phase calibration

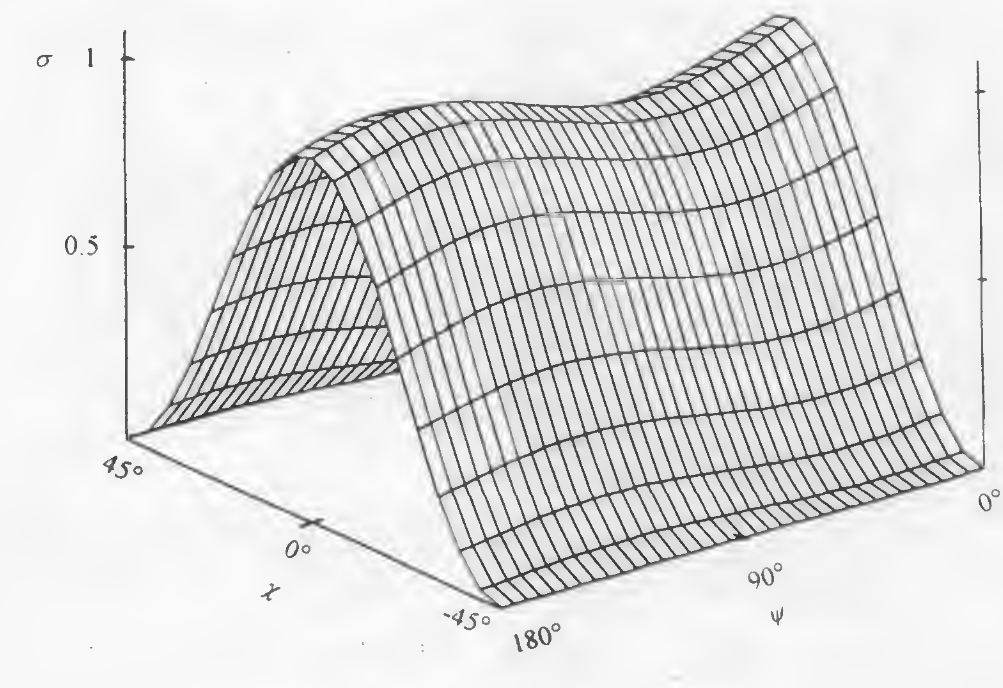

Figure 4: Same as figure 3 with phase calibration

7 Conclusion

Two phase calibration methods have been considered : the first using a smooth surface as reference, the other using trihedral corner reflectors as reference. In both cases, the assumption of symmetry of the scattering matrix is exploited, in order to obtain two equations for the two unknown phase errors.

For the first method, we have examined the validity of the assumption of equal phases for the VV and HH returns, using Rice approach for random slightly rough surfaces. The analytical expression of the ratio S_{HH}/S_{VV} is in general a complex quantity. However it appears that the phase difference is less than 3° for incidence angles less than 50°, and is less than 6° for incidence angles less than 70°, for usual moist or dry soils, and for the three NASA-JPL SAR frequencies. It has been assumed that no vegetation is present on the soil.

Therefore, the assumption of zero phase difference is a good approximation for low incidence angles (incidence near the normal) and the lowest frequencies. However the phase difference increases with increasing frequency, increasing incidence angle and increasing moisture. It can reach 10° at 15 GHz and 50° incidence angle, for a moist soil target. For the ocean surface the error is larger. Thus for calibration purposes, the preference should be given to a dry soil, without any vegetation, in particular for the highest incidence angles. No calibration should be performed over a sea surface scene, except near vertical incidence.

As far as the corner reflector method is concerned, it has been applied to polarimetric data collected above the Freiburg test-site, during the MAESTRO-1 campaign in 1989. Phase errors for the transmitter and receiver are found of the order of 90°. The polarization signature of a corner reflector is examined in order to stress the importance of the phase calibration. Before correction, the signature is completely wrong, being similar to that of a dihedral corner reflector. After phase correction, the corner reflectors signatures appear to correspond rather well to the theoretical signature to be expected.

References

[1] L. Boithias. *Propagation des ondes radioélectriques dans l'environnement terrestre.* Dunod, Paris, 1983.

[2] D.L. Evans, T.G. Farr, J.J. Van Zyl, and H.A. Zebker. Radar polarimetry : analysis tools and applications. *IEEE Trans. Geosc. Remote Sensing*, 26(6):774–789, Nov. 1988.

[3] A. Freeman, Y. Shen, and C.L. Werner. Polarimetric sar calibration experiment using active radar calibrators. *IEEE Trans. Geosc. Remote Sensing*, 28(2):224–240, March 1990.

[4] A. Ishimaru. *Wave propagation and scattering in random media, Vol.2.* Academic Press, New-York, 1978.

[5] W.H. Peake and D.E. Barrick. Scattering from surfaces with different roughness scales : Analysis and interpretation. Techn. report nr 1388-26, Electrosciences Lab., Ohio State University, Columbus, 1967.

[6] S.O. Rice. Reflection of electromagnetic waves from slightly rough surfaces. *Comm. Pure and Applied Math.*, 4:351–378, 1951.

[7] F.T. Ulaby and Ed. C. Elachi. *Radar polarimetry for geoscience applications.* Artech House, Norwood, MA, USA, 1990.

[8] F.T. Ulaby, R.K Moore, and A.K. Fung. *Microwave remote sensing - Active and passive, Vol.2*. Addison-Wesley Pu. Co., 1982.

[9] G.R. Valenzuela. Depolarization of em waves by slightly rough surfaces. *IEEE Trans. Antennas Propag.*, AP-15(4):552–557, July 1967.

[10] G.R. Valenzuela. Scattering of electromagnetic waves from a tilted slightly rough surface. *Radio Science*, 3:1057–1066, 1968.

[11] G.R. Valenzuela. Theories for the interaction of electromagnetic and ocean waves - a review. *Boundary Layer Met.*, 13:61–85, 1978.

[12] H.A. Zebker and Y. Lou. Phase calibration of imaging radar polarimeter stokes matrices. *IEEE Trans. Geosc. Remote Sensing*, 28(2):246–252, March 1990.

[13] H.A. Zebker, J.J. Van Zyl, and D.H. Held. Imaging radar polarimetry from wave synthesis. *Jl. Geophys. Research*, 92(B1):683–701, Jan. 10 1987.

[14] J. Van Zyl and al. Polcal user's manual (nasa/jpl dc-8 aircraft sar) polcal version 2.0. Report jpl d-7715, Jet Propulsion Laboratory, California Institute of Technology, Pasadena, California, August 1990. pp. 126.

[15] J.J. Van Zyl. Calibration of polarimetric radar images using only image parameters and trihedral corner reflector responses. *IEEE Trans. Geosc. Remote Sensing*, 28(3):337–348, May 1990.

[16] J.J. Van Zyl and F.T. Ulaby. Scattering matrix representation for simple targets. In F.T. Ulaby and Ch. Elachi, editors, *Radar polarimetry for geoscience applications*, chapter 2. Artech House, Norwood, MA, USA, 1990.

[17] J.J. Van Zyl, H.A. Zebker, and C. Elachi. Imaging radar polarization signatures : theory and observation. *Radio Science*, 22(4):529–543, July-Aug. 1987.

PROBLEMS IN THE LINEAR DISTORTION MODEL FOR POLARIMETRIC CALIBRATION

Shaun Quegan and Ian Rhodes
School of Mathematics and Statistics
Sheffield University
England

Abstract

The assumptions in the linear system distortion model are investigated. The unique solution of the resulting inconsistent set of equations is shown to require an additional parameter having characteristics of noise. The least squares solution [1] to these equations differs from the JPL solution [2]. The assumption of uncorrelated like and cross-responses over distributed scatterers is questioned. The current pointwise formulation of the distortion model does not represent the image distortion and the effects of azimuth point spread functions are derived.

Keywords: Polarimetric Calibration

1 The Linear System Distortion Model

The characterisation of transmit and receive system distortion of quad-polarised SAR data by a two channel linear transformation of the 2x2 scattering matrix underpins current polarimetric calibration models. Several calibration methods have been proposed for polarimetric calibration [3, 4, 5] assuming scatterer reciprocity for imbalance correction and utilising the lack of correlation between the co-polarised and cross-polarised responses of distributed targets for crosstalk removal [6]. Van Zyl's algorithm [4] requires symmetrised data in either complex or Stokes form [2] whereas Klein [3] makes no assumption of system symmetry. Yueh's algorithm [5] extends the iterative crosstalk correction of Van Zyl assuming crosstalk attenuation and selecting the crosstalk of smallest magnitude from the choice of symmetrical solutions. The least squares algorithm of Quegan [1] requires no assumptions of symmetric system distortion and yields a direct solution compensated for both complex crosstalk and imbalance ratio by direct least squares inversion of the system distortion. It will be shown that the assumption of scatterer reciprocity requires the introduction of a free parameter to resolve a unique solution for the asymmetry in the receive and transmit imbalances. Throughout this paper subscript notation will follow matrix convention with channel 1 representing horizontal polarisation and channel 2, vertical polarisation. Superscripts ^{T} and ^{H} denote the transpose and complex conjugate transpose respectively and the operator $\otimes$ is the Kronecker or tensor product.

Common to all the calibration models is the pointwise formulation of the system distortion which, assuming unsymmetrised data, is expressed

$$O \;=\; R\,S\,T \tag{1}$$

where O is the complex 2x2 matrix of observed responses, S is the complex 2x2 scattering matrix and R and T are the complex 2x2 receive and transmit matrices respectively.

1.1 Inconsistency and Noise

The assumption of scatterer reciprocity, $S_{12} = S_{21}$, leads to a system of linear equations which require 'inversion' of the system distortion matrix D, comprising the receive and transmit distortions, to yield the true scattering vector $\underline{S}$ given the observed vector $\underline{O}$.

$$\underline{O} \;=\; D\,\underline{S} \tag{2}$$

where $\underline{O} = [O_{11}, O_{21}, O_{12}, O_{22}]^T$, $D = T^T \otimes R$, $\underline{S} = [S_{11}, S_{21}, S_{12}, S_{22}]^T$

Using the 4x4 distortion matrix D in the observed covariance, assuming azimuthal symmetry and small crosstalk, leads to a system of 7 equations in 6 unknowns. This is indicated in a reduced rank, i.e a zero eigenvalue, for the ideal covariance C due to the linear dependence in the true scattering covariance C^S

$$|C| = |D\, C^S\, D^H| = 0 \tag{3}$$

The smallest eigenvector of the observed covariance C^O is used by Klein [3] to determine the crosstalks and imbalance ratio α where

$$\alpha = \frac{T_{11}}{T_{22}} \Big/ \frac{R_{11}}{R_{22}} \tag{4}$$

In practice, the system of equations arising from (1) is inconsistent, not redundant. Least squares inversion of the system distortion using the observed covariance generates two solutions, α_1 and α_2, for the imbalance ratio due to the different observed cross-responses [1]. The extra freedom in the set of observations can be parametrised by an additional 'noise' parameter N.

$$O = R\, S\, T + N \tag{5}$$

Incorporating the noise covariance C^N in the observed covariance yields the full rank system

$$|C^O| = |D\, C^S\, D^H + C^N| \neq 0 \tag{6}$$

These equations can be pseudo-inverted to give a unique least squares solution for the imbalance ratio, assuming that the noise is uncorrelated and of equal power in the cross-responses, and negligible in the co-responses, i.e.

$$< N_{ij} N_{kl}^* > = 0 \qquad \text{for } ij \neq jk \tag{7}$$

$$< N_{12} N_{12}^* > = < N_{21} N_{21}^* > \tag{8}$$

$$< O_{ii} O_{ii}^* > \gg < N_{ii} N_{ii}^* > \qquad \text{for i} = 1,2 \tag{9}$$

After the crosstalk has been corrected, the two solutions for the imbalance ratio can be written in terms of the residual covariances

$$\alpha_1 = \frac{\tilde{C}^O_{22}}{\tilde{C}^O_{32}} = \frac{\tilde{C}^S_{22} + C^N_{22}}{\tilde{C}^S_{32}} \qquad \alpha_2 = \frac{\tilde{C}^O_{32}}{\tilde{C}^O_{33}} = \frac{\tilde{C}^S_{32}}{\tilde{C}^S_{33} + C^N_{33}} \tag{10}$$

where the $\tilde{}$ denotes no crosstalk effects. As the additive noise power is real these two solutions have the same phase and differ only in their magnitudes. Assuming equal noise powers in both cross-responses, the two solutions can be combined to provide a unique imbalance ratio whose magnitude is given by

$$|\alpha| = \frac{|\alpha_1\alpha_2| - 1 + \sqrt{(|\alpha_1\alpha_2| - 1)^2 + 4|\alpha_2|^2}}{2|\alpha_2|} \tag{11}$$

Further, the assumption of equal noise in the two cross-responses provides an estimate of the noise power from the observed covariance $\tilde{C}^O_{32}$

$$C^N_{22} = C^N_{33} = \tilde{C}^O_{32}(\alpha_1 - \alpha) \tag{12}$$

The two inconsistent solutions for the imbalance ratio, α_1 and α_2, along with the noise corrected α are shown against range in Figure 2 for the JPL Maestro 1989 single look complex data over the Feltwell (UK) calibration site. The reciprocal nature of α_1 and α_2 is apparent with the noise corrected solution showing much closer adherence to the ideal unity imbalance ratio. The estimate of the noise power in the HV channel, for the same data, is shown in Figure 3 along with the total HV power. The range dependence of the noise may be a consequence of the fact that the noise has passed through all the radiometric corrections carried out in the processing.

1.2 Symmetrisation

The correction for the system imbalances, or symmetrisation, can be seen in the least squares solution for the HV cross-response S_2. With no crosstalk the observed cross-polarised responses are

$$\tilde{O}_{21} = \alpha S_{21} + N_{21} \tag{13}$$

$$\tilde{O}_{12} = S_{21} + N_{12} \tag{14}$$

The least squares estimate of the true cross-response S_{21}, assuming equal noise powers, is given by the weighted combination of both the observed cross-responses

$$\hat{S_{21}} = \frac{\tilde{O_{12}} + \alpha^* \tilde{O_{21}}}{1 + |\alpha|^2} \tag{15}$$

The rationale behind this weighting can be seen on considering the reliability of the observations in terms of signal-to-noise ratios.

If $\|\alpha\| > 1$:	SNR of $\tilde{O}_{21}$ > SNR of $\tilde{O}_{12}$ so weight $\tilde{O}_{21}$ most
If $\|\alpha\| < 1$:	SNR of $\tilde{O}_{21}$ < SNR of $\tilde{O}_{12}$ so weight $\tilde{O}_{12}$ most

In Freeman *et al* [2] the symmetrisation proposed is (where $'$ denotes the symmetrised response)

$$O'_{21} = \frac{1}{2}\left[O_{21} + O_{12}\sqrt{\langle\frac{|O_{21}|^2}{|O_{12}|^2}\rangle} e^{-j\langle\angle O_{21}O_{12}^*\rangle}\right] \tag{16}$$

whereas the least squares solution gives a symmetrisation.

$$O'_{21} = \frac{1}{1+|\alpha|^2}\left[O_{21} + O_{12}\sqrt{\frac{\langle|O_{12}|^2\rangle}{\langle|O_{21}|^2\rangle}}\, e^{-j\angle\langle O_{12}O_{21}^*\rangle}\right] \tag{17}$$

Several differences are apparent.

1. The phase correction in Eq. 16 has the wrong sign;
2. The phase needed is $\angle\langle O_{12}O_{21}^*\rangle$, not $\langle\angle O_{21}O_{12}^*\rangle$ as given in Eq. 16. These can be quite different.
3. $\sqrt{\langle|O_{21}/O_{12}|^2\rangle}$ is used to estimate $|1/\alpha|$ in Eq. 16 but is biased. An unbiased estimate is $\sqrt{\langle|O_{21}|^2\rangle/\langle|O_{12}|^2\rangle}$;
4. Even with the above change, the amplitude correction in Eq. 16 is the reciprocal of that in Eq. 17.

While point (1) is just an error, points (2)-(4) indicate that the JPL symmetrisation is not optimal.

2 Correlation of Like and Cross-Polarised Responses

The determination of system crosstalk using distributed targets assumes zero correlation of co-polarised to cross-polarised responses for azimuthally symmetric scatterers [6]. However the *calibrated* 16-look Mueller data from the 1991 DC-8 MAC-Europe campaign over the Feltwell agricultural test site exhibits cross-correlation very different from zero over extended regions. The L-band HH-HV correlation image of size 767x768 pixels is shown in Figure 1. Although the image is generally of low correlation, several regions of higher correlation are apparent. Similar correlation is also evident at P-band, although visually less so at C-band. Over the whole 16-look image, the mean HH-HV correlation coefficients were 0.27, 0.26 and 0.29 at C, L and P-band respectively. The 16-look VV-VH correlation displays similar characteristics. It remains to be determined if these correlations are statistically significant and for which cover types the assumption of zero correlation is valid.

3 Azimuth Point Spread Function

The pointwise formulation of the linear distortion model, Eq. 1, takes no account of any azimuth variation in the transmit and receive distortions. Incorporating the azimuth bearing θ in the distortion model gives

$$O(\theta) = R(\theta)\, S\, T(\theta) \tag{18}$$

where the scatterer itself is assumed isotropic over the range of azimuth bearings used in the processing.

3.1 Point Response

The observed response at azimuth point x in the image plane due to a point scatterer at azimuth x_s and slant range r_0 in the far field is, after azimuth compression (approximated by an infinitely long phase reference),

$$O(x;x_s) \approx e^{+jk\frac{(x-x_s)^2}{r_0}} \int_{x_r=x-\frac{L}{2}}^{x+\frac{L}{2}} R(\frac{x_r-x_s}{r_0})\, S(x_s)\, T(\frac{x_r-x_s}{r_0}) e^{-jk2\frac{(x-x_s)(x_r-x_s)}{r_0}} dx_r \tag{19}$$

where the small angle approximation has been used for θ and a linear approximation for slant range r_0. For example, the observed HV response can be expressed as a combination of four distortion functions comprised of the receive and transmit point spread functions.

$$O_{21}(x;x_s) \approx e^{+jk\frac{(x-x_s)^2}{r_0}} \int_{x_r=x-\frac{L}{2}}^{x+\frac{L}{2}} [T_{11}R_{11}S_{11} + T_{11}R_{22}S_{21} + T_{21}R_{21}S_{12} + T_{21}R_{22}S_{22}]\, e^{-jk2\frac{(x-x_s)(x_r-x_s)}{r_0}} \tag{20}$$

where the azimuth dependence of T and R is omitted for brevity. The point distortion functions can be concisely expressed as a 4x4 matrix-valued function P acting on the scattering vector $\underline{S}$.

$$P(x - x_s) = \int_{x_r = x - \frac{L}{2}}^{x + \frac{L}{2}} T^T\left(\frac{x_r - x_s}{r_0}\right) \otimes R\left(\frac{x_r - x_s}{r_0}\right) e^{-jk2\frac{(x - x_s)(x_r - x_s)}{r_0}} dx_r \tag{21}$$

If the system distortion is constant with azimuth, this reduces to a sinc $(\sin(x)/x)$ response in the image.

$$\underline{O}(x; x_s) = e^{+jk\frac{(x-x_s)^2}{r_0}} L \operatorname{sinc}\left(\frac{kL(x - x_s)}{r_0}\right) \left[T^T \otimes R\right] \underline{S}(x_s) \tag{22}$$

The effect of the azimuth point distortion function can be seen in Figures 4-7. For simplification the transmit and receive functions are assumed identical. Here only the effects of crosstalk will be illustrated although similar effects occur with system imbalances. Figure 4 shows a constant crosstalk over the integration length of the synthetic aperture, as assumed in the pointwise RST model. The effects of increased crosstalk off-boresight, as in Figure 5, will be shown for the example HV response quantified in Eq. 20. Although generally this is a combination of four distortion functions, weighted by the scattering elements, only the response of a trihedral scatterer is considered. The observed HV response of a trihedral is shown for constant and variable crosstalk in Figures 6 and 7 respectively, with magnitude denoted by a solid line and phase (normalised by 180^o) by a dotted line. Apparent is the increased magnitude of the observed response at all azimuth points in the image, including at boresight. This is not unexpected, given the increased integrated crosstalk over the synthetic aperture, but it should be emphasised that it is the sum of integrated products of functions which determine the observed response. As the scatterer is itself arbitrary, the observed image cannot be modeled by pointwise distortion of the true image.

3.2 Covariance

The azimuth dependence of the point response is further evident in the observed covariance of distributed scatterers. Consider the observed response from all scatterers illuminated over the synthetic aperture.

$$\underline{O}(x) = \int_{x_s = x - \frac{L}{2}}^{x + \frac{L}{2}} e^{+jk\frac{(x-x_s)^2}{r_0}} P(x - x_s) \underline{S}(x_s) dx_s \tag{23}$$

Using Eq. 21 in the observed spatial covariance at lag τ from all scatterers in the synthetic aperture

$$C^O(x + \tau, x) = < \underline{O}(x + \tau)\, \underline{O}^H(x) > \tag{24}$$

$$= \left\langle \left[\int_{x_{s_1} = x + \tau - \frac{L}{2}}^{x + \tau + \frac{L}{2}} e^{+jk\frac{(x - x_{s_1})^2}{r_0}} P(x + \tau - x_{s_1}) S(x_{s_1}) dx_{s_1}\right] \left[\int_{x_{s_2} = x - \frac{L}{2}}^{x + \frac{L}{2}} e^{-jk\frac{(x - x_{s_2})^2}{r_0}} S^H(x_{s_2}) P^H(x - x_{s_2}) dx_{s_2}\right]\right\rangle$$

If the scatterers are spatially uncorrelated, i.e. non-zero contribution only if $x_{s_1} = x_{s_2} = x_s$

$$C^O(x + \tau, x) = \int_{x_s = x - \frac{L}{2}}^{x + \frac{L}{2} - |\tau|} e^{+jk\frac{(2x\tau + \tau^2 - 2\tau x_s)}{r_0}} P(x + \tau - x_s) < \underline{S}(x_s)\underline{S}^H(x_s) > P^H(x - x_s) dx_s \tag{25}$$

Further, if the covariance is stationary, i.e. $< S(x_s)S^H(x_s) > = C^S$ and using $\chi = x - x_s$

$$C^O(\tau) = \int_{\chi = -\frac{L}{2} + |\tau|}^{+\frac{L}{2}} e^{+jk\frac{(2\chi\tau + \tau^2)}{r_0}} P(\chi + \tau) C^S P^H(\chi) d\chi \tag{26}$$

The resulting 16x16 covariance distortion function Q, as a function of azimuth, can be expressed in terms of the point distortion functions at two azimuth points.

$$Q(\tau) = \int_{\chi = -\frac{L}{2} + |\tau|}^{+\frac{L}{2}} e^{+jk\frac{(2\chi\tau + \tau^2)}{r_0}} P^*(\chi) \otimes P(\chi + \tau) d\chi \tag{27}$$

Thus the covariance measurements derived from distributed scatterers are weighted combinations of integrated fourth order products of the system distortions at different azimuth points.

4 Conclusions

The inconsistency in the linear distortion model has been shown to require an extra 'noise' freedom to obtain a unique solution for the system imbalance ratio. The assumption of equal noise power in the observed cross-responses allows both calculation of the noise corrected imbalance ratio and estimation of the uncorrelated additive noise power. The symmetrisation of the system imbalance in the JPL algorithm in [2] is not equal to that of the least squares algorithm and is not optimal in the estimates used in the complex weighting. The assumption of uncorrelated co and cross-responses of natural distributed scatterers, has been found questionable over extended regions in 16-look calibrated Mueller data. This requires further investigation of the symmetry assumptions for any natural cover types used in crosstalk calibration. The pointwise linear distortion model takes no account of azimuth variation in the system distortions and incorporating this dependence in the linear model affects both the response of point scatterers and the covariance of distributed scatterers in the observed image. It remains to quantify these effects for real systems at different frequencies.

The financial support of the Science and Engineering Research Council and the Defence Research Agency, Farnborough under contract GR/G41726 is gratefully acknowledged.

References

[1] S. Quegan. A Unified Algorithm for Phase and Crosstalk Calibration - Theory and Observations. *IEEE Transactions on Aerospace and Electronic Systems (in press)*, 1993.

[2] A. Freeman, J.J. Van Zyl, J.D. Klein, H.A. Zebker, and Y. Shen. Calibration of Stokes and Scattering Matrix Format Polarimetric SAR Data. *IEEE Transactions on Geoscience and Remote Sensing*, pages 531–539, May 1992.

[3] J.D. Klein. Calibration of Complex Polarimetric SAR imagery using backscatter correlations. *IEEE Transactions on Aerospace and Electronic Systems*, pages 183–194, January 1992.

[4] J.J. Van Zyl. Calibration of Polarimetric Radar Images using only Image Parameters and Trihedral Corner Reflector Responses. *IEEE Transactions on Geoscience and Remote Sensing*, pages 337–348, May 1990.

[5] S. Yueh, S.V. Nghiem, and R. Kwok. External Calibration of Polarimetric Radars Using Distributed Targets. Preprint, August 1992.

[6] S.V. Nghiem, S.H. Yueh, R. Kwok, and F.K. Li. Symmetry Properties in Polarimetric Remote Sensing. *Radio Science*, 27:693–711, 1992.

Fig 1. *L-band HH-HV correlation coefficient of calibrated 16-look Mueller data.*

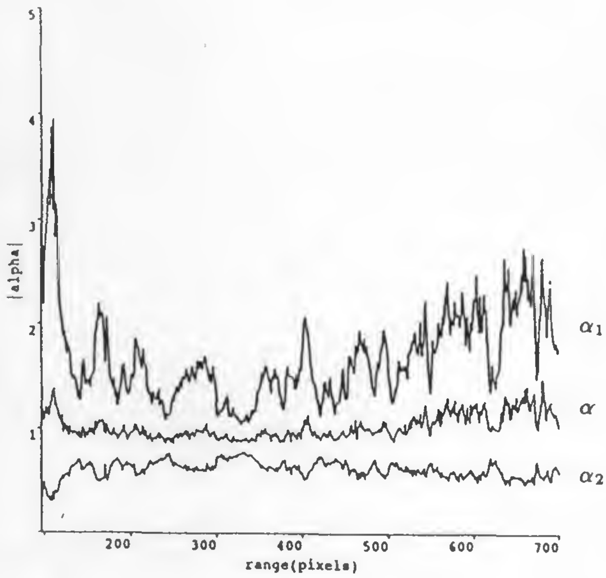

Fig 2. *Imbalance ratios α_1, α_2 and α versus range*

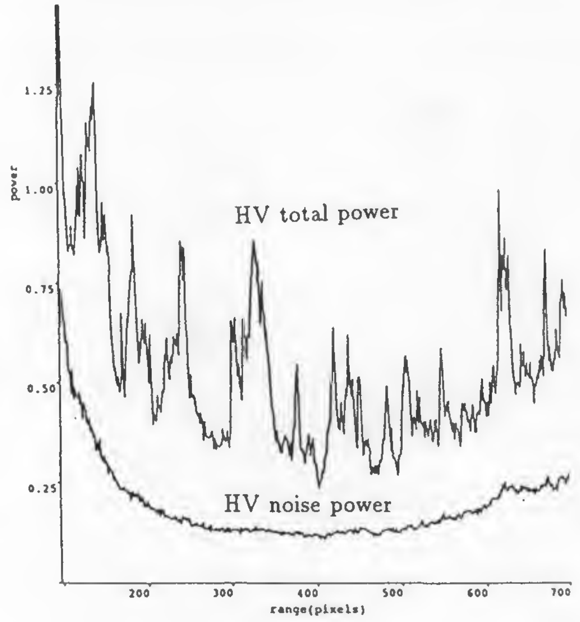

Fig 3. *HV total power and noise versus range*

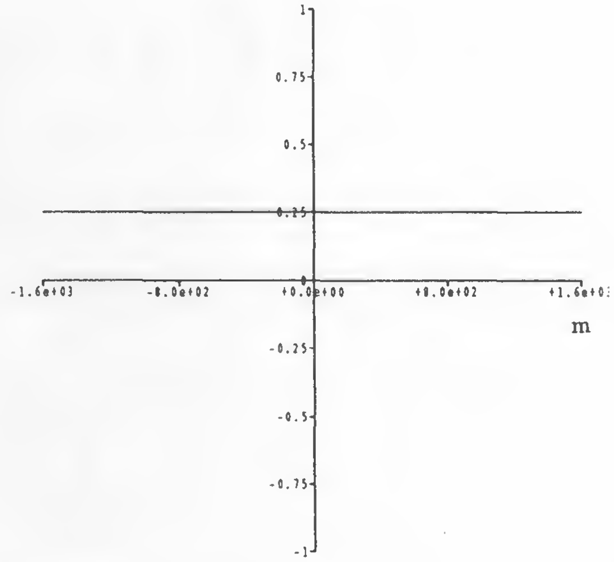

Fig 4. *HV Tx azimuth antenna pattern, constant crosstalk*

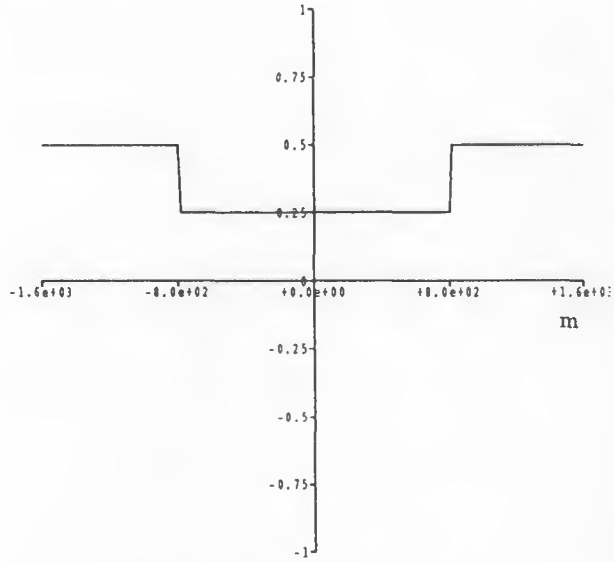

Fig 5. *HV Tx azimuth antenna pattern, variable crosstalk*

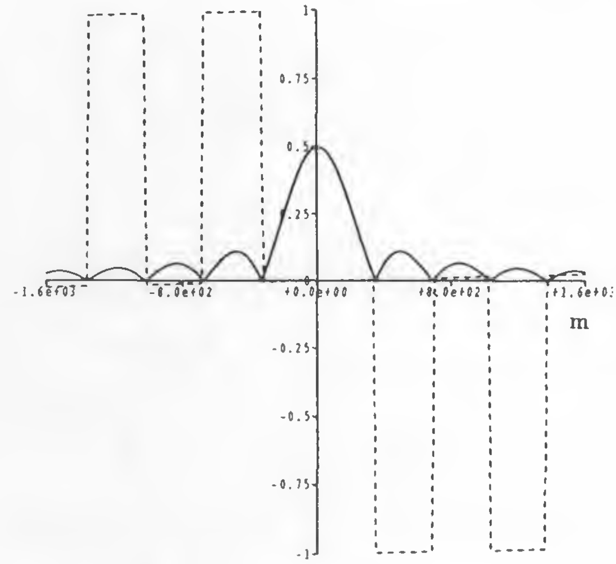

Fig 6. *HV trihedral azimuth response, constant crosstalk*

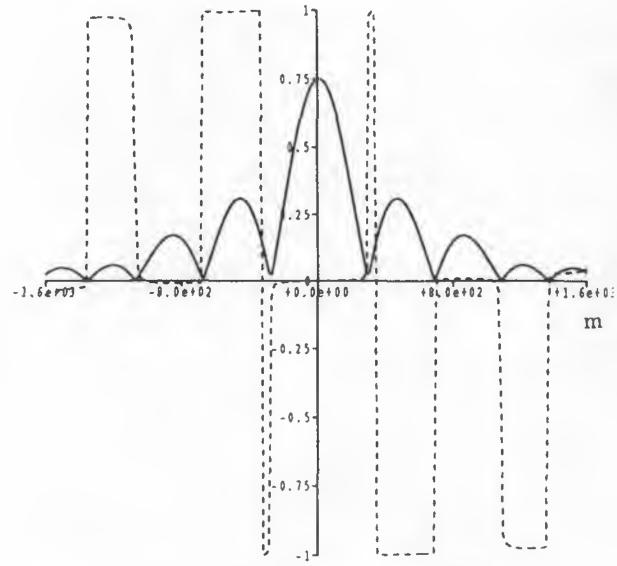

Fig 7. *HV trihedral azimuth response, variable crosstalk*

INTERFEROMETRIC SAR CALIBRATION

Session 4

Chair: S.COULSON, ESA-ESRIN, Italy

PRECISION POSITIONNING OF INTERFEROMETRIC TRACKS

Authors : D. MASSONNET, H. VADON

CNES (French Space Agency)

Abstract :

Precision positioning of interferometric tracks is of crucial importance for one of the most advanced application of radar remote sensing : the mapping of small moves by interferometry.

The importance of positioning appears in several steps of the interferometric processing. The tracks can be relatively positioned by the use of the deformation between the images of an interferometric pair. An efficient modelling of this deformation is required to obtain the sub-pixel precision required by a perfect co-registration of the images, itself led by the need to preserve coherence. Once this rough (typically one meter of precision) positioning is achieved, an interferogramme is formed and leads to a much more accurate track estimation. A simple fringe count between four ground control points is sufficient to achieve the final precision, provided that the modelling of the orbits is correct between the control points.

This paper describe the theoretical formulation we use for precision track positioning concerning all the above aspects. It also includes a discussion concerning advantages and drawbacks of the multi-pass approach versus the digital elevation approach in the field of differential interferometry.

The feasibility of using a single slant range geometric reference for many scene taken on the same site is demonstrated.

BACKGROUND OF INTERFEROMETRY

Radar interferometry was introduced almost twenty years ago (ref. 1), but its space borne multiple passes aspect was actually pioneered by Jet Propulsion Laboratory scientists (ref. 2) using SEASAT and SirB data. Radar interferometry uses the phase as an ultimate ranging tool. We proposed to eliminate the topographic fringes from an interferogramme for crustal moves monitoring (ref. 3). Actual small moves detection has been achieved using SEASAT data (ref. 4) on a relatively flat topography. The use of radar interferometry on a large scale deformation field has been demonstrated on a site where an earthquake occurred (ref. 5) using ERS1 data and the digital elevation model elimination method.

Most of the deformation between the images of an interferometric pair can be computed from correlation residuals of the image pair.

Those residuals provide also a rough estimation of relative orbital position when taking the images of the pair. They also indicate, at a very early stage of processing, whether a given pair will meet the baseline conditions (ref.6 and 7) and allow the retrieval of the bulk of the fringes due to relative orbital positions. We are then left with three kinds of information from the remaining fringes :

-the rest of the deformation, or the difference of walk, due to relative orbital positions which allows a precise orbital model tuning (typically a few centimetres) on the criterion of cancelling the fringe pattern at the edges of the interferogramme

-a stereoscopic difference of walk due to terrain topography combined with the baseline created by relative orbital position. A knowledge of the topography through a Digital Elevation Model (DEM) allows the elimination of these fringes. We call altitude of ambiguity the difference of altitude which creates one topographic fringe

-a direct difference of walk created by terrain displacement between the data takes. More precisely, the fringes measure twice the projection of the displacement of a given ground point on the line satellite-point. In other terms, due to the round trip travel of the wave, each fringe is equivalent to a projected displacement of half the radar wavelength (in ERS1 case : 28.3 millimetre)

The operations of elimination of orbital and topographic fringes are conducted in radar image, slant range geometry. The terrain model may be then used again to change the fringe pattern from radar geometry to conventional latitude-longitude map co-ordinates.

GEOMETRIC MODELLING

It is quite useful to find an approximation simple enough to allow the pursuit of analytic calculations while retaining most of the precision of an exact evaluation. Obviously, the exact evaluation will be used for the actual data processing but the approximation may be used for helping to eliminate remaining fringes by refining orbital modelling.

We use a tangential flat Earth approximation which consists in creating the geometry where the scene is projected on a plane perpendicular to local Earth radius at the centre of the scene (D being the scene width). The tangential approximation allows to continue analytical calculation using a flat Earth model and keeps most of the precision of the full scale calculation.

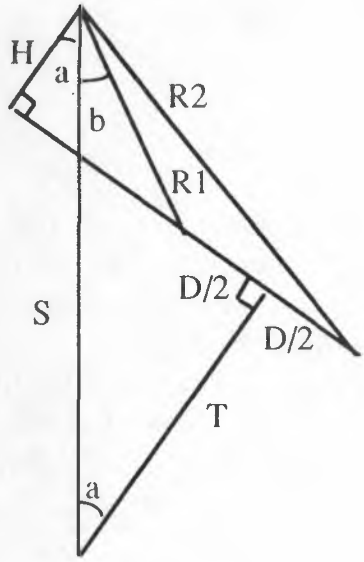

The equations which govern this approximation are the following :

S : Vector satellite position
T : local Earth radius
R1 : Range to first pixel
R2 : Range to second pixel
D : Ground distance covered
H : Orthogonal altitude (i.e. differs from S-T)
a : Terrestrial angle
b : Bore angle for first pixel

$$S \cos(a) = T + H$$

$$S \cos(a) = \frac{S^2 + T^2 + \frac{D^2}{4} - \frac{R_1{}^2 + R_2{}^2}{2}}{2T}$$

$$H = \frac{S^2 - T^2 + \frac{D^2}{4} - \frac{R_1{}^2 + R_2{}^2}{2}}{2T}$$

$$\sin(a) = \frac{R_2{}^2 - R_1{}^2}{2\ D\ S}$$

We obtain typically almost 3° for **a** in the case of ERS1, where **b** is typically 16°. Once the orbital model has been rotated by the angle a, it is almost exact to consider a "flat" Earth, the difference between the truth and the model being of the order of magnitude of the difference between two local map projections.

The "swell" due to Earth curvature is only 280 m in the middle of a 120 km swath. This kind of altitude could be found in local hills. Similarly, the difference in the vertical direction is only half a degree, which causes only mild distortions.

Again, this approximation is not used in actual data processing, but is very useful to build the commands of these data processing software.

ORBITAL MODELLING

We decide that, in an interferometric pair, one of the image will be used as a slant range geometric reference and will be called master image (with quantities indexed by **m**). The other one will be called slave image (with quantities indexed by **s**). If a third image is involved, it will be called complementary image (with quantities indexed by **c**). Index **i** is the range pixel number of the master image. We now work in our tangential flat Earth reference and assume that all the images have been co-registered to the master image.

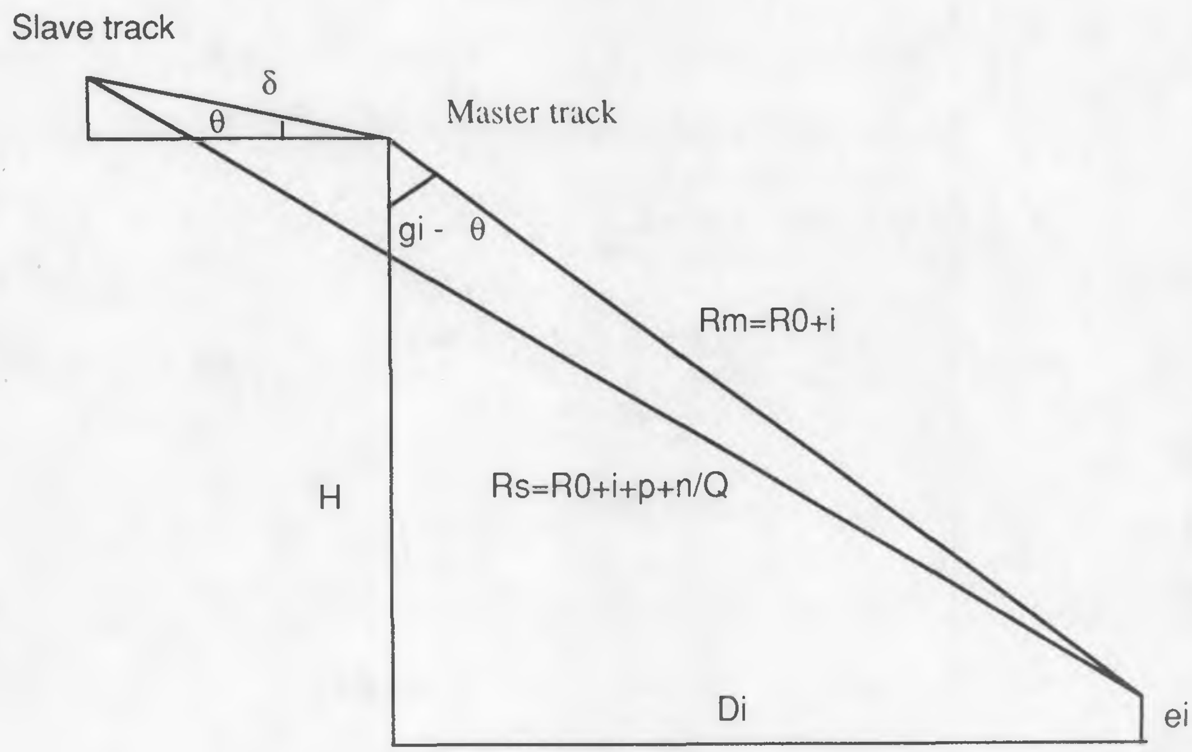

we write : $H - e_i = R_m \cos(g_i-\theta)$ and $D_i = R_m \sin(g_i-\theta)$

we have : $R_s^2 = (\delta \sin\theta + R_m \cos(g_i-\theta))^2 + (\delta \cos\theta + R_m \sin(g_i-\theta))^2$

therefore : $R_s^2 = \delta^2 + R_m^2 + 2\delta R_m \sin(g_i)$

and : $\sin(g_i) = \dfrac{R_s^2 - \delta^2 - R_m^2}{2\delta R_m}$

R_0 being the near-range of the master image, we have, using the range pixel size as a unit :

$$R_m(i) = R_0 + i$$

$$R_c(i) = R_0 + i + p + \frac{n_i}{Q}$$

Where :

-p is the range difference between master and slave image at master image near-range.

-n_i is the fringe count of the interferogramme from the near-range to pixel i, $\frac{n_i}{Q}$ is therefore the equivalent range pixel deformation (contrary to p, n and g are functions of i).

-Q is the ratio between the range pixel and the wavelength. Similarly, it represents the ratio of the sampling frequency and the carrier frequency (Q equals roughly 280 for ERS1).

In the real world, **p** is not defined for each range line, but for the whole interferogramme. **n** should therefore be indexed by the line number **j** :

$$R_s(i,j) = R_0 + i + p + \frac{n(i,j)}{Q}$$

we now have, on a given line :

$$\sin(g_i) = \frac{(R_0+i+p+\frac{n_i}{Q})^2 - \delta^2 - (R_0+i)^2}{2\delta(R_0+i)}$$

or : $$\sin(g_i) = \frac{(p+\frac{n_i}{Q})^2 - \delta^2 + 2(R_0+i)(p+\frac{n_i}{Q})}{2\delta(R_0+i)}$$

then : $$\sin(g_i) = \frac{p+\frac{n_i}{Q}}{\delta} + \frac{(p+\frac{n_i}{Q})^2}{2\delta(R_0+i)} - \frac{\delta}{2(R_0+i)}$$

In this expression, the first term is clearly the most important.

We define the altitude of ambiguity e_a as the one which causes the rotation of one fringe, therefore : $e_a = \frac{de_i}{dn}$, that is :

$$\frac{de_i}{dn} = R_m \frac{dg_i}{dn} \sin(g_i-\theta)$$

$$\frac{de_i}{dn} = R_m \frac{d(\sin(g_i))}{dn} \frac{\sin(g_i-\theta)}{\cos(g_i)}$$

$$\boxed{e_a = \frac{R_0+i+p+\frac{n_i}{Q}}{\delta Q} (tg(g_i)\cos(\theta) - \sin(\theta))}$$

Or, in meter (i.e. multiplying by the range pixel size):

$$e_a = \frac{\lambda(R_0+i+p+\frac{n_i}{Q})}{2\delta}(tg(g_i)\cos(\theta) - \sin(\theta))$$

A priori orbital parameters allow a typical accuracy of 1 to 15 metre using restituted orbit. The correlation of the image pair allows a linear modelling of the deformation between images which give p and $\frac{n_{fr}}{Q}$ (index fr stands for far-range). This estimation can be conducted at the end and the beginning of the scene.

Although the positioning of the master track cannot be improved by this correlation, the relative positioning of the slave track is bettered to less than one metre by using two control points (which we call arbitrarily near-range and far-range, although they could be any remote pair of points). With obvious notations and the help of the figure, we have :

$$(R_{sfr}^2 - R_{snr}^2) = \Delta^2 + 2\Delta(D+\delta\cos(\theta))$$
$$(R_{mfr}^2 - R_{mnr}^2) = \Delta^2 + 2\Delta D$$
$$(R_{sfr}^2 - R_{snr}^2) - (R_{mfr}^2 - R_{mnr}^2) = 2\Delta\delta\cos(\theta)$$

A good knowledge of Δ, H and D can be obtained from the master image orbital parameters and from R_{mfr} and R_{mnr}. $\delta\cos(\theta)$ is thus obtained from the above formula. $\delta\sin(\theta)$ may then be obtained by :

$$(H - \delta\sin(\theta))^2 + (D + \delta\cos(\theta))^2 = R_{snr}^2$$

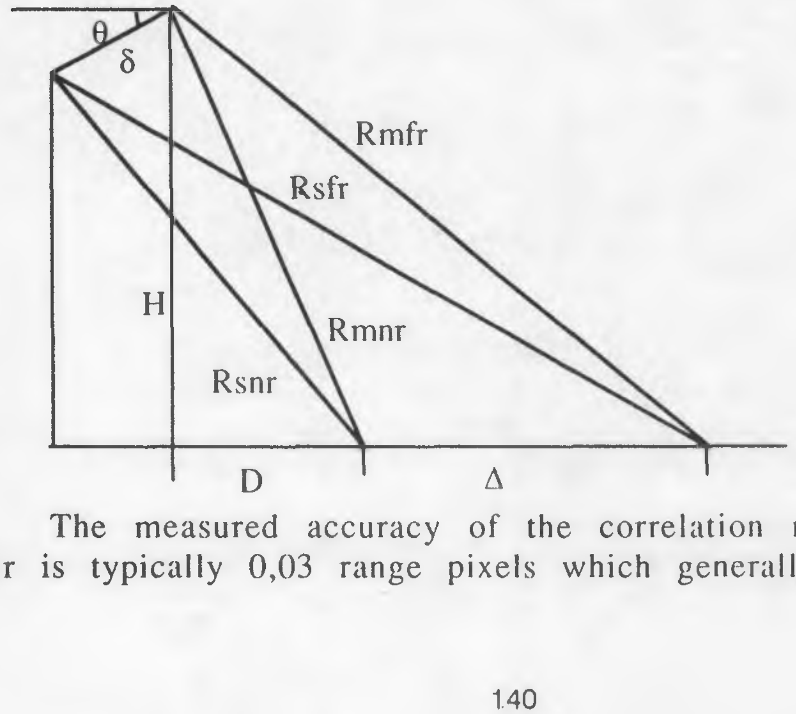

The measured accuracy of the correlation modelling of the pair is typically 0,03 range pixels which generally corresponds to an orbital accuracy of the order of one meter or better. Once we have the interferogramme, counting the fringes will give a much better estimation of $\frac{n_{Fr.}}{Q}$, and, in turn, a much better estimation of (δ,θ).

This precision can be obtained at the end and at the beginning of the scene by using a total of four ground control points (as few as possible for efficient operations !).

With small scenes (up to 100 km), we use a linear approximation of the horizontal and vertical components of the baseline. For longer scenes, this approximation is no more valid as shown by the following table, which indicates the difference between the baseline components and their linear approximations, in metres, along an acquisition lasting 300 seconds (or 2000 km on the ground).

Seconds	horizontal baseline	vertical baseline	non linear horizontal	non linear vertical
0	74,2212939	10,7090842	0	0
38,0968562	63,4887734	10,5457788	-0,2496691	-0,1268522
76,1943078	52,6492124	10,3447805	-0,3924694	-0,2160162
114,291759	41,7260931	10,1080435	-0,4517114	-0,2694414
152,389211	30,7248313	9,83372681	-0,4328108	-0,285287
190,486662	19,6726622	9,5238192	-0,3630029	-0,2655416
228,584114	8,58600857	9,17932278	-0,2587105	-0,2112074
266,681565	-2,5280246	8,79996701	-0,1270386	-0,1220139
304,779017	-13,637424	8,38779092	0	0

This linear approximation of orbital baselines is clearly inadequate for scenes longer than 300 km (up to ten "artefact" fringes were created in our example). In this case, we use what we call orbit reshaping.

Once we have the desired horizontal (d_b) and vertical (h_b) components of the baseline at scene beginning, obtained by the above orbit locking, we create the first point of a fake slave orbit by :

$$R_{sb} = R_{mb} + h_b \frac{R_{mb}}{|R_{mb}|} + d_b \frac{R_{mb} \times V_{mb}}{|R_{mb} \times V_{mb}|}$$

where R_{sb} is the slave position at scene beginning, R_{mb} is the master position at scene beginning, V_{mb} is the master speed vector at scene beginning (X is the cross product).

The problem is more complicated for the end of the scene, where orbital locking suggests d_e and h_e. We therefore propagate V_{sb} into R_{se0}, we apply three orthogonal small changes to V_{sb} and we obtain V_{sb+e_i} where $e_1 = (0,0,1\text{cm/s})$; $e_2 = (0,1\text{cm/s},0)$; $e_3 = (1\text{cm/s},0,0)$; we then propagate these three speed vectors into three R_{sei}. Since we know our desired position R_{se} at the end of the scene, a matrix inversion will give the right V_{sb}.

MULTI-DATE ACQUISITION AND SMALL MOVES DETECTION

There exist two methods of small moves detection : the three-pass method and the DEM elimination method.

The three pass method consist in predicting the fringes of a given pair (master/complementary or c-pair) by using the unwrapped fringes of another pair (master/slave or s-pair), the two pairs having one image in common. This is a way to cancel out the altitude e_i of the figure. If there are no moves, the accuracy of the prediction will be limited only by the noise. If there are moves, the prediction will fail and the moves will be detected. If the moves occur only during the time elapsed between c-pair, it will be directly observed. If it occurs only during the time elapsed between s-pair, it will be observed corrupted by the transformation used to turn s-pair into c-pair, which assumes only topographic and orbital differences between the images.

The moves may actually occur in both pairs since the image which is shared by the pair may not be the one with the median time. In the case of continuous moves (moves of glaciers for instance), the situation is even more complicated.

The procedure of pair transform is the following :
- we compute $g_s(i)$ from p_s, $n_s(i)$ et δ_s, which apply to the first interferogramme (s-pair)
- we determine the bore angle : $g_s(i) - \theta_s$, which depends only of the targets and of the master image geometry. It is therefore equal to : $g_c(i) - \theta_c$ if we change to c-pair. As a matter of fact, only : $\theta_c - \theta_s$ has to be known for obtaining g_c.
- we build $\sin(g_c)$ and, using δ_c and p_c, taking into account :

$$\sin(g_i) = \frac{(R_0+i+p+\frac{n_i}{Q})^2 - \delta^2 - (R_0+i)^2}{2\delta(R_0+i)}$$

and : $$\frac{n_i}{Q} = \sqrt{(R_0+i)^2 + \delta^2 + 2\delta(R_0+i)\sin(g_i)} - (R_0+i+p)$$

we compute : $\frac{n_c(i)}{Q}$ from which we obtain $n_c(i)$.

The DEM elimination method consist in computing directly the orbital and topographic fringes of an interferometric pair with the knowledge of the altitude e_i and of the orbital features of the pair.

One advantage of the three-pass method is that it does not require a DEM. More generally, it does not require any absolute positioning of the data.

However : the knowledge of a DEM is required anyway if we want to know where the moves occurred, which means not only to locate the satellite, but to correct for the relief. Furthermore, the DEM is the only "objective" data (i.e. we are sure that no move changed the DEM, especially if it has not been computed by interferometry).

The drawbacks of the three-pass method are :

-that the probability to find a good triplet in due time is much lower than the probability to find a good pair

-that at least one of the pairs has to be unwrapped, which means to take a difficult decision; the first solution is to unwrap the easiest pair and to inject a lot of noise into the other pair since the "baseline multiplication coefficient" from the above formulas will be greater than one. The second solution is to unwrap the most difficult pair...

-a further drawback is that, working with a triplet will combine by a logical "or" the causes of non coherence of both pairs.

The DEM elimination method worst case is to be forced to build an interferometric DEM with one of the pair of a triplet. It is probably more probable to build an interferometric DEM from a pair which is not related in time with the differential interferometry pair. All this make us think that the three pass method is actually the worst case of the DEM elimination method.

WORK WITH NON-COOPERATING PAIRS

In case of multi-date acquisition with a large number of scenes, it sounds very appealing to work with one slant range reference, that is to turn all the scenes into a slant range geometric reference which will allow to combine any pair of them into an high resolution interferogramme. We will then have a master image which will be the geometric slant range reference but will not, in general, be part of the interferometric pair. The question is then the validity of working with this master image and a fake slave image, that is the precision with which a master image/ fake slave image pair can mimic the geometric behaviour of the actual pair. We call this the quadruplet problem :
"Is there a position df,hf such that, for any ground point, the range difference between master image and fake image equals the range difference between images a and b ?" (see figure for notations)

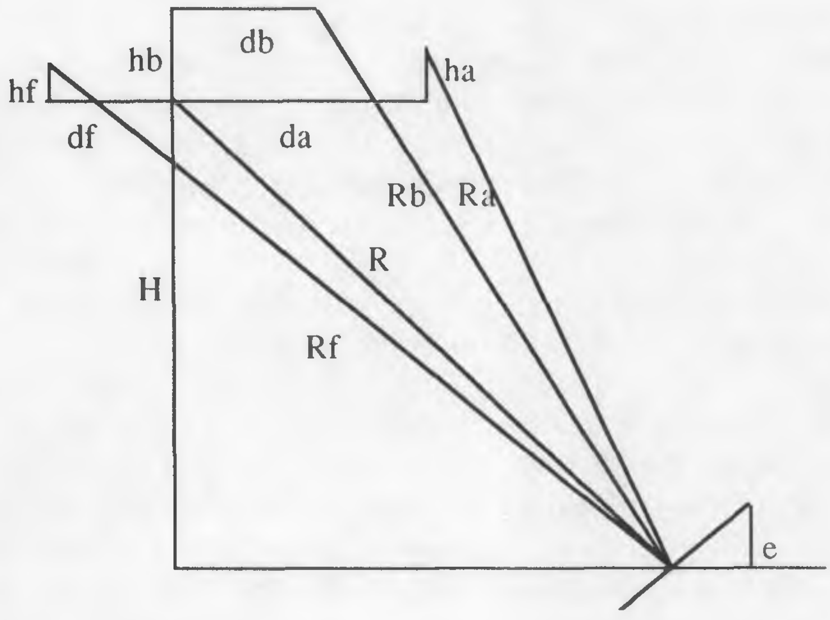

$$Ra = \sqrt{R^2+da^2+ha^2+2*ha*(H-e)+2*da*\sqrt{R^2-(H-e)^2}}$$

The solution of this problem exists, but it fully accurate only on two points of the image. If we select near-range and far-range, assuming zero altitude, as the two points where the solution is exact, we find that the error elsewhere remains very low. This proves that we may actually work in a common slant range reference without threatening the final accuracy.

As an example, if we take a typical ERS1 geometry, with da = 1000 m and ha = 100 m, we obtain the following errors :

Mid-swath : Altitude zero : 0.34 mm
Near-range : Altitude 4000 m : 1.4 mm
Mid-swath : Altitude 8000 m : 2.5 mm

REFERENCES

(1) Synthetic interferometer radar for topographic mapping
L. C. Graham - Proc. IEEE vol 62 n° 6 - 06.1974

(2) Topographic mapping from interferometric SAR observations
H. Zebker & R. Goldstein - Jour. of Geophys. Res.
vol. 91 n° B5 - 10.04.86

(3) Etude de principe d'une détection de mouvements tectoniques par radar
D. Massonnet -CT/PF/TI/AS n°326 (internal memo) - 16.11.85

(4) Mapping small Elevation Changes over large Areas : differential radar interferometry
A.K. Gabriel et al. J. Geophys. Res 94 n°B7 - 10.07.1989

(5) The Displacement Field of the Landers Earthquake mapped by Radar Interferometry
D. Massonnet, M. Rossi, C. Carmona, F. Adragna, G. Peltzer, K. Feigl and Th. Rabaute (NATURE, 8th July 1993)

(6) Radar Interferometry : Limits and Potential
D. Massonnet and Th. Rabaute IEEE (TGARS)
vol 31 n°2, 455-464 (03-1993)

(7) Sar Geocoding : Data and Systems
G. Schreier Editor (Wichmann)
chap. 18: geoscientific applications at CNES, *D. Massonnet*

USE OF INSAR FOR RADIOMETRIC CALIBRATION OVER SLOPING TERRAIN

by

L.M.H. Ulander and J.O. Hagberg
Dept. Radio and Space Science
Chalmers University of Technology
S-412 96 GÖTEBORG
FAX +46-31-164513

ABSTRACT

Radiometric calibration of SAR images over topographic terrain requires information on local surface slope. We propose two new products derived from SAR interferograms which provides the necessary data. The method used is based on estimating the instantaneous frequency in slant range and azimuth, respectively. Radiometric calibration corrections may then be derived, together with local surface slope angles. The latter may be used as input to backscattering models, which can be used for additional normalisation of the image power. The accuracy of the method depends on signal coherence, surface slopes and processing algorithms. A simulation of an algorithm based on the short-time Fourier transform is used for illustration. The algorithm is also applied to a test area in an ERS-1 SAR interferogram.

Keywords: SAR, interferometry, calibration, radiometry, slope

INTRODUCTION

Many applications of synthetic-aperture radar (SAR) data require radiometrically calibrated imagery. In recent years, calibration techniques have evolved such that the calibration accuracy is often stated to ±1 dB or better. One of the remaining problems, however, is the calibration over sloping terrain (Ref. 1). Most present calibration processors are based on an ellipsoidal Earth model which is inadequate for topographic terrain.

Radiometric calibration involves determining the backscattering coefficient (or normalised radar cross section) for an area of interest. Accurate calibration is most easily achieved by integrating the power response (noise subtracted) of reference point targets with known radar cross section (RCS) (Refs. 2, 3). The slant range geometry of the SAR implies that a geometrical projection is also necessary which depends on the local surface orientation. The backscattering coefficient σ° can be determined from

$$\sigma^\circ = \left(\frac{\sigma}{\varepsilon}\right) \cdot P \cdot \frac{dA_r}{dA_g} \qquad (1)$$

where $\mathcal{E}$ is the integrated power response of the point target [m^2], P is the mean image power (noise subtracted) in the area of interest, σ is the RCS of the point target [m^2], and dA_r and dA_g are corresponding area elements in the SAR image and on the ground surface, respectively. An alternative "backscattering coefficient" γ may also be defined according to

$$\gamma = \frac{\sigma^o}{\cos\theta_i} \tag{2}$$

where θ_i is the local incidence angle. Many terrain types approximately follow a constant-γ model, e.g. the rain forest.

Surface slope maps are thus necessary for radiometric calibration over sloping terrain. They are also required to determine the local scattering geometry for backscattering models. Slope maps may be generated from a Digital Elevation Model (DEM) or directly, without phase unwrapping, from SAR interferograms (Refs. 4 , 5). In this paper, we develop the basic theory and investigate signal processing algorithms for generating slope maps and radiometric calibration corrections from SAR interferograms. We also present simulation results and preliminary results from applying the algorithms to an ERS-1 SAR interferogram over Sardinia.

TERRAIN SLOPE FROM INSAR

Topography may be determined by SAR in an across-track interferometric mode (Ref. 6). Two focused complex images of the same area are used, acquired at two parallel but slightly displaced tracks. It can be shown that the phase difference between the two images is related to terrain altitude (Refs. 7, 8). The basis for the technique is that image speckle in the two images are correlated, which can be shown to be true up to a maximum baseline (spatial coherence) (Ref. 8). For acquisitions displaced in time, i.e. "repeat-pass", the technique also requires stable scatterers (temporal coherence) (Refs. 9, 10). This implies that the rms movement of scatterers within a resolution cell is less than about 0.1λ, where λ is the radar wavelength.

An interferogram is formed by multiplication of one image with the complex conjugate of the other image, followed by procedures to optimise fringe visibility. The phase of the interferogram is denoted by Φ. Further processing often estimates and subtracts out the phase for a horizontal flat surface forming the modified interferogram. The phase of the modified interferogram is denoted by ϕ. The differential of the interferogram phase can be related to the differential of the terrain altitude dz according to (see Fig. 1)

$$d\Phi = \frac{4\pi B_n}{\lambda R \sin\theta}\left(dz + \cos\theta\, dR\right) = C\left(dz + \cos\theta\, dR\right) \tag{3}$$

or for the modified interferogram phase

$$d\phi = \frac{4\pi B_n}{\lambda R \sin\theta} dz = C\,dz \tag{4}$$

where C is locally constant, B_n is the projected interferometer baseline perpendicular to the line-of-sight, λ is the radar wavelength, R is the slant range, and θ is the incidence angle for a horisontal surface. The factor 4π applies to a repeat-pass configuration which we consider in this paper; for a single pass configuration it should be substituted by 2π.

Eqs. (3) or (4) may be used to invert for terrain topography. Note that it is necessary to apply sophisticated phase unwrapping techniques since the phase is measured modulo(2π) (Ref. 11). Phase unwrapping becomes particularly problematic in areas of low signal correlation, e.g. due to system noise or spatial/temporal decorrelation.

Another possibility is to use (3) or (4) to retrieve terrain slope which does not require phase unwrapping. The differential modified phase is then decomposed in azimuth (x) and slant range (R) components according to

$$d\Phi = \frac{\partial\Phi}{\partial x} dx + \frac{\partial\Phi}{\partial R} dR = \Phi'_x dx + \Phi'_R dR \tag{5}$$

and a corresponding expression for ϕ.

The surface orientation is uniquely defined by the surface normal vector. The normal vector of the surface patch can be parameterised using spherical angles u and v as illustrated in Fig. 2. The angles may be conveniently determined from the modified phase derivative according to

$$\begin{aligned} \tan v &= \sin\theta \frac{\phi'_R}{\phi'_x} \\ \tan u &= \frac{\sqrt{(\phi'_x)^2 + (\sin\theta\,\phi'_R)^2}}{C + \cos\theta\,\phi'_R} \end{aligned} \tag{6}$$

Expressions may also be derived using the interferogram phase derivative Φ' although they are not separable in u and v.

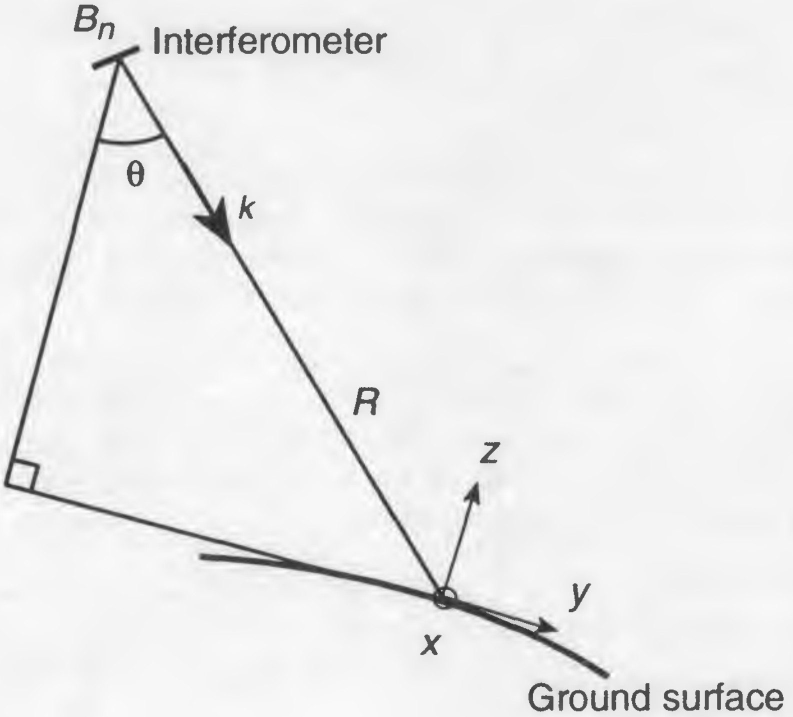

Figure 1. *Image geometry of a SAR interferometer in the slant range plane.*

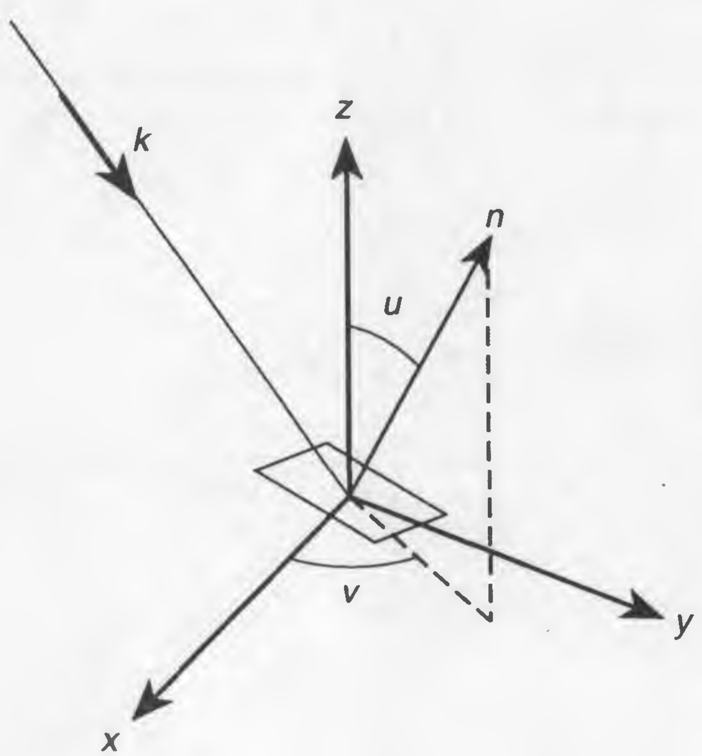

Figure 2 *The spherical angles u and v are used to define the surface orientation.*

RADIOMETRIC SLOPE CORRECTION

The radiometry in a SAR image is affected by surface orientation in two ways. Firstly, the SAR slant range and azimuth grid is projected onto the sloping ground surface. This results in increased image power in areas sloping towards the radar since the ground-projected resolution cell increases and vice versa. Secondly, the backscattering coefficient depends on polarisation state, local incidence angle and local azimuth angle. This normally also results in increased image power in areas sloping towards the radar and vice versa.

We assume that the SAR image is in its original slant range and azimuth representation. The scaling factor for the geometrical projection onto the ground can then be found by scalar multiplication of the surface normal with the normal to the SAR image plane. The result is given by

$$\frac{dA_g}{dA_r} = \sqrt{1 + \frac{\Phi_R'^2 + \Phi_x'^2}{C^2 \sin^2 \theta}} \tag{7}$$

or expressed in the modified phase

$$\frac{dA_g}{dA_r} = \frac{1}{\sin\theta} \sqrt{1 + 2\cos\theta \frac{\phi_R'}{C} + \frac{\phi_R'^2 + \phi_x'^2}{C^2}} \tag{8}$$

Eqs. (7) and (8) may be used to compute slope-corrected σ° values according to (1). After this correction, the σ° image is still effected by variations in local incidence angle due to the topography. This may be corrected for by using an appropriate model for the backscattering coefficient as a function of polarisation state, incidence angle and aspect angle. A first-order correction may be applied by converting to γ according to (2). The corresponding scaling factor can be shown to be given simply by

$$\frac{dA_g}{dA_r} \cos\theta_i = \frac{\Phi_R'}{C\sin\theta} \tag{9}$$

or

$$\frac{dA_g}{dA_r} \cos\theta_i = \frac{\phi_R'}{C\sin\theta} + \tan\theta \tag{10}$$

SAMPLING EFFECTS

The SAR spatial resolution effectively limits the spatial frequencies which can be measured in the interferogram. For simplicity, we consider a surface which has a constant phase in azimuth, i.e. which slopes towards or from the SAR only. For such a surface, the slant range frequency is given by

$$\Phi'_R = C\frac{\sin\theta}{\tan(\theta - u)} \tag{11}$$

or

$$\phi'_R = C\frac{\sin u}{\sin(\theta - u)} \tag{12}$$

where we have defined u as positive for $v = 270°$ (towards the SAR) and negative for $v = 90°$ (from the SAR).

The interval of unambiguous frequencies is given by the Nyquist limit to $2\pi/\rho_r$, where ρ_r is the slant range resolution. The maximum surface slope u_{max} which can be uniquely measured is thus given by

$$\tan(\theta - u_{\max}) = \frac{\rho_R C \sin\theta}{2\pi} \tag{13}$$

It can be shown that (13) is true for both the original and modified interferograms when positive and negative frequencies are correctly taken into account. Eqs. (11) and (12) are illustrated in Fig. 3.

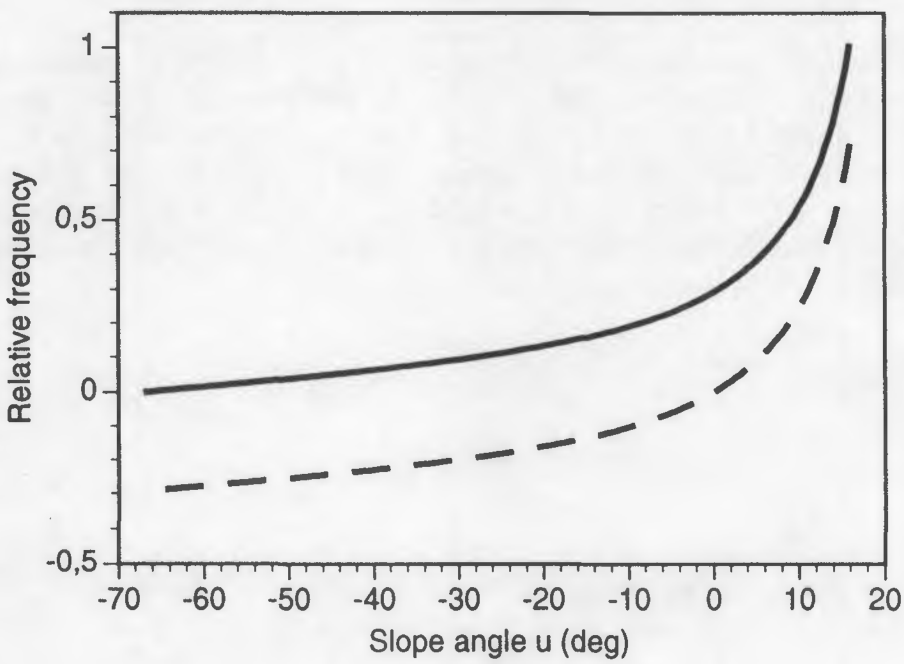

Figure 3 *Slant range frequency versus incidence angle for the original (solid) and modified (dotted) interferograms.* $C = 0.2\ m^{-1}$ *and* $\theta = 23°$.

ACCURACY REQUIREMENTS

The required accuracy for the estimation of instantaneous frequency (IF) to meet a calibration specification can be found by differentiating (7) or (8). For simplicity, we again consider the case when $v = 90°$ (u negative) or 270° (u positive). From (7) and (11), the relative calibration error simply reduces to

$$\frac{\sin^2(\theta - u)}{C\sin\theta}\Delta\Phi'_R \tag{14}$$

which shows the need for higher estimation accuracy for shorter baselines. Note also that the error has a maximum for $u = 90° - \theta$, i.e. for surfaces sloping along line of sight. The error decreases when $u \to \theta$ but sampling effects limits the performance according to (13). Aliasing will corrupt the slope estimate above u_{max}.

An example calculation using $C\sin\theta = 0.05\ m^{-1}$ and $\Delta\Phi'_R = 0.002\ m^{-1}$ gives a relative calibration error less than 0.2 dB. In practise, the size of the window used for estimating the IF can then be determined for a given SNR. The latter can be related to signal coherence Γ by (Ref. 9)

$$SNR = \frac{\Gamma}{1-\Gamma} \tag{15}$$

SIGNAL PROCESSING

Several signal processing techniques have been suggested for estimating the IF of an analytical signal (see Ref. 12 for a recent review). In this work, we have concentrated on using the short-time Fourier transform (STFT) and evaluated its performance. The maximum likelihood estimate of a single signal frequency embedded in circular white Gaussian noise can be shown to be the peak of the power spectrum. This estimate is easily implemented using an FFT followed by interpolation to find the peak power. The rms error above a SNR threshold is given by the Cramer-Rao bound (Ref. 13)

$$rms\left(\hat{f}_i\right) = \frac{\sqrt{6}}{2\pi}\frac{1}{\sqrt{SNR \cdot N^3}} \tag{16}$$

where N is the number of independent samples and $SNR = A^2/2\sigma^2$ (A is the signal amplitude and $2\sigma^2$ is the total noise variance). An example calculation using $SNR = 1$ and $N = 32$ gives an rms error of $0.002\ m^{-1}$ for the slant range frequency.

In practise, the IF is not constant but varies according to the local surface orientation. Simulation shows that the STFT performance starts to deteriorate when the relative frequency changes by about 0.02 across the window used for the FFT. Results from a simulation is shown in Fig. 4 based on a 1024-point linear FM signal with rel. frequency varying between

±0.25. The 32-point window is observed to meet the Cramer-Rao bound for $SNR > -2$ dB ($\gamma = 0.4$), whereas the 64-point window is slightly worse than the Cramer-Rao bound. Performance significantly decreases when a 128-point window is used. The relative frequency changes by 0.06 in the latter case.

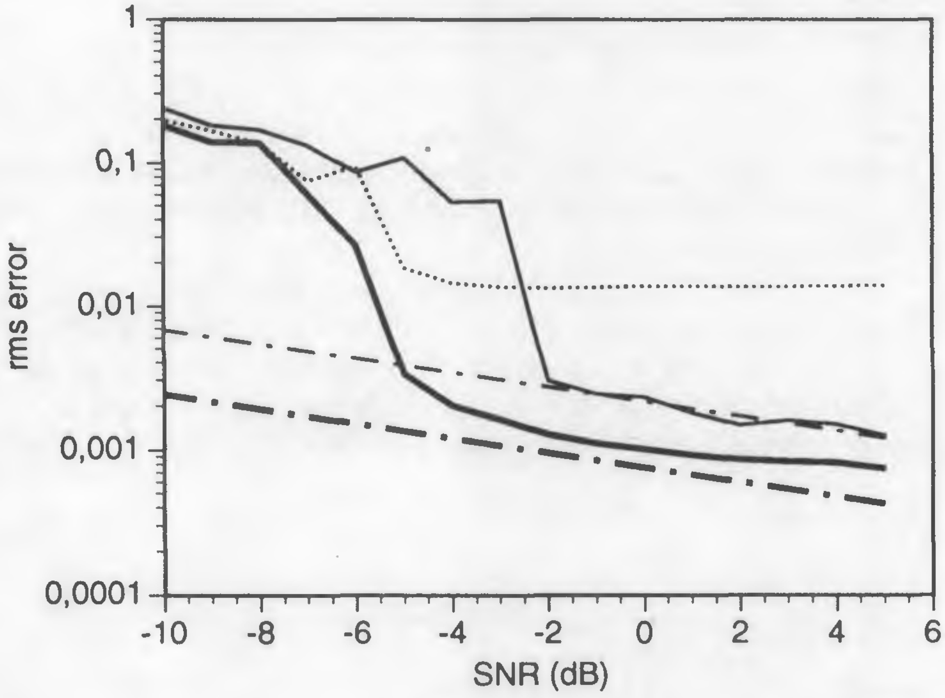

Figure 4 *Rms error of IF estimate using STFT as a function of SNR for three different window sizes: 32 (thin), 64 (thick), 128 (dotted). The Cramer-Rao bound (dot-dash) is also shown for window sizes 32 and 64. The true signal is a 1024-point linear FM signal sweeping between relative frequencies ±0.25.*

SIMULATION RESULTS

A simulation has been performed to test and illustrate the algorithm used. The surface height is modelled using a 2-dimensional Gaussian function as shown in Fig. 5. The representation is in ground range and azimuth pixels, and the surface was chosen so that no shadowing or layover occurs. The iso-heights are circles in Fig. 5 but become ellipses when the coordinates are scaled with different pixel sizes. The surface patch is then illuminated by a SAR interferometer.

Figure 5 *The surface height model used for simulation. The image is 2 km (ground range, horisontal) by 1 km (azimuth, vertical) and the Gaussian hill is 200 m in altitude. Simulation parameters: C = 0.15, θ = 23° and window size = 28 pixels.*

In Fig. 6, the result from retrieving u using (8) is shown when no system noise or speckle is included. Note that the result is displayed in slant range and azimuth coordinates, which causes the points where maximum occurs for u to be shifted towards the SAR.

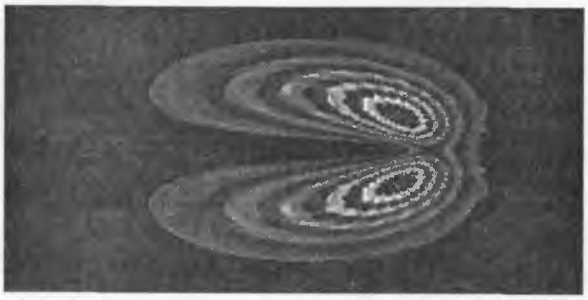

Figure 6 *The spherical angle u retrieved from a simulation of the SAR interferometer measurement. Note that the maximum slope occurs at two offset points in azimuth due to the ellipsoidal shape of the height contours.*

Fig. 7 shows the σ^o image correction according to (7) or (8), whereas Fig. 8 shows the γ correction according to (9) or (10). These images also represent the effect of topography on the SAR image radiometry for two special cases. The first case (Fig. 7) corresponds to a constant-σ^o surface which results in increased image power in a rather large area. This type of surface is, however, not very typical of a natural surface. It may be produced by a surface consisting of a many large spheres. The second case (Fig. 8) corresponds to a constant-γ surface. This results in increased image power in a smaller area since the model predicts increased backscattering coefficient closer to normal incidence. This type of surface is a simple representation of e.g. a rain forest.

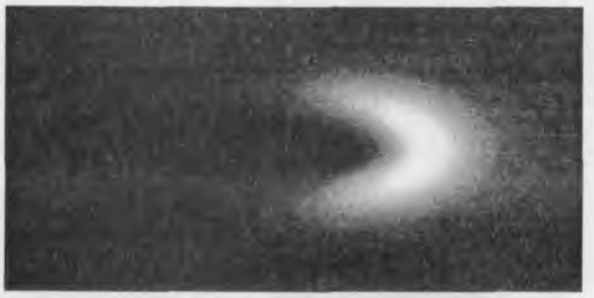

Figure 7 *The radiometric calibration correction dA_g/dA_r retrieved in the simulation. Note that the area of enhanced correction is rather large.*

Figure 8 *The radiometric calibration correction $\cos\theta_i \, dA_g/dA_r$ retrieved in the simulation. Note that the area of enhanced correction is smaller than in Fig. 7.*

The effects of system noise and speckle may be evaluated in an end-to-end simulation, and surfaces with different backscatter characteristics may also be included.

SARDINIA RESULTS

To test the algorithms for radiometric calibration over topographic terrain, we applied them to the ERS-1 SAR interferometric reference data with a baseline of 138 m. An area (16x3 km^2) at the east coast of Sardinia was used, a mountainous area with a lot of foreshortening and layover effects. In order to minimise effects of spatial variations a 28-point window, padded with zeros to 256 points, was used for the FFT IF-estimation and interpolation. The number of points should be choosen to optimise computing time, noise reduction, quantizing noise, and sensitivity to spatial varitions according to Eqs. (14) and (16).

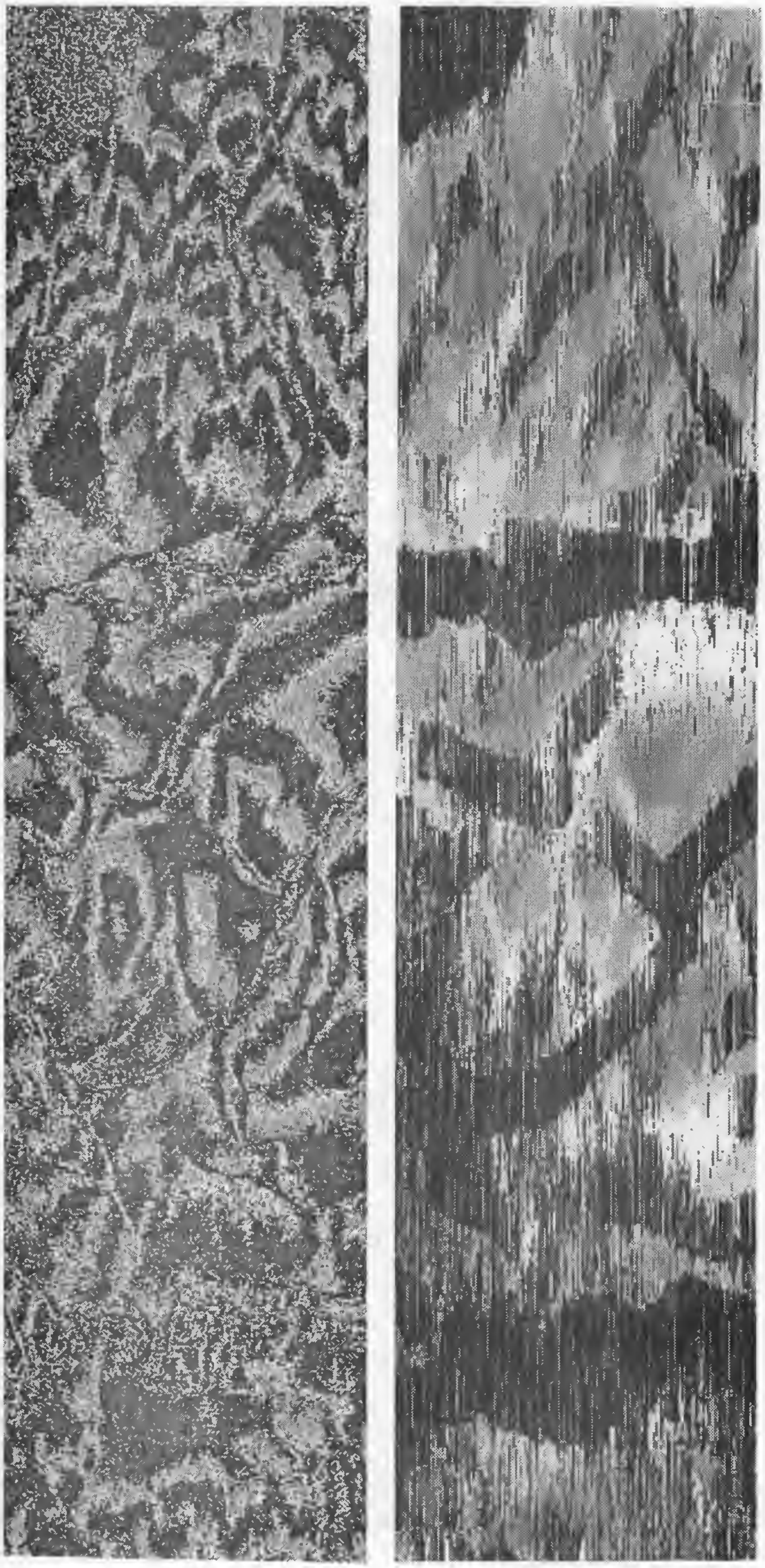

Figure 9 *The radiometric calibration correction algorithm applied to a test area in the Sardinia ERS-1 SAR interferometry data set. The interferogram (a) shows some areas of aliasing and layover which causes black areas in the calibration correction image (b).*

As a first preliminary result from this study we present the calibration correction image (Fig 9a), given by (7) for the geometrical projection onto the ground. We also show the corresponding compensated interferogram (Fig. 9b). White areas in Fig. 9a are horisontal while areas sloping away from the radar turns to gray. Steep areas sloping towards the radar can easily be identified in the interferogram as regions with high fringe rate. In such areas the STFT-algortithm fails to estimate the spatial frequency of the interferogram phase. Those areas as well as areas with low coherence (e.g. the upper left corner covering the sea) causes black areas in Fig 9a.

CONCLUSIONS

In this paper, we propose two new data products from SAR interferograms which are useful for radiometric analysis of SAR images over topographic terrain. The first product is a radiometric calibration correction according to (7) or (8) which is used for normalisation of the SAR image power. A first-order backscattering model, the constant-γ model, is also easily taken into account. The second product is the surface slope angles u and v according to (6) which can be used as input to more complicated backscattering models. Slope maps also have other important applications, e.g. for estimating drainage basins for hydrology, hydrochemistry and soil erosion modelling.

An assessment of the accuracy shows that the calibration error depends on signal coherence and the variability of the surface slope. Also, the method is ambiguous above a maximum slope towards the radar due to aliasing. Radiometric calibration and slope map generation using ERS-1 SAR is feasible but limited by the rather small incidence angle of 20-26°. A more optimised SAR interferometer system would use a higher incidence angle, e.g. 45°.

The proposed method is based on estimating the interferogram instantaneous frequency in slant range and azimuth, respectively. This can be done using the short time Fourier transform technique. Simulation has shown two limitations: Firstly, its performance degrades rapidly below a signal coherence threshold (typically, 0.4 for a 32-point window). Secondly, its performance degrades when the IF variation in the window is above a threshold (typically, 0.02). More complex algorithms will be investigated in future work with enhanced performance.

The method has also been applied to ERS-1 SAR interferometry data from the Sardinia test area. It is admittedly a difficult area with several layover ridges which results in bad performance. In the more gently undulating areas, the algorithm results in useful estimates of the radiometric calibration coefficient. It is noted that optimisation of fringe visibility is critical for the performance of the method.

REFERENCES

1. Freeman, A., SAR Calibration: An Overview, IEEE Trans. Geosci. Remote Sensing, 30, 6, pp. 1107-1121, 1992
2. Gray, A.L., Vachon, P.W., Livingstone, C.E., and T.I. Lukowski, Synthetic Aperture Radar Calibration using Reference Reflectors, IEEE Trans. Geosci. Remote Sensing, 28, 3, pp. 374-383, 1990
3. Ulander, L.M.H., Accuracy of using Point Targets for SAR Calibration, IEEE Trans. Aerospace Electron Syst., 27, 1, pp. 139-148, 1991
4. Werner, C.L., and P.A. Rosen, Topographic Slope from the SAR Interferometric Phase Gradient, Proceedings of PIERS 1993 held in Pasadena (12-16 July 1993), JPL Publication 93-17, pp. 922, 1993
5. Ulander, L.M.H., Hagberg, J.O., and J. Askne, Repeat-track SAR Interferometry over Forested Terrain, Proceedings of PIERS 1993 held in Pasadena (12-16 July 1993), JPL Publication 93-17, pp. 851, 1993
6. Graham, L.C., Synthetic Interferometer Radar for Topographic Mapping, Proc. IEEE, 62, 6, pp. 763-768, 1974
7. Prati, C., and F. Rocca, Limits to the Resolution of Elevation Maps from Stereo SAR Images, Int. J. Remote Sensing, 11, 12, pp. 2215-2235, 1990
8. Li., F.K., and R.M. Goldstein, Studies of Multi-Baseline Spaceborne Interferometric Synthetic Aperture Radars, IEEE Trans. Geosci. Remote Sensing, 28, 1, pp. 88-96, 1990
9. Zebker, H.A., and J. Villasenor, Decorrelation in Interferometric Radar Echoes, IEEE Trans. Geosci. Remote Sensing, 30, 5, pp. 950-959, 1993
10. Hagberg, J.O., Ulander, L.M.H., and J. Askne, Repeat-Pass SAR Interferometry over Forested Terrain, submitted to IEEE Trans. Geosci. Remote Sensing
11. Goldstein, R.M., Zebker, H.A., and C.L. Werner, Satellite Radar Interferometry: Two-Dimensional Phase Unwrapping, Radio Science, 23, 4, pp. 713-720, 1988
12. Boashash, B., Estimating and Interpreting the Instantaneous Frequency of a Signal - Part 2: Algorithms and Applications, Proc. IEEE, 80, 4, pp. 540-568, 1992
13. Rife, D.C., and R.R. Boorstyn, Single tone parameter estimation from discrete-time observations, IEEE Trans. Inform. Theory, 20, pp. 591-598, 1974

FIRST RESULTS OF MOTION COMPENSATION FOR TWO PASS INTERFEROMETRIC AIRBORNE SAR

Heike Büdenbender
João Moreira
Deutsche Forschungsanstalt für Luft- und Raumfahrt e. V. (DLR)
Germany
Charles Werner
Remote Sensing Laboratories, University of Zürich
Switzerland

1. ABSTRACT

In this paper a two pass interferometric airborne SAR experiment, carried out in May 1993, is described. This experiment represents the first step in the developement of a new algorithm for high precision motion compensation applied to interferometric SAR. First results are shown.

Keywords: Two pass interferometric airborne SAR, motion extraction, motion compensation

2. INTRODUCTION

Interferometric Synthetic Aperture Radar (InSAR) has been effectively used to generate Digital Terrain Models (DTMs). For a spaceborne platform (like ERS-1), this has been performed by using multiple passes of the same sensor [3]. Airborne InSAR systems require only one pass if two receiving antennas are available [4]. However, it is also possible to build a multiple-pass airborne interferometric SAR [1] It permits the creation of larger baselines that can be used for low-frequency interferometric applications.
In May 1993 a two pass interferometric SAR experiment has been carried out due to the jointeffort of the Remote Sensing Laboratories of the University of Zürich and the Institute for Radio Frequency Technologie of DLR. The goals of this experiment are:

- development of two pass interferometric SAR
- development of a new motion compensation algorithm
- time decorrelation measurements and
- differential interferometric SAR

3. TWO PASS INTERFEROMETRY WITH AIRBORNE SAR SYSTEMS

In the two pass case, the interferometric image is formed by relating the signals from two tracks with the same antenna. The geometry of a Two Pass InSAR is shown in image 1.

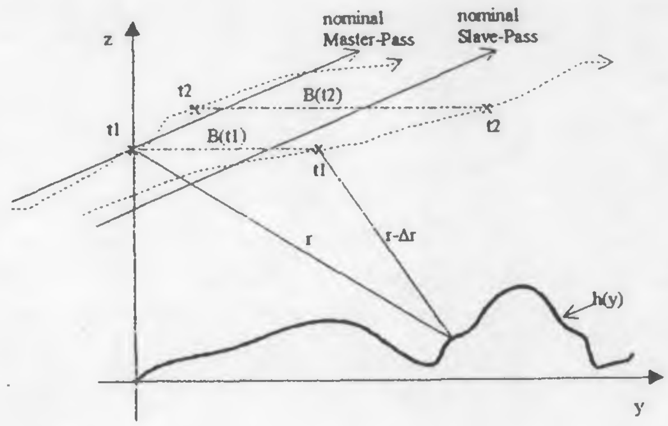

Figure 1: Geometry of the two pass interferometric SAR

The distance between the two tracks is called baseline. When the baseline increases, the coherence between the signals of the two passes decreases. The critical baseline is given by [5]

$$B_c = \frac{\lambda \cdot R_0}{2 \cdot \delta_r} \cdot \tan(\theta_D), \tag{1}$$

where λ is the wavelength, R_0 the minimum distance between scatter and sensor, θ_D the depression angle and δ_r the resolution in slant range direction. The SAR Sensor used for this experiment was the Experimental SAR E-SAR of DLR on a Do228 aircraft [2]. The parameters of the sensor and the illumination geometry are listed in table 1.

Using Eq. 1 and the parameters of table 1 the following critical baselines for the different available frequencys can be calculated:

- X-Band: $\lambda = 0.0313m$ $B_c = 21.3m$
- C-Band: $\lambda = 0.0566m$ $B_c = 38.53m$
- L-Band: $\lambda = 0.233m$ $B_c = 158.65m$

Due to the large critical baseline the L-Band has been choosen for this experiment.

PRF	1200.048Hz	pulse frequency
Δf	100MHz	chirp bandwidth
τ	$5\mu s$	chirp duration
f_{abt}	100MHz	sampling frequency
v_m	85m/s	plattform velocity
z_{nadir}	5500m	altitude
r_{near}	5852m	near range
θ_{near}	20[deg]	near range depression angle
r_{far}	8852m	far range
θ_{far}	51.6[deg]	far range depression angle
δ_r	2.2m	resolution in slant range direction

Table 1: Parameters of E-SAR system and illumination geometrie

The accuracy of height measurement is affected by decorrelation due to

- baseline decorrelation
- time decorrelation
- time variant baseline
- motion errors of the platform during the two tracks
- large differences between the two illumination geometries (high requirements for registration algorithms)

For the test site (area near Emmen/Switzerland) a high precision DTM of this area is available to verify the results. During the missions, an online radar tracker was available to direct the plane on the right track. The data from the tracker were also used to find a couple of tracks with a baseline shorter than half the critical baseline. The baseline between the two tracks is shown in fig. 2.

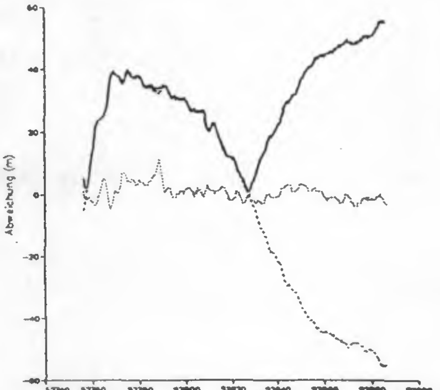

Figure 2: The dotted line is the position of track one, the dashed line the position of track two and the continous line the modulus of the baseline between the two tracks

4. MOTION EXTRACTION

The phase error due to the motion errors of the platform affects the accuracy of the hight measurement and has to be compensated. Considering the motion errors Δx, Δy and Δz one gets the following range history

$$r'(t) = R_0 + \frac{1}{2R_0} \cdot \left(\int (V + \Delta x(t))dt \right)^2 - \Delta y(t) \cos(\theta_D) + \Delta z(t) \sin(\theta_D), \tag{2}$$

where V is the ideal forward velocity. With this range history the phase error can be calculated to

$$\phi_{err}(t) = -\frac{4 \cdot \pi}{\lambda} \cdot (r'(t) - r(t)), \tag{3}$$

where r(t) is the range history without motion errors. To evaluate the motion errors, 3 different methods are combined:

- Differential GPS (which is long time stable)
- Inertial Navigation System INS (which is short time stable)
- Phase extraction from Active Radar Calibrators (ARCs) and Corner Reflectors

The new motion compensation approach is to use GPS and INS data to obtain a first level approximation of the airplane state vector during the passes. Then the phase history from a set of corner reflectors and ARCs is used to obtain the aircraft position with high precision.

To extract the phase history of one pointscatter, the data are range compressed and the range migration is compensated. After this operation, the azimuth chirp can be observed within one rangeline and compared with the expected azimuth chirp. The difference between expected and recieved azimuth chirp is related to the positioning error from Eq. 2. With three pointscatters the motion errors Δx, Δy and Δz can be triangulated.

The first approach evaluates the motion errors from the phase history of one ARC and has the following approximations:

- The forward velocity is calculated from the quadratic part of the phase history of the ARC.
- The remaining phase, calculated by subtracting the ARC phase history from its quadratic part, is related only to the motion errors in line of sight direction.
- The motion errors in line of sight direction are considered constant over range, as the range swath is very narrow (256 range bins).

Processing a small part of the two images with this first approach, we got a first interferogramm of the scene (fig. 3). The observed part of the scene is approximately flat (with exception of some buildings). That means, that the observed fringes are resulted only by the flat earth. Due to the time variant baseline, the fringes are not parallel to azimuth direction.

The first results show, that, in principal, it is possible to perform two pass interferometric SAR with the Experimental SAR of DLR.

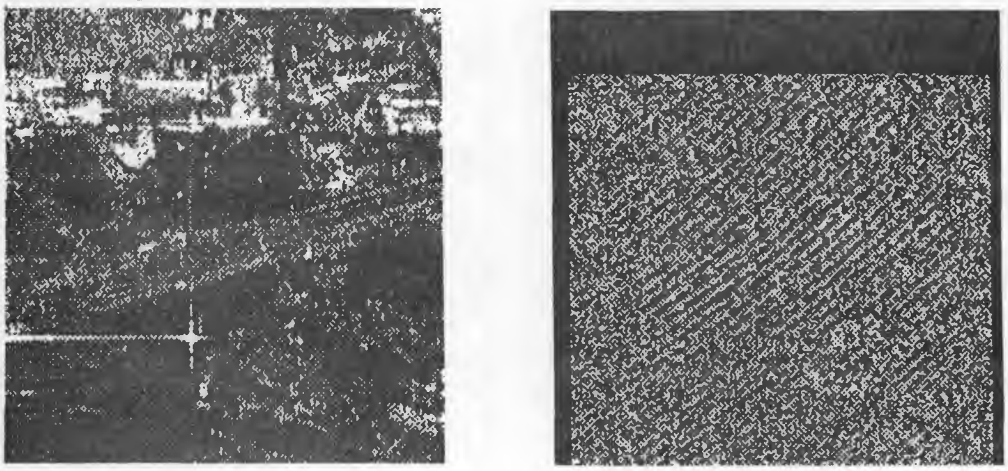

Figure 3: Processed small part of the scene with one ARC, the railway and some buildings (2048 pulse and 256 rangelines) and resultion interferogram

5. REFERENCES

[1] A. L. Gray, P. J. Farris-Manning, Repeat-Pass Interferometry with Airborne Synthetic Aperture Radar, *IEEE-Trans. Geoscience and Remote Sensing*, Vol. 31, No.1, 1993

[2] R. Horn, Das experimentelle SAR System E-SAR der DLR, *DGON, 8. Radarsymp.*, 1993

[3] F. K. Li, R. M. Goldstein, Studies of Multibaseline Spaceborne Interferometric Synthetic Aperture Radars, *IEEE Trans. Geoscience and Remote Sensing*, Vol. 28, No.1, Januar 1990

[4] S. Madsen, H. A. Zebker, J. Martin, Topographic Mapping Using Radar Interferometry: Processing Techniques, *IEEE-Trans. Geoscience and Remote Sensing*, Vol. 31, No.1, 1993

[5] H. A. Zebker, J. Villasenor, Decorrelation in Interferometric Radar Echos, *IEEE Trans. Geoscience and Remote Sensing* Vol. 30, No.5, 1992

RADIOMETRIC CALIBRATION 1 & 2

Session 5
Chair: B.HAWKINS, CCRS, Canada

Session 6
Chair: H.VADON, CNES, France

QUALITY ISSUES FOR LOW RESOLUTION SAR IMAGERY

Gaute Aarbakke SOLAAS & Henri LAUR

Projects & Engineering Department
Earth Observation Division
ERS Missions Section

ESRIN - ESA
Italy

Keywords: ERS SAR, Low Resolution SAR, Quick Look SAR, Equivalent Number of Looks (ENL).

1.0 INTRODUCTION

This paper is a short version of **ES-TN-DPE-OM-GS01, version 1.1**, an ESA technical note. The objective and a short description of the content of the complete technical note are given below. While only the introduction and the conclusive discussion are given in full in this paper.

The objective of the study is to describe and to analyse the various concepts associated with the ERS SAR low resolution imagery. This study is done in order to evaluate a range of products, to consider the trade-offs involved in product specification and to propose some recommendations for low resolution imagery of quality suitable for a broad range of potential applications.

In chapter 2 we give an overview on the concepts associated with SAR low resolution imagery. We explain the main trade-offs in SAR low resolution imagery. We then describe the techniques used during the generation of low resolution imagery with focus on the techniques for the data conversion from 16 to 8 bits.

In chapter 3 we investigate the quality of the existing ERS SAR low resolution products derived from high resolution products. For some of the analysed products, we propose quality improvements.

In chapter 4 we investigate the quality of the existing ERS SAR low resolution imagery directly derived from the raw data.

In chapter 5 we simulate different levels of speckle reduction in low resolution imagery. The simulated images are generated to demonstrate varying image quality.

Finally, in the conclusion, we make some recommendations for ERS SAR low resolution product specifications and give our view on the likely evolution of this kind of imagery.

2.0 INTRODUCTION TO LOW RESOLUTION SAR IMAGERY

A major reason to produce low resolution images is to reduce data volume and thereby to reduce time of data distribution. Another important reason for low resolution imagery generation is the possibility to make visible the ERS SAR acquisitions, i.e. the possibility to 'see' ***all*** acquired raw data.

Furthermore SAR low resolution imagery would :

1. facilitate scientific studies and surveillance applications of large scale phenomena (mainly in oceanography, sea ice kinetics and geology),
2. promote the use of high resolution data (browse function, i.e. identification of scenes to be processed at high resolution),
3. allow a closer surveillance of the SAR instrument performances.

In the case of the ERS SAR data, the term 'low resolution image' is commonly used to refer to an image with spatial resolutions ranging from 100 to 200 metres.

According to its origin, the ERS-1 SAR low resolution imagery available today falls into two categories: LR imagery derived from high resolution products and LR imagery derived from raw data.

A. LR imagery derived from High Resolution products:

Such imagery is derived from standard high resolution products (e.g. UI16 and PRI) by different techniques commented in the following chapter. At present such imagery is used for two different purposes:

- to provide scientific users with a ***digital product*** for studies of large scale phenomena. Such a product, usually called 'low resolution product', has a good radiometric resolution (usually more than 30 effective looks) and can potentially be absolute calibrated,
- to provide application users (real-time availability) and archive data centres (browse or quick-look) with a photo or screen ***display*** of the available HR products. Usually such images are generated with contrast enhancement and further data volume reduction (in comparison with the previous case). It should be noticed that screen display can be generated either from HR products or LR products.

The resulting outputs of these two purposes (digital product and screen display) are opposite because contrast enhancement and strong data reduction mean always radiometric degradation.

The major disadvantage of the LR imagery derived from HR imagery is its ***limited access*** caused by the limited generation of HR products. Within the ESA ground segment (Kiruna, Fucino and Maspalomas ground stations) ***more than 85 % of the raw data acquired have never been processed to HR products***. Although this value is large, one should not underestimate the amount of HR products already processed within the ESA ground segment : at mid-June 1993, about 23 000 standard frames (incl. double acquisition), i.e. 230 millions km^2 (Earth surface = 510 millions km^2) !

B. LR imagery directly derived from raw data :

Such imagery is derived directly from the acquired raw data. At present such imagery has one purpose:

- to provide archive data centres (browse) with a photo or screen ***display of 100 % of the acquired raw data***. Usually such images are generated as standard frames cut out of a strip corresponding to a whole SAR segment. It is mainly u sed to assist users in the choice of HR production requests. As previously such imagery can also be used for real-time applications.

To reach this goal (processing of 100 % of the raw data), the processing time of such imagery shall be very short (better than $1/8^{th}$ real time).

The major disadvantage (up to now) of the LR imagery derived from raw data is its ***poor radiometric resolution*** (usually less than 10 effective looks). This means that such an image cannot be used as a digital product for users.

However the potential exists to improve radiometric resolution without losing processing time. ***This is the main improvement to be expected in LR imagery generation for the next years***. A near real-time image with good radiometric resolution (more than 30 effective looks) could result in a digital product suitable for users and covering all ERS SAR acquisitions.

2.1 Trade-offs

Several factors must be traded off against each other in the generation of low resolution SAR imagery :

2.1.1 Spatial resolution against image size

The more coarse the spatial resolution one uses, the smaller is the volume of data per image. The problem with the distribution of high resolution products is their size, which for many users implies that tapes must be sent physically to their location. Generally the data volume decreases as the inverse square of the spatial resolution.

Reduced data volume implies reduced pixel size and by consequence reduced spatial resolution. There is however a lower limit since even large scale phenomena have a characteristic spatial sampling limit. A study of the viable applications and specific spatial resolution requirements is needed if LR imagery has to be used as digital LR product. The consensus of about 100 m pixel size (i.e. about 150 m spatial resolution) has to our knowledge not been based on such a survey. For display purposes (i.e. browsing or real-time dissemination) the dominant consideration is the data volume (less than 250 Kbytes); it means that pixel size reduction (about 200 m) or data compression are required.

Figures 2.1 to 2.3 illustrate the trade-off between radiometric and spatial resolutions that is possible to obtain when deriving LR imagery from three different ERS-1 HR products, namely the SLC (Single Look Complex), PRI (Precision Image) and UI16 (Fast Delivery Image) products [Ref. 1]. For each product the ground range resolution cell area has been calculated (SLC : 5 x 25 = 125 m^2, PRI : 22 x 25 = 550 m^2 and UI16: 25 x 28 = 700 m^2). The equivalent number of looks NL for any simulated spatial resolution is then found by taking the ratio between the simulated and the original resolution cell and multiplying by the number of looks in the original image:

$$NL_{new} = NL_{original} \times (\text{resolution cell area})_{new} \;/\; (\text{resolution cell area})_{original} \quad (1)$$

The three figures represent different intervals of spatial resolution.

The differences between the equivalent number of looks obtainable for a LR image derived from SLC, PRI and UI16 products in figure 2.1 are a clear demonstration that the quality of the LR imagery is dependent on the HR image type used to generate it. Even if the same bandwidth is used in the generation of two HR images (960 Hz for UI16 and PRI), the spatial resolution obtained for the UI16 image is poorer than the one obtained with the more thorough processing performed to generate the PRI image. The SLC product uses a larger bandwidth (about 1400 Hz) which results in a significantly better radiometric resolution in the resulting LR image.

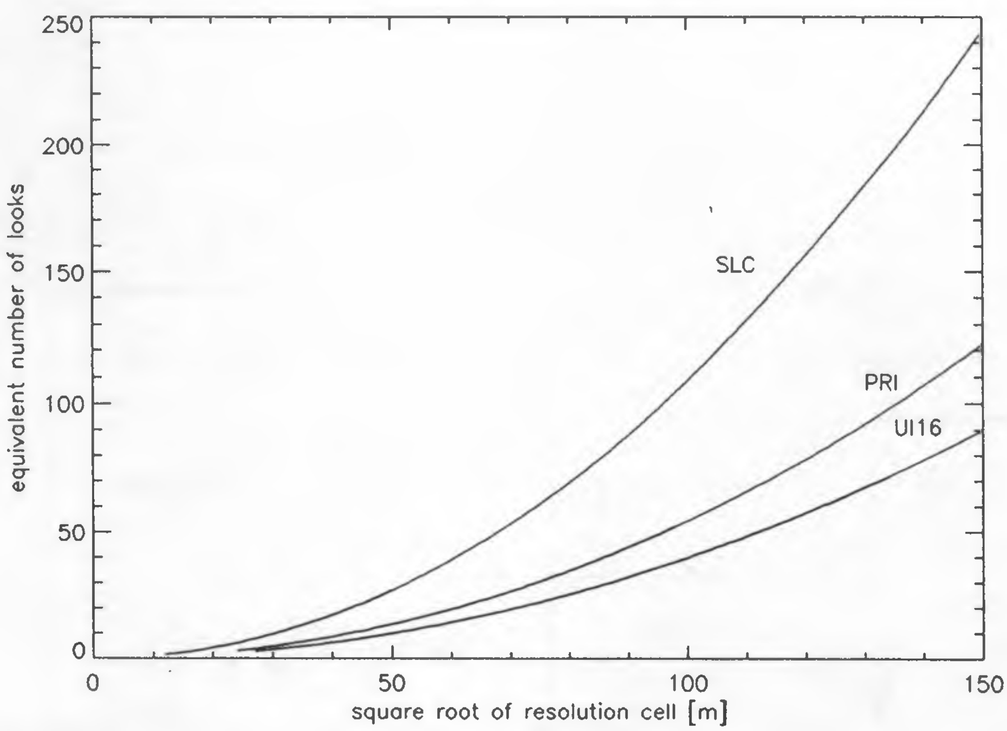

FIGURE 1: Maximum obtainable Equivalent Number of Looks for SLC, PRI and UI16 derived Low Resolution imagery (0 to 150m)

2.1.2 Speckle reduction against processing time

In order to generate LR imagery with less computation power, one can choose to use only a part of the whole information contents (bandwidth) of the raw data by subsampling techniques. This implies that the speckle reduction will be poorer, but near real-time processing can be realized with use of limited computing resources. So-called "quick-look" products are based on such an approach (see ref.1 chapter 4). The poor reduction of speckle limits the possible use of the digital product generated, but the reduced processing load enables image generation for all acquired raw data.

It should be underlined that the generation of HR products demands high computing power that significantly limit the access to the acquired raw data. Up to now more than 85 % of the acquired SAR data at the ESA ground stations are not processed.

2.1.3 Product size against dynamic range

This is mostly a question of 8 or 16 bit format on the amplitude version of the image, and is of issue because of the factor two reduction of data volume. The trade-off here is dynamic range against radiometric precision.

Here the issues are sufficiently clear that an optimal solution can be found which covers the needs of most applications. Experience has shown that most often this can be achieved with only minor loss of information (see ref.1 section 2.3.2).

3.0 DISCUSSION

ERS low resolution SAR imagery has two origins :

- **derived from high resolution products**
- **derived directly from raw data**

ERS low resolution SAR imagery serves two goals :

- **digital product for scientific applications**
- **display for browse, raw data visualization or for request of HR production**

In our study, we have described and analysed the existing ERS-1 SAR Low Resolution imagery (see next table). We have proposed improvements to the quality of some of the analysed images.

Existing ERS-1 SAR Low Resolution Imagery		**Origins**	
		Derived from HR product	Derived from Raw data
Goals	LR digital product	• LRI Tromsø • SGC Gatineau • Lo-Res Fairbanks	**Future**
	Display / Browse	• UILR Kiruna	• QL Bangkok • QL Brazil • QL Antarctica

Given the two distinctive (and potentially conflicting) goals, ERS low resolution SAR imagery should meet the following criteria:

SAR LOW RESOLUTION IMAGERY

	CRITERION	DIGITAL PRODUCT	DISPLAY / BROWSE
1	To have a good radiometric resolution	Mandatory : better than 0.75 dB, i.e. > 28 E.N. Looks Recommended : better than 0.5 dB, i.e. > 70 E.N. Looks	Recommended : better than 1 dB, i.e. > 15 E.N. Looks
2	To be relatively and absolutely calibrated	Mandatory : relative calibration (for inter-comparison) Recommended : absolute calibration (for derivation of °)	Not required
3	To have uniformly spaced pixels to limit geographic distortion [in order to avoid resampling]	Mandatory : less than 5 % difference between range and azimuth pixel spacing	Not required
4	To have a reduced data volume to allow swift and inexpensive transmission and to facilitate archiving	Mandatory : presentation : • ground range • amplitude, 8 bits • pixel spacing = 100 m	Mandatory : presentation : • amplitude, 8 bits • pixel spacing = 100 m Recommended : • data compression techniques • pixel spac. up to 200 m
5	To cover 100 % of the acquired raw data	Recommended	Mandatory
6	To be shortly available after data acquisition to allow real or near real time applications	Recommended : processing time better than $1/8^{th}$ real time	Mandatory : processing time better than $1/8^{th}$ real time
7	To have a good contrast enhancement	Not required	Recommended

3.1 Comments on the criteria

1. Good radiometric resolution

In the simulation of different radiometric resolutions for a fixed spatial resolution (chapter 5), we demonstrate (visually) that the better the radiometric resolution is, the easier the interpretation of the LR images is.

When the LR product is generated from HR product, a low pass filtering applied before the block averaging greatly improves the radiometric resolution of the LR product (section 2.2 and 3.1.3).

2. Relative and absolute calibration

Relative calibration (image-to-image)

LR digital products of the same area but of different acquisition times should be immediately comparable (without further processing). The radiometric stability measured on LR products should be identical to the one measured on high resolution products (for ERS-1, better than 0.5 dB).

In sections 2.3 and 3.1.1, we have presented two methods for 16 to 8 bit conversion of HR products. The fixed ratio conversion should be used because it does not affect the original radiometry.

Relative calibration (within one image)

LR digital products should be compensated for the antenna pattern and range spreading loss.

Absolute calibration

It should be possible to retrieve the backscattering coefficient ^{o} in LR digital products:

$$\sigma^{\circ} = I / K \qquad (2)$$

- where K is the calibration constant of the LR product and I the intensity of few pixels (mean of the square of pixel values).

If the LR product has more than 100 equivalent looks, the intensity I can be directly given by the square of <u>one</u> pixel value only.

3. Uniformly spaced pixels

This is necessary to avoid geographic distortion harmful to objects dynamics analysis in multi temporal LR products (e.g. sea ice movements).

4. Reduced data volume

In section 2.3, we have shown that the dynamic range of backscattering coefficients in ERS SAR images is completely contained in 8 bits. The pixel spacing should be 100 m and the spatial resolution about 150 m.

Previous presentation parameters give a typical size of 1 Mbyte for a LR digital product.

With pixel spacing of 200 m and use of data compression techniques, one can obtain LR imagery suitable for display purpose with a data volume of about 100 Kbytes per standard frame.

5. All acquisitions processed at Low Resolution

This criterion is particularly stringent for ground stations acquiring a large volume of raw data like the ESA Kiruna station (about 60 minutes of data per day). For such ground stations, the produced LR imagery should respect the next criteria.

6. Shortly available

For real or near real time applications, the LR imagery should be processed at near real-time (i.e. better than $1/8^{th}$ real time).

7. Good contrast enhancement

The contrast enhancement is <u>only</u> recommended for screen display purposes. In such a case, an algorithm based on the probability distribution can be applied on the image for contrast stretching (section 2.3).

3.2 SAR Low Resolution Imagery Evolution

The Figure 6.1 gives an overview of the current status and the evolution of ERS SAR Low Resolution imagery.

The ***existing*** LR imagery derived from raw data is able to provide ***visualization of all SAR acquisitions*** albeit with degraded image quality (case of Bangkok QL).

The *existing* LR imagery derived from HR products is able to provide ***LR digital products*** for scientific applications (case of Norwegian LRI product) but is far from covering all SAR acquisitions. At near term the quality of such LR digital products can be improved to better satisfy user needs.

The ***future*** LR imagery should be able to provide ***LR digital product with high image quality of all SAR acquisitions***. This goal is reachable if increased computer power is available.

Increased computer power means reduction of HR processing time, i.e. possibility to have HR products of all SAR acquisitions (and by consequence LR products of all SAR acquisitions). But in such a scenario one would have ***to drastically increase the archiving capacities of HR products***.

Increased computer power means quality improvement in LR imagery derived from raw data and by consequence possibility to have LR digital products with a good image quality. However in such a scenario, there would be the need to ***reprocess the data for HR products generation.***

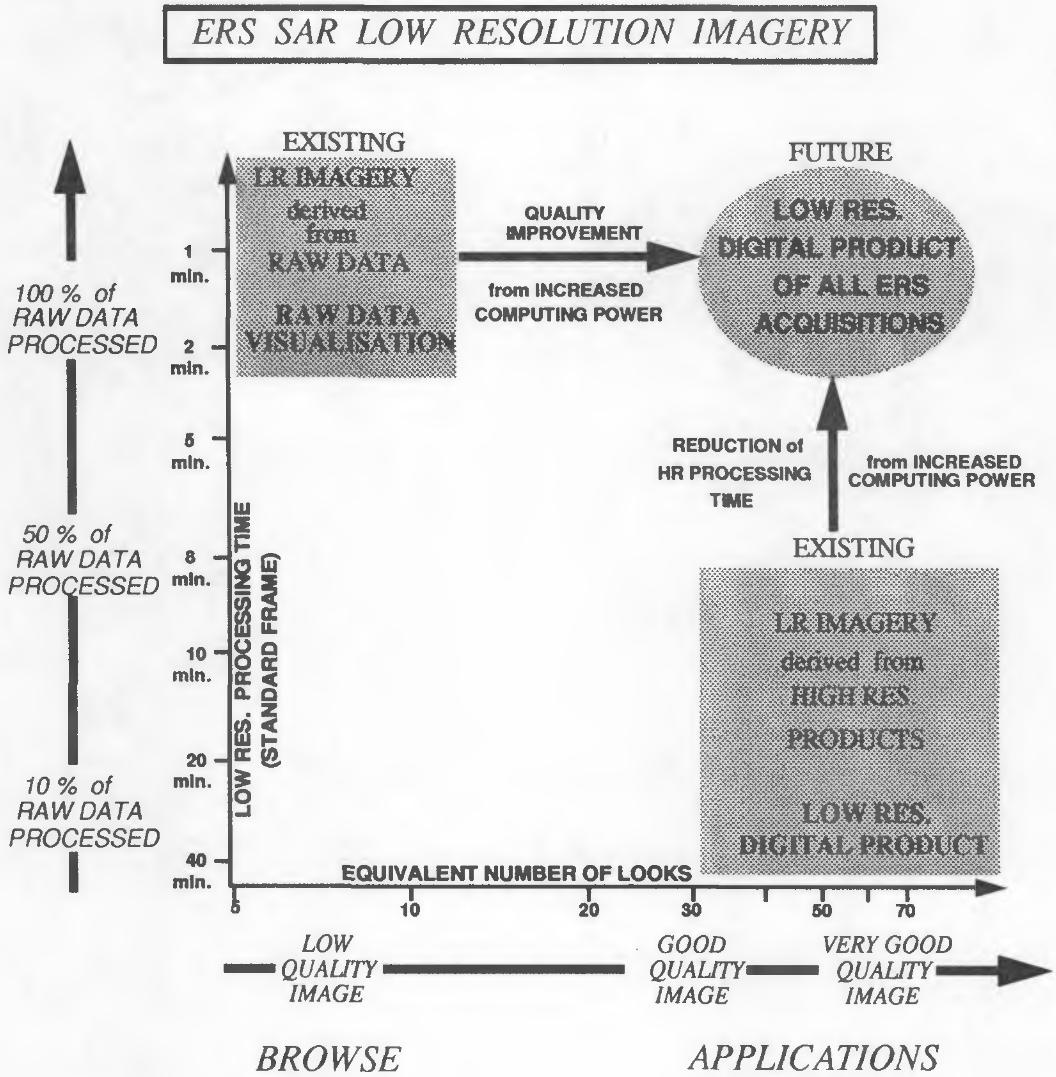

FIGURE 2: **Current status and evolution of the SAR Low Resolution imagery.**

4.0 References

1. European Space Agency, *An Assessment of ERS SAR Low Resolution Imagery*, ESA/ESRIN, Ref. ES-TN-DPE-OM-GS01, version 1.1, July 1993.

THE CCRS AIRBORNE SAR
STC FUNCTION

L.D. Teany[1] and R.K. Hawkins
Canada Centre for Remote Sensing
588 Booth St., Ottawa, Ontario, Canada K1A 0Y7

ABSTRACT

The CCRS airborne SAR does its range expansion and compression stages by using matched pairs of surface acoustic wave devices (SAWs). Six-bit A/D conversion then follows the downconversion of the signal to baseband. Due to the wide dynamic range of the signal across the swath, a sensitivity timing control (STC) attenuation function is applied to the incoming signal before and after range compression in order to limit the signal dynamic range and to level the grey scale across the swath.

This paper examines the implementation of the STC function in the CCRS C/X SAR systems and models the effect of STC on the amplitude of the resultant data. Results are compared with measurements completed using BITE test signals. Understanding the STC function and correctly modelling its effect is an essential part of the calibration of this airborne SAR.

Keywords: Sensitivity Timing Control, SAR Receiver Characterization, Calibration

1. INTRODUCTION

The STC is a voltage controlled, range-dependent attenuation applied to all samples in the radar receive window of the CCRS airborne SAR. Its function is to reduce the incoming signal dynamic range and to level the grey scale across the swath. The STC function is computed within the Preprocessor Control Unit (PCU) of the SAR, based on SAR configuration parameters. However, the actual implementation of this function is performed in the ERU (Exciter Receiver Unit) of the SAR where the ideal STC is approximated by the non-linear device characteristics, control signal slewing, timing offsets, etc. In order to calibrate CCRS airborne SAR data, it is essential that knowledge of the true applied STC function be available.

For calibration, the STC function is modelled within the CCRS calibration software, SARCAL (Synthetic Aperture Radar CALibration), see (Ref. 1). This software is a key element in the CCRS airborne calibration methodology (Ref. 2). For accurate STC modelling, the implementation of the STC in the ERU has to be examined thoroughly. This paper shall address how the STC function is physically implemented for the CCRS SAR, examine the parameters which are modelled within SARCAL, and show the resulting improvement to the modelled STC.

2. SENSITIVITY TIMING CONTROL (STC) FUNCTION

Figure 1 illustrates the STC function concept. For each transmitted pulse, a typical radar return[2] may resemble the curve shown. Note that there is a large signal dynamic range and signal shape to the expected return. To balance these range-dependent signal levels, and to obtain a more constant output level across the swath[3], a STC function is applied. The STC is therefore a programmed control of the receiver gain, having essentially the inverse shape to the expected radar return.

The variation of the radar return across the swath is dependent on the SAR viewing geometry, the antenna gain pattern, and the terrain type (Ref. 3). This dependence is depicted in Eq. 1, which is a proportionality equation for the SAR received power (at the receive antenna). When azimuth compression is included, the dependence is R^{-3}.

---

[1] Intera Information Technologies (Canada) Ltd., Under Contract to CCRS. 2 Gurdwara Rd., Nepean, Ontario, Canada K2E 1A2

[2] This shape most resembles that of a Nadir mode configuration. For Narrow Swath and Wide Swath modes, the expected radar return may have less signal dynamic range and/or shape.

[3] Ideally, assuming a homogeneous target, the resultant signal level would be constant. In reality however, terrain variations across the swath and variations in SAR configuration parameters to actual parameters, result in a small residual level fluctuation.

$$P_R \propto \frac{P_T G_{TR} e^{-\alpha R} \sigma_o}{R^4 \sin\theta} \quad (1)$$

The applied STC function is computed at configuration time, based on operator input configuration parameters (such as swath mode, antenna depression angle, antenna polarization, altitude, and an applicable terrain reflectance law). This function is then implemented in real-time in the SAR receiver.

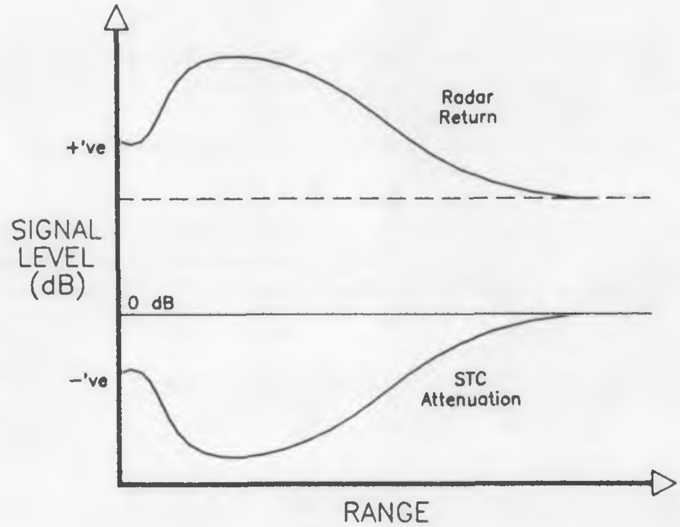

Figure 1: *STC Function Concept*

3. IMPLEMENTATION OF STC

3.1 C-Band Exciter Receiver Unit (ERU)

The STC function is physically implemented in the exciter receiver unit of the SAR. Figure 2 illustrates the C-band ERU, with the RF signal path highlighted.

The basic transmit signal path consists of the radar pulse signal generation, range expansion through the SAW device[4], up conversion from IF (300 MHz) to RF (5.3 GHz) frequency, and transmission through the SAR antenna. Upon reception, the signal enters one of two channels of functionally identical modules. Normal SAR configuration assigns channel A for co-polar reception and channel B for cross-polar reception. This received signal passes through a bandpass filtering stage, a downconversion stage back to IF frequency, receiver gain control stages, the application of the precompression STC (STC1), signal compression through a second SAW device, and application of the postcompression STC (STC2).

Near the receiver front end is a RF switch which is used to optionally inject a BITE (Built In Test Equipment) test signal. This signal is typically used for receiver noise/gain characterization, and can be used to recover the effective STC applied to the incoming data stream.

The drive signal to the STC attenuators originates from within the PCU module. This module, together with the IF Amplifier module, the SAW Compressor module, and the Coherent Video Detector module, form the fundamental modules in which the STC is implemented. These modules will be examined more thoroughly in Section 3.3.

3.2 Computation of STC

The computation of the STC function is done in the PCU module, and it consists of several steps (Ref. 4) as illustrated in Figure 3.

[4] The 1 us pulse is expanded into a 7.0 us pulse for the C-band high resolution mode, an 8.0 us pulse for the C-band low resolution mode, a 14.8 us pulse for the X-band high resolution mode, and a 30.0 us pulse for the X-band low resolution mode.

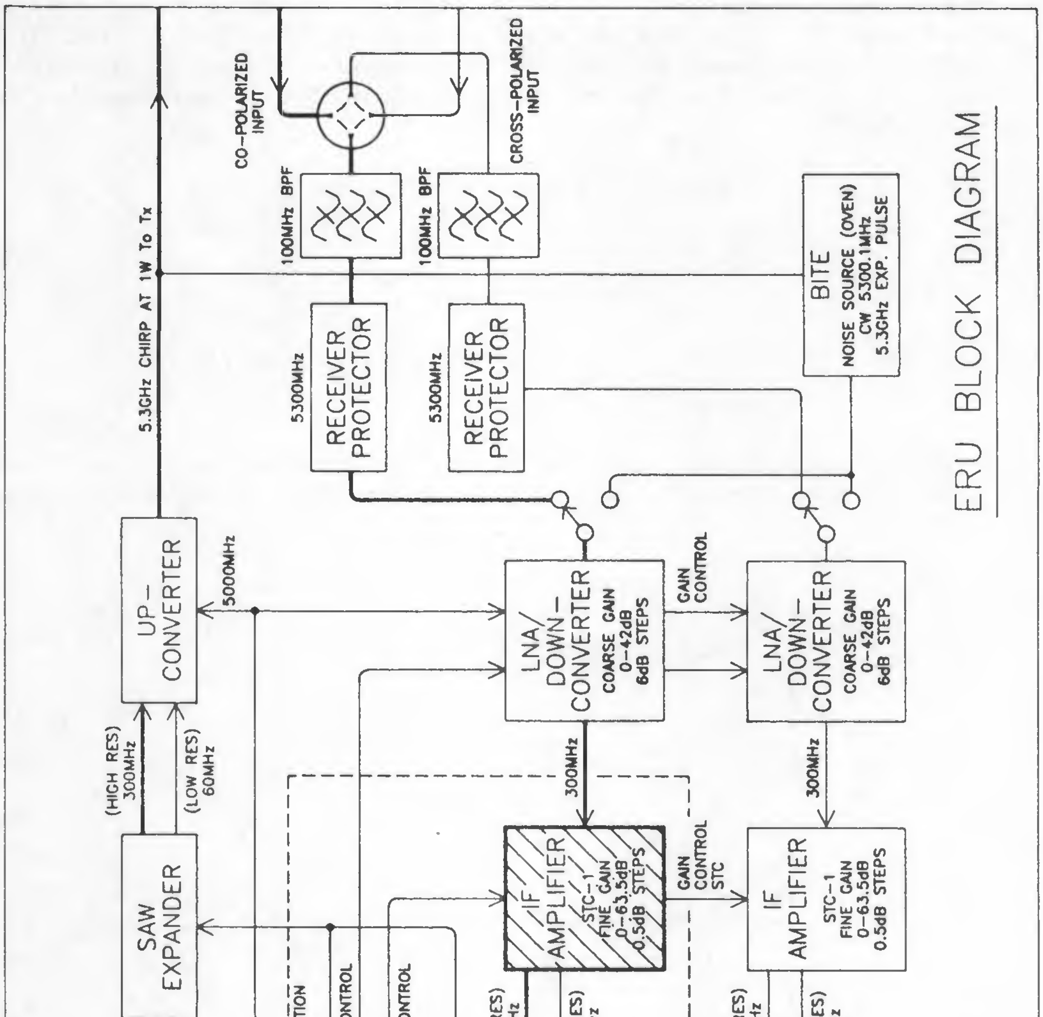

Figure 2: *Block Diagram of CCRS C-Band Exciter Receiver Unit*

First, the total attenuation is computed in decibels, and specified to 64 coarse intervals over the swath. These values are then adjusted by the specified threshold setting[5], and a linear interpolation is performed to compute the STC to a fine time interval of 1.0 μs samples. Now the STC is split into two components, one before (STC1) and one after (STC2) range compression. The magnitudes of the STC divisions are based on the total STC dynamic range, as shown in Eq. 2.

$$
\begin{array}{llll}
Att_{tot} < 52.5\ \mathrm{dB}, & STC1 & = & 2/3\ Att_{tot}\ (\mathrm{dB}) \\
, & STC2 & = & 1/3\ Att_{tot}\ (\mathrm{dB}) \\
52.5\ \mathrm{dB} \leq Att_{tot} < 70\ \mathrm{dB}, & STC1 & = & 35\ (\mathrm{max})\ (\mathrm{dB}) \\
, & STC2 & = & \mathrm{remainder}\ (\mathrm{dB})
\end{array}
\tag{2}
$$

The STC1 and STC2 components are then converted from decibel units to digital control units, and are rounded to 8-bit unsigned integers. STC1 is shifted forward in time, by the range compression SAW delay (to the nearest integer number of 1 μs sample periods).

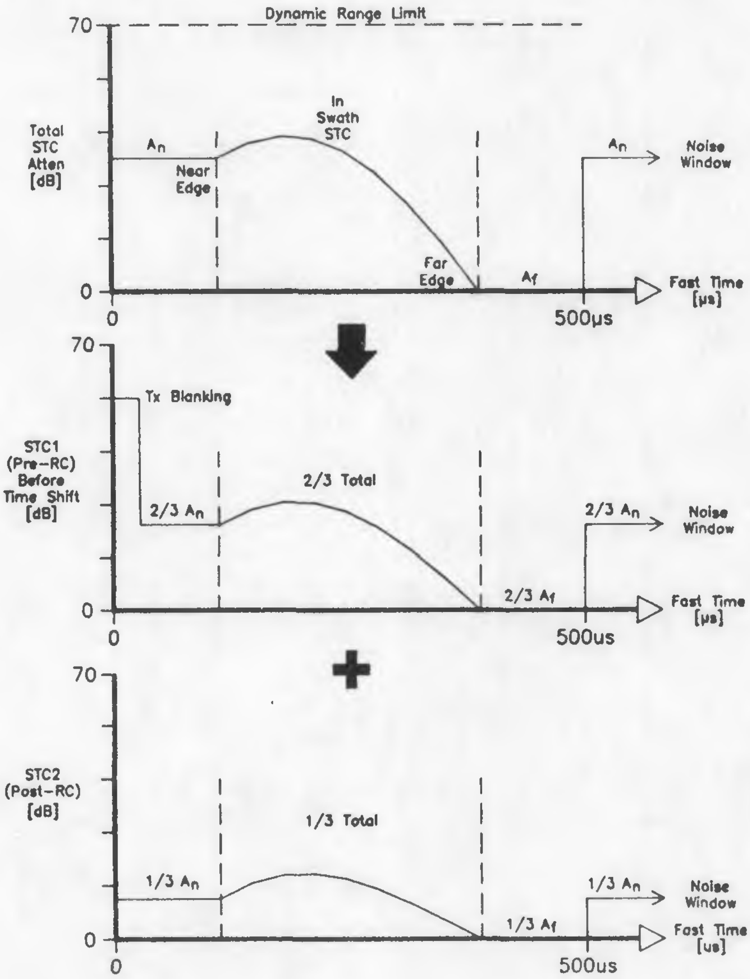

Figure 3: *Illustration of STC Computation*

[5] Threshold setting is a SAR configuration option, used to limit the received signal dynamic range.

3.3 STC Modelling Concerns

Shown in Figure 4 is a block diagram of the four modules within the ERU, which directly affect the STC function implementation.

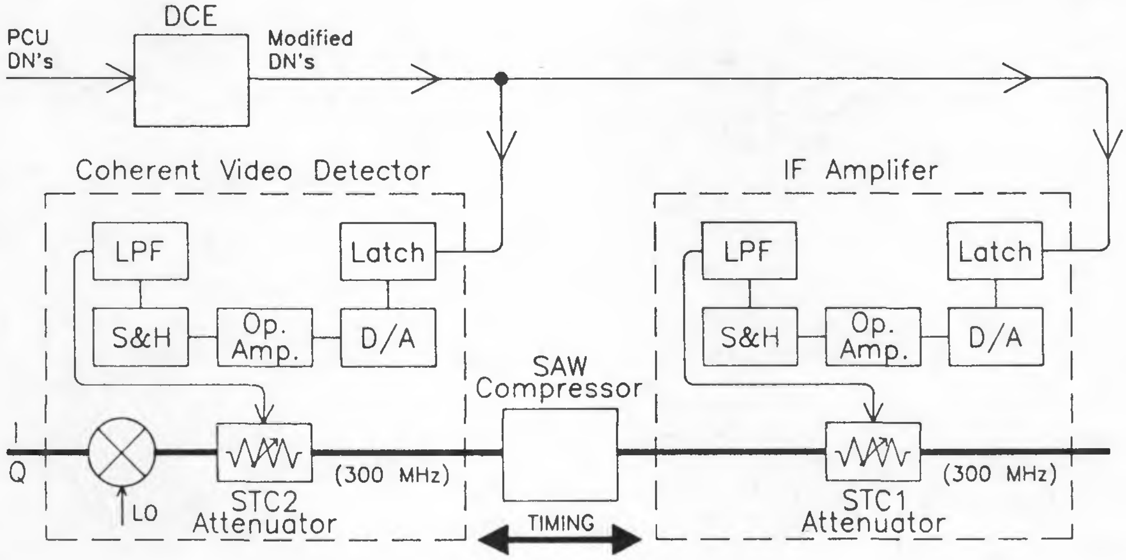

Figure 4: *STC Modules within ERU*

There are three key calibration issues here, which have the greatest impact on the STC modelling:

1) The STC attenuators are non-linear devices which have to be fully characterized (Ref. 5). In addition the conditioning of the drive signals to these attenuators must be considered. A STC Gain Control board is located within the DCE of the ERU. The input STC values to this board are digital numbers (DNs) computed in the PCU, and these DNs serve as the control signals (after a digital to analog conversion, a sample and hold stage, and a low pass filtering) to the voltage controlled STC attenuators. The STC attenuators[6] require a minimum operating voltage level, and in addition they suffer from nonlinearities in the output response. In some instances the attenuator nonlinearity is so great[7] (Ref. 6) that a LUT was applied to modify the attenuator digital drive signal accordingly. Furthermore, the control signal is altered by the effect of the LPF in the path after the D/A which drives the attenuator.

2) The STCs are applied before and after the range compression SAW device (STC1 is applied to an uncompressed pulse) and this distinction must be accounted for. The applications of STC1 and STC2 to the incoming data are separated by the SAW compressor. STC1 attenuation is applied as if the returned pulse were already compressed in time; this however is not the case. The true applied STC1 attenuation is thus a function of the computed attenuation, convolved with the uncompressed pulse replica weighting function.

3) There are absolute and relative timing considerations to be made in the applications of STC1 and STC2. Further to the compression issues of the STC separation are timing considerations. Due to the transmission delay inherent in the SAW compressor[8], STC1 must be shifted forward in time to add with STC2. Absolute timing then has to be considered for the actual application of the attenuations relative to the TMIT signal.

4. MODELLING STC

4.1 STC Attenuator Non-linearities

A series of LUTs were implemented in code, see Figure 5. A Mapping and Offset LUT was used to modify the original DNs, to account for the severity of the attenuator nonlinearities and for the initial flat knee response of the attenuator

[6] The attenuators are Daico P/N DA0098 devices.

[7] The attenuators failed to comply with the specified acceptance test procedures.

[8] The SAW compressor delays, in units of us, are 6.6 and 8.0 for C-band high and low resolution respectively, and 9.6 and 19.0 for X-band high and low resolution respectively.

with control voltage. Secondly a LPF smoothing transformation was used, in which the DNs were remapped to new values in order to account for the slewing aspects inherent in the attenuator drive signal path. The final LUT was the actual DAICO Attenuator LUT which is a steady-state mapping of applied digital drive signal to resultant attenuation, for all four C-band attenuators.

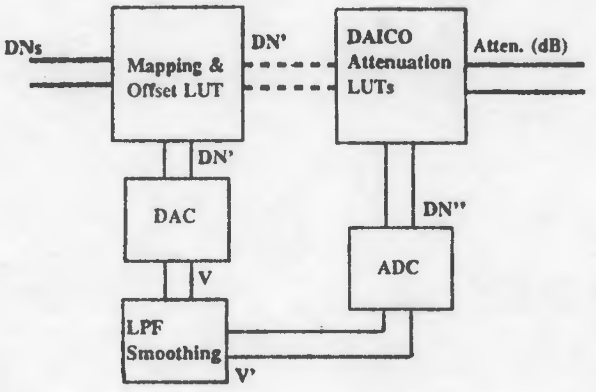

Figure 5: *Implementation of STC Attenuator Characterization*

4.2 STC1 Averaging over Uncompressed Pulse

Averaging STC1 over the uncompressed pulse was accomplished by convolving the calculated STC1 attenuation, G_{STC1}, with the pulse replica weighting function, $\Re_{pulse}$, see Eq. 3.

$$G'_{STC1} = G_{STC1} * \Re_{pulse} \tag{3}$$

4.3 Timing Considerations

The absolute and relative STC timing definitions are illustrated in Figure 6. Start times of STC1 and STC2 are specified in the code as system delays relative to TMIT. In addition, the measured SAW delays are used to quantify the forward time shift of STC1.

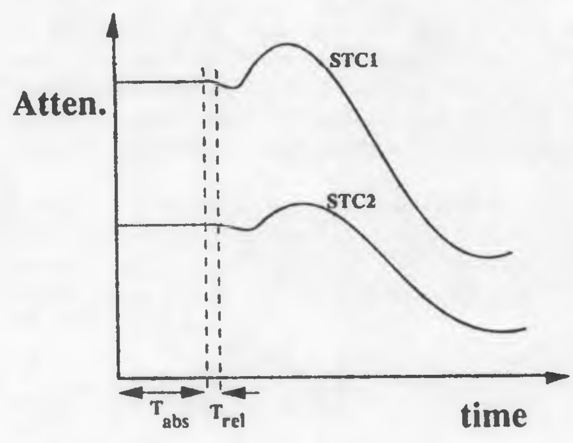

Figure 6: *Absolute and Relative Timing Considerations*

5. RESULTS

A BITE signal was injected into the receiver front end (for a configured near half swath, Nadir mode case), and used as a reference for analyzing the modelling impact of the various stages. The effect of the individual modelling components were analyzed separately[9], as is observed in the graphs of Figure 7.

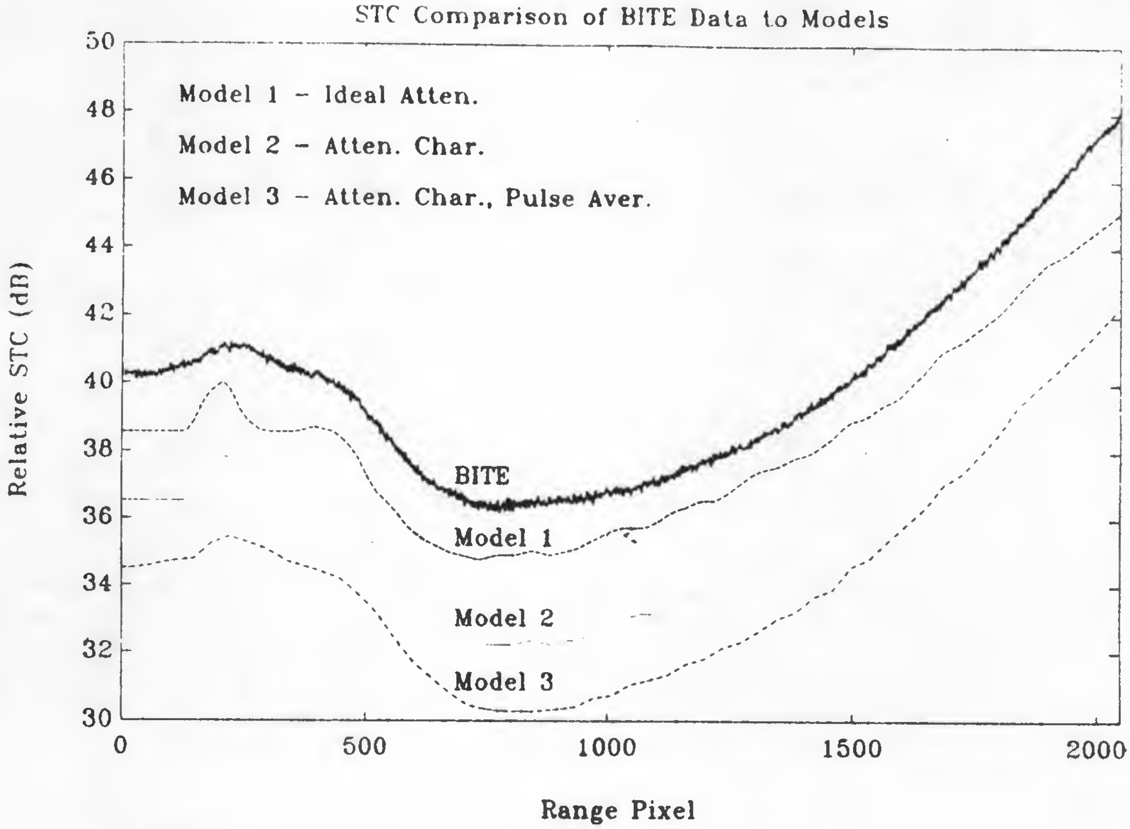

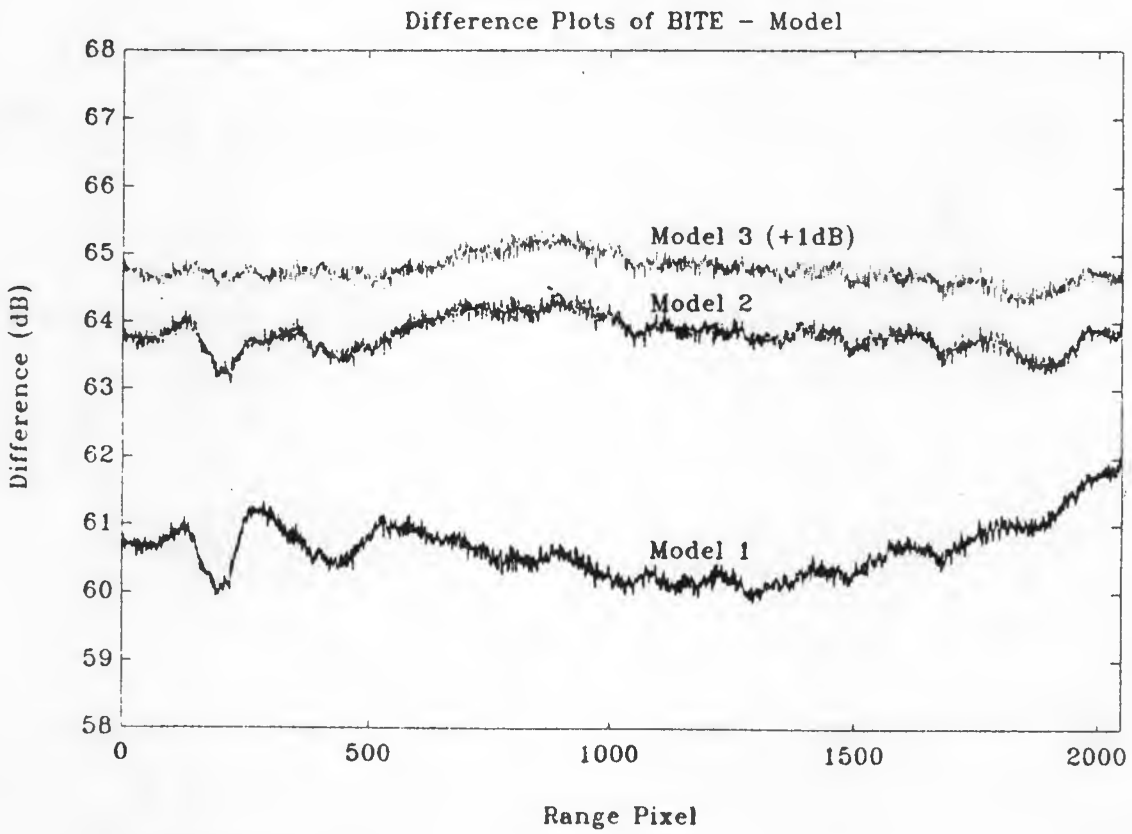

Figure 7: *STC Modelling Results*

The first plot shows the relative STC attenuation versus range pixel, of the BITE signal and of the three models. Model 1 represents the modelling of the STC attenuators as ideal devices (no non-linearities) and with no control signal slewing. As observed, model 1 shows significant response shape at the near range pixels, and nonlinear response variations throughout.[10] Model 2 represents the modelling of the STC attenuators with their measured nonlinear behaviour, and uses the actual control signal slewing. The improvement of the results from model 2, compared with those of model 1, are dramatic (not so much in terms of improved response shape, but in terms of more accurate signal levels). Model 3 represents the combination of true attenuator characterization, plus STC1 pulse averaging. The incremental improvement provided by this modelling over that of model 2, may best be observed as 'fine tuning'. The response shape is smoothed out to more accurately agree with the BITE response, but little change occurs in the overall STC signal level.

The second plot in Figure 7 illustrates these same results, but plotted as difference measurements versus range[11]. Important to note is the 3 dB amplitude shift between model 1 and model 3, and the degree of response flatness observed in model 3.

6. CONCLUSION

The physical implementation of the STC function in the CCRS C-band SAR is quite complex in nature, as has been observed; yet, the accurate modelling of the actual applied attenuation forms an essential part of the CCRS calibration procedure.

Modelling of the STC has been done, with focus being placed on three main issues: 1) STC attenuator characterization, 2) STC1 pulse averaging, and 3) absolute and relative timing considerations. The attenuator characterization had the greatest impact towards the improvement of the STC modelling, followed next by pulse averaging, and lastly by timing considerations. With these factors properly modelled, the STC may be simulated to better than 0.5 dB over the whole swath.

7. REFERENCES

1. Lukowski T I, & Daleman P S 1991, User's Guide for A/B SAR Radiometric Calibration: SAR_RAD_CAL, Tech. Memo No. DMD-TM-91-742, 54 p.

2. Hawkins R K, & Daleman P S 1991, Calibration Implementation for the CCRS Airborne SAR, 60 p.

3. Hawkins R K, Livingstone C E, Gray A L, Olsen R B, Halbertsma J G, & Deane R A 1987, CCRS C-Band Airborne Radar: System Description and Test Results, *Proceedings of the 11th Canadian Symposium on Remote Sensing*, pp. 503-515

4. Ulander Lars M H 1990, Theory of SAR Radiometric Calibration, Department of Radio and Space Science, Research Report No. 167, 42 p.

5. Knight T A 1990, CCRS Airborne SAR Software Modifications, Macdonald Dettwiler Report AB-RP-50-2721.

6. 1987, X-band Acceptance Test Procedures, Macdonald Dettwiler Associates 07-0196, pp. 4.14-4.27

---

[9] The effect of timing offsets on the modelled STC was found to be small in comparison with the other contributions, and thus such results are not shown.

[10] A small amplitude displacement has been imposed between all the models, for response shape comparison purposes; thus the actual disagreement of model 1 to the BITE response is larger than appears. Also, a large amplitude shift has been imposed on all of the models (the modelled STC actually levels to 0 dB at the far range pixel (4096)).

[11] Note that model 3 has been amplitude shifted by 1 dB, to separate it from the model 2 response.

An Estimation of JERS-1's SAR Antenna Elevation Pattern using Amazon Rain Forest Images

Masanobu Shimada
Earth Observation Center / NAtional Space Development Agency of Japan
1401 Numanoue Ohashi Hatoyama Hiki Saitama, Japan, 350-03

ABSTRACT

It is well known that the radar backscattering characteristics of the rain forest show very small dependencies on the incidence angle for wide range of the radar frequencies through several experiments /1,2,3/. Based on these facts, an estimation of the SAR elevation antenna pattern for the JERS-1 satellite was conducted through two steps, (1) the statistical screening of the rain forest SAR data to obtain the same characterized uniform images, and (2) the application of the correlated SAR image model including the noise bias, which should be considered for more correct estimation of the antenna beam width, to the screened SAR images by means of the least square method. Finally, one way antenna elevation pattern was obtained as 5.44 deg in terms of 3 dB down beam width, with the accuracy of 0.17 degree. It was also estimated that the beam width does not change between before and after launch significantly, but, SAR off nadir angle is 34.91 degree, which is 0.3 degree smaller than the original SAR antenna deployment.

Introduction

The main advantage of JERS-1 synthetic aperture radar, JSAR, is to enable the observation of Earth surface almost directly by L band frequency with some specific recurrence cycle and regardless the weather and day/night conditions. In the movement of the recent global monitoring, the normalized radar cross section, NRCS, was assessed as a parameter for expressing Earth surface characteristics, and also necessary to be absolutely calibrated for the qualified SAR product. NRCS may be obtained in straightforward by an arrangement of the processed image intensity with a radar-processor response function, which includes the antenna elevation pattern, or shortly AEP. The accuracy of AEP may affect the SAR product quality. This is because JSAR antenna is deployed in space to the large scale structure in 11.9 meter length and 2.2 meter width, then, becomes difficult to grasp the AEP before the launch of the satellite. The possible deformation of JSAR antenna due to the vibration in launching phase and in deployment process, may cause the change of the antenna pattern, therefore, the AEP measurement is absolutely necessary in after the launch of the satellite.

Several approaches in determination of AEP were taken for the past spaceborne SARs. As examples, approach-(1) to use the distributed target data such as the tropical rain forest data in Amazon or boreal forests, approach-(2) to use the known signal references such as corner reflectors and active radar calibrators. Moore et al. analyzed the SIR-B's AEP using Amazon data and Illinois data /4, 5/. Laur calculated AEP for ERS-1 using Amazon data also /6/. Hawkins succeeded to obtain the airborne SAR's AEP using the Canadian forest images /7/. Dobson's result is an example of latter approach /8/. However, the latter's standard deviation is slightly bigger than the former.

These researches foresee that the distributed targets in approach-(1) may offer the better results than the approach-(2). This is because the number of the back scatterers in former is much bigger than the latter, and may contribute to minimize the statistical error. It is also easy to deal with the tropical rain forest data because its scattering coefficient, γ, defined as the NRCS/cos(incidence angle) may not change within the SAR imaging swath.

In this study, a correlation power model for JSAR was constructed considering the characteristics of JSAR and SAR processor, and applied to the 17 Amazon JSAR images to estimate AEP by means of the statistical way. The assumption given is that the scattering coefficient, γ, is constant within the imaging swath, which corresponds to 6 degree change in incidence angle. The features of this study is twofold, (1) to screen the similar scatterers which belongs to the same distribution function using the texture analysis, then (2) to express the JSAR correlation power model as the function of AEP and noises of receiver and AD converter.

2. SAR received signal model and antenna pattern estimation

2.1 Received signal power

Received signals from the JSAR imaging swath of 75 Km are injected into the AGC, Automatic Gain Control, where the signal power level is controlled to around 0 dBm whatever the target intensity is, then injected into the STC, Sensitivity Time Control, where the signal power level is controlled to almost constant by canceling the AEP. The output level of the AD converter is expressed as follows:

$$P_{ADC}(R) = \{P_r(R) \times G_{LNA} + P_{n,REC}\} \times G_{AGC} \times G_{STC}(R) + P_{n,ADC} \qquad (1)$$

$$P_r(R) = \frac{P_t \times G_0^2 \times G_{ele}(R)^2 \times \lambda^2}{(4\pi)^3 R^3} \gamma \cdot \cos\theta_{inci} \frac{C \times \tau}{2\sin\theta_{inci}} \beta \qquad (2)$$

where, $P_{ADC}(R)$:Averaged power of the AD converter's output, R: Slant Range, $P_r(R)$: Received power at the Low Noise Amplifier, LNA, input port, G_{LNA} : Gain of the LNA, $P_{n,REC}$: Noise power generated by LNA and receiver, $G_{STC}(R)$: Sensitivity Time Control, G_{AGC} : Gain of AGC, $P_{n,ADC}$: Noise by AD converter, which includes saturation and bit redundancy noises, G_0 : Antenna one-way peak gain, P_t, Transmission power, $G_{ele}(R)$: Antenna relative elevation pattern or AEP, λ : wave length (23 cm), γ :

back scattering coefficient, which is defined by $\sigma^0/\cos\theta_{inci}$, θ_{inci} : Incidence angle, C : Light speed (300,000 Km/sec), β : azimuth antenna half width (0.98 degree), σ^0 : normalized radar cross section.

2.2 Correlation signal power

We consider the correlation processing of the SAR signal received from the rain forest region like Amazon. Supposing that both of the JSAR received signal components, one is from amazon rain forest and the other is noise generated inside receiver, distribute in Gaussian, same correlation gain is applied to both of the signals. Level change in STC's 1 dB step is averaged over the correlation length in the range correlation processing. NASDA SAR processor determines the azimuth correlation length proportional to the slant range for keeping the azimuth resolution same over the whole image. Then, the correlation power is expressed by the followings /12/ :

$$P_{corr}(R) = G_{proc}(R) \times \sum_{i=1}^{N_{rg}} \frac{P_{ADC}(R_i)}{N_{rg}} \tag{3}$$

$$G_{proc}(R) = \tau \times f_{sample} \times \frac{0.4 \times PRF^2 \times \lambda}{V_g^{\,2}} \times R \tag{4}$$

where, $G_{proc}(R)$: SAR processor gain, N_{rg} : correlation length in range, f_{sample} : sampling frequency (17.076 MHz), PRF : pulse repetition frequency, V_g : satellite's relative ground speed, τ : pulse width(35 μsec).

Rearranging, (1) through (4), correlation power is expressed by the followings :

$$P_{corr}(R) = A \cdot \frac{G_{ele}(R)^2 \cdot \cot\theta_{inci}}{R^2} \cdot \overline{G_{STC}(R)} + R \cdot B(R) \tag{5}$$

$$A = \frac{P_t \cdot G_0^{\,2} \cdot \lambda^2 \cdot \gamma \cdot C \cdot \tau \cdot \beta \cdot G_{LNA}}{2 \cdot (4\pi)^3} \cdot \frac{G_{proc}(R)}{R} \cdot G_{AGC} \tag{6}$$

$$B(R) = \frac{G_{proc}(R)}{R} \cdot (P_{n,REC} \cdot G_{AGC} \cdot \overline{G_{STC}(R)} + P_{n,ADC}) \tag{7}$$

Because γ is assumed constant and $\overline{G_{STC}(R)}$ cancels $G_{ele}(R)^2$, first term of the right side of (5) behaves proportional to R^{-2}, where $\overline{G_{STC}(R)}$ is defined as the moving average of $G_{STC}(R)$ with pulse duration. $B(R)$ in (5) which contains LNA and AD conversion noise may behaves in complex way over an observation window of 360 μsec. Then, the order estimate of these terms was made using the Amazon data.

Fig 2 shows two raw data power patterns, where the upper curve (Curve_1) is the typical Amazon data acquired for GRS 395-306 on May 17 '92, and the lower curve (Curve_2) is the ocean data acquired for GRS 49-230 on May 21 '92 which is also dominated by the receiver and AD noise. Automatic Gain Control (AGC) of JSAR sets the receiver gain appropriate in 1 dB unit so that the amplified signal can be AD converted with the best sensitivity. AGC level changes in response to the target brightness and its value is down linked to the ground in the satellite telemetry. In Fig. 2, AGC values for Amazon and ocean are 4 dB and 0 dB respectively, where AGC value is the attenuation value applied to the maximum receiver gain, and this also means that the more AGC value is set, the brighter the target is. If ocean is observed by 4 dB AGC, Curve_2 should go down 4 dB in total. Based on the error analysis /13, 14/, averaged AD conversion error is 0.45 dB when input power exists between 5 and 10 dB. This error is fairly bigger than the modified Curve_2 which went 4 dB down. Finally, *B(R)* can be constant over the imaging swath.

2.3 Estimation of AEP using MLE, Maximum Likelihood Estimation

We assume that the same γ area is extracted from the SAR correlated power image as shown in Fig 3 - (2), where more detailed description is given later and white strip parts correspond to the extracted areas. Each extracted strip parts are calculated for the averaged correlated power, incidence angle, slant rage, etc. Expressing averaged correlated power over i^{th} strip by $\overline{P_i}$, and its power model by $P_m(R_i / \boldsymbol{a})$, then, AEP is given by minimizing the χ^2 defined below. In this case, $\boldsymbol{a}$ stands for the parameters defining the AEP. This model was assumed 4 th order power expression referring the SIR-B data analysis /9/.

$$\chi^2(\mathbf{a}) = \sum_{i=1}^{N} \frac{\{\overline{P_i} - P_m(R_i \mid \mathbf{a})\}^2}{\sigma_i^2} \Rightarrow \min imum \tag{8}$$

$$10\log_{10} G_{ele}(\phi) = a(\phi - \phi_0)^2 + b + c(\phi - \phi_0)^4 \tag{9}$$

where, $\boldsymbol{a}$ includes off nadir angle, ϕ_0, and the other coefficients a, b, and c. σ_i is the standard deviation of $\overline{P_i}$.

In the analysis, level 1.1 three look power images are incorporated. The slant range of each strip, R_i, can be determined by using the header information in image record. Then, the off nadir angle, ϕ_i, is also calculated by using the satellite position (x, y, and z) and geodetic latitude of at the center of the image, φ, both of which are stored in CCT header (see Fig. 4).

$$\phi_i = \cos^{-1}\{\frac{R_i^2 + (x^2 + y^2 + z^2) - R_{et}^2}{2 \cdot R_i \cdot \sqrt{x^2 + y^2 + z^2}}\} \tag{10}$$

$$R_{et} = R_e \cdot (1 - f \sin^2 \varphi) \tag{11}$$

where, R_{et}, R_e, and f are Earth radius at the center of the SAR image, equatorial Earth radius, and flattening, respectively. Finally, $\boldsymbol{a}$ is determined by the following equation.

$$\frac{\partial}{\partial a_k}\chi_m^2(\mathbf{a}) = 2\sum_{i=1}^{N}\frac{\{\overline{P_i} - P_{m,i}(\mathbf{a})\}}{\sigma_i^2}\frac{\partial}{\partial a_k}P_{m,i}(\mathbf{a}) = \mathbf{0} \quad k = 1,2,\ldots,L \tag{12}$$

where, L is the maximum number of the unknowns. To solve above nonlinear equation, Levenberg-Marquardt method was adopted because of non necessity for the preparation of the second order derivatives.

2.4 Determination of B in the power model.

While the parameter B can be estimated as the solution of equation (12), its accuracy is not the satisfactory /9/. Then, B should be determined separately before the estimation of $\boldsymbol{a}$. In the consideration of the integration of power model (5) over S^{th} strip to E^{th} strip, which is expressed by P_{total}, following three equivalent expressions are obtained (see Fig. 3-(2)).

$$P_{total} = \sum_{i=S}^{E}\int_{R_{near,i}}^{R_{far,i}}\{A\cdot\frac{G_{ele}{}^2(\phi_i|\mathbf{a})\cot\theta_i}{R^2}\cdot\overline{G_{STC}(R)} + BR\}dR \tag{13}$$

$$= P_{\text{int}}(\mathbf{a}) + \sum_{i=S}^{E}\frac{B}{2}(R_{far,i}^2 - R_{neqr,i}^2) \tag{13-1}$$

$$= P_{\text{int}}(\mathbf{a})\,(1 + SNR^{-1}) \tag{13-2}$$

$$= \sum_{i=S}^{E}\overline{P_i}\cdot\Delta R \tag{13-3}$$

where, $P_{int}(\boldsymbol{a})$ corresponds to the first term in the right side of the equation (13). Introducing the SNR of the raw data at this integration area, (13-1) becomes (13-2), and then it becomes (13-3) for the screened data.
where, $\overline{P_i}$; averaged correlation power over screened area in i^{th} strip, ΔR ; range pixel spacing (8.78 m), $R_{near,i}$, $R_{far,i}$; slant ranges at the near and far edges of i^{th} strip, SNR ; Signal To Noise Ratio of the integration area, which can be obtained by the frequency analysis of the raw data.

Finally, unknown constant B is obtained below;

$$B = \frac{2\cdot\sum_{i=S}^{E}\overline{P_i}\cdot\Delta R}{(SNR+1)\cdot\sum_{i=S}^{E}(R_{far,i}^2 - R_{near,i}^2)} \tag{14}$$

Table 1 shows B values for all the examined Amazon scenes.

3. Error criteria

3.1 Error criteria for the averaged correlation power

Error criteria for the averaged correlation power to be applied to the AEP estimation and its derivation method are discussed in this section. Regarding the AEP error, $\Delta Gele$, which is defined by the difference of the estimated AEP, $\overline{G_{ele}(\phi)}$ in dB and the measured AEP, $G_{ele}(\phi)$ in dB, its error criteria is settled below referring the SIR-C and SIR-B /15/;

$$|\Delta G_{ele}| \leq 0.3dB\ (3\ sigma) \tag{15}$$

After differentiating (5) expressed in dB, the root sum square of all the right side error sources is calculated, where $B \cdot R$ is not considered because they are negligibly smaller than the first term.

$$\Delta P_{corr} = \sqrt{(\Delta A)^2 + 4(\Delta G_{ele})^2 + 4(\Delta R)^2 + (\Delta \cot \theta_{\mathrm{int}})^2 + (\Delta \overline{G_{STC}(R)})^2} \tag{16}$$

In this analysis, $\Delta\overline{G_{STC}(R)}$, ΔR, $\Delta cot\theta_{inci}$ are much smaller than ΔA and ΔG_{ele}, then, neglected. While γ in A is changeable, however, L band SAR data over Amazon shows γ constant in several experiments of AIRSAR /9/ and JSAR imaging swath has only 6 degree change in incidence angle. Then, the above equation is simplified and error criteria for the ΔP_{corr} is determined as follows;

$$\Delta P_{corr} = 2\Delta G_{ele} \leq 0.2dB(1\ sigma) \tag{17}$$

3.2 Number of the data for averaging

It is considered on how many data should be averaged to obtain the P_{corr} satisfying the condition (17). It is ideal that all the data are independent each other in averaging. Even Amazon data, however, this condition is not realized as its autocorrelation coefficients are shown in Fig. 5 (non zero values around at the several pixels away from the origin depend partially on the characteristics of the SAR processor). We consider that the averaging is done over N samples, each of which is subsampled from the original data characterized by the standard deviation of σ, with D pixels in azimuth and range direction. This offers the standard deviation σ_z for averaged data.

$$\sigma_Z = \sqrt{\frac{1+2\rho_1+2\rho_2}{N}}\sigma \tag{18}$$

where, ρ_1 and ρ_2 are the auto correlation coefficients at pixel distances D and $2D$ respectively. Obtaining the standard deviation of correlated power in dB ($\sigma_{p,dB}$), then, inserting it to (18) instead of σ and comparing with (17), the number of the data, N, satisfying the condition (17) is obtained as follows;

$$N \geq (1+2\rho_1+2\rho_2)\left(\frac{\sigma_{p,dB}}{0.2}\right)^2 \tag{19}$$

Table 1 also shows the $\sigma_{p,dB}$, ρ_1, ρ_2 and N_{min}(minimum number of N). Generally, N_{min} is taken by 460 for Amazon data.

4. Screening processing for the distributed target

4.1 Screening processing.

Most of the Amazon images dealt in this data analysis seemed uniform and to satisfy the above mentioned conditions qualitatively. But, careful watching offers, even minor, not only several dark areas by forest cutting and rivers, but also bright areas by mountain ridges (see one example for Amazon 395-308 acquired on May 17 '92 in Fig. 8-1).

Extraction of the uniform areas or same γ areas from the full image increases the creditability of the calculation results. For this purpose, a similarity test as a part of the screening processing is very helpful. As shown in Fig. 6, one image is meshed into many small rectangular cells, each of which has a dimension of N_{az} and N_{rg} in azimuth and range direction respectively. Each cell is identified by $\mathrm{Cell}^{i,j}$, where i corresponds to the strip address in range direction and j does in azimuth direction. The continuous function of AEP in slant range R is canceled by STC function roughly, however, 1 dB step changes in STC makes the correlation power model in step wise. Then, N_{rg} should be selected in such a way that correlation power is non correlated with the AEP. Finally, several non similar cells will be taken away from each strip by using the χ^2 similarity test.

4.2 Similarity check of the two cells using χ^2 test

Similarity test based on χ^2 test decides "whether or not two distributions are different" /16, 17/. Let $C_l^{i,j}$ and C_l^i be assumed the histogram of $\mathrm{Cell}^{i,j}$ and its averaged histogram(C_l^i = $\overline{C_l^{i,j}}$), respectively. If χ^2 defined below is smaller than or equal to a criteria parameter X_α, it is decided that two distributions are not different with confidence of α %.

$$\chi^2 = \sum_{l=1}^{N} \frac{\left(C_l^{i,j} - \mathrm{C}_l^i\right)^2}{C_l^{i,j} + \mathrm{C}_l^i} \tag{20}$$

$$Q(\chi^2 \le X_\alpha | r) = \int_0^{X_\alpha} \frac{1}{\Gamma(\frac{r}{2})2^{r/2}} w^{\frac{r}{2}-1} e^{-\frac{w}{2}} dw \tag{21}$$

where, $\Gamma()$, r are gamma function and degree of freedom, respectively. X_α is the upper limit for the integration when Q in (21) is set to α. In the following data analysis, 99% is settled to α based on /9/.

4.3 Determination of N_{rg}

Defining the $H(X_k/i)$ and $H(X_k/i+L)$ as the histograms of the data on i^{th} and $i+L^{\mathrm{th}}$ azimuth lines, respectively. Then, χ^2 is calculated for these histograms. If similarity is confirmed, 0 is given to the intermediate parameter I_d. 1 is given to I_d for the non similarity confirmed. An averaged intermediate parameter$\overline{I_d}$ over range direction is defined as $I_D(L)$ and the sample results for Amazon three scenes are shown in Fig. 7. In result;

(1) Setting the criteria of $I_D(L)$ as 5% under which no data correlation is supposed, azimuth lines difference L is adequate between 20 and 50. Then, 20 is given to N_{rg}. This is also similar to the previous result /9/.

4.4 Determinations of N_{az} and I_a

N_{az} and whole image size in azimuth I_a are determined under the following conditions;

(1) Number of the data which are incorporated in the averaged correlation power is bigger than N_{min}.

(2) Only when number of the cells identified similar dominate over the non similar ones, the strip is considered to offer the averaged correlation power.

(3) Number of the data which are subsampled from each cell is big enough for keeping the calculation accuracy. However, it is difficult to be determined. Then, 55 was set in this calculation.

Finally, conditions (1) and (2) determines I_a and (3) determines N_{az} as follows;

$$I_a \ge \frac{2N_{\min}D^2}{N_{rg}} \qquad N_{az} \ge \frac{55D^2}{N_{rg}} \tag{22}$$

The results are also shown in Table 1. Most of Amazon data take 1200 for I_a. This is much smaller than the azimuth pixel number of level 1.1 product, 8448.

4.5 Method of the screening

Each strip contains M_{az} ($=I_a/N_{az}$) cells. Among of them, the extraction of similar cells is conducted by the following procedure (see Fig. 6).

(1) To calculate the histogram of each cell, $C_l^{i,j}$), and its average, $\boldsymbol{C}_l^i$.

(2) To calculate the χ^2 for each cell using $\boldsymbol{C}_l^i$.

(3) If χ^2 of the cell is smaller than X_α, the cell is identified as similar to the general of the all the strip areas with the confidence of 99 %.

(4) If the strip of the interest contains complex areas, such as forest and dark intensity objects, river or deforested or cut area, $\boldsymbol{C}_l^i$ may be different from the finally selected cells' histogram. For this difficulty, the number of the similar cells should dominate over non similar cells. The cells satisfying these conditions will be considered for the calculation of averaged correlated power, incidence angle, slant range, etc. for the further calculation.

As an example, the screened result for the Amazon 395-308 is given in Fig. 8-2. Comparing the above with the original image in Fig. 8-1, it is confirmed that the non similar area, which corresponds to black square, is coincident with the vein like pattern at the left top of Fig 8-1. This screening processing seems effective for obtaining the similar characteristic area.

5. Estimation of AEP.

5.1 Procedure of the AEP estimation

Procedure of the AEP estimation is summarized in Fig. 3.

(1) To select the scenes from the Amazon tropical rain forest area.

(2) To conduct the screening processing for the selected images, and obtain the averaged correlation power, incidence angle, slant ranges, etc.

(3) To estimate the AEP by the MLE for screened data and correlation power model including the noise reduction.

5.2 Images selected for the AEP estimation

While JSAR is in activation since April 13 '92, it succeeded to observe the Amazon forest areas, especially on both of April 23 '92 and May 17 '92. Each activation was lasted over eight minutes and gathered 40 contiguous scenes. Following condition was applied to pick the appropriate scenes out of these scenes.

(1) AGC should be constant over a whole scene

In AGC, data which is received during 7 μsec from 22 μsec after the origin of the whole observation window is taken into account to set up the suitable AGC gain for the next 64 pulses /10. 11/. If AGC is changed, the power change may occur at some address in azimuth. But, saturation error of AD converter makes it difficult to correct the power change due to the AGC change. Then, the condition that AGC should be constant over a whole image was settled.

(2) STC start time should not change in a scene.

STC start time is controlled to make the SAR observation window cover the SAR illumination area centered at the antenna boresite direction in order to acquire the signal as in good condition as possible. This is motivated by the fact that Earth is not sphere. STC start time changes in 10 μsec step wise, which corresponds to 1.5 Km in slant range. For the calculation simplicity, the condition that STC start time should not change is also placed.

Among of 80 Amazon scenes, 17 are picked under the above two conditions and inputted to the calculation. The calculation results is shown in Table 2.

5.3 AEP estimation results and discussions

5.3.1 Determination of the best AEP model and its comparison with on ground AEP

The average of all the AEP coefficients over 17 scenes is conducted and gives best AEP. These parameters are also shown below;

a = -0.39971, SD = 0.0372

c = - 0.00133, SD = 0.0072

ϕ_0 = 34.91, SD = 0.160 degree

The reason why the coefficient b in (9) is not written above is such that b is actually obtained in the estimation process, but, it depends on γ of each scene. AEP estimation is originated for the relative calibration. Determination of b is connected to the absolute calibration which will be achieved by the corner reflector or the active radar calibrator deployed on ground.

Fig. 9-1 and 9-2 show the coincidences of the best fitted correlation power model and screened correlation powers for two representative scenes, such as 395-309 and 415-313. In these Figs, white circle shows the screened data represented also by **mea**, black circle shows the best fitted correlation power model, represented also by **mod**. In Fig, 9-1, there is some area missing white circles, which correspond the truth that screening processing failed. Figures also show the successful estimation of AEP.

Comparison of the best AEP and ground measured AEP is given in Fig. 10. The ground measurement is made by the combination of the actual measurement for one antenna sub paddle, whose dimension is 2.2 x 1.5 m, and the antenna array theory. As a result, antenna elevation pattern is almost similar between before and after the launch of the satellite.

The 3 dB one way beam width of AEP was calculated 5.44 degree with the standard deviation of 0.17 degree, which is almost equal to the value of before launch, 5.4 degree. This result was obtained considering the *SNR* of raw data. However, the calculation without the noise consideration gave almost same value, where half width and off nadir angle are 5.51 degree and 35.021 degree, respectively. The fact that the half widths for all the sample images are distributed equally around the average shows the consistency of the calculation.

The averaged residual which is defined as the averaged difference between best fitted correlation power model in dB and averaged correlation power in dB has taken 0.104 dB as shown in Fig. 11. The maximum and minimum are 0.184 dB and 0.061 dB, respectively. This residual generally satisfies the condition (17), but, far from 0.01 dB obtained in SIR-B data analysis /9/. This is explained as follows; STC in JSAR changes in stepwise of 1 dB between 0 dB and 5 dB. One dB step in receiver is lost some certain level in AD converter because of its saturation and bit redundancy error. This missed power is not perfectly corrected in the SAR processor as the screened image shows several stripes along azimuth /13, 14/.

5.3.2 Repeatability

Repeatability error (E) defined below is to know the stability of the estimated AEP over all the images.

$$E = \sqrt{\Delta G_{ref}^2 + \Delta G_{target}^2 + \left(\overline{G_{ref}} - \overline{G_{target}}\right)^2} \quad [dB] \tag{23}$$

where, ΔG_{ref}: standard deviation of the referenced AEP, 0.104 dB, ΔG_{target}: standard deviation of AEP obtained for each target image, $\overline{G_{ref}}$: gain of reference, -3dB, $\overline{G_{target}}$: gain of AEP in target where the half width of reference AEP is measured.

The repeatability of all the target images is shown in Table 2. Except scene 11, rest of the data are confirmed within 0.2 dB. The value of 0.2 dB is also reasonable value considering that reference gain error has contained already 0.1 dB. Scene 11 shows a small standard deviation, however, different AEP derives the perturbed error.

5.3.3 Stability of the off nadir angle

It is confirmed that the antenna off nadir angles distribute between 34.7 degree and 35.2 degree around the 35.0 degree. The averaged value is 34.91 degree with the standard deviation of 0.17 degree. This means that the antenna was deployed in smaller off nadir angle than designed, also illuminates about 4 km closer region to nadir. Originally, it was expected that SAR antenna was deployed at 35.2 degree, however, the confirmation telemetry data was not obtained yet from the satellite. After the deployment of SAR antenna, several estimations for the antenna off nadir angle were conducted by using the satellite dynamic analysis. This study also qualitatively meets the previous results.

Comparing the results with path 395, whose Scene_IDs correspond to 1 to 10, and the ones with path 415, whose Scene_IDs correspond to 11 to 17, it seems that (1) these results are grouped, (2) more south the scene goes, the bigger the error does as shown in Fig. 12. Regarding the former result, there is some relationship with SAR transmission characteristics. While the SAR has three transmitters, two of which were supposed to activate in normal transmission mode, however, one of three is used in the normal operation in order to keep the arcing off and recover the resultant image degradation when two transmitters were turned on. Path 415 and 395 correspond to one and two transmitters' operation respectively. The arcing may affect the boresite direction of JSAR antenna. Then, the former phenomena may be related to this fact. For the latter, more detailed data analysis is expected in future.

6. Summary

Elevation antenna pattern of JSAR installed on JERS-1 was estimated by the image data analysis for the Amazon tropical rain forest SAR data whose back scattering coefficient is expected constant over the small off nadir angle. First, screening processing was applied to the correlated power image over these area to remove the non similar area from the total image, which are slightly dark area, such as river and deforested area, and brighter area such as mountain ridges. Second, correlated power model as the function of antenna elevation, receiver and AD converter noises, etc. was developed and applied to obtain the antenna pattern in the maximum likelihood estimation method. As a result, 3 dB down one way beam width was estimated as 5.44 degree as almost same as the before launch data of 5.4 degree. The off nadir angle was estimated as the 34.91 degree which is 0.3 degree smaller than the designed value.

Acknowledgment

This research was conducted as a part of the joint project between NAtional Space Development Agency of Japan and Ministry of International Trade and Industry. Author would like to express his great thanks to RESTEC, Remote sensing technology center, and NEC, Nihon Electric Corporation for their data processing in the large amount of Amazon data.

References

/1/ Emedio M. Bracalente, Langrey Research Center Jon L. Sweet Kentron International Inc./NASA-TM-85779 1984" Analysis of normalized RADAR cross section(sigma 0) signature of Amazon rain forest using SEASAT scatterometer data"

/2/ M.AUTRET, et al, "Theoretical Study of the sensitivity of the microwave backscattering coefficient to the soil surface parameters", INT., J. Remote Sensing, 1989, VOL. 10, NO. 1, 171-179.
/3/ R.Bernard, D. Vidal-Madjar, "C-Band Radar Cross Section of the Guyana Rain Forest : Possible Use as a Reference Target for Spaceborne Radars", Remote SENS. ENVIRON. 27:25-36(1989)
/4/ Richard K. Moore and Mehrzad Hemmat, 1988, "Determination of the vertical pattern of the SIR-B antenna", INT.J.REMOTE SENSING, VOL. 9, NO. 5, 839-847
/5/ Moore R. K, Frost V. S, Westmore Land H., Frank D. and Hemmat M, "Determining the vertical antenna pattern of a spaceborne SAR by observation of uniform targets", proceedings IGARSS'86, Zurich, Switzerland, Vol. 1, pp. 469-472,1986
/6/ Henri LAUR, "Derivation of Backscattering Coefficient s0 in ERS-1.SAR.PRI Products", Issue 1, Rev. 0, 17 Oct. 1992, ESA documents
/7/ R.K.Hawkins, 1988, CCRS, "Determination of Antenna Elevation Pattern for Airborne SAR using the rough target approach", IEEE TRANSACTIONS ON GEOSCIENCE AND REMOTE SENSING, Sept. 1990, pp. 896-905.
/8/ Myron C Dobson, et al., "External Calibration of SIR-B Imagery with Area extended and point targets", July, 1986. IEEE TRANSACTIONS ON GEOSCIENCE AND REMOTE SENSING, VOL. GE-24, NO. 4. pp. 453-461
/9/ Masanobu Shimada, Anthony Freeman, "A technique for measurement of spaceborne SAR antenna patterns using distributed targets", to be published to IEEE TRANSACTIONS ON GEOSCIENCE AND REMOTE SENSING
/10/ Y. Nemoto, Japanese Earth Resources Satellite-1 Synthetic aperture Radar, June 1991, pp. 800 - 809, Proceedings of the IEEE. Vol. 79 no. 6
/11/ Chu Ishida, et al, "JERS-1 DEVELOPMENT STATUS", 40th CONGRESS OF THE INTERNATIONAL ASTRONAUTICAL FEDERATION, 1989, Beijing, China
/12/ A.Freeman and J C Curlander, 1990, "Radiometric Correction and Calibration of SAR images", Photogrammetric Engineering and Remote Sensing, Vol. 55, No. 9, pp. 1295-1301,1989.
/13/ Masanobu Shimada, "First result of the SAR characterization(in Japanese)" Technical Report of IECE SANE92-58(1992-11)
/14/ M.Shimada, et al., "Inflight Evaluation of L band SAR of Japanese Earth Resources Satellite-1", COSPAR, 1992
/15/ J.D.Klein "Spaceborne Imaging RADAR-C/SIR-C Engineering Calibration Plan", Feb. 1990, JPL Report JPL-D-6998
/16/ Numerical Recipes in C, The art of scientific Computing. Press, Flannery, Teukolsky, Vettring, Cambridge University Press
/17/ Robert V Hogg, Allen T Craig "Introduction to Mathematical Statistics", Macmillan, 1978

Table 1 A summary of the images evaluated

Scene_ID	Path	Row	Acq.Date	SNR	B	σp,dB	ρ1	ρ2	D	Nmin	Naz
1	395	305	May 17 '92	4.16	0.046	3.307	0.125	0.112	5	403	69
2	395	307	May 17 '92	4.37	0.043	3.307	0.177	0.141	5	447	69
3	395	308	May 17 '92	4.37	0.048	3.307	0.105	0.083	5	376	69
4	395	309	May 17 '92	4.80	0.046	3.568	0.053	0.038	5	394	69
5	395	311	May 17 '92	5.25	0.049	3.568	0.148	0.110	5	482	69
6	395	312	May 17 '92	4.97	0.049	3.568	0.163	0.122	5	500	69
7	395	314	May 17 '92	5.69	0.053	3.568	0.148	0.120	5	489	69
8	395	317	May 17 '92	4.87	0.050	3.568	0.128	0.093	5	459	69
9	395	318	May 17 '92	4.93	0.057	3.568	0.134	0.122	5	481	69
10	415	301	Apr. 23 '92	5.78	0.054	3.832	0.06	0.033	5	435	69
11	415	304	Apr. 23 '92	5.67	0.055	3.832	0.118	0.088	5	518	69
12	415	309	Apr. 23 '92	5.82	0.056	3.568	0.071	0.050	5	394	69
13	415	310	Apr. 23 '92	5.80	0.057	3.832	0.093	0.08	5	494	69
14	415	311	Apr. 23 '92	5.80	0.059	3.832	0.126	0.085	5	521	69
15	415	313	Apr. 23 '92	5.78	0.057	3.831	0.042	0.026	5	416	69
16	415	317	Apr. 23 '92	5.80	0.056	3.831	0.092	0.064	5	481	69
17	415	319	Apr. 23 '92	5.32	0.055	3.83	0.097	0.08	5	496	69
			[dB]	x1016	[dB]						

Table 2 A summary of antenna patterns obtained by 17 Amazon images

Scene_ID	Path	Row	3dB half width	off nadir(deg)	residual(dB)	repeat error(dB)
1	395	305	5.491	34.754	0.0794	0.1543
2	395	307	5.465	34.751	0.0946	0.1510
3	395	308	5.561	34.685	0.0942	0.1956
4	395	309	5.591	34.707	0.0924	0.2322
5	395	311	5.415	34.780	0.1245	0.1620
6	395	312	5.472	34.681	0.1836	0.2209
7	395	314	5.337	34.973	0.1134	0.1790
8	395	317	5.288	34.900	0.1138	0.2118
9	395	318	5.385	34.853	0.1335	0.1744
10	415	301	5.451	35.015	0.0636	0.1295
11	415	304	5.924	34.980	0.0613	0.4162
12	415	309	5.573	34.873	0.1108	0.2122
13	415	310	5.345	35.020	0.1052	0.1671
14	415	311	5.293	35.066	0.0884	0.2325
15	415	313	5.242	35.074	0.0798	0.2740
16	415	317	5.371	35.047	0.1019	0.1508
17	415	319	5.207	35.218	0.1210	0.3320
average			5.436	34.905	0.1036	0.2115
standard dev			0.170	0.160	0.0289	0.0732

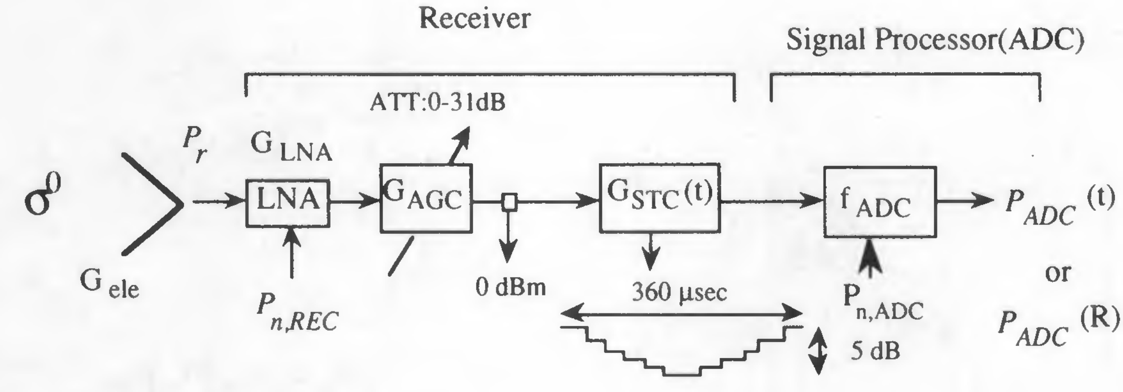

Fig. 1 A block diagram of JERS-1 SAR

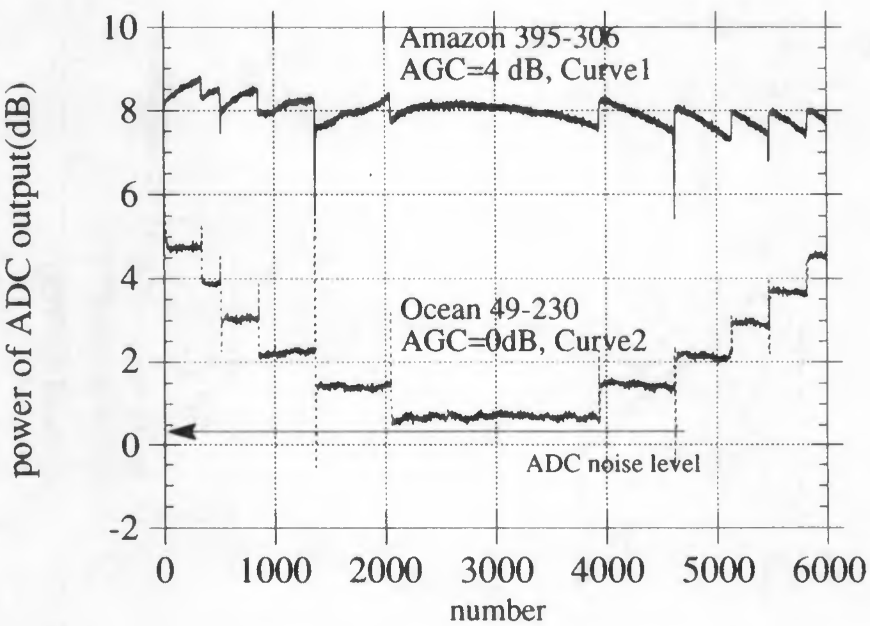

Fig. 2 A comparison of the AD noise and receiver noise.

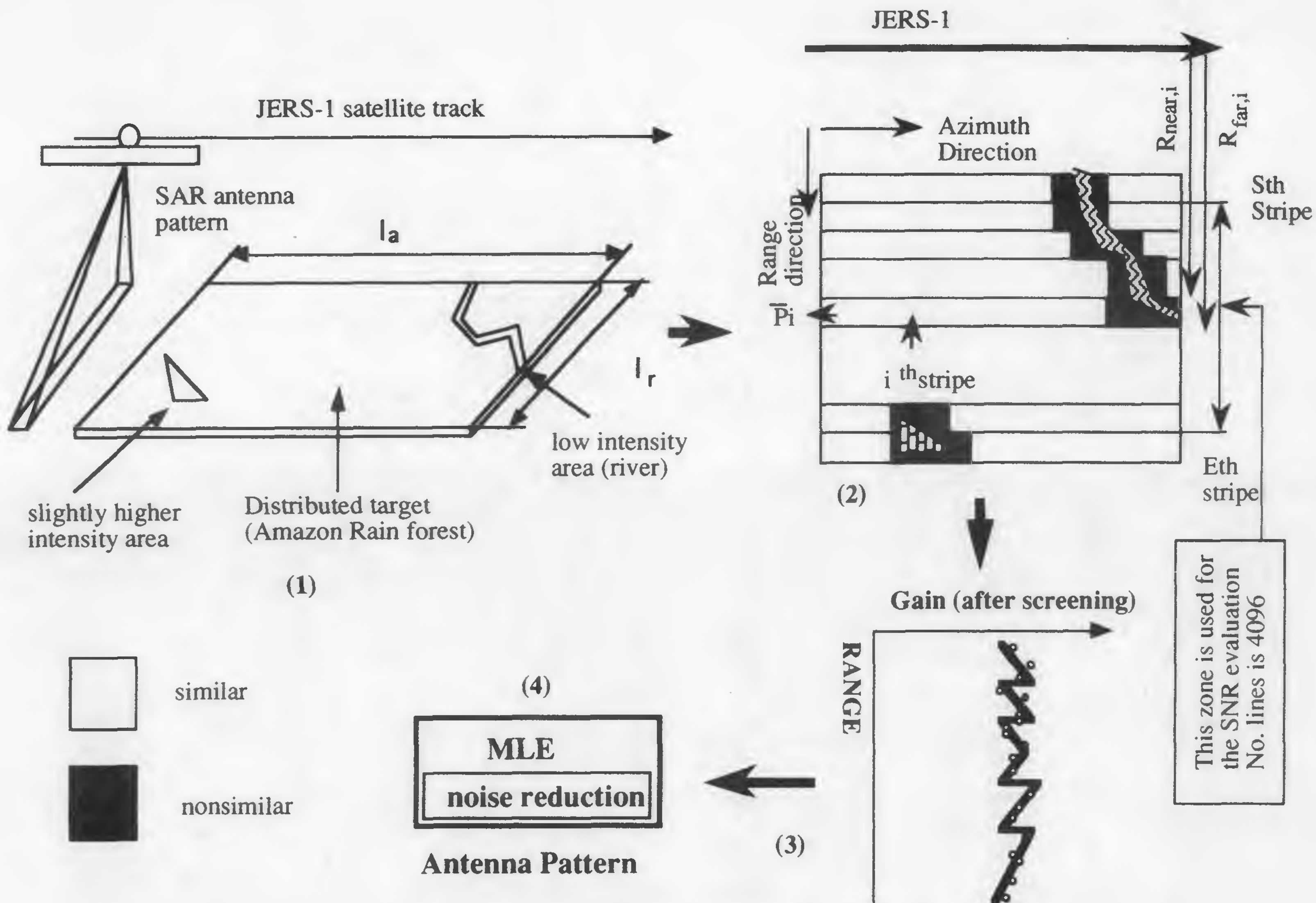

Fig. 3 A procedure to estimate the Antenna pattern by rain forest data

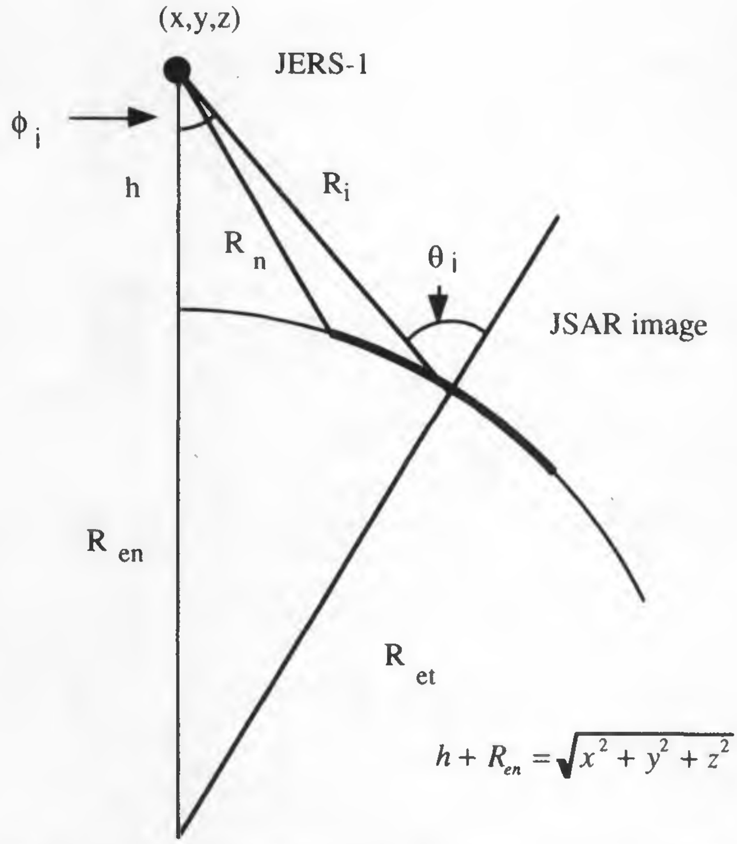

Fig. 4 A coordinate of the SAR observation, where SAR is moving from the top to the behind of the paper.

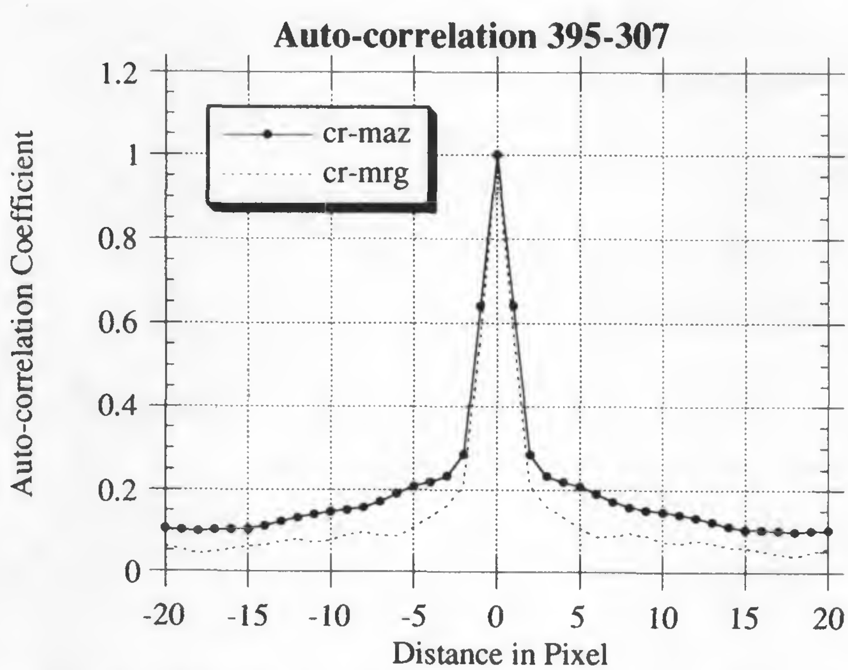

Fig. 5 An example of the autocorrelation coefficients for Amazon 395-307

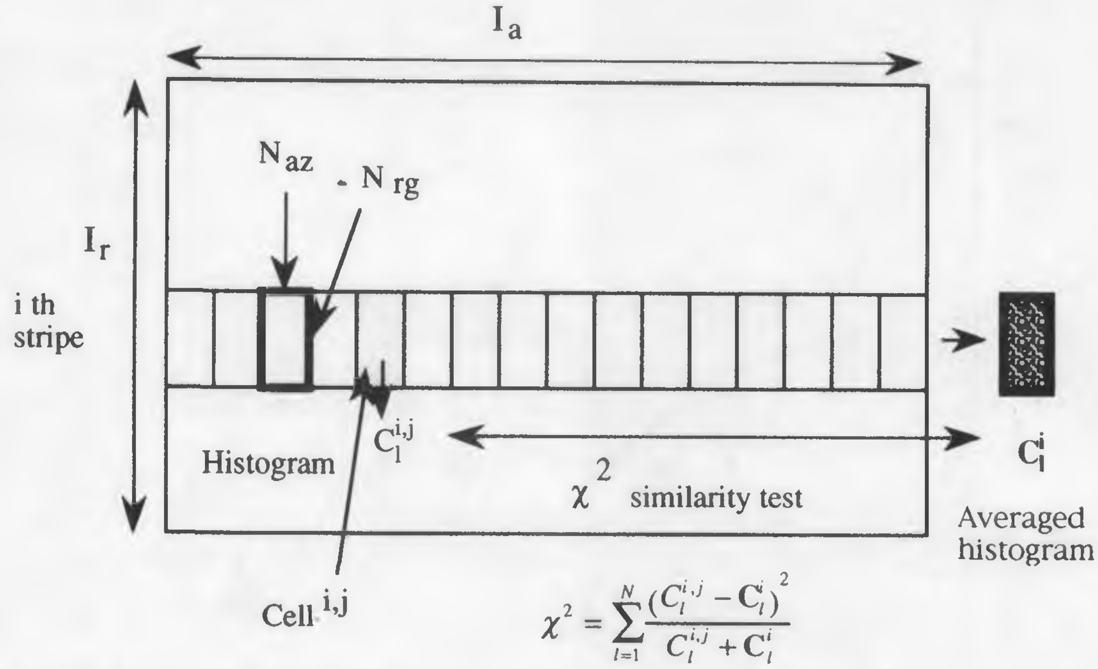

Fig. 6 A general of the screening processing and its similarity test.

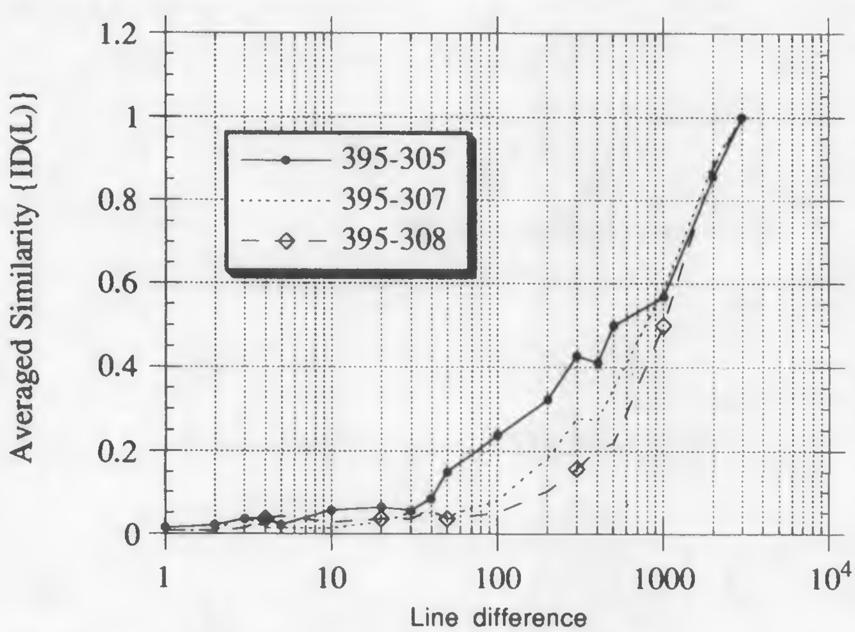

Fig. 7 Averaged similarity over range direction for Amazon data ($I_D(L)$)

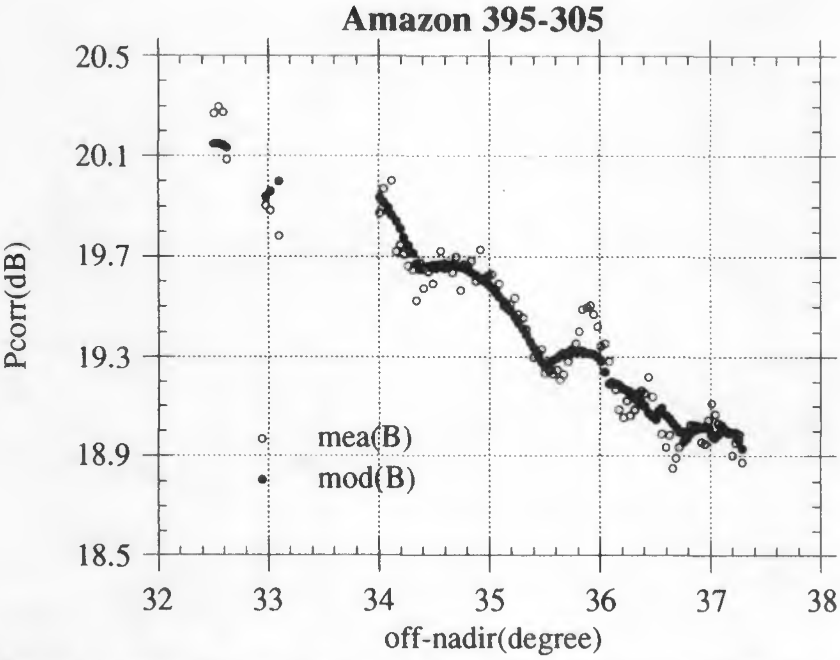

Fig. 9-1 An example of the fitted SAR correlation power model, $P_{m,i}(\boldsymbol{a})$, which is expressed by black square, and averaged correlation power, $\overline{P_i}$, which is expressed by white square for Amazon 395-305

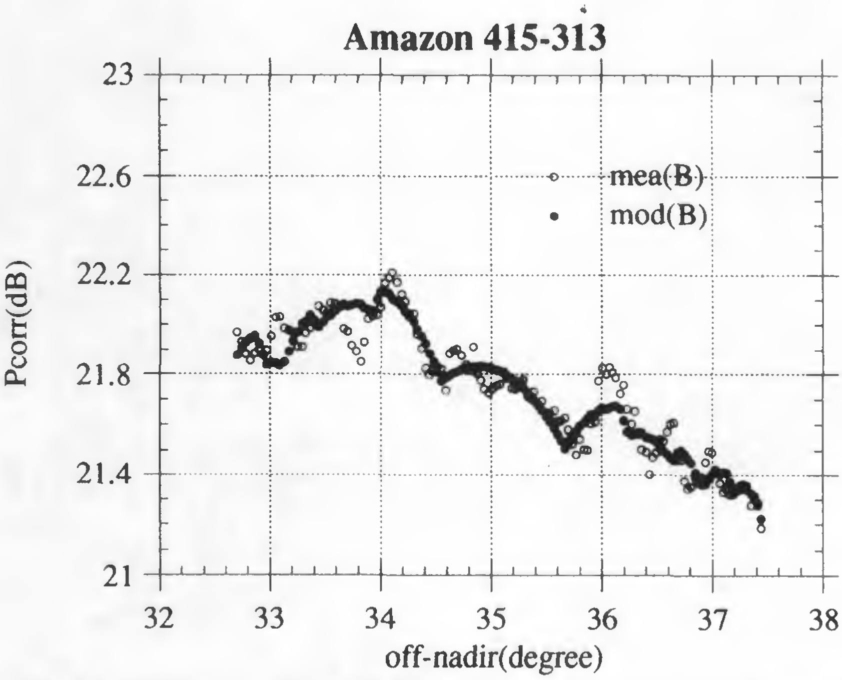

Fig. 9-2 An example of the fitted SAR correlation power model, $P_{m,i}(\boldsymbol{a})$, which is expressed by black square, and averaged correlation power, $\overline{P_i}$, which is expressed by white square for Amazon 415-313

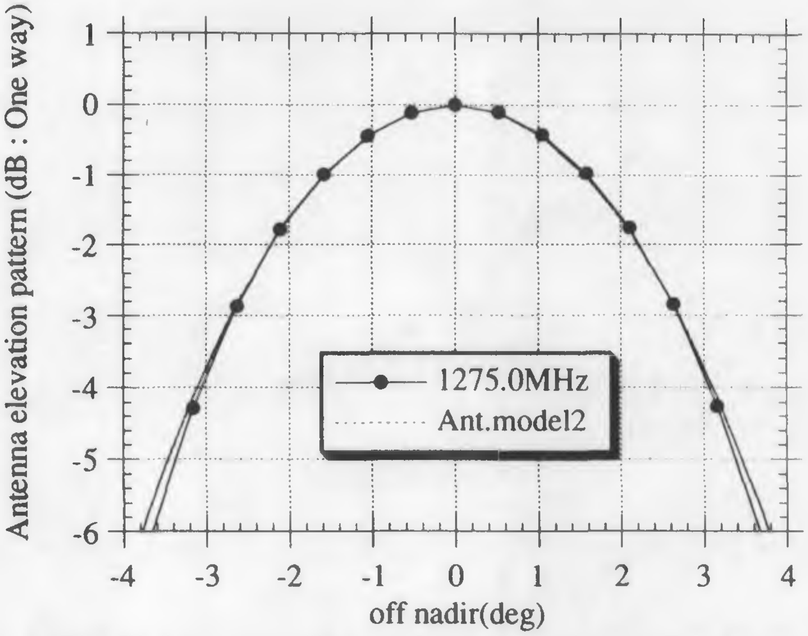

Fig. 10 A comparison of estimated antenna elevation pattern, which is broken line, and ground based measurement, which is solid line with black circles.

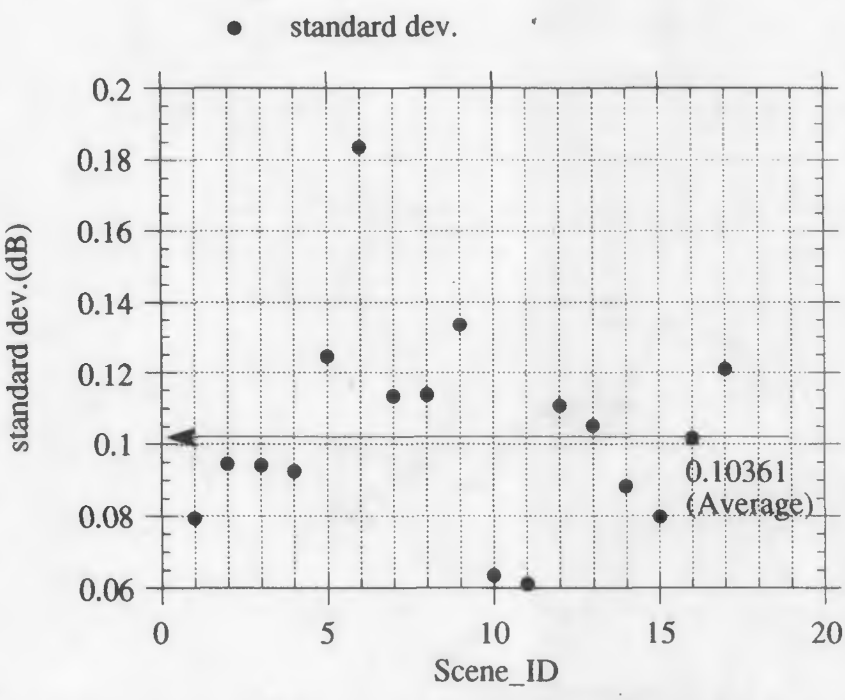

Fig. 11 A distribution of the mean residual errors for all the evaluated images.

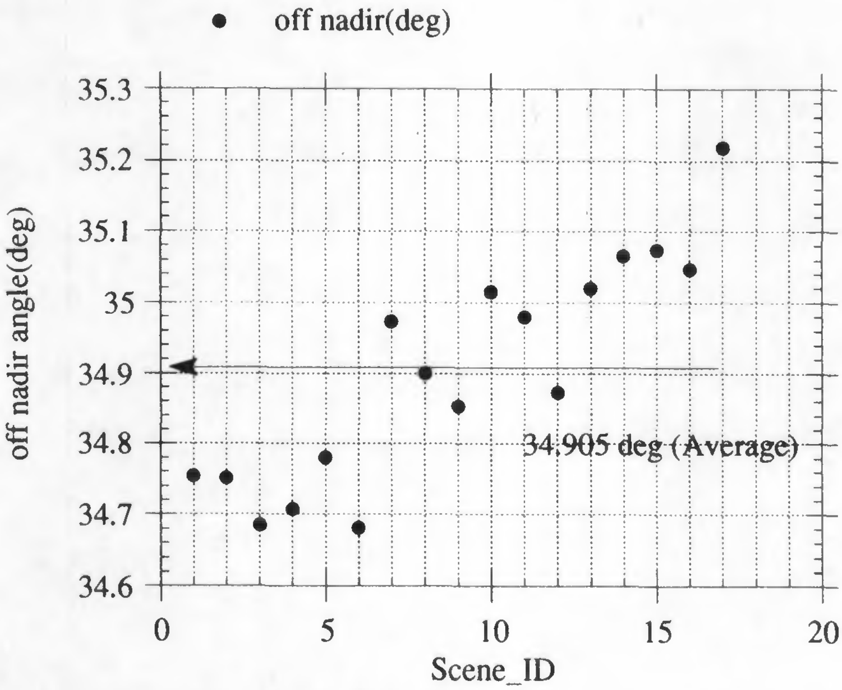

Fig. 12 A distribution of the off-nadir angles of the evaluated images.

Fig. 8-1. Amazon SAR image acquired on May 17 '92, GRS = 395-308

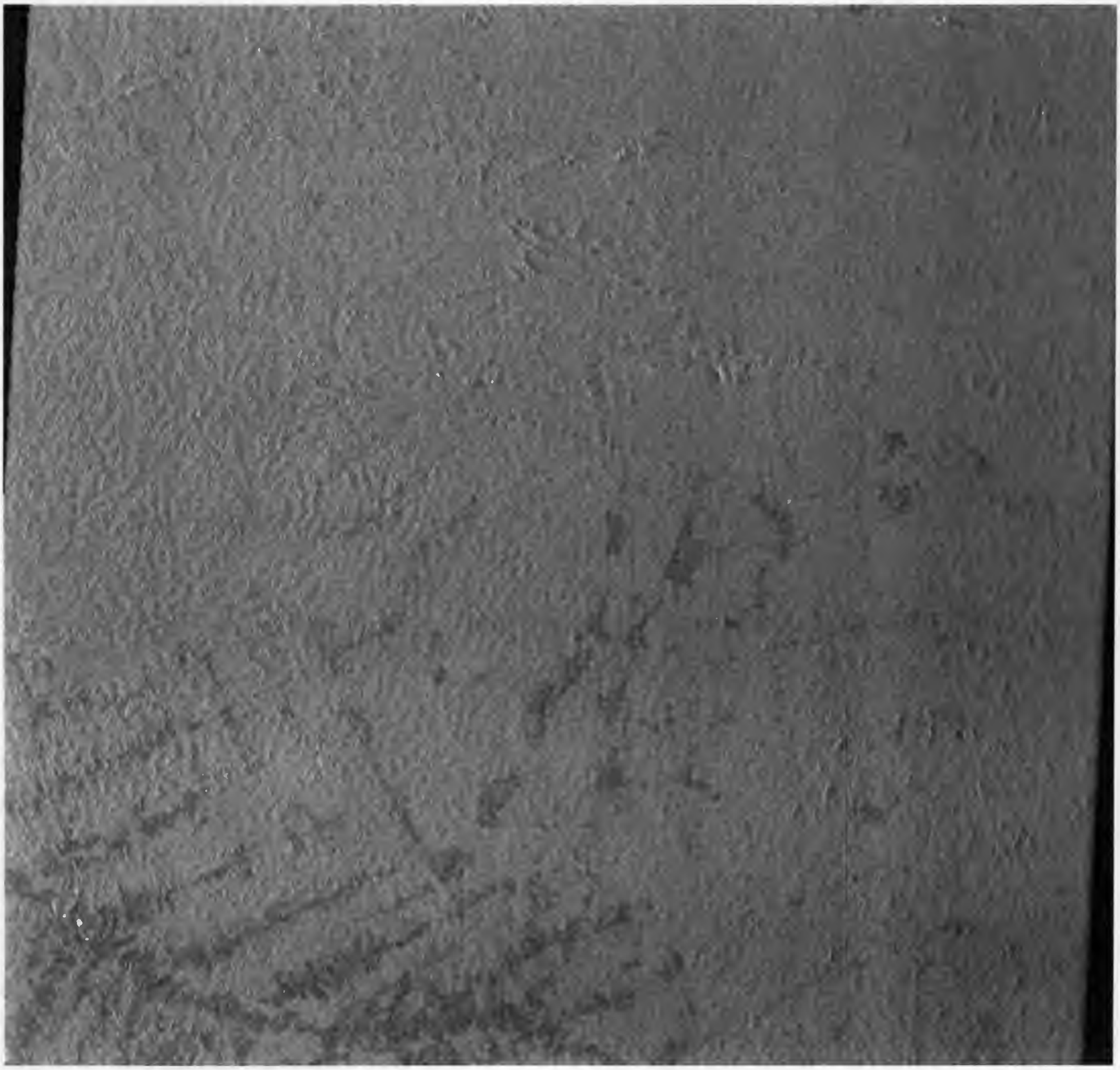

Fig. 8-2. An example of the screening processing for the Amazon SAR image, GRS = 395-308. Black area is recognized non similar, and looks same to the darker area of Fig. 8-1.

ON THE USE OF FORESTED AREAS FOR CALIBRATION : RESULTS FROM MAESTRO_1 AND MAC_EUROPE EXPERIMENTS

J.C. Souyris, T. Le Toan, A. Beaudoin
Centre d'Etude Spatiale des Rayonnements
CNRS - Université Paul Sabatier
Toulouse, France

C.C. Hsu, J.A. Kong
Massachusetts Institute of Technology
Cambridge, MA, USA

ABSTRACT :

The objective of this paper is to study spatial and temporal variations of the radiometric and polarimetric properties of forest stands in order to assess their use for calibration purposes. The study is based on an analysis of NASA/JPL AIRSAR data acquired on the Landes forest during Maestro_1 (1989) and Mac_Europe (1991) campaigns. The data have been first calibrated using corner reflectors and natural extended targets (clear-cut).

Backscattering coefficients at P-, L- and C- band, HH, VV, HV and difference of phases between HH and VV were analyzed. Also, data at C- VV and L- HH were compared with ERS-1 and JERS-1 data acquired on the same site.

The analysis showed that full polarimetric measurements of forest stands could be experimentally evaluated with a good accuracy as a function of forest age. The results have been validated by theoretical modeling. Finally, those specific properties of forest stands have been assessed for calibration purposes.

I. INTRODUCTION :

The calibration of radar data frequently relies on the use of man-made passive calibration point targets such as corner reflectors or active devices such as Polarimetric Active Radar Calibrators (PARCs). Calibration has been performed with accuracy on both airborne and spaceborne data in recent years. However, the deployment of the calibration point targets is not always practical. There has been an increasing interest in specific natural extended targets which can substitute the use of point target for calibration.

In this paper, we investigate the polarimetric properties of forest stands for this purpose. The study is based on an analysis of NASA/JPL AIRSAR data acquired over the Landes forest test-site during Maestro_1 (1989) and Mac_Europe (1991) campaigns. Also, ERS-1 data and JERS_1 data acquired on the same site have been compared to airborne data.

The site under test is the Landes forest in South-Western France which is the largest plantation forest in France, constituting nearly one million hectares on flat topography, producing 20% of the French timber. This forest is almost totally formed of maritime pine, and is managed in a consistent fashion, which ensures the canopy to be homogeneous. This site has been studied for ERS-1 and JERS-1 missions and has been selected for the space shuttle SIR-C/XSAR missions scheduled in 1994.

The main objective of the first airborne campaign (Maestro_89) was to assess the use of SAR data at different frequencies and polarizations for observation and monitoring of forest environments. The specific application objective was to retrieve forest biomass (Le Toan et al. 1992, Beaudoin et al. 1993). Two years later, the second experiment (Mac_Europe_91) has been led on the same site in order to study spatial and temporal variations of forest responses by comparison between the two sets of airborne data and comparison with ERS-1 data.

The airborne data were from the NASA/JPL imaging radar system (AIRSAR), operating at P- Band (0.44 Ghz), L- Band (1.25 Ghz) and C- Band (5.3 Ghz).

II. CALIBRATION OF AIRSAR DATA :

The calibration procedure has been done using the algorithm proposed by Van Zyl (Van Zyl, 1990). The basis of calibration is to use targets with known polarimetric backscattering characteristics. Calibration targets under consideration include natural distributed targets and manmade point calibration targets such as corner reflectors. For both airborne campaigns, trihedral corner reflectors have been deployed on the site in order to achieve the full polarimetric calibration. In Maestro_89, 16 trihedral corner reflectors (1.8 m, 0.70 m, 0.44 m) for P-, L-, C- Band were deployed. In Mac_Europe_91, 5 triangular basis trihedral corner reflectors of 2.5 m were deployed.

In the case of Maestro_89 campaign, the delivered data format can be either compressed 4-look Stokes matrix or 1-look full resolution complex scattering matrix. We have used the first format, comprising the 4 complex terms of the unsymmetrized scattering matrix. For Mac_Europe_91, two pulse bandwidth modes were available. From the 1-look full resolution image, we have used the 40 MHz mode that generates a 8-look image with a resolution of approximatively 6.05 m (azimuth)*3.33 m (slant range).

Spaceborne data include ERS-1 data (3-look, C- Band, VV polarization) acquired in 1991 and JERS-1 data (3-look, L- Band, HH polarization) acquired in 1992.

II.1. Phase calibration of Stokes matrices :

A preliminary step in the calibration procedure consists in achieving the phase equalization scheme, in order to correct phase differences between different transmitting and receiving paths (Zebker and al., 1990).

S_{ij} being the components of the true scattering matrix **[S]**, the received matrix **[R]** can be written as :

$$[\mathbf{R}] = e^{j\phi_0} . \begin{bmatrix} S_{hh} . \exp j(\phi_t + \phi_r) & S_{hv} . \exp j(\phi_r) \\ S_{vh} . \exp j(\phi_t) & S_{vv} \end{bmatrix}$$

where $\phi_t=\phi_{t,h}-\phi_{t,v}$ and $\phi_r=\phi_{r,h}-\phi_{r,v}$.

The above phase factors correspond to the phase paths of the four distinct polarization measurements.

Two equations are required to provide an estimation of ϕ_t and ϕ_r.

First, the reciprocity theorem imposes equality between S_{hv} and S_{vh}. Under this assumption, we make up the complex product :

$$R^*_{hv} . R_{vh} = S^*_{hv} . S_{vh} . \exp j(\phi_t - \phi_r)$$

and average it over the full image. For each pixel, the argument of this product mainly depends on the phase difference ϕ_t-ϕ_r (providing that the system noise between channels is uncorrelated). An average of this quantity over many pixels will provide an estimation of ϕ_t-ϕ_r.

Another assumption is nevertheless required to derive the values of ϕ_t and ϕ_r. This relies on the knowledge of phase difference between hh and vv signals on a particular area of the image. We currently assume that the mean of this difference is 0° on bare soil surfaces (this hypothesis being discussed later). A local estimation of the complex product :

$$R^{*}_{hh} \cdot R_{vv} = S^{*}_{hh} \cdot S_{vv} \cdot \exp j(\phi_t + \phi_r)$$

thus allows to estimate ϕ_t+ϕ_r.

Finally, we get estimations of ϕ_t and ϕ_r with possible errors of π.

II.2. Calibration procedure :

After this first step, the calibration procedure of Van Zyl, using the system model of a symmetrized measured scattering matrix **[Z]** decomposed as follows :

$$\begin{bmatrix} Z_{hh} & Z_{hv} \\ Z_{hv} & Z_{vv} \end{bmatrix} = A.e^{i\phi}.\begin{pmatrix} 1 & \delta_2 / f \\ \delta_1 & 1 \end{pmatrix}.\begin{pmatrix} 1 & 0 \\ 0 & f \end{pmatrix}.\begin{pmatrix} S_{hh} & S_{hv} \\ S_{hv} & S_{vv} \end{pmatrix}.\begin{pmatrix} 1 & 0 \\ 0 & f \end{pmatrix}.\begin{pmatrix} 1 & \delta_1 \\ \delta_2 / f & 1 \end{pmatrix}$$

will allow to estimate cross-talk parameters δ1 and δ2/f, channel imbalance factor f and absolute radiometric calibration factor A, provided that for every step of the calibration procedure, one or several simplifying assumptions are available.

In the case of cross-talk calibration, one required condition is that the magnitudes of δ1 and δ2 are small compared to 1, i.e. the system is supposed well isolated. This condition insures the convergence of recursive algorithms used to determine cross-talk parameters. A second assumption, which is more delicate to check, is the hypothesis of zero correlation between like- and crosspolarized backscatter for natural clutters, which can be expressed as follows :

$$\langle S_{hh}^{*}.S_{hv} \rangle = \langle S_{vv}^{*}.S_{hv} \rangle = 0$$

This assumption has been validated in the case of a multifrequency image dataset acquired by the NASA/JPL AIRSAR over natural clutter (Cordey 1993). It appears to be of particular importance, especially if we aim at estimating the crosspolarized power with a good accuracy. Using simulation, it was shown (Cordey 1993) that the error in the cross-polarized power is less than 0.1 dB, provided that the amplitude of the correlation between like- and cross-polarized signals is less than about -10 dB.

In the case of channel imbalance correction and absolute radiometric calibration, a certain number of point targets with known backscattering characteristics have to be deployed on the site under test. We usually use trihedral corner reflectors characterized by the following relationships between the co-polarized components of the scattering matrix :

$$\frac{S^{*}_{vv} \cdot S_{vv}}{S^{*}_{hh} \cdot S_{hh}} = 1 \qquad \text{and :} \qquad \text{Arg } (S^{*}_{hh} \cdot S_{vv}) = 0°$$

These two results will be useful to estimate respectively amplitude and phase of the channel imbalance f, for a given range (i.e. for a given incidence), and has to be achieved for various ranges of the image.

Finally, the knowledge of theoretical corner reflector cross section σ_{cr} will allow to determine the absolute radiometric calibration factor A. To reduce errors due in particular to corner reflector positioning, the calibration factor should be estimated from several corner reflectors located at different ranges.

The full polarimetric calibration has been achieved for Maestro_89 and Mac_Europe_91 datasets at P- band, L- band and C- band. **Fig 1-a** presents the co-polarized signatures of a 1.8 m square-base trihedral corner reflector located at an incidence of 30° in Maestro_89 data. Signatures from uncalibrated data exhibit strong distortions at all frequencies. After cross-talk removal, significant improvement is observed in L- Band, whereas the signature is not significantly different at P- Band. Cross-talk removal had not been taken into account in the case of C- Band, as $\delta 1$ and $\delta 2/f$ are very weak for this frequency. Then column 3 shows the channel balanced signatures (both phase and amplitude). **Fig 1-b** presents initial and final polarimetric signatures of a 2.5 m triangular basis corner reflector located at an incidence of 53° in Mac_Europe _91 data. In this case, we have used POLCAL, which is a software developed by JPL, to achieve AIRSAR image calibration.

In the two cases, the calibrated polarimetric signatures are in good agreement with theoretical signatures. This result suggests that the quality of the overall calibration is sufficient to further the data analysis.

III. STUDY OF SPATIAL AND TEMPORAL VARIATIONS OF FOREST STANDS RADIOMETRY:

III.1. Results derived from AIRSAR experiments :

In previous studies (Le Toan and al. 1992, Beaudoin and al. 1993), it was demonstrated that the radar backscattering coefficients of forest stands are related to the forest age or forest biomass, which is generally strongly correlated to age.

In the following, both Maestro_89 and Mac_Europe_91 data were analyzed together as a function of forest age.

Fig 2-a to **fig-2d** show the forests responses at P-HH, P-HV, L-HH and C-VV. We observe a good agreement between data derived from the two campaigns, showing the temporal stability of the radar responses to forest age.

At P-HH (**fig 2-a**) we observe an increase of backscatter with forest age. This trend has been interpreted by theoretical modeling (Hsu and al. 1993). The model indicated that the major contribution to P-HH return are the trunk-ground double scattering at forest age > 30 years. For young stands, the scattering results from multiple sources including crown scattering and the crown-ground interaction. The modeling result (**fig 2-a**) shows good agreement with the experimental data, especially in the case of forest age > 30 years where the data dispersion is reduced. For young forest, the data dispersion and the discrepancies between theory and data can be due to the multiple sources of scattering.

In the case of P-HV (**fig 2-b**), the increase of backscatter responses as a function of age is the most important. Modeling result shows the same trend with nevertheless underestimated predicted values of backscattering coefficients, especially for young forest stands. It was found that the main contribution of the backscattering coefficient comes from the direct scattering of the primary branches in the crown layer. When the forest grows older, the primary branches get bigger and the HV return increases in spite of the decrease of tree density.

Fig 2-c shows L- Band HH backscattering coefficients (which is the configuration of JERS-1 SAR) as a function of forest age. A good agreement is observed between theoretical and experimental results. A smaller increase of backscattering coefficients compared to that of P- band frequency is also observed. Simulations suggest that the HH return is mainly from the direct crown return and crown-ground reflection for young forest, while for older forests, it rather comes from the direct crown return and trunk-ground interaction.

Finally **fig 2-d** shows C- Band VV backscatter (which is the configuration of ERS-1 SAR) as a function of the forest age. The data show an almost flat response for the backscattering coefficients . The theory indicates that the main contribution is from the direct crown scattering for all polarizations and all ages of forests.

III.2. Comparison with spaceborne data :

Fig 3-a shows a comparison between ERS-1 data acquired in November 1991 and Maestro_89 AIRSAR data at C- band VV selected in the incident angle range 20°-25°. A good agreement is observed between the two sets of data. It was found to be nearly independent of forest stand age.

Fig 3-b presents comparison between JERS-1 data acquired in August 1992 and Maestro_89 AIRSAR data at L- band HH selected in the incident angle range 40°-50°. There is also a good agreement between these two sets of data. The JERS-1 data are slightly higher (around 0.7 dB in mean). This difference may be explained by the incident angle of JERS-1 (35°) which is lower than the AIRSAR incident angle range (40°-50°).

The overall result suggests that backscatter coefficients of different forest stands at different dates and different seasons, retrieved from different data sets, remain stable when expressed as a function of forest age. In particular, the data dispersion at L- band and C- band was found of the order of 1 dB.

IV. POLARIMETRIC BEHAVIORS OF CLEAR-CUTS AND FOREST STANDS:

IV.1. (hh-vv) phase difference behaviour for forests :

In addition to the backscattering coefficients, polarimetric parameters are studied. Here, we are more particulary interested in the phase of correlation between hh and vv signals, for forest stands and bare surfaces. In the present work, this is the unique polarimetric parameter under study. Moreover, it has to be noticed that in most cases of natural clutter, the phase of correlation equals the mean phase difference between hh and vv signals (Dutra and al. 1991).

Fig 4-a shows the phase of correlation between hh and vv signals for both Maestro_89 and Mac_Europe_91 forest stands at L- Band, as a function of age. In both cases, the mean of the phase distribution is about 0° and the standard deviation is about 5°. However, we observe a slight increase of this mean as forest grows older. This trend can be explained by a partial coherent effect related to ground-trunk interactions.

Fig 4-b represents the phase of correlation between hh and vv signals for C- Band. The result is similar to that observed at L- band, i.e. with the same standard deviation for phase distribution. Nevertheless, the slight increase at L- band is not observed at C- band, as no ground-trunk interaction has been present in the scattering.

In the case of P- band, the behaviour of correlation between hh and vv signals is different. As it is shown in **fig 4-c**, the first feature is that the mean of phase distribution is not equal to 0° any more. Secondly, we observe an increase of the mean phase as the forest grows older. This behaviour has been confirmed by the theoretical model which indicated that the large phase difference is caused by the trunk-ground interaction (i.e. a two-bounce effect) which becomes dominant when the forest age increases.

IV.2. (hh-vv) phase difference behaviour for bare surfaces :

Fig. 5-a,b,c present the phase of correlation between HH and VV signals for various clearcuts located at various incidence angles in Mac_Europe_91 images, at P-, L- and C-bands.

At C- band, the observed mean of phase of correlation is -2°, close to 0° as expected, while at L- and P- bands, the mean values are respectively -5.2° and -3.6°. This result can be used to readjust the phase difference to 0° after full calibration, if it was not the case.

The standard deviations of the distributions are of 6°, 4° and 3° for respectively P-, L- and C- bands. The large dispersion at P- band (maximum dynamic 17°), due probably to both surface and volume inhomogeneities of the areas, will lead to a large uncertainty in the phase evaluation.

V. USE OF FOREST STANDS AND CLEAR-CUTS AREAS FOR POLARIMETRIC CALIBRATION :

V.1. Properties derived from forest observations :

The study performed on different data sets acquired at the Landes forest indicates that the radar backscattering coefficients of different forest stands at P-, L- and C- bands and HH, VV, HV polarizations can be known with an uncertainty of the order or less than 1 dB. At C-band, as the radar backscatter does not change with forest age, a priori knowledge of forest/non forest areas is sufficient for radiometric calibration. At P- and L- bands, an updated forest stand age map is necessary.

The polarization phase difference for forest stands is also known, with an observed standard deviation of the order of 10°. For a reduced uncertainty, polarization phase difference of clear-cut areas should be preferred, especially at L- and C- bands, where the observed standard deviation is of the order of 3°, 4°.

V.2. Properties derived from the literature :

In addition to the above results, the following information on the properties of forested areas have been derived from the literature.

The first information concerns the zero correlation between like- and crosspolarized backscatter for natural clutter. This assumption has been theoretically assessed by Borgeaud and al. (1987) who have discussed the problem in terms of second-order Born approximation. It was shown that, for an azimuthally isotropic distribution of scatterers, there is no correlation between like- with crosspolarized signals. Moreover, we have already mentioned that this assumption has been validated by Cordey in the case of a multifrequency image dataset acquired by the NASA/JPL AIRSAR, and is of particular importance if we have to estimate the crosspolarized intensity with a good accuracy.

The second information concerns symmetry properties of natural media published by Nghiem et al. (1992, 1993). The authors defined the following different symmetry properties of extended targets. The azimuthal symmetry -found for most geophysical media at normal incidence- is the combination of the reflection symmetry (with respect to a vertical plane) and the rotation symmetry. The reflection symmetry, which induces the zero correlation between co- and crosspolarization can be used to estimate the two complex cross talk parameters. The rotation symmetry which induces equality between $\sigma^{o}hh$ and $\sigma^{o}vv$ can be used to remove channel imbalance. Finally, the centrical symmetry generalizes the azimuthal symmetry to all incidence angles. Therefore, the centrical symmetry is of particular importance for cross-talk removal and channel balance at oblique incidence. The results showed evidences of the centrical symmetry in forest canopies at C- band. Unfortunately, centrical symmetry of forest canopies has not been proved for P- and L- Band.

V.3. Application to external calibration of polarimetric radars :

We expose hereafter to what extent the knowledge of natural clutter responses can be used at every step of the calibration procedure :

* *Phase equalization* : The phase equalization scheme will be improved by estimating the phase of correlation between hh and vv signals on several clear-cuts of the image, in order to reduce the uncertainties. A standard deviation of 6° has been observed on the distribution of phases at P- band. It drops to 3° for L- and C- bands.

* *Cross-talk calibration* : We will use natural clutter of clear-cuts and forests over the whole image, considering that the assumption of zero correlation between like- and cross-polarized backscatter is reliable.

* *Channel imbalance calibration* : It can be totally achieved by using forest stands responses at C- band, relying to the centrical symmetry properties of forest canopies for this frequency. The estimated uncertainty on the imbalance phase is ± 3°. The use of forest stands responses is more delicate for P- and L- bands. Nevertheless, they can be used for amplitude imbalance, taking into account theoretical differences between σ^{o}_{hh} and σ^{o}_{vv} at these frequencies, for a given incidence angle (the uncertainty in this case being difficult to estimate, due to the incidence dependence). For phase imbalance, a possibility is the use of clear-cuts located at specific ranges. In this last case, the estimated uncertainty on the phase reachs ± 10° at P- Band and is ± 3° for L- and C- Band.

* *Radiometric calibration* : It can be achieved with backscattered intensity of forest stands at the three frequencies. At L- and C- bands, the respective uncertainties will be of ± 0.7 dB and ± 0.5 dB). In the case of P- band, the responses reach a fairly stable value for age > 35 years. If only stands > 35 years are used, we achieve a radiometric calibration with an uncertainty of ± 0.5 dB.

In summary, full polarimetric calibration can be achieved using exclusively natural extended targets such as the Landes forest stands. Compared to the use of corner reflectors, the forest stands can provide radiometric calibration with equivalent uncertainties. Polarimetric calibration appeared adequate at C- band, while at P- and L- bands, the uncertainties are more important.

VI. CONCLUDING REMARKS :

It was demonstrated that forests have specific properties that can be used for calibration purposes. The resulting uncertainties have been estimated in the case of The Landes forest. These preliminary results will be assessed during the space shuttle SIR-C/XSAR mission scheduled for April and November 1994.

To generalize this method, further works must be done, on various forest types and environment conditions. It should be also important to estimate to what extent meteorological conditions involve variations of natural clutter polarimetric responses.

REFERENCES :

Beaudoin, A., T. Le Toan and Q.H.J. Gwyn, "SAR observations and modeling of the C-band backscatter variability due to multiscale geometry and soil moisture," IEEE Trans. on Geoscience and Remote Sensing, vol. 28, n°5, Sept 1990.

Borgeaud, M., R.T. Shin and J.A. Kong, "Theoretical models for polarimetric radar clutter," Journal of Electromagnetic Waves and Applications, vol. 1, pp. 73-89, 1987.

Cordey, R.A., "On the accuracy of crosstalk calibration of polarimetric SAR using natural clutter statistics," IEEE Trans. on Geoscience and Remote Sensing, vol. 31, n°2, March 1993.

Dutra, L.V., S. Quegan and R.G. Caves, "The information content of Maestro-1 Images," Proceedings IGARSS'91, Espoo, Finland, June 1991.

Hsu, C.C., H.C. Han, R.T. Shin, J.A. Kong, A. Beaudoin and T. Le Toan, "Radiative transfer theory for polarimetric remote sensing of pine forest," International Journal of Remote Sensing, September 1993.

Le Toan, T., A. Beaudoin, J. Riom and D. Guyon, "Relating forest biomass to SAR data," IEEE Trans. on Geoscience and Remote Sensing, vol. 30, n°2, March 1992.

Le Toan, T., A. Beaudoin, S. Goze, J.A. Kong, C.C. Hsu, H.C. Han and R.T. Shin, "Microwave interaction and analysis of polarimetric data : retrieval of forest biomass," Final report ESA ESTEC / Contract n° 9352/91/NL/LC(SC), December 1992.

Nghiem, S.V., S.H. Yueh, R. Kwok, and F.K. Li, "Symmetry properties in polarimetric remote sensing," Radio Science, vol. 27, n°5, pp. 693-711, September-October 1992.

Nghiem, S.V., S.H. Yueh, R. Kwok, and D.T. Nguyen, "Polarimetric remote sensing of geophysical medium structures," accepted for publication in Radio Science, 1993.

Van Zyl, J.J., "Calibration of polarimetric radar images using only image parameters and trihedral corner reflector responses," IEEE Trans. on Geoscience and Remote Sensing, vol. 28, n°3, May 1990.

Zebker, H.A., Y. Lou "Phase calibration of imaging radar polarimeter Stokes matrices," IEEE Trans. on Geoscience and Remote Sensing, vol. 28, n°2, March 1990.

Acknowledgment :

The work was supported by the Direction des Recherches et Etudes Techniques (DRET). The authors would like to thank the MIT Lincoln Laboratory for providing us the calibration targets and Son Nghiem for his help during Mac_Europe_91 campaign.

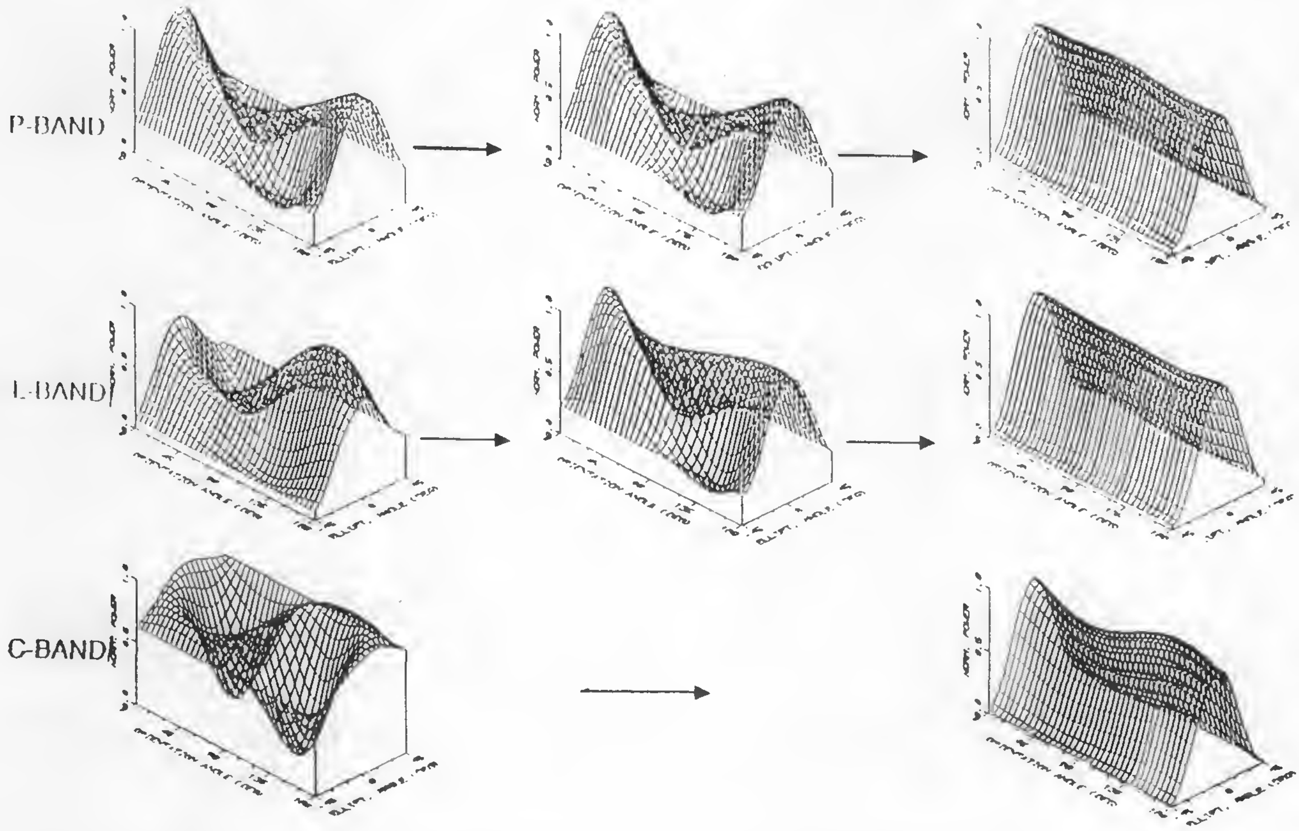

Fig 1-a - Calibration of MAESTRO 89 data : Co-polarized polarimetric signatures of a trihedral corner reflector at 30° incidence angle for P-, L- and C- Band. Column 1 : uncalibrated. Column 2 : after crosstalk removal. Column 3 : after full calibration.

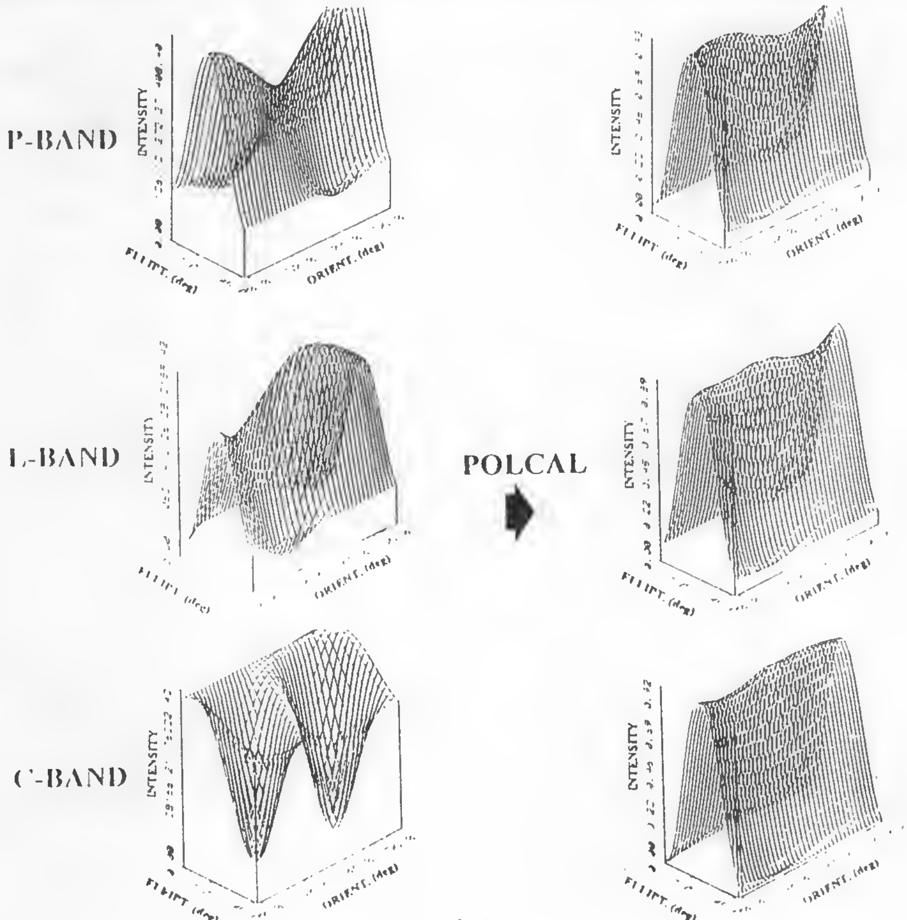

Fig 1-b - Calibration of MAC EUROPE 91 data : Co-polarized polarimetric signatures of a trihedral corner reflector at 53° incidence angle for P-, L- and C- Band. Column 1 : uncalibrated. Column 2 : after crosstalk removal. Column 3 : after full calibration.

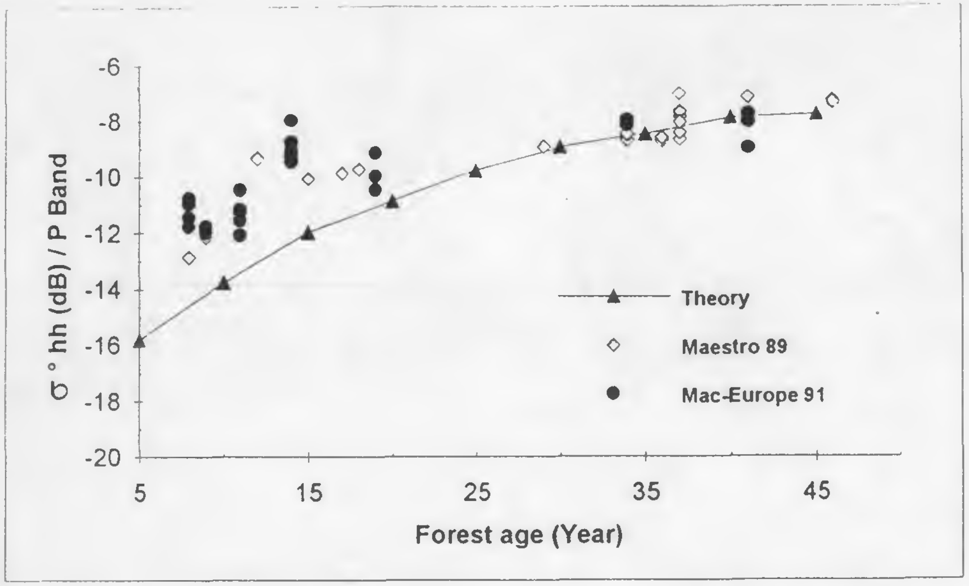

Fig 2 a - Backscattering characteristics of forest as a function of age. P Band, HH

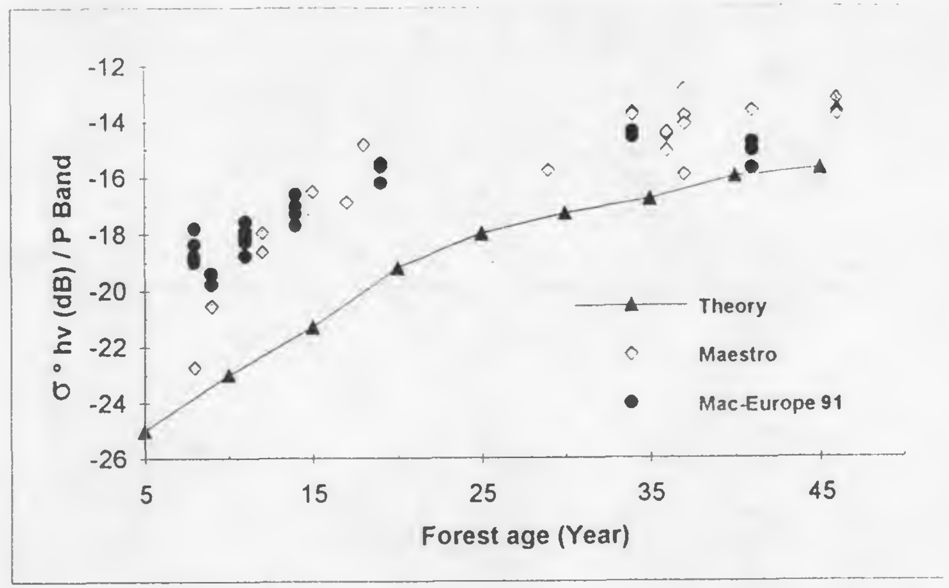

Fig 2 b - Backscattering characteristics of forest as a function of age. P Band, HV

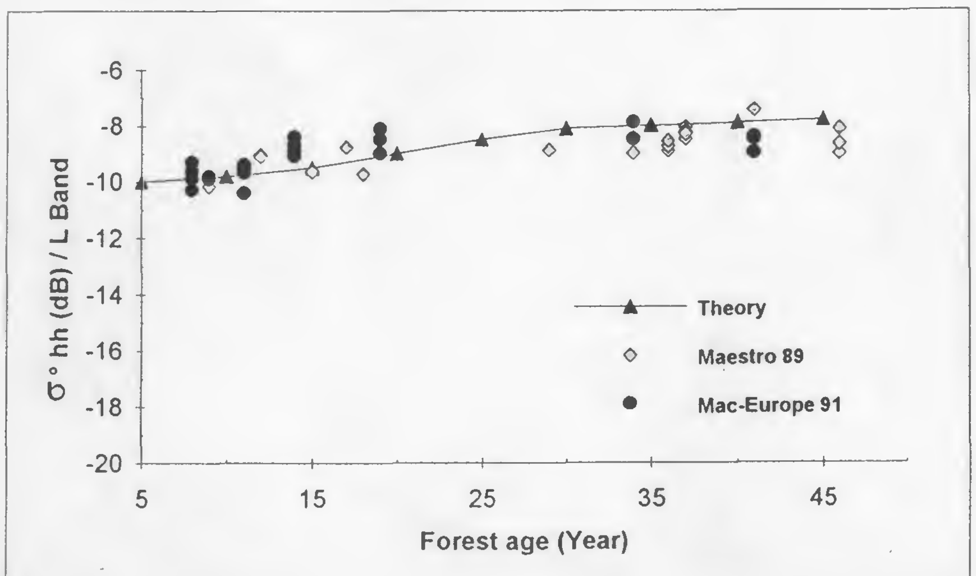

Fig 2 c - Backscattering characteristics of forest as a function of age. L Band, HH

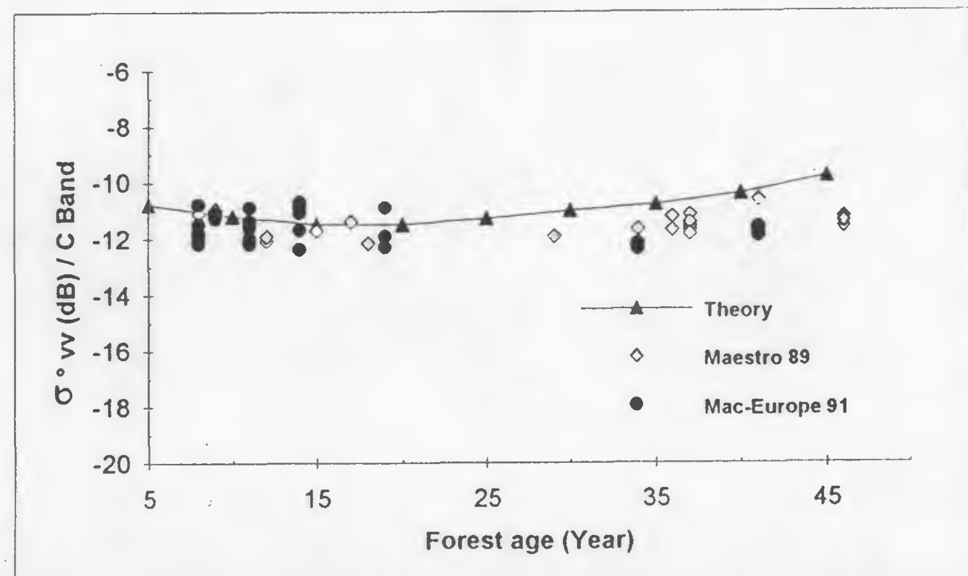

Fig 2 d - Backscattering characteristics of forest as a function of age. C Band, VV

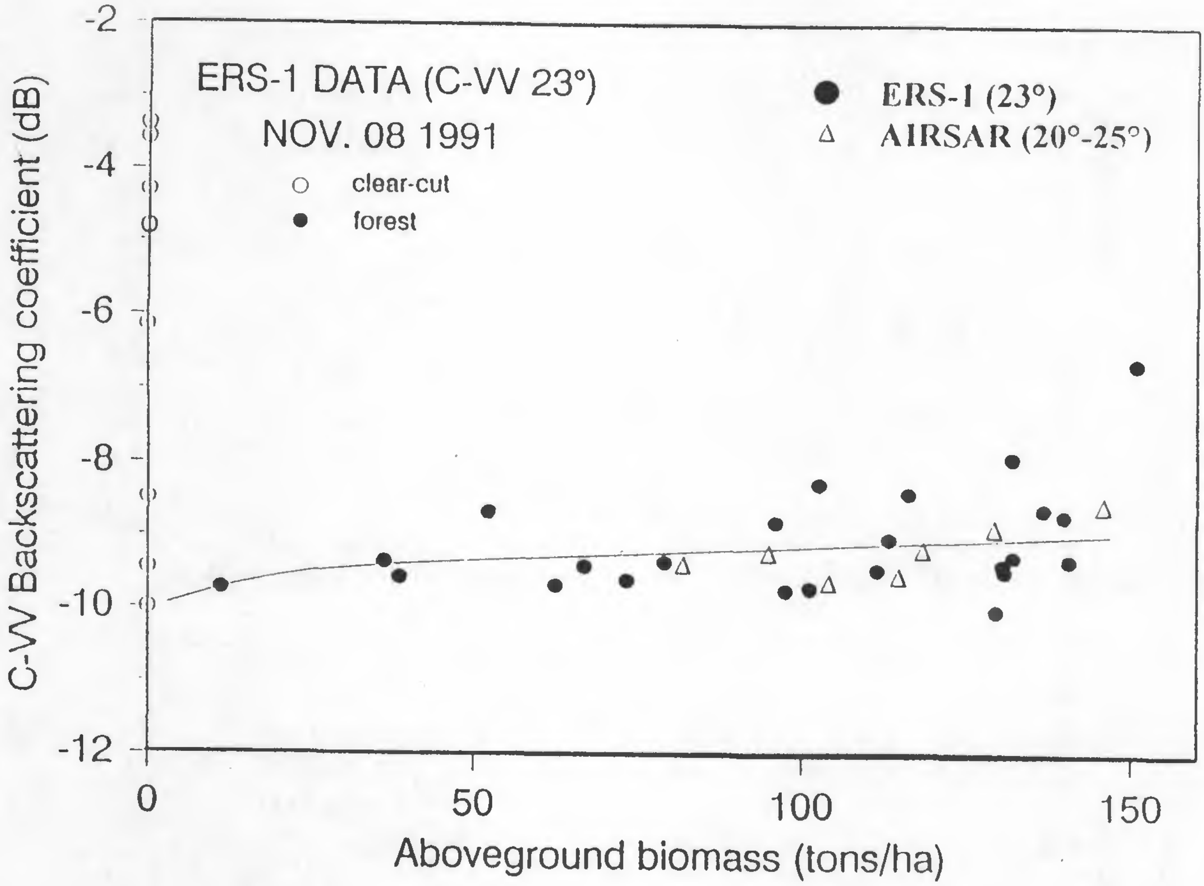

Fig 3-a - Comparison between ERS-1 (Nov. 1991) and AIRSAR (Aug. 1989) data as a function of forest biomass.

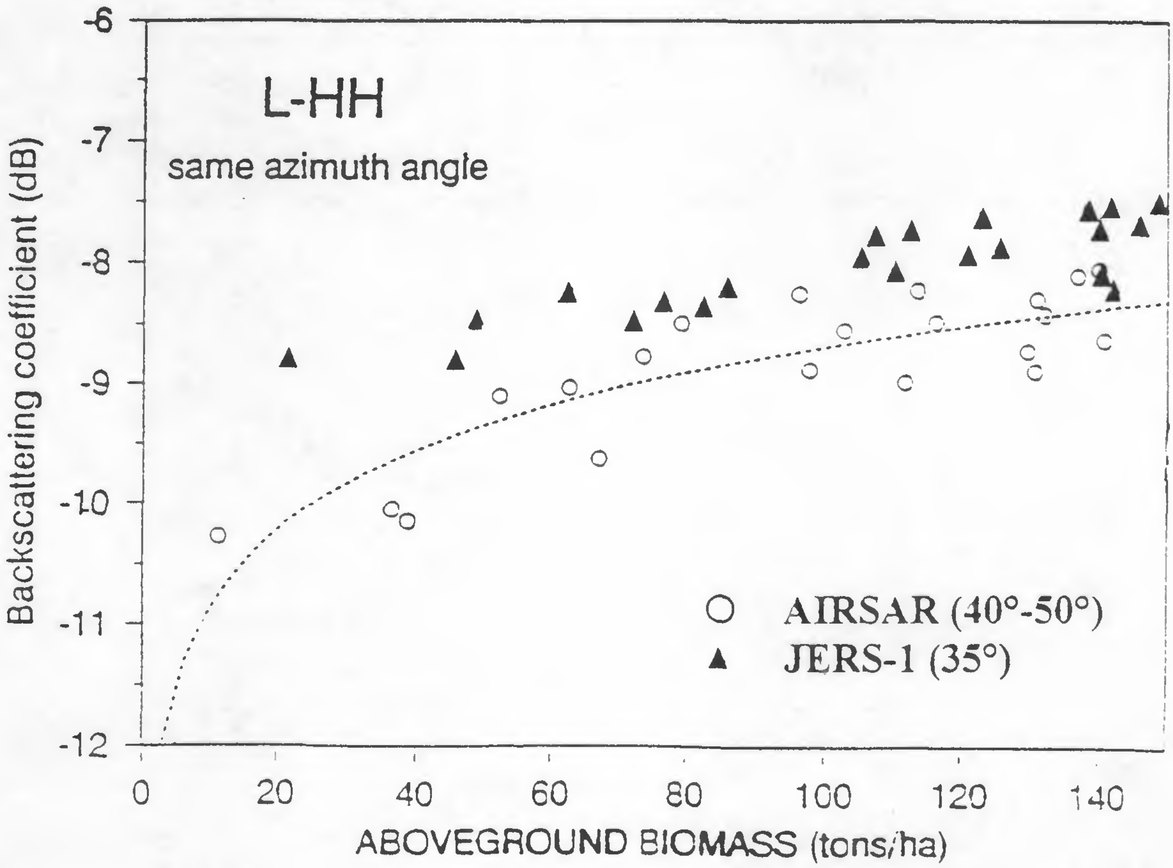

Fig 3-b - Comparison between JERS-1 (Aug. 1992) and AIRSAR (Aug. 1989) data as a function of forest biomass.

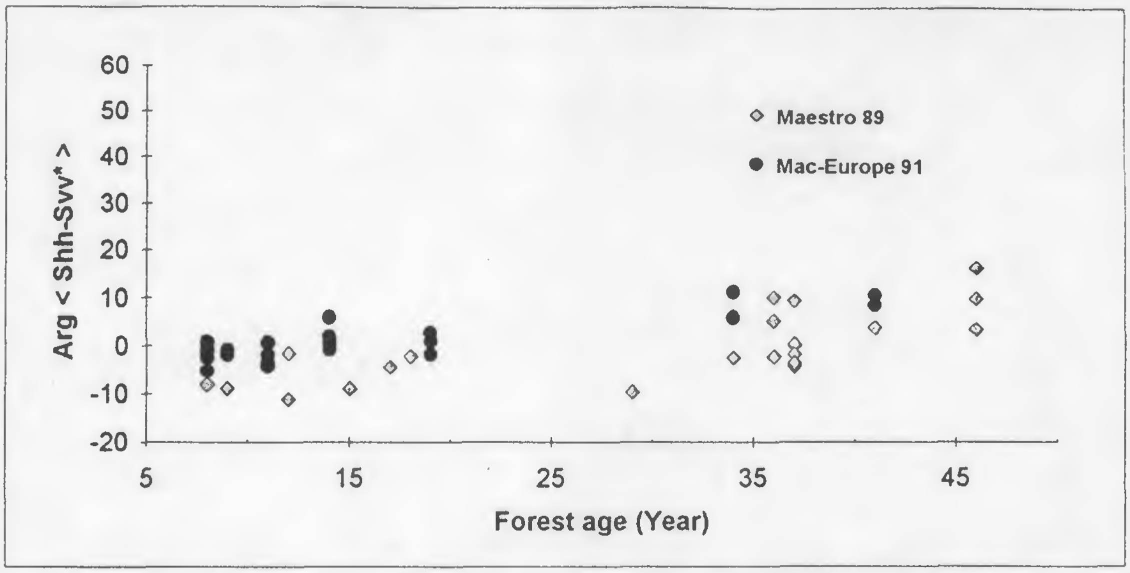

Fig 4 a - Phase of correlation between HH and VV signals for forest stands / L Band

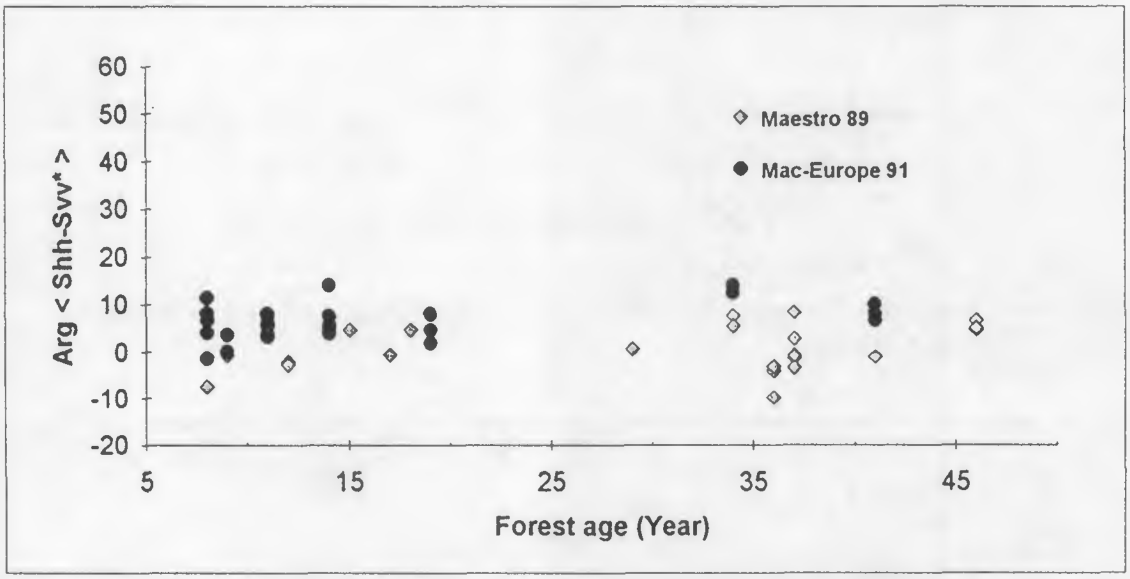

Fig 4 b - Phase of correlation between HH and VV signals for forest stands / C Band

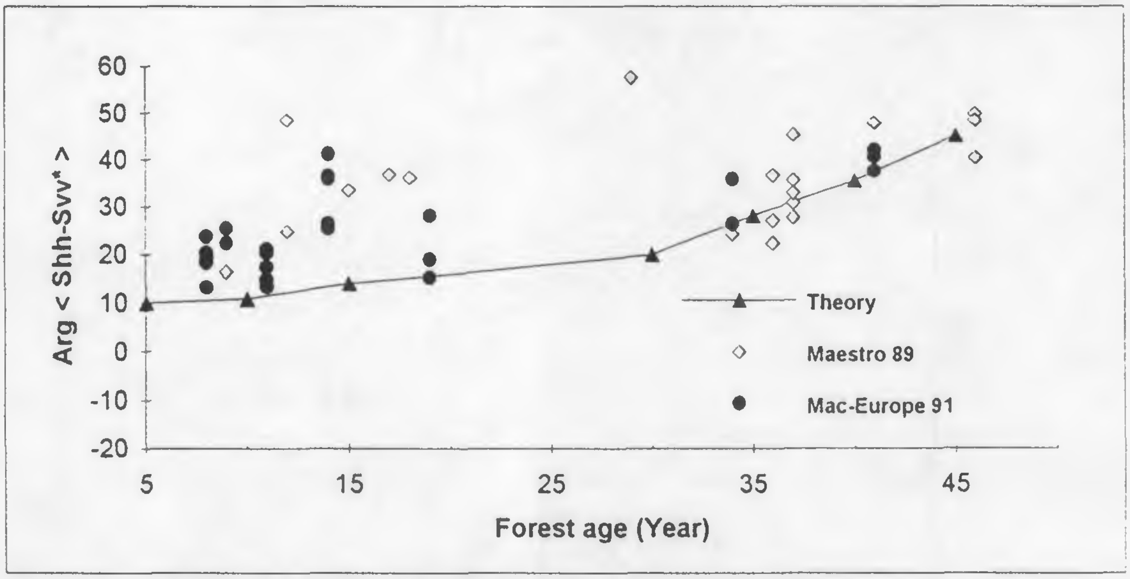

Fig 4 c - Phase of correlation between HH and VV signals for forest stands / P Band

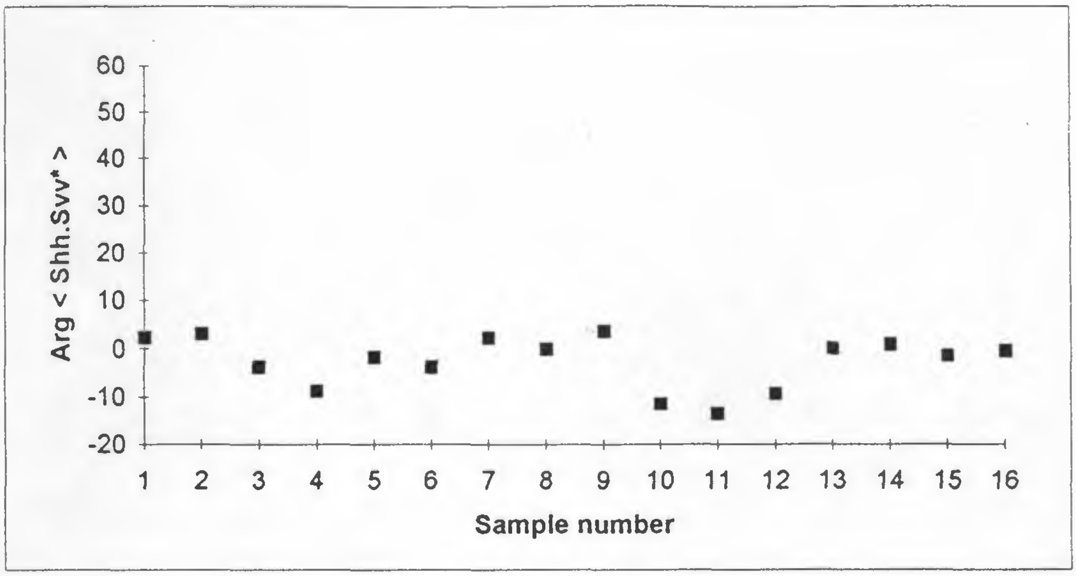

Fig 5-a - Phase of correlation between HH and VV signals at P Band, on clearcut areas.

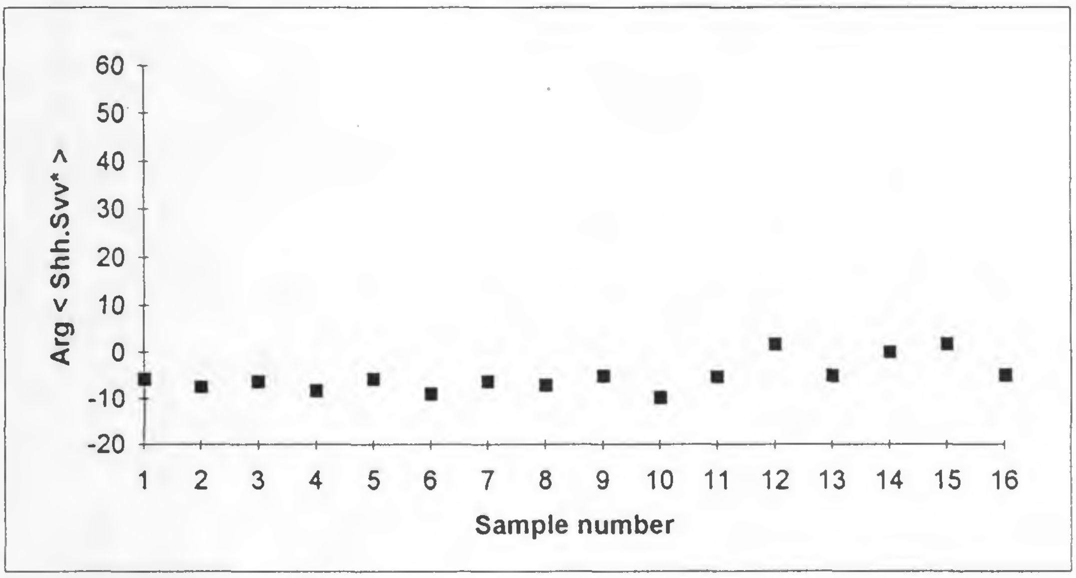

Fig 5-b - Phase of correlation between HH and VV signals at L Band, on clearcut areas.

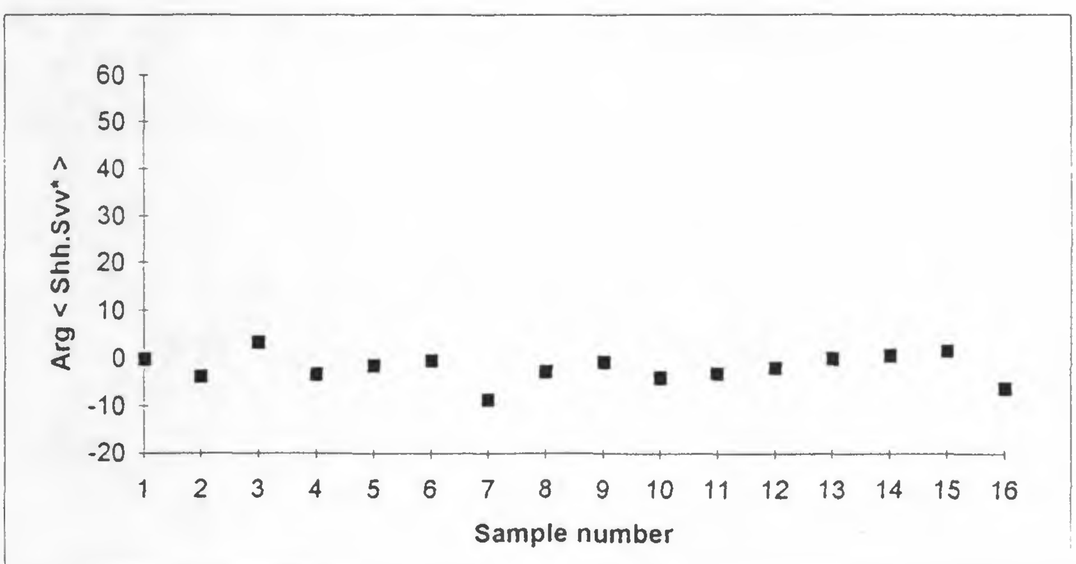

Fig 5-c - Phase of correlation between HH and VV signals at C Band, on clearcut areas.

SAR PROCESSOR CALIBRATION

Session 7

Chair: R.BAMLER, DLR, Germany

ON THE CALIBRATION ALGORITHMS OF X-SAR

Franco NIRCHIO
Agenzia Spaziale Italiana
Centro di Geodesia Spaziale
Matera (Italia)

Massimo BIAGINI
TELESPAZIO S.p.A.
Via Tiburtina, 965
00156-ROMA (Italia)

ABSTRACT

A concise background is given on the algorithms, which are applicable for the radiometric correction and calibration of the data to be acquired during the X SAR experiment. The calibration algorithm of the receiver based on the data included in the header of the High Rate data stream of the instrument and the various ways to make corrections of the antenna boresight angle during post processing are also presented which are to be installed at the Italian Processing & Archiving Facility (I-PAF) in the Centro di Geodesia Spaziale in Matera, Italy.

Keywords: Synthetic Aperture Radar, SIR C, X-SAR, Calibration, Radiometric Correction

1.RADIOMETRIC CORRECTION OF ANTENNA PATTERN AND RANGE

1.1 General Concerns

Conventionally the radar equation gives the received power from a backscattering target. Regarding the Radar Cross Section (RCS) as σ and the target-to-sensor-range dependent term of K'(R), which includes all the system parameters, we obtain Equations 1 and 2, when no noise is present.

$$P_r = K'(R)\sigma \qquad (1)$$

$$K'(R) = P_t G_r \frac{(G\lambda)^2}{(4\pi)^3 R^4} \qquad (2)$$

The RCS of the target in case of an extended image is: $\sigma = \sigma^0 \delta A$, where $\delta A = \delta x \delta R_g$, with the δx resolution in azimuth and δR_g in range for an image pixel.

After the calculation of the pixel value in the SAR image additional terms should be included, to account for the number of samples, which are used in the image pixel synthesis. Thus the power of a pixel is expressed as follows:

$$P_r^I = K'(R)\sigma L N_I^2 W_I, \qquad (3)$$

where L is the number of looks, N_I is the number of samples included in the pixel calculation and W_I is the loss term accounting the losses due to the weighting in the range and azimuth reference functions. $N_I = L_r L_{az}$ with the number of samples in range and azimuth. To find the number of samples in azimuth, we need the length of the radar real-aperture (L_{ap}), the velocity of the SAR platform (v_{sens}) and the pulse repetition frequency (f_p):

$$L_{az} = \frac{\lambda}{L_{ap}} \frac{R}{v_{sens}} f_p \qquad (4)$$

Using the latter dependence of the azimuth weighting function length results in an azimuth resolution which is independent from range, i.e. δx fixed, so in the final SAR image an R^{-2} dependence of the power will be observed because of the R^2 law of the resulting N_I^2.

Finally we can rewrite the full expression of a SAR image pixel power and find the differential RCS of the pixel as:

$$\sigma^0 = \frac{P_r^I}{K'(R) L N_I^2 W_I \,\delta x \delta R_g} \qquad (5)$$

The parameters in Equation 5 are partly flight and sensor data, which are supplied with the input data, or they depend on the processing of the raw data. The latter ones are the weighting function dependent loss and length values, defined by the functions, which are used in the range and azimuth compression.

For a completely calibrated image, using Equations 1 and 2 for the absolute calibration with point targets of known RCS, and using Equations 3-5 the correct sigma nought values are found throughout an entire image.

1.2 Imaging over the EARTH's surface

Figure 1 gives the geometry for imaging over a spherical surface, where γ and η are the boresight angle from nadir and the local angle of incidence at the pixel from zenith, respectively, and Equations 6 and 7 give the necessary links between the individual parameters of the sensor distance from the Earth center (R_c), Earth radius (R_e), the pixel-sensor distance (R) and the bandwidth used in the range-compression of the raw data (B_r).

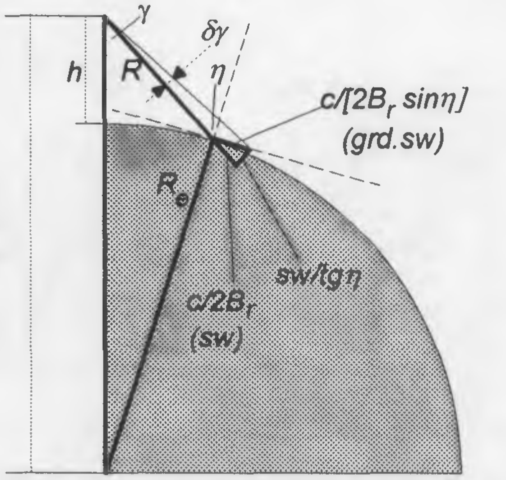

Figure 1. Imaging geometry of X-SAR over the Earth

$$\cos\eta = \frac{R_c^2 - R^2 - R_e^2}{2RR_e} \qquad (6)$$

$$\cos\gamma = \frac{R_c^2 + R^2 - R_e^2}{2RR_c} \qquad (7)$$

Equations 6 and 7 are to be used to evaluate the antenna pattern dependence of the K'(r) term, where the elevation antenna pattern as seen in Figure 2 should be used to solve Equation 5 for a given γ and the corresponding R.

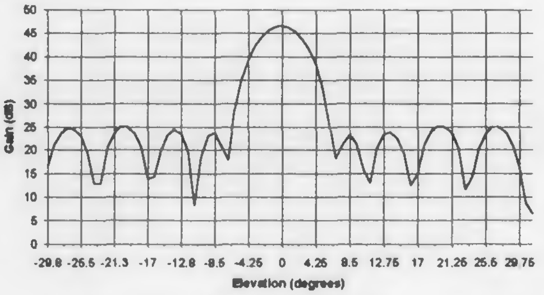

Figure 2 X-SAR antenna elevation-pattern

R has to be expressed as the smaller root of the second order Equation 7, which yelds Equation 8.

$$R = R_c\left[\cos\gamma - \sqrt{\left(\frac{R_e}{R_c}\right)^2 - \sin^2\gamma}\right] \qquad (8)$$

It also should be noted, that any Earth surface model can be used in the evaluation of Equation 8, when the instantaneous Earth radius at the nadir point below the space shuttle (R_c-h) and the same at the investigated pixel (R_e) are known.

To investigate the effect of the changing boresight-angle, the beamwidth taken by the swath projected on the surface should be calculated. From Figure 1 one can see that this angle denoted as $\delta\gamma$ corresponds to the slant range swath (*sw*) according to Equation 9.

$$sw = \delta\gamma \, tg\eta \, R \qquad (9)$$

1.3 Evaluation of the useful data window within a data-take

If the swath-width projected on the ground surface (*grd.sw*) is of interest, one has to account the local angle of incidence (η), also seen in Figure 1, and has to project *sw* on the surface as *grd.sw* of Equation 10.

$$grd.sw = \frac{sw}{\sin\eta} \qquad (10)$$

To find the required number of pixels (*pxl*) covering this swath, the slant extension of the swath (*sw*) should be divided by the spacing of the adjacent pixels in slant range, based on the sampling interval of τ, as Equation 11 shows.

$$pxl = \frac{slt.sw}{c\tau/2} \tag{11}$$

The useful range of the swath is limited by the 3 dB elevation mainlobe of the antenna, and on the other hand a limitation exists due to the fixed data rate, so the number of pixels within the slant swath decreases by increasing *PRF*. The minimum of the resulting two swath values should be regarded as the real swath, and the number of pixels is defined by this lower value.

The previous equations are used in a spreadsheet calculation, and with the existing data for X-SAR at coarse resolution setting, when the sampling rate is *STALO/8*. The resulting beamwidth values are listed and plotted for 4 bit and 6 bit sampling modes in Figure 3. It seems, that for boresight angles below 30 degrees the full swath does not contain useful data due to the widening of the projected swath. Only for angles greater than 30 degrees is expectable a beamwidth around or less than 10 degrees, which matches to the mainlobe of the elevation antenna pattern, which is about 5.5 degree wide, regarding a 3 dB drop from the maximum gain.

The number of pixels in the 4 and 6 bit data take are also tabulated in Table 1, and they vary from 533 to 3024, depending on the variation of the boresight angle of the antenna axis, i.e. the center of the mainlobe, and also on the *PRF*. The latter dependence is apparent only, if the limiation is set by the data rate, when all the received values are within the mainlobe. If the 3 dB mainlobe sets the limitation, the condition is purely geometrical, so the number of pixels within the mainlobe does not depend on the pulse repetition frequency. In this case the two sides of the mainlobe fall out of the range, which is spanned by the slant swath at the maximum data rate.

To find the useful window of pixels in the data-stream, the entire data-window should be positioned so, that the central pixel of each swath data series shall coincide with the backscattered signal coming from the centre of the antenna beam. Thus the data stream covers simmetrically the swath between near and far range, measured in slant direction, though the ground cover is not perfectly simmetrical due to the curved surface. Regarding this position of the data-window, as reference, the start and stop of the window defined by the 3 dB mainlobe of the antenna can be found, measured from the transmission of the radar-pulse.

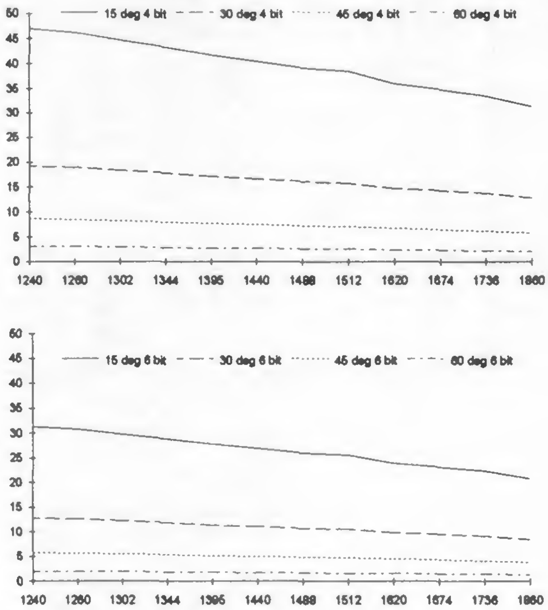

Figure 3 Beamwidth in degrees over *PRF*

2. *RECEIVER CALIBRATION OF X-SAR*

2.1 System Concerns

Figure 4 shows the simplified block-diagram of the X-SAR trasnsceiver. With reference to [4] the error sources are:

A. uncertainties of the high power AMPLIFIER output power

B. transmission path losses and its variation from AMPLIFIER to ANTENNA (TR loss)

C. TX calibration loop with COUPLER+ATTENUATOR loss ambiguities (TX loss)

D. variations of the LOW NOISE Amplifier (LNA) gain

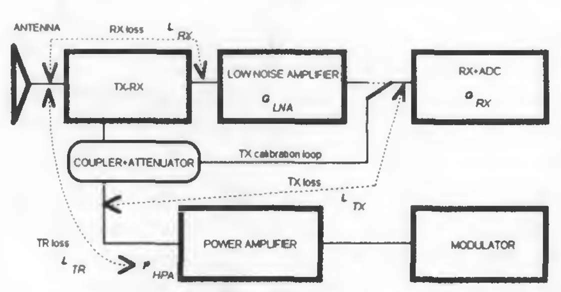

Figure 4 The X-SAR System-blocks

Tau [ns]	c [km/s]	alt [km]	Re [km]	Rcentral [km]	fs [MHz]	Data-rate [Mb/s]	3dB [deg rad]	Pixsp [m]
88.89	300000	255	6500	6755	11.25	44.997	5.505 0.096	13.33333

PXL 4	SW 4	PXL 6	SW 6	Ground Swath [km] (4 bit)				Ground Swath [km] (6 bit)				PRF
[num]	[meters]	[num]	[meters]	15	30	45	60	15	30	45	60	[Hz]
4536	60,484	3024	40,323	26.43	33.43	52.41	67.2	26.43	33.43	52.41	44.8	1240
4464	59,524	2976	39,683	26.43	33.43	52.41	66.14	26.43	33.43	52.41	44.09	1260
4320	57,604	2880	38,402	26.43	33.43	52.41	64	26.43	33.43	52.26	42.67	1302
4185	55,804	2790	37,202	26.43	33.43	52.41	62	26.43	33.43	50.63	41.34	1344
4032	53,763	2688	35,842	26.43	33.43	52.41	59.74	26.43	33.43	48.78	39.82	1395
3906	52,083	2604	34,722	26.43	33.43	52.41	57.87	26.43	33.43	47.25	38.58	1440
3780	50,403	2520	33,602	26.43	33.43	52.41	56	26.43	33.43	45.73	37.34	1488
3720	49,603	2480	33,069	26.43	33.43	52.41	55.11	26.43	33.43	45	36.74	1512
3472	46,296	2315	30,864	26.43	33.43	52.41	51.44	26.43	33.43	42	34.29	1620
3360	44,803	2240	29,869	26.43	33.43	52.41	49.78	26.43	33.43	40.65	33.19	1674
3240	43,203	2160	28,802	26.43	33.43	52.41	48	26.43	33.43	39.19	32	1736
3024	40,323	2016	26,882	26.43	33.43	52.41	44.8	26.43	33.43	36.58	29.87	1860

									PRF [Hz]
Bores [deg]	15	30	45	60	15	30	45	60	
Bores [rad]	0.26	0.52	0.79	1.05	0.26	0.52	0.79	1.05	
Slant-r [km]	264.4	296.4	368	544.2	264.4	296.4	368	544.2	
Incid [cos]	0.963	0.854	0.678	0.436	0.963	0.854	0.678	0.436	
Incid [deg]	15.6	31.3	47.3	64.2	15.6	31.3	47.3	64.2	
Beamwidth [deg]>	46.94	19.22	8.692	3.084	31.29	12.82	5.794	2.056	1240
>	46.19	18.92	8.554	3.035	30.8	12.61	5.702	2.023	1260
>	44.7	18.31	8.278	2.937	29.8	12.21	5.519	1.958	1302
>	43.31	17.74	8.019	2.845	28.87	11.82	5.346	1.897	1344
>	41.72	17.09	7.726	2.741	27.82	11.39	5.151	1.828	1395
>	40.42	16.55	7.485	2.656	26.95	11.04	4.99	1.77	1440
>	39.12	16.02	7.243	2.57	26.08	10.68	4.829	1.713	1488
>	38.5	15.77	7.128	2.529	25.66	10.51	4.752	1.686	1512
>	35.93	14.72	6.653	2.361	23.95	9.81	4.435	1.574	1620
>	34.77	14.24	6.438	2.284	23.18	9.494	4.292	1.523	1674
>	33.53	13.73	6.208	2.203	22.35	9.155	4.139	1.469	1736
>	31.29	12.82	5.794	2.056	20.86	8.544	3.863	1.371	1860
Near Slant [km]	261.2	288.3	350.2	496.1	261.2	288.3	350.2	496.1	
Far Slant [km]	268.3	305.7	388.8	605.8	268.3	305.7	388.8	605.8	
Slant Swath [km]	7.11	17.37	38.51	109.7	7.11	17.37	38.51	109.7	
3 dB grd-sw [km]	26.43	33.43	52.41	121.9	26.43	33.43	52.41	121.9	
SWATH PIXELS	533	1303	2888	8225	533	1303	2888	8225	
Pixels within swath of 3 dB mainlobe limit (above) and 4 & 6 bit beam and data rate limit (below)									PRF [Hz]
Useful pixels	533	1303	2888	4536	533	1303	2888	3024	1240
	533	1303	2888	4464	533	1303	2888	2976	1260
	533	1303	2888	4320	533	1303	2880	2880	1302
	533	1303	2888	4185	533	1303	2790	2790	1344
	533	1303	2888	4032	533	1303	2688	2688	1395
	533	1303	2888	3906	533	1303	2604	2604	1440
	533	1303	2888	3780	533	1303	2520	2520	1488
	533	1303	2888	3720	533	1303	2480	2480	1512
	533	1303	2888	3472	533	1303	2315	2315	1620
	533	1303	2888	3360	533	1303	2240	2240	1674
	533	1303	2888	3240	533	1303	2160	2160	1736
	533	1303	2888	3024	533	1303	2016	2016	1860
	Pixels (4 bit)				Pixels (6 bit)				

Table 1 Calculations for the useful window size

Terms A and C are included in the TX calibration procedure, which means, that at 60 dB mid gain value one-second-long calibration raw-data are recorded before and after each data take. This yelds a term including the product of the output power of the transmitter and the receiver gain (LNA excluded). Term B has an approximate value of 0.2 dB, with a slight temperature dependence (from 0.11 to 0.32 dB). Term D has an individual temperature dependence look-up-table. Some of these temperature dependent terms are listed in Table 2 and are plotted in Figure 5.

The overall system budget is discussed in an estimation as given in Table 3. For the given 255 km flight altitude an approximate 187 dB loss is assumed, including all the terms of the radar equation, except the target RCS and receiver gain.

Table 2 Temperature Dependence of Receiver

Temp deg C	TR loss dB	TX loss dB	RX loss dB	G(LNA) dB	Offset dB
-10	0.11	-0.41	0.91	---	↓
0	0.14	-0.37	0.98	2.3	↓
10	0.16	-0.34	1.05	2.2	↓
20	0.19	-0.3	1.12	1.8	↓
30	0.22	-0.27	1.17	1.7	↓
40	0.25	-0.23	1.22	1.5	↓
50	0.28	-0.20	1.27	1.3	↓
60	0.31	-0.17	1.32	1.2	↓
65	0.32	-0.15	1.34	---	↓
	TX loss and LNA gain are offset				30

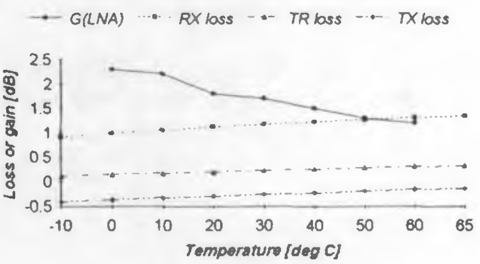

Figure 5 Temperature dependence of receiver

If the illuminated area is approximated from the maximum antenna gain, and a -10dB differential RCS is observed, the receiver output power after 80+30dB amplification will be approximately 4 mW.

Table 3 System budget estimation of X-SAR

Wavelength		0.03 *m*
Antenna gain		47 *dB*
Range		280 *km*
S antenna & space		-187 *dB*
Illum.area.		72.94 *dBdBm*^{2}
Cal power (ADC)	*saturation*	10 *dBmW*
Data take power		6 *dBmW*
GRX(cal)		60 *dB*
GRX(take)		50 *dB*
LTR(take)	(30°)	0.22 *dB*
LRX(take)	(30°)	1.12 *dB*
GLNA(take)	(30°)	31.7 *dB*
LTX(cal)	(30°)	100 *dB*
sigma		63.0 *dBm*^{2}
sigma nought		-10.0 *dB*

2.2. Correction of the Individual Terms

The two major variations, aroused by the LNA temperature dependence and the whole MODULATOR-AMPLIFIER-COUPLER-RECEIVER loop can be corrected based on the amplitude detection of the RAW data from the TX calibration data take.

Given an amplitude value detected from the TX calibration raw data at a certain temperature of T_{TX} during the calibration period, which utilizes the TX loop the total power at the detector input is:

$$P_{RX}^{CALTX} = \frac{P_{HPA}\left(T_{HPA}^{CALTX}\right) G_{RX}\left(T_{RX}^{CALTX}\right)}{L_{TX}\left(T_{TX}^{CALTX}\right)} \tag{12}$$

At the regular measurement data take period another temperature set is supposed to be in effect, and the signal route is also different:

$$P_{RX}^{TAKE} = \frac{P_{HPA}\left(T_{HPA}^{TAKE}\right) G_{LNA}\left(T_{LNA}^{TAKE}\right) G_{RX}\left(T_{RX}^{TAKE}\right)}{L_{TR}\left(T_{TR}^{TAKE}\right) L_{RX}\left(T_{RX}^{TAKE}\right)} S_{ANT\&SPACE}^{TAKE}\, \sigma_{target} \tag{13}$$

Finally from Equation 1 and the necessary temperature dependence look-up tables the target RCS will be:

$$\sigma_{target} = \frac{P_{RX}^{TAKE}}{P_{RX}^{CALTX}} \frac{P_{HPA}\left(T_{HPA}^{CALTX}\right)}{P_{HPA}\left(T_{HPA}^{TAKE}\right)} \frac{G_{RX}\left(T_{RX}^{CALTX}\right)}{G_{RX}\left(T_{RX}^{TAKE}\right)} \cdots$$
$$\cdots \frac{L_{TR}\left(T_{TR}^{TAKE}\right) L_{RX}\left(T_{RX}^{TAKE}\right)}{G_{LNA}\left(T_{LNA}^{TAKE}\right) L_{TX}\left(T_{TX}^{CALTX}\right) S_{ANT\&SPACE}^{TAKE}} \tag{14}$$

In Equation 14 the G and L parameters are the corresponding gain and loss values, obtained from the temperature dependence of the LNA and SAW device etc., and these values are read from the look up tables of these parameters, based on the housekeeping temperature data, stored in the RAW DATA header of the SAR data stream.

On the right hand side of Equation 14 the first three terms express the correction of those parameters, which are in the TX calibration loop and data TAKE as well. In the last term each parameter is accounted only for either TX calibration or data TAKE. The S term expresses the antenna and free space effects, as $(G\lambda)^2/(4\pi)^3/R^4/L_{atmosphere}$, which means, that the corrections due to the atmosphere, antenna and range can be performed by accounting this term. Note, that Equation 14 expresses the RCS, so a different R correction can be required, when evaluating the differential cross section on an image, when the pixel area also counts.

3. BORESIGHT-ANGLE CORRECTION

3.1. Available information

For the estimation and correction of the X-SAR antenna boresight angle, the High Rate data header contains the shuttle state and attitude data and the antenna tilt angle of the SIR-C antenna. Also is apriori knowledge of the antenna pattern.

The images of interest for boresight angle investigaton are the Amazonian rain forest areas, where a uniform sigma nought distribution is expected, and those areas, where more point targets with uniform or known radar cross section are available, e.g. corner reflectors and active transponders.

3.2. Applicable algorithms

One group of these algorithms are based on the acquired images. Without the antenna pattern correction, the images hold the boresight direction information, which can be extracted by using either the:

- **rain forest data**, by fitting the apriori known antenna pattern to the image, obtained by imaging an area of extended radar target, with uniform σ^0 distribution, or using

- **point target areas**, where a similar fitting of the antenna pattern can be carried out, if the point targets have the same *RCS* values, all the distinct *RCS* values are apriori known. The positions of these points shall be of different boresight directions, and the boresight angle of the points should be extracted from the image or given by the ground truth measurements of the positions of the calibrating point targets (GPS reading).

If there are ground based microwave receivers available, and they are deployed in different boresight directions, their recordings will show the one-way signal strength, measured at the radar target, and a similar estimation can be done, based on the antenna pattern of the X-SAR.

4. CONCLUSIONS

The presented algorithms can be used in the radiometric correction and range, antenna and boresight calibration of the images obtained by the X-SAR.

These algorithms shall use a priori information, such as the navigation data in the header of the High Rate data tapes, and calibration scenes, among which the Amazonian rain forest areas and test sites with calibration targets are found.

The presented algorithms are of more general use, in other similar Synthetic Aperture Radar systems.

5. ACKNOWLEDGEMENTS

The authors wish to express their thanks to Mr.Manfred Zink and Mr.Richard Bamler for their cooperation concerning the X-SAR project. Also special thanks to Mr.Sandor Mihaly, at the Department of Microwave Telecom-municatiions, Technical University of Budapest, for his contribution regarding the analytical aspects of the calibration problems.

The presented algorithms have been investigated in the framework of the Italian PAF activities, the processor that will generate the X-SAR products is developped under the contract between Italian Space Agency and TELESPAZIO.

6. REFERENCES

1. Skolnik 1980, Introduction to Radar Systems, McGraw Hill.

2. T.Freeman, J.Curlander 1989, Radiometric Correction and Calibration of SAR images, Photogrammetric Eng. & Remote Sensing Society Journal, 1989

3. S.Mihály, R.Seller, B.Farkas, I.Bozsóki 1992, X-band Scatterometry in SLAR Image Evaluation, Proc. IGARSS, Espoo, Finland, IEEE cat n 91CH2971-0, 613-616.

4. M.Zink 1993, X-SAR Calibration Plan, Part 1, System Analysis and Test Results, DLR, Oberpfaffenhofen, Germany, 16p.

5. R.Bamler 1991, Proposal for calibration of X-SAR products, 15.10.91.

6. Space segment / Ground segment interface specification, Doc. SC-2042-1200-DS/06, 10.08.90, Dornier.

7. Space segment requirements, Doc. SC-2042-1200-DS/01, 05.10.87, Dornier.

CALIBRATION OF THE DLR/INPE SAR PROCESSOR FOR ERS-1 INTERFEROMETRY

José C. Mura
INPE
12201 São José dos Campos, Brasil

João R. Moreira
DLR NE-HF
82234 Oberpfaffenhofen, Germany

Abstract. A SAR Processor for airborne and spaceborne plataforms is presented. A bidimensional azimuth reference function and a hybrid correlation algorithm is used in order to correct the range migration during the azimuth compression. The interferometic capability of this SAR Processor is evaluated using two scenes of the ERS-1 System and the results are presented.

1 Introduction

This work is based in the results obtained from the joint work carried out in cooperation with the Institute for Radio Frequency Technology (NE-HF) of DLR and INPE, suported by the agreement between DLR (German Aerospace Research Establishment) and INPE (Brazilian Institute for Space Research) for space research. A SAR Processor architecture for airborne (E-SAR/DLR) and spaceborne (ERS-1) plataforms is presented. This SAR Processor is based on a hybrid correlation algorithm, and look filters are used to increase its performance. The Spaceborne SAR Processor is used to generate complex images from ERS-1, for interferometric evaluation. The methodology to generate a terrain elevation map and the results obtained are presented.

2 INPE/DLR SAR Processor

A SAR system is a side-looking radar, with time-coherence from pulse to pulse. The discrimation in range direction (across track) is accomplished by a short Frequency Modulated pulse, of period τ, called "chirp". In order to increase the resolution in range direction this pulse has a large time-bandwidth product, τB_r, where B_r is the bandwidth of the system pulse. In this case the range resolution, δ_r, obtained after the pulse compression is $\delta_r = c/2B_r$, where c is the speed of the light. The discrimination in azimuth direction (along track) is accomplished by a coherent integration of the radar return from a target point at a slant range r. The coherent integration depends on the phase history of the point, given by
$\theta(t) = -2r(t)/\lambda$, where 't' is the time along track, r(t) is the slant range on t and λ is the radar wavelength. The attainable resolution in azimuth direction, δ_a is $\delta_a = 1/B_D$, where B_D is the Doppler spectrum bandwidth. The Doppler spectrum is given directly by viewing a point target from different angles as the plataform moves. A SAR Processor consists of carring out a range compression of the raw radar signal and an azimuth compression (coherent integration) of the data in the azimuth direction, in order to obtain a high range and azimuth resolution respectively.

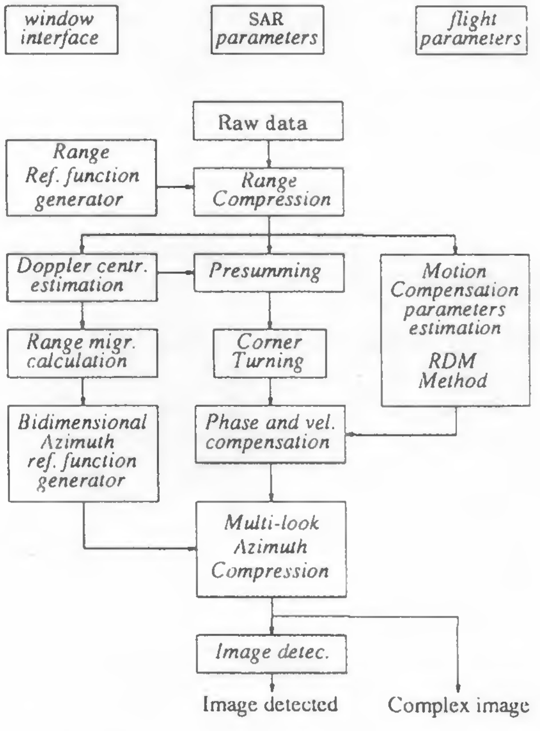

Figure 1: Block diagram of the INPE/DLR SAR Processor

2.1 E-SAR system

The SAR Processor for the E-SAR system was implemented in C and C++, and uses window interfaces based in motif for use in wokstations. These interfaces allow the operator to load the SAR and scene parameters, and also to check the processor status during the processing. The block diagram of the SAR Processor for E-SAR system is shown in Figure (1).

In this Processor the raw data are first range compressed using a frequency domain fast correlation. A range reference function is generated from the chirp pulse parameters and correlated with the raw data to make the range compression.

The clutterlock technique is used to estimate de Doppler spectrum shift due to the errors in the antenna pointing (squint angle not zero). This frequency shift, called Doppler Centroid Frequency, f_{Dc}, is obtained from the range compressed data.

The phase history of a point target is not ideal due to the motion errors. The motion compensation parameters have to be calculated to conform with the data and to allow an accurate coherent integration of these data (azimuth compression). The Reflectivity Displacement Method (RDM) proposed by [1] is used to calculated the velocity variation of the aircraft and the variation of the phase, due to the other motion errors. These parameters are calculated from the range compressed data.

The range compressed data are low-pass filtered in azimuth direction (presumming), through a moving average, in order to decrease the Doppler bandwidth, B_D, for an attainable azimuth resolution.

After the pressuming the array of data has to be transposed to make the access to the data in azimuth direction easier, this process is called "Corner Turning".

The array of data arranged in azimuth lines has to be motion compensated, for the azimuth compression. Each azimuth line is ressampled according to the variation of the velocity, to compensate de PRF constant, and the Doppler spectrum is shifted according to the variation of the phase. After this processing step the data can be compressed in azimuth direction.

To avoid the range migration correction of the raw data, the two dimensional azimuth referencce function is generated, with the ideal range migration and the ideal phase history.

A hybrid correlation algorithm is used for the azimuth compression. This algorithm uses a frequency domain fast correlation in azimuth direction, with a time domain colvolver operation in range dimension, in order to handle the finite amount of dispersion of the azimuth reference function, due to the range migration.

The multi-look azimuth compression is the most intensive step of a SAR Processor, mainly due to the length of the FFTs to transform the data in frequency domain. In order to decrease the computation time of this step, data are filtered centered in each look-frequency and sampled. The resulting data can be tranformed in frequency domain using smaller FFTs.

After the look somation the complex image can be detected using a linear or square detection.

Due to some different characteristics of the original E-SAR System Motion Compensation Processor of the DLR, such as, look-filters, corner turning and motion compensation after pressuming, this SAR Processor can process a scene in the same condition about 30% faster than the original, suplying the same image quality. The Figure (2) shows a E-SAR System 8 looks image of Munich (Germany) processed by INPE/SAR Processor, with 2.0 m of the range resolution and 3.0 m of the azimuth resolution.

Figure 2: E-SAR System image of Munich

2.2 ERS-1 System

The SAR Processor for ERS-1 data has the same structure of the E-SAR System Processor, without the modules of Presumming, Motion Compensation and Phase and Velocity Compensation . For the ERS-1 System the processor does not need motion compensation due to de stability of the plataform, and the Doppler bandwidth is small enough that the Presumming step can be removed.

The same hybrid correlation algorithm, to compensate the range migration, is used in this processor to make the azimuth compression of the data. Figure (3) shows an image of Flevoland (Holand) processed by this Processor with 8 looks and about 25.0 m by 25.0 m of range and azimuth resolution respectively.

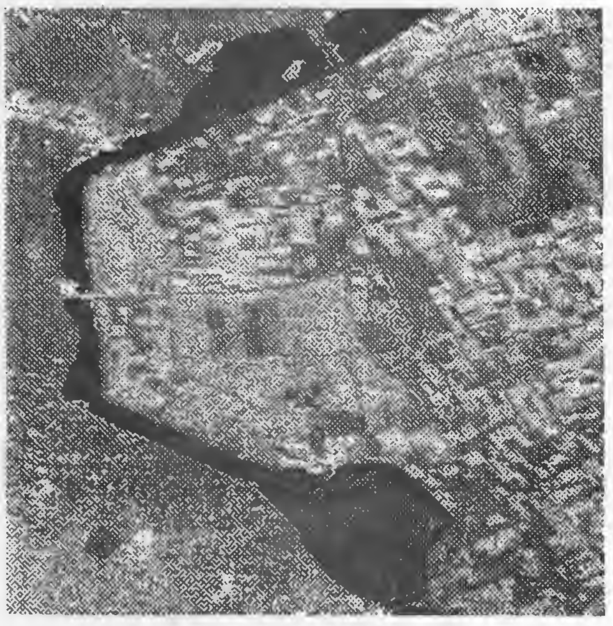

Figure 3: ERS-1 image of Flevoland

3 Interferometric capabilities for ERS-1 System

The INPE/DLR SAR Processor for ERS-1 data has been demonstrated to be a good phase preserving processor during the simulations, carried out with simulated point target and small squint angle. In order to verify its use for interferometry aplication two ERS-1 images were processed and evaluated.

3.1 Two pass interferometry

Interferometric radar image has been used to generate topographic mapping. An interferometric image is formed by relating the signals from two separated sensors (antennas). The separation of the two sensors (antennas) is called "baseline". The baseline can be achieved by using two antennas in the same platform, one pass interferometry, or using one antenna, two pass inteferometry. In the last case, the radar illuminates a given surface at two different times but with nearly the same viewing geometry.

In this work the two pass case to obtain the terrain elevation is used . The two images (Sardegna - Italy) were obtained with six days interval.

The phase of the interferometric image is related to the terrain elevation, but unfortunately this phase is represented in a 2π modulus. To estimate the height of the terrain it is necessary transform this relative phase (modulus 2π) to the absolute phase. The phase transformation is called "phase unwrapping". After estimating the absolute phase it is possible to calculate the terrain elevation.

Figure (4) shows the interferometric radar geometry, where S_1 and S_2 are the two sensors (antennas), H the altitute of the sensor 1, r the slant range, Δr the slant range difference, B the baseline, θ the look angle, α the baseline angle and z the height of the terrain.

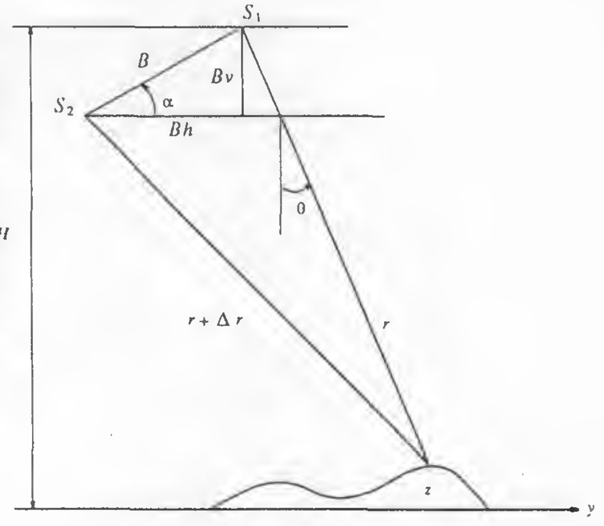

Figure 4: Interferometric radar geometry

The relationships for height estimation are given by the followings equations: (1) for phase difference estimation ($\Delta\phi$), (2) for baseline angle determination (α), (3) to get the look angle (θ), (4) to estimate the height (z).

$$\Delta\phi = \frac{4\pi}{\lambda}\Delta r \quad (1)$$

$$\alpha = arctan(\frac{Bv}{Bh}) \quad (2)$$

$$sin(\theta - \alpha) = \frac{(r + \Delta r)^2 - r^2 - B^2}{2rB} \quad (3)$$

$$z = H - r\cos\theta \quad (4)$$

3.2 Processing steps

The processing levels to estimate the terrain elevation, using SAR interferometry, are shown in the Figure (5). The processing consists of the phase estimation, baseline determination and the terrain altitude determination.

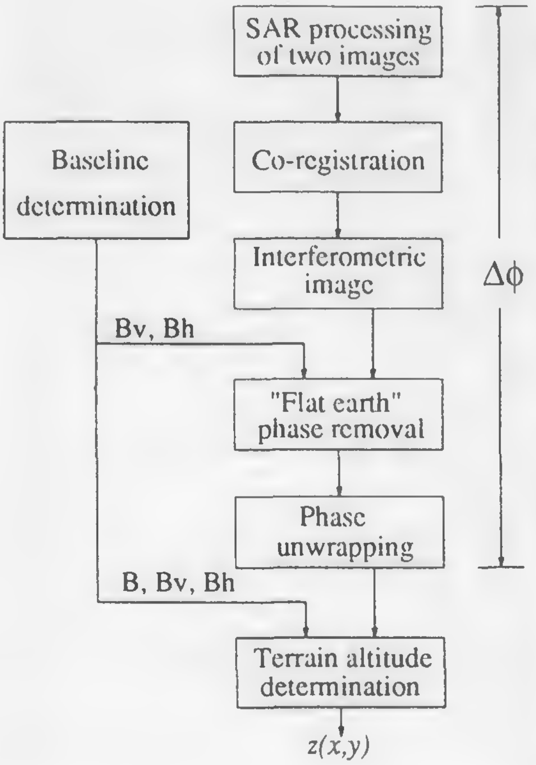

Figure 5: SAR inferferometry processing steps

Figure 6: ERS–1 one look image of Uzurlei region (Sardegna - Italy)

3.2.1 SAR Processing

The first step consists of the SAR processing, where the two complex images are generated. The complex images are necessary to obtain the phase information. Figure (6) shows the first one look ERS–1 image processed, of the Uzurlei region (Sardegna - Italy)

3.2.2 Corregistration

Because the two images were obtained in different dates they need to be corregistrated. To minimize the phase noise it is necessary to make a good corregistration. In this work first the coarse offset between the two images using the cross correlation peak is calculated , following by a fine offset with 0.12 pixel accuracy, using the maximun spectrum method.

The fine offsets in the whole image vary in range and azimuth. Two linear polinomials for range and azimuth direction are used to resample the two images by a quadratic interpolation.

3.2.3 Interferometric image

An interferometic image is generated by multiplying the first image with the complex conjugate of the second. In order to minimize the phase variance, the interferometric image is filtered in range and azimuth direction using a box filter with two points in range and ten points in azimuth. In this case the interferometric image used has a spatial resolution of approximately 40 meters in range and 40 meters in the azimuth direction.

3.2.4 Flat earth phase removal

In order to facilitate the phase unwrapping, the phase due to the flat earth is removed. Because this phase component does not have any information about the terrain elevation, it can be removed. Figure (7) show the interferogram used to estimate the terrain elevation.

3.2.5 Phase unwrapping

The phase of the interferometric image (interferogram) is represented in a 2π modulus. The interferogram represents the phase difference due to the terrain elevation, the interferogram looking like waves called "fringe". To estimate the height of a certain point it is necessary to know the absolute phase value of this point. The absolute phase value is recovered from the relative phase. When there are noises in the

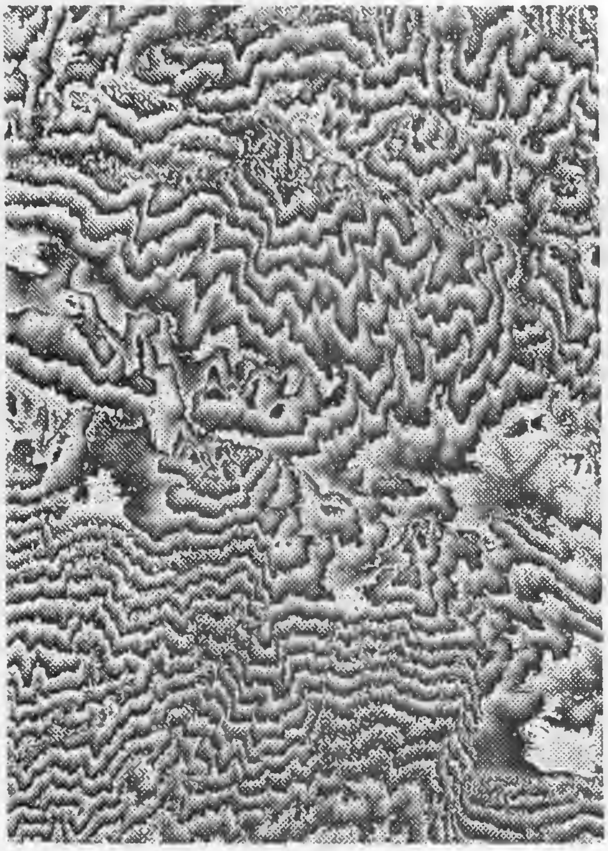

Figure 7: Interferogram

Figure 8: Cut lines to avoid the propagation error

phase, caused by termal noise, speckle noise, SAR processing errors, time decorrelation, baseline decorrelation and layover efects, it can be very difficult or even impossible to get the absolute phase. In this case propagation errors can occur.

In order to avoid the propagation errors during the phase unwrapping, the "residues method" [Goldstein et.al. (1988)] is used. This method identifies the points where there are phase noises (residues) and warning the phase unwrapping algorithms (cut lines) to avoid these points. Figure (8) shows the cut lines generated to avoid the propagation error.

3.2.6 Baseline determination

In the two pass case, the baseline is not fixed and needs to be determinated. To determine the baseline and its vertical and horizontal components, the state vector positions of the satellite are used as well as the information of the SAR processing offset and azimuth offset between the two images. For the two images used the baseline estimated was 144.73 m, 10.76 m and 143.73 m for the vertical and horizontal components respectively.

3.2.7 Terrain elevation determination

The terrain elevation is determined from the absolute phase obtained, and the baseline determinated using equations (1), (2),(3) and (4).

Figure (9) shows the 3 dimensional representation of the terrain elevation of the Urzulei region in the Sardegna island (Italy).

4 Conclusion

The INPE/DLR SAR Processor has proved to be very flexible, fast and able to handle data from different SAR Systems. The processor has a high phase fidelity for images with small squint angle. The results for interferometry proved to be good. Unfortunately is was not possible to check how accurate the elevation map obtained of the Uzurlei region (Sardegna - Italy) was, due to the fact that the local DTM was not available.

5 Reference

[1] J. R. Moreira, Estimating the residual error of the reflectivity displacement method for aicraft motion error extraction from SAR raw data, *Proc.*

Int. Radar Conf., (1990) 70–75.
[2] R. M. Goldstein, H. A. Zebker and C. Werner, Satellite radar interferometry: two-dimensional phase unwrapping, *Radio Sci.*, **23** (1988) 713–720.

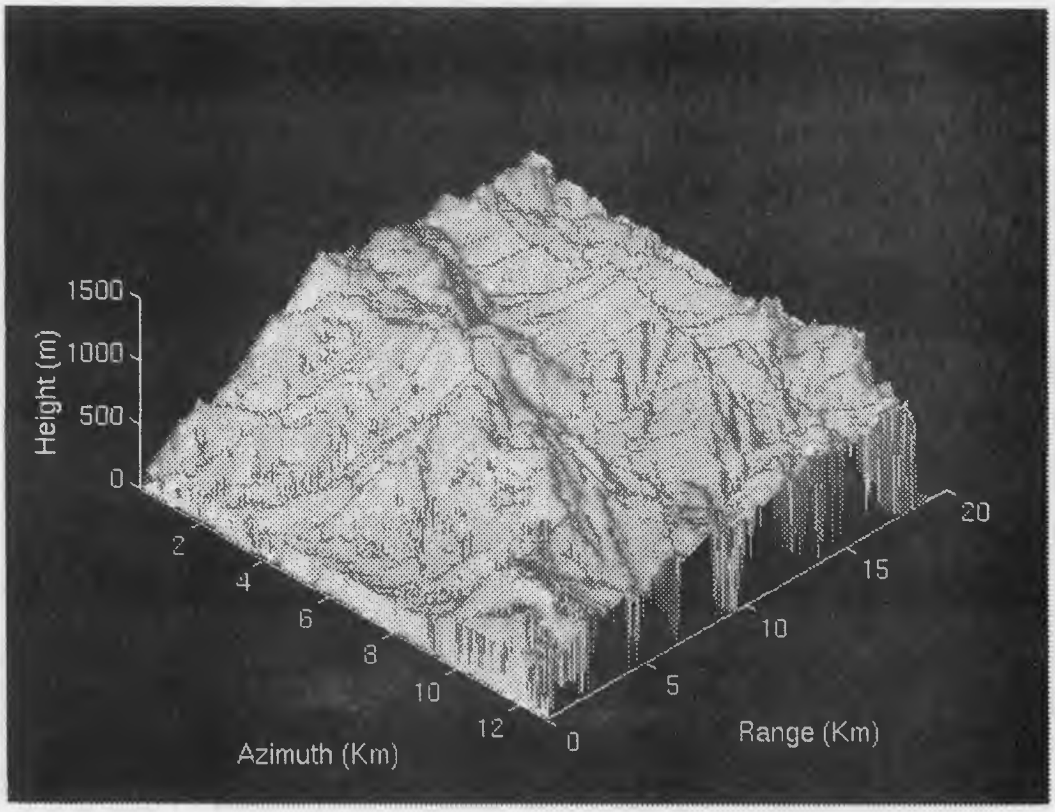

Figure 9: 3D elevation map of the Uzurlei region

ESA WPP-048

SAR CALIBRATION WORKSHOP

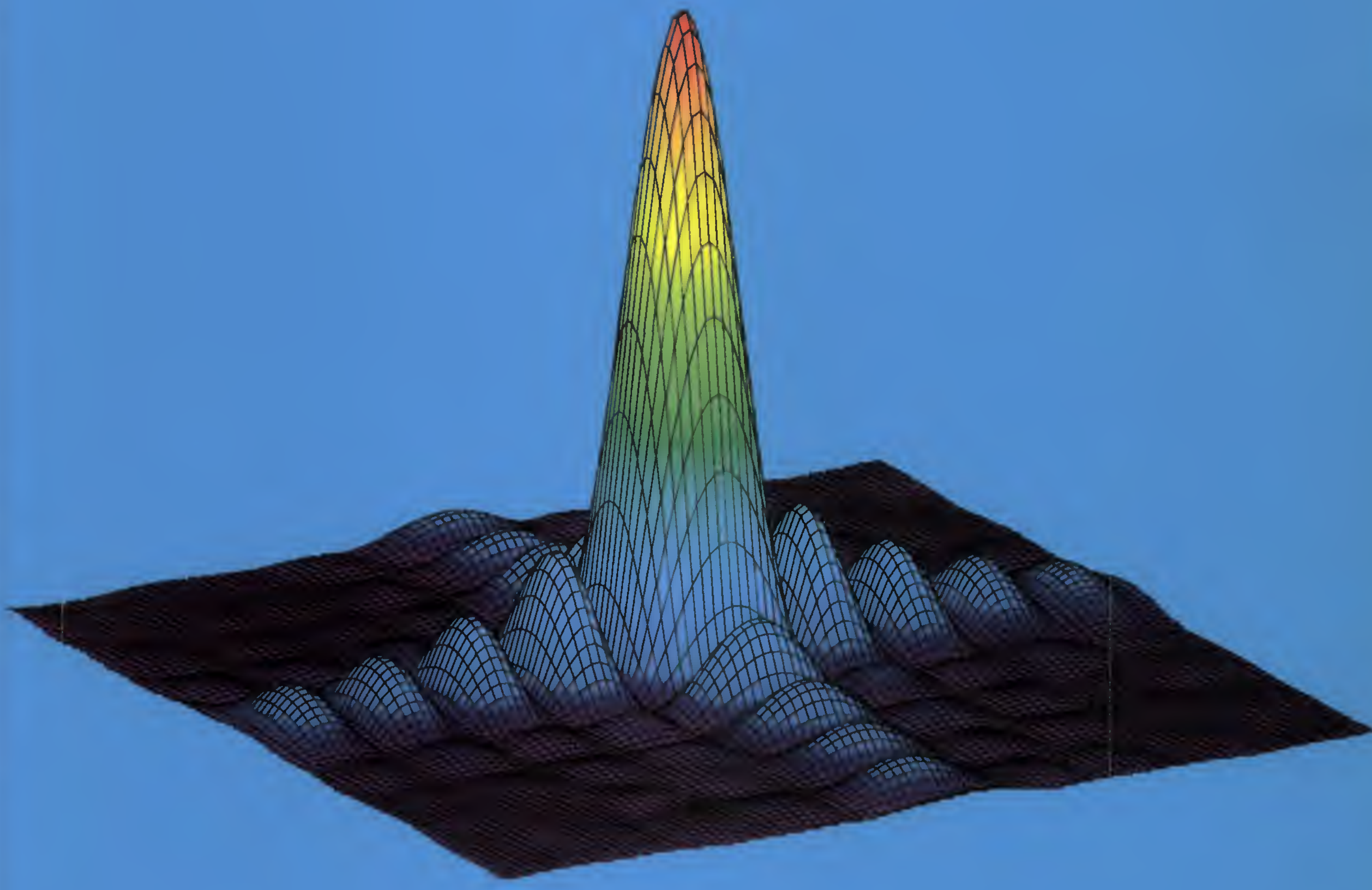

CEOS CALIBRATION/VALIDATION WORKING GROUP
SAR CALIBRATION SUB-GROUP

20 - 24 SEPTEMBER 1993
ESTEC, NOORDWIJK, THE NETHERLANDS

esa
european space agency

NOISE CALIBRATION OF ERS−1 SAR PRODUCTS

M. Eineder, R.Bamler

German Aerospace Research Establishment (DLR)

German Remote Sensing Data Center

Oberpfaffenhofen

P.O. Box 1116

82230 Wessling, Germany

Tel.: +49−8153−28−1396, FAX: +49−8153−1446

ABSTRACT

This paper gives guidelines to estimate the thermal noise component in ERS−1 SAR images processed at the German Processing and Archiving Facility D−PAF. Simulated noise data are used to characterize the noise gain of the processing chain. The analog digital converter (ADC) influence on the recording of noise and of SAR signals is investigated. The results are verified using a low backscatter ERS−1 scene. The history of ERS−1 thermal noise power since launch is presented.

1. INTRODUCTION

Like any SAR images ERS−1 images carry a thermal noise component essentially caused by the receiver electronics. To allow an estimation of the noise power the ERS−1 sensor records some lines of data with the transmitter turned off at the begin and at the end of an imaging sequence. Due to the different spectral properties of the reflected SAR signal and the noise, the processor calibration constant does not hold for noise data. Instead the noise gain of the processing chain has to be determined separately.

Together with every processed scene the Verification Mode Processor (VMP) used at D−PAF analyses the recorded noise data from the begin of the imaging sequence. The analysis is performed using the first activities of the SAR processor i.e. raw data correction, range compression and chirp power normalization. The average power of the 'compressed' noise lines is annotated in the image product. Note however, that this number is not yet the noise floor in the image as the image data encounters additional scaling, filtering and resampling operations. The relationship between the processor measured noise power and the actual noise power in the image is given by the processor noise gain K_N.

At D−PAF the processor noise gain for different products was determined by feeding simulated noise data to the processor's raw data input and analyzing the processed image.

To get an idea about the variation of the ERS−1 noise power since launch, the annotation data of all scenes processed at D−PAF were analyzed. The results allow noise calibration even on products, where no noise measurements are available.

2. PRELIMINARIES

The VMP uses several scaling factors during processing to keep the signal amplitude within the dynamic range of internal data formats. Those scaling factors or gains are tuned in a way that normal image data are well quantized and the ESA transponders deployed at Flevoland used for radiometric calibration are not clipped (See [2], [3]). The gains are constant for all D–PAF products processed after September 1st, 1992.

The following VMP gains are used for PRI and SLC products:

	RC_gain	Az_FFT_gain	AC_gain
PRI	1.175	0.02	32.0
SLC	1.175	0.02	6.21

For the measurements the **range spread compensation** (R^{-3}) and the **antenna elevation pattern correction** have been switched **off** for PRI (and of course for SLC) to make K_N constant of range.

The VMP compensates drifts of the ERS–1 transmitter power during range compression. This is done by normalizing the compression chirp's power to the inverse power of the chirp replica rather than to unity. This compensation method makes the image power independent of the replica power but the noise power gain of range compression is then inverse proportional to the replica power. Therefore all measurement results depend on the current replica power (annotated in field 166 of the VMP product header) . The replica power used as a reference for the measurements from Chapter 4 was

$$\boxed{P_{REP,\,ref} = 182046.352}$$

The noise power level depends on the setting of the satellite's receiver gain. The measurements are valid for the normal gain code 15.

Depending on the way the azimuth compression filters are normalized, the processor's noise gain may depend on the pulse repetition frequency PRF. The measurements are made with PRF = 1680 Hz and are valid for all current D–PAF products since their PRFs vary only between 1660Hz and 1680Hz.

3. SYSTEM AND MEASUREMENT MODEL

3.1 Definition of Processor Noise Gain

In a noise–only measurement receiver noise of power N passes the ADC onboard ERS–1 and is recorded in 5 bit / 5 bit representation. The power of the quantized noise be denoted by $N_{5/5}$. The ICAL module of the VMP performs a range compression of the noise lines and estimates the noise power per sample N_{CAL}.

In normal imaging mode signal and noise are recorded in 5 bit / 5 bit quantization. After processing the image noise power per sample is the unknown quantity N_{PRI} or N_{SLC}. The **processor noise gain** is defined as

$$K_N := \frac{N_{PRI/SLC}}{N_{CAL}}. \qquad [1]$$

Note that the range compression of ICAL also includes the power normalization according to $1/P_{REP}$. Hence,

$$N_{CAL} \propto \frac{N_{5/5}}{P_{REP}}\,. \qquad [2]$$

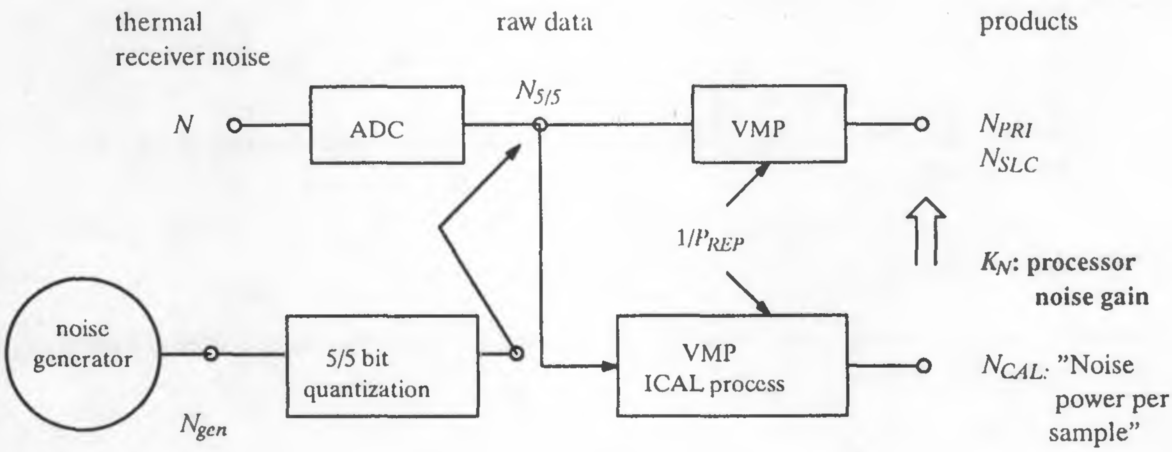

Figure 1: *Signal flow of thermal noise and of synthetic noise*

3.2 Noise Gain Measurement Procedure

For measuring K_N circular Gaussian noise sequences of different variances have been generated, quantized to 5 bit / 5 bit and injected into the VMP at the raw data stage. This noise sequences have been first analyzed by ICAL giving values for N_{CAL} and then processed. The image noise powers were finally measured from the PRI and SLC products. Measurement areas were 300 x 300 samples.

Since both N_{CAL} and N_{image} are measured after range compression, the measurement method is valid if the shape of power density spectrum (PDS) of thermal noise and of simulated noise are equal within the compression chirp's bandwidth. Indeed the typical noise PDS was found to be 'white' in this area.

4. MEASUREMENT RESULTS

The following table summarizes the results of the noise–only measurements:

N_{gen}	$N_{5/5}$	N_{CAL}	N_{PRI}	N_{SLC}	$K_{N,PRI}$	$K_{N,SLC}$
8.00	8.17	15.044	7464	767	496.1	51.0
16.01	16.17	29.818	14706	1528	493.2	51.2
32.02	32.18	59.364	29186	3056	491.6	51.5
64.05	63.69	117.443	57650	6042	490.9	51.4
128.06	117.50	216.882	106367	11160	490.4	51.5

A raw signal power of $N_{gen} = 64$ is most representative for ERS–1 data acquisition and is still little affected by saturation; hence, we derive the **processor noise gain** from these values:

$K_{N,PRI} = 490.9$
$K_{N,SLC} = 51.45$

A further useful result is that N_{CAL} and $N_{5/5}$ are related by

$$\frac{N_{CAL}}{N_{5/5}} = 1.844 \cdot \frac{P_{REP,ref}}{P_{REP}} = \frac{335690}{P_{REP}} \qquad [3]$$

i.e. due to internal scaling factors in the range compression of ICAL the parameter 'noise power per sample' is about 1.84 times the real raw data power.

5. CONSIDERATION OF QUANTIZATION EFFECTS

Onboard ERS−1 noise and signal are digitized using a 5 bit / 5 bit ADC which introduces quantization noise and saturation effects.

5.1 Quantization of Thermal Noise Only

The noise lines are recorded using the same receiver gain as with regular SAR data acquisition, i.e. the noise is quantized with high bit redundancy; most of the values are only ± 0.5 as can be seen in Fig. 2 and Fig. 3.

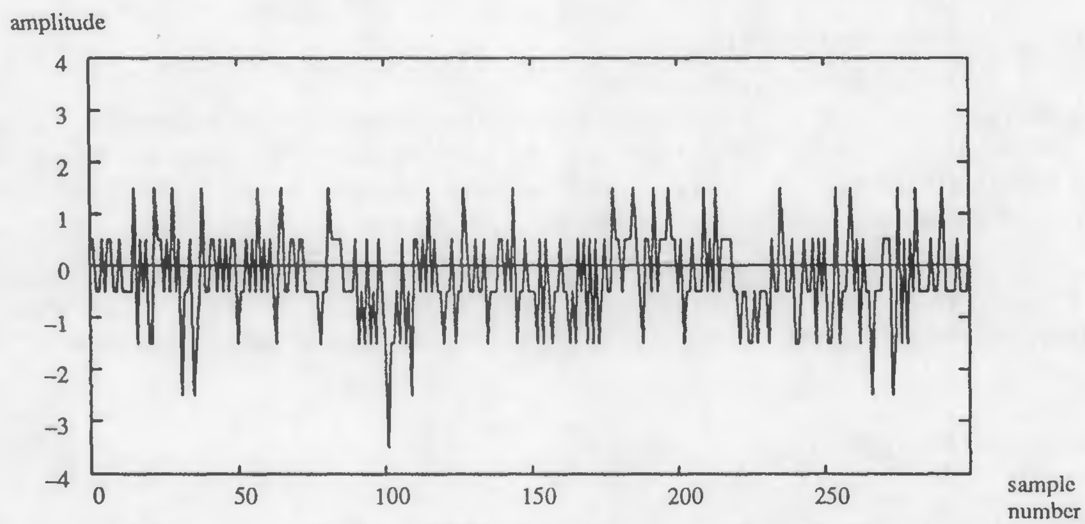

Figure 2: *In phase component of a typical ERS−1 noise line after subtraction of the nominal bias 15.5*

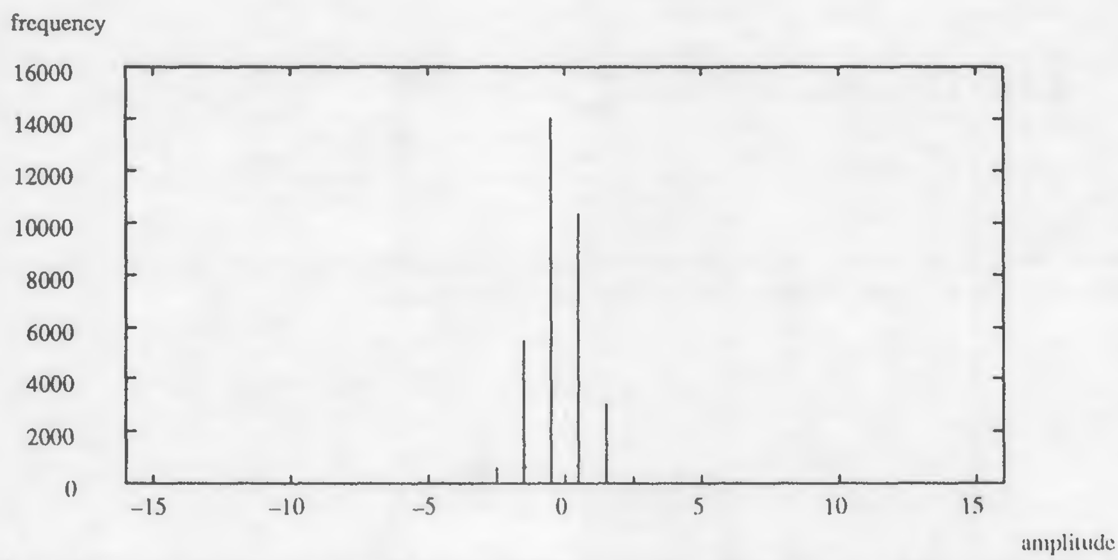

Figure 3: *Amplitude histogram of a typical ERS−1 noise line after subtraction of the nominal bias 15.5*

For such noise powers the ADC adds considerable quantization noise. Fig. 4 shows the difference between output ($N_{5/5}$) and input power (N) of an ideal 5 bit / 5 bit ADC as a function of input power.

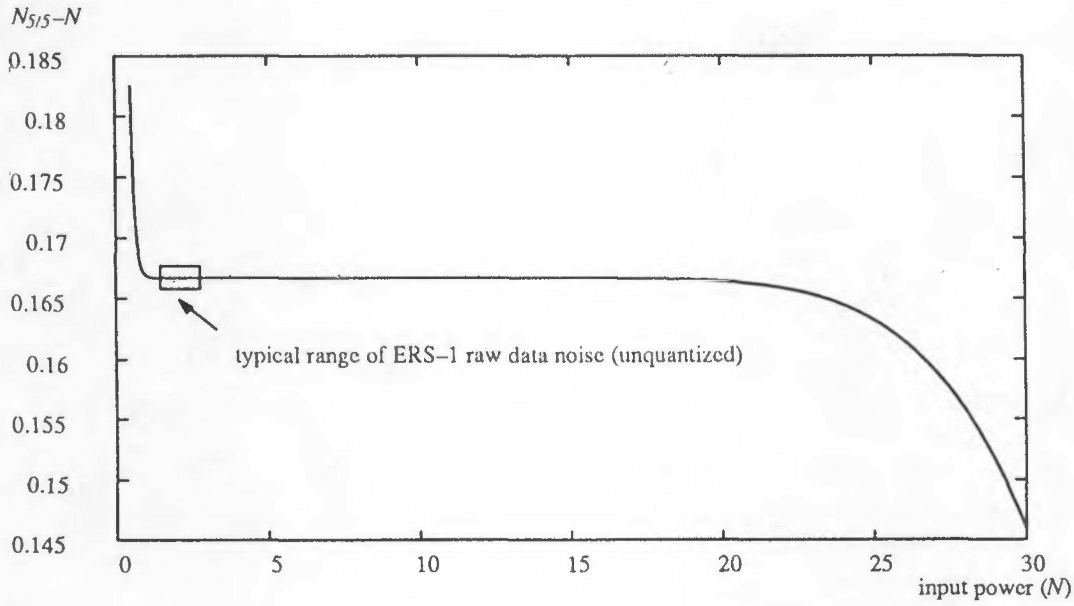

Figure 4: *Difference between output ($N_{5/5}$) and input power (N) of an ideal 5bit/5bit ADC as a function of input power*

Since for all analyzed imaging sequences $N_{5/5} \geq 1.8$ (see Chapter 7), the noise powers are in a region where

$$N_{5/5} = N + 1/6\,, \qquad [4]$$

i.e. the ICAL measurement will always **overestimate** N by

$$\frac{1}{6} \cdot \frac{P_{REP,ref}}{P_{REP}} = \frac{55948}{P_{REP}}\,. \qquad [5]$$

5.2 Quantization of SAR Data

For real SAR acquisition the noise is superimposed on the signal and the amplitude clipping of the ADC causes a reduction of the effective noise power at the ADC output. Therefore in SAR acquisition mode the ADC's differential power gain

$$g_{ADC} = \frac{dN_{5/5}}{dN} \qquad [6]$$

has to be considered together with the processor noise gain K_N. Note that for non–homogenous images the power gain has to be evaluated with an average power value measured from the raw data rather than from the image data. The VMP measures this raw data powers for blocks of approximately the synthetic aperture size. It is annotated in field 223 of the product header.

The image noise power depending on the noise power N before quantization is then

$$N_{image} = N \cdot g_{ADC} \cdot 1.844 \cdot \frac{P_{REP,ref}}{P_{REP}} \cdot K_N \qquad [7]$$

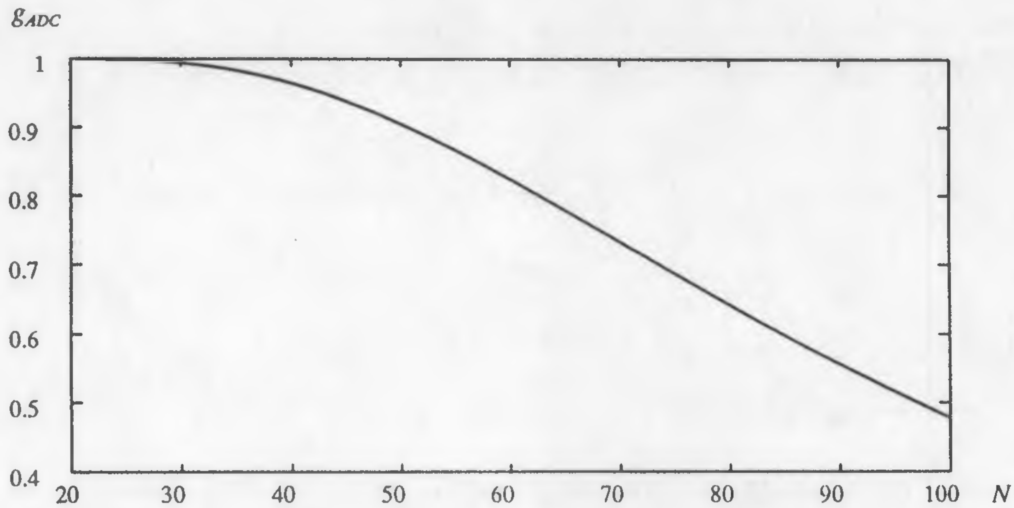

Figure 5: *Differential power gain g_{ADC} of an ideal 5 bit / 5 bit ADC as a function from input power N*

For a typical raw data set with a signal power of 64 the differential power gain is

$$\boxed{g_{ADC}(64) \approx 0.8} \; .$$

It may significantly vary however in an image with large dark and bright areas.

6. SUMMARY IMAGE NOISE POWER

Using equations [3], [4] and [7], the **image noise power per sample** is finally found as

$$N_{image} = g_{ADC} \cdot (N_{CAL} - \frac{55948}{P_{REP}}) \cdot K_N \qquad [8]$$

i.e:

$$\boxed{N_{PRI} = g_{ADC} \cdot (490.9 \cdot N_{CAL} - \frac{27.46 \cdot 10^6}{P_{REP}})} \; , \qquad [9]$$

$$\boxed{N_{SLC} = g_{ADC} \cdot (51.45 \cdot N_{CAL} - \frac{2.879 \cdot 10^6}{P_{REP}})} \; . \qquad [10]$$

For PRI the antenna gain correction and the range spread correction have to be applied additionally as e.g. described in [1].

For products where no noise power values are available, the average ERS−1 raw data noise level from the analysis in the next chapter can be used to get an estimate of the image noise floor of

$N_{PRI} \sim 1724 \cdot g_{ADC}$,

$N_{SLC} \sim 180 \cdot g_{ADC}$.

7. ERS−1 NOISE POWER HISTORY

This investigation is based upon 2381 valid noise measurements out of 3582 VMP processing reports available. 1201 measurements had to be discarded for one the following reasons:

a) $N_{CAL} = 0.0$: (774 times)

This happened when no noise data were available.

b) $0.922 < N_{CAL} < 1.480$: (58 times)

In these cases case P_{REP} had the abnormal value of 703.0. This may have been caused by shifts of the replica pulse in the window which is a known problem.

c) $N_{CAL} = 1.903$: (1 time)

The Receiver gain had the abnormal gain code 18 instead of the normal value 15.

d) $N_{CAL} = 8.85$: (3 times)

All 3 measurements origin from the same imaging sequence, i.e. the same noise record. The reason for the abnormal high noise power is unknown.

e) $549 < N_{CAL} < 14949$: (365 times)

A bug in an early VMP software version caused these totally wrong values.

Typical values for N_{CAL} for 9400 orbits are shown below. N_{CAL} varies in the interval

$3.0 \leq N_{CAL} \leq 6.1,$

$\mu(N_{CAL}) = 3.67, \ \sigma(N_{CAL}) = 0.40$

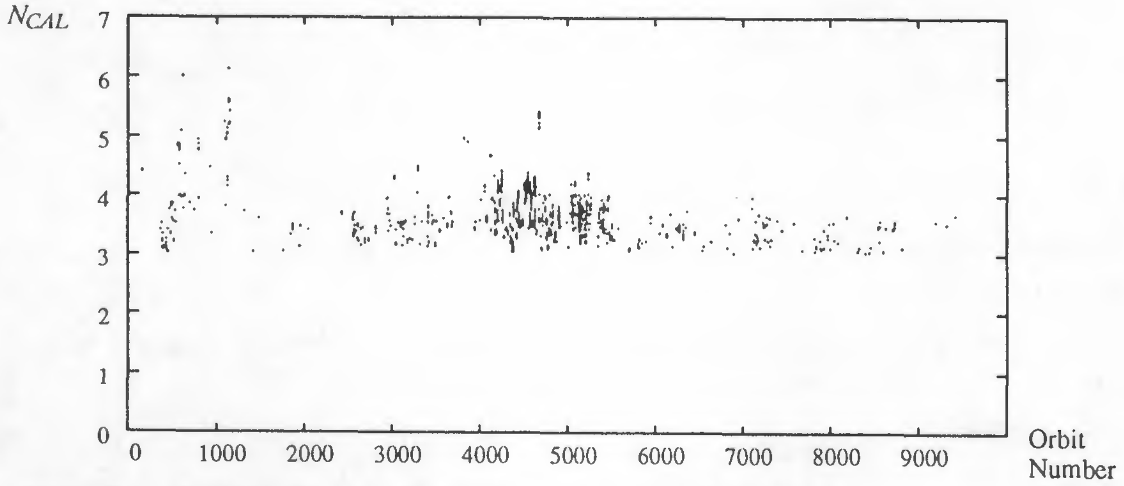

Figure 6: *The Noise Power per Sample N_{CAL}, as measured by the VMP*

In fact most of the variation of N_{CAL} is due to the chirp normalization method used during range compression. The effect of this normalization can be compensated by multiplying N_{CAL} with the replica chirp power P_{REP} and relating it to the reference replica chirp power:

$$N'_{CAL} = N_{CAL} \cdot \frac{P_{REP}}{P_{REP,ref}} = 1.844 \cdot N_{s/s} . \qquad [11]$$

The values of N'_{CAL} show less variation from than those of N_{CAL}:

$3.3 \leq N'_{CAL} \leq 5.5,$

$\mu(N'_{CAL}) = 3.82, \ \sigma(N'_{CAL}) = 0.25 .$

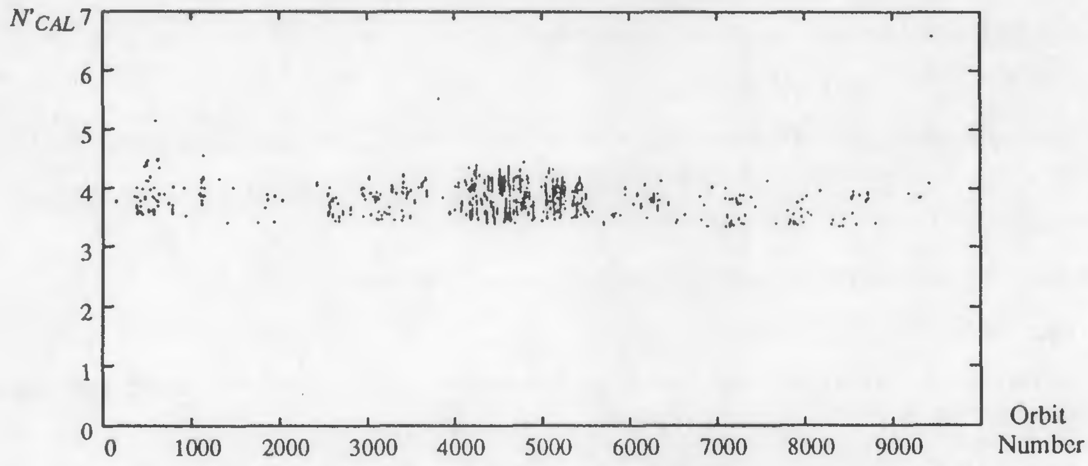

Figure 7: *The Noise Power per Sample, when corrected for P_{REP}*

Obviously the noise level is rather stable so that the average level N'_{CAL} =3.82 can be used for images where no noise measurement is available.

8. EXPERIMENTAL VALIDATION

To verify the above findings for noise calibration low backscatter areas in a PRI and an SLC product have been analyzed. The ERS−1 scene is

Orbit : 5349

Frame : 2547

UTC : 24−JUL−1992 10:40:41

PRF : 1680 Hz .

The VMP reported the following values for the PRI / SLC product:

N_{CAL} = 3.298 / 3.300

P_{REP} = 204114 / 204279 .

The scene shows a part of the dutch coast line and contains large almost black ocean areas. The lowest intensities averaged over 500 x 500 pixel areas have been found as:

$N_{PRI,measured} = 1596$

$N_{SLC.measured} = 154$.

These values compare well with the expected ones (g_{ADC}=1.0 because of low raw data power)

$N_{PRI,expected} = 1485$

$N_{SLC,expected} = 156$.

REFERENCES

[1] H. Laur, ERS−1 SAR Calibration: Derivation of Backscattering Coefficient σ^0 in ERS−1.SAR.PRI Products, ESA/ESRIN , 17 Oct. 1992.

[2] B. Schättler, R. Bamler, "SLC Calibration, Comparison between old and new gains at D−PAF", Technical Note, DLR, 19 Jan. 1993

[3] R. Shumann, "ERS−1 SAR Processors: Tuning the gains". ESA ESRIN, 24 Jan. 1992

ERS-1 SAR CALIBRATION STUDIES

T.I. Lukowski
Canada Centre for Remote Sensing
588 Booth St.
Ottawa, Canada.
K1A 0Y7

R. St-Jean
Calian Communications Systems Ltd.
(Under Contract to the Canadian Space Agency)

R. K. Hawkins
Canada Centre for Remote Sensing

K.J. Draper, P.L. Hamm, R.Z. Moucha, T.C. Khandelwal
Canada Centre for Remote Sensing
(On Work Term from University of Waterloo Co-operative Education Program)

ABSTRACT

Calibration studies are being conducted at the Canada Centre for Remote Sensing (CCRS) using data obtained from the ERS-1 SAR system. These studies are providing input to the development of the Radarsat Image Data Calibration System.

SAR data of the Ottawa region containing passive and active point targets received during the ERS-1 Multi-disciplinary Phase beginning in June, 1992 have been analyzed. Processing has been performed at the Canadian Data Processing Facility at the Gatineau Satellite Station.

A variability in the system calibration constant for ERS-1 of ± 1.0 dB has been found over a 13 month period. Variations in the power of the pulse replica of ± .2 dB have been observed between June 6, 1992 and July 31, 1993.

Keywords: Calibration, ERS-1, CERS-1 Processor

1. INTRODUCTION

Effective use of Synthetic Aperture Radar (SAR) data by some science applications requires their calibration. To assist in the development of the RADARSAT Image Data Calibration System (Ref. 1), calibration studies are being conducted using the available spaceborne SAR on the ERS-1 satellite.

The Canada Centre for Remote Sensing has been receiving ERS-1 SAR data and recording these on High Density Digital Tapes at the Canadian data reception facilities at the Gatineau Satellite Station (GSS) and Prince Albert, Sask (PASS). These data are correlated to imagery by the Canadian ERS-1 SAR Processor (CERS-1) located at GSS which was designed and built by *MacDonald Dettwiler and Associates* (Ref. 2). A number of products are output including raw data, first-level products (georeferenced), system geocoded and precision geocoded images. Some images are available in slant range projections and others in ground range projection (Ref. 3).

Because ERS-1 was initially an experimental satellite the design and development of the CERS-1 processor were carried out prior to the growth of requirements of the scientific community for radiometrically calibrated imagery. As a result, the CERS-1 processor was not designed to perform radiometric calibration and performs no corrections for changes in system gain. The intention was rather to allow all fluctuations in the sensor to flow through to the data. Any stability that it does produce is therefore inherent in the sensor itself. There are no normalizations for slant range, incidence angle or antenna pattern dependencies (Ref. 3).

2. RADIOMETRIC CALIBRATION

2.1 DETERMINATION OF β^o

The relation that can be generally used to relate the DN_{ij} (digital number of a pixel at coordinates (i,j)) in a processed image to the β^o (image brightness coefficient) for the geometry given in Fig. 1 is: [1]

$$\beta^o_{ij} \quad = \quad \mathrm{I} - \mathrm{K} + 10 \log_{10}\left[\left(\frac{\mathrm{R}_n^3}{\mathrm{R}_o^3}\right) \frac{1}{\sin\alpha_o} \frac{G_{sys_o}}{G_{sys}\, g(\theta_n)} \right] \tag{1}$$

where:

$$\begin{aligned}
\mathrm{I} &= \text{Intensity [dB]} \\
&= 10 \log_{10}\left(\mathrm{DN}_{ij}^2 - \mathrm{DN}_n^2\right) \\
\mathrm{DN}_n^2 &= \text{System Noise} \\
\mathrm{K} &= \text{Calibration Constant [dB]} \\
\mathrm{R}_n &= \text{Slant range to target area [m]} \\
\mathrm{R}_o &= \text{Reference slant range [m] (847000m)} \\
\alpha_o &= \text{Reference incidence angle [deg] } (23^o) \\
g(\theta_n) &= \text{Two-way antenna gain at elevation angle } \theta_n \\
\theta_n &= \text{Elevation angle to target area [deg]} \\
G_{sys} &= \text{System gain} \\
G_{sys_o} &= \text{System gain at which K was determined}
\end{aligned}$$

2.2 CALIBRATION CONSTANT: K

The calibration constant (K) is used to relate the digital values in a SAR image to the clutter backscatter coefficient for the area under study. Consequently, the behaviour of this constant directly reflects system radiometric stability.

K, the calibration constant, can be determined using backscatter from a point target with correction for the accompanying mean clutter: [2]

$$\mathrm{K} \quad = \quad \mathcal{E} - \sigma + 10 \log_{10}\left[\left(\frac{\mathrm{R}_t^3}{\mathrm{R}_o^3}\right) \frac{1}{\sin\alpha_o} \frac{1}{g(\theta_t)} \right] \tag{2}$$

where:

$$\begin{aligned}
\sigma &= \text{Radar cross section of point target [dBm}^2\text{]} \\
\mathcal{E} &= 10 \log_{10}\left(\left[\sum_{ij}^{B} DN_{ij}^2 - \frac{B}{B-A} \sum_{ij}^{B-A} DN_{ij}^2\right] \delta_s \delta_a \right) \\
\mathrm{B} &= \text{Samples of point target and adjacent clutter} \\
\mathrm{A} &= \text{Samples of point target accompanied by clutter} \\
\delta_s &= \text{Slant range coordinate sample spacing [m]} \\
&= \delta_g \sin\alpha_t \\
\delta_g &= \text{Ground range coordinate sample spacing [m]}
\end{aligned}$$

[1] This is modified from the formulation for ERS-1 presented in (Ref. 4).
[2] Modified from (Ref. 5).

α_t = Incidence angle at point target [deg]

δ_a = Azimuth coordinate sample spacing [m]

R_t = Slant range to point target [m]

$g(\theta_t)$ = Two-way antenna gain at elevation angle θ_t

Some of the variations in the hardware gain are obtained by use of a replica of the transmit pulse obtained by coupling a small fraction of the power in the transmit chain at RF through a path bypassing the antenna and converting to an IF sample that is input into the receiver IF chain. This IF replica is thus available during imaging and is included (subcommutated over 24 pulse echos) in the signal data (Ref. 6). However, since the replica does not pass through all of the RF hardware, some variations may not be reflected by this signal.

In the scheme implemented in the CERS-1 processor, the reference function for range compression is given by the replica function alone. The first complete and uncorrupted replica corresponding to the data being imaged is extracted from the signal data and is used *without normalization* for the processing of the whole scene (Ref. 3). Consequently, variations in the replica in power which are not reflected by the transmitted pulse may result in variations in the output image which do not reflect clutter backscatter changes.

3. DATA ACQUISITION

For these studies, SAR data are being acquired on descending (daytime) passes every 35 days (beginning in June of 1992) centering on an array of corner reflectors deployed at Shirley's Bay on the western outskirts of Ottawa, Ontario (Latitude: 45" N, Longitude: 76" W) and on targets positioned behind the laboratories of the Canada Centre for Remote Sensing near the Ottawa International Airport.

A large trihedral (Ref. 7) was obtained with a nominal cross section of 46.7 dBm^2 which was deployed in the array at Shirley's Bay. After receipt, this target was reinforced to improve stability. All targets were revisited prior to each satellite overpass to monitor positioning and condition. Data studied have included raw data and SAR Georeferenced Fine-Resolution (SGF) ground range and Multi-Look Detected (MLD) slant range images.

4. ANALYSIS AND RESULTS

A number of studies were performed related to the radiometric calibration of ERS-1 imagery using the raw signal and processed imagery obtained for this Ottawa test site.

4.1 REPLICA STUDIES

Replica data were examined to study variations in the replica and to determine how these are reflected in accompanying imagery. Code has been developed to extract the replica data from the signal data and to analyze them for the period from June, 1992 to July, 1993. A number of such replicas have been extracted from the signal data corresponding to imagery of the Ottawa test site. Examples from April 17, 1993 and November 28, 1992 of "the first acceptable replica" in the signal data are shown in Fig. 2. Even though the replica in Fig. 2b was incomplete, this was not detected and the range compression was performed using this replica as the reference function. This was accompanied by decreased range resolution and a shift in range of the imagery. On reprocessing, a replica of the form in Fig. 2a was obtained.

The total power in the replicas is indicated in Fig. 3. A mean value of 53.0 dB with a standard deviation of 0.2 dB has been obtained.

4.2 CALIBRATION CONSTANT K

The calibration constant, K, has been calculated for the SGF (ground range) and MLD (slant range) products of the CERS-1 processor. The power corresponding to each point target was determined using the integration method (Ref. 8). K were then calculated [3] as given in Tables 1 and 2 and plotted in Fig. 4.

Significant K value variations from the mean are noted for January 2, 1993 (ice buildup on the corner reflector) and for October 24, 1992.

In order to more accurately determine the calibration constant, raw data of Oct. 13, 1991 containing Active Radar Calibrators of the ESA Flevoland calibration site were processed on the CERS-1 processor. Unfortunately, this resulted in saturated output.

It was therefore decided to reprocess imagery of both the Ottawa Test Site and from Flevoland on a newly available PC-based SAR processor developed by *Atlantis Scientific Systems Group, Inc.* under contract to CCRS. [4] Corrections for saturation of the raw data in the Flevoland scene have been made according to the methodology indicated in (Ref. 10). Comparison of outputs indicates that the assumed corner reflector cross-section is approximately 2.1 dB too high thus resulting in a calibration constant, K, of 66.4 $\pm$1.1 dB for MLD and 66.1 $\pm$1.0 dB for SGF products.

Variations in the replica do result in variations in the K. However, in comparing variations in both of these, it is seen that the variations of the K cannot, in general be explained solely by those of the replica.

5. CONCLUSIONS

Stability of the ERS-1 space segment and CERS-1 ground processing system on the order of $\pm$ 1.0 dB has been obtained by study of the calibration constant.

The replica for range compression in the Radarsat system shall be obtained in a manner similar to that for ERS-1 (Ref. 11). Based on this study, it is clear that variations in the replica path which are not reflective of variations in the backscattered signal data must be minimized in the Radarsat system. As well, more stringent verification of replica integrity and appropriate normalization must be included in Radarsat processing.

Minimization of the effects of contributions from background terrain would require larger corner reflectors (Ref. 12). These would be difficult to manufacture, support and maintain to the tolerances required for accurate knowledge of their cross section. The variations noted in this study support the decision in the development of the Radarsat Image Data Calibration System to utilize Active Radar Calibrators of significantly higher radar cross section than the corner reflector used here.

6. REFERENCES

1. Srivastava S.K., Shepherd N., Hawkins R.K., Lukowski T.I., and Luscombe, A.P. 1992, Calibration for Radarsat, *Proceedings of the 4th CEOS Workshop on SAR Calibration*, Ottawa, Canada

2. Kavanagh P.F., Wong I.H., Guindon B. and Princz G.J. 1989, Canada's Fast Operational ERS-1 SAR Precision Processing and Geocoding System, *Proceedings of IGARSS'89*, Vancouver, Canada, pp. 1795-1798.

3. *Canadian Radar Data Centre ERS-1 Data Processing Facility Synthetic Aperture Radar Processor Subsystem Detailed Design Manual*, MacDonald Dettwiler and Associates Ltd., Richmond, Canada, 1991

4. Laur H. 1992, *ERS-1 SAR Calibration: Derivation of Backscattering Coefficient σ^0 in ERS-1.SAR.PRI Products*, ESA Report, ESRIN, Frascati, Italy

[3] Geometric parameters and antenna gain have been determined using software code implemented at CCRS by C. Livingstone (Ref.9).

[4] J. Princz, Private Communication.

5. *Ecisar Test Image Quality Analysis and Calibration Measurements. ESA Technical Note ER-TN-EPO-GP-1902 Issue 1, Rev. 1,* ESA Report, ESRIN, Frascati, Italy, 1991

6. *ERS-1 Satellite to Ground Segment Interface Specification ER-IS-ESA-GS-0001 Issue 2C,* ESTEC, Noordwijk, Holland, 1991

7. Fatland R. and Freeman A. 1992, Calibration and Change Detection of ASF/ERS-1 SAR Image Data, *Proceedings of IGARSS'92,* Houston, U.S.A., pp. 1164-1166

8. Ulander L.M.H., Hawkins R.K., Livingstone C.E., and Lukowski T.I. 1991, Absolute Radiometric Calibration of the CCRS SAR, *IEEE Trans. Geosci. Remote Sensing,* Vol 29, Nr 6, pp. 922-933

9. Livingstone C.E., Maxwell D.A., and Lafontaine J.R.C. 1992, The ERS-1/CV580 SAR Cross-Calibration Experiment: Sault Ste Marie, October 26 - November 2,1991, *Proceedings of ERS-1 Workshop,* Cannes, France

10. Laur H., Meadows, P., Sanchez, J.I., and Dwyer, E. 1993, ERS-1 SAR Radiometric Calibration, *Proceedings of the 5th CEOS Workshop on SAR Calibration,* Noordwijk, Holland

11. Raney R.K., Luscombe A.P., Langham E.J., and Ahmed S. 1991, Radarsat, *Proceedings of the IEEE,* Vol 79, Nr 6, pp.839-849

12. Ulander L.M.H. 1991, Accuracy of Using Point Targets for SAR Calibration, *IEEE Trans. Aerospace and Electronic Systems,* Vol 27, Nr 1, pp.139-148

Table 1: Calibration Constant for SGF: Ground Range

DATE	DATA MAX (dB)	S/C RATIO (dB)	INTEGRATED RESPONSE (dB)	K (dB)
July 11, 1992	81.8	24.7	111.5	65.2
August 15	81.2	22.3	111.0	64.6
September 19	81.1	24.7	111.1	64.8
October 24	79.0	25.6	108.6	62.2
November 28	80.9	24.2	110.4	64.0
January 2, 1993 ‡	76.3	20.2	106.1	59.7
February 6	79.9	25.8	109.7	63.3
March 13	79.2	25.4	109.0	62.5
April 17	79.2	22.1	109.1	62.7
May 22	81.1	21.3	110.7	64.3
July 31	82.4	22.9	111.7	65.3
Mean ± Std. Dev.				64.0 ± 1.0

Table 2: Calibration Constant for MLD: Slant Range

DATE	DATA MAX (dB)	S/C RATIO (dB)	INTEGRATED RESPONSE (dB)	K (dB)
July 11, 1992	81.8	25.1	107.6	65.3
August 15	81.9	22.6	107.5	65.1
September 19	81.3	24.3	107.4	65.1
October 24	78.2	24.5	104.5	62.1
November 28	81.9	24.7	107.1	64.7
January 2, 1993 ‡	75.8	19.2	102.1	59.7
February 6	77.8	24.9	104.2	61.8
March 13	78.6	24.1	105.8	63.4
April 17	80.1	22.3	105.9	63.5
May 22	80.7	20.5	106.9	64.6
July 31	82.1	23.0	108.3	66.0
Mean ± Std. Dev.				64.3 ± 1.1

‡Not included in determination of mean.

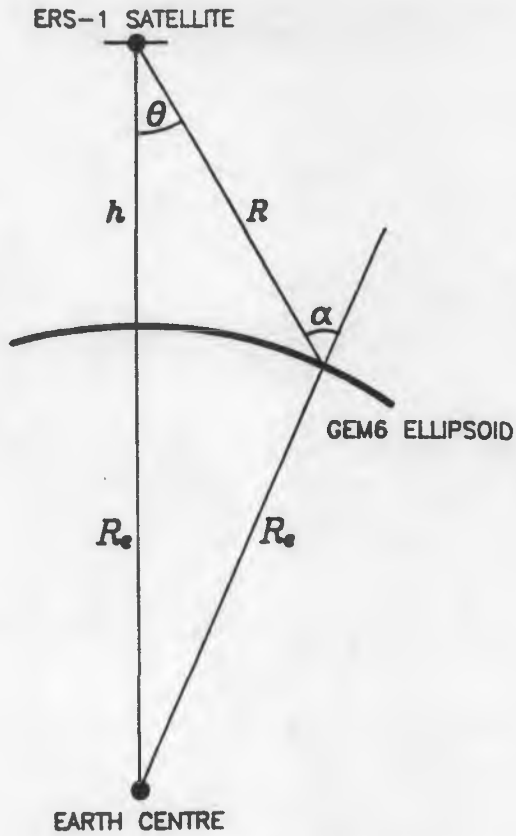

Figure 1: *Geometry for ERS-1 Imaging.*

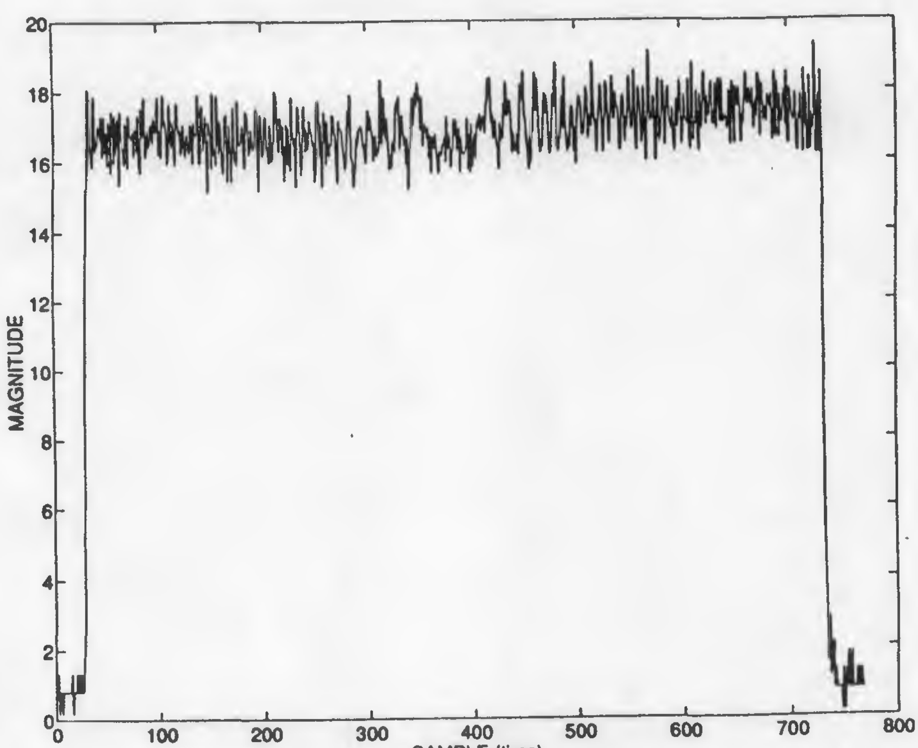

Figure 2a: *ERS-1 Replica from April 17, 1993. This is a "good" replica.*

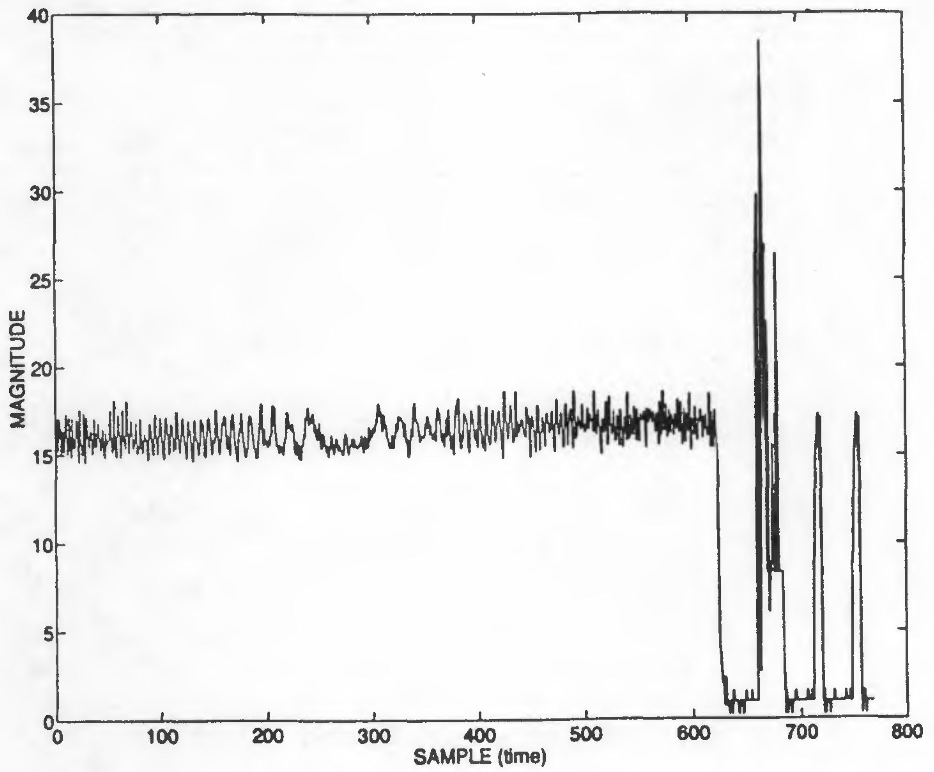

Figure 2b: *ERS-1 Replica from November 28, 1992. This "bad" replica (incomplete) was accompanied by a range shift of the image and degraded range resolution.*

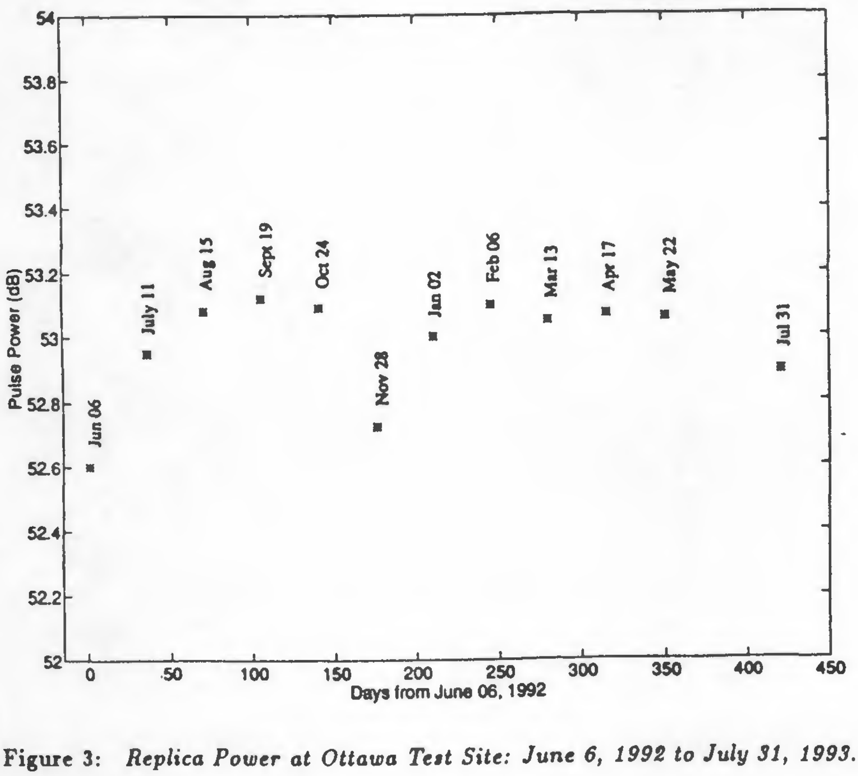

Figure 3: *Replica Power at Ottawa Test Site: June 6, 1992 to July 31, 1993.*

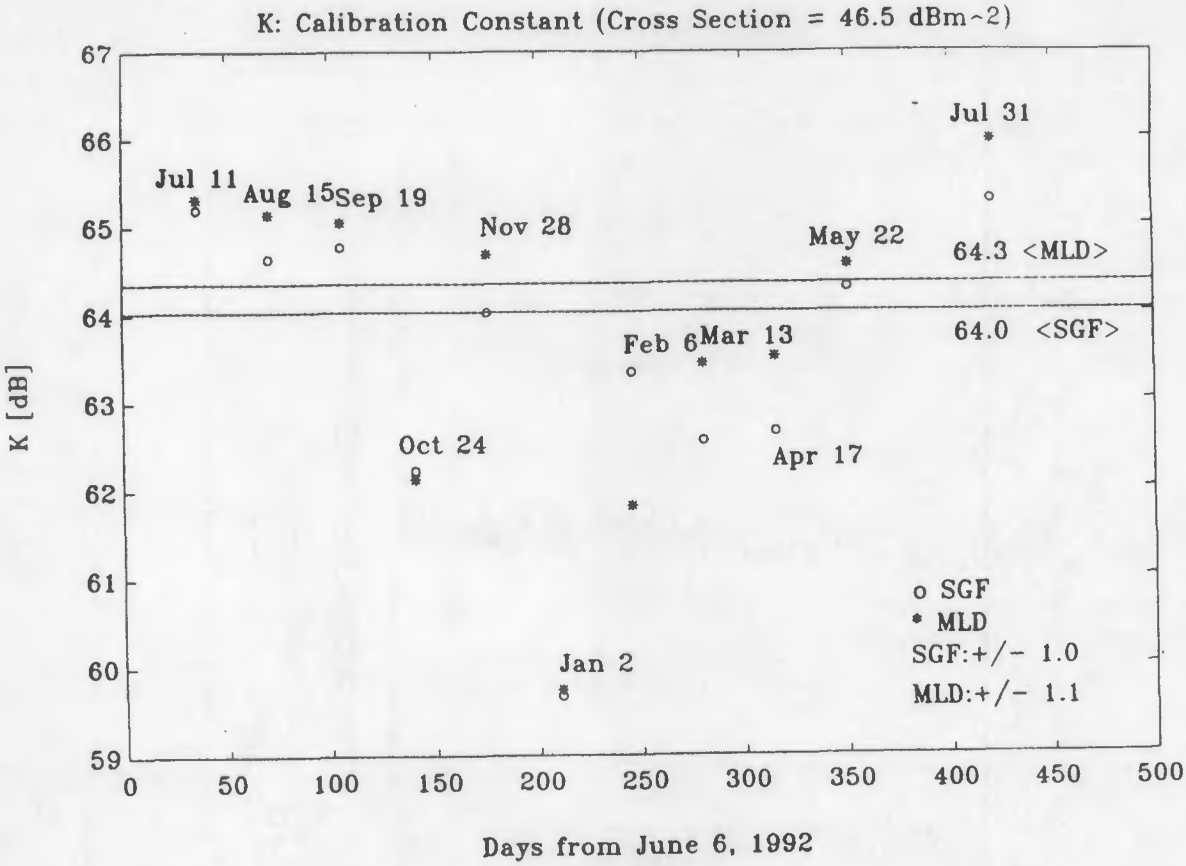

Figure 4: *Calibration Constant from July 11, 1992 to July 31, 1993 for SGF and MLD (slant range products).*

SPACEBORNE SAR CALIBRATION

Session 8

Chair: M.SHIMADA, NASDA, Japan

ERS-1 SAR RADIOMETRIC CALIBRATION

H. LAUR [1], P. MEADOWS [2], J.I. SANCHEZ [1], E. DWYER [1]

[1] European Space Agency / ESRIN, Frascati, Italy
[2] GEC-Marconi Research Centre, Chelmsford, United-Kingdom

1. INTRODUCTION

The European Space Agency perceives ERS SAR as an end to end system combining high on-board performances with accurate on-ground performance measurements, precise data processing and suitable transmission of data related information to the user community. Such a synergy between ERS space and ground segments is well illustrated by the SAR radiometric calibration activities. The combination of internal calibration parameters availability with accurate on-ground measurements gives to the ERS-1 user community the first opportunity to work with precisely calibrated SAR products acquired over a long time period.

This paper describes the status of the ERS-1 SAR radiometric calibration with updated measurements on the radiometric stability. The calibration measurements are performed using the transponders deployed by ESA/ESTEC in Flevoland, The Netherlands (Ref. 1). The calibration measurements are the result of a joint effort between the ESA Processing and Archiving Facilities (PAF) and the ERS Central Facility at ESA/ESRIN.

2. INTERNAL CALIBRATION PARAMETERS

Two types of internal calibration parameters are measured in the ERS-1 SAR Active Microwave Instrument (AMI). At the start and end of each SAR imaging sequence, a set of four calibration pulse measurements and eight noise measurements are made. During the imaging sequence, copies of the transmitted pulses (replicas) are generated and appended to the raw data. One complete replica pulse is transmitted with every 24 raw data range line records (Ref. 2).

These two stage internal calibration parameters are required to ensure that the ERS-1 SAR image products are internally calibrated, especially as the ERS-1 AMI does not have an automatic gain control system. The system gain can drift due to temperature changes and ageing. The gain changes are monitored via the replica pulse powers as they are passed through the SAR system. The calibration pulse measures the majority of the gain drift with the replica pulse being used to monitor the gain drift during the imaging sequence when the more representative pulse is not available. The thermal noise is measured when pulses are not being transmitted at the start and end of each imaging sequence.

2.1 Replica Pulses

Within the ESA SAR processors, a single replica pulse associated with the image product being processed is extracted and used for gain normalisation and range compression.

Two problems were identified with replica pulses. The first was that the replica pulse was being extracted from the raw data incorrectly such that the start of the replica was mis-identified by one or two range line records. The second problem was associated with the fact that the replica pulse itself is corrupt in that one or more of the 704 samples that make up the replica can have spurious values. This leads to a spike and/or null for one or more of the replica samples. The analysis of two raw data sets acquired during a corruption period shown that one in sixty replica pulses and one in every one hundred pulse were corrupt (Ref. 3).

The effect of these two problems on the resultant imagery was different at the UK-PAF and at the D-PAF (Ref. 4). For UK-PAF processed imagery, the only problem identified were streaks up to 10 km in length in range which emanated from bright point targets (Ref. 5). At the D-PAF, the images processed were severely corrupted. Quality checking has now been incorporated at the UK-PAF since April 1993 and at the D-PAF since May 1993 to identify the two problems and if found select another suitable replica pulse to be used for image generation.

Effect of the replica pulses corruption on the radiometric calibration :

The use of a replica pulse within a processor assumes that the replica pulse power is directly proportional to the transmitted pulse power. Thus, if this were the case, any transmitter pulse power variations would be compensated for in the resultant SAR image. Figure 1 shows that the above assumption is invalid (i.e. there is no direct relationship between the replica pulse and calibration pulse power). Identical results are found by (Ref. 6). The consequence of this is that any replica pulse power variations introduced by a SAR processor need to be removed.

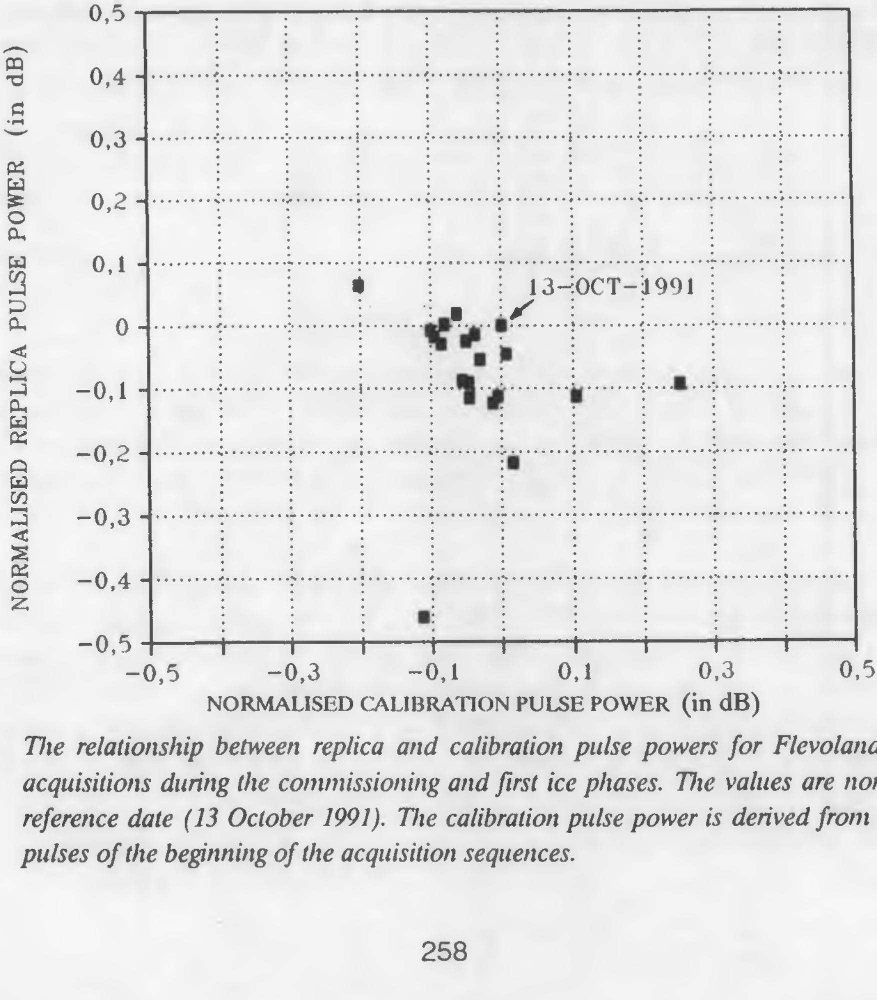

Figure 1 *The relationship between replica and calibration pulse powers for Flevoland and Zeeland acquisitions during the commissioning and first ice phases. The values are normalised to the reference date (13 October 1991). The calibration pulse power is derived from the calibration pulses of the beginning of the acquisition sequences.*

Examination of the replica pulse power variations since the beginning of the ERS-1 mission in July 1991 (Figure 2) show that usually the replica pulse power is stable to within ± 0.1 dB but can, for short periods, be within a band of ± 1.0 dB. Identical results have been reported by (Refs. 7, 8).

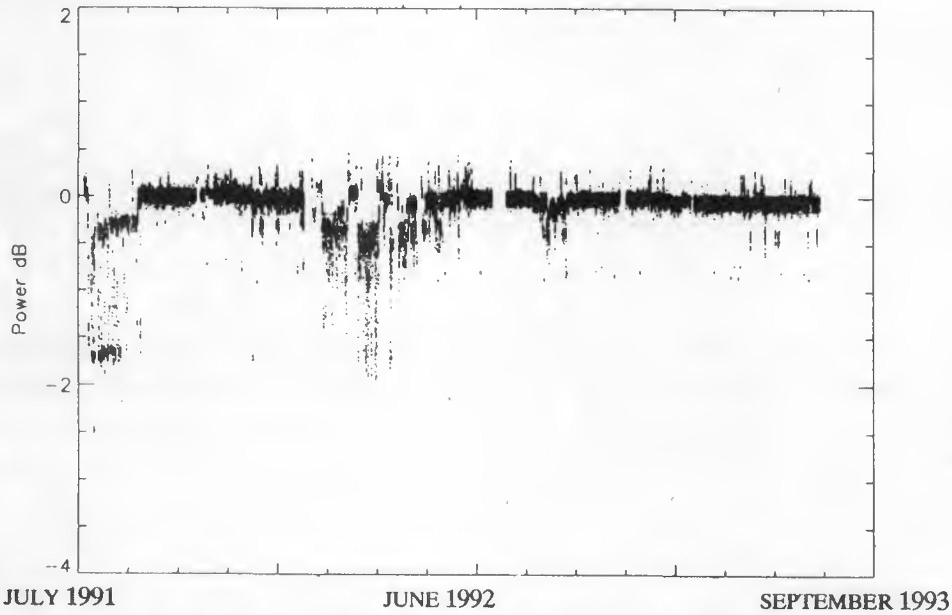

Figure 2 *Replica pulse power variations since beginning of ERS-1 mission. The replica pulse power is normalised to the reference date (13 October 1991).*

From Figure 2, it can be seen that two main periods of high replica pulse power variations occurred since beginning of the ERS-1 mission :

- during the early commissioning phase (from July to early October 1991)
- during the early multi-disciplinary phase (from May to July 1992)

Periods when the replica power variations were higher than 0.4 dB correspond to 7.8 % of the acquisitions since beginning of the mission and 6.0 % of the acquisitions apart from the commissioning phase. 2.4 % of the acquisitions (mainly in August and September 1991) exhibit replica power variations higher than 1 dB. Figure 3 shows that in 1993 the variations of the replica pulse power are fairly small, i.e. within ± 0.1 dB.

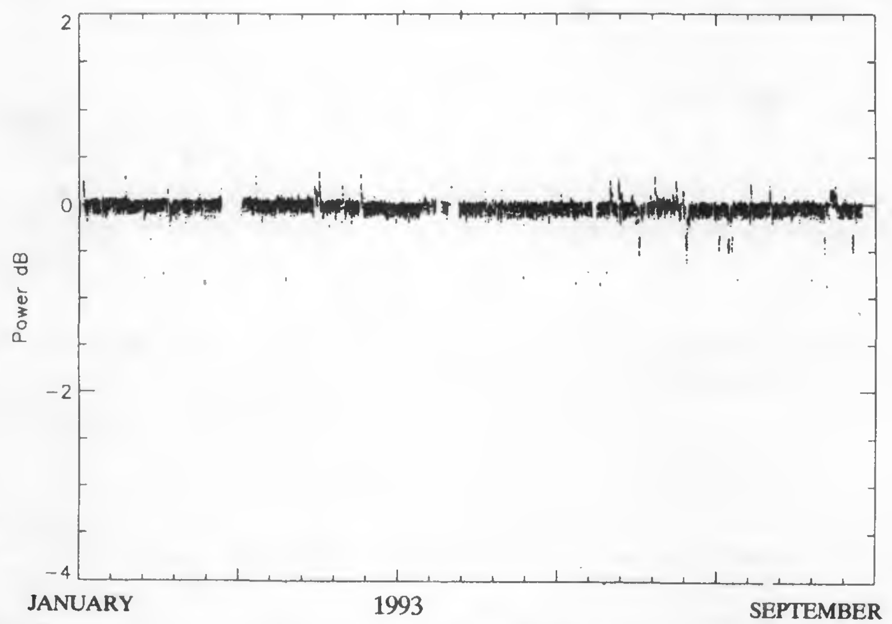

Figure 3 *Replica pulse power variations during year 1993 (from January to September).*

Figure 4 shows that during the early commissioning phase, in September 1991, the replica pulse power variations were high. In fact during this period the descending passes (morning acquisitions over Europe) had a replica pulse power about 1.6 dB lower than the replica pulse power of the ascending passes (close to the mean reference value).

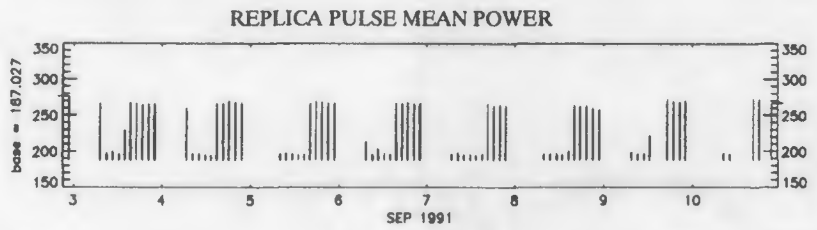

Figure 4 *Replica pulse power variations from 3 to 10 September 1991.*

During the Commissioning Phase, the imaging of the DRA Calibration Site at Romney-Marsh, Kent (Ref. 9) occurred during the descending passes. A comparison of point target powers and replica pulse powers (Figure 5) clearly shows a close link, i.e.: as the replica pulse power decreased, the point target powers increased by a similar amount (Ref. 10).

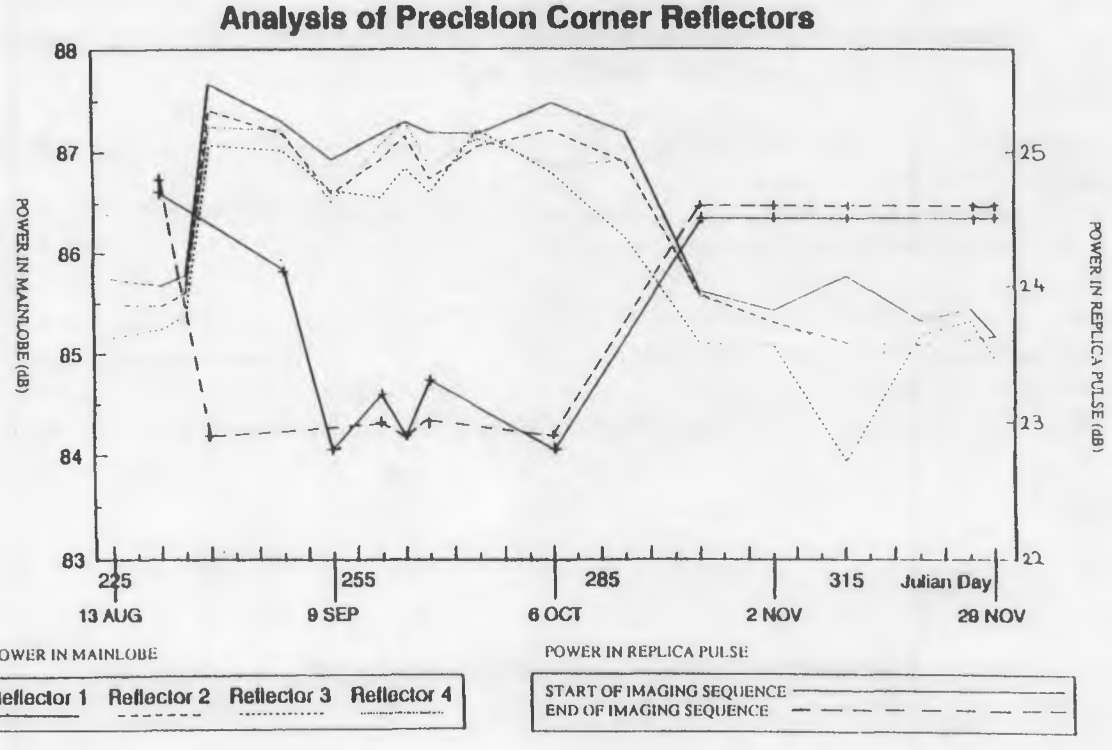

Figure 5 *Variation in calibration point target power and replica pulse power during the commissioning phase (from analysis of DRA precision corner reflectors responses).*

The imaging of the ESA calibration site in Flevoland (NL) occurred during the ascending passes when the replica pulse power was close to the reference value. The corrections to apply to the measured radar cross sections of the ESA transponders was lower than 0.5 dB during the commissioning phase.

Table 1 gives the values of the radiometric stability and the radiometric accuracy measured with the ESA transponder 2 before and after the correction of the replica pulse power variations.

Transponder 2 *(38 measurements over 2 years)*	**before** correction of replica pulse power variations	**after** correction of replica pulse power variations
radiometric stability	0.43 dB	0.38 dB
radiometric accuracy	0.38 dB	0.32 dB
max. variation of the measured RCS	± 0.92 dB	± 0.75 dB

Table 1 *Radiometric calibration measurements before and after correction of replica pulse power variations.*

The **radiometric stability** is defined as the standard deviation of the (time serie) measurements of the radar cross section of a calibration target (using the same calibration constant) (Ref. 11).
The **radiometric accuracy** is defined as the (time serie) average of the absolute difference between the nominal radar cross section and the measured radar cross section (using the same calibration constant) of a calibration target (Ref. 11).

Similar results are found for transponders 1 and 3.

Users of ERS-1 SAR imagery need to correct their imagery to obtain correctly calibrated results. This is done by comparison of the replica pulse power used to generate the image in question with that used to generate the reference image of Flevoland from which the calibration constant was derived [13 October 1991] (Ref. 12). The replica pulse power used for image generation is given in the CEOS header of each image product. Similarly, users comparing two images need to take into account any difference in replica pulse powers.

The expression used for this correction is:

$$\frac{\text{image replica power}}{\text{reference replica power}}$$

As a consequence, the full expression to apply in order to determine the backscattering coefficient σ^o of an area located at incidence angle α is (for an ESA SAR PRI product) :

$$\sigma^o = \frac{\langle I \rangle}{K} \cdot \frac{\sin \alpha}{\sin \alpha_{ref}} \cdot \frac{\text{image replica power}}{\text{reference replica power}}$$

where $\langle I \rangle$ is the mean pixel intensity, K the calibration constant and α_{ref} the mid range incidence angle equal to 23 degrees.

The reference replica power is 205229 (value on 13 October 1991 at 21:40 UTC).

2.2 Calibration Pulses

Calibration pulse measurements are performed only at the start and the end of an imaging sequence. This creates practical difficulties. When the start or the end of the imaging sequence is outside the area of reception of an acquisition ground station. In such a case, the calibration pulses are not recorded. The calibration pulse power is the mean power of the 4 calibration pulses at the start and the end of the imaging sequence.

Since the beginning of the ERS-1 mission, the calibration pulse power appears stable: 87 % of the calibration pulse power measurements are within the range ± 0.2 dB. Figure 6 shows the variations of the calibration pulse power during the year 1993 (from January to September). The calibration pulse correction is by consequence fairly small.

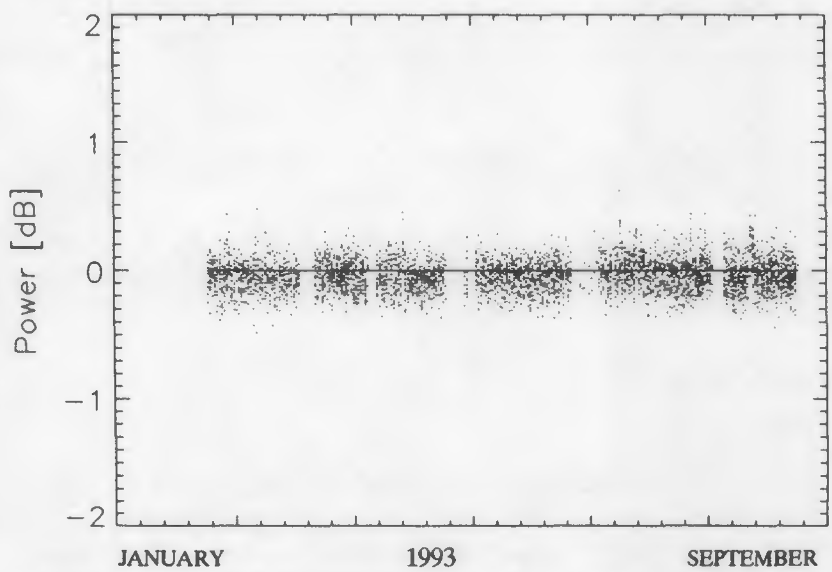

Figure 6 *Calibration pulse power variations during year 1993. The values are normalised to the reference date (13 October 1993).*

When applied on ESA transponder responses, the calibration pulse correction do not improve the measurements results (see Table 2).

The correction has been applied on the original measurements and on the measurements previously corrected for the replica pulse power variations. The method of correction is similar to the one used for the replica pulse power correction with a reference value (calibration pulse power on 13 October 1991 at 21:40 UTC).

Transponder 2 *(20 measurements during commissioning phase and ice phase)*	original measurements	**after** correction of **calibration** pulse power variations	**after** correction of **replica** pulse power variations	**after** correction of **replica & calibration** pulse power variations
radiometric stability	0.36 dB	0.39 dB	0.33 dB	0.35 dB
radiometric accuracy	0.30 dB	0.33 dB	0.27 dB	0.29 dB

Table 2 *Radiometric calibration measurements before and after correction of calibration pulse power variations. The effect of the replica pulse power correction is shown for comparison.*

No corrections are made for the calibration pulse power variations within the ESA ground segment SAR processors. Because the calibration pulse power information is difficult to access for users and because the correction of its variations do not improve the calibration measurements, it is not proposed to apply such a correction in the derivation of σ^0 in ESA SAR products.

3. RAW DATA QUALITY PARAMETERS

3.1 Raw Data Quality

SAR raw data obeys a certain statistical distribution (zero mean, Gaussian amplitude and uniform phase). Statistical checks on the data can establish whether the data has been corrupted during on-board processes such as in-phase (I) and quadrature (Q) channel separation and analogue to digital conversion (ADC).

A selection of parameters which can be derived from a block of raw data include (once the raw data for both channels have been suitably unpacked from 5 bit values to 8 bit values):

1. I and Q Channel Means

This is the arithmetic mean of the data in the I and Q channels. The expected mean value in each channel is zero. Any bias on either channel can be easily corrected by subtracting the appropriate value from the I or Q channel values. This is indeed carried out for all ESA ground segment SAR processors. The I & Q channel means are stable parameters. Table 3 shows the stability of both channel means and a slight negative bias (corrected in the ESA processors).

Channel mean	Jan. 1992 to Sept. 1993 *(18415 products)*	May 1993 *(837 products)*	July 1993 *(962 products)*
I channel mean (mean ± s.d.)	- 0.158 ± 0.030	- 0.152 ± 0.028	- 0.159 ± 0.032
Q channel mean (mean ± s.d.)	- 0.137 ± 0.030	- 0.119 ± 0.029	- 0.107 ± 0.031

Table 3 *I & Q channel mean from SAR products of different time periods.*

2. I and Q Channel Standard Deviations

This is the standard deviation of the data in the I and Q channels. For ERS-1 SAR image mode (On-Ground Range Compressed) the I and Q channels are quantised within the Analogue to Digital Convertor (ADC) to 5 bits each. This allows the quantised data to take integer values in the range -16 to 15 and with each channel having a Gaussian distribution. Thus, the distribution should have a maximum at 0 and should ideally fall to zero at -16 and 15. In addition, the ratio of the I and Q Standard Deviations (gain imbalance) should be one. Any gain imbalance can be corrected by multiplying the Q channel values by the gain imbalance. This is also carried out for all ESA ground segment SAR processors.

3. I and Q Channel Top and Bottom Saturation

The saturation parameters are defined as the percentage of the samples occupying the highest or lowest quantisation levels for the I and Q channels.

The ERS-1 ADC can be easily simulated using routines to generate a Gaussian distribution with a zero mean and a specified input standard deviation together with quantisation to 5 bits for each of the channels. Figure 7 (from Ref. 6) shows histograms for the simulated I and Q channels for a selection of *input* standard deviations. When the *input* standard deviation has a value greater than approximately 5, tails in the distribution appear at the highest and lowest channel bins. This indicates that saturation has occurred in the top and bottom bins of the ADC. For each of the histograms, a Gaussian distribution has been derived and is superimposed on the histograms. The fitted Gaussian distribution is the one which was measured using

ERS-1 raw data (i.e. the ADC output parameters). Note that as the input standard deviation increases, the fitted Gaussian fails to fit the histogram.

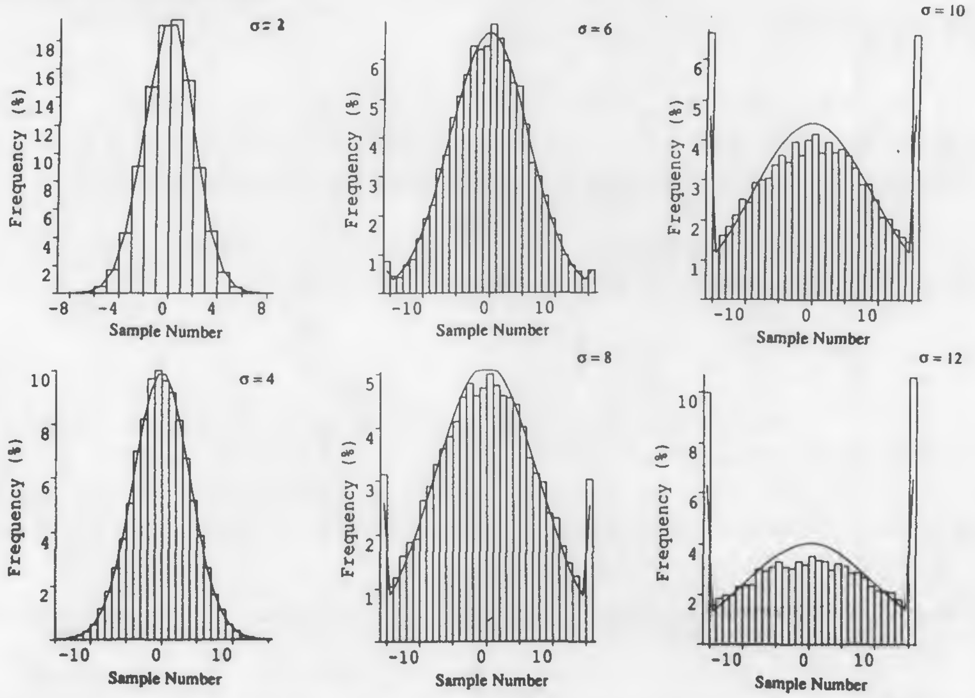

Figure 7 *Simulated I & Q channels after quantisation by the ADC for various input standard deviations.*

The zero mean used for the simulations is applicable for ERS-1 raw data as any non-zero bias is removed prior to processing as is any gain imbalance. The validity of using a Gaussian distribution can be deduced by comparing the simulated relationship between measured I & Q Top & Bottom Saturation and I & Q Standard Deviation values with actual ERS-1 raw data parameters. This has been carried out using a selection of raw data blocks from imaging sequences of Flevoland and Zeeland as Figure 8 (from Ref. 7) shows. The solid line in this figure is based on the simulations. A good agreement exists between the actual raw data and the simulations.

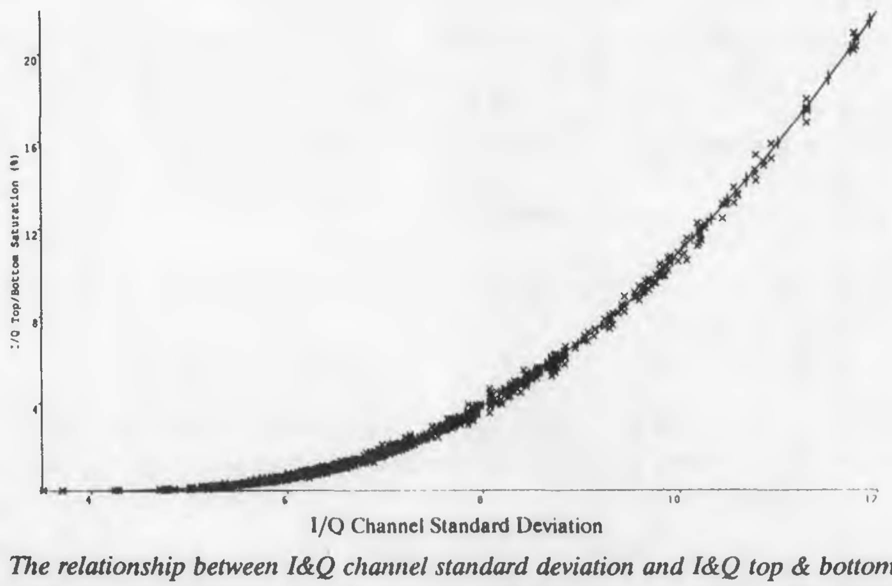

Figure 8 *The relationship between I&Q channel standard deviation and I&Q top & bottom saturation for all the raw data blocks of the Flevoland and Zeeland image sequences. The solid line is derived from simulations using a zero mean Gaussian to represent the I&Q raw data channels.*

The effect of saturation within the ADC leads not only to a difference in input and output standard deviations but more importantly to a difference in input and output powers. An ideal ADC should preserve the power of the raw data.

Figure 9 shows the difference between the simulated input and output ADC power as a function of *output* ADC standard deviation. This shows that for *output* standard deviations between 2 and 6, the power change introduced by the ERS-1 ADC is small (<0.1 dB). The power gain for small output standard deviations (<2) is a consequence of quantisation noise. For higher standard deviations, there is a significant power loss. This raw data power loss will be reflected in a correspondingly similar image power loss. Thus the high power losses have severe implications for distributed target radar cross-section measurements as well as for ERS-1 SAR radiometric stability determinations and ERS-1 SAR calibration.

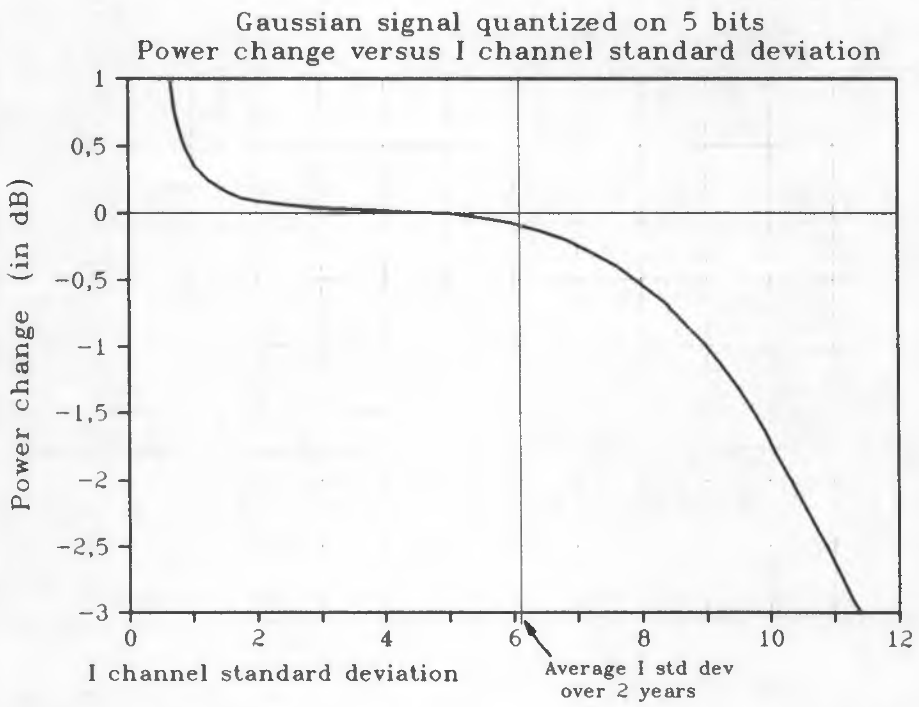

Figure 9 *The ADC power change versus output I&Q channel standard deviation.*

3.2 Effects of ADC saturation

3.2.1 Dependence of ADC power loss on surface types

Examination of ERS-1 SAR raw data for the period January 1992 to September 1993 indicate an average I channel standard deviation of 6.15 (corresponding to a power loss of 0.1 dB) together with a range of from approximately 2 to 12. These findings indicate that a significant proportion (22 %) of the ERS-1 SAR raw data suffers from an ADC power loss higher than 0.5 dB.

Table 4 and Figure 10 give the monthly averages of the I channel standard deviation and the output image mean for a large quantity of SAR products. These SAR products correspond to acquisitions within the ESA ground stations of Kiruna (SW), Fucino (I) and Maspalomas (E), i.e. over Europe, North and West Africa, Greenland and North Atlantic.

Month	Number of SAR products analysed	Average I standard dev.	Output image mean
January 1992	1206	6.40	1779
February 1992	1151	6.25	1745
March 1992	1245	6.51	1787
April 1992	628	5.67	1627
May 1992	709	5.86	1542
June 1992	753	6.31	1816
July 1992	634	5.91	1510
August 1992	935	5.95	1589
September 1992	914	6.41	1781
October 1992	793	6.46	1748
November 1992	941	6.30	1872
December 1992	765	6.58	1809
January 1993	1147	5.91	1712
February 1993	977	6.07	1603
March 1993	1019	6.13	1606
April 1993	755	6.25	1580
May 1993	841	6.14	1562
June 1993	891	5.92	1613
July 1993	993	5.80	1485
August 1993	922	5.86	1470
September 1993	196	6.58	1627
Total	**18415**	**6.15**	**1668**

Table 4 *Monthly average of I channel standard deviation and SAR image output mean.*

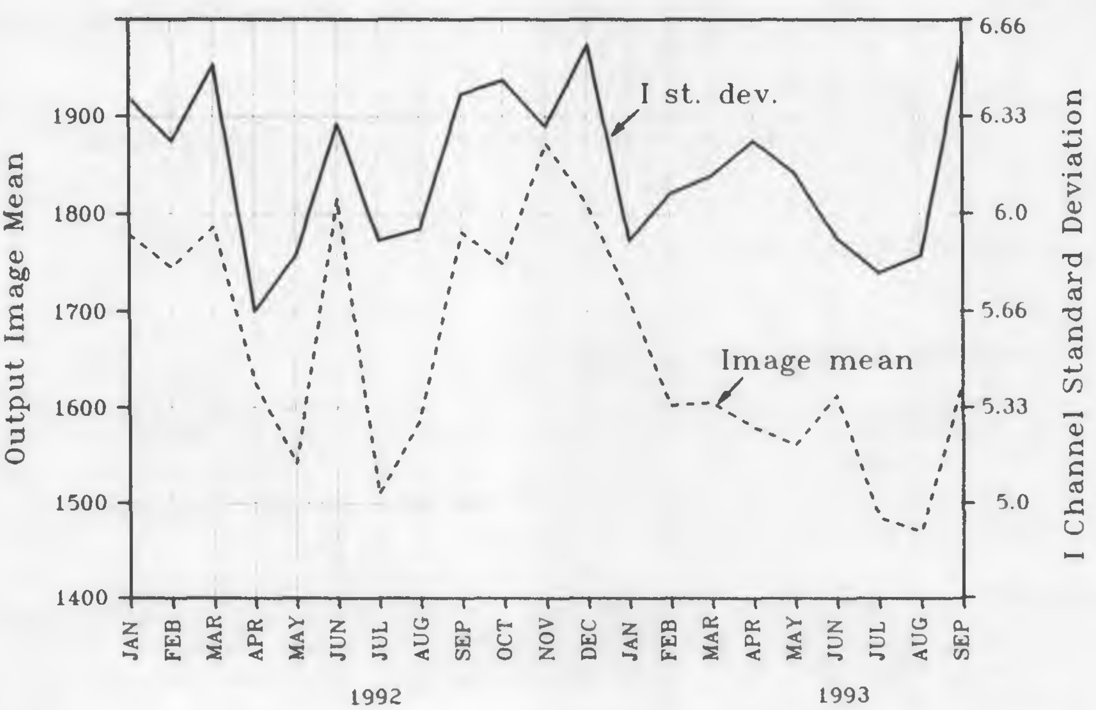

Figure 10 *Monthly measurements of I channel standard deviation and image mean.*

Table 5 gives a confirmation of the occurrence of ADC saturation mainly over sea areas.

Measurements from January 1992	Number of SAR products analysed	Average I standard dev.	Average ADC power loss
Sea area : Norwegian sea between lat. 60N & 70N between long. 12W & 3E	998	6.71	***0.18 dB***
Sea area : East Atlantic between lat. 40N & 60N between long. 20W & 10W	249	8.76	***0.87 dB***
Land area : Central Europe between lat. 47N & 52N between long. 10E & 30E	378	5.58	*0.03 dB*
Land area : France between lat. 44N & 50N between long. 0E & 7E	164	5.65	*0.04 dB*

Table 5 *Average I channel standard deviation and ADC power loss over sea areas and land areas.*

The previous results give a global scale overview of ADC saturation. Examination of raw data products corresponding to an 100 km by 100 km ERS-1 image can be used to map the precise variation of I channel standard deviation and hence ADC power loss with location in the image and surface type. The raw data is examined by determining the standard deviation for a series of blocks. Each block has a range length equivalent to the replica pulse length (704 samples) and an azimuth length equivalent to the synthetic integration period (about 1300 samples). The blocks overlap each other by half a block size in both azimuth and range. For the raw data products examined below, the raw data has been sampled in range and azimuth by a factor of 10.

Two raw products (Kent, UK and Flevoland, NL) have been examined. Figure 12-a shows the I channel standard deviation in the form of a contour plot for Kent (orbit 865). The land mass of Kent is towards the top left of these plots while the English Channel occupies the remainder. Note that the highest standard deviations occur at near range and over the ocean. The average I channel standard deviation for each of these scenes is 7.44, while the range of values is 4.41 to 9.81. Clearly for this scene there is a significant variation in the I standard deviation. This variation is reflected in the power loss as Figure 12-b shows. A power loss of up to 1.5 dB occurs at near range which is coincident with the ocean. Over the land, the power loss is much less, except for coastal regions.

Figure 13-a shows the I channel standard deviation of a Flevoland scene for the calibration reference date (13 October 1991). The Flevoland polder is at the bottom centre of these plots while the Ijselmeer is at the centre. Note that the highest standard deviations occur once again at near range and over the ocean. Figure 13-b shows the power loss over the scene. The power loss is as high as 0.65 dB over Flevoland. The measured power loss in a raw data block centred on transponder 2 is 0.39 dB.

As expected, the image mean is correlated with the I channel standard deviation. Figure 10 shows an increase of the output image mean during winter. This is an effect of the storms over the North Atlantic ocean during winter. This suggests that the ADC saturation occurs mainly over large areas having an high backscattering level (e.g. water surface during storms). Figure 11 confirms this suggestion.
Figure 11 is a map of I channel standard deviation over Western and Central Europe. The black triangle indicates a scene with I channel standard deviation (for the whole 100 x 100 km scene) higher than 7, i.e. an ADC power loss higher than 0.25 dB. The diamond indicates a scene with I channel standard deviation lower than 7. The map shows that ADC saturation occurs mainly over the sea.

Figure 11 *Map of I channel standard deviation over Europe. The ADC saturation (black triangles) occurs mainly overthe sea.*

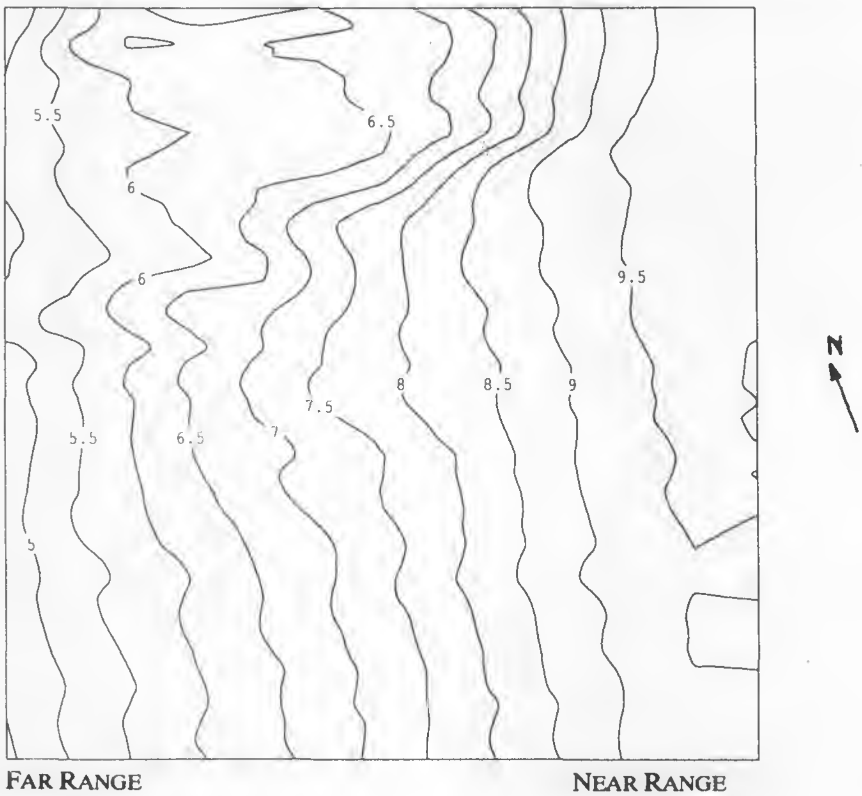

Figure 12-a *I channel standard deviation of a raw data scene over Kent (UK). The scene covers an area of about 105 x 105 km and has been acquired on 15 September 1991. The Kent coast is in the top left of the scene. The English Channel occupies the rest of the scene. Note the high values of I channel standard deviation over the sea, particularly at near range.*

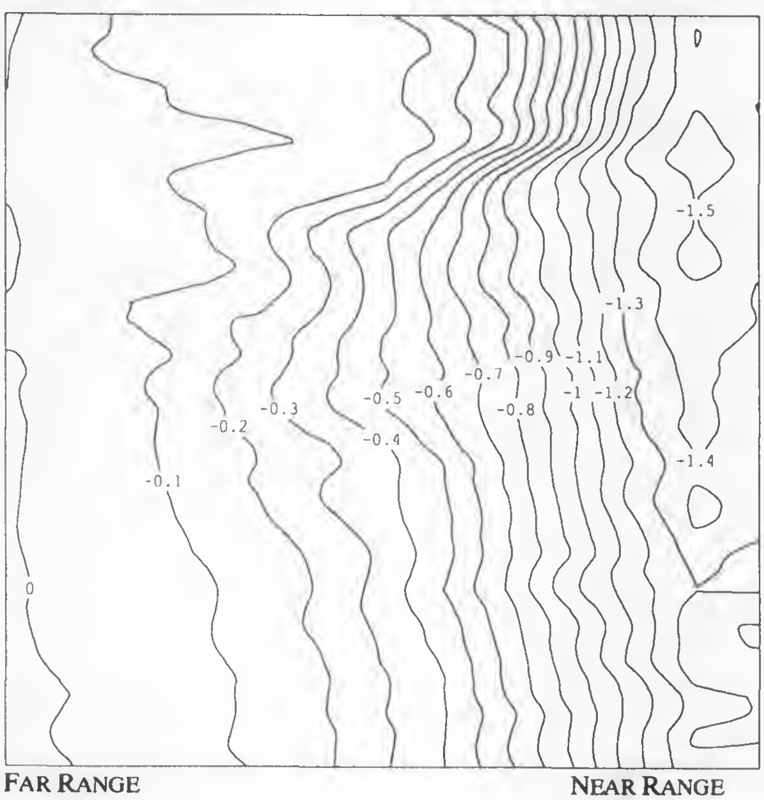

Figure 12-b *ADC power loss over Kent (15 September 1991). Note that the ADC power loss is as high as 1.5 dB at near range. Over land the ADC power loss is less than 0.2 dB.*

I Channel Standard Deviation

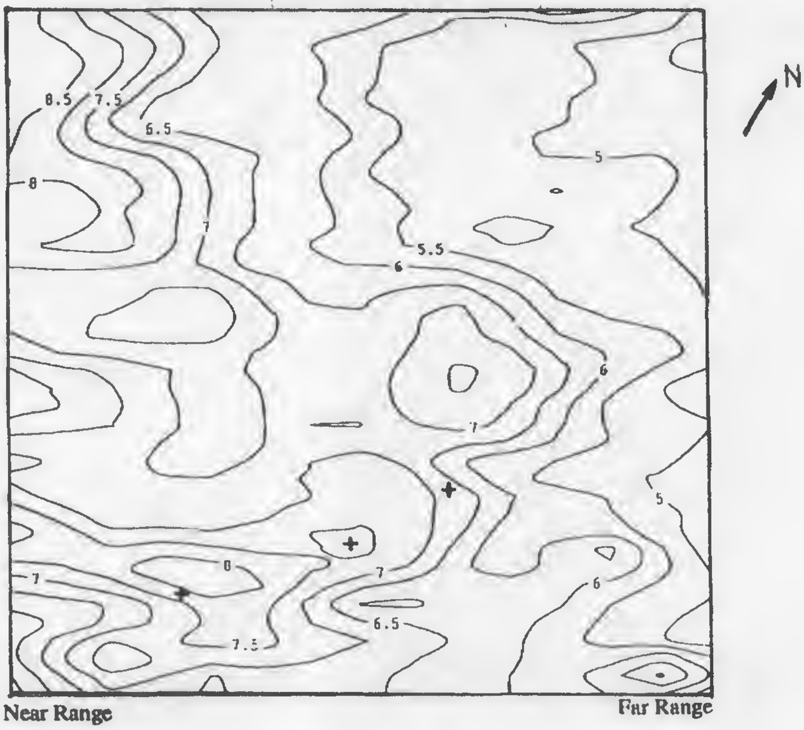

Figure 13-a *I channel standard deviation of a raw data scene over Flevoland (NL). The scene covers an area of about 105 x 105 km and has been acquired on 13 October 1991 (refence date for calibration constant derivation). The Ijsselmeer is in the middle in the image and the Flevoland polder in the bottom centre. The transponders location is indicated by a cross (see Figure 14)*

ADC Power Change

Figure 13-b *ADC power loss over Flevoland (13 October 1991). Note the ADC power loss values in Flevoland polder area ranging from 0.2 dB to 0.5 dB (see Figure 14).*

3.2.2 Implications for the radiometric stability measurements

The previous results clearly indicate the need to correct for ADC non-linearities when measuring the radar cross sections of calibration target, especially when the target is located close to the sea (coastal area). In such a case the raw data would be required for the correction analysis. This means practical difficulties when a big number of scenes have to be analysed.

Another solution, provided by the SAR Verification Mode Processor (VMP) installed at ESA/ESRIN and at the D-PAF, is to generate a raw data power table for each processed product. Each entry in the table corresponds to the mean power of a block of raw data. The raw data block size is approximately the synthetic aperture length (1300 range lines) in the azimuth direction and the replica length (704 samples) in the range direction.

The average power of the raw data from each block is given by :

$$Po = \frac{1}{NM} \sum_{k=1}^{N} \sum_{j=1}^{M} \left(I^2 + Q^2 \right)$$

where N = number of range lines used
M = number of samples used per line

From the raw data power table is derived an ADC nonlinearity correction table using the table and figures given in chapter 3.1.

The ESA transponders are then located in the table in order to apply the ADC nonlinearity correction to their measured radar cross section. The location of the transponders is done with the following method:

Azimuth direction:

The transponder is first located in the image (PRI product) by its pixel position in metres relative to the first pixel of the first image line. Then the time shift Δt between the first raw data line (defined by the acquisition time) and the first image line (defined by the zero Doppler azimuth time of the first azimuth pixel) is calculated and converted in position shift using the satellite ground velocity (Vg = 6640 m/s) :

$$\text{Azimuth position}_{\text{(Raw data table)}} = \text{Azimuth position}_{\text{(PRI product)}} + (\Delta t \,.\, Vg)$$

Ground range direction:

The transponder is located in the image (PRI product) by its pixel position in metres relative to the first pixel of the first image line. This value is converted in slant range position. Half of the replica length (352 samples) is then subtracted to take into account discarding of samples during range compression:

$$\text{Range position}_{\text{(Raw data table)}} = \text{Slant range position}_{\text{(PRI product)}} - 352 \text{ samples}$$

When the transponder is located close to the limit between two blocks in the ADC correction table, then an average is done between the two blocks.

Table 6 gives the ADC correction to be applied on the measured radar cross sections of the ESA transponders during the commissioning phase and first ice phase. During the commissioning phase the transponders were located in Flevoland. During the first ice phase, they were located in Zeeland (Figure 14).

	ADC correction to applied on measured R.C.S. (values in dB)		
	Transponder 1	Transponder 2	Transponder 3
Commissioning Phase (Flevoland)			
07-SEP-1991	0.28	0.06	0.05
19-SEP	0.17	0.17	0.00
25-SEP	0.30	0.26	n.d.
01-OCT	1.98	0.57	0.39
07-OCT	0.32	0.22	0.26
13-OCT	0.30	0.39	0.21
19-OCT	0.67	0.32	0.38
25-OCT	0.25	0.30	n.d.
31-OCT	0.24	0.09	0.04
06-NOV	0.75	0.88	0.57
12-NOV	1.05	1.34	1.00
18-NOV	0.62	1.11	0.81
24-NOV	0.52	0.76	0.54
30-NOV	0.35	0.73	0.33
06-DEC	0.57	0.48	0.49
First Ice Phase (Zeeland)			
11-JAN-1992	0.42	0.17	n.d.
17-JAN	n.d.	0.80	0.37
23-JAN	0.17	0.05	0.02
29-JAN	0.40	0.30	0.12
01-FEB	0.40	0.03	0.06
10-FEB	1.17	0.62	0.34
16-FEB	1.00	0.77	0.56
22-FEB	1.39	0.69	0.32
28-FEB	0.21	0.13	0.22
05-MAR	0.96	0.41	0.32
08-MAR	0.26	0.28	0.06
11-MAR	0.61	0.37	0.18
Flevoland + Zeeland Mean ± Standard deviation			
27 dates	0.59 ± 0.43	0.45 ± 0.33	0.32 ± 0.25
Flevoland only Mean ± Standard deviation			
15 dates	0.56 ± 0.45	0.51 ± 0.37	0.39 ± 0.29
Incidence angle	20.7 deg.	22.7 deg.	23.6 deg.
Zeeland only Mean ± Standard deviation			
12 dates	0.64 ± 0.40	0.39 ± 0.26	0.23 ± 0.16
Incidence angle	20.4 deg.	23.1 deg.	26.0 deg.

n.d. = no data

Table 6 *ADC non-linearity corrections to apply on the measured radar cross sections of the ESA transponders in Flevoland and Zeeland.*

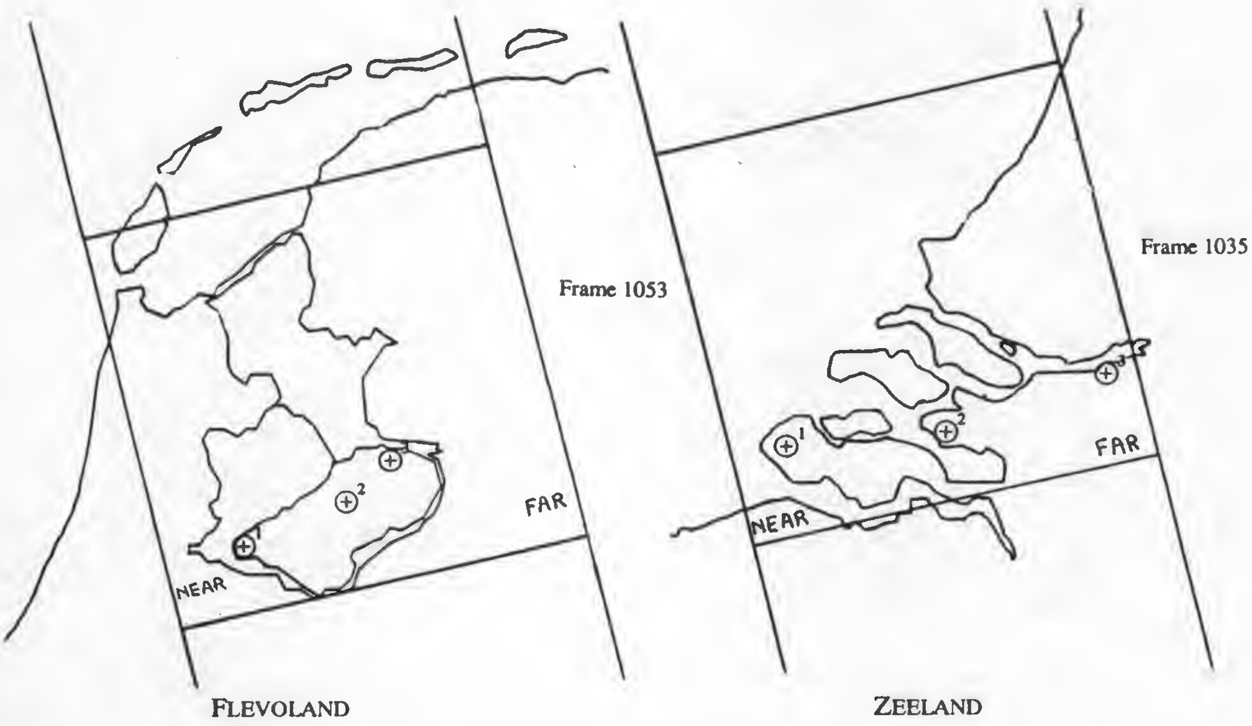

Figure 14 *Localisation of the ESA transponders in Flevoland (Commissioning Phase and Multi-Disciplinary Phase) and Zeeland (Ice Phases).*

The mean ADC non-linearity correction for the transponders depends on two effects (for both calibration sites):

- ***the transponder location in range***: the mean ADC correction decreases along range from 0.59 dB at near range (mean incidence angle of about 20.5 degreees for transponder 1) to 0.32 dB at far range (mean incidence angle of about 24.8 degreees for transponder 3). This an effect of the elevation antenna pattern.

- ***the vicinity of high backscattering large distributed targets*** (e.g. rough water surface areas): this is reflected by the standard deviation of the ADC correction. Transponder 1 is located close from the Ijsselmeer during the commissioning phase and close to the North Sea during the first ice phase. The areas of open water can produce a wide range of backscattering levels according to the state of the water surface and by consequence a large range of ADC correction to apply. As an example, a scene over Flevoland acquired on 14 March 1993 exhibits very low backscattering for the Ijsselmeer. Figure 15-a & b are plots of I channel standard deviation of the scene and ADC power change. Note that the I channel standard deviation can be as low as 1.04, which gives actually a positive ADC power change (i.e. a power gain) of up to 0.3 dB.

I Channel Standard Deviation

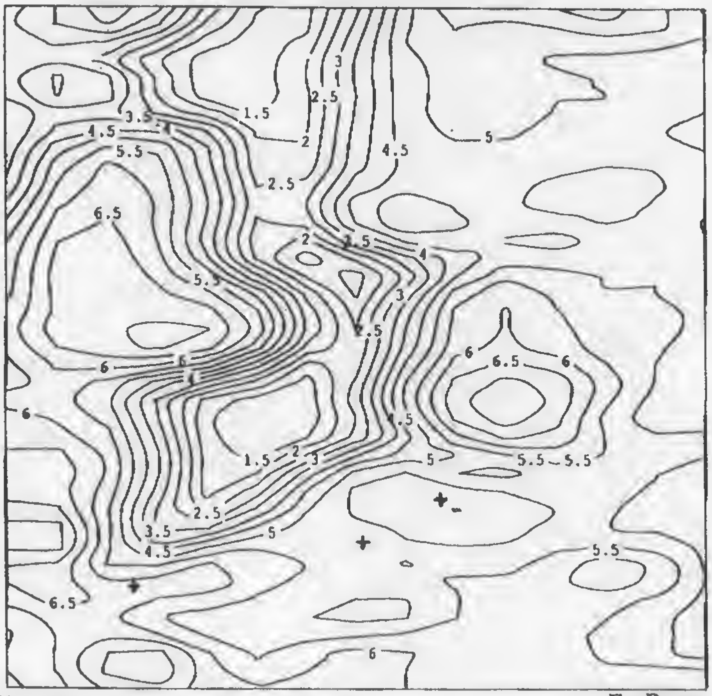

Figure 15-a *I channel standard deviation of a raw data scene over Flevoland (NL). The scene covers an area of about 105 x 105 km and has been acquired on 14 March 1993. Very low values of I channel standard deviation (down to 1.04) can be seen in the Ijsselmeer. The lake has a very low backscattering level.*

ADC Power Change

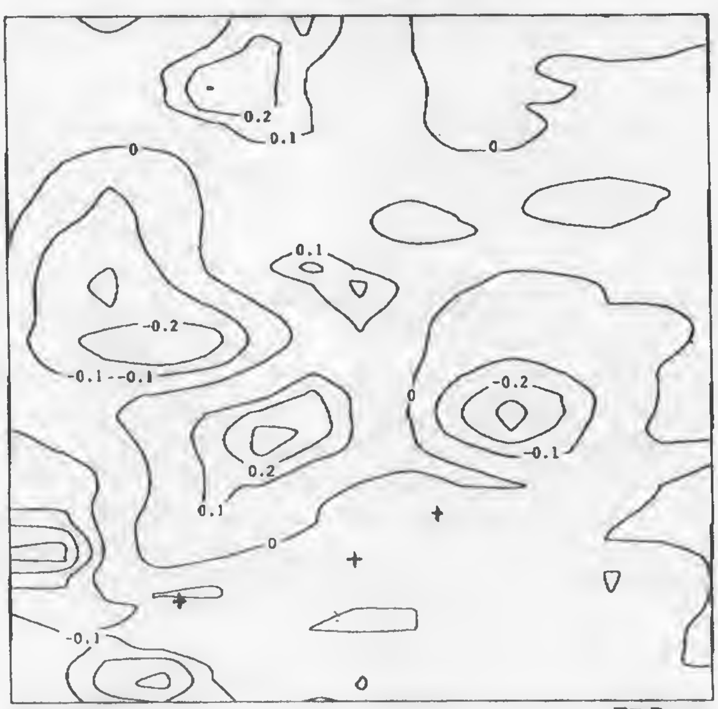

Figure 15-b *ADC power loss over Flevoland (14 March 1993). Note that there is no ADC correction to apply on the transponder responses.*

Table 7 gives the values of the radiometric stability and the radiometric accuracy measured with the transponder 2 before and after the ADC correction. The values before the ADC correction are values corrected for the replica pulse power variations.

Transponder 2 (38 measurements over 2 years)	**before** correction of ADC power loss estimate	**after** correction of ADC power loss estimate
radiometric stability	0.38 dB	***0.18 dB***
radiometric accuracy	0.32 dB	***0.16 dB***
max. variation of the measured RCS	± 0.75 dB	***± 0.42 dB***

Table 7 *Radiometric calibration parameters with correction of ADC non-linearities.*

Similar results are found for transponders 1 and 3. Detailed results are shown in Table 8.

From the results in table 7, it appears that ***the ADC non-linearities correction gives a substantial improvement in the precision of the radar cross sections measurements***. The derived radiometric parameters like the radiometric stability and the radiometric accuracy are ***reduced by half***.

Due to the high precision of the previously derived parameters, further radiometric corrections (which are usually neglected in SAR radiometric calibration) can be applied in the derivation of the ERS-1 calibration measurements. Potentials corrections are :

- correction of distributed target ambiguity
- correction of atmospheric propagation loss

All values are in Decibels	Measured RCS			Measured RCS with Replica Pulse Variations Correction			Measured RCS with ADC Non-linearities Correction			Measured RCS with updated calibration constant (+ 0.39 dB)		
	Tr. 1	Tr. 2	Tr. 3	Tr. 1	Tr. 2	Tr. 3	Tr. 1	Tr. 2	Tr. 3	Tr. 1	Tr. 2	Tr. 3
Commissioning Phase - Flevoland												
07-SEP-1991	0.60	0.68	0.56	0.14	0.22	0.10	0.42	0.28	0.15	0.03	-0.11	-0.24
19-SEP-1991	0.55	0.61	0.65	0.28	0.34	0.38	0.45	0.51	0.38	0.06	0.12	-0.01
25-SEP-1991	0.34	0.34	n.d.	0.07	0.07	n.d.	0.37	0.33	n.d.	-0.02	-0.06	n.d.
01-OCT-1991	-0.88	0.19	0.29	-1.10	-0.03	0.07	0.88	0.54	0.46	0.49	0.15	0.07
07-OCT-1991	0.42	0.57	0.68	0.17	0.32	0.43	0.49	0.54	0.69	0.10	0.15	0.30
13-OCT-1991	-0.03	***0.00***	-0.09	-0.03	***0.00***	-0.09	0.27	***0.39***	0.12	-0.12	***0.00***	-0.27
19-OCT-1991	-0.28	0.10	-0.56	-0.28	0.10	-0.56	0.39	0.42	-0.18	0.00	0.03	-0.57
25-OCT-1991	0.04	-0.03	n.d.	0.03	-0.04	n.d.	0.28	0.26	n.d.	-0.11	-0.13	n.d.
31-OCT-1991	0.18	0.34	0.21	0.16	0.32	0.19	0.40	0.41	0.23	0.01	0.02	-0.16
06-NOV-1991	-0.60	-0.19	-0.29	-0.54	-0.13	-0.23	0.21	0.75	0.34	-0.18	0.36	-0.05
12-NOV-1991	-0.59	-0.81	-0.86	-0.52	-0.74	-0.79	0.53	0.60	0.21	0.14	0.21	-0.18
18-NOV-1991	0.03	-0.61	-0.74	0.05	-0.59	-0.72	0.67	0.52	0.09	0.28	0.13	-0.30
24-NOV-1991	-0.28	-0.38	-0.61	-0.28	-0.38	-0.61	0.24	0.38	-0.07	-0.15	-0.01	-0.46
30-NOV-1991	-0.16	-0.08	-0.45	-0.18	-0.10	-0.47	0.17	0.63	-0.14	-0.22	0.24	-0.53
06-DEC-1991	-0.34	-0.01	-0.32	-0.34	-0.01	-0.32	0.23	0.47	0.17	-0.16	0.08	-0.22
First Ice Phase - Zeeland												
11-JAN-1992	0.23	0.33	n.d.	0.20	0.30	n.d.	0.62	0.47	n.d.	0.23	0.08	n.d.
17-JAN-1992	n.d.	-0.14	-0.07	n.d.	-0.15	-0.08	n.d.	0.65	0.29	n.d.	0.26	-0.10
23-JAN-1992	0.56	0.71	0.30	0.51	0.66	0.25	0.68	0.71	0.27	0.29	0.32	-0.12
29-JAN-1992	0.06	0.47	0.19	-0.05	0.36	0.08	0.35	0.66	0.20	-0.04	0.27	-0.19
01-FEB-1992	-0.27	0.54	n.d.	-0.32	0.49	n.d.	0.08	0.52	n.d.	-0.31	0.15	n.d.
10-FEB-1992	-0.52	-0.13	-0.15	-0.63	-0.24	-0.26	0.54	0.38	0.08	0.15	-0.01	-0.31
16-FEB-1992	-0.70	-0.15	-0.39	-0.81	-0.26	-0.50	0.19	0.51	0.06	-0.20	0.12	-0.33
22-FEB-1992	-0.37	-0.33	0.05	-0.48	-0.44	-0.06	0.91	0.25	0.26	0.52	-0.14	-0.13
28-FEB-1992	0.39	0.46	-0.16	0.30	0.37	-0.25	0.51	0.50	-0.03	0.12	0.11	-0.42
05-MAR-1992	-0.30	-0.24	n.d.	-0.39	-0.33	n.d.	0.57	0.08	n.d.	0.18	-0.31	n.d.
08-MAR-1992	0.13	0.41	0.18	0.04	0.32	0.09	0.30	0.60	0.15	-0.09	0.21	-0.24
11-MAR-1992	-0.15	0.11	0.32	-0.27	-0.01	0.20	0.34	0.36	0.38	-0.05	-0.03	-0.01
Multi-Disciplinary Phase - Flevoland												
03-MAY-1992	0.71	1.03	0.77	0.34	0.66	0.40	0.49	0.68	0.59	0.10	0.29	0.20
07-JUN-1992	0.55	0.81	0.55	0.15	0.41	0.15	0.42	0.57	0.36	0.03	0.18	-0.03
12-JUL-1992	n.d.	0.54	0.42	n.d.	0.44	0.32	n.d.	0.53	0.49	n.d.	0.14	0.10
20-SEP-1992	n.d.	0.57	0.53	n.d.	0.50	0.46	n.d.	0.57	0.54	n.d.	0.18	0.15
25-OCT-1992	n.d.	n.d.	-0.44	n.d.	n.d.	-0.52	n.d.	n.d.	0.09	n.d.	n.d.	-0.30
29-NOV-1992	n.d.	-0.60	-0.48	n.d.	-0.83	-0.71	n.d.	-0.09	0.07	n.d.	-0.48	-0.32
03-JAN-1993	n.d.	n.d.	0.56	n.d.	n.d.	0.45	n.d.	n.d.	0.47	n.d.	n.d.	0.08
14-MAR-1993	0.51	0.65	0.64	0.42	0.56	0.55	0.45	0.56	0.60	0.06	0.17	0.21
18-AVR-1993	-1.03	-0.28	-0.91	-1.02	-0.27	-0.90	-0.24	0.41	-0.08	-0.63	0.02	-0.47
23-MAY-1993	n.d.	0.39	0.47	n.d.	0.29	0.37	n.d.	0.31	0.38	n.d.	-0.08	-0.01
27-JUN-1993	0.20	0.59	0.53	0.11	0.50	0.44	0.32	0.52	0.47	-0.07	0.13	0.08
01-AUG-1993	0.22	0.18	0.12	0.11	0.07	0.01	0.34	0.33	0.19	-0.05	-0.06	-0.18
Mean	-0.02	0.17	0.05	-0.13	0.07	-0.06	0.40	0.45	0.25	0.01	0.06	-0.14
Standard Dev.	0.45	***0.43***	0.48	0.40	***0.38***	0.41	0.22	***0.18***	0.22	0.22	0.18	0.22
Max. Range	1.74	1.84	1.68	1.61	1.49	1.46	1.15	0.84	0.87	1.15	0.84	0.87

n.d. = no data

Table 8 *R.C.S. measurements of the transponders over 2 years (only ascending passes). The values are expressed in decibels. They are referenced to the measured radar cross section of transponder 2 on 13th October 1991 .The same calibration constant K is used to derive these measurements, except for the last columns set where the updated calibration constant Ku (Ku = K + 0.39 dB) is used. The standard deviation of the measurements is by definition the radiometric stability.*

3.2.3 Implications for the derivation of the calibration constant

The calibration constants for ESA ERS-1 products are derived from transponder 2 radar cross section on 13 October 1991 (Ref. 12). The estimation of the ADC non-linearities correction (computed from the raw data block power analysis) to apply on transponder 2 radar cross section for this date is 0.39 dB (see Table 6). A confirmation of the estimate is given by the mean ADC correction of 0.45 dB. An updated calibration constant is obtained when applying the ADC correction:

$$K(\text{updated}) = K + 0.39 \text{ dB}$$

The updated calibration constant K is ***consistent*** with previous K estimate error bounds given at the end of the commissioning phase. The updated K error bounds ± 0.42 dB are indeed within the previous estimation of ± 0.75 dB (Figure 16).

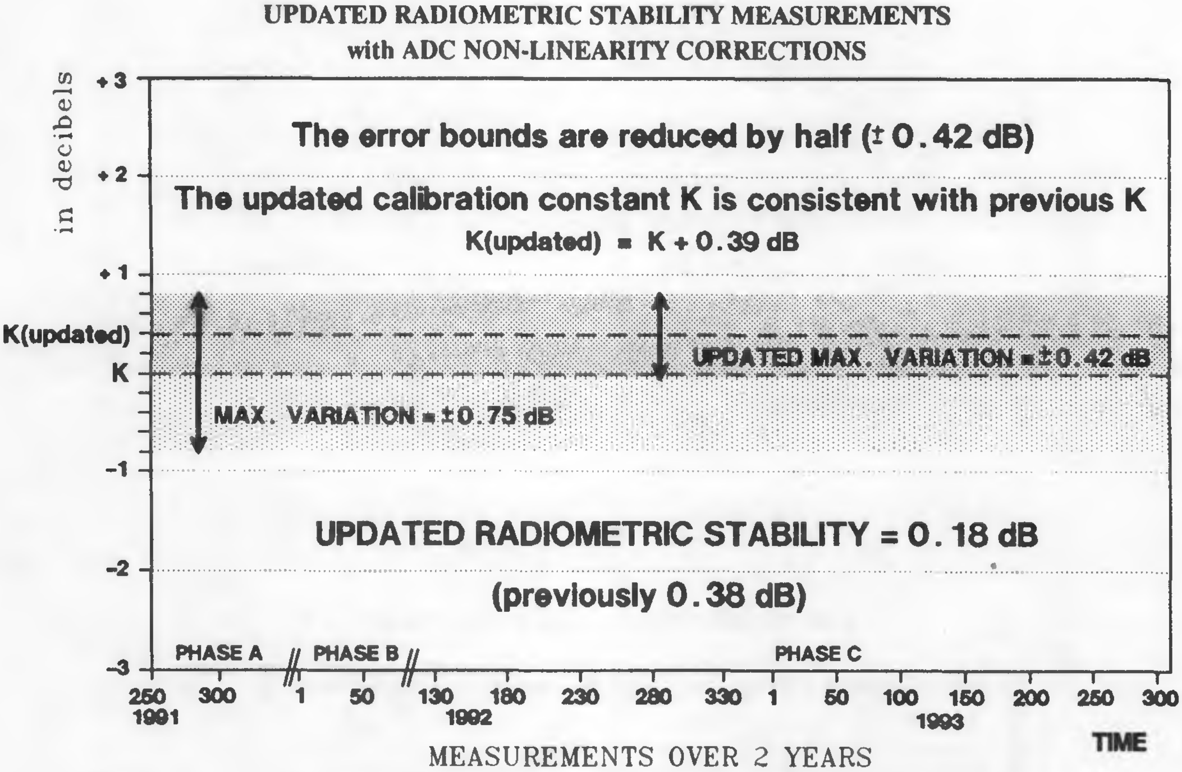

Figure 16 *Updated radiometric stability measurements with ADC non-linearity correction.*

3.2.4 Implications for the derivation of the in-flight antenna pattern

The in-flight ERS-1 SAR antenna elevation pattern has been estimated using detected images over the Brasilian rain forest. The derivation of the antenna pattern was done using the mean range profile of 10 images of uniform rain forest with the assumption that $\gamma = \sigma^o / \cos\alpha$ is a constant value for the rain forest (for the ERS-1 SAR incidence angles α). The derived mean polynomial of range profiles was set to zero at the boresight angle (look angle θ = 20.35 degrees). Noise compensation was applied. The estimated in-flight antenna pattern was then compensated in ESA PRI product (Ref. 12).

In order to check the effect of ADC non-linearities over the rain forest, a raw data image was analysed. Figure 17 gives the contour plots of the I channel standard deviation of the scene. The derived ADC power loss in the scene versus the look angle θ is given in Figure 18.

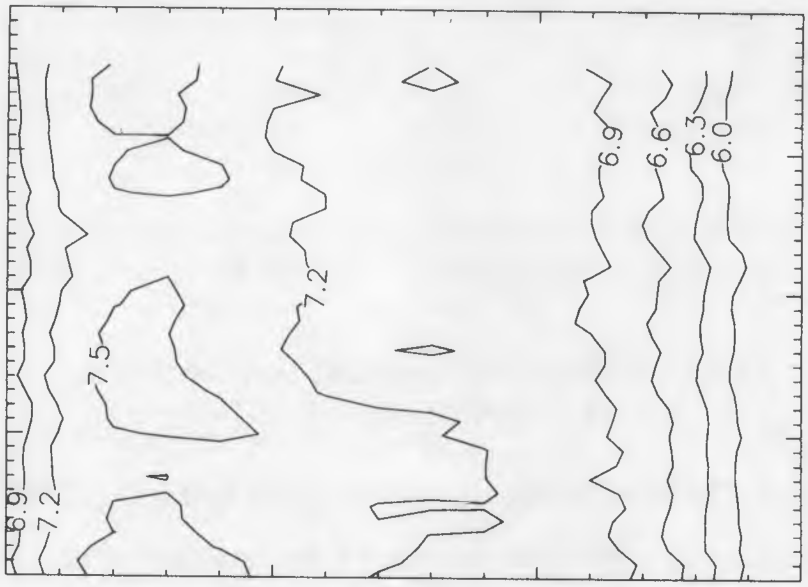

NEAR RANGE FAR RANGE

Figure 17 *I channel standard deviation of a raw data scene over the Brazilian rain forest. Note the high values of I channel standard deviation at near range.*

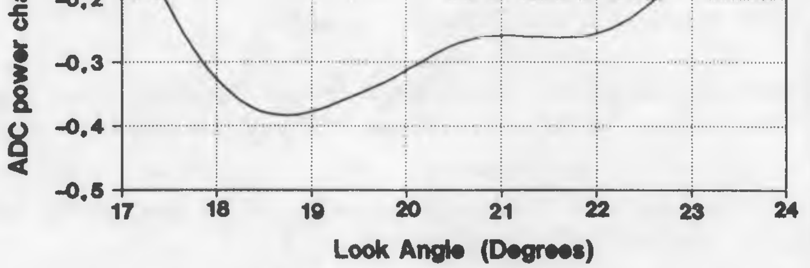

NEAR RANGE FAR RANGE

Figure 18 *ADC power loss in the preceding scene (Figure 17).*

The estimated ADC power loss correction is then applied on the previously derived in-flight antenna pattern. The new estimation of the antenna pattern has then to be set to zero at boresight angle in order to be comparable with the previous one. The result is given in Figure 19.

Figure 20 shows the difference between the new and previous antenna pattern estimation. Note that the difference is lower than 0.1 dB in the scene except at extreme far range (up to 0.3 dB).

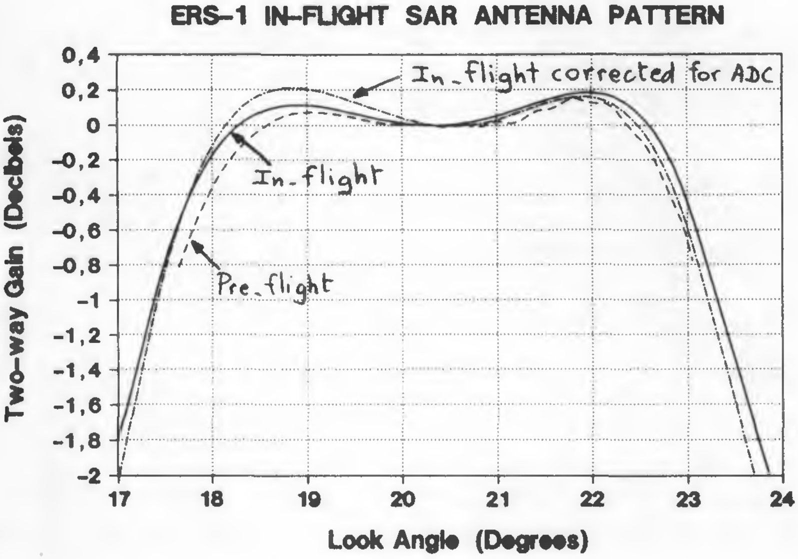

Figure 19 *ERS-1 in-flight antenna pattern estimations.*

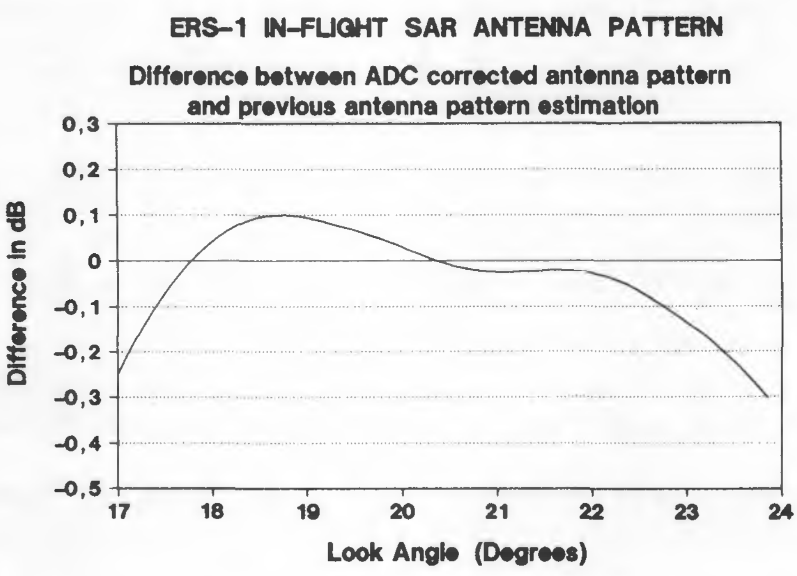

Figure 20 *Difference between ADC corrected antenna pattern and previous antenna pattern estimations.*

4. Conclusions

This study confirms the high radiometric stability of the ERS-1 SAR since beginning of the mission. When including the Analogic to Digital Converter (ADC) non-linearity corrections, we obtain a reduction by half of the radiometric calibration parameters such as the radiometric accuracy or the radiometric stability. The values of the calibration constants previously given within maximum bounds of about ± 0.8 dB are now given within maximum bounds of about ± 0.4 dB. The radiometric stability measured over two years is about 0.2 dB, well within the specifications.

The study has identified the ADC non-linearity as the main source of errors in the measurements of radar cross sections or backscattering coefficients. The ADC non-linearity occurs over large distributed targets having high backscattering level such as rough sea surfaces.

ERS-1 SAR calibration requirements have been carefully established following expert recommendations. One of these recommendations formulated ten years ago (Ref. 13) was the following : *"Calibration of ERS-1 to a level of ± 1 dB would be a major achievement"*.

Acknowledgments

The authors wish to thank their ESA colleagues (including M. Doherty and E. Attema) for useful discussions and the ESA Processing and Archiving Facilities of Germany and United Kingdom for their contribution.

References

1. H.D. Jackson & A. Woode, 'Development of the ERS-1 Active Radar Calibration Unit', *IEEE Trans. on Microwave Theory and Techniques*, Vol. 40, No. 6, pp. 1063-1069, June 1992.

2. D.C. Lancashire, 'ERS-1 AMI Calibration and Characterisation Plan', *Marconi Space Systems Report*, ER-PL-MSS-AM-0008, Issue 13, March 1987.

3. P.J. Meadows, 'ERS-1.SAR.RAW Replica Pulse Analysis', *GEC-Marconi Research Centre Report*, PF-TN-MRC-0002, Issue 2.0, October 1992.

4. J. Sanchez & H. Laur, 'ERS-1 SAR Products Validation', *to appear in same proceedings*, September 1993.

5. P.J. Meadows, 'The Effect of using Corrupt Replica Pulses on UK-PAF Processed ERS-1.SAR.PRI Imagery', *GEC-Marconi Research Centre Report*, PF-TN-MRC-0005, Issue 1.0, December 1992.

6. P.J. Meadows, 'ERS-1.SAR.PRI Status Report', *GEC-Marconi Research Centre Report*, PF-TN-MRC-0006, Issue 1.0, January 1993.

7. B. Schättler, W. Noack, H. Wilhelms, 'Die Verarbeitung von SAR-Daten des ERS-1 bei der D-PAF', *Proceedings of the 8th Radar Symposium*, Neupiperg, pp. 186-191, September 1993.

8. P.A. Wright, 'ERS-1 SAR CATA of the Raw Data Quality Parameters and the Internal Calibration Parameters for September 1991 to December 1992', *GEC-Marconi Research Centre Report*, PF-TN-MRC-0010, Issue 1.0, June 1993.

9. P.J. Bird, D.R.D. Kenward, G.E. Keyte, 'An Experiment for the Radiometric Calibration of the ERS-1 SAR', *Proceedings of the First ERS-1 Symposium*, Cannes, ESA SP-359, pp. 195-200, November 1992.

10. P.J. Meadows & C.M. Stapleton, 'Replica Pulse Power and Absolute Calibration Scaling Factor Variations', *GEC-Marconi Research Centre Report*, PF-TN-MRC-0001, Issue 1.0, September 1992.

11. GEC-Marconi Research Centre, 'SAR Data Quality Assessment and Rectification', *ESA contract report No. 6635/86/HGE-I*, March 1988.

12. H. Laur, 'ERS-1 SAR Calibration: Derivation of Backscattering Coefficient σ^{o} in ERS-1.SAR.PRI Products', *ESA/ESRIN Technical Note*, Issue 1, Rev. 0, October 1992.

13. 'Radar Calibration', *Proceedings of EARSEL Workshop*, Alpbach, Austria, December 1982.

PLANNED RADIOMETRIC CALIBRATION SCHEME FOR THE ENVISAT-1 ASAR INSTRUMENT

D L Hurd

Matra Marconi Space Uk Limited
Portsmouth

ABSTRACT

The ENVISAT-1 ASAR instrument requirements for radiometric calibration are embodied in a specification for the overall system readiometric accuracy (In contrast, only the radiometric stability of the spaceborne instrument was specified for ERS-1 AMI (SAR). The paper describes the planned calibration scheme for achieving the radiometric accuracy requirements for the ASAR instrument. Four areas are covered:

a) Internal calibration An internal calibration loop is built into the ASAR equipment which enables the characteristics of all the active circuits in the instrument, in particular the TR Modules in the active antenna, to be monitored in-flight.

b) External calibration End to end system calibration using ground transponders is proposed.

c) External characterisation In-flight characterisation of the passive radiator, the calibration loop itself, and the antenna mechanical pointing is planned using a ground receiver.

d) Ground processor requirements The requirements placed on the ground processor by the proposed calibration scheme are outlined.

The predicted performance of the scheme is quantified and compared with the radiometric accuracy requirement.

Keywords: SAR, Calibration, Active phased array SAR.

1. INTRODUCTION

1.1 Background

The first ESA Polar Orbit Earth observation Mission (POEM; Ref. 1), designated ENVISAT-1, will include the Advanced Synthetic Aperture Radar (ASAR) instrument. The ENVISAT-1 ASAR (Ref.2) is an active phased array radar, and is the first instrument of this type to be included in an ESA mission. Previously, the ERS-1 mission included the Active Microwave Instrument (AMI), part of which is a SAR incorporating a passive antenna (Ref.3).

The ENVISAT-1 ASAR instrument requirements for radiometric calibration are embodied in a specification for the overall system radiometric accuracy, including the ground segment. In contrast, only the radiometric stability for the spaceborne instrument was specified for the ERS-1 AMI SAR. The specified radiometric accuracy for ASAR is 1.75dB. This is to be interpreted as a worst case (i.e three sigma) value. For ERS-1, the SAR radiometric stability was specified as 0.95dB, and this was to be interpreted as an RMS value rather than worst case. Therefore the requirement, as specified, is more stringent for ASAR than for ERS-1. It should be noted that the observed ERS-1 SAR radiometric stability is significantly better than its specification value. Thus the more stringent specification on ASAR is necessary to ensure that the user will obtain data of comparable or better accuracy from ASAR than that obtained from ERS-1.

The principal engineering challenge for ASAR radiometric calibration is presented by the active antenna. The antenna includes 320 Transmit-Receive (TR) modules, each of which is connected to a radiating sub-array. Each TR Module includes transmit and receive chains of active components which provide amplification, and programmable amplitude and phase adjustment. Instabilities in the gain and phase characteristics of these will distort the antenna gain pattern of the phased array. This would potentially cause a radiometric error in the SAR image. The need to calibrate the active antenna for ASAR requires a calibration scheme radically different from that employed for the ERS-1 SAR.

1.2 TR module temperature compensation

The TR module amplitude and phase characteristics will vary principally as a function of temperature. However, the characteristics may also be subject to ageing, and in the extreme, TR modules may fail completely. The instrument control concept includes a TR Module temperature compensation scheme. The variation with temperature of the amplitude and phase characteristics of each individual TR Module is established on-ground. Each TR module includes a thermistor for temperature measurement. The on-ground characterisation data is reduced to a set of coefficients which approximately define the observed temperature dependence of the amplitude and phase characteristics. These coefficients are stored on-board, and are used in conjunction with the in-flight temperature measurements in an algorithm which calculates the required control settings for the amplitude and phase shifter devices within each TR Module. The calculated settings compensate for the TR Module variations so that the amplitude and phase shift along each path through the antenna is stable with temperature. This stabilises the antenna transmit and receive gain patterns.

Using the temperature compensation scheme, it is anticipated the active antenna will possess a high degree of stability. However the scheme will not account for ageing effects, or TR Module failures. Also, under conditions of rapid temperature variations, such as those occurring close to eclipse, the temperature distribution within each TR Module may differ significantly from that occurring during on-ground characterisation. This may lead to compensation errors. Thus the compensation scheme alone may not achieve adequate antenna stability over the lifetime of the instrument to meet the radiometric accuracy requirements.

1.3 Overview of the ASAR calibration scheme

The planned radiometric calibration scheme for ASAR is performed by four distinct functions:

a) Internal calibration
b) External calibration
c) External characterisation
d) Ground processor corrections

1.3.1 Internal calibration

The basic principle followed in the ASAR internal calibration scheme is similar to that employed in AMI. Distinct calibration paths are built into the instrument, and special calibration pulses are routed around the instrument via the calibration paths. The calibration pulses are sampled, and linked to the ground along with the science data. The ground processor measures the calibration pulses and this gives an indication of drifts in the instrument gain.

However, the detailed implementation in ASAR is quite different from that employed in AMI, as necessitated by the particular problems concerned with calibration of the active antenna. The key feature of the ASAR internal calibration scheme is that a distinct calibration path is provided to each of the 320 TR modules. This enables transmit pulses at each TR module output to be sampled. It also allows calibration pulses to be injected into the receiver front end of each TR module. Effectively, the scheme provides a multi-pathed calibration loop that encompasses all the active electronic circuits in the instrument transmit and receive paths. In particular, the scheme provides a solution to the potential shortcomings of the TR module temperature compensation scheme, as discussed in Section 1.2 above. Ageing of TR Module characteristics and module failure can be sensed using the calibration loop.

1.3.2 External calibration

The internal calibration scheme is intended to allow relative drifts in the instrument gain to be monitored by the ground processor. In order to meet the requirements for absolute accuracy of the radar cross section information in the image, it is necessary to provide an absolute end to end calibration facility. This facility comprises an external reference transponder target whose radar cross section has been accurately determined. The transponder characteristics can be similar to those of the ERS-1 AMI, but the additional feature of dual polarisation is required for the transponder, since ASAR is a dual polarisation instrument (horizontal and vertical).

External calibration measurements are made infrequently, at intervals of at lease six months. The interval calibration scheme maintains the radiometric accuracy in the interval between external calibrations.

1.3.3 External characterisation

The internal calibration scheme monitors drifts in the gain of the majority of the instrument. However, drifts in elements outside the calibration loop are not monitored and therefore are not compensated. Specifically these elements are the passive part of the antenna (i.e the radiator), and the calibration paths themselves. Also drift in the antenna mechanical pointing is not compensated.

The characteristics of the uncompensated element are monitored infrequently (at intervals of at least six months) using an external characterisation ground receiver. This enables any gross bias effects introduced at launch to be characterised. Also ageing and failure effects associated with the uncompensated elements can be monitored.

1.3.4 Ground processor corrections

The ground processor uses the information obtained from internal and external calibration, and external characterisation measurements, and also from satellite attitude and slant range measurements to correct the image magnitude such that a calibrated image is produced.

2. INTERNAL CALIBRATION SCHEME

2.1 Calibration loop

Each TR module contains separate transmit and receive chains for operation in horizontal (H) and vertical (V) polarisations. There are separate H and V feeds from each TR module to its associated radiator sub-array, each feed being used for both transmit and receive. Within each TR module, a directional coupler is located immediately before each of the feeds to provide a calibration path. The pair of couplers within each TR module are combined via a passive hybrid network, which is connected to a calibration input/output port. Calibration pulses are coupled into or out of each TR module via its calibration port. The 320 connections from the calibration ports of all the TR Modules are combined through a passive distribution network to provide a single calibration connection between the antenna and the instrument central electronics assembly. The calibration distribution network is in fact very similar to the primary distribution network which provides the main transmit/receive paths between the central electronics and the antenna. Figure 1 shows a schematic of the calibration loop.

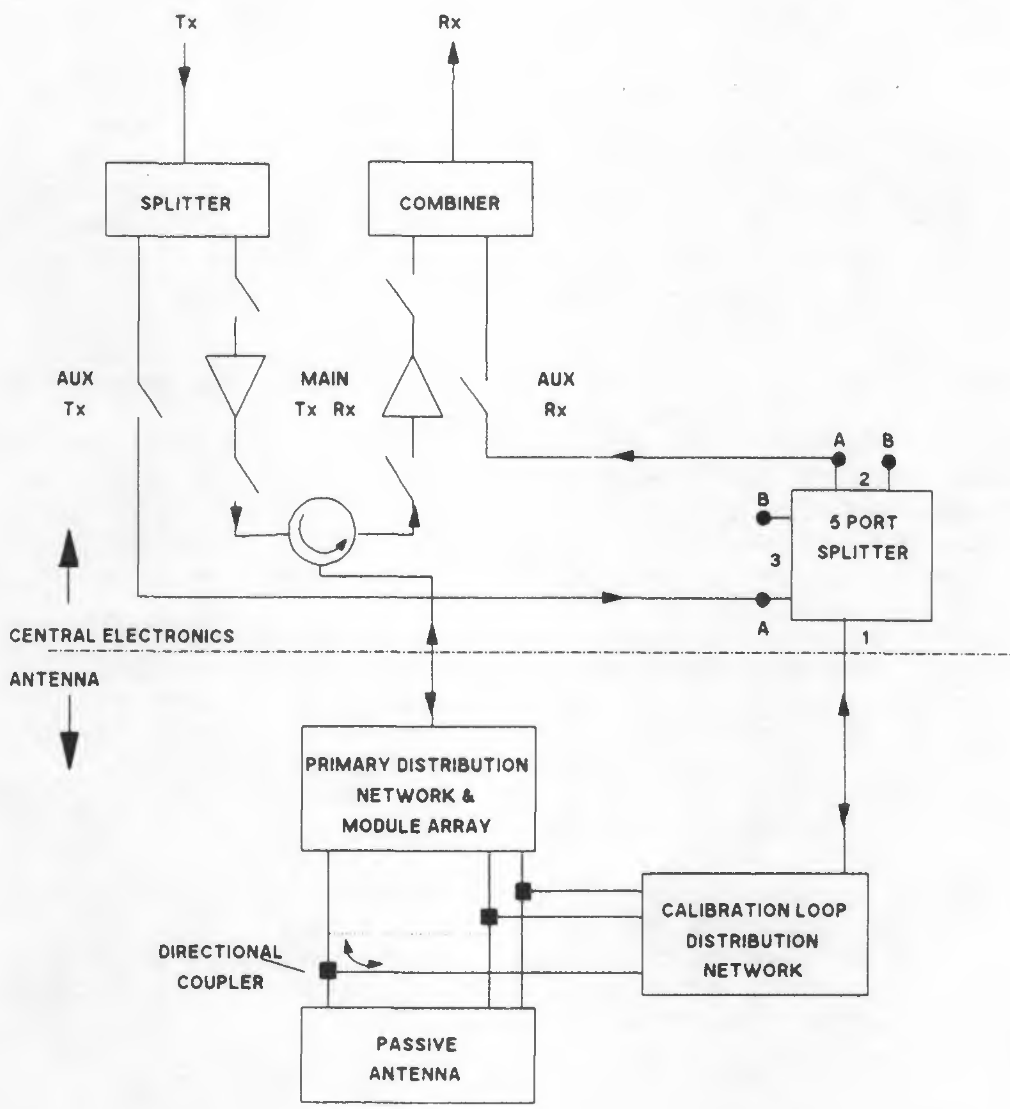

Figure 1 : Calibration loop schematic

In the central electronics, the calibration path connects to a five port passive network. This is used to route calibration pulses from the antenna to the main receiver chain via an auxiliary receive path, and to inject calibration pulses into the antenna via an auxiliary transmit path. It is also used to route pulses around the majority of the central electronics via the auxiliary transmit and receive paths. The central electronics transmit and receive chains are dual redundant (labelled A and B). Figure 1 shows the connections to the A side only.

The calibration paths, between the directional couplers in the TR modules and the five port network contain no active components. This maximises the reliability and stability of the calibration loop. Both primary and calibration distribution networks on the antenna are designed as equi-time, equi-phase networks.

2.2 Calibration pulses

The 320 TR modules, and their associated radiator sub arrays are arranged in 32 rows with 10 modules in each row along the length of the antenna. ASAR is essentially an elevation steering instrument, therefore in normal operation the phase settings are nominally equal for the ten modules in each row. The phase is varied between rows in order to steer and shape the elevation beam. Also, uniform amplitude weighting is applied along each row.

The planned internal calibration scheme for ASAR characterises the active part of the antenna on a row by row basis. Calibration pulses from one row of modules are combined in the distribution network, nominally with equal phase and amplitude. During normal operation, a sequence of calibration pulses is interleaved with the normal radar pulses. This sequence characterises each row in turn for both transmit and receive.

The instrument also has a special module stepping mode in which the antenna is characterised on a module by module basis. However, during normal operation, row stepping is preferred to module stepping because it characterises the antenna more quickly (one tenth of the time) and the combined signal from the distribution network is 20dB bigger for a row than for a module, and therefore can be measured more accurately.

The calibration scheme relies on the characteristics of a row when measured in isolation being representative of its characteristics when operating normally in conjunction with all other rows. Therefore interference from leakage signals through the modules in other rows that are nominally off during a calibration pulse needs to be minimised. Also there is one specific feature of the design that has necessitated special consideration in the calibration scheme. Each TR module shares a power supply with three other modules, which are in different rows. Therefore the transient load on each power supply will be different for the cases where one row only transmits, and all rows transmit. This could cause a change in the transmit characteristics of a row between the two cases. This potential problem is avoided by the following scheme. For transmit calibration, rows are turned on in groups of four corresponding to the power supply demarcations, but only one of the four is the 'wanted' row, whose characteristics are to be measured. The modules within the wanted row take the amplitude and phase settings appropriate to normal operation. The phases of the modules in the three unwanted rows are set so that their combined signal out of the calibration distribution network is nominally zero. Thus their interference to the measurement of the wanted row characteristics is minimised. The amplitude setting on each of the unwanted rows is set to its normal operating value to produce the same power supply loading as in normal operation. The transmit calibration pulse in which four rows are excited is referred to as pulse 1. Pulse 1 is routed to the central electronics receiver via the auxiliary receive path (see figure 1).

A second type of transmit calibration pulse, referred to as pulse 1A, is also included in the scheme. The purpose of this pulse is to characterise the residual unwanted signal arising from imperfect cancellation of the three unwanted rows during pulse 1. During pulse 1A, the three unwanted rows alone are excited with the same amplitude and phase settings as in pulse 1, and the residual signal is measured. The power supply loading will be not quite representative during pulse 1A since only three of the four rows sharing a power supply are excited. Therefore there could be a small error on the estimation of the small residual signal. This is acceptable since the error involved will be very small compared with the wanted row contribution to the pulse 1 signal.

For receive characterisation, one row of module receivers is activated while so-called calibration pulse 2 is injected into the calibration distribution network using the auxiliary transmit path (see figure 1). Pulse 2 passes along the main receive chain in the central electronics.

The central electronics transmit and receive paths are included in both the transmit and receive row characterisation. It is thus necessary to characterise the central electronics separately so that its effect can be removed (in the ground processor) from the receive row measurements. Its effect is then included once only, in the transmit row measurements. Characterisation of the central electronics is achieved by calibration pulse 3, using both transmit and receive auxiliary paths (see Figure 1).

The various calibration pulses, the means of controlling them using the switches in the auxiliary transmitter and receiver in Figure 1, and the associated module states are summarised in Table 1.

PULSE NO	FUNCTION	SWITCH STATE				MODULE STATE		
		TRANSMIT		RECEIVE				
		MAIN	AUX	MAIN	AUX	WANTED ROW	UNWANTED ROW (3)	OTHER
1	Sense wanted row transmission	ON	OFF	OFF	ON	TX	TX	OFF
1A	Sense unwanted row transmission	ON	OFF	OFF	ON	OFF	TX	OFF
2	Inject into wanted row receivers	OFF	ON	ON	OFF	RX	OFF	OFF
3	Route around central electronics	OFF	ON	OFF	ON	OFF	OFF	OFF

Note: The unwanted rows consist of the modules sharing the power supplies with the modules in the wanted row.

Table 1: Calibration pulses

Pulses 1, 1A and 2 are repeated for each of the 32 rows. Together with pulse 3, this then constitutes a complete internal calibration cycle of the instrument.

2.3 Timelining of calibration pulses

The ASAR instrument includes five operational modes (Ref.2)

- image mode
- wave mode
- wide swath mode
- alternating polarisation mode
- global monitoring mode

The basic principles of the internal calibration scheme, as described in Sections 2.1 and 2.2, are followed in each of the operational modes. The detailed timelining of the calibration pulses is tailored to meet the particular features of each mode.

For all modes, a complete row calibration cycle is performed at the beginning of the mode, prior to the start of the imaging sequence. For wide swath and global monitoring modes, which use the ScanSAR principle across five sub swaths, the initial row cycle is repeated for each sub swath. For alternating polarisation mode, the initial row cycle is repeated for each polarisation. The initial calibration sequences occupy less than 1 second.

During the imaging sequence itself, calibration pulses are periodically inserted into the timeline. A row cycle is completed within typically 15 - 30 seconds. The instrument performance degradation due to inserting the calibration pulses is negligible. In wave, wide swath and global monitoring modes, there are natural gaps in the imaging sequence which can be used for calibration. In image and alternating polarisation modes, typically one echo in 1000 is lost due to the insertion of the calibration pulses.

2.4 Noise measurements

The internal calibration scheme also includes measurements of the instrument noise level. The measurements are included in the initial calibration sequences at the beginning of a mode. The echo window is sampled at a time when no echoes are present.

In the modes with natural gaps in the imaging sequence (wave, wide swath and global monitoring modes), noise measurements are also made during the normal operation of the mode. In image and alternating polarisation modes, noise measurements are not made during normal operation, because it would be necessary to cease transmissions to allow all echoes to die away. For these modes, it is assumed the noise level tracks the receiver gain during the imaging sequence. The receiver gain drift is monitored (in the ground processor) from measurements of Pulse 2 at the auxiliary transmit output and the main receiver output.

3. EXTERNAL CHARACTERISATION SCHEME

External characterisation is a dedicated instrument mode, performed while over flying a receiver located on the ground. During the mode, the SAR transmits a sequence of pulses from each antenna row in turn. These pulses are received and digitised on the ground, and the data are recorded for off-line processing. The pulses are also coupled into the SAR receiver using the calibration loop, and the resulting data are down-linked.

Ideally the ground receiver should lie at the centre of the azimuth beam pattern of each row at the time of the row transmission cycle, which would require very accurate knowledge of the orbit. This is avoided by repeating the cycle of transmissions from the rows continually over a 0.5 second period. Each cycle has a duration of approximately 12 ms. The particular cycle for which the receiver was at beam centre can be determined from the processed data.

To aid demodulation of the row transmission sequence, a carrier acquisition sequence is transmitted from one column of subarrays of the SAR antenna before and after the 0.5 second period of the row sequence. The carrier acquisition sequence is recorded by the ground receiver, and demodulation is performed in the off-line processing.

The phase and amplitude of the pulse from each row is determined and compared for the two measurement data sets - that from the ground receiver, and that downlinked from the SAR. The relative amplitude and phase characterises the row of radiating sub arrays and the calibration path from the row. The linear component of phase variation across the rows is used to determine the elevation angle of the ground receiver. This can be compared with the elevation angle predicted by the satellite orbit and attitude, and the ground receiver location in order to characterise the mechanical pointing of the antenna.

External characterisation is performed for both H and V polarisations.

4. EXTERNAL CALIBRATION SCHEME

External calibration is proposed using three target transponders, positioned along an East-West line with approximately 20Km spacing between adjacent transponders. The aim is to make transponder observations over the full range of the ASAR swaths, but mainly using one mode only (image mode).

The ENVISAT-1 orbit repeat period is 35 days, but the orbit almost coincides every 3 days, being shifted by approximately 100km at latitude 50°N. Therefore on five successive near coincient orbits, the transponders can be observed over a range of 400km in off nadir distance, compared with a total coverage of the ASAR swaths of 490km. A second series of five observations can be made with the satellite direction reversed; ie both ascending and descending passes can be used.

The proposed transponder positioning enables all three transponders to fall within a single swath and therefore be observed on most of the passes. Overall it is anticipated that 22 transponder observations in image mode can be made within one 35 day period. These observations would be split between H and V polarisations. A few observations would be made in other modes as a cross check on the ground characterisation of instrument variations between modes.

5. GROUND PROCESSOR CALIBRATION REQUIREMENTS

In outline, the ground processor must perform the following functions associated with calibration. The amplitude and phase of the calibration pulses 1, 1A, 2 and 3 are measured for each row. The amplitude and phase of pulse 2 relative to the amplitude and phase of pulse 3 are calculated, and pulse 1A is vectorially subtracted from pulse 1, as discussed in Section

2.2. The derived amplitude and phase values for the 32 rows on transmit and receive are used to estimate the two way instrument gain at a reference elevation angle for the swath. This calculation makes use of the ground characterised radiation patterns (amplitude and phase) of the 32 rows; and also the external characterisation data, as discussed in Section 3. The ratio of the estimated instrument gain at the reference angle to its ground characterised value is determined. This ratio is used to scale the complete ground characterised instrument gain pattern. The scaled pattern is then used as the instrument gain reference pattern.

The instrument gain reference pattern is converted from antenna to orbit coordinates, making corrections for the antenna pointing error, as determined from external characterisation, and also for the satellite attitude variations.

The replica of the transmitted pulse is calculated from the pulse 1 measurements (after vector subtraction of the pulse 1A measurements), the ground characterised row patterns, and the external characterisation data. The constructed replica tracks variations in all the instrument active circuits apart from the TR module receive circuits, and the central electronics main receiver up to the auxiliary receiver injection point (see Figure 1). The replica is used to determine the range reference function for use in the range compression processing.

The ground processor includes a Doppler tracker, which corrects for azimuth pointing errors.

The ground processor makes corrections for variations in the instrument gain reference pattern, and the instrument noise level (see section 2.4) and also applies an overall scaling factor determined from external calibration (see section 4).

Figure 2 shows a schematic of the data flow for the ASAR calibration process.

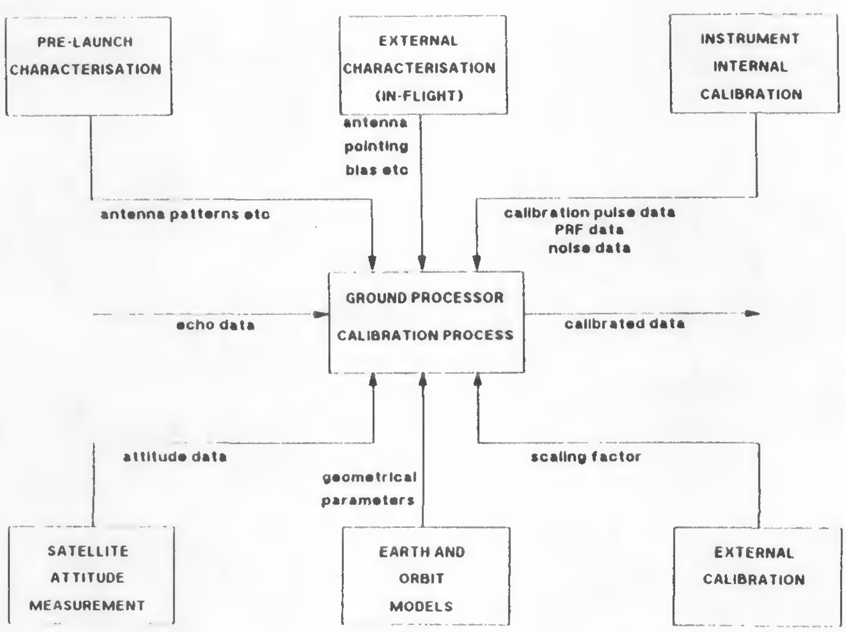

Figure 2: Calibration data flow

6. RADIOMETRIC ACCURACY PERFORMANCE

A detailed computer model for the ASAR radiometric accuracy performance has been implemented. The model includes over one hundred instrument parameters, as well as assumptions for the ground segment and satellite parameters. Using the model, the performance has been determined from the current estimates of the input parameters.

The estimated radiometric accuracy depends on the operational mode, and also the swath, and lies in the range 1.1 - 1.5dB compared with the requirement of 1.75dB. Thus the ASAR instrument is predicted to exceed the stringent requirement for radiometric accuracy.

7. REFERENCES

1. Mr Rast and C Readings 1992, The first mission of the ESA Earth Observation Polar Platform, Proc. of European 'International Space Year' Conference 1992, pp 1131-4.

2. D J Q Carter et al 1992, The Advanced Synthetic Aperture Radar (ASAR) for POEM-1, Proc of European 'International Space Year' Conference 1992, pp 1165-72.

3. S J Austin et al 1991, ERS-1 Spacecraft - Active Microwave Instrumentation : a Major Achievement, The GEC Journal of Research, 09,01, pp 2-12.

ERS-1 SAR PRODUCTS VALIDATION

Sánchez J.I., Laur H.

ESA/ESRIN
Frascati
Italy

ABSTRACT

Validation and quality monitoring of the ERS-1 SAR products is a vital task in order to ensure the success of the ERS 1 mission. This article explains the criteria used during the validation of ERS-1 SAR products (image mode) as well as the quality procedures implemented to control systematically the production in the ground stations and in the PAFs (Processing and Archiving Facility), once the products have been validated.

Some key quality results obtained after the two first years of mission are also presented.

Keywords: ERS-1, SAR, Validation, Quality, PAF, Ground Station.

1. INTRODUCTION

Since July 1991, ERS-1 has been providing the international community with a huge amount of data. To allow the exploitation of the data by the international scientific community and also by commercial users, a major effort must be invested in monitoring the quality and the consistency of the SAR products processed within the decentralised ESA ERS-1 ground segment.

2. SAR PRODUCT VALIDATION

2.1 ESA SAR Product Validation

2.1.1. ESA SAR Products

The ESA ERS-1 ground segment has been established using a decentralised set of processing facilities with central monitoring and control at ESA/ESRIN (EECF=ESRIN ERS Central Facility). The ERS-1 SAR products are generated at the ESA ground stations (Fucino, Kiruna and Maspalomas), at the PAFs (D-PAF at Oberpfaffenhofen, I-PAF at Matera and UK-PAF at Farnborough) and at ESA/ESRIN.

Four processors are involved in the generation of SAR products:

- **Fast Delivery Processor (FDP)** at the ground stations

  Provided by MDA
  DEC VAX 6210
  2 ST 50 Array Processors

- **Verification Mode Processor (VMP)** at D-PAF and ESRIN

  Provided by MDA
  DEC VAX 6210
  2 ST 50 Array Processors.

• **EMMA 2 Processor** at I-PAF

Provided by Telespazio/ELSAG
DEC VAX 6005
Special dedicated processor EMMA 2

• **EODC SAR processor** at UK-PAF

Provided by EDS SCICON
Microvax + Amteck
3 numeric array processors

In addition two geocoding systems, GEOS at D PAF and GEO at I PAF (under validation) are responsible for production of the geocoded products:

• **GEOS system** at D PAF

Provided by DLR/IPI/RSL/DIBAG
SUN SparcStations (SUN4)

• **GEO system** at I PAF

Provided by Telespazio
VAX 9000
Vector processing option

The different products generated are:

- **RAW**: annotated raw data in 8 bit format
- **SLC**: single look, complex, slant range image in 16 bit format (quarter scene)
- **UI16, FDC (UI16 off-line copy), PRI**: three look, detected, ground range image in 16 bit format
- **GEC**: Geocoded Ellipsoid Corrected product, derived from PRI
- **GTC**: Geocoded Terrain Corrected product, derived from PRI

A complete product description can be found in the document **ESA ERS-1 Product specification (ESA SP-1149).**

2.1.2 Strategy and status of validation.

The main tool used at ESA/ESRIN to analyse, validate and calibrate the SAR products is the **SARCALQ** system (SAR CALibration & Quality analysis) developed by EDS Scicon.

Fast delivery image quality is systematically monitored. Periodic updates of the FDP software have been performed to continuously improve the FDP's performance. Since February 1993 FDP SAR 4.2 processor has been running in all the ground stations. As the processing performed by the FDP SAR processor is simpler than that done by the off-line processors (e.g., there is not antenna pattern correction), anomalies are also less frequent.

Before a PAF starts to produce images operationally, the product must be validated by ESA/ESRIN. The PAF forwards a validation report with some examples (digital product on exabyte or on CCT, and photographic hardcopys), to ESA/ESRIN. After analysis, the product is either validated or recommendations are made for improvement of the product quality.

ESA/ESRIN and the PAFs work together to bring the different products inside the specifications previously determined by ESA.

Different checks are carried out:

• Image Visual Inspection

• Point Target QA (FDC, SLC, PRI)

- Spatial resolution (3 dB width in azimuth and range)
- Peak to Side-Lobe Ratio
- Integrated Side-Lobe ratio
- Localisation Accuracy
- Radar Cross Section (for PRI & SLC product)

• Distributed target QA (FDC, SLC, PRI)

- Radiometric resolution
- Backscatering coefficients (for PRI product)
- Verification of the antenna pattern implementation

In addition the linearity of the processor has to be demonstrated (with point targets and distributed targets).

For geocoded products the residuals (distance between a point in the image and the real position in the map) are measured. It is also verified that the geocoding processing retains the radiometric characteristics of the scene.

Different reference scenes have been chosen to perform the measurements needed to establish the quality of the product. The main test site is the Flevoland area in The Netherlands. Three transponders have been deployed by ESA/ESTEC in this area to allow the calibration and the quality analysis of ERS-1 SAR products. The transponder produces in the image the Impulse Response Function of the system. This IRF is used to determine some of the radiometric characteristics of the SAR image as well as the localisation accuracy of the scenes.

Additional test sites are found in Zeeland (NL)(during the ice phases the ESA transponders are moved to this area), Kent (UK/DRA calibration test site), ...Low and high latitude scenes are also used to investigate problems which may be due to latitude (e.g. antenna pattern correction).The Frankfurt area is the test scene used to control the quality of geocoded products. This area presents a mean height value of about 250 m, and an irregular relief.

The current status of the validation is summarised in the next table. To date 20 products have been validated with 5 different processors.

On-Line SAR Image Product

Detected Data	UI16	Fucino (I), Maspalomas (S), Kiruna (SW)	through satellite link

Off-Line SAR Image Product

Raw Data	RAW	D-PAF, EECF, I-PAF, UK-PAF	Telemetry Data + Annotations
Complex Data	SLC	D-PAF, EECF, I-PAF	Quarter Frame, Bandwidth=1400 Hz
	SLCF	UK-PAF	Full Frame, Bandwidth=1100 Hz
Detected Data	PRI	D-PAF, EECF, I-PAF, U-PAF	Pixel 12.5x12.5m, radiometrically corrected
	FDC	D-PAF, EECF	Pixel 16x20m, not radiometrically corrected
Ellipsoid Corrected	GEC	D-PAF, ***I-PAF****	From PRI product
Terrain Corrected	GTC01	D-PAF	If Digital Elevation Model available
	GTC02	D-PAF	If Digital Elevation Model available

Figure 1: *Table showing the validation status of ESA ERS-1 SAR image products*
** The GEC product from I PAF is under validation*

2.2. National & foreign stations SAR product validation

All around the world, different agencies are acquiring and processing ERS-1 SAR data. These agencies must demonstrate the quality of the ERS-1 SAR product that they generate. To control the products, the following information must be provided by the stations to ESA/ESRIN:

- Description of the SAR Processor
- Detailed SAR Products Specification
- Detailed Validation Procedures and Results
- Sample Products on CCT or Exabyte and on Slides (with annotations)

The stations validated to date are:

- Fairbanks (NASA/UAF,USA)
- Gatineau + Prince Albert (CCRS,Canada)
- Tromsö (TSS,Norway)
- Aussaguel (CNES,France)
- Hyderabad (NRSA,India)
- Alice Springs (ACRES,Australia)

3. QUALITY MONITORING

3.1. SAR performance monitoring

Systematically, the three ESA ground stations send to ESA/ESRIN the annotations of all the fast delivery images processed. These headers contain important information as to where and when the data were collected, the parameters used in the processing, quality flags showing the status of the communications link and statistical information about the raw data and the final image product. Other information about the noise measurements, calibration pulse and chirp replica is also sent. All this information is kept in a database at ESA/ESRIN to allow the monitoring and further investigation of trends or anomalies that may appear in the satellite's performance or in the image data acquired.

Daily, some UI16 samples are also sent from the stations, and backed up at ESA/ESRIN. These products are used to carry out further investigations after detection of anomalies. A report is produced monthly by ESA/ESRIN showing the results of the month's investigation. The next three figures (fig. 2,3 & 4) illustrate some of the controls performed at ESA/ESRIN to ensure the quality of the ERS-1 SAR products.

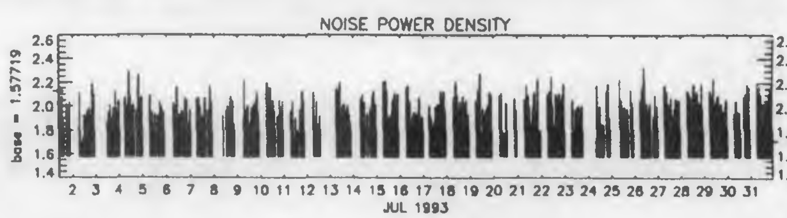

mean value=1.92957 std dev=0.146968

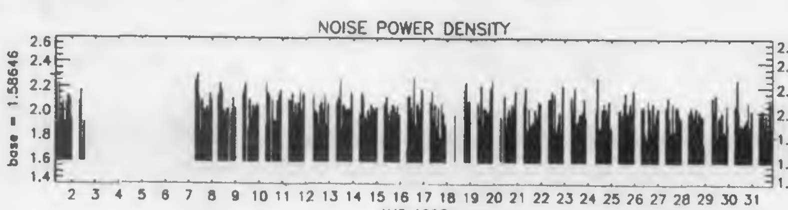

mean value=1.93026 std dev=0.146132

Figure 2: *Comparison of noise power in the radar system (July and August 1993)*

From fig.1 and fig.2 it is possible to compare the noise power density during July 1993 against the same parameter measured during August 1993.

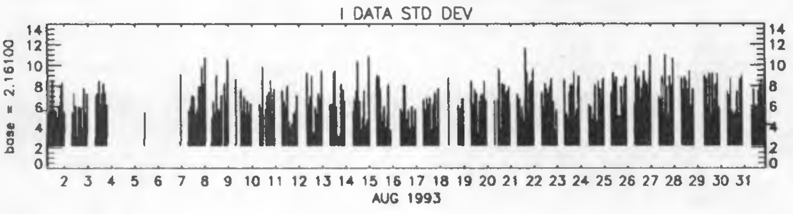

Figure 3: Raw data I channel std dev during August 1993

Figure 3 shows the ***standard deviation*** of the ***raw data*** in the ***I channel*** during August 1993. This information indicates if there is saturation in the raw data recorded by the satellite. This saturation has an important effect in every SAR Image product generated, independently of the processor used.

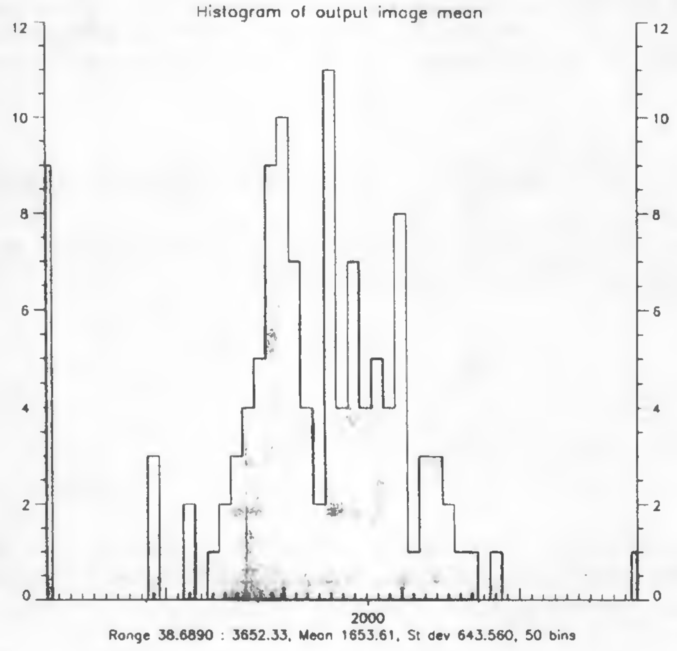

Figure 4: *Mean output value histogram of the FD products processed at Fucino station during February 1993*

Figure 4 shows a histogram of the ***mean output value*** of fast delivery images produced at Fucino station during February 1993. Because of a problem in the parameters used to process the data after the installation of a new FDP software version, Fucino station was producing low quality products for more than one week. These products had an output mean much lower than normal. After detection of the problem corrective actions were taken to resolve it.

3.2. SAR Image product quality results

The user community should have identical product quality independent of the ESA processor used to process the raw data. In other words, the ESA facility providing the SAR product should be transparent to the user. Unfortunately, different hardware and software means that it is very difficult to achieve exactly the same performance everywhere.

This table summarises the characteristics of the different products in the different PAFs.

PRI	ESRIN/D-PAF	UK-PAF	I-PAF	ESA Spec.
range resolution	24.88 m	24.5 m	29.62 m	< 30 m
azimuth resolution	21.5 m	20.00 m	24.04 m	< 30 m
islr	-9.44 dB	-14.20 dB	-9.75 dB	< -8 dB
range peak side lobe ratio	-20.73 dB	< -21 dB [1]	-22.83 dB	< -18 dB
azimuth peak side lobe ratio	-16.43 dB	< -21 dB [1]	-20.21 dB	< -18 dB

SLC	ESRIN/D-PAF	UK-PAF[2]	I-PAF	ESA Spec.
range resolution	9.8 m	9.48 m	9.60 m	< 10 m
azimuth resolution	5.3 m	5.27 m	6.05 m	< 10 m
islr	-14 dB	-10.47 dB	-14.55 dB	< -8 dB
range peak side lobe ratio	-22.37 dB	-13.99 dB	-18.63 dB	< -18 dB
azimuth peak side lobe ratio	-28.4 dB	-24.45 dB	-29.59 dB	< -18 dB

Figure 5: *PRI and SLC quality parameters for the different PAFs*
[1] *worst peak side lobe ratio*
[2] *SLCF: different bandwidth*

It should be noted that ESA Specifications refer to parameters measured on the transponders. The validation measurements are calculated as the average of the results from both transponders and point targets of opportunity (this explains why the range peak side lobe ratio for UK PAF products is outside the validation threshold).

The measurements always refer to the same area, Flevoland, but not always the same date. The date depends on the products used by the PAF to prepare the validation report. However, it is always October 1991.

These parameters are very stable through time. The standard deviation for these quality indicators for transponder 2 (PRI ESRIN product) in the Flevoland area during the multidisciplinary phase (since April 1992) are:

- range resolution 0.32 m
- azimuth resolution 0.47 m
- islr 0.53 dB
- range peak side lobe ratio 0.84 dB
- azimuth peak side lobe ratio 1.3 dB

The radiometric resolution is defined as $10\log_{10}(1+\sigma/\mu)$, σ being the standard deviation and μ the mean of the intensity of homogenous distributed targets.. Different measurements show that for the different facilities the radiometric resolution is always close to the nominal value:

- 1.98 dB for PRI products
- 3.01 dB for SLC products

3.3. SAR Image product troubleshooting

During ERS 1's life time, different problems have appeared in the various image products processed.

These problems are detected by:

- ESA/ESRIN
- PAFs
- External Users via ERS-1 Help Desk

Once a problem is confirmed, there is a discussion with the people concerned in order to clarify exactly the anomaly and the actions to be taken.

Some actions that could be agreed are:

• Modification of the parameters used in the processing
• Reprocessing of the data
• PAF asked for modification
• New version software
• Additional information for the user to correct the problem

The following flowchart shows the methodology used.

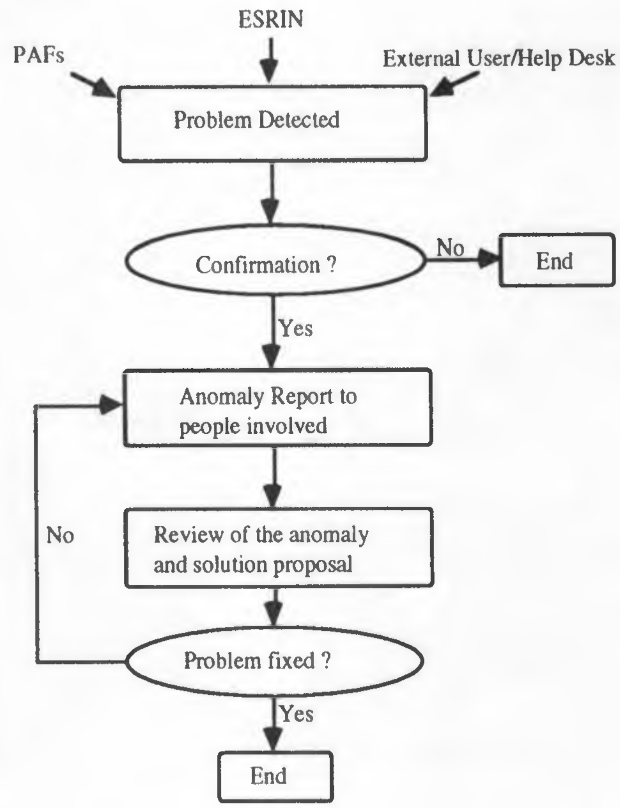

Figure 6: *Flowchart showing the methodology followed to solve the quality anomalies*

Some major problems that have been investigated and fixed during recent months are:

• Antenna Pattern Correction wrongly applied at UK-PAF
• Occasional corruption of the Chirp Data
• CEOS format anomalies
• Incorrect information on the ERS-1 Image catalogue
• Bad data supplied by the PAFs

Let's illustrate these anomalies with some examples:

At the beginning of this year, in UK-PAF PRI images over the Greenland area, an anomaly was detected. In near and far range, the images were clearly brighter than in mid range. One of these Greenland images is presented in figure 7. In a normal SAR scene the backscattered power usually decreases from near to far range. After investigations it was found that the antenna pattern correction was applied wrongly. Users affected by this problem were informed and provided with information to solve the anomaly. Some scenes were also reprocessed using the right correction. This anomaly was not detected during the validation checks because the Flevoland and Kent scenes used to verify the correct implementation were not affected by the anomaly. The problem

appeared only at low and high latitudes because the antenna pattern correction wrongly applied was latitude dependent.

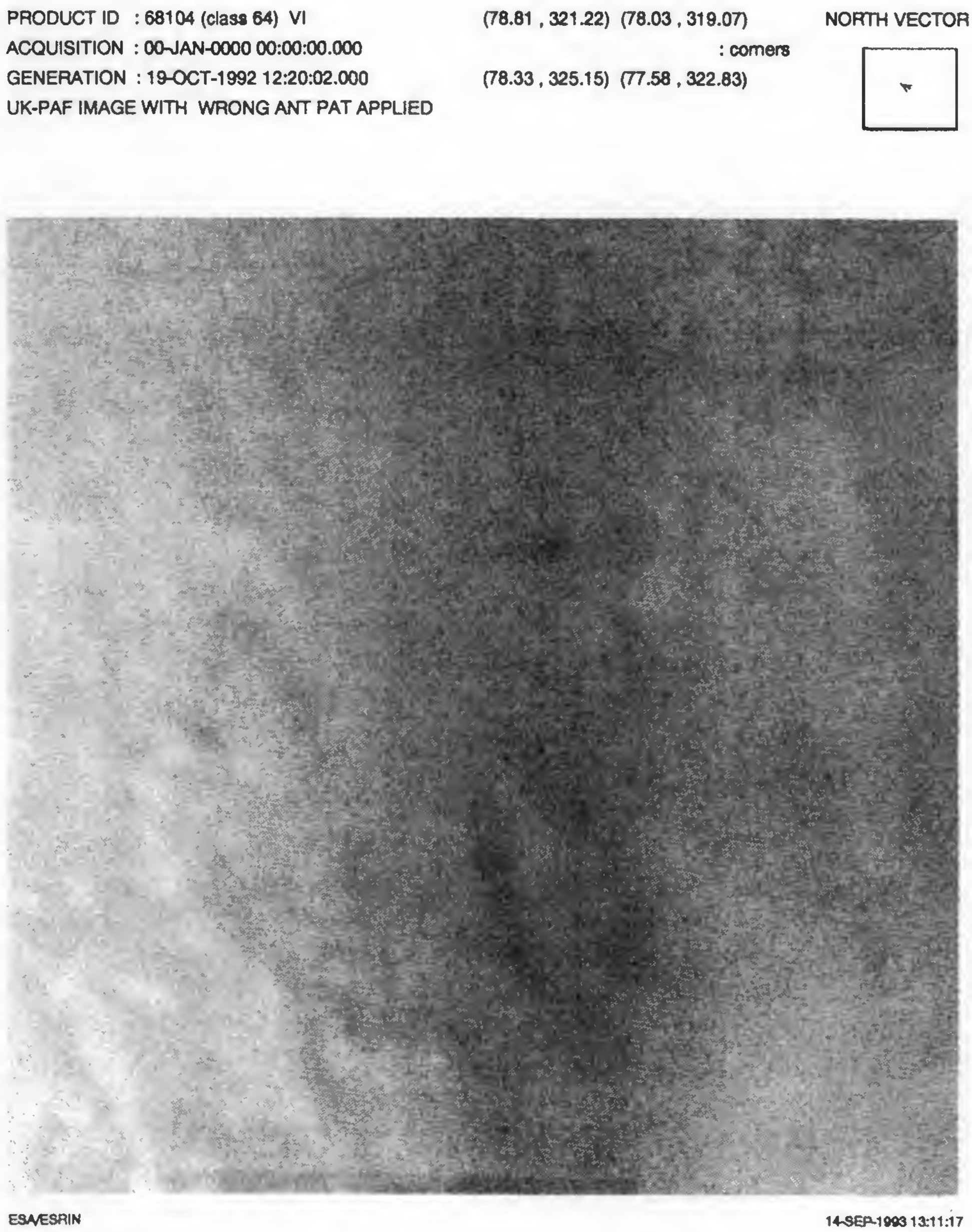

Figure 7: *Greenland PRI image with incorrect antenna pattern correction*

Another major problem analysed is the corruption of chirp data during telemetry. As the chirp data is used to process the whole scene, the anomaly affects the whole final image. This problem is characterised by strips emerging from bright points. One of these scenes is presented in the figure 8.

After detection and investigation it was decided to improve the chirp quality control before processing and discard the corrupted chirps.

Figure 8: *Image processed with corrupted chirp data*

The third example refers to the geographical information contained in the ERS-1 central catalogue about the different products produced in the PAFs. In early '93 major discrepancies among the nominal co-ordinates (generated before the data acquisition), the information provided by the archiving report and the actual location of the image were found.

Figure 9 shows the frame co-ordinates of one of these scenes. After investigation it was found that the archiving report sent by the PAF was wrong. The PAF fixed the problem and the anomaly was closed.

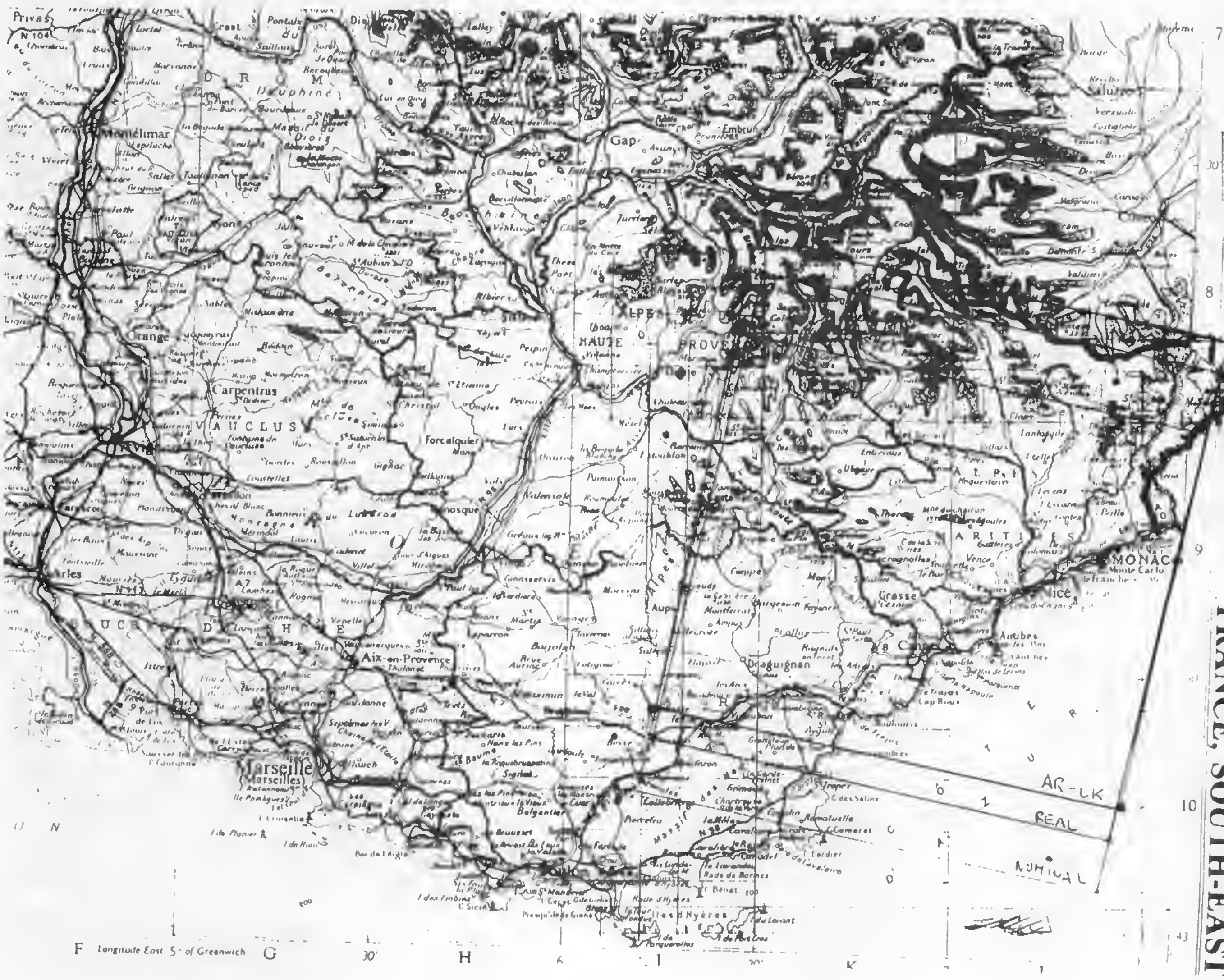

figure 9: *Frame location of one PRI product with incorrect archiving report*

4. CONCLUSION

This paper has shown the large amount of work that is being invested in the validation and ongoing monitoring of ERS-1 SAR image products. It is important that the products delivered to users have a consistent quality irrespective of ESA processing facility. ESA/ESRINs work in validating ground station and PAF products has been a key issue in guarenteeing this consistency.

We have also illustrated the stability and extremely good performance of the ERS-1 SAR during the first two years of mission.

The experience gained by the ground segment in the analysis and solving of problems and anomalies will be extremely useful for future ESA SAR missions, among them the imminent ERS-2 mission.

ACKNOWLEDGEMENTS

The authors would like to thank the people involved in the validation of SAR products at the PAFs:

R. Bamler, M. Eineder, A. Roth, B. Schättler (DLR)
P. Meadows (MRC), R. Cordey, M. Hutchins (DRA)
L. Candela, E. Lopinto, C. Tarantino (Telespazio)

The authors also acknowledge H. Jackson and Y. L. Desnos (ESA/ESTEC), E. Dwyer and M. Doherty (ESA/ESRIN) for their contribution.

SCANSAR and CALIBRATION

Session 9

Chair: M.JIN, NASA-JPL, USA

SCANSAR PROCESSING AND SIMULATION

Knut Eldhuset

Norwegian Defence Research Establishment (NDRE)
Kjeller
Norway

ABSTRACT

This paper presents results from the first phase of an ESA study on scanSAR processing and simulation taking into account the ASAR system parameters. An important part of the study is to use ERS–1 raw data in both normal mode and roll tilt mode for Doppler centroid estimation, processing and simulation. Special attention is devoted to azimuth gain variations and azimuth ambiguity ratios for different scanning strategies and to the effect of individual beam pointing errors. A scanning strategy with two scan cycles has been selected and a processing scheme with three range looks and two azimuth looks. SPECAN is considered very favourable for azimuth processing. The degradation in image quality is investigated by imposing individual beam pointing errors on real ERS–1 data. The beam pointing errors and Doppler centroid estimation errors are assumed to be kept so small that azimuth intensity variation (due to gain variations) should be compensated.

Keywords: ScanSAR, ASAR, processing, simulation, ERS–1

1 INTRODUCTION

During the ERS–1 mission Norway has demonstrated fast SAR image processing (Ref. 1) and distribution and a number of interesting applications. NDRE has been involved in some of these applications such as agriculture (Ref. 4), iceberg detection, oil slick detection (Ref. 2) and automatic ship detection (Refs. 2,3). Based on the successful experiences with ERS–1 Norway also plans fast processing and distribution of RADARSAT (Canada) and ASAR (ESA) data. As a step towards this goal NDRE is presently doing an ESA study on scanSAR processing and simulation. This paper presents some results in this study. Although this study has been concentrated on the ASAR specifications, it will also prepare Norway's ability for RADARSAT processing.

The scanSAR operation introduces additional problems which are not present in a conventional SAR system. The ASAR scanSAR system is specified to cover a swath of 400 km with a resolution better than 100 m. The beam scanning procedure causes the azimuth data stream to be discontinuous and also individual beam pointing errors. In a scanSAR system point targets with different azimuth locations have different azimuth signal histories if they are illuminated by different parts of the azimuth beam. This fact has consequences for the azimuth gain variation, the azimuth ambiguity ratio, and the azimuth processing scheme. In this study a scanning strategy is selected which maximizes such image quality parameters and a suitable azimuth processing method is investigated.

2 BASIC PRINCIPLES AND DEFINITIONS FOR SCANSAR

A fundamental difference between a conventional SAR and a scanSAR is the azimuth imaging. For a conventional SAR a point target on the ground traverses all the antenna beam and all point targets get the same phase history. For a scanSAR different point targets will have different frequency signatures dependent on the section of the beam pattern where the point target is imaged. In Fig. 2.1 is illustrated the situation using 2 scan cycles. In that case a given point target is illuminated twice by the beam (full processing bandwidth). We define the dwell time, T_D, as the time interval in which the beam is directed towards a given range subswath. We also define an effective dwell time, $T_{D,eff}$, which corresponds to the time interval reflected pulses are detected. The difference between these two times is dependent on the number of pulses lost when the beam is switched between subswaths with different PRF's. In Fig. 2.1 the two shaded regions correspond to the integrated power of the point target in two different scan cycles. The width of each column can be referred to in terms of bandwidth, and the dwell bandwidth is defined as

$$B_D = f_{DR}\ T_{D,eff} \tag{2.1}$$

where f_{DR} is the azimuth Doppler frequency rate. The return time, T_R, is defined as the time interval between the beginning of one dwell time and the beginning of the next dwell time in the same subswath. In Fig. 2.1 this time corresponds to the return bandwidth defined as

$$B_R = f_{DR}\ T_R \tag{2.2}$$

Finally, we define the full integration time or the imaging cycle time, T_F, and the full bandwidth or the imaging cycle bandwidth:

$$B_F = f_{DR}\ T_F \tag{2.3}$$

The needed full bandwidth is dependent on the sum of the dwell times over all subswaths and the number of scan cycles, denoted n. A scan cycle is an ordered number of subswaths (SS1,SS2,SS3,SS4,SS5). SS1 is the subswath at near range and SS5 is the subswath at far range. The nominal look angles for ASAR scanSAR mode (wide swath mode) and ERS–1 normal and roll tilt mode are defined as in Table 2.1.

Subswath	SS1	SS2	SS3	SS4	SS5	Normal (ERS)	Roll Tilt (ERS)
Look ang. near (^{0})	15.1	23.0	27.2	31.3	34.1	17.0	26.5
Look ang. far (^{0})	23.3	27.5	31.7	34.3	37.1	23.0	32.5

Table 2.1 Nominal look angles for ASAR scanSAR mode and ERS–1 normal and roll tilt modes

We denote the number of looks n_l. The situation in Fig. 2.1 corresponds to two scan cycles, and one look from each scan cycle can be generated. We denote this situation $(n = 2\ n_l = 2)$. If only one scan cycle is used and we imagine that the two columns in Fig. 2.1 are adjacent we may form two looks and get the same resolution. We denote this situation $(n = 1\ n_l = 2)$.

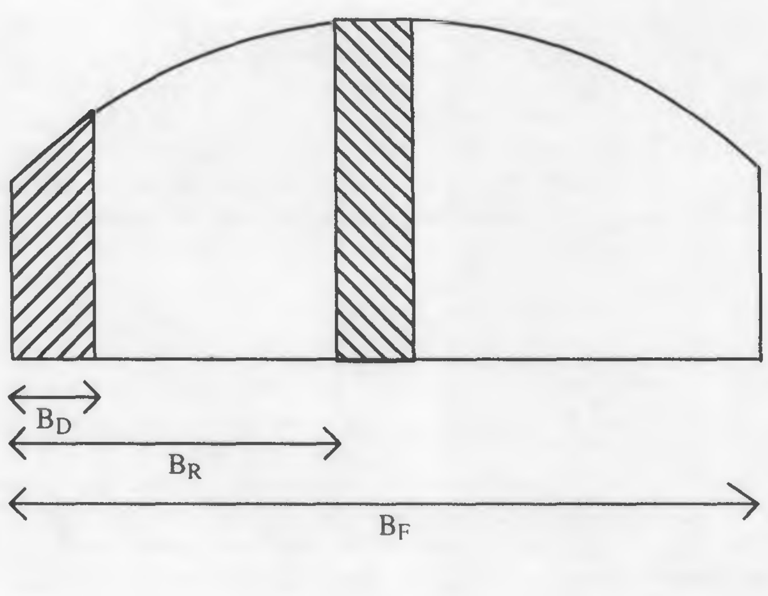

Figure 2.1 Gain of a point target where the number of scan cycles is n=2. One look from each scan cycle can be generated

3 SCANNING STRATEGY

3.1 Estimation of dwell times and imaging cycle times

In order to calculate azimuth ambiguity ratios and azimuth gain variations one has to know the full integration time (imaging cycle time). The requirement for the ASAR wide swath mode is an azimuth resolution better than 100m. Here we study what dwell times, $T_D(j_{ss})$, we need for the different 5 subswaths (SS1–SS5), j_{ss} = 1, 2, 3, 4, 5 and what the full integration time $T_F(j_{ss})$ has to be for each subswath j_{ss}. We first set up the fundamental relation which must yield to achieve a specified image quality :

$$\sum_{i=1}^{5} T_D(i) = \frac{T_F(j_{ss}) - T_{D,eff}(j_{ss})}{n} \quad , \quad j_{ss} = 1,2,3,4,5 \qquad (3.1)$$

where n is the number of scan cycles. The right or left side of Eq. 3 .1 can be interpreted as the return time. Since the sum of the dwell times is independent of subswath number a common return time is defined for a scanSAR:

$$T_R = \frac{T_F(j_{ss}) - T_{D,eff}(j_{ss})}{n} \quad , \quad j_{ss} = 1,2,3,4,5 \qquad (3.2)$$

The dwell times can be expressed by two terms:

$$T_D(j) = \frac{V_B(j_{ss})}{|f_{DR}(j_{ss})|\varrho} + \frac{N_{lost}(j_{ss})}{PRF(j_{ss})} \qquad (3.3)$$

where ϱ is the required azimuth resolution, $V_B(j_{ss})$ is the beam speed on the earth for subswath j_{ss} and $f_{DR}(j_{ss})$ is the azimuth Doppler rate (smallest absolute value) in subswath j_{ss} .The first term in Eq. 3 .3 expresses the time needed to get the required resolution and the second term the time needed to generate all the pulses on the air at the beginning of the dwell time. The maximum number of pulses lost due to beam switching is the number of pulses which are on the air when the beam switches to another swath. As mentioned in (Ref. 5) a careful choice of subswath order and by rapid switching the number of lost pulses can be substantially reduced. For a given subswath the azimuth Doppler rate is largest in near range. Hence, to calculate the needed dwell times Eq. 3 .3 is calculated at far range in each subswath . The dwell times can then be selected such that the required resolution is achieved in far range in each subswath. If uniform azimuth resolution is required over all subswaths shorter azimuth filters can be used in near range than in far range of a given subswath. We also define the effective dwell time in terms of the desired azimuth resolution.

$$T_{D,eff}(j_{ss}) = \frac{V_B(j_{ss})}{|f_{DR}(j_{ss})|\ \varrho} \qquad (3.4)$$

Eq. 3 .4 expresses the time needed to achieve a specified azimuth resolution and is valid for a specified Hamming window used on the azimuth filter. To get an expression for the full integration time for a given subswath, we put the expression in Eq. 3 .3 into Eq. 3 .1 and using the Doppler rates at far range in each subswath (since the resolution is at worst at far range). The full time of integration (imaging cycle time) is then given by:

$$T_F(j_{ss}) = \frac{n}{\varrho}\left[\sum_{i=1}^{5} \frac{V_B(i)}{|f_{DR,f}(i)|}\right] + n\sum_{i=1}^{5} \frac{N_{lost}(i)}{PRF(i)} + \frac{V_B(j_{ss})}{\varrho\ |f_{DR}(j_{ss})|} \qquad (3.5)$$

The first term in Eq. 3 .5 expresses the total effective integration time for all subswaths to achieve the required resolution . The second term includes the time corresponding to the number of pulses lost. It is proportional to the number of scan cycles (n).

3.2 Azimuth ambiguity ratio (AAR) and azimuth gain (AG)

Two important quality parameters for scanSAR are the azimuth ambiguity ratio, AAR, and azimuth gain , AG. For a scanSAR AG will vary since different point targets are illuminated by different portions of the beam. In a scanSAR system the aim is to keep this variation as low as possible. The variation is reduced by using several scan cycles and then averaging looks from different scan cycles. The two concepts will here be defined for a scanSAR system. But, first we need the azimuth two–way gain function in terms of frequency, f, when no beam shaping is used (e.g. Ref. 7):

$$G(f) = \frac{\sin^4\left(\frac{\pi L}{2V} f\right)}{\left(\frac{\pi L}{2V} f\right)^4} \tag{3.6}$$

where V is the speed of the satellite and L is the antenna length. For n scan cycles ($n = 2$ in Fig. 2.1), the processed unambiguous power can be written:

$$S(f_R, \Delta f_{DC}) = \sum_{i=1}^{n} \int_{f_{DC}-\frac{B_F}{2}+(i-1)B_R}^{f_{DC}-\frac{B_F}{2}+(i-1)B_R+B_D} G(f - \Delta f_{DC} - f_{DC} + f_R)df \quad , f_R \in [0, B_R] \tag{3.7}$$

where f_R is the frequency within the return bandwidth interval and f_{DC} is the Doppler centroid. Δf_{DC} is a Doppler centroid error and may be caused by inaccurate Doppler centroid estimation. Geometrically a variation in the variable f_R can be interpreted as moving the two columns under the antenna pattern in Fig. 2.1 to the right. In this way we get a curve which represents the azimuth gain variation in the unambiguous signal. The azimuth gain in a scanSAR is defined as the unambiguous power per look:

$$AG(f_R, \Delta f_{DC}) = \frac{S(f_R, \Delta f_{DC})}{n_l} \tag{3.8}$$

The azimuth ambiguity ratio is defined:

$$AAR(f_R, \Delta f_{DC}) = \frac{S(f_R, \Delta f_{DC})}{\sum\limits_{\substack{j=-j_{max} \\ j \neq 0}}^{j_{max}} S(f_R + j\ PRF)} \tag{3.9}$$

where j_{max} is selected to obtain sufficient accuracy. Geometrically this is the ratio between the unambiguous power (in the main lobe) and the ambiguous power (power located an integer number of PRF's from the unambiguous columns). We also introduce the azimuth gain variation:

$$AGV = AG_{max} - AG_{min} \tag{3.10}$$

In Fig. 3.1 is shown an example of the azimuth gain variation for 4 different scanning strategies.The curve ($n = 2$ $n_l = 2$) corresponds to two scan cycles($n = 2$) and two looks ($n_l = 2$) as in Fig. 2.1 . The curve ($n = 1$ $n_l = 2$) corresponds to one scan cycle ($n = 1$) and two looks ($n_l = 2$) . The two curves show that adding 2 looks from 2 different scan cycles yields less AGV than adding looks from neighbouring sections under the antenna pattern, and also a higher gain which also means a higher SNR (signal–to–noise ratio) . The azimuth gain curves for a 3–look system are also plotted. Here we have assumed that one shall obtain the same azimuth resolution as for the 2–look system. AGV for the ($n = 3$ $n_l = 3$) curve is slightly less than for the ($n = 2$ $n_l = 2$) curve, but the last one has higher gain. In Fig. 3.1 we have assumed that all pulses on the air are lost due to beam switching between subswaths, that is that the second term in Eq. 3 .5 is maximum. If one assumes rapid beam switching procedure between subswaths that collects incoming pulses in another swath, the curves in Fig. 3.1 change only slightly. In Fig. 3.1 the AGV is about 0.51 dB for the ($n = 2$ $n_l = 2$) curve. If all pulses could be collected (hypotetical), the AGV is reduced to 0.42 dB.

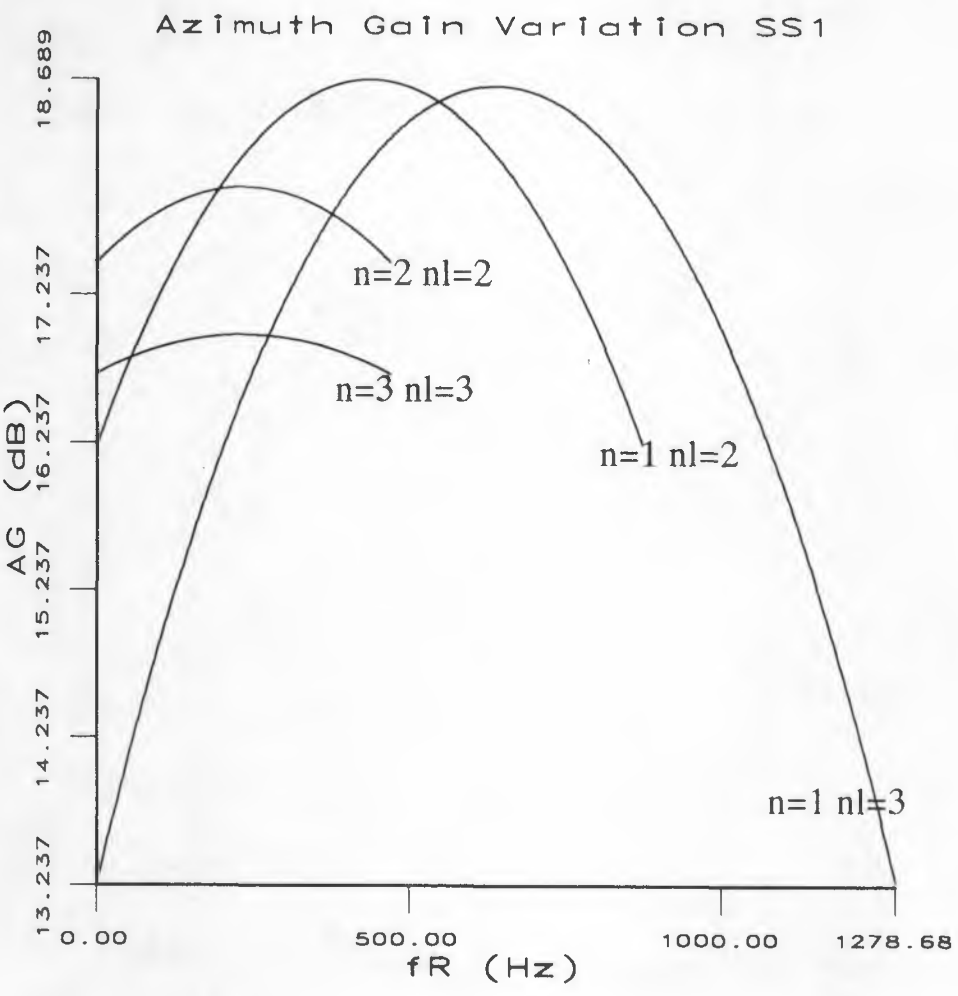

Figure 3.1 *Azimuth gain variation for some scanning strategies for ASAR scanSAR (all pulses on the air due to subswath switching are assumed lost)*

In Fig. 3.2 is shown the azimuth ambiguity ratio for the same scanning strategies as for the azimuth gain variation curves in Fig. 3.1. Concerning the AAR 2 scan cycles with 2 looks ($n = 2$ $n_l = 2$) is clearly favourable. The lowest AAR for ($n = 2$ $n_l = 2$) is 24.54 dB while the lowest AAR for ($n = 3$ $n_l = 3$) is 15.91 dB, that is about 8.6 dB lower. Azimuth ambiguities is considered very inconvenient in connection with detection of point target like scatterers. Although the azimuth gain variation is slightly less for the n=3 than n=2, the gain is always higher for the n=2 case. A strategy with 2 scan cycles and two looks should be preferred based on this analysis.

Another important conclusion can be drawn from Fig. 3.1. and Fig. 3.2 concerning the ($n = 2$ $n_l = 2$) strategy. If gain compensation is not done during azimuth compression a gain variation (or approximately the same as the intensity variation) in the processed image of about 0.5 dB will be present using correct value for the Doppler centroid. (If an error of 150 Hz is used there is an azimuth gain variation of about 1.35 dB.) Corresponding analysis has been performed for the other subswaths, but SS1 has the lowest numbers for the AAR numbers and largest azimuth gain varitaion, that is the worst case situation. It should also be mentioned that if all pulses could be detected (hypotetical) the AAR curves is about 2 dB higher. Lowest value in SS1 for ($n = 2$ $n_l = 2$) is 26.6 dB.

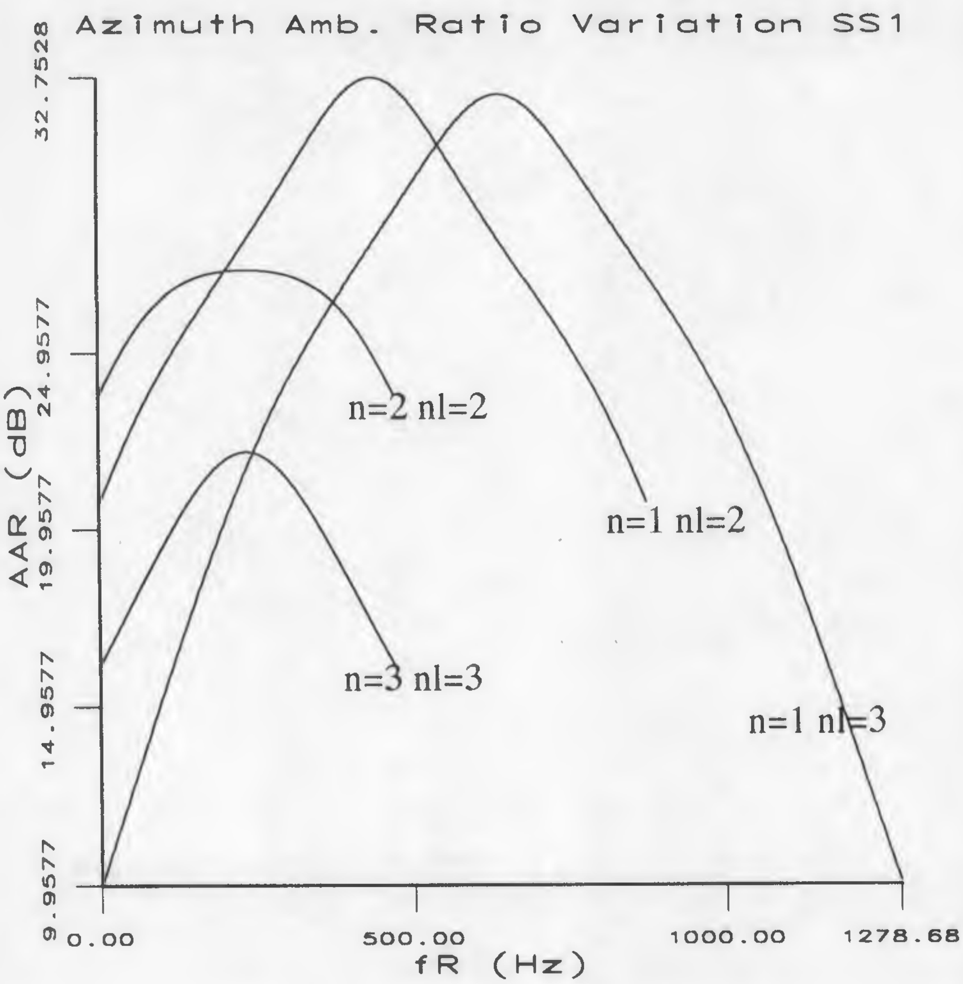

Figure 3.2 *AAR for some scanning strategies (all pulses on the air lost)*

4 AUXILIARY DATA PROCESSING

4.1 Spectrum based Doppler centroid estimator

We used an optimum spectrum based Doppler centroid estimator in the study. The method is correlation based with the weighting kernel (Jin's kernel Ref. 9):

$$B(f) = A'(f)/A(f)^2 \quad (4.1)$$

where f is Doppler frequency and A(f) is the azimuth spectrum intensity. The approximation in (Ref. 8) has been used and is given by:

$$A(f) = 1 + m\ cos(2\pi\ f/PRF) \quad (4.2)$$

where m is a parameter which accounts for the degree of aliasing and additive noise level, PRF is the pulse repetition frequency. For ERS–1 normal mode m=0.65 was used and for ERS–1 roll tilt mode m=0.5 was used. In Fig. 4.1 is illustrated how the actual raw data vectors are selected from ERS–1 raw data. The vertical lines represent raw data vectors which are selected for scanSAR simulation. The rest of the raw data vectors are thrown away. Typical number of raw data vectors may be 56 in each scan cycle. In this case a 64–point FFT is used for spectrum estimation. To improve the accuracy of the Doppler centroid estimate raw data from several scan cycles were selected.

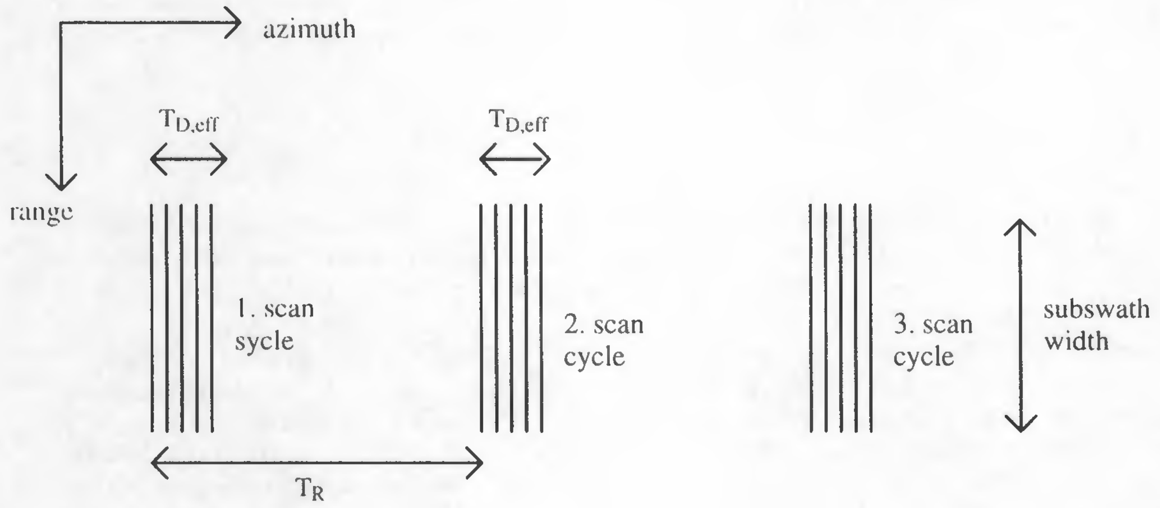

Figure 4.1 *Effective dwell time, $T_{D,eff}$, and return time, T_R, defined in a raw data set for a given subswath.*

For the ERS–1 raw data scenes tested standard deviations of 2.8 Hz for the normal mode scene in Fig. 7.1 and 8.6 Hz for the roll tilt mode scene in Fig. 7.4 were achieved using 75 scan cycles for averaging spectrum estimates. In this way accurate mean Doppler centroids over a scene in azimuth direction is obtained. Since the ASAR beam shall be directed near zero Doppler there is small variations in Doppler centroid along track. There may however be some harmonic and random variations.

4.2 Individual beam pointing errors

One potential problem using scanSAR data is the individual beam pointing errors due to electrical beam pointing in the beam forming network. Simulation of such pointing errors were simulated in the study assuming a Gaussian random process as in Section 7.1. If the beam pointing errors are sufficient large the accuracy of the along track average Doppler centroid may be degraded. For given yaw and pitch errors on the error Doppler centroid, Δf_{DC}, can be estimated according to Eq. 7 .1 . In Table 4.1 is shown the AAR and AGV numbers for some Doppler centroid errors. If the standard deviations for both pitch and yaw are equal to 0.016^0 the Doppler centroid error is 75 Hz (using Eq. 7 .4). Although a very accurate mean Doppler centroid has been achieved, AAR and AGV in each scan cycle will be degraded as in Table 4.1 depending on the pointing errors.

Δf_{DC} (Hz)	0	60	120	180	240
AAR(dB) SS1	24.7	22.7	20.1	17.4	14.8
AGV(dB) SS1	0.51	0.79	1.16	1.59	2.10

Table 4.1 *Azimuth ambiguity ratio (AAR) and azimuth gain variation (AGV) for some Doppler centroid errors (Δf_{DC}).*

5 CORE PROCESSING

5.1 Range compression

The range compression is performed with 3 looks. The available bandwidths must be 15.5 ,10.3, 8.8 ,7.7 and 7.1 Mhz at near range in each subswath. This yields 96 m resolution. To achieve uniform range resolution the bandwidth is reduced stepwise with increasing range such that the variation in range resolution between range blocks is less than 2 m.

5.2 Azimuth compression

In Fig. 5.1 is sketched the principles of scanSAR azimuth processing. The vertical lines correspond to the raw data vectors available in a given subswath. The triangles correspond to the full time of integration beam width. In the first scan cycle the satellite moves from a to b, and in the second scan cycle from c to d.

The time corresponding to the distance from a to c is the return time, T_R . During the effective dwell time, $T_{D,eff}$, the raw data vectors are collected. Note that each of raw data vectors contains backscatter signals from the region covered by the triangle at the instant when a pulse was reflected from ground. From the data collected in one scan cycle the azimuth compression yield output corresponding to a distance on the ground which is covered by the defined full beam width T_F. This is illustrated by the shaded rectangles for two scan cycles. Two azimuth looks can be formed by adding the data corresponding to the overlapping part of the two rectangles. In this way we get 6 looks using 3 range looks.

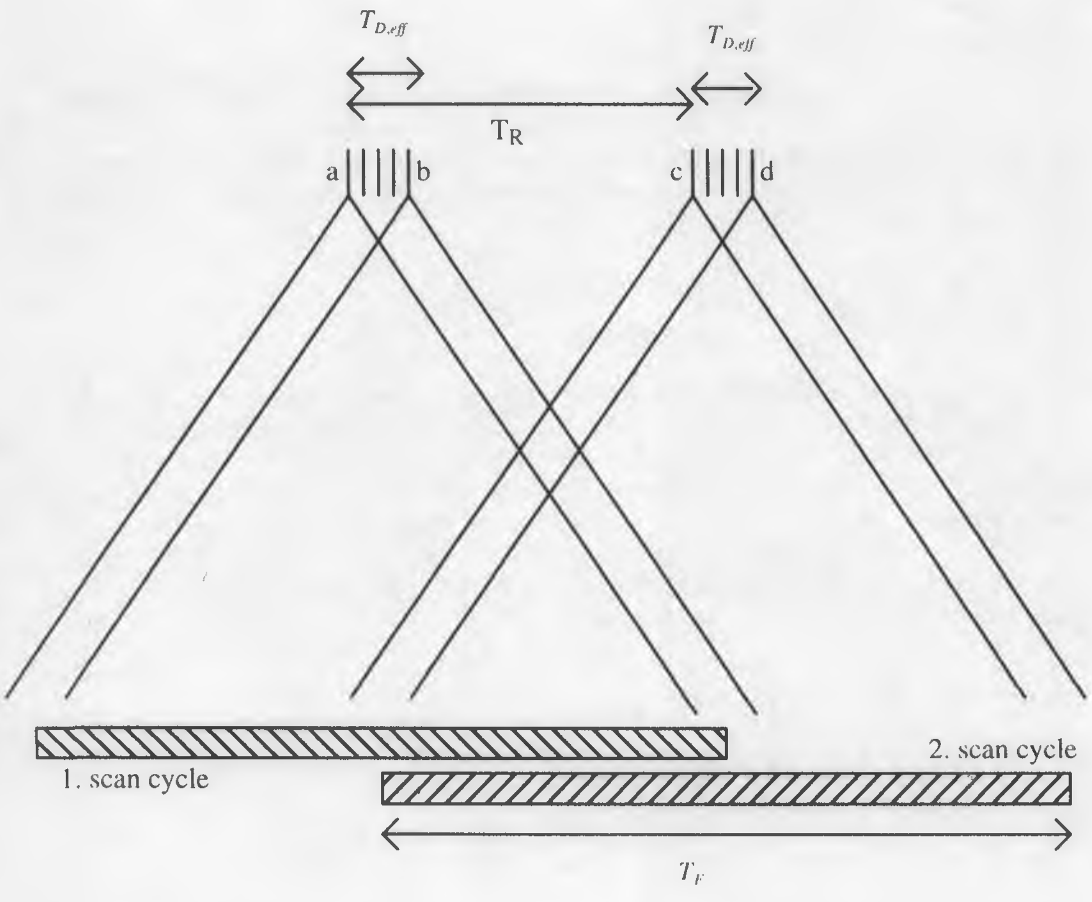

Figure 5.1 ScanSAR azimuth look generation with 2 scan cycles (n=2))

Time domain and SPECAN have been implemented for azimuth compression. SPECAN is described e.g. in (Ref 7). SPECAN (64–point FFT) needs about 16 % of the arithmetic operations needed by time domain implementation. In this estimate interpolation is included after SPECAN. Since the PRF's in different subswaths are different, interpolation in azimuth direction is necessary to get the same pixel spacing. Both methods yield azimuth gain variations as calculated in Section 3.2 if gain compensation is not performed. Although gain variations are quite small using 2 scan cycles (0.5 dB) such variations can be observed if the backscattering is quite homogeneous from large sea areas. Compensation can be done with both methods and the intensity variations will be calculated in Section 6.2 with and without compensation at different erroneous Doppler centroids.

6 IMAGE QUALITY

6.1 Uniform resolution

Since the incidence angle change from approximately 17^0 to 43^0 from near range at subswath SS1 to far range in subswath SS5, the range bandwidth for different subswaths should be different to achieve a more constant range resolution. To achieve uniform resoultion across subswath boundaries, the look bandwidth of the range filters are also changed in our processor. The variation in range resolution is in this way less than 2 meters if the range resolution is on the average 98 m. The azimuth resolution is also refined by changing the azimuth filter length within each subswath and the variation is less than 2 m.

6.2 Calculation of azimuth intensity variations (AIV)

In Chapter 5 we mentioned two methods for azimuth compression for scanSAR data. In Section 3.2 we calculated azimuth gain variations. Here we calculate the intensity variations which occur in the azimuth compressed image. The expression for the azimuth spectrum intensity in Eq. 4 .2 also takes into account the aliased reflections from the antenna sidelobes assuming homogeneous scenes. Here we also include the m as a function dependency. We set up an equation like that in Eq. 3 .7 for the total processed power (unambiguous + ambiguous power), but also divide with the compensation function which is used. If M=m, the compensation is accounted for. If M=0, no compensation is done. Strictly speaking, Eq. 6 .1 is only valid for calculation of the power using time domain processing. For SPECAN followed by azimuth spectrum compensation, the A(,M) function in the denominator in Eq. 6 .1 should be outside the integral with the function value in the middle of the integration interval. It may however be shown that the difference between the estimated total power in the two cases is negligible.

$$S(f_R, \Delta f_{DC}, m, M) = \sum_{i=1}^{n} \int_{f_{DC}-\frac{B_F}{2}+(i-1)B_R}^{f_{DC}-\frac{B_F}{2}+(i-1)B_R+B_D} \frac{A(f-\Delta f_{DC}-f_{DC}+f_R, m)}{A(f-f_{DC}+f_R, M)} df \quad , f_R \in [0, B_R] \qquad (6.1)$$

To calculate the azimuth intensity (AI) for a given frequency f_R within the return bandwidth interval and a given Doppler centroid error Δf_{DC} the total processed power (all scan cycles) is divided by the number of looks:

$$AI(f_R, \Delta f_{DC}, m, M) = \frac{S(f_R, \Delta f_{DC}, m, M)}{n_l} \qquad (6.2)$$

The azimuth intensity variation is then given by the difference between the maximum and minimum value of Eq. 6 .2 :

$$AIV = AI_{max} - AI_{min} \qquad (6.3)$$

In Fig. 6.1 we have calculated the azimuth intensity variation for some situations. The two upper curves correspond to ERS–1 normal mode (m=0.65). The curve with M=0.65 corresponds to intensity compensation during or after azimuth compression while the curve with M=0 represents the case with no compensation. The two lower curves are calculated with m=0.5 which corresponds to ERS–1 roll tilt mode. What we can say is that if the estimated Doppler centroid is too erroneous, compensation is not favourable. For normal mode the two curves cross at about 67 Hz and for roll tilt mode at 77 Hz. If the Doppler centroid error is less than these values, compensation is favourable and the azimuth intensity variation is kept lower than if azimuth spectrum intensity is not compensated. Larger Doppler centroid errors caused by beam pointing errors are not very likely to occur since random beam pointing errors are assumed to be less than 0.01^0 (3σ) (Ref. 12). According to Eq. 7 .4 this corresponds to approximately 45 Hz. In Section 4.1 it was demonstrated that mean Doppler centroids could be estimated to better than 10 Hz. Hence, intensity compensation should be performed. It should be noted that azimuth intensity compensation does not improve the signal-to-noise ratio.

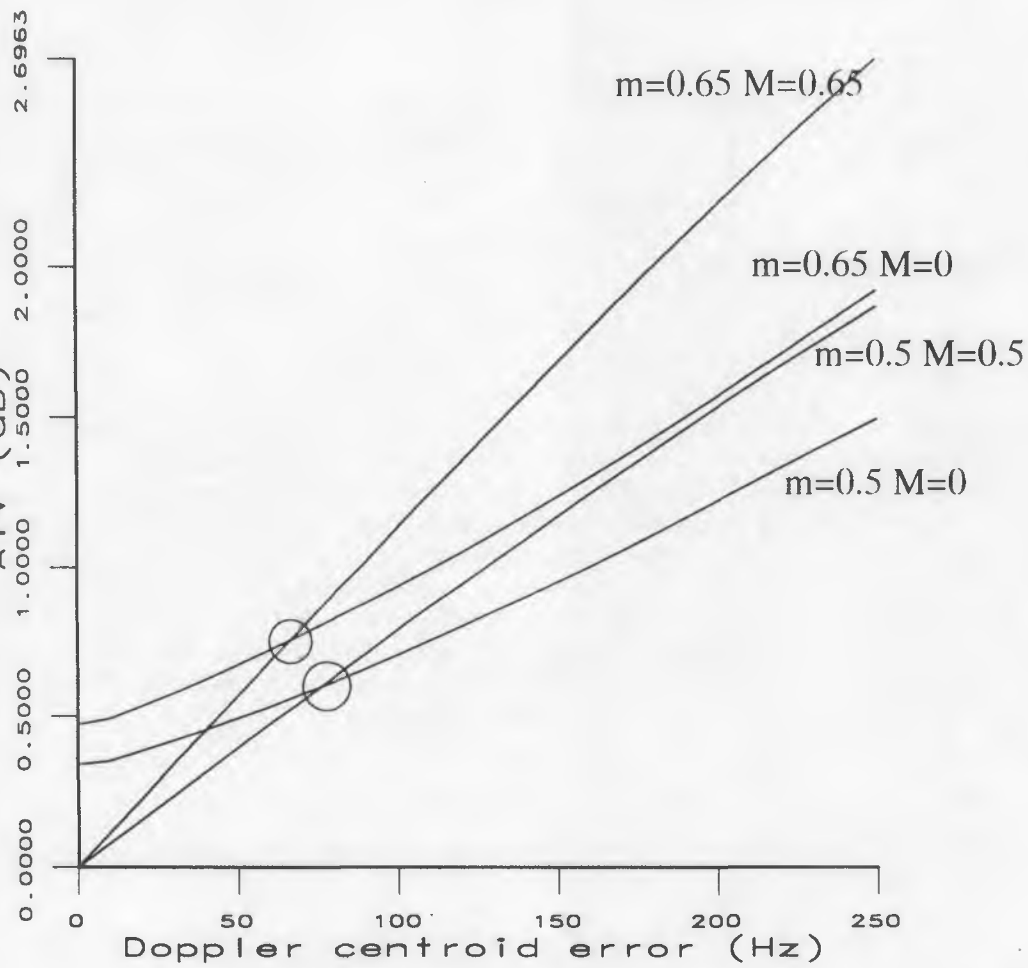

Figure 6.1 *Azimuth intensity variations (AIV) as function of Doppler centroid error used in the processor with (M=m) and without (M=0) azimuth spectrum intensity compensation. For ERS–1 normal mode m=0.65 and for roll tilt mode m=0.5*

7 SCANSAR PROCESSING AND SIMULATION

7.1 Simulation of individual beam pointing errors

It may be shown that the relation between Doppler centroid error, $\Delta f_{DC}(k,n)$, is related to a yaw (Y_n) and pitch (P_n) by (has been used in Refs. 10,11) :

$$\Delta f_{DC}(k,n) = -\frac{2\,V_{rel}}{\lambda}\,(sin(\theta_k)Y_n + cos(\theta_k)P_n) \tag{7.1}$$

where V_{rel} is the relative speed between satellite and a point on the earth. In Eq. 7 .1 it is assumed that yaw and pitch are small angles. The Doppler centroid error relative to a nominal Doppler centroid (e.g. according to a yaw steering rule) is zero if the yaw and pitch angles are 0. The index n in Y_n and P_n indicates the scan cycle. The index k indicate the range pixel number and θ_k is the look angle for a given range pixel (k). The yaw and pitch variations may be of harmonic character with random variations. In this paper we only consider random variations from scan cycle to scan cycle and may be considered as the electrical beam pointing errors in the beam forming network. In this work we assume that Y_n and P_n are independent Gaussian zero mean random processes, that is $E[Y_n]= E[P_n] = 0$, where $E[\ ]$ denotes expectation. Assuming zero mean processes the variance of Eq. 7 .1 is:

$$\sigma^2_{\Delta f_{DC}} = \frac{4\,V^2_{rel}}{\lambda^2}\,(sin^2(\theta_k)\,\sigma^2_Y + cos^2(\theta_k)\,\sigma^2_P) \tag{7.2}$$

$$\sigma^2_Y = E\,[Y^2_n] \quad , \quad \sigma^2_P = E\,[P^2_n] \tag{7.3}$$

If the variances of yaw and pitch are equal Eq. 7 .2 can be simplified to:

$$\sigma_{\Delta f_{DC}} = \frac{2\,V_{rel}}{\lambda}\,\sigma_Y \quad when \quad \sigma_P = \sigma_Y \tag{7.4}$$

Eq. 7 .4 tells us that the standard deviation of the Doppler centroid error is independent of look angle if the standard deviations on the yaw and pitch are equal (also assuming that the variation of V_{rel} over range is small)

Let $A_{k,n}(f)$ be the azimuth spectrum (where we assume that the Doppler centroid is at f=0) in azimuth line number k and scan cycle number n. The simulation of individual beam pointing errors is then completed by modulating the azimuth spectrum (estimated from ERS–1 raw data) in azimuth line k and scan cycle n in the following way:

$$\hat{A}_{k,n}(f) = A_{k,n}(f)\,\frac{1 + m\,cos\left(2\pi\,\frac{f + \Delta f_{DC}(k,n)}{PRF}\right)}{1 + m\,cos\left(2\pi\,\frac{f}{PRF}\right)} \tag{7.5}$$

This operation is perfomed before SPECAN is applied in the azimuth compression. Hence, the modulated azimuth spectrum given by Eq. 7 .5 is then inverse FFT transformed and then deramped. Finally, one forward FFT completes the azimuth compression.

7.2 Examples of scanSAR simulation and processing with ERS–1 data

We now apply the scanSAR simulation and processing algorithm on ERS–1 raw data in both normal mode and roll tilt mode. Fig. 7.1 shows a scanSAR processed ERS–1 normal mode image. This image has also been compensated by using the azimuth spectrum intensity function in Eq. 4 .2 . In this image no intensity variations can be seen, but if no intensity compensation is performed, the intensity variations can be seen as faint azimuth travelling wave patterns which vary as fast as the scan cycles. From Fig. 6.1 we see that the AIV is approximately 0.5 dB (m=0.65, M=0) .This image is not shown here since the variations are quite faint and may be lost during the photo copy process. In Fig. 7.2 is shown the same image where the Doppler centroid error is 100 Hz. The wave patterns can now clearly be seen and the curve (M=m=0.65) in Fig. 6.1 tells us that the azimuth intensity variation is about 1.2 dB. From Fig. 6.1 we see that for m=M=0.65 AIV=0.5 dB for Doppler centroid error equal to 50 Hz. That is, if intensity compensation is performed a Doppler centroid error of 50 Hz causes 0.5 dB intensity variation. As explained above 0.5 dB may be visible, so that the Doppler centroid error should not be larger than 50 Hz. Using only a few scan cycles for Doppler centroid estimation or using geometrical Doppler centroid estimators might give such degradations in the image. The AAR reduction and AGV number can be interpolated from Table 4.1. In Fig. 7.3 is shown a

Figure 7.1 ScanSAR processed ERS–1 normal mode image ,6 looks, 98 m resolution, azimuth intensity compensated, Flevoland Netherlands, Orbit 1789, 18. Nov. 1991–21:40:27

Figure 7.2 ScanSAR processed ERS–1 normal mode image, azimuth intensity compensated, and Doppler centroid error 100 Hz

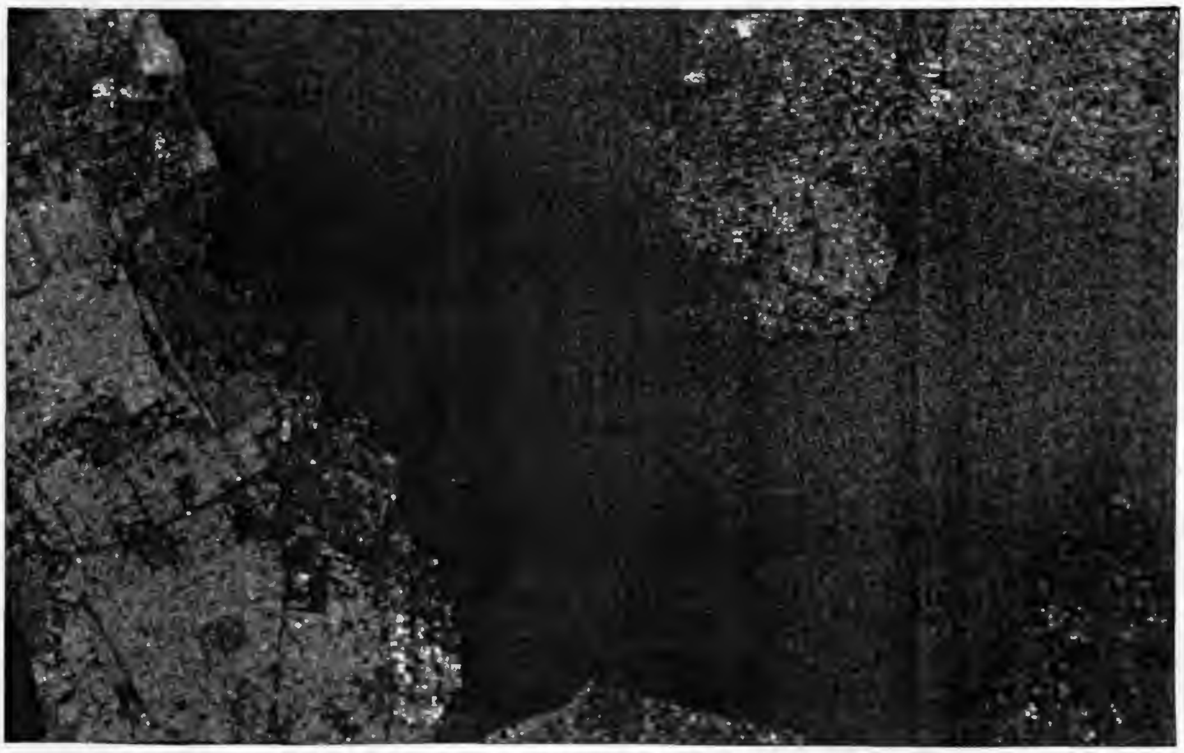

Figure 7.3 ScanSAR processed ERS–1 normal mode image, intensity compensated, simulation of individual beam pointing errors, $\sigma_Y = \sigma_P = 0.016^0$

Figure 7.4 ScanSAR processed ERS–1 roll tilt mode image, 6 looks, 98 m resolution, intensity compensated, Flevoland Netherlands, Orbit 3767, 4. April 1992–21:52:05

simulation of individual beam pointing errors where the standard deviation of the Gaussian noise process on yaw and pitch is 0.016^0. A wave pattern with randomly varying intensity can be observed. Such patterns are still weakly visible (especially in the sea at moderate wind conditions) using pitch and yaw standard deviations of 0.007^0. The individual beam pointing errors are expected to be kept considerably lower than that. (random beam pointing errors is expected to be $3\sigma < 0.01^0$ (Ref. 12)). In Fig. 7.4 is shown a scanSAR processed roll tilt image with azimuth intensity compensation. Even here the intensity variations are practically invisible (original image).

7.3 Implementation on CESAR array processor

The current CESAR computer system at Tromsø Satellite Station (TSS) is capable of processing a 100 km x 100 km ERS–1 scene in 8 minutes. A new version of the CESAR system (Ref. 1) with increased functionality has been developped at NDRE. Phase 2 of the ESA study shall be devoted to implementation on CESAR of the scanSAR processing algorithm described in this paper. A rough estimate shows that processing of an ASAR scanSAR scene covering 400 km x 400 km will take about 16 minutes with one MALU (Multifunctional ALgorithm Unit) and 2 minutes with an 8–MALU system.

8 CONCLUSIONS

This study has demonstrated scanSAR simulation and processing using ERS–1 rawdata in both normal mode and roll tilt mode. The ERS–1 raw data provided a unique possibility to study phenomena which are present in scanSAR systems like RADARSAT and ASAR. Especially the azimuth intensity variations could be studied using scanSAR azimuth processing algorithms. The work has assessed different scanning strategies and selected two scan cycles as favourable with respect to azimuth ambiguity ratios and azimuth gain variations. The work has also demonstrated how individual beam pointing errors can be simulated and imposed on ERS–1 data. For azimuth processing SPECAN appears to be very efficient and also provides the possibility to compensate remaining azimuth intensity variations when two azimuth looks are generated from two different scan cycles. Doppler centroid estimation has been investigated with an optimum method for homogeneous scenes and sufficient accuracy may be achieved using data from many scan cycles. Both Doppler centroid errors and beam pointing errors are expected to be so small that intensity compensation is favourable. Uniform azimuth and range resolution can be obtained with variation of 2% over 5 subswaths covering 400 km. The processing time for a 6–look ASAR scanSAR algorithm on the current version of CESAR will be about 2 minutes with an 8–MALU system.

9 ACKNOWLEDGMENT

This paper presents some results from a study under contract with European Space Agency which started in January 1993. The first phase shall be finished in October 1993. The author would like to thank Yves Louis Desnos (ESTEC) and Jean–Luc Marchand (ESTEC) for valuable discussions and comments on the work during the study. The author also appreciates good collaboration and support from Per Atle Våland. Also thanks go to Ola Gråbak for doing some programming work in the beginning of the study. Finally, thanks go to Henry Kjell Johansen and Terje Wahl for giving motivation for this work.

10 REFERENCES

(1) Toverud M , Våland P A, Desnos Y L, Guignard J P, The CESAR computer architecture the fastest in Europe, Proc. IGARSS'92, Houston, Texas, 1992

(2) Wahl T, Eldhuset K, Skøelv Å 1993, Ship traffic monitoring and oil spill detection using ERS–1 , Proc. Int. Symposium on Operationalization of Remote Sensing, Enschede, Nederland, pp. 151–160

(3) Wahl T, Eldhuset K, Skøelv Å 1993, Ship traffic monitoring using the ERS–1 SAR, Proc. 1st ERS–1 Symposium, Cannes Nov 1992, France, ESA SP–359 (March 1993)

(4) Weydahl D J, Solberg R 1992, Monitoring land use and soil erosion in agricultural areas using ERS–1 SAR images, 2nd Scandinavian SAR Symposium, Bergen, Norway

(5) Wilson C, Corr D G 1991, SAR data processing techniques and operational considerations for scanSAR systems, Proc. IGARSS'91, pp. 271–274

(6) Li F K et al 1985, Doppler Parameter Estimation for Spaceborne Synthetic Aperture Radars, *IEEE Trans. Geosci. Remote Sensing*, Vol. GE–23, pp. 47–56

(7) Curlander J C, McDonough R N 1991, *Synthetic aperture radar; Systems and Signal Processing*, New York Wiley & Sons , pp. 303–305

(8) Bamler R 1991, Doppler Frequency Estimation and the Cramer–Rao Bound, *IEEE Trans. Geosci. Remote Sensing*, vol GE–29, pp. 385–390

(9) Jin M 1989, A Doppler centroid estimation algorithm for SAR systems optimized for quasi–homogeneous source, JPL Publication 89–9

(10) Wu C, Curlander J C, Cenzo D A 1980, Determination of spacecraft attitude using synthetic aperture radar, JPL publication, 80–1922

(11) Loffeld O 1990, Doppler centroid estimation with Kalman filters, Proc IGARSS'90, Washington D.C.

(12) ESTEC information

ASAR SCANSAR OPERATION

M.A. Brown,

GEC-Marconi Research Centre,
West Hanningfield Road,
Gt. Baddow, Chelmsford,
Essex. CM2 8HN
United Kingdom

ABSTRACT

The first ESA polar platform mission, ENVISAT-1, includes an advanced synthetic aperture radar (ASAR) within its complement of instruments. At the heart of ASAR is an active phased array antenna, offering great flexibility in terms of the generation and control of the radar beam. ASAR is capable of operating in a number of modes to maximise the potential of the instrument. The ScanSAR imaging technique is utilised in several modes to provide either wide swath coverage from a number of subswaths, or multi-polarisation imaging of a single swath. The paper describes the ASAR operating modes which use the ScanSAR technique, and details the implications for image quality with performance trade-off examples for the current design.

KEYWORDS

Synthetic aperture radar, SAR, ENVISAT-1, ScanSAR, image quality.

1 INTRODUCTION

Spaceborne synthetic aperture radar systems are capable of providing high quality radar backscatter images of the Earth's surface. The all-weather, day and night operating capability, coupled to a spatial resolution of the order of tens of metres offers an enhanced surveillance tool for many applications compared to other instruments. The continuing operation of ERS-1, launched on 17th July 1991, and producing extremely reliable and consistent SAR data, further extends the data provided by earlier, somewhat limited spaceborne missions such as the SEASAT-A SAR and the shuttle based SIR-A and SIR-B instruments.

In the longer term, continuity of SAR data will be provided by ERS-2, essentially a clone of ERS-1, due for launch in 1995, and then the polar platform missions, which commence with ENVISAT-1, intended for launch in 1998. The latter's payload includes an advanced synthetic aperture radar (ASAR), which is now in its Phase C/D development stage. Its basis was the versatile SAR (VSAR) proposed by the British National Space Centre (BNSC) as an alternative to the ERS-1 technology based AMI-2 and SAR-C instruments (Reference 1). The ASAR concept offers greater flexibility and development potential from the active-array antenna design without compromising the overall mission timescale.

The main objectives of the ASAR instrument are to provide information on both the geosphere and the hydrosphere through measurements of the radar backscatter. Applications include

- Land surface composition and soil moisture

- Ocean waves and circulation

- Sea ice characterisation and extent

- Surface topography and snow and ice extent

Clearly such a wide variety of objectives requires an instrument which is flexible in both the modes of operation and performance capabilities.

2 ASAR DESIGN OVERVIEW

The ASAR instrument (Reference 2) consists mainly of an active-array antenna and a central electronics unit. The antenna is 10 m x 1.3 m when deployed, but consists of five panels (c.f. ERS-1), which can be folded up in order to fit into the launch vehicle shroud. Each panel is subdivided into four tiles, each 1 m x 0.67 m, all of which are identical electrical and mechanical sub-assemblies. The tiles are fully interchangeable and can be tested separately. They represent the active part of the antenna and are supported by a rigid mounting structure.

Each tile contains 16 transmit/receive (T/R) modules, each of which feeds a row of 26 front-fed printed patch radiators allowing either horizontal (H) or vertical (V) polarisation signals to be transmitted or received. The potential to operate ASAR with a full multi-polarisation capability therefore exists, but the current requirements are only for HH or VV (i.e. the same polarisation on both transmission and reception) operation. The T/R modules provide the final output power in the transmit path and the low-noise amplification in the receive path. Full control of both the amplitude and phase of the signals passing through each module is available. This allows the two-way radar beam shape to be optimised in terms of both the radiated power onto the target area (for good radiometric performance) and low sidelobe levels (for good ambiguity suppression).

The central electronics provide the signal generation, control equipment, data handling, and power distribution. Digital chip generation is used to provide flexibility. Pulse durations can be adjusted to vary power consumption, and the bandwidth can be matched to the required performance (spatial resolution and multiple looks).

3 ASAR OPERATING MODES

The ENVISAT-1 ASAR is capable of operating in five different modes as shown in Table 1. These range from single swath, high spatial resolution, high data rate imaging through to multiple subswath, low spatial resolution, low data rate coverage.

The Image mode utilises a single swath conventional SAR imaging approach. The advantage over ERS-1 comes from the ability to steer the elevation beam over a range of incidence angles. Figure 1(a) shows the ground coverage extent over Europe for ERS-1, with a 100 km swath width centred on 23° incidence, for 43 orbits (approximately 3 days) out of a repeat cycle of 501 orbits (35 days). Over the full repeat cycle complete coverage at most latitudes (except the poles) is possible. However, the ability to steer the beam and select the imaging geometry will reduce the revisit time to a particular target region (at the expense of coverage of another ground area).

The basic coverage capability of a SAR is determined by the antenna length. In conventional SAR operation the minimum pulse repetition frequency (PRF) is essentially constrained by the antenna length, through the need to adequately oversample the Doppler bandwidth being processed. Generally, this is about the 3-dB width of the one-way azimuth gain pattern (typically a $Sinc^2$ function from uniform amplitude illumination along the antenna) and the PRF is selected some 20-25% higher in order to control the suppression of unwanted azimuth ambiguities. Swath coverage is then limited by the interpulse periods available for echo reception as the same antenna is used for transmission and reception.

The ASAR coverage space is shown in Figure 2, and the baseline swaths are shown. Seven swaths (IS1-IS7) are used to cover the complete range of 15-45° incidence utilising two PRF ranges (1590-1765 Hz and 1996-2149 Hz). Individual swath widths vary from 100 km at low incidence down to 56 km at high incidence. The two PRF sets are necessary to permit continuous across track coverage whilst avoiding both pulse transmission periods (solid lines) and the strong specular nadir returns (dashed lines). Data is produced at a high rate, thereby limiting coverage within sight of a ground station (unless data relay satellites (DRS) are available).

Wave mode operation is a sampled version of Image mode. Up to 2 across track image vignettes from within any Image mode swath are produced covering a 5 km square region of the Earth's surface. Along track sampling separation is also selectable. This mode is therefore an enhanced version of the equivalent ERS-1 mode. On-board range compression is used to reduce data rates, and on-board data recording allows global coverage, with data transmission to ground stations at a low rate.

Wideswath mode achieves an increase in across track coverage (by a factor of 4) at the expense of a decrease in spatial resolution along track by a similar factor. The ScanSAR technique (see Section 4) is utilised to achieve the desired coverage with 5 subswaths (labelled SS1-SS5 on Figure 2). These provide continuous across track coverage over 17-43° incidence. The improvement for global coverage can be seen by comparing Figure 1(b) which shows the coverage over Europe for a 400 km wide swath (also from 43 orbits) with the ERS-1 case (Figure 1(a)). Revisit times to particular ground locations are reduced significantly, whilst the penalty in terms of reduced spatial resolution is not a problem for many applications (e.g. ice monitoring). Data is produced at a high rate requiring direct transmission to a ground station or DRS.

The Alternating Polarisation mode provides two images, one at HH and the other at VV polarisation. Once again the ScanSAR technique is used, but rather than imaging different subswaths to increase swath coverage, the same swath is imaged using alternate blocks of transmission and reception at each polarisation. Swath coverage is then the same as for Image mode (swaths IS1-IS7 on Figure 2), as indeed is the data rate.

The Global Monitoring mode uses the same subswaths as Wideswath mode to achieve good across track coverage. The low spatial resolution requirement (1 km) leads to small data rates for each subswath, and the on-board data recording permits virtually complete coverage (orbit

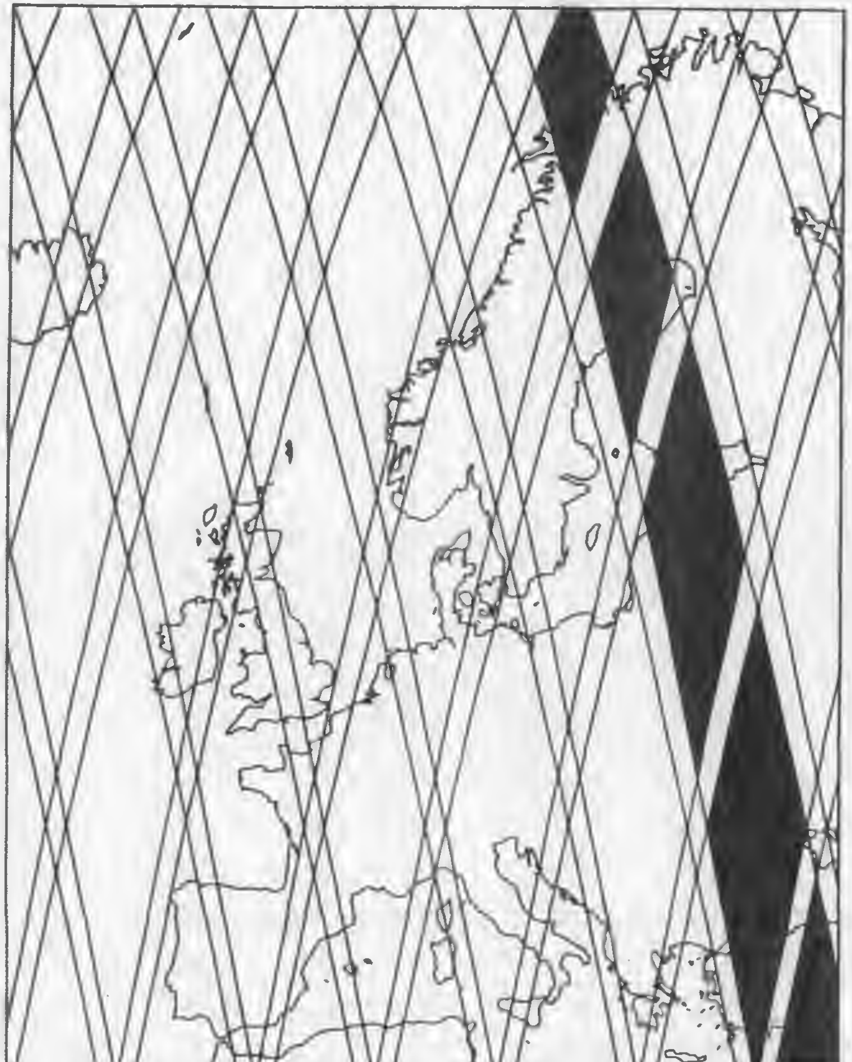

Figure 1(a): *ERS-1 Swath Coverage, 100km*
43 Orbits (~3 days) From 501 Orbit Repeat Cycle (35 days)

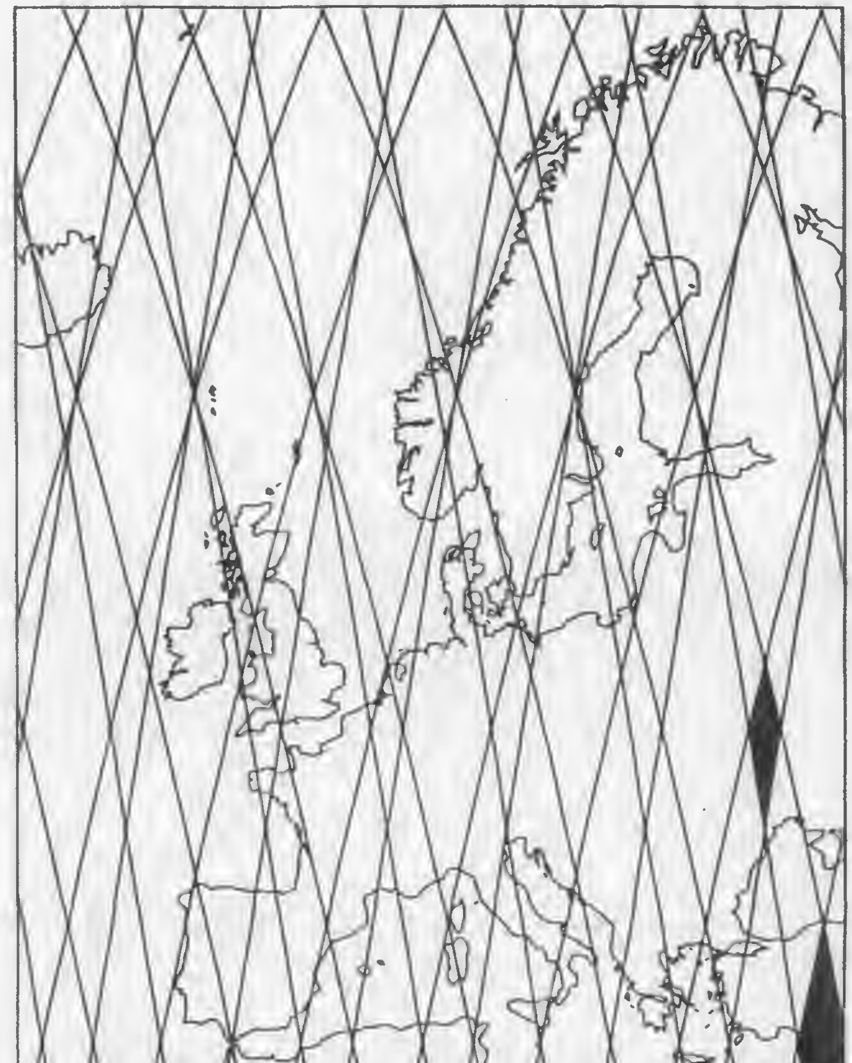

Figure 1(b): *ASAR Wideswath Mode Coverage, 400km*
43 Orbits From 501 Orbit Repeat Cycle

dependent) before data transmission to the ground. In order to conserve power this mode uses a reduced number of azimuth imaging periods, but recovers the radiometric performance through multiple range looks.

Operating Mode	Technique	Swath Coverage (km)	Spatial Resolution (m)	Data Rate (Mb/s)	Description/Comments
Image	Conventional	≥100	≤30	97.5	Swath widths to be optimised within 20-45° incidence
Wave	Conventional	2x5	≤30	1.8	Dual vignettes, 100 km along track intervals, within Image mode swaths
Wideswath	ScanSAR	≥400	≤100	97.5	Multiple subswaths, continuous across track coverage
Alternating Polarisation	ScanSAR	≥100	≤30	97.5	Using Image mode swaths, alternate HH and VV polarisation imaging
Global Monitoring	ScanSAR	≥400	≤1000	0.9	Using Wideswth mode subswaths, on-board data storage (c.f. Wave mode)

Table 1: ASAR Operational Modes

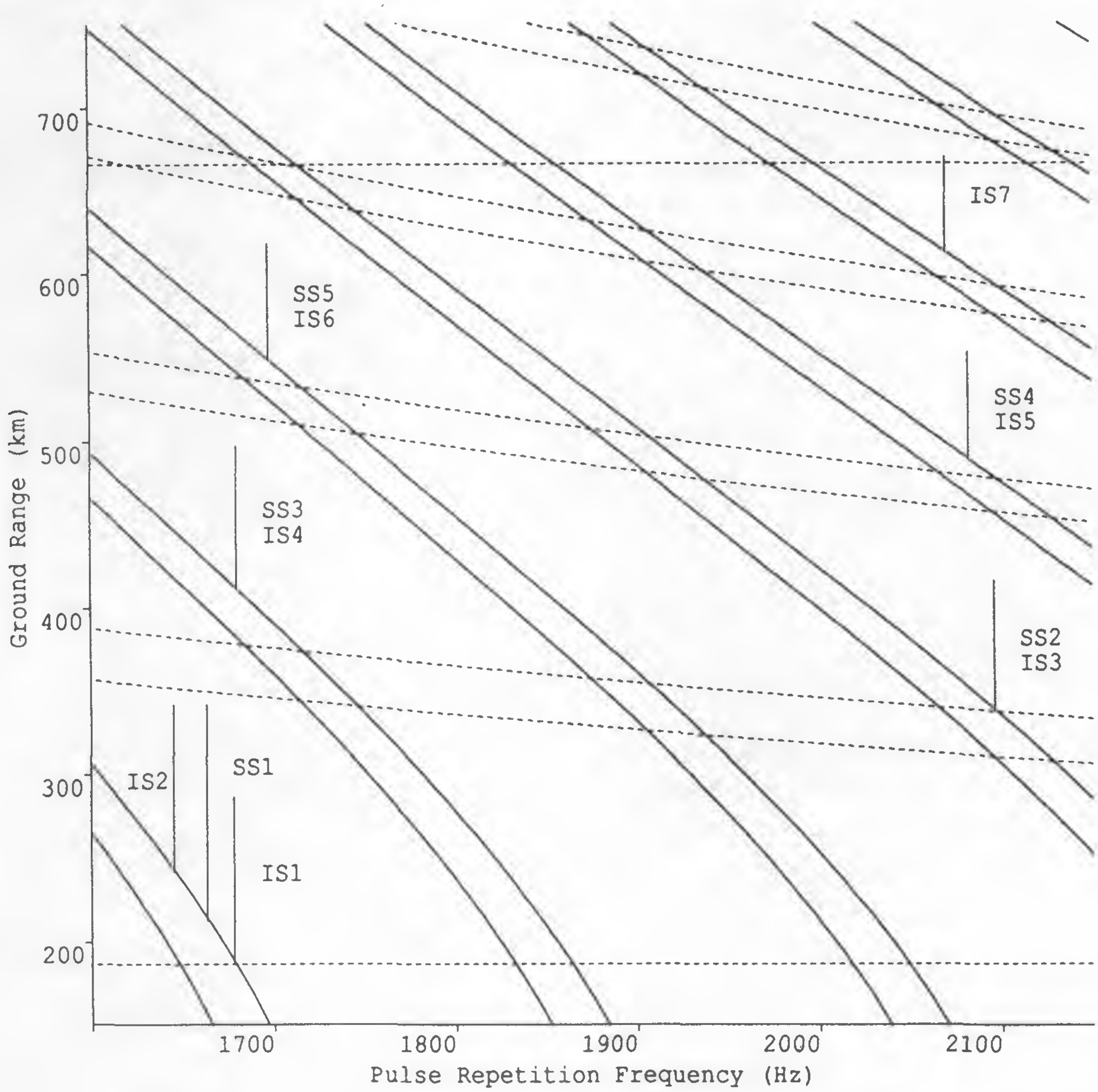

Figure 2: *ASAR Swath Coverage (Minimum Altitude)*
Image, Wave, Alternating Polarisation Modes - IS1-IS7
Wideswath and Global Monitoring Modes - SS1-SS5

4 SCANSAR OPERATION

The ScanSAR technique was originally proposed (References 3,4) as a means of broadening the across track swath coverage of the conventional SAR mode. Individual (continuous) swath widths are constrained by the need to measure the echo during the interpulse periods. Longer echo windows imply lower pulse repetition frequencies (PRFs), which in turn must satisfy the Nyquist sampling rate of the processed Doppler bandwidth. Maintaining image quality (azimuth ambiguity suppression) requires long antennas, to provide narrow azimuth beams, but this entails associated mass increases.

Multiple subswath imaging also has its problems. The use of a single PRF provides only disjoint coverage (for broadside imaging) and requires isolation between the signals from each swath. Solutions include pulse coding (bandwidth limitations) and/or stringent elevation gain pattern formation (large antenna height). Continuous coverage further requires the use of multiple PRFs. Data handling is complex with multiple receive channels.

The ScanSAR technique achieves the wide multiple subswath coverage by imaging a number of subswaths sequentially. It requires only a single transmit/receive beam pair at any one time and makes use of a single transmit/receive chain. A beam steering/pointing capability is necessary, but this is easily achieved with an active-array antenna.

Consider the beam 'footprint' as shown in Figure 3. In a conventional SAR this would pass over all azimuth ground target positions. The optimum spatial resolution is then determined by the Doppler bandwidth corresponding to the width of the footprint. The corresponding spatial resolution and coherent integration period are given by

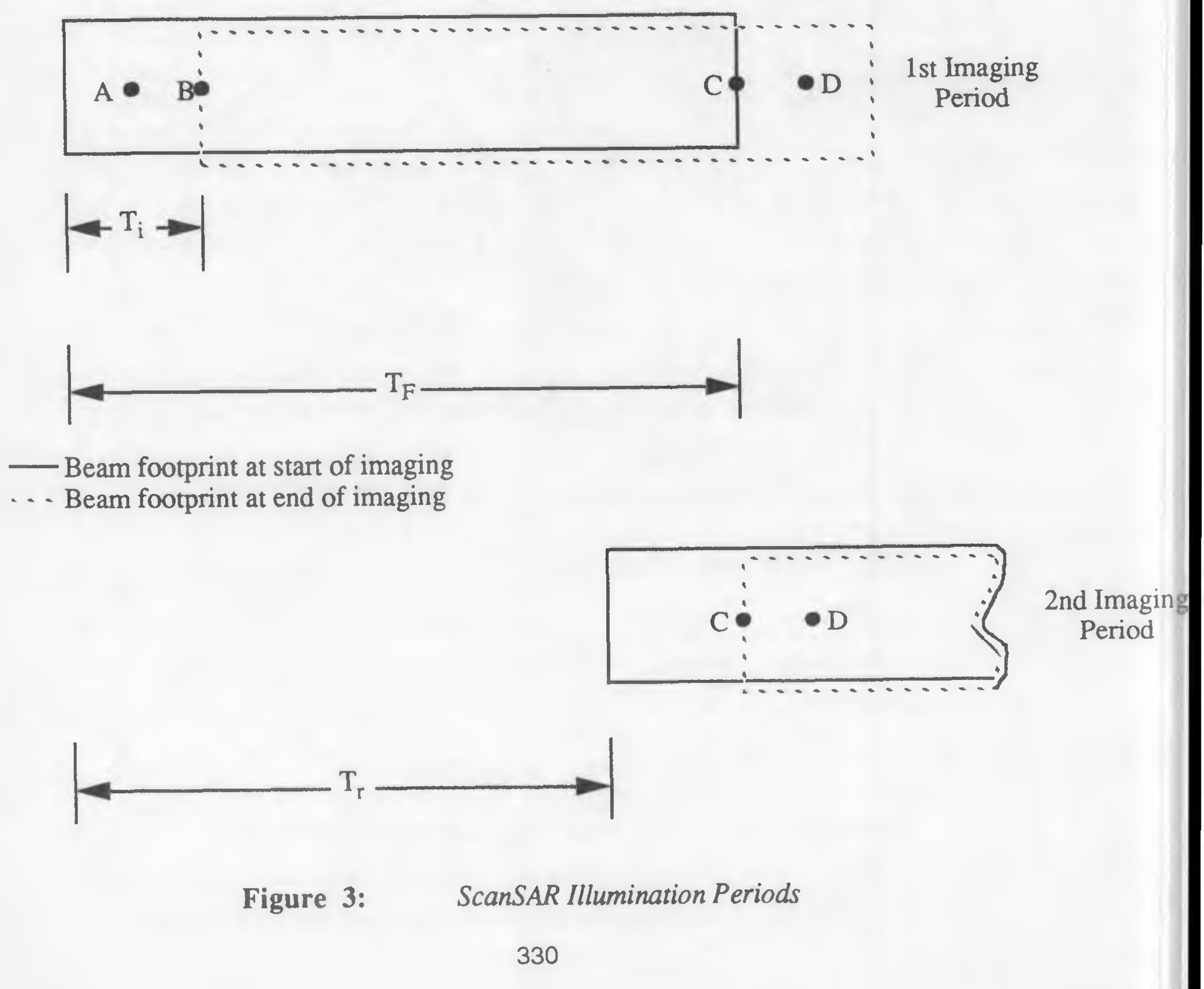

Figure 3: *ScanSAR Illumination Periods*

$$\rho_{opt} = f_A V_g / B_F \qquad \text{..... (1)}$$

where ρ_{opt} is the optimum azimuth spatial resolution

f_A is the broadening factor from the compression weighting

V_g is the velocity of the beam over the ground

B_F is the full Doppler processing bandwidth

$$T_F = \lambda R f_A / 2 V_s \rho_{opt} \qquad \text{..... (2)}$$

where T_F is the full coherent integration period

R is the slant range

V_s is the satellite velocity.

Typically, a conventional SAR uses a bandwidth corresponding to the 3-dB beamwidth of the one-way azimuth gain pattern (Sinc^2 from a uniform amplitude illumination).

Now consider the effect of imaging for a shorter period, T_i. Referring to Figure 3, target A leaves the footprint, targets B and C remain illuminated for the whole duration T_i, whilst target D enters the footprint. To ensure continuity in along track coverage, and ensure that all positions are illuminated for a time T_i, then imaging must return to this swath at a time T_r after the start of the previous imaging period. Thus, we have

$$T_r \leq T_F - T_i \qquad \text{..... (3)}$$

Note that target D is then imaged for the full duration T_i in the next (2nd) imaging period whilst target A would have been imaged fully in the previous (0th) period if it existed. Within this time T_r we are free to image other swaths and so we can increase the across track coverage at the expense of along track spatial resolution.

From the above equations it is clear that to achieve a given spatial resolution we must increase the integration period as the slant range increases. Similarly, the beam footprint on the ground increases in length with increasing slant range. If we assume that we image N subswaths, then we have

$$T_{rj} \leq T_{Fj} - T_{ij} \qquad j = 1, N \qquad \text{..... (4)}$$

Also, we have

$$T_{rj} = \sum_{k=1}^{N} T_{ik} \qquad \text{..... (5)}$$

Substituting, gives

$$\sum_{k=1}^{N} T_{ik} \le T_{Fj} - T_{ij} \qquad j = 1,N \qquad \text{..... (6)}$$

In particular this inequality must hold for the subswath with the smallest return time, that is the subswath (subscript n) closest to the nadir track. If we also assume that we aim to achieve the same azimuth spatial resolution in each subswath then

$$\sum_{k=1}^{N} \lambda R_k f_A / 2V_s \rho_A \le \lambda R_n f_A / 2V_s \rho_{opt} - \lambda R_n f_A / 2V_s \rho_A \qquad \text{..... (7)}$$

This then implies that the imaging periods increase with subswath position. Rearranging leads to

$$\rho_A \ge \rho_{opt}\left(\sum_{k=1}^{N} R_k / R_n + 1\right) \qquad \text{..... (8)}$$

Thus, the spatial resolution increases at a rate greater than N+1 since $R_k \ge R_n$ for all k. Figure 4 shows the trade-off between swath coverage and azimuth spatial resolution using the ASAR Wideswath mode subswaths as the baseline.

The preceding analysis has assumed that each subswath is imaged only once during each imaging cycle which therefore consists of an ordered series of subswaths (e.g. for 4 subswaths we could have 1/2/3/4 or 1/3/2/4 etc.). As with conventional SAR operation we can split the integration period up into looks to provide imagery at a lower spatial resolution, but with a better radiometric resolution. However, we may wish to introduce multiple scan cycles (Reference 5) within each imaging cycle as shown in Figure 5. Both the top two cycles will give 2 azimuth looks (of the same spatial resolution corresponding to an integration period T) but in one case the looks are adjacent for any particular target, whilst in the other case the looks are separated. If the kth subswath is imaged m_k times in an imaging cycle, then the spatial resolution becomes

$$\rho_A \ge \rho_{opt}\left(\sum_{k=1}^{N} m_k R_k / R_n + 1\right) \qquad \text{..... (9)}$$

In general m_k will be fixed for all subswaths, but may vary depending upon system performance capabilities and requirements (it could be traded-off against multiple range looks). In the first instance we may have [{1/2/3/4}{1/2/3/4}] where { } denotes a scan cycle and [ ] denotes an imaging cycle. In this example each subswath is imaged twice. Alternatively, we could have [{1/2/3/4/1/2/3}]. In this example all subswaths are imaged twice except number 4 which is imaged only once. Also shown in Figure 5 is the spatial resolution trade-off for a two look imaging cycle. Note that the total Doppler processing bandwidth or integration period is smaller for the second case (Figure 5(ii)) when the two looks are separate. Alternatively, the same spatial resolution could be achieved by using a reduced total processing bandwidth, that is, a smaller value for T_F (see Figure 5 (iii)), but with only one azimuth look.

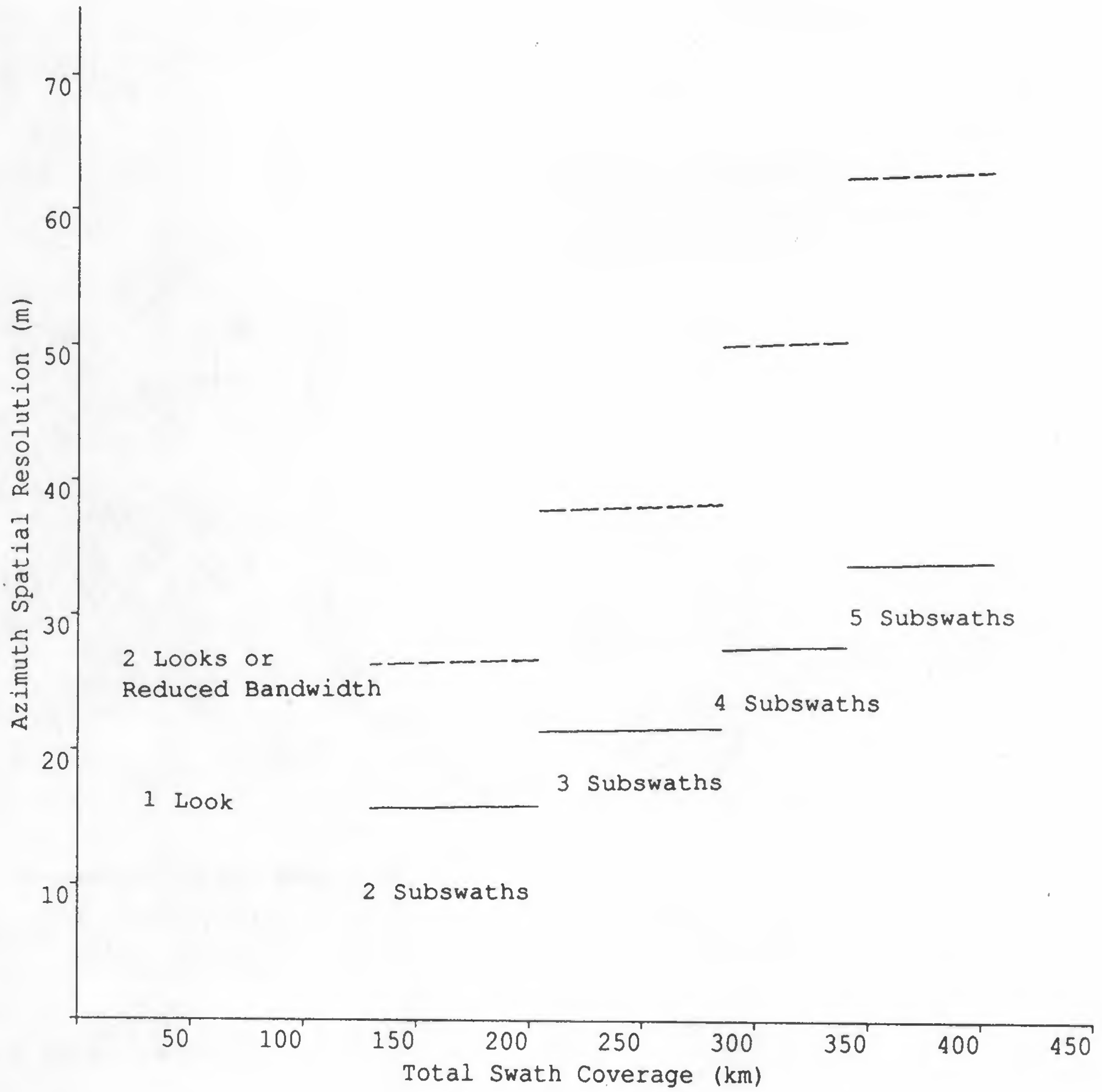

Figure 4: *Swath Coverage/Spatial Resolution Trade-off*

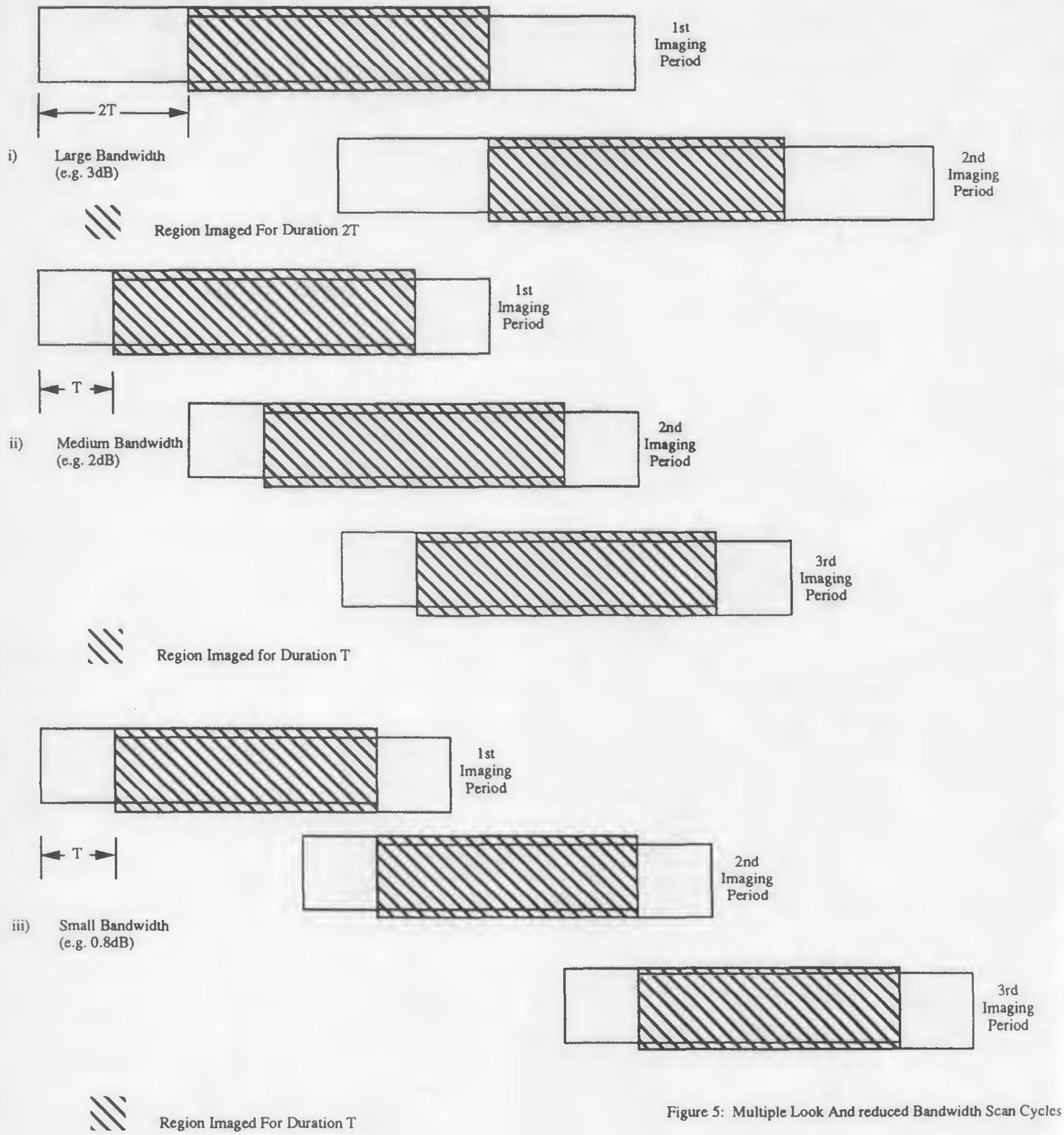

Figure 5: *Multiple Look and Reduced Bandwidth Scan Cycles*

The scan cycle must also ensure that every along track position in each subswath is illuminated continuously for the imaging period necessary to produce the required spatial resolution. Combining echo data from different imaging periods (e.g. for targets A or D in Figure 3) is not possible since there is a target position dependent phase discontinuity between adjacent data blocks.

The azimuth gain pattern is typically non-uniform (e.g. Sinc^2) and so this implies that image quality parameters such as radiometric resolution (γ) or noise equivalent sigma zero ($NE\sigma_o$), or azimuth ambiguity suppression will vary in the along track direction. The requirements on such parameters help to determine the optimum imaging cycle in addition to spatial resolution and coverage trade-offs. Ambiguity suppression and good $NE\sigma_o$ performance requires small total processing bandwidths (i.e. small T_F), whilst good γ values require large bandwidths (i.e. large T_F) to allow multiple looks.

Figure 6 shows the peaks of a number of point targets at different along track positions. The effect of the azimuth gain pattern can clearly be seen. In this simulation of raw data and block processing the total Doppler processing bandwidth is some 1340 Hz and the look bandwidth 400 Hz. Each image block contains 773 azimuth samples corresponding to a distance of 3.075 km. No correction has been made for the gain pattern effects, and so the point target impulse response functions will also have a non-uniform (cyclic) shape dependent upon the relevant portion of the gain pattern. Radiometric corrections could be made to keep image levels uniform, but this will still result in a residual variation in signal-to-noise ratio.

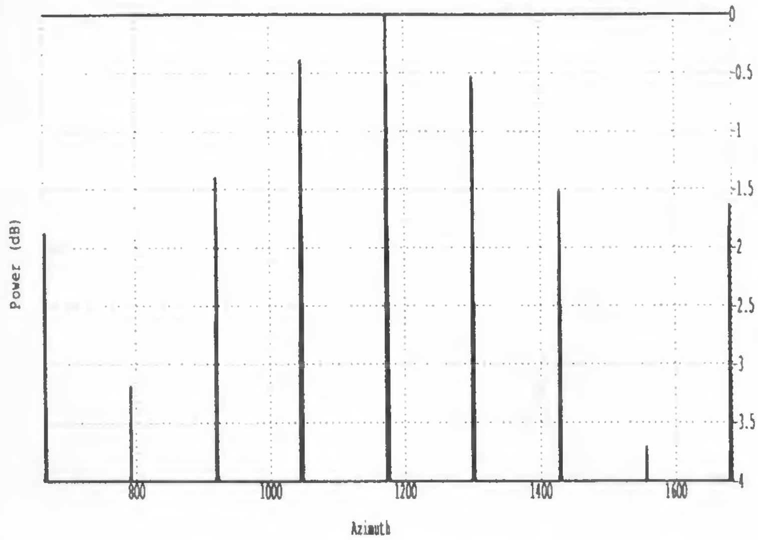

Figure 6: *ScanSAR Simulation Demonstrating Along Track Cyclic Variation*

As mentioned previously, for a ScanSAR system to produce continuous across track coverage requires the use of multiple PRFs (Figure 2). In general a small overlap between subswaths should be allowed for in the design to facilitate geometric and radiometric registration of the overlapping portions of the subswaths. The preceding derivation of spatial resolution has not included an allowance for beam switching between subswaths. In spaceborne SAR imaging there are typically 9 or more pulses in flight between the time of one pulse transmission and reception of the corresponding ground echo. This round trip delay means that the effective integration period can be smaller than the imaging period, and so the spatial resolution is proportionally larger. Potentially 'fast switching' of the antenna beam between the two subswaths, with pulse transmissions into one and echo reception from the other, could be used if the two PRFs are suitably linked. This would then reduce the number of lines of 'lost' echo to only one or two (actually the difference in the subswath ambiguity ranks). Where multiple subswaths using only two PRFs are involved the scan cycle scheme could be ordered to optimise the number of PRF changes.

A further consideration is that the fixed integration period for each subswath means that the azimuth spatial resolution increases across track in proportion to the slant range. This is most noticeable at lower incidence angles. Two approaches can be considered to accommodate this effect. Firstly, and the approach adopted for ASAR in Wideswath mode currently, the integration periods are selected to equalise azimuth spatial resolution at the near edge of each subswath. Secondly, the integration periods could be made the same thereby giving a smooth transition between subswaths, but a much larger variation across the full swath coverage. RadarSAT (Reference 6) adopts an approximation of this approach.

It has been shown that the return time for the subswath nearest to the nadir is the driver in the imaging cycle. The general ScanSAR timing cycles equations result in different maximum return times for each subswath. However, if we wish to achieve contiguous imaging of all subswaths then we must use the minimum return time. That is,

$$T_{rj} = T_r = \sum_{k=1}^{N} m_k T_{ik} \qquad j = 1,N \qquad \text{..... (10)}$$

This implies that the full integration period for each subswath will vary, and will in fact decrease with increasing slant range.

Also, from a practical operational viewpoint it makes sense to fix all imaging periods to be an integer multiple of the pulse repetition interval. This will ensure that a regular duty cycle can be maintained at the subswath boundaries. That is,

$$T_{ik} = n_k / PRF_k \quad k = 1,N \qquad \text{..... (11)}$$

This will require slight adjustments to the timing cycle.

5 ASAR ScanSAR Modes

In this section we examine the current ASAR design for those operating modes which utilise the ScanSAR technique.

5.1 Alternating Polarisation Mode

This mode replaces the typical wideswath multiple subswath imaging scheme with a dual polarisation imaging scheme using a single swath. Since the same swath is imaged continuously the same PRF is used for both polarisations and there is no loss of data due to the round trip delay and swath switching. Indeed, the imaging process is the same as for conventional (Image mode) SAR imaging save for the block nature of the echo (HH and VV). The timing cycle is set up to produce two distinct azimuth looks (one per imaging period) at each polarisation.

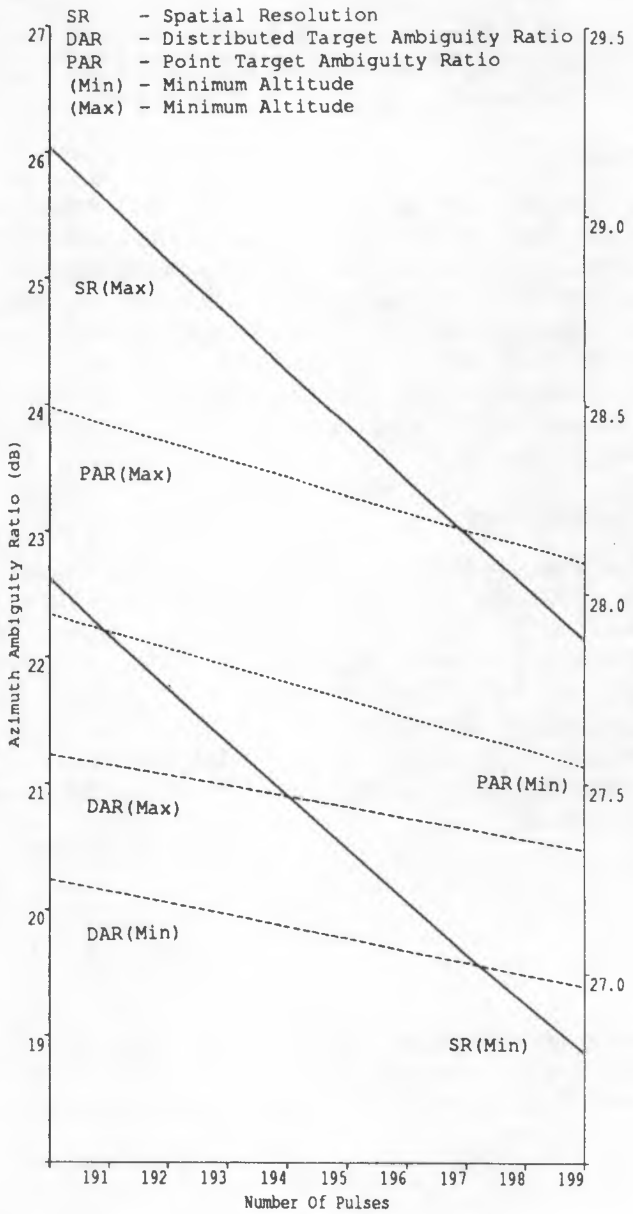

Figure 7: *Image Quality Trade-offs*

The satellite altitude for ASAR varies between 786 km and 813 km around the near-polar orbit. If the imaging times are allowed to vary around the orbit, the corresponding processing bandwidths can be kept essentially constant and the spatial resolution variation is then minimal (<0.25 m). However, this means that the return time between the same polarisation varies by about 5% between the two extremes in the orbit altitude, corresponding to a difference in the number of pulses in the imaging period of about 10. The current ASAR design uses a fixed number of pulses in each imaging period around the entire orbit. A reduction in the number of pulses (i.e. smaller T_i) leads to poorer azimuth spatial resolution, but improved azimuth ambiguity suppression as shown in Figure 7. Spatial resolution is worst (largest) at maximum altitude, whilst ambiguity suppression is poorest at minimum altitude. For the example shown, swath IS1, the current design uses 194 pulses in each imaging period. Figures 8 and 9 show the variation in $NE\sigma_o$ and azimuth ambiguity suppression with along track target position, that is for targets illuminated by different sections of the beam. In this mode a total processing bandwidth of some 1200-1275 Hz is used with individual look bandwidths of 240-255 Hz.

5.2 Wideswath Mode

Wideswath mode currently uses an imaging cycle which produces two azimuth looks for four of the subswaths (SS1, SS3-5), but only one for the other subswath (SS2). This timing cycle is a result of attempting to equalise radiometric performance across the subswaths, after satisfying the spatial resolution requirements. Radiometric performance (γ) can be recovered by using multiple range looks. The total processing bandwidth varies between 987 Hz (SS1) down to 838 Hz (SS5), whilst the look bandwidth is 77 Hz. The number of echoes in each block is some 10-14 less than the number of pulses due to the round trip delay. In this mode the number of pulses is variable whenever the PRF is changed. Currently, only two PRFs are used for any one subswath.

5.3 Global Monitoring Mode

This mode uses the Wideswath mode subswaths, but with a regular timing cycle. Originally, a 7 look timing cycle was derived to satisfy the spatial resolution requirements and provide excellent radiometric performance. However, in order to reduce the power requirements the timing cycle was reduced to cover just 4 imaging periods for each subswath in the 7 look timing cycle. Consequently, there are gaps in the pulse transmissions. Radiometric performance is once again recovered using multiple range looks. Bandwidths are small (817-684 Hz in total, 8 Hz per look) due to the low resolution (1 km). Also, in range the impulse response function shape is poor due to the small time-bandwidth products and the impact of Fresnel ripples.

6 SUMMARY

The ScanSAR imaging technique has been described. Various design trade-offs have been highlighted, and the current ASAR approach detailed. Given the inherent functionality of ASAR there is on-going potential for adjustment to the operational schedule after launch provided that flexible processing is available.

7 ACKNOWLEDGEMENTS

The ASAR design work was carried out under a contract to Matra Marconi Space UK Ltd funded by ESA. The author gratefully acknowledges the contributions made on the instrument design by colleagues within MRC and the European industrial consortium and ESTEC.

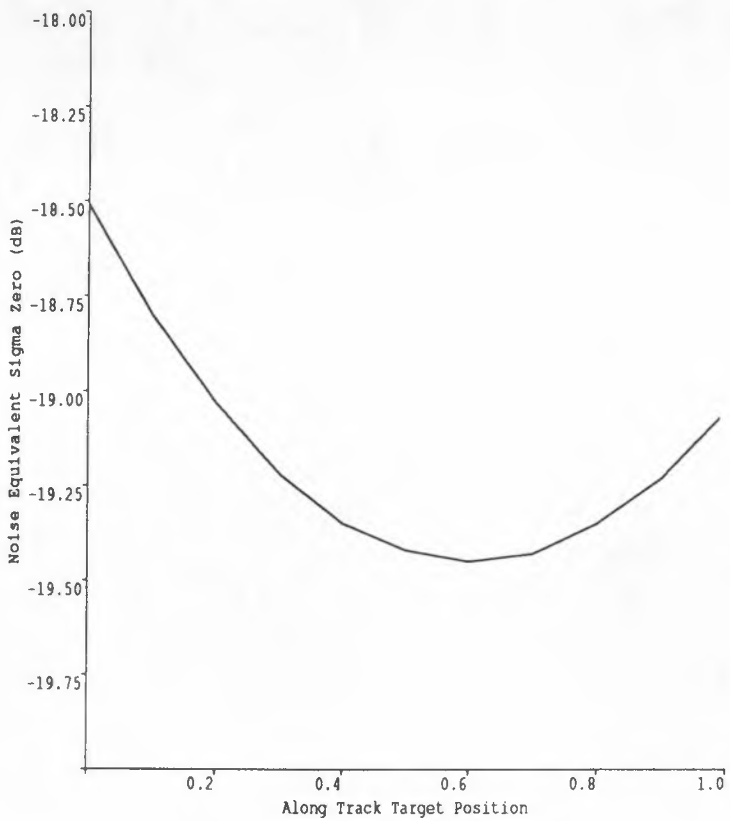

Figure 8: *Along Track Variation in $NE\sigma_0$*

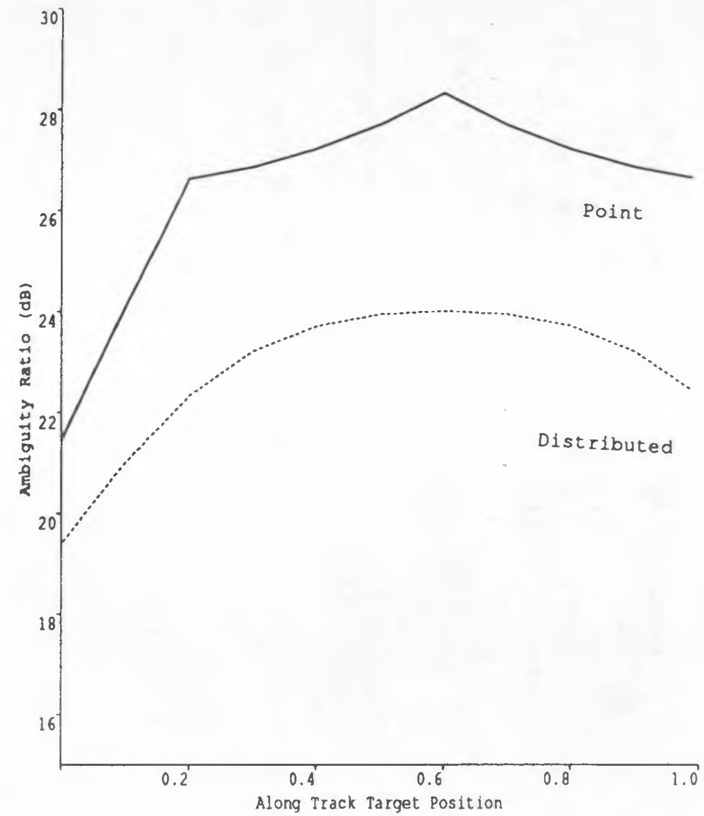

Figure 9: *Along Track Variation in Azimuth Ambiguity Suppression*

8 REFERENCES

1. Sawyer, F.G., et al., 1991, Versatile SAR for the first Polar Platform, *GEC Journal of Research*, 09/01, pp13-22.

2. Carter, D.J.Q., et al., 1992, The advanced synthetic aperture radar (ASAR) for POEM-1, *Proc. European 'International Space Year' Conference*, pp1165-1172.

3. Tomiyasu, K., Conceptual performance of a satellite borne wide swath synthetic aperture radar, *IEEE Trans*., April 1981, GE-19, (2), pp108-116.

4. Moore, R.K., Scanning spaceborne synthetic aperture radar with integrated radiometer, *IEEE Trans*., May 1981, AES-17, (3), pp410-420.

5. Currie, A. and Brown, M.A., 1992, Wide-swath SAR, *IEE Proceedings* - F, Vol. 139, No. 2, pp122-135.

6. Luscombe, A.P., 1988, Taking a broader view: RadarSAT adds ScanSAR to its operation, *Proc. IGARSS*'88, pp1027-1030.

USING THE OVERLAP REGIONS TO IMPROVE SCANSAR CALIBRATION

Anthony P. Luscombe

Spar Aerospace Ltd.
Sainte-Anne-de-Bellevue
Québec, Canada

ABSTRACT

ScanSAR images are constructed from blocks of pixels from different subswaths in range and from discrete sets of pulse returns in azimuth. The principal additional calibration errors which arise from ScanSAR operation are due to variations across each block, leading to discontinuities at the transitions. In the regions where the adjoining blocks overlap in each dimension, there are two independent backscatter measurements for the same area. Any difference between these backscatter values contains information about system errors, and this paper suggests some ways in the overlapping measurements can be used to provide improved calibration. The principal focus is on radiometric calibration, but the paper also considers briefly how the same approach can be applied to geometric calibration and phase calibration.

Keywords: ScanSAR, calibration.

1. INTRODUCTION

The signal obtained during ScanSAR imaging differs from that obtained during normal single swath imaging in that it is divided up into discrete blocks of pulse returns from different subswaths (Ref. 1). Modified algorithms must therefore be used for processing. Each block of pulses is converted to a section of image in one subswath, and the final image is pieced together from these various sections and subswaths. Because of the discrete form of both the raw data and the image sections, calibration has been seen as presenting more of a problem for ScanSAR than for conventional SAR imaging. This paper suggests some ways in which the form of the ScanSAR data can actually be used to our advantage in calibration.

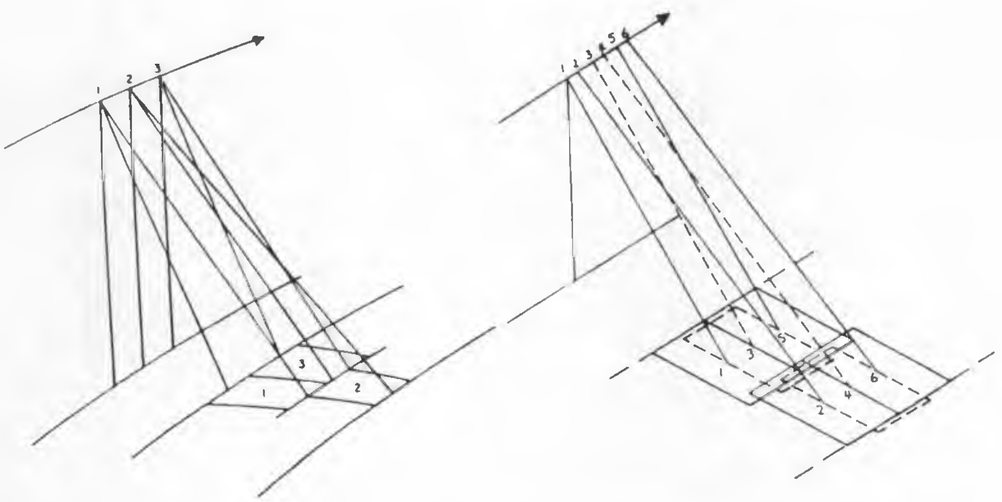

Figure 1: Examples of ScanSAR image formation.

As an illustration of the basic approach, consider the radiometric calibration in range across a SAR image. In most systems, a major error component is due to uncertainties in beam pattern and pointing, and in ScanSAR operation this problem is increased because adjoining subswaths are imaged with different beams. The suggested approach makes use of the data from the overlap regions between these adjoining beams. Within these regions, two measurements of backscatter are available, and these are obtained from data when the area was at the near edge of one beam and the far edge of the other. With knowledge of the likely cause (in this case, elevation pointing error) of any difference in these measurements, a correction can be applied not just to equalise levels at the join, but to do so in a manner which can improve calibration accuracy across the rest of each subswath.

The first section of this paper describes some of the features of ScanSAR operation and processing which are related either to the need or the suggested means for additional calibration operations. The outline of the method given in the previous paragraph was given in terms of radiometric calibration, and specifically in the range dimension of the image. A similar approach can also, however, be used for calibration in the azimuth dimension and for other types of calibration (e.g. geometric and phase), and the later sections of the paper consider these applications.

2. SCANSAR IMAGING AND PROCESSING

In conventional SAR imaging, the raw signal data are obtained in the form of a continuous series of pulse returns from a single swath swept out by the radar beam footprint. When a SAR system is operating in a ScanSAR mode, however, the full wide coverage is obtained by switching the beam between a set of adjoining subswaths. The signal data are generated in the form of discrete blocks of pulse returns from each of the subswaths in turn. Each block of returns is processed to form a section of image for the corresponding subswath, and the final image is obtained by combining the various sections in azimuth within each subswath and by connecting the resulting strips of image from the different subswaths in range. The piecewise construction of the image, and the consequent need for accurate spatial and radiometric registration of adjoining segments, is therefore intrinsic to ScanSAR.

Althouch conventional single swath data may also in practice be processed in blocks, there is no inherent variation requiring correction across the block, as there is with ScanSAR data, and there are no enforced breaks in the coverage in range. To image a given point with single swath data, the set of returns used in the processing corresponds to the period while the point to be imaged was within the radar beam. This interval of returns therefore shifts progressively with the azimuth position of the pixel at the same rate as the beam sweeps along the ground. For ScanSAR operation, only a subset (or multiple discrete subsets) of the returns from this interval are available, and data divided in this way require a modified form of processing. The same block of pulse returns must be used to image a series of points at different along-track positions, and so there is a progressive shift in the signal Doppler band used in processing, rather than in the time interval. Since Doppler frequency can be directly related to azimuth angle, this is equivalent to saying that the angular segment of the beam in azimuth which is used varies across the block of image. If the characteristics of the beam (principally radiometric, but perhaps also in phase or polarization) are not known perfectly, any variations across the block can only partially be corrected for. There will therefore be a residual cyclic relative calibration error (e.g. the 'scalloping' seen in some images). For single swath data, these relative errors do not occur, even when beam information is inaccurate, because any error effects are consistent.

The division of the ScanSAR data into discrete blocks of pulse returns from different subswaths therefore leads to potential variations and discontinuities in both the range and the azimuth dimensions of the image. Image calibration can, however, include corrections for any known variations, and the residual relative errors can be reduced to negligible levels if the corrections are based on sufficiently accurate information. The regions where any relative errors will be most apparent are the transitions between the image segments: i.e. between subswaths in range and between areas imaged with different blocks of pulses in azimuth. The overlap regions at these transitions also, however, offer an opportunity to measure directly the differences between the data obtained in the adjoining sections, and the suggested operations described in the following sections involve corrections made on the basis of measurements in those overlap regions.

3. RADIOMETRIC CORRECTIONS IN RANGE

The artifact of ScanSAR operation which is most likely to be visible in an image is the radiometric misregistration between adjoining subswaths. The regions on either side of the join will have been imaged with different beams, and being near the edges of these respective beams they are also in the regions where gain variations are generally greatest and so radiometric calibration is likely to be least accurate. Within an image produced with a single beam, a certain amount of residual radiometric variation in range may not be visually noticeable. The juxtaposition of two regions with different radiometric errors in a ScanSAR image will, however, be obvious. In practice, the regions covered by the two adjoining beams must be overlapped by a small amount to ensure there is no gap in the image. If the radiometric levels are equalized in this region, the image will be improved visually. More important than this cosmetic improvement, however, is the opportunity that this overlap presents for actually determining the required range-dependent corrections more accurately. The image data from the two beams can be equalized in a variety of ways, but the optimum method of correction suggested here is based on a knowledge of the likely cause of any radiometric discrepancy.

The principal range-dependent factors which must be included in the radiometric calibration of all SAR images are due to the elevation beam pattern and to geometric factors (slant range and incidence angle). In addition, for ScanSAR data, any differences in operating or processing parameters between different beams must be taken into account. There may, for example, be a change in the mean transmitted power between one beam and another because different PRFs are used, and there may be a difference in the lengths of the blocks of pulse returns used in processing. In the overlap region between beams, all these factors except one are either common to the data for both beams or are accurately known (and therefore assumed to be accurately corrected for). Any discrepancy can therefore be attributed to the one remaining factor, which is the antenna gain pattern. Various types of error can contribute to antenna gain uncertainties, and three in particular could cause the discrepancy in the overlap region:

- an error in the elevation pointing information,
- an error in the information about the shapes of the gain patterns in elevation, and
- an error in the information on relative overall gains of the two beams.

The form of correction which is applied to equalize levels within the overlap region would be different for each type of error. For the first, it would involve a pointing adjustment; for the second, a form of radiometric 'rubber-sheeting'; and for the third, a radiometric adjustment of one whole subswath relative to the other. Although errors of all three types will be present, when the overlap is within the regions where the gain is falling off at the edges of the beams, it is likely that the pointing uncertainty is the major cause of the error. (This conclusion may depend partly on the system being considered, and a different form of optimum equalization might apply in other cases.) Any mechanical pointing error, and a significant part of any electrical pointing error, will be common to both of the overlapping beams. It can be seen from Figure 2, which shows the gain patterns for two such beams, that any given radiometric difference in the overlap region can be converted back to an offset in elevation pointing. If the nominal transition from Beam A to Beam B occurs at the point where the gains are equal, then a positive pointing error would raise the level of the Beam A image relative to B and vice versa. The magnitude of the error can be determined from the relative gain slopes of the two beams in the overlap region.

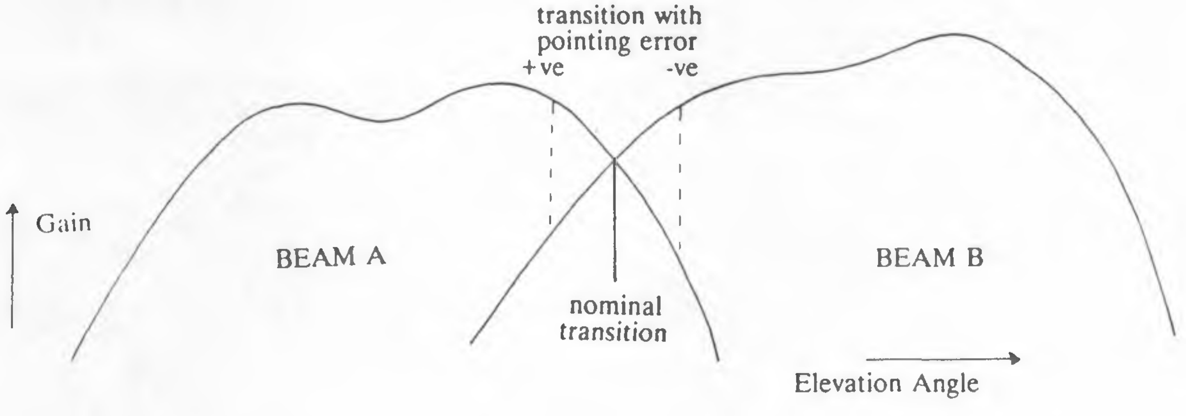

Figure 2: Relative Radiometric Levels in Overlapping Subswaths

If the radiometric corrections for the elevation beam patterns include the pointing adjustment derived in this way, then there will be no radiometric discontinuity or mismatch at the transition between subswaths. More importantly, however, this radiometric registration is obtained through a refined elevation pointing data, and therefore gives a potential improvement in radiometric accuracy across the full swath.

As a means for estimating elevation pointing from signal returns, this method can be related both to 'echo-tracking' and 'null-tracking'. With 'echo-tracking', the pointing is estimated by finding the best fit of the echo to the beam shape, particularly the edges of the mainlobe (Ref. 2). The method using ScanSAR overlap regions also involves fitting of beam patterns to signal data, but the effects of backscatter variation are removed because signals from the same area are being compared. With 'null-tracking', a beam pattern with a central null is formed, typically by an inversion of phase across half the antenna width, and the position of this null is located in the signal return (Ref. 3). This approach, like the ScanSAR overlap method, involves a comparison of signals from the same area with different beam patterns, although for 'null-tracking' the signals are electronically combined in the nulled-pattern, with cancellation at the null. The ScanSAR method has several advantages. It is not limited to the occasional pulse return. It is based on the actual beam patterns employed in imaging, rather than on special patterns used only for this purpose. And the

comparison is in a region of rapid gain variation with angle, making the ratio a sensitive measure of pointing error. Possible disadvantages: there may be more uncertainty in the relative gains of the two beams than between the beams from the two halves of the antenna, and the signal levels near the edges of beams are lower and therefore more susceptible to noise effects.
(Note: The method has been described here for a single overlap between a pair of beams. When the ScanSAR image covers more than two beams, separate pointing estimates can be obtained for each of the overlaps, and the radiometric correction can involve a combination of pointing adjustment and either relative radiometric adjustment between beams or expansion/compression of the beam width. The choice between these alternatives can be made on the basis of an assessment of the relative magnitudes of the different gain error factors listed earlier in this section.)

4. RADIOMETRIC CORRECTION IN AZIMUTH

In ScanSAR processing, the same fixed set of pulse returns is used to produce all points within a block of image. The radiometric variations in azimuth within each image block arise because the segment of the beam pattern to which the set of returns corresponds depends on the azimuth position of the imaged point. Points at the beginning of the image block, for example, were at angles in the trailing edge of the beam during the interval of returns, whereas points at the end of the block were in the leading edge. With perfect information on the beam pattern and pointing, the form of this radiometric variation could be determined from the processing parameters, and a correction could be applied. In practice, however, there will be some errors in both items of information, and so some residual radiometric variation will remain. The technique described in this section is intended to provide improved information on both beam pattern and pointing to ensure that residual variations are reduced even further.

The method suggested here is essentially the same as that of Section 3, but applied in the azimuth dimension. In this case, the overlap regions are between blocks of image obtained from succesive sets of pulse returns within a single subswath, rather than between the different subswaths. When the ScanSAR switching has been timed to give multiple looks of each area, the image blocks will overlap by at least 50%. For single-look operation, the switching is only required to ensure that consecutive image blocks adjoin, but in practice the same set of returns can be processed for a region which is slightly larger in azimuth to ensure that overlapping data are available (even if not directly used in the final image).

The technique is also modified slightly because the signal returns combined to image a given point cover a series of different azimuth angles in the beam, but are at essentially a fixed elevation angle. The azimuth beam patterns which must considered therefore correspond to signals integrated across a sliding segment of constant width within the beam. (The function also depends on the processing and should take into account both the length of the set of returns and any weighting applied across the set.)

Within any given block of image processed from one set of pulse returns, the signal level for a uniform scene would vary in azimuth in accordance with the integrated beam pattern. Ideally, the block would be centrally placed in this pattern. For a second image block, the same pattern would apply, but displaced in azimuth by a distance corresponding to the difference in time between the two sets of pulse returns. In the overlap region between blocks, a comparison of relative levels would remove any backscatter dependence and would give a measure of the beam position relative to the imaged area at the times of the two sets of pulses. In Figure 3, for example, the image blocks are displaced from the beam centre, and so the signal levels are not equal at the nominal transition. This indicates that the Doppler centre frequency used in processing is inaccurate, and provides a more accurate measurement for use with the next set of pulses. The information can also be used to determine the point at which to make the transition between one image block and the next, and to position the correction function to remove the radiometric 'scalloping' within each block.

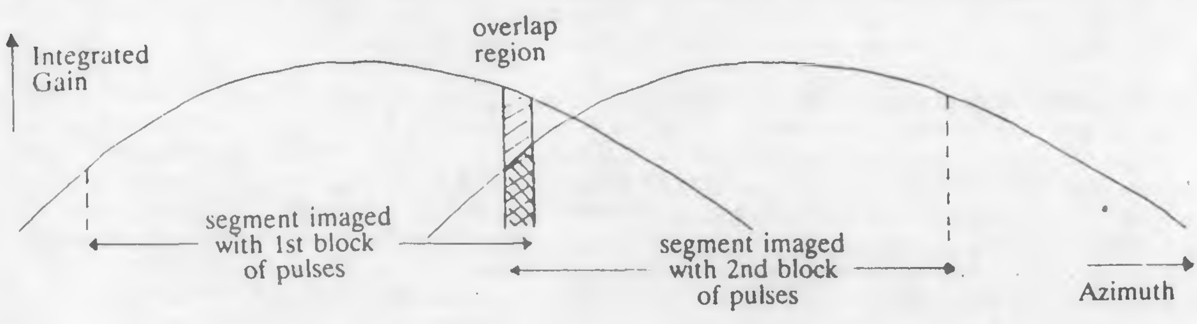

Figure 3: Radiometric Variations in Azimuth

The procedure described in the previous paragraph is effectively a means for obtaining a refined beam centre Doppler frequency estimate (and is very similar to the method based on comparison of mean levels in different looks of the image (Ref. 4)). It has the advantage over the common spectrum centroid method as applied to pulse-compressed data in that the estimate is not significantly affected by backscatter variations. Not only does the suggested method provide this Doppler tracking function, however, it can also provide information about the form of the required radiometric correction function. This information can be obtained when the overlaps between successive image blocks are large, particularly when the switching is sufficiently rapid to give multiple looks at each area. In this case, the relative levels can be measured as a function of azimuth position across the overlap region; this function corresponds to the difference between the two sections of the integrated beam patterns. With knowledge of the basic form of the beam pattern, the difference function can be converted back to the required radiometric correction function.

The suggested method of signal level comparison in the block overlap can potentially therefore provide improved information about both the shape of the radiometric function and where it should be applied relative to each block. Together, these two pieces of information should enable any 'scalloping' effects to be reduced to a minimal, near-negligible level.

5. GEOMETRIC CORRECTIONS

The methods discussed in the previous two sections for radiometric calibration are equally applicable to geometric calibration in that the images of any point in an overlap region should ideally be coincident, and any misregistration indicates an error and can potentially be used to characterise and correct that error. Because the misregistration is likely to vary systematically within the overlap region, the measurements should be made at several points across the region to characterise the effect fully. In order to detect and measure any misregistration, some features have to be present to provide a strong peak in the autocorrelation function. The features need not necessarily be point-like, and could instead be linear, possibly boundaries between regions. A single point might show directly the two-dimensional displacement, but each line gives a measure of displacement in the direction perpendicular to it, and so full information on the displacement will be available from an area containing multiple features.

As with the radiometric measurements, these location misregistrations can be examined both in overlaps between subswaths and in overlaps between image blocks in a single subswath. Displacements in range and azimuth in both types of overlap region can result from inaccuracies and approximations in the processing. Errors in certain items of the auxiliary data used in the processor will also, however, cause particular forms of displacement. In the overlap region between blocks in one subswath, for example, a Doppler ambiguity error will cause a misregistration in range, and an error in the Doppler FM rate will cause a misregistration in azimuth. Indeed, the suggested operations with ScanSAR data are closely related to the look-correlation methods which have been used for Doppler ambiguity resolution (Ref. 5) and autofocus (Ref. 6).

In ScanSAR imaging, there is a consistent (or, at worst, slowly varying) geometric relationship between the positions of the successive image blocks that are generated, and a consistent geometry within each block. In order to avoid the need to repeat processing for a given scene, therefore, I suggest incorporating any correction determined from misregistrations in one overlap region for subsequent image formation for equivalent regions. Any misregistration measurements for these later regions will then be used to track variations and make any necessary adjustments. If the misregistrations indicate a Doppler ambiguity error or an FM rate error which could cause significant defocusing, a correction could be applied in the azimuth processing stage. Otherwise, the corrections required are in scaling and placement of the image blocks. Because the distortions are likely to be linearly varying within each block, if linear operations (e.g. stretches, transpositions, rotations) are applied to give registration in the overlap regions, there should also be an improvement in geometric calibration across the rest of each block.

6. PHASE CORRECTION

Certain algorithms are particularly appropriate for efficient processing of data divided into discrete blocks of pulses, such as are produced in ScanSAR operation. In general, these algorithms have been designed to produce intensity images and have not been required to be accurate in retaining information about phase. The phase information is present in the raw ScanSAR signal, however, just as it is in any other SAR data from the same sensor. In this section of the paper, I make some suggestions as to how phase information might be obtained from ScanSAR images without a major change in the processing algorithms, and how the overlap regions might be used to refine the accuracy of these phase data.

The SPECAN processing algorithm, which has been shown to be effective for ScanSAR data, consists of a deramping for the Doppler slope followed by a Fast Fourier Transform (Ref. 7). All operations in this (and any similar) method of processing are mathematically well-defined, and so it should be possible to determine the form of the phase variation it introduces by analysis of the algorithm (or, at worst, by passing test signals through the processor and examining the output). For the algorithm described here, it is likely that the phase variations caused in processing will be linear along each line in azimuth and/or slant range, possibly with a slope which changes linearly across the block. The precise phase slopes in each dimension may depend on the exact signal characteristics and processing parameters, but if known variations are removed the residual part of the processor-induced phase variation should be significantly smaller. The next step in the suggested scheme for phase calibration is the equivalent of the radiometric and geometric calibration operations discussed earlier in this paper. The phases of the data from a series of areas across the overlap region between two image blocks are compared to determine the residual misregistration of phase. Because these overlap regions cover at least three, and possibly all four, sides of each block, a two-dimensional phase correction function giving the required phase registration can be determined. (Any phase unwrapping should be relatively simple because the most rapid phase variations will have been removed in the correction for known phase effects.) Since any phase variations will be essentially separable into the two dimensions of the image, the operation to remove phase misregistration around the perimeter of the block should also be effective in removing most of the error within the block. Potentially, therefore, this procedure could allow ScanSAR data to be used in interferometry, for example.

7. SUMMARY

ScanSAR images are formed from blocks and it is this blockwise formation of the image, with discontinuities between blocks and variations across blocks, which is seen as making it more difficult to achieve good calibration, particularly relative calibration, for ScanSAR data. The suggested calibration approach is based on the principle that if an error effect is visible (or otherwise detectable) in the data, it can be measured and can be used to provide information about the causal error, which can in turn be used to improve the calibration. With ScanSAR data, there are regions of overlap between successive blocks both in range and azimuth, and these areas provide the opportunity to measure the discontinuities in radiometric levels, geometry and phase. This paper suggests that these measurements can be used to enhance the image data, at worst by removing any discontinuities, but in a number of cases by providing more precise information about system characteristics which can potentially be used to enhance calibration across the full image. The principal example considered in the paper concerned derivation of improved elevation pointing information for radiometric calibration. This measurement supplements any that are available with single swath data; others, such as Doppler tracking and Doppler ambiguity estimation, may be performed in any case, but may be particularly convenient in the suggested form.

8. REFERENCES

1. Luscombe A P 1988, Taking a Broader View: Radarsat Adds ScanSAR to Its Operations, Proceedings of IGARSS '88, Edinburgh, Scotland, September 1988, pp. 1027-1032.

2. Curlander J C and McDonough R N 1991, Synthetic Aperture Radar: Systems and Signal Processing, New York, Wiley, p. 349.

3. Honeycutt B L 1989, Spaceborne Imaging Radar-C Instrument, IEEE Trans. Geosci. and Remote Sensing, GE-27, pp. 164-9.

4. Curlander J C, Wu C and Pang A 1982, Automated Preprocessing of Spaceborne SAR Data, Proceedings of IGARSS '82, Munich, pp. FA.1.3-6.

5. Cumming I G, Kavanagh P F and Ito M R 1986, Resolving the Doppler Ambiguity for Spaceborne SAR, Proceedings of IGARSS '86, Zurich, Austria, September 1986, pp. 1639-1643.

6. Bennett J R and Cumming I G 1979, A Digital Processor for the Production of Seasat Synthetic Aperture Radar Imagery, Workshop on Seasat SAR Processors, Frascati, Italy, December 1979, ESA SP-154, pp. 21-43.

7. Sack M, Ito M R and Cumming I G 1985, Application of Efficient Linear FM Matched Filtering Algorithms to SAR Processing, Proc. IEE, 132, pp. 45-57.

Radiometric Compensation and Calibration for Radarsat ScanSAR

Michael Y. Jin

Jet Propulsion Laboratory
California Institute of Technology
Pasadena, California 91109, USA

Abstract

Due to lack of a standard for modeling the radar echo signal in terms of signal unit and coordinates as well as lack of a standard in designing the gain factors in each stage of a processor, absolute radiometric calibration of a SAR system is usually performed by treating the sensor and processor as one inseparable unit. This often makes the calibration procedure complicated and requiring the involvement of both radar system engineers and processor engineers in the whole process. This paper introduces a standard for modeling the radar echo signal and a standard in designing the gain factor of a ScanSAR processor. In this paper, the radar equation is derived based on the amount of energy instead of the power received from a backscatterer. These efforts lead to simple and easy-to-understand equations for radiometric compensation and calibration.

1. INTRODUCTION

This paper describes the radiometric compensation algorithm proposed for the Radarsat ScanSAR processor. A detailed analysis for the radar signal and noise energy distribution is also given to facilitate the understanding of the compensation equation. A radiometric calibration procedure similar to that applied to the Magellan SAR data is then described.

It starts with the discussion of proper scaling for the SAR raw data. It then shows the scale factors that must be incorporated in each stage of the processing module for designing a unit gain processor. Signal and noise analysis in terms of energy are introduced then. It follows by the description of the radiometric compensation process and calibration steps.

2. UNITS OF SAR SIGNAL AND COORDINATES

The original radar signal is one dimensional with its unit given by voltage. Its instantaneous power can be formulated by the square of the signal times the reciprocal of the output impedance of the receiver. The energy over a time period is given by the integration of the instantaneous power over that period. This can be expressed by

$$E_t = \int Z^{-1} \cdot s^2(\tau)\ d\tau \qquad (1)$$

For a SAR system, a SAR processor engineer usually treats its signal as a two-dimensional one with one coordinate named the fast time τ and another coordinate named the slow time t. In this case, the interpretation of the unit of the SAR signal may require some consideration. A simple approach is to make a reasonable assumption that the two-dimensional integration of the square of the signal is equal to the total signal energy. This can be expressed by

$$E_t = \iint s'^2(t,\tau)\ dt d\tau \qquad (2)$$

In order for (2) to be consistent with (1), $S'(t,\tau)$ must equal to the product of $S(\tau)$ and $\sqrt{PRF / Z}$ where PRF is the pulse repetition frequency. Thus, the unit of the SAR input signal becomes $(\text{joule}\cdot\text{Hz})^{1/2}$. Since digital SAR data is quantized by the quantization level of the ADC, dV , the scale factor for the SAR raw data must also include dV. Therefore, one must convert a SAR input signal by a scale factor of $\sqrt{PRF / Z} \cdot dV$ before input to the SAR processor.

3. SAR CORRELATION WITH UNITY GAIN

For a burst mode SAR like the Radarsat ScanSAR, the correlation process involves fast Fourier correlation in range and azimuth deramp-FFT process. Both processes may introduce additional gain if they are not properly scaled. To ensure unity gain from SAR correlation process, the standard process described below should be followed.

A fast Fourier correlation is an implementation approach for a correlation or convolution process through the use of FFT algorithm. In a range compression process, the convolution can be expressed by

$$R(t) = \int C(\tau)\ g_r(t-\tau)\ d\tau$$

where $C(t)$ is the range echo data and $g_r(.)$ is the range reference function designed for both resolution compressing and impulse response shaping. Since $C(t)$ is a random process, in order to maintain $\int R^2(t)\ dt = \int C^2(t)\ dt$, the following condition must be satisfied

$$\int g_r^{\,2}(t)\ dt = 1$$

Also to be noticed is that the gain of the standard FFT is not the same as that of a Fourier transform. A Fourier transform is given by

$$\hat{S}(f) = \int S(t)\ e^{-j\ \omega\ t} dt$$

In discrete form, it is given by

$$\hat{S}(k\ \Delta f) = \sum_{1}^{N} S(i\ \Delta t)\ e^{-j\ 2\pi\ i\ k\ \Delta f\ \Delta t}\ \Delta t$$

A conventional FFT routine gives a normalized result such that a factor of Δt is ignored, i.e.,

$$\hat{S}(k\ \Delta f) = \sum_{1}^{N} S(i\ \Delta t)\ e^{-j\ 2\pi\ i\ k\ \Delta f\ \Delta t}$$

Therefore, in evaluating the signal power in spectral domain, the gain of the power differs by a factor of Δt^2. Based on this, the following steps must be implemented in the Radarsat ScanSAR process:

[1] In range compression, after the forward FFT, a factor of Δt must be multiplied to the spectrum, where Δt is the range sampling interval.

[2] In range compression, after the inverse FFT, a factor of $\Delta f = f_s/N_{fft}$ must be multiplied to the spectrum, where f_s is the range sampling frequency and N_{fft} is the range FFT length. However, standard inverse FFT does have a scale factor of $1/N_{fft}$, therefore, the factor to be multiplied is f_s. It should be noted that the scale factor introduced in step [2] is the reciprocal of the scale factor introduced in step [1].

[3] In azimuth compression, after FFT, a factor of $\Delta t = 1/PRF$ must be multiplied to the spectrum.

In azimuth processing for the ScanSAR data, the deramp reference function is the composite function of the deramp phase function and a weighting function. The deramp phase function does not affect the radiometric gain, but the weighting function could introduce a gain factor. To ensure unity gain in azimuth processing, the weighting function must be normalized, i.e.

$$\sum_{1}^{N_p} w^2(k\,\Delta f)\cdot\Delta f = PRF \quad \text{or} \quad \sum_{1}^{N_p} w^2(k\,\Delta f) = N_p$$

4. SIGNAL ENERGY FROM TARGET

Let the power and duration of a radar pulse given by P_t and τ_p respectively, the energy contained in a burst of radar pulses is then given by

$$E_t = N_p \int_0^{\tau_p} P_t\, dt = N_p\, P_t\, \tau_p$$

where Np is the number of pulses in the radar burst. The energy of each radar pulse is distributed to all directions in the space with a percentage proportional to the gain of the antenna pattern. In a SAR system, the radar beam is pointed to the ground, therefore, this energy is finally distributed to areas within the antenna footprint. If the burst interval is relatively short, the amount of along-track migration of the antenna footprint during the burst interval will be small as compared to the dimension of the footprint. Under this assumption, we may consider that the energy of all Np pulses is distributed to the footprint with the same distribution function as that of a single pulse. For a small area dA within the footprint, the amount of energy reflected in a burst of radar pulses is given by

$$E_r = N_p\, P_t\, \tau_p\, \frac{G(\theta,\phi)}{4\,\pi\, R^2}\, \cos\theta_L\, dA$$

where R is the distance between the radar and the target, $G(\theta,\phi)$ is the antenna gain, and θ_L is the radar look angle. Let σ be the cross section of a point-like target, the energy reflected from this target is then given by

$$E_1 = N_p\, P_t\, \tau_p\, \frac{G(\theta,\phi)}{4\,\pi\, R^2}\, \sigma$$

If the scatterer is iso-tropic, the energy received by the radar antenna from the signal reflected from dA is given by

$$E_2 = N_p\, P_t\, \tau_p\, \frac{G(\theta,\phi)\, A_e}{(4\,\pi\, R^2)^2}\, \sigma \qquad (3)$$

where Ae is the effective antenna area. Since Ae is given by $(\lambda^2/4\,\pi)\ G(\theta,\phi)$ and the receiver gain can be expressed by G_r, the energy received by the receiver can be rewritten as

$$E_2 = N_p\, P_t\, \tau_p\, G_r \frac{G^2(\theta,\phi)\ \lambda^2}{(4\pi)^3\ R^4}\, \sigma$$

For a distributed target, a cross section is substituted by the integral of the product of the backscattering coefficient σ_0 and an infinitesimal area of the target dA, i.e.

$$E_2 = N_p\, P_t\, \tau_p\, G_r \int_A \frac{G^2(\theta,\phi)\lambda^2}{(4\pi)^3 R^4}\, \sigma_0\, dA \qquad (4)$$

5. NOISE ENERGY

The noise power of a radar is usually modeled by

$$P_n = K\ T_e\ B\ G_r$$

where K is Boltzmann's constant, T_e is the equivalent noise temperature, and B is the bandwidth of the radar receiver. Within a collected burst echoes, the total noise energy is given by

$$E_n = K\ T_e\ B\ G_r\ N_p\ \tau_{echo}$$

The amount of noise energy over a fraction of the echo duration $d\tau$ and a fraction of the frequency bandwidth df can be expressed as

$$E_n = K\ T_e\ B\ G_r\ N_p\ d\tau\ \frac{df}{PRF} \tag{5}$$

In range-Doppler image domain, the amount of area covered by the corresponding window of $d\tau\ df$ can be shown to be $dA = dx\ dy$, where $dx = c\ d\tau/(2\sin\theta_i)$ and $dy = \lambda\ R\ df/(2V_s \sin\theta_{sq})$, R is the distance between the radar and the target, θ_i is the incidence angle, and θ_{sq} is the radar squint angle. Equation (3) can therefore be rewritten as

$$E_n = K\ T_e\ B\ G_r\ N_p\ dx\ dy \frac{4V_s \sin\theta_i \sin\theta_{sq}}{c\ \lambda\ R\ PRF} \tag{6}$$

From the signal and noise energy given in (4) and (6), the signal-to-noise ratio can be formulated as

$$SNR = \frac{P_t\ G^2(\theta,\phi)\lambda^3(c\,\tau_p/2)\ \sigma_0\ PRF}{2\ (4\pi)^3 V_s\ R^3 (K\ T_e B)\ \sin\theta_i\ \sin\theta_{sq}}$$

6. GEOMETRIC RECTIFICATION WITH UNITY GAIN

In burst mode SAR processing, a range-Doppler image is formed after range and azimuth compression processes. To allow mosaicking for image framelets obtained from SAR bursts, geometric rectification must be made for each range-Doppler image. As shown in section 2, there are conversion factors between the delay time and the cross-track ground distance and between Doppler frequency and along-track ground distance. To preserve energy level, these conversion factors must be properly applied to the rectified framelets. In equation form, it is given by $E_1\ d\tau\ df = E_2\ dx\ dy$. It is obvious that the scale factor $S = E_2/E_1$ should be equal to

$$S = \frac{d\tau\ df}{dx\ dy} = \frac{4\ V_s\ \sin\theta_i\ \sin\theta_{sq}}{c\ \lambda\ R} \tag{7}$$

In Radarsat ScanSAR processing, two elevation maps will be used; a smooth geode model and a fine DEM. When a fine DEM is applied, the above scale factor will vary significantly within the radar footprint such that it must be computed frequently. If a smooth geode is applied, S could be a single constant for the whole framelet.

In implementation, we may consider to combine this scale factor multiplication with the radiometric compensation process to reduce the overall computation load. If it is done in the geometric rectification process, $\sqrt{S}$ instead of S should be used since the signal is still in amplitude instead of intensity (amplitude square).

7. RADIOMETRIC COMPENSATION EQUATION

Now we may formulate the radiometric compensation equation under the assumption that (1) the range and azimuth compression processes are with unity gain, (2) the geometric rectification is already compensated by the scale factor given in equation (7), and (3) the final image framelet represents the normalized backscattering coefficient. Then, based on equation (4), the radiometric compensation equation is

$$\sigma_0(x,y) = I_n^2(x,y) \frac{4\pi^3 R^4}{\tau_p N_p P_t G_r G^2(\theta,\phi)\lambda^2} \tag{8}$$

where $I_n^2(x,y)$ is the square of the framelet pixel value in unit of joule/meter^2 if the radiometric compensation process not performed, P_t is the transmitted radar pulse power in watt, and G_r is the net receiver gain which includes gain factors from the antenna down to the ADC.

To output pixel with value in term of the backscattering coefficient, the gain factor of $4\pi^3 R^4(\tau_p N_p P_t G_r G^2(\theta,\phi)\lambda^2)^{-1}$ should be multiplied to the SAR framelet data in the radiometric compensation process which is usually done right before or after the geometric rectification process.

The above equation is useful to come to the understanding of the radiometric compensation, but, it is difficult to realize due to many unknown factors like G_r, Z, and P_t. A practical approach is to model all the unknown factors through the radiometric calibration process. This calibration process will be described below.

8. RADIOMETRIC CALIBRATION

When the gain of a SAR processor is unity, the radiometric calibration can be broken down as the processes to calibrate the sensor and to verify the processor gain of being unity.

To calibrate the sensor, it may be accomplished by (1) model the gain factor g_1 of the link between the transmitter end and the antenna end which may involve a cable and the antenna itself and (2) to collect a rechirp from an attenuated echo box directly connected to the transmitter end and to compute the sensor gain based on the attenuation factor, the transmitter power, the radar pulse width, and the energy of the collected echo at the end of an ADC. This calibration will give us a constant representing the product of the uncertain factor of the transmitter power and the receiver gain from the transmitter end to the ADC digital output. This calibration constant times the product of the estimated radar power and the gain factor g_1 will be used to replace the product of $1/(P_t G_r)$ in equation (8).

To verify that the gain of the processor is unity, we need (1) simulated raw data of either a point-target response or a Gaussian random process, (2) an assumed set of radar parameters including PRF and range sampling frequency, (3) an assumed set of radar platform parameters including radar position, velocity, terrain elevation, and radar look angle. The SAR raw data will be processed with a set of processing parameters derived from data given in step (2) and (3). This process will, however, exclude the radiometric compensation process. To satisfy the verification of processor, the total energy after this process should be equal to the total energy in the raw data.

9. CONCLUSION

Some scale factors are ignored in the above analysis for simplification. These may include the scale factors introduced along range as an automatic gain control for the range intensity variation, the transmitter power variation factor, the receiver gain variation factor, and the atmosphere attenuation factor.

The radiometric compensation process for Radarsat ScanSAR data is given in this paper. This process requires a unity gain processor which has the advantage that the signals in all modules are calibrated such that they can be used for measuring the amount of energy. The concept of this processor is simple, clear, and easy for implementation. The sensor calibration requires to collect only one radar pulse echo reflected from an echo box. This should not be difficult to obtain.

ACKNOWLEDGMENTS

The research described in this paper was carried out by the Jet Propulsion Laboratory, California Institute of Technology, under a Contract with the National Aeronautics and Space Administration.

Seed Questions prepared for the Working Group Discussions

SEED QUESTIONS

SESSION 1: CALIBRATION REQUIREMENTS

1. Actions from the last workshop

During the previous workshop it was decided to publish radiometric calibration needs for different applications and scientific disciplines. It was also decided to publish current and planned SAR sensors with associated calibration parameters.

2. New calibration requirements

New calibration requirements to consider in this meeting are regarding the following parameters.

Geometric calibration, DEM accuracies
Polarimetric calibration (e.g. vv-hh phase differences)
Interferometric calibration (e.g. relative phase, phase reference, decorrelation).

3. Calibration requirements derived from geophysical parameters

The basis for SAR calibration requirements is a relation between the primary radar measurement (sigma nought, phase difference, decorrelation etc...) and the geophysical parameter of interest (soil moisture, biomass, ocean wave height etc...). Is it possible to establish a list of geophysical parameters observable by radar, the sensitivity of these w.r.t. the primary radar measurement and the derived calibration requirement.

SEED QUESTIONS

SESSION 2: CALIBRATION DEVICES

1. With regard to the costs, is there a need for transponders with very high phase stability?

2. Considering a limited budget, is there a need for response-shifting transponders or should we focus on conventional devices?

3. We had only very few responds to our inventory list for calibration devices. Should we circulate it once more?

4. A question which often comes from universities: do we need further low cost receivers and transponders with limited accuracy? Maybe for the purpose of SAR-sensor monitoring?

5. Are there any experiences with radomes used for weather protection of active devices?

6. If several transponders are deployed, would it be reasonable to have approximately the same RCS for easier identification or should we keep an eye on transfer function verification by means of different RCS-values?

7. If we use ground based devices is there a need to measure in-flight patterns in a few hours?

8. Should we put a significant effort in beam alignment measurement procedures which deliver a result in a few hours? (absolute and between frequency bands?)

9. Even in the case of very large and important campaigns like XSAR/SIR-C there might be some calibration devices which are not involved. Can they be pooled? It is necessary? Which test site should be selected?

10. At Munich Tony Freeman suggested that all Calibration Transponders should be traceable to some fundamental standard, such as a metal plate. What steps have been taken to implement this?

11. Is there a need for accurate active transponders able to calibrate H.V or V.H? There are fundamental problems of accuracy generated by the geometry for the methods used to date.

SEED QUESTIONS

SESSION 3: POLARIMETRIC CALIBRATION

1. Radar systems and image formation models:
   - what is the impact of a finite point-spread function?
   - what is the effect of realistic noise models on calibration procedures?

2. Algorithm selection for calibration
   - what are the ranges of validity of procedures given realistic system performances and likely satellite capabilities?

3. What impacts do ambiguities have on polarimetric performance?

4. Can cover types be defined polarimetric calibration requirements (e.g. having decorrelated like -and crosspol return, or having known hh-vv phase differences)?

5. What is the status of any programme to define polarimetric calibration requirements?

6. What is the status of ASAR dual-polarisation calibration requirements and procedures?

SEED QUESTIONS

SESSION 4: INTERFEROMETRIC SAR CALIBRATION

1. How should height accuracy be defined or specified for interferometrically derived products?

2. Definitions of correlation measures:
    - raw correlation
    - fringe visibility
    - normalizations (baseline, surface slope)

    What has been your experience with various correlation measures?

3. What is the potential of an ERS-1/ERS-2 tandem mission?
    What should one concentrate on?
    What baseline, repeat cycle, coverage, mission length should be chosen?

4. What is the potential for better orbit data from ERS-2?

5. What new products (esp. InSAR) does ESA foresee during the ERS-2 timeframe?

6. What are the requirements in terms of Instrument and Processor performance for the INSAR Technique (Phase Fidelity, etc)?

7. What is the status of INSAR Processing System?
    - data input (raw data/complex image)
    - automated registration
    - automated phase unwrap

8. What are the proposed INSAR experiments/activities for ERS-1 2nd Ice Phase?

SEED QUESTIONS

SESSION 5 & 6: RADIOMETRIC CALIBRATION

What is the appropriate general form for the "SAR equation"?

What form should calibrated SAR data be distributed in?

- Product nature: calibration data or calibrated data?
- Ancillary quality information requirements: noise, looks, sampling, resolution, ambiguity levels, etc. Does the CEOS format handle this adequately?
- How can scene-dependant calibration factors: elevation/slope be separated from system-dependent factors?

What are the preferred methods of getting at the in-situ antenna pattern of a SAR after launch? -azimuth and elevation patterns.

What are the appropriate methods for intercalibration of spaceborne, airborne, and ground-based RCS measurements?

SEED QUESTIONS

SESSION 7: SAR PROCESSOR CALIBRATION

1. Last year's workshop did not give an answer to the problem of compensating quantization noise. Is there more knowledge now?

2. What are the additional calibration requirements for high resolution complex data compared to detected images (phase, radiometry precision, geometry precision, Doppler centroid precision, FM rate precision)?

3. How does resampling/averaging of magnitude detected images affect calibration accuracy? Is multi-looking a necessity?

4. Are there further comments/contributions to K. Raney's white paper presentation on the radar equation from the processor point of view?

SEED QUESTIONS

SESSION 8: SPACEBORNE SAR CALIBRATION

1. What is the recommendation for specification of future SARs with regard to calibration and image quality?

2. Are there standard scenes for sensor calibration at several frequencies? Comment: We have assumed, e.g. that the Amazon is OK. Are there geographical areas with well-documented coordinates that one or more users have used that we should select as standards?

3. What is the recommended measurement method for SAR long term stability?

4. What is the recommended saturation level of A/D converted raw data under which the SAR is well calibrated?

5. Based on experiences with SIR, ERS-1, and JERS-1, what recommendations are there for future systems with respect to calibration? (Anything new since 1992 meeting?)

6. Does the use of AGC and STC pose any problems in the calibration of SAR imagery of systems employing them?

7. It is assumed that the Space Segment, Atmospheric Propagation and Ground Segment all act linearly on the microwave signals? Is this a reasonable assumption for spaceborne SARs? How large are the linear regions for the various systems?

8. What operations should be required of the data user to obtain calibrated imagery for his science studies or operational utilization of imagery and which operations should be performed by the supplier of the imagery products?
   Are we expecting too much of the users if we do not give them a "completely" calibrated product to which they can directly apply their analysis algorithms?

9. What functions related to calibration should be performed and which data should be supplied by a satellite operator for those users who wish themselves to process raw data to a calibrated product? Is this a practical approach?

10. How frequently should calibration operations, using deployment of point targets, be performed?

11. Intercalibration of the various processors of a spaceborne SAR.

12. Quality and calibration of low resolution SAR products (low resolution means spatial resolution between 100 and 200 m). Low resolution SAR products are often required by ERS-1 users.

SEED QUESTIONS

SESSION 9: SCANSAR AND CALIBRATION

1. **Standard Performance Measures**
Such as radiometric resolution, radiometric error, spatial resolution, geometric error, ISLR, PSLR, noise equivalent sigma-zero, number of looks and phase performance.

2. **Requirements**
What are the requirements from the users of the ScanSAR products?

3. **ScanSAR Design Issues**
What are the trade-offs between number of sub-swath, resolution, and radiometric performance? What should be the approach for designing the integration time and number of sub-swaths?

4. **Ideal Processor performance**
What is the noise equivalent sigma-zero, radiometric resolution, resolution, ISLR, PSLR, and number of looks.

5. **Realistic Processor Performance**
Due to pointing error effect.
Due to ephemeris error effect.
Due to antenna pattern error effect.
Due to processing algorithm imperfection.

6. **SAR Algorithms**
In refining pointing knowledge.
In refining ephemeris knowledge.
SAR Processing.
State of the art algorithms, practical algorithms.

7. **ScanSAR Processor Calibration Approach**
What must be accomplished in processor calibration?
What are the appropriate steps?

8. **ScanSAR Output Measure**
Sigma-zero, normalized sigma-zero, gamma, or TBD measures?

Summary Report of Working Groups

WG 1-2 chair: E.ATTEMA (ESA)
WG 3-4 chair: A.FREEMAN (NASA-JPL)
WG 5-6-7 chair: K.RANEY (CCRS)
WG 8-9 chair: M.SHIMADA (NASDA)

SUMMARY REPORT OF

WORKING GROUP 1

CALIBRATION REQUIREMENTS

Chairman: E. Attema (ESA/ESTEC, The Netherlands)
Co-Chair: M. Borgeaud (ESA/ESTEC, The Netherlands)

Presentation of Papers

A paper was presented by G. D'Urso on the dielectric behaviour of soils and the importance of a careful description of what is imaged by the radar.

Actions from last meeting

Two actions were taken at the last CEOS meeting. The publication of two papers in the Canadian Journal of Remote Sensing at the end of September 93. The working group felt if was very important to have the results of the previous year available before the next meeting takes place.

Seed questions

Geometric Calibration:

A sub-pixel requirement was discussed as geometric requirement and it was felt that this is achievable by current sensors and processors. It was noted that not only the accuracy of the product, but also the delivery time and the cost were important. For each application a requirement list should be established for the accuracy and the delivery time.

It was noted that geometric calibration was not only required for geodetic referencing but also for terrain slope corrections. However it was observed that for non-flat terrains not only the local incidence angle was important but a model for the area under observation was required (trees tend to grow vertically, not perpendicular to the surface on mountain slopes).

Polarimetric calibration

Of the new parameters introduced with radar polarimetry σ^0_{vv}, σ^0_{hh}, σ^0_{vh} and the phase between hh and vv were felt to be the most important for hydrology, agriculture and forestry. Before specification of accuracy requirements a better understanding of the implications of these (further signature research) is needed.

Interferometry

The group thought that it might be too early to specify requirements. Only after seeing exactly what can be achieved with this new technique requirements should be defined. It may be more appropriate to have this aspect discussed in the subgroup on terrain mapping.

Geophysical models

Radiometric calibration requirements were derived from simple regression models defining the sensitivity of σ^0 to geophysical parameters (e.g. soil moisture, forest biomass). This was felt a good first approach, but the next step should be a refined specification on the basis of more advanced electromagnetic interaction models describing the underlying physics.

Discussion on Calibration Requirements

Tony Freeman
As far as polarimetric calibration is concerned SIR-C polarimetric calibration requirements are the baseline for discussion (reference IEEE GRS special issue on SAR calibration):

SNR requirement 20 dB (open to question: excessive?)
Phase balance of 10 degrees
0.5 dB amplitude balance between channels
30 dB polarisation isolation

Evert Attema
Thank you. Is there anybody who want to challenge these numbers?
No. This means it is the world consensus.

Bob Hawkins
A comment on Tony's own paper.
May be we can relax calibration requirements if more than a single (SAR) parameter is considered. It is worth keeping this in mind when trying to specify the requirement for a particular parameter.

Evert Attema
If you need data from other sources one should consider accuracy of those other data as well as the SAR data because it has an impact on the quality of the final data product.

S. Tam
How does the phase accuracy play in the physical application? ...because it is almost impossible to achieve such high requirement (mm scale) on a reflector deployed in a field under adverse conditions I wonder if we should be considering phase distribution...

E. Attema
We considered your question in the WG1. Your suggestion to look at phase information in a statistical sense in a useful one. I want to ask Tony about this who has made more progress than us in this field.

T. Freeman
We have a specification on phase error within 10° for polarimetry. This number includes all contributions (e.g. noise imbalance between polarisation channels). For interferometry the requirement has to come from a height determination requirement.
All requirements placed on our systems must be related to some sort of measurable quantity (soil moisture, height or correlation coefficient...).
Bob's comment on that you can relax calibration requirements perhaps if you are using more than one parameter from different measurement systems being radar or other is quite on the mark.

Using calibration devices to measure phase: it is difficult to do it with a transponder and probably expensive. A reflector can do it if you keep the edges very rigid ("concrete" type of reflector for the lifetime of the experiment). My suggestion is to use a reflector or transponder for early validation experiments and then after that find a junk of granite that is stable to do the job for you. Another suggestion is to use a radiotelescope dish.

S. Tam
What is the physical signification of the absolute phase of forest, soil, whatever... Stating requirements on absolute phase is asking for a meaningless quantity...

E. Attema
It depends on the application: specific applications in interferometry require this.

T. Freeman
1) In Polarimetry the requirement on phase difference between HH/VV = 10° is suggested. That does carry a lot of information (e.g. strongest discriminator between different crop types, flooded versus non flooded forest etc...).

2) Correlation coefficient and distribution of HH/VV phase often have a one to one relationship.

3) I believe this is a similar type relationship between correlation coefficients in interferometric pair and the "interferometric phase" standard deviation.

SUMMARY REPORT OF WORKING GROUP 2

CALIBRATION DEVICES

Chairman: H. Lentz (INS, Germany)
Co-Chair: A. Woode (ESA/ESTEC, The Netherlands)

Calibration Standards

The need for traceability of the standards used for calibrating the calibration devices was considered as part of the maturing of the SAR Calibration Working Group and was something that all participants in calibration campaigns should now consider. This calibration standard could be a suitably designed flat plate.

It was considered that a flat plate by itself was not enough to obtain correct calibration, this should be allied to accurate measurements made on a suitable range. One organization with suitable facilities should be nominated on each continent able to carry out such calibration.

Interferometric calibration

When using an active transponder for external calibration, very high phase stability of the electronics is not by itself sufficient. The antennas must also have a very good sidelobe and multipath behaviour to ensure the overall system phase stability (requirement < 1mm).

Corner reflectors can have good phase stability provided their mechanical structure is strong enough to withstand temperature variations and wind influences.

In either case, calibration devices for interferometric purposes should be mounted in a very stable manner.

Transponders

Response shifting transponders:

Response shifting transponders are in principle useful provided they are used within an amplitude correction loop or with an appropriate look up table.

Transponder RCS during deployment:

For calibration during deployment the use of transponders with the same radar cross section is the preferred option, they should also all be

calibrated at this same value. This simplifies the response identification in the image as well as the detection of a malfunction.
Transfer function verification of the SAR can be carried out by its own internal calibration.

Low cost calibration Devices:

Recommendation for all who intend to contribute but have a very limited budget. Don't spend your money on devices without matching the accuracy requirements. At the stage we have now reached it would be more reasonable to contribute with a good corner-reflector than use of a transponder/receiver with low accuracy.

Some Technical points

Radomes:

Radomes are necessary under adverse weather conditions. There is very little experience, especially for the case where the radome is covered with raindrops. In this situation transponders might suffer from an increase in antenna coupling. Investigations into the influence of radomes are highly desired.

Faraday-rotation:

This effect might have an important influence on signal-propagation in L-band. Although the inflight antenna pattern measurements for JERS-1 carried out by INS/DLR revealed no significant faraday-rotation effect some degradation was expected. It is very important to study this effect because it might have a significant impact on calibration with polarization dependent targets.

Transponder Horn Polarisation:

Where transponders are used with a 45° antenna polarisation alignment to facilitate calibration of VV or HH signals, it is necessary that this is taken into account when the error budget is compiled.

Inventory of calibration devices

There was not a very big response to the circulated inventory list of calibration devices. People who wish to add their devices to the list should contact Derek Kenward, DRA as soon as possible.

People who have devices to rent, or would like to rent devices should also contact him.

Discussion on Calibration Devices

A. Woode
There should be an organization responsible for calibrating devices used in campaigns.

Y-L Desnos
As far as Europe is concerned I think that the Joint Research Centre (Ispra Italy) of the European Community has the facility to calibrate properly our calibration devices.

K. Raney
You mentioned transponders shifting in range. Their counter part shift in azimuth can be achieved by a very low cost doppler modulator and is compatible with certain isolation between transmit and receive. So I would suggest greater attention to the doppler shift technique as well as the range shift technique.

A. Woode
This was not discussed in the WG. The range shift technique is easy to apply. The Doppler modulation technique is slightly more difficult.

E. Attema
Did you work out the pointing mechanism for a concrete block?

A. Woode
No. The idea is to have this type of corner reflector with a broad polar diagram.

F. Rocca
For the Naples experiment we use corner reflectors in concrete because this is the cheapest way to get the 1mm requirement for interferometry.
My proposal is to set up a single reflector that could be used for both ascending and descending path as a unique geodetical reference (multifrequency capability).

A. Woode
A possible solution is four C.R. corner to corner (as used on ships). If that sort of structure could be set in concrete that is the solution!!

F. Rocca
If we could arrive to some sort of standardisation of such a C.R. with 1mm stability this could help the expansion of SAR interferometry for practical application.

G. Keyte
To answer F. Rocca's question such reflectors exist. We use them at Romney March. They are under test for precisely that purpose, ascending and descending orbits.

Another point I think it is important to establish what is actually required rather than to tell us how to do the job. Practical consideration for example trying to put a reflector in concrete and expecting it to remain stable will be very difficult.

A. Woode
Requirement:

- orthogonality of the plate
- flatness of the plate. We are not interested in the actual radiometric return. We are only interested as a phase center.

E. Attema
This comment about concrete is an implementation question. If somebody can do it in another way and achieve it in another way it is even better.

G. Keyte
What is the requirement for interferometry?

- is it that you have the reflector stable i.e. non of the phases move more than 1 mm

or - is it that the reflector characteristics are known to within 1 mm

T. Freeman
It is that the phase center of the reflector does not move by more than 1 mm. Now, the requirement that one should place on the edge alignment, and the movement of the overall reflector are not known currently.

<u>There is some work to be done...</u>

G. Keyte
Are you saying the phase difference between HH and VV?

T. Freeman
No, a corner reflector if you look at all the ray paths, in an ideal reflector all the reflections look as if they come from the same point. That is what I mean by the phase center. The position of that point should not change by more than 1mm.

F. Rocca
The best engineering solution for such a phase stable reflector is something that has to be studied.

T. Freeman
This is worth a paper. So I would suggest that someone volunteered to study the problem and come up with the answer. Requirement can be defined as 1mm precision for the phase center.

F. Rocca
Adding as wide as possible opening to accept ascending and descending orbits and multifrequency capability.

E. Attema
Who is going to write the paper?

Tam
Environmental conditions should be taken into account, water, even bird dropping!...

E. Attema
Last meeting we went over the implications of bird dropping extensively and that is a big problem!

A. Woode
After the war there were a lot of papers written on corner reflectors for both phase and amplitude: the flatness of the plate and any movements were very sensitive parameters...

K. Raney
Comment on Faraday rotation:

1) Faraday rotation can be circumvented by using right circular and left circular as the orthogonal pair for quadrature polarimetry

2) In the case of +45°/-45° calibration devices you can measure Faraday rotation by having a pair of Transponders set orthogonally.

T. Freeman
Actually you can measure using only one.

SUMMARY REPORT OF WORKING GROUP 3

POLARIMETRIC SAR CALIBRATION

Chairman: R. Cordey (GEC-Marconi, UK)
Co-Chair: Y. Lou (JPL, USA)
Secretary: S. Quegan (Univ. of Sheffield, UK)

Calibration models and the point-spread function

- Discrepancies between "point" approaches to calibration and integral methods are expected for some forms of cross-pol antenna patterns in azimuth. Magnitude is not quantified.

Calibration/Interpretation and Noise

- Calibration model of Rhodes (Sheffield University) includes a noise-like term. How does this term relate to expected noise for JPL AIRSAR for which model was run? Not yet known.

- Very important to understand noise for the interpretation of polarimetric data (e.g. in identification of dominant scattering mechanism).
  Freeman (JPL) suggested that suppliers of data should include information on (range-dependent) noise floor and ambiguity levels.
  Range ambiguities may be a very significant source of noise in hv channel for certain satellite geometries operating interleaved h&v pulses.

Q: Should complex data be noise-corrected and if so, how?

A: In practice, not needed (probably) because:

(1) For distributed targets only noise power is relevant
(2) For point targets measurements should only be done with large signal-to-clutter ratio (and hence SNR).

Reference Distributed Targets

- Modelling using Rice model suggests some slightly-rough targets are unsuitable for hh-vv phase calibration (ocean at high incidence angle).

- Problems include the expected low SNR for slightly rough surfaces. This gives a reduced coherence and increased phase variance.

Q: Can we identify reference targets for hh-vv phase from historical data (at JPL in particular)?

Action: JPL to prepare statement on current status as regards reference surfaces.

Q: Do we have confidence in universal applicability of assumption of $<S_{ii} S_{ij}^*> = 0$ used in crosstalk verification?

A: Clearly need to avoid towns and there are difficulties from terrain effects in knowing appropriate antenna boresight angle.

. The wider validity of $<S_{ii} S_{ij}^*> = 0$ was discussed. Significant values have been repeated over agricultural areas but relatively little data investigated.

Action: Cordey to confirm to Freeman the expected insensitivity of crosstalk calibration to this assumption.

Calibration Requirements for Polarimetry

Q: How near are we to specifying applications requirements?

A: For an explanation of SIR-C requirements, see IEEE TGARS special issue.

ASAR Polarimetry

. Suggestions concerning ASAR modes (especially polarimetric ones) are probably best directed through ESA's science working group (Chair: E. Attema).

Other Issues

. Explicit discussion of different polarimetric calibration algorithms not conducted. Remains a possible issue for future discussion?

Recommendations

. The point-spread function is ignored in current calibration procedures; this leads to possible errors if point measurements on images are used. The likely impact for real radars should be quantified.

- (As in 1992) Data on noise should be supplied to users. Noise levels in different channels (e.g. as plots vs. range) and ambiguity data should be made available.

- More work is required to identify reliable distributed reference targets for calibration/verification of systems. Existing datasets should be used to further:

  (a) the identification of phase references for hh-vv phase verification

  (b) the verification of the assumptions of $\langle hh\text{-}vv^{*} \rangle = 0$ for crosstalk verification.

- Developing polarimetric calibration requirements should be monitored (possibly by future CEOS SAR calibration meetings). It is noted that the definition of requirements is complex and we are less able to identify requirements on individual parameters than in the case for single-channel SARs.

- Polarimetric modes of ESA's ASAR are of great user interest and attention should be paid by the appropriate ESA working group to requirements on polarimetric calibration and to verification techniques.

Discussion on Polarimetric SAR Calibration

Editor's Note: Due to technical problems the detailed discussion is not reported.

In addition to the discussion on the points raised in the working group report, two points concerning polarimetry were made by E. Attema:

1. The recommendation that ESA's ASAR working group should be aware of polarimetric calibration issues was noted and would be acted on.

2. What are the implications/requirements for polarimetry of scansar operation? This question remains open.

SUMMARY REPORT OF WORKING GROUP 4:

INTERFEROMETRIC SAR CALIBRATION

Chairman: Dr Steve Coulson (ESRIN, Italy)
Co-Chair: Prof. Fabbio Rocca (POLIMI, Italy)
Secretary: Dr Charles L. Werner (RSL, Univ. of Zurich, Switzerland)

Our group met to discuss calibration and verification problems associated with Interferometric SAR (INSAR). We began with a presentation of the current research topics being addressed by group members in the areas coherence and change detection, multiple-pass interferometry, both with satellite/aircraft, and single aircraft systems, and interferometric measurement by surface slope. This was followed by a guided discussion on aspects of SAR processor design, and verification, recommendations for Mission operation of ERS-1, ERS-2, Radarsat and Envisat.

Summary

The presentation by Dr Zakharov from the Russian Academy of Sciences demonstrated the potential for interferometric processing of Almaz data. Small test interferogram from the Antarctic region demonstrated that coherence could be maintained over the 5-day duration between orbits at the design frequency of the radar of 2.3 GHz. Work is continuing on improved coregistration algorithms.

A presentation by H. Budenbender et al of the German DLR of multiple pass airborne interferometry with the DLR ESAR instrument over Switzerland demonstrated the usefulness of active radar calibrators (ARCs) for determination of platform motion for improved motion compensation of the radar data. Temporal decorrelation studies are possible with this platform since regions with varying temporal decorrelation signatures were observed. Other applications the system will be differential interferometric studies of glaciers, earthquakes and vulcanism.

Prof. F. Rocca et al of the Politecnico di Milano in Italy proposed an innovative investigation combining SAR data from the Seasat L-band orbital SAR with airborne L-band data such as that recorded by the JPL L-band Airsar instrument. The long time period between the Seasat data acquisition and the current time requires that only study sites with a slow rate of surface change would maintain coherence. Death valley in California is suggested as an excellent candidate both because of the slow rate of surface change in the desert, and because of the current interest in tectonic related displacements in the Valley. Dr Rocca also presented recent results in resolution enhancement of SAR data using multiple pass interferograms.

Topographic surface slopes are important parameters which can be extracted for interferograms. Dr C. Werner and associates from the University of Zurich and JPL have developed algorithms for the extraction of surface slope from ERS-1 data. One algorithm does not require phase unwrapping and determines slope from the interferometric phase gradient. Slope information can be used both for correction of scattering cross section and temporal decorrelation for resolution element dimensions in range and azimuth. Results from a test site on the Alaska North slope were presented as maps of surface backscatter and correlation coefficient.

Recommendations

Processor Verification:

The importance of processor testing for phase accuracy was stressed. The auto-interferogram test was suggested by Keith Raney and Richard Bamler. In this test the same scene, either simulated or real, is shifted by an integer number of pixels in range & azimuth and passed through the processing system. An interferogram made with the two SLC products will reveal phase discontinuities and phase noise introduced by the processor. We recommend the following:

- adopt the auto interferogram as a standard test for processor phase performance

- develop a set of requirements for phase accuracy and standard deviation for interferometric SAR Processors

ERS-1, ERS-2, Envisat, Radarsat missions

With the second Ice Phase of ERS-1 coming up it is important to quickly select Interferometric test sites. Roll-tilt mode opportunities are also an option. A list of interferometric baselines for ERS-1 has been produced by Steve Coulson and is available in hard copy and accessible by computer networks.

Recommendations

The Radarsat commissioning phase orbit should be chosen to permit Interferometry.

High accuracy Orbit data (meter error scale) at 30 second intervals are desirable for automated INSAR processing.

- The ASAR instrument can be improved for interferometry through the capability for shifting the starting frequency of the transmit chirp over a range of 10-20 MHz. This is especially useful for low resolution wide swath mapping in order to maintain correlation.

- The ASAR dual polarization mode must function in Pulse interleave mode for interferometry.

- An ERS-2, ERS-1 dual mission is strongly recommended. A 1-day interval between sensor passes is preferred to a 8-day overflight schedule. This mission will permit global scale topographic mapping because the coverage restriction of the 3-day orbit is eliminated. ERS-1 & ERS-2 can be placed in a 35-day repeat orbit during the global mapping experiment duration.

Discussion on Working Group 4

K. Raney
New recommendation to the Canadian Space Agency that at least during the commissioning phase Radarsat uses a 3-day repeat orbit.

E. Attema
A roll-tilt mode campaign was held in April 1992. Technically there is a possibility to do another roll-tilt mode campaign, next year around April at the end of the ice mode. Those interested in repeating some roll-tilt mode operations should let me know.

F. Rocca
The Working Group recognised the usefulness of a phase stable ARC.
Problems of atmospheric dephasing by ionosphere (proposal of Zakharov) and by water vapour should be studied.

About ASAR:
- check the possibility of interferometry in the nominal mode
- interferometry in SCANSAR (we need a synchronization of the scanning patterns, in order to have the same wave number in the two following paths) to be studied
- the capability to change the chirp as a function of the orbit position could relax orbit maintenance requirements
- a listing of orbits suitable for interferometry is available for ERS-1 prepared by ESRIN

T. Freeman

- a short paper on how to validate the processors for interferometry should be written providing simple numbers (i.e. phase accuracy of the processor, correlation coefficient accuracy of the processor)
- problems like ionosphere, day/night coherence need to be studied but should not stop us going forward planning systems and designing systems
- the point of interferometry being represented at this Working Group meeting is the contact with processor people and calibration devices

people. Issues about terrain mapping validation are the brief of the Terrain mapping validation group.

C. Werner
Encourage further study on SCANSAR for interferometry

K. Raney
Just a clarification. Just simply because SCANSAR is a wide swath one gets global coverage every 3 days does not mean it repeats the interferometric geometry that frequently.

F. Rocca
If you look at the same place from the same angle with the same wave number why should you not be able to do interferometry.

K. Raney
That is precisely the statement and SCANSAR does not increase your opportunity to have the same position in space at the same angle.

T. Freeman
Recommendation to the Radarsat Project to facilitate interferometry over part of the mission by a proper repeat orbit. Radarsat's unique contribution is access to areas not yet covered previously through proper selection of incidence angle.

SUMMARY REPORT OF WORKING GROUP 5 & 6

RADIOMETRIC CALIBRATION

Chairman: R.K. Hawkins (Canada Centre for Remote Sensing, Canada)
Co-Chair: L. Ulander (Chalmers University of Technology, Sweden)
Secretary: M. Zink (DLR, Germany)

In the area of radiometric calibration there were 10 presentations given: 6 in the Plenary, and 4 minipapers in the working group meeting. As the list below indicates, a wide range of topics were covered. Some represent incremental results from on-going research, some review of previous results and still others describe work on new topics. It is clear from the discussion and the range of topics, that Radiometric Calibration remains an active area of interest and that another meeting is in order.

It could be observed that in many cases calibration involves correction of system non-linearities. The non-linearity of A/D converters is one example of this.

1. Calibration of DLR's Experimental Airborne SAR System E-SAR (presented by Zink, DLR)

2. Effect of Doppler Centroid mis-tracking on the Parameter Estimation of Point Target Complex Signals (presented by Touzi, CMR/CAN)

3. ERS-1 and JERS-1 External Calibration Experiments (presented by Zink, DLR)

4. Antenna Pattern Determination of Japanese SAR using Amazon Rain Forest (presented by Shimada, NASDA)

5. On the use of Extended Targets for Calibration: results from Maestro-1 Data and Mac-Europe data (presented by Souyris, CNRS)

6. Multi-frequency, Polarimetric Radar Cross Section Measurements of the Amazon Rain Forest (presented by Freeman, JPL)

7. The STC Function in the CCRS Airborne SAR (presented by Teany, CCRS)

8. Quality Issues for Low Resolution SAR Imagery (presented by Solaas, ESA/ESRIN)

9. Azimuth Banding in Airborne SAR Imagery (presented by Hawkins, CCRS)

10. Generation of Invisible SAR Targets Using Coded Transponders (presented by Hounam, DLR)

Following the presentations in the working group, there was a discussion on the nature of the participant's interest in calibration. In general, it appears that two groups exist: a) those who are interested in calibration in its own right and b) those for whom calibration is a necessary evil and their interest in calibration problems stems from the fact that adequately calibrated products did not exist. The user community interest in calibrated data products is growing and it is clearly the responsibility of the data providers to remove the system errors as far as possible from the output product. It is equally clear that the provision of derived geophysical products is the responsibility of the users, not the radar data provider.

A group of "seed" question were considered in the discussion with conclusions as follows:

a) What is the appropriate general form for the "SAR equation"?

Because a general paper was given in the plenary and in the session on processor calibration by Raney and Bamler, this question was not generally discussed except in relation to the questions below. A white paper is being prepared on the subject and will be included in the proceedings.

A general outcome of the SAR equation discussion was however that contrary to common thought, a SAR does not measure normalized radar backscattering coefficient, sigma-0 (this quantity can be derived if detailed knowledge about the local terrain slopes is available, but it is not intrinsically measured). Instead what is available from the instrument after radiometric calibration is radar brightness, Beta-0. It was highly recommended that SAR data products be calibrated to or traceable to this quantity rather than sigma-0. This recommendation was brought to the plenary and endorsed to be brought forward to CEOS generally.

(Despite the above recommendation which appears to eliminate the need to know the terrain elevation model in calibrating the data, the terrain comes into this problem also because it affects the antenna angle viewed on the ground pixel. Limited knowledge of the viewing geometry and the antenna gain are the largest sources of calibration uncertainty in most systems).

b) What form should calibrated SAR data be distributed in?

. Product nature: calibration data or calibrated data?

Unless the output of the processor is a floating point product, the output will be as a minimum a scaled amplitude product for which some factors must be supplied. For products where there is a large dynamic range across the swath, further range dependent scaling (and offset) factors may be required. It will be a challenge to supply this in the least user frustrating mode.

It was generally agreed that SAR image data should be calibrated before noise subtraction. After scaling and noise subtraction the obtained values are proportional to radar brightness, Beta-0.

Implementation details is a format question, but there seems to be general agreement that a common output format is highly desirable and that the flexibility now offered by the CEOS format was problematic.

. Ancillary quality information requirements: noise, number of looks, sampling, resolution, ambiguity levels, etc... Does the CEOS format handle this adequately?

We did not get a chance to consider this question.

. How can scene-dependent calibration factors: elevation/slope be separated from system-dependent factors?

See a) above.

c) What are the preferred methods of getting at the in-situ antenna pattern of a SAR after launch? -azimuth and elevation patterns.

Several papers in the workshop have dealt with this question adequately. For satellite SAR use of the Amazon rain forest is yielding highly reliable data for the elevation pattern and use of ground receivers is the preferred method of yielding the azimuth pattern.

d) What are the appropriate methods for intercalibration of spaceborne, airborne, and ground-based RCS measurements?

This question was not addressed due to limitations of time.

Discussion on Working Group 5 & 6

R. Bamler
I am very happy that you came back to the sigma 0 divided by the sinus of incidence angle (radar brightness) because I am convinced this is the quantity that is really measured and that should be delivered.
Is it broad consensus or is it because some people were not there.

B. Hawkins
To measure this consensus can we have a short hands out?

K. Raney
Let's first give the debate one chance to unfold!

T. Freeman
Imagine you are from a small University in an obscure town in the UK and you have been working with ERS-1 data in the last year. Suddenly along comes a new format unit sigma 0 divided by sinus theta.
Your software does not work any more your data are let's say 5dB off... you scratch your head and you wonder why?

K. Raney
The reason is that UK does not want to go metric!...

T. Freeman
An obscure University in Canada then!

B. Hawkins (back on Radar Brightness)
... We seem to be putting out this number for ERS-1 in every PAF. About the shift in several dB we have seen shift in several dB presented already in PAF's so users are used to that...

E. Attema
Many years ago we asked for sigma 0 and the answer was you can't get it... The fundamental discussion is: do we maintain the sigma 0 as a fundamental parameter or do we change to brightness, gamma value or something else? What is put on an image or a tape is a slightly secondary matter!

K. Raney
Some comments:
We are working with calibration in this case in the radiometric sense and for years I think we have been struggling with the ambiguities about where the instrument stops and where terrain interaction begins.
The difficulty with the sigma 0 definition is that it has embedded in it the assumption that there is prior knowledge of the terrain (one must know the local incidence angle)...

1) By moving to radar brightness definition... (β_0) it removes the incidence angle normalisation...
2) None of us had been presenting sigma 0 data. Sigma 0 is an intrinsic material property like is mass, ... One of the reasons for presenting new terminology for this (radar brightness) is to help clarifying the issue when it comes to radiometric calibration.

B. Hawkins
I feel this is important for this group to think in a serious way and ratify. I recognize the problem of tradition.
We present here a real "philosophic" change in the user community if we adopt a new terminology for what we are putting out and shift the responsibility to the users to deal with these data.
I hope we can endorse this recommendation.

K. Raney
Bob suggested a poll? Do you want to conduct a poll so I can vote... The question is: "shall we recommend that the presentation of our data be in terms of Beta 0 (radar brightness digital number per pixel)"? So the answer will be:

- yes if you agree with that change from current sigma 0 to radar brightness
- no if you do not agree with that change

Question: Who is providing the angle?

K. Raney
Nobody provides the angle. The number that is given is radar brightness and clearly the imaging geometry will be provided but there is no effort to normalize the data with respect to that angle to first order.

H. Laur
Should I understand your conversation as a theoretical conversation or as a practical conversation? My job is to try to communicate our thoughts in terms of calibration to the users who want to get calibrated data. So I have written this document last year on how to derive sigma 0 in ESA PRI products. Should I call that how to derive brightness in PRI products?

R. Bamler
But Henri that is exactly what we want to do, this is exactly what you have done already. You give the ERS-1 data as Beta0 data, they are not sigma 0 data and you tell the user how to convert them to sigma 0 using terrain slope and ellipsoid and so on.

H. Laur
Not yet!

R. Bamler
But then this is not correct, the conversion from beta0 to sigma0 is via terrain slope! In your technical note you are giving beta0.

K. Raney
It is beta0 scaled by a fixed angle...

R. Bamler
What is given in ERS-1 images is beta 0 not sigma 0.

H. Laur
Another thought in ESA, we have products called GTC which terrain corrected product (produce at D/PAF) and which is including a mask of local incidence angle. Actually I have some problems to speak about the calibration of such a product. So generally speaking I think there is a weakness also in our group how to derive sigma0 from terrain corrected products...

R. Bamler
Don't do anything to the data!...

K. Raney
The strength of Radar Brightness is that it is what is observed by the radar is its highest precision. There is no geometrically dependent interpretation attached to it. In the application you turn radar brightness in a number which is meaningful to your application in the geometric projection at hand. As an instrument provider you need to provide a number which is a reliable output of the instrument...

S. Tam
What is the difference between beta0 and gamma?

R. Bamler
Gamma is sigma 0 divided by cosinus of incidence angle and that is the natural quantity which is measured a CW scatterometer (you have an infinitely long pulse and the integrated area is limited by the beamwidth). In SAR the integrated area on ground is limited by the pulse length that is why the natural quantity measured by a SAR is sigma0 divided by sinus of incidence angle.

K. Raney
... The natural quantity measured by a radar is reflectivity per unit pixel:
- gamma is the projection making an assumption about incidence angle into one plane
- Sigma0 is a projection of that number based on several assumptions into another plane
- beta0 has no incidence angle assumption. It simply reports faithfully the number measured by the radar.

Let's poll:

Question:

- those as representative of the professional SAR community preferring that the output of radar is being expressed in terms of beta0 raise you hands? (YES) OK
- those in favour of retaining the current notation? (NO)
- abstention please indicate?

More abstentions than negations, and they were by the eyes of this chair about 5 times as many affirmatives as negatives.

Do people agree with that assessment? Thank you. Let's at least show the sense of this meeting to that opinion poll and then we will try to decide what to do with it. Further actions arising from your working group?

B. Hawkins
We have to make sure that format people can accommodate this... I suggest that this is brought forward to the format people in a recommendation.

SUMMARY REPORT OF WORKING GROUP 7:

SAR PROCESSOR CALIBRATION

Chairman: R. Bamler (DLR, Germany)
Co-chair: J.L. Marchand (ESA/ESTEC, The Netherlands)

Presentation of papers

H. Budenbender reported on the performance of the ERS-1 interferometry processor implemented at DLR/INPE.

M. Biagini presented the plan for X-SAR calibration at I-PAF.

R. Bamler described the implications of sensor parameter variation on processor gain for X-SAR.

Discussion of seed questions

1 - Revision of SAR signal & noise equations

It was criticised that in the presentation by K. Raney & R. Bamler the graphical representation of the model was misleading. It should be modified to show more explicitly the noise pre-filtering and the input of the noise. Concerns have been raised about the validity of the assumption that range signal and range noise have the same spectral properties. This will be added to a more complete revision of the paper.

It was agreed that such basic foundation of the SAR signal & noise equations should be set up now.

The authors have agreed to circulate the revised version of the paper to the interested attendants for technical discussion.

It was recommended that in a second step the model is extended to the polarimetric case.

2 - Errors introduced by ADC

R.B. proposed to use 2 different "gains" describing the effect of ADC behaviour close to saturation: (1) ratio of output power to input power to describe large signal attenuation and (2) the differential gain to describe the attenuation of small signals (noise, point scatterer response) superimposed on strong background clutter. K.R. objected that the ADC operates on complex signals rather that on powers.

No agreement was reached on this point. It was questioned whether the subject is an important point at all.

Recommendation: Use floating point quantization in future sensors.

3 - Additional Requirements on Single Look Complex data for Possible Interferometric Use

The paper by R. Touzi raised questions about the meaning of the complex integration method for phase measurements.
It was concluded that the phase of the peak is one of the important parameters. Measuring it requires careful resampling and is subject to errors. The relationship between the peak value and the more robust integral measure (vis-a-vis Dopcen) is not yet fully clear.

It was agreed that coherence (or phase variance) is a primary quality measure for a processor. High coherence results also in good geometric resolution. As a definition of coherence it was proposed to use the complex correlation coefficient between the output of the processor to be evaluated and of an ideal (aberration-free) processor.

Under simplifying assumptions it was shown that this coefficient is equal to the complex value of the normalised impulse response at the expected peak position.

The question was raised for setting up a quantitative standard table of interferometric processor quality vs. coherence.

A discrepancy was resolved, that appeared in the WG on interferometry: the coherence and phase standard deviation corresponding to a S/N ratio of 20dB are:

$$S/N = 20\text{dB} \quad \text{--->} \quad |\gamma| \approx 0.99 \quad \text{--->} \quad \sigma_\varphi \approx 15.03^\circ$$

The question of estimating coherence was briefly addressed, but not solved (cf. recommendation).

Recommendations

- To include coherence (γ) in the standard set of quality measures for SAR processors. The exact evaluation method for γ has to be standardised.

- To relate the coherence requirement on the processor to the maximum coherence (or minimum phase standard deviation) achievable under given S/N.

4 - Multi-look vs. post-detection averaging

There was a large consensus that post-detection averaging is at least equivalent to multi-looking. Nevertheless there were doubts on the validity of this statement for ocean imaging.

Strong concern were raised about the idea of providing the user with SLC only and letting him/her do the detection/averaging.

5 - Test data sets

As for interferometry is it feasible to establish a standard test data set for SAR processors? Several aspects were discussed. Among other it was proposed to stick with real data.

No conclusion was reached.

Action items

K. Raney & R. Bamler:	circulate revised paper on equation set
R. Touzi & S. Quegan:	discuss sensitivity results of their methods to measure the peak phase
F. Rocca & S. Quegan:	exchange information on estimator for γ and on pdf $[\,|\gamma|\,]$ and make results available.

Discussion on Working Group 7

K. Raney
Comment about multi-looking in the frequency domain and integration in the image domain: they are not equivalent, whenever there is the possibility of time variation in the incoming signal (i.e.: motion compensation, movement of oceanic surface).
So I would suggest the statement is amended with the proviso about time variation.

R. Bamler
Is there a reference?

K. Raney
There are several references.

Action Item
I will provide a list of references.

R. Touzy
One comment, there is a relationship between the phase estimated by the complex integration method and the "absolute phase" of the point target. Now if you want test coherence if you admit that for a coherent processor you have to measure the phase of the peak... you don't have to apply the complex integration method... but what we showed is that the peak value is very sensitive to zero doppler offset... If you want to have a good measurement of coherence you have to be sure that the peak value is in good condition so that it can be considered as a good estimate of phase.

R. Bamler
Yes exactly. We need the value at the peak. The other question is how we measure it. Of course the integration method is more robust but this is not enough...What we want to know is what the value of integration method is with respect to the peak value specially in the presence of aberration or doppler centroid variations. I think this was not fully resolved in the discussion.

K. Raney
The suggestion that the peak value of the impulse response is an estimate of the coherence of the processor is already strong. This makes some assumptions on the linearity and the spatial stationarity of the processor neither of which a real processor is completely satisfying. I think one needs to have a test which is realistic not just a prediction by linear theory.
So I would suggest that the statement itself be subject to further examination as well as means for testing it.

E. Attema
About the non linearity issue. As much as I enjoy public debate with K. Raney I tend to agree with the statement that non linearities operate on the complex data (I, Q) one has to look into that... I was a little bit disappointed about the recommendation of the group on this point because to say that using floating point quantization is a solution to this is misleading. Because wether you use floating point of any other form of coding doesn't really solve the problems of non linearities.
Keith has earlier put up this week a simplified model of a radar system with a linear part and a non-linear part being the detector but everybody knows, that it is an over-simplification, that in the so-called "linear Part" there are non linearities and they come partly from the ADC and also from the analog part of the system...
If you are really responsible for a system design: the question is what level of non linearity can you afford giving all the design constraints?

F. Rocca

This subject is relevant. Floating point quantization has other problems, for example:

- quantisation noise will be different from point to point. Just that is a complication. In other words we are gaining on one thing we are loosing on another. It is worth looking into non linearity problems because the possibility of reducing by a factor of two (i.e. ERS-1 example) the dispersion is extremely interesting.

So in conclusion the question of non linearity is very important.

K. Raney
From the standpoint of the Chair I think it is worth noting that the importance of the subject itself should be supported?

H. Laur
I agree with Evert and Prof. Rocca. I am a poor calibration engineer who has to deal with ADC saturations. We are looking for recommendations from this community what is the best way to correct these saturations either in the processor or the products.
I would have liked to see recommendation at this level.

K. Raney
1) Answer to question: What is the appropriate saturation effect? Could not be answered during time available yesterday.
2) The issue is far more fundamental than that. I consider to be correct on that we are talking about one extremely large ensemble of signals that go through pulse compression in two dimensions and for which the ADC is statistically independent between the two I and Q components. This changes the level of the question...

Those people who have done simulations or use classical references will find their results far more pessimistic than the actual performance of systems that are built that way.
We are all aware about 1/2 bit radars that have rather reliable output dynamic range and the 2 bit radar is making rather good estimates of return power output. There is an area for active investigation both theoretically and by simulations. I would suggest any recommendation in this area to be in.

R. Bamler
Last year we had the same question and no one was really interested in discussing it... This year we spent almost half an hour, I expect that next year we will have the solution!...

SUMMARY OF WORKING GROUP SESSION 8:

SPACEBORNE SAR CALIBRATION

Chairman: M. Shimada, NASDA, Japan
Co-Chairman: H. Laur, ESA/ESRIN, Italy
Secretary: T. Lukowski, CCRS, Canada

The session began with four presentations:

J. Sanchez and H. Laur of ESA/ESRIN presented "ERS-1 SAR Products Validation" giving a summary of their work which is a joint effort between ESA/ESRIN and the PAFs. Examples of three problems that have arisen with data presented along with the solutions that were worked out.

D.L. Hurd of Matra Marconi Space UK Limited discussed calibration aspects of the ASAR in "Planned Radiometric Calibration Scheme for the ENVISAT-1 ASAR Instrument". The design of internal calibration is further advanced than the ground segment as the hardware design will be the first to be completed.

F.M. Seifert and J.R. Moreira of DLR presented "Determination of Phase Errors in Spaceborne SAR". Various sources of phase error were discussed along with a method to determine atmospheric and instrumental phase errors of a spaceborne SAR. A method of estimation of satellite velocity was presented.

G. Solaas and H. Laur of ESA/ESRIN summarized the necessity of developing low resolution imagery of high quality for the ERS satellites, stressing the two most significant parameters (radiometric and spatial resolutions), in "Quality Issues for Low Resolution SAR Imagery".

These presentations were followed by a short discussion period based on a number of seed questions. Discussions were able to reflect the experience of those involved with existing and soon to be launched SAR systems due to the participation of representatives of organizations involved with ERS-1, JERS-1, SIR-C and Radarsat.

From these discussions, it is clear that the investment of time and money in the planning of calibration is invaluable. The success of a SAR mission depends on the best possible characterization of the SAR system.

The usefulness of a SAR system demands a close tie between geophysical requirements and the specification of the system, a relationship that is not easy to develop.

There is an evolution of SAR systems and phase measurement and stability are expected to be an important aspect of future SARs.

A number of lessons can be drawn based on practical experience in calibration of SARs:

1. The use of distributed targets in the determination of antenna gain patterns assumes constant γ with varying incidence angle. Various areas that can be considered include ice-shelf (Antarctic) areas and Amazon rain forest areas. H. Laur has agreed to distribute coordinates of a well-behaved area of the Amazon (from ERS-1 Scatterometer data).
   Action: H. Laur

2. The measurement of SAR long-term stability has been carried out using corner reflectors and Active Radar Calibrators. In either case, high cross-sections are required to obtain high signal ratios minimizing the clutter contribution to the integrated power at the point target location in the image.
   Raw data for calibration containing external point targets should be acquired as often as possible, but routine calibration operations should be minimized. This is best carried out by design of a system requiring as little external calibration as possible.

3. The ERS-1 experience has shown the effects of A/D converter saturation which must be considered in radiometric calibration.

4. When a spaceborne SAR has been made operational it is believed (by a number of the participants in this group) that the minimum of changes should be made that would impact data interpretation or utilization by users.

5. The system products and ancillary information should be specified in such a way as to minimize the effort required by users to obtain clutter backscatter information in a form useful to them (σ_0, γ, or βo as discussed elsewhere in these summaries).

6. The linearity of end-to-end SAR systems should be verified and corrections performed (if necessary) in the processing chain.

7. For effective use of data by the user community, processor intercalibration is essential. This is made difficult by incompatibilities (e.g. of tape formats) that must be overcome.

8. As phase behaviour becomes more important, the phase behaviour of variable gains in the receiver should be well characterized. It would be preferable to avoid AGC and STC functions in spaceborne SARs, if possible.

Due to the large number of questions, discussions on each of these topics were quite brief and could have profited from a longer discussion period.

Discussion on Working Group 8

E. Attema
About minimizing gain changes during a satellite SAR mission taking ERS-1 as an example: the possibility exists to set the gain over a wide range before each individual imaging sequence... We have set the gain at a specific value after launch and we have not touched the gain, the advantage of that is to minimize errors in the processing chain. We could have chosen the other option to optimize the A/D setting for each average signal level. Was that discussed in the group?

T. Lukowsky
There was little said.

K. Raney
BFPQ is an AGC system!

A. Freeman
You will probably have to vary the gain if you are going to look at different incidence angles over a very wide range of targets. I cannot see how you can avoid that unless you modulate the antenna pattern which effectively will change the gain anyway.

T. Lukowsky
Yes, but we want the user to see an identical product, so if there are any changes they have to be compensated for the users in the processor.

H. Laur
For clarification our suggestion was: after the commissioning phase, the agency should not touch anymore whatever will make trouble to users (on the condition that the satellite behaves well).
Typical example: we have seen with ERS-1 in some little cases mainly over sea we may have some ADC saturation and obviously we could tune the system gain to avoid that but we are not going to do it simply because it will create much more trouble for users than the correction itself that is the recommendation. Evert I am sure that you will agree?

E. Attema
I assume I should answer this as it was addressed to me directly. I think we have to be careful what we are talking about: ideally, if the on-board gain is changed and the information is properly communicated to ground processors we don't create problems to users. I feel I am pessimistic, but I am not completely confident that the information is timely communicated to everybody so we may find products on the market to which this correction is not properly applied.

H. Laur
You are right to be pessimistic "ideally" is the perfect world... to be sure some corrections will have the same effect in all processors...
... i.e. adjustment of gain of SLC produced at German PAF has created problems to users...

The problem is to always have the right information to the right people at the right time.

T. Freeman
I think you guys are very fortunate in having such a stable system with ERS-1 by design of course as it is reminded me constantly! But with Radarsat, SIR-C we have variable pointing angles, we have perhaps more of the earth to cover and we have to change the gain. A recommendation from this group not to change the gain we can't accept it...
Second comment: I have a question: "Did you change the gain in Roll tilt mode with ERS-1?"

H. Laur
I don't think so.

T. Freeman
The other question I have is, you are proposing to do a differential gain change across the image distributed spatially for each data product?
That doesn't square with don't change the gain really.
The two statements are conflicting.

K. Raney
The suggestion of the Working Group is a practical one and is meant to be interpreted for a given mode or a given product don't change the parameters downstream. And clearly for the larger incidence angle of multimode satellites is opposed to smaller incidence angle: gain level of the systems have to be different. But one month later don't throw a curve to the users!

H. Laur
We want the user to have to do as less as possible when doing calibration that is the idea...

T. Freeman
I think we agree that we have only to tell system engineer to change the gain. Your comment earlier suggested we didn't trust the system engineer in the past they are doubtful.

M. Shimada
I have a comment: JERS-1 SAR has a kind of trouble with saturation of data. AGC works every scene for every 64 or 128 pulses and input level to the A/D converter is set a little higher than the design value. Whenever data are acquired some part of the data are saturated...
From the view of the users, even if the SAR data is saturated, the data are well converted to Beta 0 or Sigma 0. My question is: even if the data is saturated can we find Sigma 0 (or Beta 0) from saturated digital number?

H. Laur
Yes. Perhaps it is something we have to do now... We have to find a proper way to provide users with a correction of products already processed.

T. Freeman
If you want to do a linearisation on the data product I would not do it at the PAF I would recommend that you distribute software to allow the user to do it. May be not even describe what the algorithm does, just execute it.

H. Laur
But software available for any kind of SAR product?

T. Freeman
That I don't know.

T. Lukowsky
Tony, by the discussion in this group we would suggest that it is not the answer. That is adding something else for the user to do.
We were suggesting that we want to keep it as simple as possible.

H. Laur
Tony's suggestion may be good for users who want accurate derivation of Sigma0. In any case without correction we are within +/- 1dB.

E. Attema
Two comments:

1) General consensus is we should try to provide users with Radar brightness and from time to time technical people try to push problems to the users and I am not in favour of that. I think there is a consensus that we should not do that.

2) How to remove non linearities. Statements both in Working Group and plenary have been made on that. What was suggested is something that is build in ESA processors: you look at radar brightness presented by the processor without non linearity corrections, you apply a low path filter on the image to estimate the loading of the ADC, at the time data was taken prior to compression and then you can derive correction factors from that... So I think it is not really a big deal.

T. Freeman
So you are going to have product 2.1A or B product, I wonder which one would have been corrected after a certain day and which would not have been corrected. That is the difficulty.

E. Attema
I think if you spread products in the user community without the system correction it goes against our agreement to keep the things simple for the users.

SUMMARY REPORT OF WORKING GROUP 9

SCANSAR AND CALIBRATION

Chairman: M. Jin (JPL, USA)
Co-Chair: A. Luscombe (Spar, Canada)
Secretary: M. Brown (GEC-Marconi, UK)

1. Standard Performance Measures

i) It is agreed that one performance figure for each measure is not sufficient. We suggest that either mean (μ) and worst case ($\mu \pm 3\sigma$) values or minimum and maximum values are given. For example point spread function (IRF) measures such as spatial resolution, PSLR, and ISLR could use the former approach, whilst measures such as radiometric resolution, noise equivalent sigma zero, and range ambiguity ratios could use the latter. Furthermore, full characterization of ScanSAR mode performance requires values for all subswaths.

ii) Is there anything to be gleaned from the phase information, in particular for a multiple azimuth look product? If not, is it necessary to retain it throughout the processing?

2. Requirements

i) What are the main requirements for ScanSAR modes from users? Potential users of Radarsat ice imagery have requested 100m spatial resolution with many looks.

3. ScanSAR Design Issues

i) The number of azimuth looks is determined by the SAR operation (timing cycle between subswaths). Thus, it is fixed before imaging, and cannot be selected at the processing stage. It is a selectable process, but it must be undertaken prior to the SAR operation.

ii) In terms of design trade-offs the following priority was agreed. Firstly, coverage is most important (giving the number of subswaths). Secondly, the number of azimuth looks. This will then allow trade-offs between azimuth spatial resolution and azimuth ambiguity suppression. It is felt that the same number of looks should be used for each subswath (this will help to reduce the variation between different subswaths) although this is ultimately system-dependent.

O/R For ASAR it was felt that the 100m spatial resolution requirement should be relaxed to allow the timing cycle to accommodate 2 azimuth looks in each subswath.

O/R iii) It is preferable that both multiple range look processing and spatial averaging be available with the processor. Given the choice, a constant range resolution is preferred to a constant number of range looks.

4. Ideal Processor performance

O i) Margins should be included in performance prediction to allow for processor introduced errors/effects. The level of such margins will be dependent upon the processing strategy.

5. Realistic Processor Performance

O i) Antenna pointing errors need to be constrained and tracked during processing. This applies both for subswath-to-subswath and for block-to-block within each subswath. There will be an impact on performance and these effects should be budgeted for in the system design.

6. SAR Algorithms

O/R i) PRF/ambiguity determination is still recommended (but is mission specific).

R ii) The image quality at the joint between subswaths should be equalized. This will have an impact on the processors.

O iii) The de-ramp FFT (SPECAN) algorithm is efficient for ScanSAR processing. It does not give optimum quality, but (based on Magellan data) the difference is small. This then impacts back to the error margin allowances for the processor.

O iv) The requirement for a linear phase correction in the image can be removed if the block of data is centred on the time origin before processing.

7. ScanSAR Processor Calibration Approach

O i) For the purposes of radiometric calibration, the processor should ideally be an invisible black box with unity gain (as described in the session paper (Jin)).

8. ScanSAR Output Measure

R/Q i) There will be a significant radiometric variation across the full coverage in ScanSAR mode, typically of the order of 2-2½ due to the incidence angle range (e.g. 20°-45°). We recommend that some form of incidence angle dependent function be applied (e.g. gamma function rather than just $\sigma°$). However, we request clarification on the preferred function.

Nomenclature:

O: Observation
R: Recommendation
Q: Question

Discussion on Working Group 9

A. Luscombe
Can I ask a question about phase information in SCANSAR data: "Does anybody see any application for phase information other than interferometry?"

M. Jin
I'd like to say something about the unity gain processor: For Scansar (burst mode) processing is quite different from continuous mode...

K. Raney
I think the question of M. Jin has to do with appropriate SNR equation in azimuth for Scansar?
Processing gain derives from oversampling by the PRF of the input Spectra. The other factor in the azimuth processing gain is the number of pulses summed which in Scansar is shorter than the total aperture available. So both factors are important:

- oversampling factor
- number of pulsed summed

For the noise you have already statistical independence pulse to pulse so you have an azimuth gain for the noise of 1 and you have a non-coherent gain for the noise which is proportional to the number of pulses summed. So even in Scansar you find out there is an azimuth processing gain which is proportional to the oversampling ratio: PRF modulo bandwidth of the input signal.

F. Rocca
If you consider the 3-day global observation orbit and with a proper synchronization they might be opportunity for an interferometric Scansar. Has anybody looked at this?

A. Luscombe
Based on discussions I have heard I don't think there has been any question that in principle Scansar data could be used for interferometry. It has been more a question of practicality.

B. Hawkins
In Scansar, the switching operation determined the number of looks you can obtain. If I fold the argument correctly, the operation determine the multilooking and therefore that is the first parameter you would have to specify. Why don't we produce everything single-look at the highest resolution, then degrade the data at the resolution that you want and the number of looks that are required?

A. Luscombe
If you try to do a single-look with two beam something like 1/3 of the information is being thrown away (not used in processing).
If you do 4 looks with 4 beams something like 1/17 of information is not used. Multiple looking also reduces the radiometric variation, so seems more optimum form of operation.

K. Raney
In principle there is no limit on the number of looks you can apply in Scansar. Look extraction in range and azimuth are purely symmetrical. We are in the habit of thinking of looks only in azimuth but it works both ways: Scansar if well designed takes advantage of that.

A. Luscombe
Discussion took place in our Working Group about alternative ways about getting range looks either through the processing, separate channel or spatial averaging... Within Scansar because we cover such a large range of incidence angles there is a choice of retaining the same number of looks in range or equalizing the range resolution and getting effectively a variable number of looks across the swath it is a design choice...

K. Raney
A comment: as is done on ASAR you can transfer a pulse with different bandwidth larger bandwidth for nearer range as for further range which allows you to have the same image quality across the swath in terms of number of looks and resolution and also protect SNR.
Radarsat uses the same pulse length from near range to far range that is not optimum. Adapting range pulse bandwidth to the near range to far range transition is going in the direction of optimality.

A. Luscombe
The advantage of the Radarsat scheme that we are more able to use data rate capacity efficiently so that we can obtain 500 km with four beams as opposed to 400 km with five beams. So there are trade-offs.

E. Attema

We had previously statements that for a system like ASAR there was some interest in the phase difference between HH and VV.
Now nobody seems interested in phase information in Scansar. What is the difference from an application point of view between normal mode and Scansar?

A. Luscombe
I understood that there might be some more constraints on coordination of timing so you always look imaging from the same aspect angle for the HH/VV phase comparison to be valid.

E. Attema
It might be safe to keep the option of the phase fidelity in the processor because you never know what is going to happen in our next meeting.

Recommendations for CEOS Calibration/Validation Working Group

RECOMMENDATIONS FOR

CALIBRATION/VALIDATION WORKING GROUP

By A. Freeman, Chairman CEOS Sub-group on SAR Calibration (JPL, USA)

- Need to establish straightforward relationships between user requirements (e.g. for mapping biomass) and calibration requirements.
- Calibration should be traceable to a known standard, (e.g. a flat plate). Need for a single organization within each continent to calibrate these devices.
- Work needs to be done on design of phase-stable calibration devices (with 1mm stability) for interferometry.
- Calibration device inventory needs to be completed by SAR Calibration Sub-group.
- Need for further work on validation of processors and quality measures (e.g. coherence, phase error) for interferometry.
- Use of ERS-1 in roll-tilt mode would enable interferometry at large incidence angles and is recommended.
- Recommend orbit repeat phase for Radarsat to enable interferometry over a reasonable time interval. This would allow interferometry in otherwise unreachable areas and at different incidence angles.
- 1-day repeat orbits for ERS-1 and ERS-2 would enable interferometry over large areas and is recommended.
- There is a need for high quality restituted orbits (meter scale) for global DEM generation using interferometry.
- SAR Calibration sub-groups recommends that data be distributed in β° (radar brightness) format.

$$\beta^\circ = F(DN)$$
$$\sigma^\circ = \beta^\circ \sin\theta_i$$

- Recommend that advanced ADC's be studied for future sensors to minimize non-linearity problems.
- SIR-C polarimetric calibration requirements serve as a useful baseline-need to be updated by SAR calibration Sub-group as knowledge advances.

- Users should be provided with noise level estimates for SAR data sets.
- Stable distributed target sites (e.g. Amazon) need to be located.
- Intercalibration of SAR processors is needed for effective use of data on a global scale.
- Paper a S+N equations to be generated by SAR Calibration Sub-group.

Action Items and Study Areas

MEETING ACTION ITEMS AND FURTHER STUDY AREAS

- Encourage people to fill out inventory on calibration devices (WG2)

- Effects faraday rotation and radomes on calibration devices shall be studied (WG2).

- JPL to prepare statement on status of reference surfaces for HH/VV phase calibration (WG3).

- Confirmation of the expected insensitivity of crosstalk calibration to the assumption <Sii Sij*> = 0 (R. Cordey).

- Explicit discussion on different polarimetric calibration algorithms is encouraged (WG3)

- Paper on best engineering solution for a phase stable reflector encouraged (requirement 1 mm for phase center) (WG4).

- Problems of phase errors due to ionosphere and atmospheric water vapour should be studied (WG4).

- Recommendations regarding change to radar brightness shall be brought to the attention of the WG on data (WG 5/6).

- Provide list of references regarding time varying phenomena and multi-looking versus single looking (action K. Raney).

- Circulate revised paper on set of radar equations (K. Raney - R. Bamler).

- Discuss sensitivity of the method to measure the peak phase (R. Touzi and S. Quegan).

- Exchange information on estimator for gamma and P.D.F. [gamma] and make results available (F. Rocca - S. Quegan).

- Question of saturation effect shall be studied (WG7).

- Distribute coordinates of amazon rain forest areas suitable for antenna pattern verification (H. Laur).

- How to find Sigma0 or Beta0 from saturated digital numbers shall be studied (WG8).

- Interferometric and polarimetric aspects (HH/VV phase difference) of SCANSAR shall be studied (WG9).

Workshop Closing Remarks

WORKSHOP CLOSING REMARK

Chair: A. Freeman

Do people like this format?

The format is OK, except we need shorter presentation in the WG... mini papers are too long... It should have been 10 minutes with 15 minutes allowed: this is a forum to interchange your ideas with your colleagues not to present the work you have done last year.

What about the timing?

People felt that timing is OK and next September will be a good time to hold another meeting.

Location

Suggestions: CNES (Toulouse), A.S.F. (Alaska), U.K. and Japan.
Chairman to sollicit offers....

Output of the Meeting: Concrete results of the meeting were:
- recommendations to cal/val WG
- workshop proceedings
- interchange of ideas (difficult to measure but certainly very real).
- CAL/VAL questionnaire circulated.
- expert papers.

Regarding Topics:

. Interferometry: I think this is the right place for the dialog between interferometry, calibration devices and processor people but a lot of the issues should be tackled under the CEOS terrain mapping subgroup.
. Scansar: should it be a regular group or part of the SAR processor calibration group?
. Distributed scatterers: part of radiometric calibration or seperate group?

Actions:
- write down output we generated and send that to CAL/VAL WG.
- keep the workshop format with shorter papers in the W.G.

B. Hawkins:

Where do we get information on the output of this group? we should propose to make a record of results obtained by the CEOS Subgroup on SAR cal/val.

A. Freeman:

Very good idea, it will be quite simple to generate a copy of all material, pass it on to the CEOS CAL-VAL and have it included in the newsletter as a list of available material for distribution.

I'd like to thank you all for attending, for your hard work in listening, presenting and discussing.
I'd like to thank ESTEC for organizing this workshop and I declare the workshop closed.

Workshop Participants List

A

ADRIAN, V.
Alcatel Espace
26, Av. J.F. Champollion
P.O. Box 1187
31037 Toulouse
33 61 19 6108
33 61 19 6163
FRANCE

ALVAREZ, A.
ESA/ESTEC/XRM
Keplerlaan 1
2200 AG Noordwijk
01719 83535
NETHERLANDS

ARBESSER-RASTBURG, B.
ESA/ESTEC/XEP
Keplerlaan 1
2200 AG Noordwijk
NETHERLANDS

ATTEMA, E.
ESA/ESTEC/JWS
Keplerlaan 1
2200 AG Noordwijk
NETHERLANDS

B

BAMLER, R.
DLR
German Aerospace Research Est.
Oberpfaffenhofen, P.O.Box 1116
82230 Wessling
49 8153 28 1364
49 8153 28 1446
GERMANY

BARBIER, C.
Centre Spatial de Liege
Av. du Pre Aily
B-4031 Angleur
32 41 67 6668
32 41 67 5613
BELGIUM

BHAGAVATHULA, S.
Daimler Benz Research Center
Division Radar Systems (F3B)
Wilhelm-Runge Str. 11
D-89081 Ulm
0049 731 505 2136
49 731 505 4104
GERMANY

BIAGINI, M.
Telespazio
Via Tiburtina 965
Roma
39 6 407 93787
39 6 407 93628
ITALY

BIRD, P.
Defence Research Agency
Farnborough
Hants GU14 6TD
44 252 393425
44 252 372982
UNITED KINGDOM

BONNEFOY, R.
ESA/ESTEC/J
Keplerlaan 1
2200 AG Noordwijk
NETHERLANDS

BORGEAUD, M.
ESA/ESTEC/XEP
Keplerlaan 1
2200 AG Noordwijk
01719 84830
01719 84999
NETHERLANDS

BROOKER, G.
ESA/ESTEC/JW
Keplerlaan 1
2200 AG Noordwijk
01719 83611
NETHERLANDS

BROWN, M.
GEC-Marconi Research Centre
West Hanningfield Road
Great Baddow, Chelmsford
Essex CM2 8HN
44 245 473 331
44 245 475 244
UNITED KINGDOM

BUEDENBENDER, H.
DLR
Muenchenerstr. 20
82234 Wessling
49 8153 282378
49 8153 281449
GERMANY

C

CANTONI, M.
Telespazio
Via Tiburtina 965
00156 Roma
39 6 4069 3695
39 6 4069 3628
ITALY

CHATURVEDI, D.
ESA/ESTEC/WDP
Keplerlaan 1
2200 AG Noordwijk
NETHERLANDS

COIRAULT, R.
ESA/ESTEC/XR
Keplerlaan 1
2200 AG Noordwijk
NETHERLANDS

CORDEY, R.
GEC-Marconi Research Centre
West Hanningfield Road
Great Baddow, Chelmsford
Essex CM2 8HN
44 245 473 331
44 245 475 244
UNITED KINGDOM

COULSON, S.
ESA/ESRIN
Via Galileo Galilei
Frascati
39 6 941 80 295
39 6 941 80 361
ITALY

D

D'URSO, G.
University of Molise
Dept. S.A.V.A.
Via Cavour 50
I-86100 Campobasso
39 874 98744
39 874 98743
ITALY

DALL, J.
Technical University of Denmark
B 348
DK-2800 Lyngby
45 42 88 14 44
45 45 93 16 34
DENMARK

DE MATTHAEIS, P.
ESA/ESTEC/JIR
Keplerlaan 1
2200 AG Noordwijk
01719 85724

DERAUW, D.
Centre Spatiale de Liege
Av. du Pre Aily
B-4031 Angleur
32 41 67 6668
32 41 67 5613
BELGIUM

DESCHAUX-BEAUNE, M.
Alcatel Espace
26, Av. J.F. Champollion
P.O. Box 1187
31037 Toulouse
33 61 19 5339
33 61 19 6163
FRANCE

DESNOS, Y-L.
ESA/ESTEC/XRI
Keplerlaan 1
2200 AG Noordwijk
31 1719 84927
31 1719 84596
NETHERLANDS

E

EINEDER, M.
DLR
German Remote Sensing Data Cent.
Oberpfaffenhofen
82230 Wessling
49 8153 28 1396
49 8153 28 1446
GERMANY

ELDHUSET, K.
Norwegian Defence Res. Est.
P.O. Box 25
2007 Kjeller
47 6380 7467
47 6380 7212
NORWAY

F

FELTHAM, S.
ESA/ESTEC/XRL
Keplerlaan 1
2200 AG Noordwijk
NETHERLANDS

FOURNET, P.
Thomson-CSF/RCM
La Clef de Saint Pierre
1 Bvd. Jean Moulin
78852 Elancourt cedex 1
33 1 34 59 6766
33 1 34 59 5990
FRANCE

FREEMAN, A.
Jet Propulsion Laboratory
M/S 300-325
Pasadena
CA 91109
1 818 354 1887
1 818 393 6943
UNITED STATES

FREUNDT, E.
ESA/ESTEC
Keplerlaan 1
2200 AG Noordwijk
01719 83388
NETHERLANDS

G

GARRIDO, C.
ESA/ESTEC/JWO
Keplerlaan 1
2200 AG Noordwijk
NETHERLANDS

GRAF, G.
ESA/ESTEC/NT
Keplerlaan 1
2200 AG Noordwijk
NETHERLANDS

GREINER, W.
ESA/ESTEC/XRF
Keplerlaan 1
2200 AG Noordwijk
NETHERLANDS

GROOT, J.
TNO-FEL
P.O. Box 96864
2509 JG Den Haag
31 70 3264221
31 70 3280961
NETHERLANDS

GUIJARRO, J.
ESA/ESTEC/ORP
Keplerlaan 1
2200 AG Noordwijk
NETHERLANDS

GUISSARD, A.
Universite Catholique de Louvain
Batiment Stevin
Place du Levrant 2
B-1348 Louvain la Neuve
32 10 147 2306/2300
32 10 147 2089
BELGIUM

H

HAGBERG, J.
Chalmers University of Technology
Dept. of Radio and Space Science
S-41296 Gothenborg
46 31 772 1839
46 31 164513
SWEDEN

HARDANGE, J-P.
Thomson-CSF
La Cle de Saint-Pierre
1 Boulevard Jean Moulin
78852 Elancourt Cedex
33 1 34 59 5244
33 1 34 59 5224
FRANCE

HAWKINS,
Canada Centre for Remote Sensing
3483 Limebank Road
Ottawa
Ontario KIA OY9
1 613 998 9060
1 613 993 5022
CANADA

HEER, C.
Dornier GmbH
Abtg RSX-230
An der Bundesstr. 31
D-88039 Friedrichshafen
49 7545 84319
49 7545 83378
GERMANY

HOLECZ, F.
University of Zurich
Inst. of Geography, Remote Sensing Labs.
Winterthurstr. 190
8057 Zurich
0041 1 257 5164
41 1 362 5227
SWITZERLAND

HOUNAM, D.
DLR
GERMANY

HURD, D.
Matra Marconi Space UK Ltd.
Anchorage Road
Portsmouth
Hampshire PO3 5PU
44 705 664966
44 705 690455/690403
UNITED KINGDOM

HUTCHINS, M.
Defence Research Agency
Space & Communications Dept., R16 Blg.
Farnborough
Hants GU14 6TD
44 252 392 534
44 252 522 959
UNITED KINGDOM

J

JACKSON, H.
ESA/ESTEC/XRI
Keplerlaan 1
2200 AG Noordwijk
01719 83382
NETHERLANDS

JENSEN, N.
ESA/ESTEC/XE
Keplerlaan 1
2200 AG Noordwijk
NETHERLANDS

JIN, M.
Jet Propulsion Laboratory
4800 Oak Grove Drive
Pasadena
California 91109
818 1354 3778
818 1383 6943
UNITED STATES

JUST, D.
DLR
German Aerospace Est.
P.O. BOx 1116
82230 Wessling
49 8153 28 1395
49 8153 28 1446
GERMANY

K

KARNEVI, S.
ESA/ESTEC/NTM
Keplerlaan 1
2200 AG Noordwijk
NETHERLANDS

KATO, Y.
MITI
Electrotechnical Laboratory
1-1-4 Umezono, Tsukuba
Ibaraki-Ken
81 298 58 5628
81 298 58 5640
JAPAN

KENWARD, D.
Defence Research Agency
Space & Communications Dept.
Farnborough
Hants GU14 6TD
44 252 393172
44 252 372982
UNITED KINGDOM

KEYTE, G.
Defence Research Agency
Space & Communications Dept. Q134
Farnborough
Hants GU14 6TD
44 252 393026
44 252 372982
UNITED KINGDOM

KLEIJWEG, J.
ESA/ESTEC/XRI
Keplerlaan 1
2200 AG Noordwijk
01719 84643
01719 84596
NETHERLANDS

KROGAGER, E.
Danish Defence Research Establishment
Ryvangs Alle 1
P.O. Box 2715
DK-2100 Copenhagen
45 39 27 8888/5942
45 31 20 3315
DENMARK

L

LANCASHIRE, D.
MMS-UK
Anchorage Road
Portsmouth PO3 5PU
44 705 674468
44 705 674 642
UNITED KINGDOM

LAUR, H.
ESA/ESRIN
Via Galileo Galilei
P.O. Box 64
I-00044 Frascati
39 6 941 80 235
39 6 941801
ITALY

LE TOAN, T.
CESR
9 Avenue Colonel Roche
31029 Toulouse Cedex
33 61 55 66 71
33 61 55 67 01
FRANCE

LENTZ, H.
University of Stuttgart
Inst. of Navigation
Keplerstr. 11
70174 Stuttgart
49 711 121 3400
49 711 121 3500
GERMANY

LIFERMANN, A.
CNES
18, Av. E. Belin
31077 Toulouse
33 61 282143
33 61 281815
FRANCE

LIN, C.
ESA/ESTEC/JIM
Keplerlaan 1
2200 AG Noordwijk
01719 85813
NETHERLANDS

LOPRIORE, M.
ESA/ESTEC/X
Keplerlaan 1
2200 AG Noordwijk
NETHERLANDS

LOU, Y.
Jet Propulsion Laboratory
4800 Oak Grove Drive
MS-300-243
Pasadena California 91107
1 818 354 2647
1 818 354 6943
UNITED STATES

LUKOWSKI, T.
Canada Center for Remote Sensing
588 Booth St.
Ottawa KIA 0Y7
1 613 998 9060
1 613 993 5020
CANADA

LUSCOMBE, A.
Spar Aerospace Ltd.
21025 Trans-Canada Highway
Sainte-Anne-de Bellevue
Quebec H9X 3R2
1 514 457 2150
1 514 457 2724
CANADA

M

MACCOLL, D.
ESA/ESTEC/XRI
Keplerlaan 1
2200 AG Noordwijk
NETHERLANDS

MANCINI, P.
ESA/ESTEC/XRI
Keplerlaan 1
2200 AG Noordwijk
01719 84552
NETHERLANDS

MARCHAND, J.
ESA/ESTEC/JWP
Keplerlaan 1
2200 AG Noordwijk
31 1719 83666
31 1719 85617
NETHERLANDS

MARCORELLES, B.
ESA/ESRIN/DEX
Via Galileo Galilei
CP 64
00044 Frascati
39 6 94 18 04 03
ITALY

MARTIN-NEIRA, M.
ESA/ESTEC/XRI
Keplerlaan 1
2200 AG Noordwijk
01719 84052
NETHERLANDS

MASSENZIO, M.
ESA/ESTEC/XRM
Keplerlaan 1
2200 AG Noordwijk
NETHERLANDS

MEHL, C.
ESA/ESTEC/XRI
Keplerlaan 1
2200 AG Noordwijk
NETHERLANDS

MESZAROS, M.
Earth Observation Sciences Ltd
Broadmede
Farnham Business Park
Farnham GU9 8QL
44 252 721444
44 252 712552
UNITED KINGDOM

MEYNARD, Y.
ESA/ESTEC/JIR
Keplerlaan 1
2200 AG Noordwijk
01719 84167
NETHERLANDS

MICA, S.
ACS
Via Lazzaro Belli 23
Frascati
39 6 940 8823
39 6 940 8783
ITALY

MULDER, N.
ITC
P.O. Box 6
7500 AA Enschede
31 53 874480
31 53 874335
NETHERLANDS

N

NAGLER, T.
University of Innsbruck
Inst. fuer Meteorologie u. Geophysik
Innrain 52
A-6020 Innsbruck
43 512 507 2171
43 512 507 2170
AUSTRIA

NOLL, J.
ESA/ESTEC/XEP
Keplerlaan 1
2200 AG Noordwijk
31 1719 85158
31 1719 84999
NETHERLANDS

O

OTTEN, M.
TNO/FEL
P.O. Box 96864
2509 JG Den Haag
31 70 326 4221
328 0961
NETHERLANDS

P

PETITVILLE,
ESA/ESTEC/JWO
Keplerlaan 1
2200 AG Noordwijk
NETHERLANDS

PETZ, F.
ESA/ESTEC
Keplerlaan 1
2200 AG Noordwijk
31 1719 84954
NETHERLANDS

PHILLIPS, P.
Systems Engineering & Assessment Ltd.
Beckington Castle
P.O. Box 800
Bath BA3 6TB
44 373 831 800
133
UNITED KINGDOM

PONTE, S.
Univ. of Naples "Federico II"
Inst. of Gasdynamics
Piazzale V. Tecchio 80
80125 Napoli
39 81 7682158/59/76
39 81 7682160
ITALY

POSA, F.
Dipartimento di Fisica
Via Amendola 173
70126 Bari
39 80 243171
39 80 242434
ITALY

Q

QUEGAN, S.
University of Sheffield
Dept. of Applied & Computional Maths.
Western Bank
Sheffield S10 2TN
44 742 824 432
44 742 824 292
UNITED KINGDOM

R

RANEY, K.
Canada Centre for Remote Sensing
588 Booth Street
Ottawa
Ontario KIA OY7
1 613 947 1812
1 613 947 1383
CANADA

RHODES, I.
Sheffield University
Dept. of Applied + Computional maths.
Western Bank
Sheffield S10 2TN
44 742 824 932/363
44 742 824 292
UNITED KINGDOM

ROCCA, F.
Politecnico di Milano
Piazzia L. da Vinci 32
20133 Milano
39 2 2399 3585
39 2 2399 3413
ITALY

ROMBACH, M.
University of Muenchen
Inst. fuer Geographie
Luisenstr. 37
80333 Muenchen
49 89 5203 335
49 89 5203 321
GERMANY

ROSELLO, J.
ESA/ESTEC/WDP
Keplerlaan 1
2200 AG Noordwijk
01719 84058
NETHERLANDS

S

SAN MIGUEL-AYANZ, J.
ESA/ESTEC
Keplerlaan 1
2200 AG Noordwijk
01719 85795
NETHERLANDS

SANCHEZ, J.
ESA/ESRIN
Via Galileo Galilei
P.O. Box 64
I-00044 Frascati
39 6 941 80 682
39 6 941801
ITALY

SARDAR, A.
ESA/ESTEC/XRI
Keplerlaan 1
2200 AG Noordwijk
NETHERLANDS

SCHAETTLER, B.
DLR
Oberpfaffenhofen
WT-DA-SD
82234 Wessling
49 8153 281352
49 8153 28 1446
GERMANY

SCHMULLIUS, C.
DLR
Inst. of Radio Frequency Technology
P.O. Box 1116
82230 Wessling
49 8153 28 2337
49 8153 28 1135
GERMANY

SEIFERT, F.
DLR
NE-HF
Muenchenerstr. 20
D-82234 Wessling
49 8153 28 2377
49 8153 28 1449
GERMANY

SHIMADA, M.
NASDA
1401 Numanoue Ohashi
Hatoyama Hiki
Saitama
81 492 98 1215
81 492 98 1001
JAPAN

SKOU,
University of Denmark
B 348
DK 2800 Lyngby
45 42 88 1444
42 45 93 1634
DENMARK

SMALL, D.
University of Zurich
Dept. of Geography, Remote Sensing Labs.
Winterthurerstr. 190
8057 Zurich
41 1 257 5164
41 1 362 5227
SWITZERLAND

SNOEIJ, P.
Delft University of Technology
Mekelweg 4
2628 CD Delft
31 15 781046
31 15 784046
NETHERLANDS

SOLAAS, G.
ESA/ESRIN
Via Galileo Galilei
P.O. Box 64
I-00044 Frascati
39 6 941 80 609
39 6 941 1801
ITALY

SOUYRIS, J.
CESR
9, Av.du Col. Roche
31029 Toulouse Cedex
33 61 55 64 83
33 61 55 67 01
FRANCE

SRIVASTAVA, S.
Canadian Space Agency
Radarsat Program, Bldng 14
3701 Carling Avenue
Ottawa, Ontario, K2H 8S2
613 991 9123
613 998 2817
CANADA

STRIJK, S.
ESA/ESTEC/XRL
Keplerlaan 1
2200 AG Noordwijk
01719 83946
NETHERLANDS

SULTAN, N.
Canadian Space Agency
6767 Route de l'Aeroporte
Saint-Hubert
Quebec J3Y 8Y9
1 514 926 4633
1 514 926 4613
CANADA

T

TAM, S.
MPB Technologies Inc.
151 Hymus Boulevard
Pointe Claire
Quebec H9R 1E9
1 514 694 8751
1 514 695 7492
CANADA

TEANY, L.
Canada Centre for Remote Sensing
3483 Limebank Rd.
KIA OY1 Ottawa
Ontario
1 613 998 9060
1 613 993 5022
CANADA

TOUZI, R.
College Militaire Royal de Saint-Jean
Richelain J0J 1R0
Quębec
1 514 358 6582
1 514 358 6749
CANADA

TU, M.
ESA/ESTEC/CSP
Keplerlaan 1
2200 AG Noordwijk
NETHERLANDS

U

ULANDER, L.
Chalmers University of Technology
Dept. of Radio and Space Science
S-41296 Gothenberg
46 31 772 1835
46 31 164 513
SWEDEN

V

VADON, H.
CNES
18, Av. E. Belin
31055 Toulouse
FRANCE

VALERO, J.
ESA/ESTEC/XRI
Keplerlaan 1
2200 AG Noordwijk
01719 84638
NETHERLANDS

VAN 'T KLOOSTER, C.
ESA/ESTEC/XEA
Keplerlaan 1
2200 AG Noordwijk
0171 83940
NETHERLANDS

VAN DEN BROEK, A.
TNO-FEL
P.O. Box 96864
2509 JG Den Haag
31 70 3264221
31 70 3280961
NETHERLANDS

W

WERNER, C.
University of Zuerich
Dept. of Geography
Winterthurer str. 110
CH-8057 Zuerich
41 1 257 5185
41 1 362 5227
SWITZERLAND

WESSELS, G.
INTERA Information Technologies
Suite 200
2 Gurowara Road, Nepean
Ontario K2E 1A2
1 613 226 5442
1 613 226 5529
CANADA

WILLIAMS, J.
University of Alaska
Alaska SAR Facility
Fairbanks, AK 99775-0800
1 907 474 6715
1 907 474 5195
UNITED STATES

WOODE, A.
ESA/ESTEC/XRP
Keplerlaan 1
2200 AG Noordwijk
NETHERLANDS

WOODING, M.
Remote Sensing Applications Consultants
Merlin Court
82 Alexandra Rd, Farnborough
Hants GU14 G0D
44 252 371211
44 252 370995
UNITED KINGDOM

Z

ZAITSEVA, Z.
ESA/ESTEC/XRI
Keplerlaan 1
2200 AG Noordwijk
01719 85888
NETHERLANDS

ZAKHAROV, A.
Russian Academy of Science
Inst. of Radioengineering & Electronics
Bldg. 1, Vvedensky Square
141120 Fryazino, Moscow region
7 095 526 9047
7 095 203 8414
RUSSIA

ZINK, M.
DLR
German Aerospace Research Establishment
P.O. Box 1116
D-82230 Wessling
49 8153 282386
49 8153 281449
GERMANY

Acknowledgments

ACKNOWLEDGEMENTS

We should like to acknowledge the ESTEC Conference Bureau for continuous efficient support in the preparation and running of the Workshop in particular, G. Elfering, Charlotte Brikenaar and hostesses at the Reception.

We should also like to acknowledge R. Guerrand for his availability and his continuous support during the workshop preparation.

Special thanks to Sandrine Albin who did all of the typing for the abstracts, programme and working group summaries.

Finally thanks to the Reproduction Service of ESTEC for a fast and well done job.

Printed by ESTEC Repro